Flexure and Rheology of Pacific Oceanic Lithosphere

A thesis submitted for the degree of Doctor of Philosophy

Johnny Hunter
St. Catherine's College



Supervised by:
Prof. A.B. Watts, FRS
Department of Earth Sciences
University of Oxford

Michaelmas 2015

This thesis is dedicated to my Mum and Dad —
Thank you for everything.

Flexure and Rheology of Pacific Oceanic Lithosphere

A thesis submitted for the degree of Doctor of Philosophy

Johnny Hunter
St. Catherine's College

Michaelmas 2015

Abstract

The idea of a rigid lithosphere that supports loads through flexural isostasy was first postulated in the late 19th century. Since then, there has been much effort to investigate the spatial and temporal variation of the lithosphere's flexural rigidity, and to understand how these variations are linked to its rheology. In this thesis, flexural modelling is used to first re-assess the variation in the rigidity of oceanic lithosphere with its age at the time of loading, and then to constrain mantle rheology by testing the predictions of laboratory-derived flow laws.

A broken elastic plate model was used to model trench-normal, ensemble-averaged profiles of satellite-derived gravity at the trench-outer rise system of circum-Pacific subduction zones, where an inverse procedure was used to find the best-fit T_e and loading conditions. The results show a first-order increase in T_e with plate age, which is best fit by the depth to the 400 ± 35 °C plate-cooling isotherm. Fits to the observed gravity are significantly improved by an elastic plate that weakens landward of the outer rise, which suggests that bending-induced plate weakening is a ubiquitous feature of circum-Pacific subduction zones.

Two methods were used to constrain mantle rheology. In the first, the T_e derived by modelling flexural observations was compared to the T_e predicted by laboratory-derived yield strength envelopes. In the second, flexural observations were modelled using elastic-plastic plates with laboratory-derived, depth-dependent yield strength. The results show that flow laws for low-temperature plasticity of dry olivine provide a good fit to the observations at circum-Pacific subduction zones, but are much too strong to fit observations of flexure in the Hawaiian Islands region. We suggest that this discrepancy can be explained by differences in the timescale of loading combined with moderate thermal rejuvenation of the Hawaiian lithosphere.

Flexure and Rheology of Pacific Oceanic Lithosphere

A thesis submitted for the degree of Doctor of Philosophy

Johnny Hunter
St. Catherine's College

Michaelmas 2015

Extended Abstract

The idea of a rigid lithosphere that supports loads through flexural isostasy was first postulated in the late 19th century. Since then, there has been much effort to investigate the spatial and temporal variation of the lithosphere's flexural rigidity, and to understand how these variations are linked to its rheology. In this thesis, flexural modelling is used to first re-assess the variation in the rigidity of Pacific oceanic lithosphere with its age at the time of loading, and then to constrain mantle rheology by testing the predictions of laboratory-derived flow laws.

A common method of constraining the lithosphere's flexural rigidity is to model observations of flexure using an elastic plate overlying an inviscid substrate, where the rigidity is generally expressed through the effective elastic thickness of the plate, T_e. One of two methods is generally used to constrain T_e: forward methods, in which bathymetric or gravimetric deflections are compared with a range of elastic plate models; or spectral methods, in which the relationship between the Fourier spectra of observed bathymetry and gravity are compared to theoretical relationships for a range of elastic plate models. In the oceans, these methods have been used to constrain the T_e at the trench-outer-rise system seaward of subduction zones, at Mid-Ocean Ridges (MOR), at seamounts and ocean islands, and at fracture zones. One of the most important results to have emerged from these studies is that there is a general increase in T_e with the age of oceanic lithosphere at the time of loading. This finding is in agreement with ideas on the thermal cooling of the lithosphere as it moves away from the MOR, and with ideas on the thermally-activated ductile processes by which lithospheric minerals, such as olivine, deform. Somewhat surprisingly, therefore, a recent global study (Bry and White, 2007) modelled bathymetry and gravity profiles at the trench-outer rise system of subduction zones and found no relationship between T_e and plate age.

In light of the study of Bry and White (2007), we have re-assessed the relationship between T_e and the age of oceanic lithosphere at the time of loading, as it has implications for our understanding of the lithosphere's rheology and its thermal structure. To do this, we have modelled ensemble-averaged, trench-normal profiles of free-air gravity at the trench-outer rise system of all the major circum-Pacific subduction zones. This is an ideal dataset with which to investigate the relationship between T_e and the lithosphere's age and thermal structure. Firstly, it provides a wide range of plate ages, from 2 to 157 Ma; secondly, subduction zone outer-rises are generally not affected by active volcanism, thus avoiding the complications of thermal rejuvenation; and thirdly, the subducting plate is being loaded at the present-day, thus avoiding complications caused by variation in the time since loading. In addition, by producing ensemble-averaged profiles, we have removed much of the short-wavelength noise that is unrelated to the long-wavelength flexure caused by subduction, thus improving the accuracy of T_e estimates. We modelled the observed gravity profiles using a 2-D broken (semi-infinite) elastic plate model, where the plate-break was located at the trench axis and was subject to two end-loads: a vertical shear force, V_0, and a bending moment, M_0. Physically, these end-loads represent the forces and stresses that exist in the subducting plate at the trench axis due to tectonic forces such as slab pull, collision resistance and slab suction. To find the best-fit T_e and end-loads, we used an inversion procedure in which T_e was iterated over a range of values and M_0 and V_0 were optimized using a damped least squares algorithm.

The results of this inversion show that there is a first-order increase in T_e with the age of the subducting plate. For example: at the Middle America trench, where the lithosphere is youngest (2–27 Ma), the mean T_e is 13.7 ± 1.4 km; at the Aleutian trench (52–66 Ma), it is 25.0 ± 2.4 km; and at the Izu-Bonin-Mariana trench (132–157 Ma), it is 29.5 ± 1.5 km. The relationship between T_e and plate age is reasonably well fit by the depth to the 400 ± 35 °C plate-cooling isotherm, which suggests that the lithosphere's thermal structure exerts first order control on its flexural rigidity. However, there is scatter in the relationship between T_e and age, particularly for older lithosphere, which we attribute to inaccuracies in the T_e estimates and the influence of factors other than plate age on the lithosphere's rigidity. For example, the accuracy of T_e estimates might be affected by: short-wavelength noise such as hotspot volcanoes; trade-offs between T_e and the end-loads; failure of the 2-D elastic

plate model to account for arcuate trench geometry or oblique plate convergence. Factors other than plate age that might affect the lithosphere's rigidity include, for example: thermal anomalies related to hotspot-induced thermal rejuvenation; variations in plate weakening due to variations in plate curvature and mantle hydration via bend-faults; variations in axial (horizontal) loading; variations in the style of bend-faulting on the outer-trench slope.

Our finding that there is a general increase in T_e with the age of subducting lithosphere is at odds with the results of Bry and White (2007). In order to understand this discrepancy, we conducted a series of modified inversions, inverting both the observed circum-Pacific gravity profiles and a suite of synthetic profiles. The results suggest that the discrepancy can be explained by differences in: the treatment of the long-wavelength gravity anomalies, the gravity calculation method, the optimization constraint placed on M_0, and the trench axis location. Of these differences, the treatment of the long-wavelength anomalies is the most important factor: whilst we removed a long-wavelength spherical harmonic gravity signal prior to inversion, Bry and White (2007) inverted for a linear gravimetric slope. Results from inversion of the synthetic profiles suggest that this has caused Bry and White (2007) to underestimate the rigidity of older, stronger lithosphere, thus masking the relationship between T_e and plate age.

Several studies of individual oceanic subduction zones have suggested that the subducting plate is weakened as it bends into the trench. Indeed, our inversion results show that in general, an elastic plate of constant T_e cannot simultaneously fit the steepness of the outer-trench slope and the wavelength and amplitude of the outer rise. Therefore, in order to asses the extent of plate weakening at circum-Pacific subduction zones, we conducted a second inversion in which the ensemble-averaged gravity profiles were modelled using a variable T_e elastic plate. We inverted for two T_e values—a 'landward T_e' and a 'seaward T_e'—where prior to inversion, observed plate curvatures were used to define the location of the linear transition between the two values. Results show that the variable T_e elastic plate significantly improves the fits to the observed gravity, where the RMS error is improved by a mean of 39 % and by up to 73 %. The plate weakens in 42 out of 43 best-fit models, where the average reduction in T_e between the seaward and landward values is 51 ± 11 % and the range is 20–72 %. This suggests that significant plate weakening is a ubiquitous feature of the outer-trench slope and

outer-rise seaward of subduction zones. This plate weakening is likely to be caused primarily by bending-induced inelastic yielding—a combination of shallow, brittle and deep, ductile failure—and perhaps also by mantle hydration and serpentinization via bend-faults on the outer-trench slope.

Using laboratory-derived flow laws to infer the plastic deformation mechanisms by which the lithosphere deforms involves large and uncertain extrapolations in timescale and space-scale. Therefore, it has been of great interest to use observations of flexure to constrain the rheology of the lithosphere, providing a link between large-scale, long-timescale geological deformation and small-scale, short-timescale laboratory deformation. It is thought that oceanic lithosphere has a dry olivine rheology, as olivine is the most abundant and probably weakest mineral, and as partial melting of the upwelling mantle at the MOR is thought to leave a dry residuum (e.g., Karato et al., 1986; Hirth and Kohlstedt, 1996; Morgan, 1997). Laboratory studies and geophysical observations suggest that dislocation creep is the dominant ductile deformation mechanism in the olivine-rich oceanic lithosphere, and that Low-Temperature Plasticity (LTP) dominates in long-term lithospheric flexure. However, Zhong and Watts (2013) recently used a 3-D finite-element viscoelastic model to show that laboratory-derived LTP flow laws for dry olivine are much too strong to fit flexural observations in the Hawaiian Islands region, and that the recent LTP law of Mei et al. (2010) must be significantly weakened (by increasing the pre-exponential factor by $\sim$ 8 orders of magnitude) to fit the observed data. In light of this study, we have attempted to constrain the mantle rheology using observations of flexure at the trench-outer system of circum-Pacific subduction zones. This is perhaps a better location to constrain rheology than the Hawaiian Islands, as the subducting plate is generally not affected by the thermal alteration and magmatic processes associated with hotspot volcanism.

We used two methods to constrain the LTP rheology seaward of circum-Pacific subduction zones, where we tested four laboratory-derived flow laws for dry olivine (Goetze, 1978; Evans and Goetze, 1979; Raterron et al., 2004; Mei et al., 2010) and one for wet olivine (Katayama and Karato, 2008). In the first method, dubbed the 'YSE-curvature method', we compared the T_e derived by inversion of observed ensemble-averaged gravity profiles to the T_e predicted by elastic-plastic Yield Strength Envelopes (YSE) based on laboratory-derived failure criteria

for frictional sliding and ductile creep. The results show that regardless of the assumed friction coefficient, all of the laboratory-derived LTP flow laws provide a reasonably good fit to the observed T_e at the subduction zones. This result contrasts with the findings of Zhong and Watts (2013) at the Hawaiian Islands. Therefore, to test the validity of the YSE-curvature method, we used this approach to also constrain the rheology in the Hawaiian Islands region, where we estimated the observed T_e by modelling seismically-constrained crustal deflections in the flexural moats surrounding Oahu. The results show that, in agreement with Zhong and Watts (2013), laboratory-derived LTP flow laws for dry olivine are much too strong to fit the observed T_e and that the law of Mei et al. (2010) must be significantly weakened.

The second method used to constrain the rheology at circum-Pacific subduction zones was to model the observed ensemble-averaged gravity profiles using elastic-plastic plates with laboratory-derived, depth-dependent yield strength. The results show that in the absence of axial loading, regardless of the assumed LTP flow law, the observed gravity anomalies cannot be explained by such a model, even if the law of Mei et al. (2010) is significantly weakened. However, when axial loading is accounted for, the laboratory-derived LTP flow laws all provide a reasonably good fit to the observations, in agreement with the results of the YSE-curvature method and in contrast with the findings of Zhong and Watts (2013) at the Hawaiian Islands. Once again, to test the validity of the elastic-plastic plate model, we used it to constrain the rheology in the Hawaiian Islands region by modelling seismically-constrained crustal deflections, and the results are in general agreement with those of Zhong and Watts (2013).

The results of the YSE-curvature method and elastic-plastic plate modelling suggest that there is a discrepancy between the LTP rheology at the Hawaiian Islands and that at the trench-outer rise system of circum-Pacific subduction zones. Laboratory-derived olivine flow laws are much too strong to fit the observations at the Hawaiian Islands, but provide a reasonably good fit to the observations at subduction zones. Another way of saying this is that the lithospheric rocks in the Hawaiian Island region appear weaker than those seaward of subduction zones. One possible cause of this discrepancy is the difference between the two study regions in the timescales of loading and the implications that this has for the viscoelastic behaviour of the lithosphere. Previous studies have shown that on relatively short timescales,

oceanic lithosphere exhibits viscoelastic behaviour, such that following loading, it takes 1–2 Myr to relax from the initial seismic thickness to the long-term elastic thickness. At the trench-outer rise system of subduction zones, the subducting plate is continuously bending such that much of the strain has accumulated within the past 100^{s} kyr; in contrast, the Hawaiian island of Oahu was emplaced in a discrete burst of volcanism 4–2 Ma. Thus, it is possible that there are significant unrelaxed viscoelastic stresses at the subduction zones but not at the Hawaiian Islands, which could explain the apparent relative strength of the lithospheric rocks in the former region. To explore this possibility, we developed a modified YSE-curvature method that accounts for viscoelasticity by assuming a Bingham-Maxwell rheology, and used it to constrain the rheology in both regions. The results show that viscoelasticity can account for at least some of the discrepancy in rheology between the trenches and Hawaiian islands, as the laboratory-derived LTP laws for dry olivine are too strong to fit the observed T_e in both regions. However, the flow law of Mei et al. (2010) must be weakened by more at the Hawaiian Islands than at the subduction zones, which could be due to the effects of thermal rejuvenation, magma-assisted flexure, or concave-upwards bending in the former region. For example, tests show that a combination of viscoelasticity and moderate thermal rejuvenation of the Hawaiian lithosphere can explain almost all of the discrepancy in rheology between the two study regions. When both of these factors are accounted for, the dry olivine LTP laws are too strong to fit the observations at both the Hawaiian Islands and circum-Pacific subduction zones, and the law of Mei et al. (2010) must be weakened by increasing the pre-exponential factor by ~ 4 orders of magnitude in both regions. In addition, the wet LTP law of Katayama and Karato (2008) provides quite a good fit to the observed T_e in both regions.

There are many factors that might cause oceanic lithosphere to be weaker than predicted by laboratory-derived LTP flow laws for dry olivine. For example: flexural deformation might occur in the transient creep regime; the lithosphere might be wetter than is predicted by mid-ocean ridge melting models; weakening by strain localization and grain size reduction; the weakening effect of small inclusions of pyroxene; problems with the extrapolation from laboratory conditions to geological conditions; semi-brittle deformation. It has been suggested using geodynamic convection models that a relatively weak lithosphere, much weaker than predicted by experimental rock mechanics, is required for plate tectonics to occur on Earth.

Thus, our finding that, when a Bingham-Maxwell rheology is assumed, dry olivine LTP flow laws are too strong to fit observations at oceanic subduction zones and the Hawaiian Islands may have implications for the existence of plate tectonics.

Contents

Abstract i

Extended Abstract iii

Table of Contents xi

List of Figures xvii

List of Tables xxxix

List of Abbreviations xli

Acknowledgements xliii

1 Introduction 1
- 1.1 Early ideas on flexural isostasy . . . 1
- 1.2 Elastic plate models of oceanic lithosphere . . . 2
  - 1.2.1 T_e vs. the age of oceanic lithosphere at the time of loading . . . 4
  - 1.2.2 Plate weakening at oceanic subduction zones . . . 6
- 1.3 Elastic plate models of continental lithosphere . . . 6
- 1.4 Elastic-plastic and viscoelastic plate models of the lithosphere . . . 7
- 1.5 Laboratory-derived flow laws for the upper mantle . . . 9
- 1.6 Constraining the rheology of the sub-lithospheric upper mantle . . . 10
- 1.7 Constraining the rheology of oceanic lithosphere . . . 12
- 1.8 Constraining the rheology of continental lithosphere . . . 14
- 1.9 Thesis aims . . . 15
- 1.10 Software used in this thesis . . . 19

2 Data preparation 21
- 2.1 Circum-Pacific subduction zones . . . 21
- 2.2 Gravity and bathymetry data . . . 23
- 2.3 Ensemble-averaging . . . 23
- 2.4 Data corrections . . . 28
  - 2.4.1 Plate cooling . . . 28
  - 2.4.2 Long-wavelength gravity anomalies . . . 29
- 2.5 Flexural wavelength vs. plate age . . . 29
- 2.6 Chapter summary . . . 31

3 Flexure and gravity modelling **33**
3.1 Elastic plate model . . . 33
3.1.1 Cylindrical bending model . . . 34
3.1.2 Broken elastic plate model . . . 39
3.1.3 Axial loading . . . 43
3.2 Gravity model . . . 46
3.2.1 Modelling observed trench-outer rise gravity anomalies . . . 49
3.3 Chapter summary . . . 51

4 Inversion methodology and synthetic testing **53**
4.1 Inversion methodology . . . 53
4.1.1 Uncertainty in T_e . . . 54
4.1.2 Optimization constraints . . . 54
4.1.2.1 Constraints on M_0 . . . 55
4.1.2.2 Constraints on V_0 . . . 59
4.2 Synthetic testing . . . 60
4.2.1 Generating synthetic profiles . . . 60
4.2.1.1 Trench-outer rise flexure . . . 60
4.2.1.2 Short-wavelength noise . . . 62
4.2.1.3 Landward of the trench axis . . . 66
4.2.1.4 Gravity anomalies . . . 67
4.2.2 Synthetic test 1 – gravity vs. bathymetry . . . 68
4.2.3 Synthetic test 2 – profile length . . . 69
4.2.4 Synthetic test 3 – input profiles with variable rigidity . . . 69
4.3 Chapter summary . . . 70

5 Inversion A1 - constant T_e **73**
5.1 Profile fits . . . 73
5.2 T_e vs. plate age . . . 76
5.3 Trade-offs between T_e, M_0 and V_0 . . . 78
5.4 Sensitivity tests . . . 80
5.4.1 Profile length . . . 81
5.4.2 Wavelength of the removed spherical harmonic anomaly . . . 81
5.4.3 Constraint on M_0 . . . 84
5.4.4 Young's modulus . . . 85
5.4.5 Densities . . . 86
5.4.6 Axial loading . . . 87
5.4.7 Summary . . . 88
5.5 Comparison with the results of Bry and White (2007) . . . 89
5.5.1 Profile binning . . . 90
5.5.2 Understanding the discrepancy between the two studies . . . 91
5.5.2.1 Inversion B1 . . . 93
5.5.2.2 Inversion B2 . . . 94
5.5.2.3 Summary . . . 96
5.6 Chapter summary . . . 96

6 Inversion A2 - variable T_e **99**
6.1 Defining the location of weakening . . . 99
6.1.1 Estimating plate curvature . . . 100
6.1.2 Using the observed curvature to define the location of plate weakening 102
6.1.3 Summary . . . 103
6.2 Inversion methodology . . . 103
6.3 Profile fits . . . 104
6.4 T_e vs. plate age . . . 107
6.4.1 Landward T_e . . . 107
6.4.2 Seaward T_e . . . 109
6.4.3 Comparison to Inversion A1 . . . 109
6.4.4 Plate weakening vs. plate age . . . 110
6.5 Causes of plate weakening . . . 110
6.5.1 Bending-induced inelastic yielding . . . 111
6.5.2 Observational evidence for inelastic yielding . . . 111
6.5.3 Mantle hydration and serpentinization . . . 113
6.6 Chapter summary . . . 116

7 Discussion on circum-Pacific T_e variations **119**
7.1 Regions at variance with a simple relationship between T_e and plate age . . . 127
7.1.1 Old lithosphere . . . 127
7.1.2 Peru-Chile . . . 128
7.1.3 Middle America . . . 128
7.2 Short-wavelength noise . . . 130
7.3 Thermal rejuvenation . . . 131
7.3.1 Depth anomalies . . . 132
7.3.2 Effective thermal age, t_{eff} . . . 132
7.3.3 Peru-Chile . . . 134
7.3.4 Mariana-Izu-Bonin . . . 135
7.3.5 T_e vs. effective thermal age . . . 136
7.4 Plate weakening . . . 138
7.4.1 Plate curvature . . . 138
7.4.2 Mantle hydration and bend-faulting . . . 140
7.5 Axial loading . . . 140
7.6 Model assumptions . . . 142
7.6.1 Observations . . . 142
7.6.2 Discussion . . . 143
7.7 Style of bend-faulting . . . 145
7.7.1 Observations of bend-faulting . . . 148
7.7.2 Bend-faulting and the geometry of the outer rise . . . 149
7.7.3 Bend-faulting and T_e . . . 152
7.8 Trade-offs between T_e and the end-loads . . . 152
7.9 Strain rate . . . 152
7.10 Strain history . . . 153
7.11 Chapter summary . . . 154

8 Constraining the rheology of oceanic lithosphere using the YSE-curvature method **157**
8.1 Constructing the Yield Strength Envelope (YSE) . . . 158
8.1.1 Brittle faulting . . . 158
8.1.2 Plastic flow . . . 159
8.1.3 Semi-brittle regime . . . 163
8.1.4 Yield strength envelope . . . 163
8.2 Calculating the predicted T_e . . . 165
8.2.1 Predicted T_e vs. plate curvature . . . 168
8.3 Constraining LTP flow laws at circum-Pacific subduction zones . . . 170
8.3.1 Strain rate . . . 170
8.3.2 Geotherm . . . 174
8.3.3 Comparing the predicted T_e to the observed T_e . . . 174
8.3.4 Results – Byerlee's friction coefficients . . . 176
8.3.5 Results – $\mu_f = 0.3$ . . . 180
8.3.6 Results – effective thermal age . . . 182
8.3.7 Discussion . . . 182
8.4 Constraining LTP flow laws in the Hawaiian Islands region . . . 186
8.4.1 Tectonic setting . . . 186
8.4.2 Deriving the observed T_e . . . 187
8.4.2.1 Data . . . 187
8.4.2.2 Model . . . 187
8.4.2.3 Inversion methodology . . . 190
8.4.2.4 Inversion results . . . 190
8.4.3 Calculating the predicted T_e . . . 193
8.4.3.1 Plate curvature . . . 193
8.4.3.2 Geotherm . . . 195
8.4.3.3 Strain rate . . . 195
8.4.3.4 LTP flow laws . . . 196
8.4.4 Results – comparison with Zhong and Watts (2013) . . . 196
8.4.5 Results – comparison with circum-Pacific subduction zones . . . 199
8.4.6 Summary . . . 201
8.5 Chapter summary . . . 201

9 Constraining the rheology of oceanic lithosphere using elastic-plastic plate models **203**
9.1 Elastic-plastic plate model . . . 204
9.1.1 Yield strength . . . 205
9.1.2 Iterative method . . . 205
9.1.3 Runge-Kutta method . . . 209
9.1.4 Comparison between the iterative and Runge-Kutta methods . . . 214
9.1.5 Comparison between the elastic-plastic and variable T_e elastic plate models . . . 214
9.2 Constraining LTP flow laws in the Hawaiian Islands region . . . 216
9.2.1 Data . . . 216
9.2.2 Modelling technique . . . 218
9.2.3 Results . . . 218
9.2.3.1 Comparison with Zhong and Watts (2013) . . . 218
9.2.3.2 Varying the friction coefficient . . . 221

9.2.3.3 Summary . . . 224
9.3 Constraining LTP flow laws at circum-Pacific subduction zones . . . 224
9.3.1 Data and inversion technique . . . 225
9.3.2 Results . . . 225
9.4 Effect of axial loading on the stress distribution in an elastic-plastic plate . . . 229
9.5 Effect of axial loading on the deflection of an elastic-plastic plate . . . 232
9.6 Axial loading at circum-Pacific subduction zones . . . 235
9.6.1 Inversion results: axial force applied before bending . . . 235
9.6.2 Inversion results: axial force applied after bending . . . 236
9.6.3 Summary of inversion results . . . 237
9.6.4 Best-fitting axial force . . . 242
9.7 Chapter summary . . . 246

10 Reconciling mantle rheology at circum-Pacific subduction zones and the Hawaiian Islands 249
10.1 Thermal rejuvenation . . . 250
10.2 Thermal stresses . . . 251
10.3 Magma-assisted flexure . . . 252
10.4 Viscoelasticity . . . 252
10.4.1 Accounting for viscoelasticity in the YSE-curvature method . . . 253
10.4.2 Circum-Pacific subduction zones . . . 257
10.4.2.1 Method . . . 257
10.4.2.2 Results . . . 260
10.4.3 Hawaiian Islands . . . 264
10.4.3.1 Method . . . 264
10.4.3.2 Results . . . 265
10.4.4 Discussion . . . 266
10.5 Weakening mechanisms in the LTP regime . . . 269
10.5.1 Transient creep . . . 269
10.5.2 Water . . . 270
10.5.3 Grain size . . . 271
10.5.4 Pyroxenes . . . 272
10.5.5 Extrapolation from the laboratory to geological conditions . . . 272
10.5.6 Semi-brittle deformation . . . 273
10.6 Implications for plate tectonics . . . 273
10.7 Chapter summary . . . 274

11 Conclusions and future work 277
11.1 Conclusions . . . 277
11.2 Future work . . . 283

A Tectonic setting of circum-Pacific subduction zones 287
A.1 Middle America . . . 287
A.2 Peru-Chile . . . 289
A.3 Aleutian . . . 290
A.4 Tonga-Kermadec . . . 292
A.5 Kuril-Japan . . . 293
A.6 Izu-Bonin-Mariana . . . 295

B Profile fits from Inversion A1 **297**
B.1 Segment-bins 298
B.2 Trench-bins 307

C Profile fits from Inversion A2 **309**
C.1 Segment-bins 310
C.2 Trench-bins 319

References **321**

List of Figures

1.1 Cartoon illustrating the trench-outer rise system of a subduction zone. The trench-outer rise system is the flexural feature immediately seaward of the trench axis, which forms as the subducting plate descends beneath the overriding plate. It comprises the flexural depression known as the outer trench-slope, and the flexural bulge known as the outer rise. 3

1.2 Oceanic T_e estimates plotted against the age of lithosphere at the time of loading, from Watts and Zhong (2000). Note that the majority of the values from trenches (blue triangles) have been corrected for the effects of plate curvature, and thus are actually mechanical thickness estimates, not T_e estimates. The figure also shows two estimates of the seismic thickness of oceanic lithosphere (blue stars). 5

2.1 Seafloor age in the Pacific from the grid of Müller et al. (2008, v3.2). The trench axes of the subduction zones considered in this study are marked in solid black. 22

2.2 Free-air gravity anomaly map of the Pacific Ocean (Sandwell et al., 2014, v23.1), showing the locations of the geographic bins within which the ensemble-averaged profiles were calculated. The red dash shows the 'trench-bins' and the solid black shows the 'segment-bins'. 24

2.3 Bathymetry map of the Pacific Ocean (GEBCO One Minute, v2.0; Ioc et al., 2003), showing the locations of the geographic bins within which the ensemble-averaged profiles were calculated. The red dash shows the 'trench-bins' and the solid black shows the 'segment-bins'. 24

2.4 The segment-bin numbering system that is used throughout this thesis. The thick black lines show locations of trenches and the thinner black lines show the locations of the segment-bins. 25

2.5 Figure illustrating the calculation of the trench-bin ensemble-averaged gravity profile at the Tonga-Kermadec trench. (a) Free-air gravity anomaly map (Sandwell et al., 2014, v23.1) with the locations of the profiles that were ensemble-averaged. (b) The black lines show the free-air gravity along the profiles shown in Figure 2.5a (for clarity, only every other profile is shown), and the red line shows the ensemble-averaged profile. 26

2.6 Figure illustrating the calculation of the trench-bin ensemble-averaged bathymetry profile at the Tonga-Kermadec trench. (a) Bathymetry map (GEBCO One Minute, v2.0; Ioc et al., 2003) with the locations of the profiles that were ensemble-averaged. (b) The black lines show the bathymetry along the profiles shown in Figure 2.6a (for clarity, only every other profile is shown), and the red line shows the ensemble-averaged profile. 27

2.7 Long-wavelength gravity anomalies of the Pacific Ocean, synthesized from EGM2008 spherical harmonic coefficients up to and including degree and order 16. Trench axes are shown in thick black, segment-bins in thin black and trench-bins in red dash. 30

2.8 Corrected trench-bin ensemble-averaged profiles of (a) free-air gravity and (b) bathymetry, ordered from top to bottom with increasing age of the subducting plate. (c) Distance from the trench axis to the first flexural node, x_0, from the gravity and bathymetry profiles shown in Figures 2.8a and 2.8b respectively. 31

3.1 Illustration of broken elastic plate undergoing cylindrical bending, and the coordinate system used in this study. 34

3.2 Forces and torques acting on a small element of a thin elastic plate during cylindrical bending. 36

3.3 Illustration of the normal stresses, σ_{xx}, and strains, $\varepsilon_{xx} = \Delta l/l$, in an element of a thin elastic plate undergoing cylindrical bending. 37

3.4 Cartoon of the broken elastic plate model that was used to model flexure at the trench-outer rise system. There is a break in the plate at the trench axis, where a bending moment M_0 and vertical shear force V_0 are applied. 40

3.5 Comparison between analytical and finite difference solutions for a broken elastic plate with a bending moment M_0 and vertical shear force V_0 applied at the plate-break. (a) shows the plate deflection, (b) shows the bending moment and (c) shows the vertical shear force. 42

3.6 Comparison between analytical (Hetényi, 1946) and finite difference solutions for a broken elastic plate loaded by a rectangular end load. 42

3.7 Figure showing the effect of an axial force, F, on the deflection of a broken elastic plate. (a) shows the effect of the maximum tensional axial force that might be expected to occur in nature, and (b) shows the effect of the maximum compressional axial force that might be expected to occur. Each plot show deflections for plates with $T_e = 20$ km and $T_e = 30$ km, which were calculated with $M_0 = 1 \times 10^{16}$ N and $M_0 = 5 \times 10^{16}$ N respectively, with $V_0 = 1 \times 10^{12}$ $\mathrm{N\,m^{-1}}$ in both cases. 45

3.8 Illustration of the gravity calculation method of Bott (1969). The total anomaly is obtained by summing the anomalies due to a series of semi-infinite slabs with edges defined by the edges of the polygon. 47

3.9 (a) Comparison between analytical and numerical gravity anomalies over a buried cylinder, shown in (b). 47

3.10 Comparison between trench-outer rise gravity anomalies calculated using the methods of Bott (1969) and Levitt and Sandwell (1995). The gravity anomalies, shown in (a), due to the bathymetry shown in (b) were calculated with a density contrast typical of that between oceanic crust and seawater. The grey shade illustrates the semi-infinite slabs that are used to calculate the gravity anomaly in the method of Bott (1969). 48

3.11 Figure illustrating the calculation of gravity anomalies when modelling observed trench-outer rise profiles. (a) shows the density contrasts that were included the calculation—the seafloor, the top of the crust, the Moho—and illustrates the density in each layer. (b) shows the gravity anomalies arising from each of these density contrasts. These anomalies were summed to give the total anomaly, shown in black. 50

4.1 Illustration of how the uncertainty in T_e was estimated. The upper and lower bounds on T_e were defined as the values at which Δg_{rms} exceeds 1.25 times the minimum Δg_{rms}. 55

4.2 Active-source seismic velocity models from the (a) central Japan and (b) north Chile trenches, modified from Miura et al. (2005) and Ranero and Sallares (2004) respectively. 57

4.3 An example of the synthetic model used to constrain the bending moment at the trench axis, M_0. See text. 58

4.4 Figure illustrating the generation of synthetic gravity anomaly and bathymetry profiles. (a) A broken elastic plate was defined with constant or variable (shown) T_e. (b) A bending moment M_0 and vertical shear force V_0 were applied at the plate-break to produce a long-wavelength trench-outer rise flexure profile. This was then shifted to a typical seafloor depth (black) and Moho depth (grey). (c) Short-wavelength bathymetric noise (black) was generated using a spectral synthesis method; the corresponding synthetic power spectrum is shown in Figure 4.4g. Its flexural compensation (grey) was calculated assuming that the noise was emplaced on hot, weak lithosphere. (d) The bathymetric noise was added to the long-wavelength trench-outer rise bathymetry (black) and its flexural compensation was added to the Moho (grey). (e) The landward wall of the trench and the descent of the subducting plate beneath it were simulated for the 50 km landward of the trench axis. The dashed black line shows the top of the subducting plate, solid grey shows the Moho of the subducting plate, and solid black shows the seafloor bathymetry. (f) The free-air gravity anomalies arising from the synthetic bathymetry and Moho were calculated and then summed to give the final synthetic gravity anomaly. (g) The synthetic power spectrum corresponding to the bathymetry shown in Figure 4.4c. . . . 61

4.5 Figure illustrating the spectral analysis of ensemble-averaged bathymetry profiles. (a) De-trended, low-pass filtered, windowed ensemble-averaged bathymetry from the abyssal region of segment-bin 22 (Middle America trench). (b) The power spectrum of the bathymetry shown in Figure 4.5a, as estimated using the periodogram. 64

4.6 Average power spectrum estimates (black lines) for the abyssal ensemble-averaged bathymetry seaward of circum-Pacific subduction zones. Best-fit curves are shown in red; the equation that defines these curves was used in the generation of the synthetic noise profiles. 64

4.7 Results from inversion of the constant rigidity synthetic profiles, showing the effect of varying profile length and data type (labelled on each plot). Also shown on each plot is the R^2 value, and the mean and RMS difference between the input and recovered T_e. 68

4.8 Results from inversion of the variable rigidity synthetic profiles, showing the effect of varying profile length and data type (labelled on each plot). Also shown on each plot is the R^2 value, and the mean and RMS difference between the input and recovered T_e. 70

5.1 Examples of segment-bin profile fits from Inversion A1, in which a constant T_e plate was fitted to circum-Pacific trench-outer rise gravity anomalies. For each bin, the top plot shows the observed and best-fit free-air gravity profile; the trench, bin number, average seafloor age and best-fit T_e are labelled. Beneath each gravity anomaly plot is the corresponding best-fit bending moment and plate curvature profile. Beneath that is the corresponding plot of T_e vs. Δg_{rms}; the grey line shows 1.25 times the minimum Δg_{rms}, which was used to estimate the uncertainty in T_e. For clarity, only the first 600 km of the profile fits are shown, but the inversions were conducted on 750 km profiles. *Figure continued on next page...* 74

5.2 T_e from Inversion A1 plotted against seafloor age for the (a) segment-bins and (b) trench-bins. The uncertainties in T_e and age are shown as straight grey lines. The grey curves show the depth to the plate-cooling isotherms of Parsons and Sclater (1977). The isotherms that best fit the T_e-age relationship are shown in solid black and the 95 % confidence intervals in dashed black; the temperatures of these isotherms are labelled in the top right of each plot. . . 77

5.3 Plots showing the trade-offs between M_0, V_0, and T_e for the trench-bin profiles; the trench is labelled on the top right of each plot. To calculate this, M_0 and V_0 were iterated and T_e was optimized at each iteration using a damped least squares algorithm. The colour map shows the best-fit T_e. The RMS error between the observed and calculated gravity, Δg_{rms}, is contoured every 1 mGal up to a maximum of 3 times the minimum Δg_{rms}. The white contour is 1.25 times the minimum Δg_{rms}, which was used to estimate the T_e uncertainty in Inversion A1. The red star shows the best-fit solution from Inversion A1. . . . 79

5.4 T_e plotted against seafloor age from inversion of different profile lengths. The profile length is labelled on the bottom left of each plot, where '(A1)' indicates the results from our preferred inversion, Inversion A1. The top and bottom rows show the segment-bin and trench-bin results respectively. The grey curves show the depths to the 300, 600, 900 and 1200 °C plate-cooling isotherms. The isotherms that best fit the T_e-age relationship are shown in solid black and the 95 % confidence intervals in dashed black; the temperatures of these isotherms are labelled in the top right of each plot. The T_e estimates are coloured by trench as in Figure 5.2. 80

5.5 Long-wavelength gravity anomalies of the Pacific Ocean, synthesized from the EGM2008 spherical harmonic coefficients (Pavlis et al., 2012). The maximum degree and order of the harmonics used in the synthesis is labelled at the bottom left of each plot. Solid black lines mark the trenches modelled in this study and dashed black lines show the trench-bin locations. 82

5.6 Trench-bin ensemble-averaged profiles of long-wavelength gravity anomalies. The black lines show the long-wavelength anomalies, where the pattern (legend on the top left plot) indicates the maximum degree and order of the spherical harmonics used in the synthesis. The observed free-air gravity anomalies are shown in grey; these profiles have not had any long-wavelength signal removed. Note that we have shown an ensemble-averaged profile for the entire Peru-Chile trench. 83

5.7 T_e plotted against seafloor age from inversion of profiles that have had different wavelength gravity anomalies removed prior to inversion. The maximum degree and order of the removed spherical harmonic anomaly is shown on the bottom left of each plot, where '(A1)' indicates the results from our preferred inversion, Inversion A1. The top and bottom rows show the segment-bin and trench-bin results respectively. The curves show plate-cooling isotherms as described in Figure 5.4. 84

5.8 T_e plotted against seafloor age from inversions where (a,c) M_0 was constrained to be positive (Inversion A1), and (b,d) M_0 was unconstrained. The top and bottom rows show the segment-bin and trench-bin results respectively. The curves show plate-cooling isotherms as described in Figure 5.4. 85

5.9 T_e plotted against seafloor age from inversions where different values for Young's modulus, E, were assumed. The assumed E is labelled on the bottom left of each plot, where '(A1)' indicates the results from our preferred inversion, Inversion A1. The top and bottom rows show the segment-bin and trench-bin results respectively. The curves show plate-cooling isotherms as described in Figure 5.4. 86

5.10 T_e plotted against seafloor age from inversions where different mantle densities were assumed. The density is labelled on the bottom left of each plot, where '(A1)' indicates the results from our preferred inversion, Inversion A1. The top and bottom rows show the segment-bin and trench-bin results respectively. The curves show plate-cooling isotherms as described in Figure 5.4. 87

5.11 T_e plotted against seafloor age from inversions where (a,c) axial loading was neglected (Inversion A1) and (b,d) an axial force was inverted for. The top and bottom rows show the segment-bin and trench-bin results respectively. The curves show plate-cooling isotherms as described in Figure 5.4. 89

5.12 Figure comparing the results of this study to those of Bry and White (2007). (a) Segment-bin T_e and (b) trench-bin T_e from Inversion A1 plotted against seafloor age. (c) Circum-Pacific T_e estimates digitized from Bry and White (2007), which were obtained by inversion of 700 km-long, averaged profiles of free-air gravity; arrows on error bars indicate an unconstrained upper bound on T_e. The figure shows that in contrast to this study, Bry and White (2007) found no relationship between T_e and plate age. 90

5.13 Results from our preferred inversion, Inversion A1, compared to Inversions B1 and B2. The inversion name is labelled on the bottom left of each plot. (a) and (b) show T_e against seafloor age, as derived from inversion of the circum-Pacific segment-bin and trench-bin profiles respectively. Arrows on error bars indicate an unconstrained upper bound on T_e. (c) shows recovered T_e against input T_e, as derived from inversion of the variable rigidity synthetic profiles. The input T_e is given as a weighted average of the input T_e profile, where the weights are given by the squared magnitude of the input gravity anomaly. . . 92

5.14 Plots showing the position of the plate-break in Inversion B2. The plate-break was placed 10 km landward of the bathymetrically defined trench axis. (a) and (b) show observed ensemble-averaged bathymetry and gravity respectively from the Izu-Bonin trench-bin. (c) and (d) show bathymetry and gravity from a synthetic profile. 95

6.1 Plots illustrating how the plate curvature was estimated at the outer trench-slope of circum-Pacific subduction zones. (a) is from the Middle America trench-bin and (b) is from the Kuril trench-bin. (i) The observed ensemble-averaged bathymetry and free-air gravity. (ii) The black line shows the curvature estimated by fitting an elastic plate to 170 km long gravity profiles (the 'observed curvature'), and the grey line shows the curvature estimated from the bathymetry using a moving window regression. 101

6.2 Figure showing how the observed curvature (black) was used to define the location of plate weakening (grey) in Inversion A2. 103

6.3 Examples of segment-bin profile fits from Inversion A2, in which a variable T_e plate was fitted to circum-Pacific trench-outer rise gravity anomalies. For each bin, the top plot shows the observed and best-fit free-air gravity profile; the trench, bin number and average seafloor age are labelled. Note that these are the same bins as shown in Figure 5.1. *Figure and caption continued on next page...* 105

6.3 Beneath each gravity anomaly plot is the corresponding best-fit T_e profile, and beneath that, the corresponding bending moment and curvature profile. Beneath that is the corresponding plot of landward T_e (black line) and seaward T_e (grey line) vs. Δg_{rms}. For clarity, only the first 600 km of the profile fits are shown, but the inversions were conducted on 750 km profiles. 106

6.4 T_e from Inversion A2 plotted against seafloor age for the (a,b) segment-bins and (c,d) trench-bins. (a,c) shows the landward T_e and (b,d) shows the seaward T_e. The uncertainties in T_e and age are shown as straight grey lines; arrows on error bars indicate an unconstrained upper bound on T_e. The grey curves show the depth to the plate-cooling isotherms of Parsons and Sclater (1977). The isotherms that best fit the T_e-age relationship are shown in solid black and the 95 % confidence intervals in dashed black; the temperatures of these isotherms are labelled in the top right of each plot. 108

6.5 Plate weakening from Inversion A2 plotted against seafloor age, for the (a) trench-bins and (b) segment-bins. 110

6.6 Figure illustrating bending-induced inelastic yielding. The black curves show a yield strength envelope for 80 Ma oceanic lithosphere, and the red curve shows the stress distribution induced when the plate is bent to a curvature of $\kappa = 5 \times 10^{-7}\,\mathrm{m}^{-1}$ (assuming an elastic-perfectly plastic rheology). The flow laws are labelled on the plot; the brittle regime was calculated assuming hydrostatic pore fluid pressure. 112

6.7 (*Figure on previous page*) Plots showing seismicity and bend-faulting at the outer trench-slope of the Tonga-Kermadec trench. (a) GEBCO bathymetry overlain with all earthquakes, as of 2013, in the ISC (black dots) and CMT (focal mechanisms) catalogues. Only events seaward of the trench axis and within the trench-bin (black dash) are shown. CMT events have been plotted at their respective EHB positions, as these are more accurate (e.g., Bürgmann et al., 2005; Ranero et al., 2005). (b) Histograms of ISC, EHB and CMT seismicity against distance from the trench, where the bin width is 10 km. This shows the landward increase in seismicity due to outer trench-slope bend-faulting. (c,d) Swath bathymetry, gridded at 200 m resolution, from the boxes shown in Figure 6.7a. This is from a newly compiled, cleaned dataset comprised of all available data in the region, totalling 36 cruises. The incoming fabric of oceanic crust strikes at high angles to the trench and therefore new, large-offset, horst-and-graben style faults are formed. (e) Swath bathymetry along the profiles shown in Figures 6.7c and 6.7d. This shows the horst and graben structures, which are bounded by bend-faults with offsets up to > 1.5 km. . . 115

7.1 Segment-bin T_e estimates from the Middle America trench. (a) Free-air gravity anomaly map (Sandwell et al., 2014, v23.1); the white lines show seafloor isochrons at 5 Ma intervals (Müller et al., 2008, v3.2) and the dashed white line marks the East Pacific Rise (EPR). The solid black boxes show the segment-bins and the dashed red boxes show the bins described in Section 7.1.3. The black arrows show plate convergence vectors from the MORVEL plate motion model (DeMets et al., 2010). (b) T_e from Inversion A1, and the ensemble-averaged seafloor age 100 km from the trench axis, plotted against longitude. (c) T_e from Inversion A2 plotted against longitude. Arrows on error bars in Figures 7.1b and 7.1c indicate that the upper bound is outside the plot range. (d) Strike of seafloor isochrons to the trench axis, plotted against longitude. The grey shade marks the transition in the style of bend-faulting from abyssal hill fault reactivation (< 25–$30°$) to newly formed, trench-parallel faults (> 25–$30°$). 121

7.2 Segment-bin T_e estimates from the Peru-Chile trench. (a) Free-air gravity anomaly map (Sandwell et al., 2014, v23.1); the white lines show seafloor isochrons at 5 Ma intervals (Müller et al., 2008, v3.2). The solid black boxes show the segment-bins, and the black arrows show plate convergence vectors from the MORVEL plate motion model (DeMets et al., 2010). The dashed red lines mark aseismic ridges and the black stars mark hotspot locations (Zhao, 2007). (b) T_e from Inversion A1, and the ensemble-averaged seafloor age 100 km from the trench axis, plotted against latitude. (c) T_e from Inversion A2 plotted against latitude. Arrows on error bars in Figures 7.2b and 7.2c indicate that the upper bound is outside the plot range. (d) Strike of seafloor isochrons to the trench axis, plotted against latitude. The grey shade marks the transition in the style of bend-faulting from abyssal hill fault reactivation (< 25–$30°$) to newly formed, trench-parallel faults (> 25–$30°$). (e) Black line shows trench-normal axial stresses digitized from Wortel and Cloetingh (1985) and the grey shade shows regions of flat-slab subduction (from Manea et al., 2012). 122

7.3 Segment-bin T_e estimates from the Aleutian trench. (a) Free-air gravity anomaly map (Sandwell et al., 2014, v23.1); the white lines show seafloor isochrons at 5 Ma intervals (Müller et al., 2008, v3.2). The solid black boxes show the segment-bins, and the black arrows show plate convergence vectors from the MORVEL plate motion model (DeMets et al., 2010). (b) T_e from Inversion A1, and the ensemble-averaged seafloor age 100 km from the trench axis, plotted against longitude. (c) T_e from Inversion A2 plotted against longitude. Arrows on error bars in Figures 7.3b and 7.3c indicate that the upper bound is outside the plot range. (d) Strike of seafloor isochrons to the trench axis, plotted against longitude. The grey shade marks the transition in the style of bend-faulting from abyssal hill fault reactivation (< 25–$30°$) to newly formed, trench-parallel faults (> 25–$30°$). 123

7.4 Segment-bin T_e estimates from the Tonga-Kermadec trench. (a) Free-air gravity anomaly map (Sandwell et al., 2014, v23.1); the white lines show seafloor isochrons at 5 Ma intervals (Müller et al., 2008, v3.2). The solid black boxes show the segment-bins, and the black arrows show plate convergence vectors from the MORVEL plate motion model (DeMets et al., 2010). (b) T_e from Inversion A1, and the ensemble-averaged seafloor age 100 km from the trench axis, plotted against latitude. (c) T_e from Inversion A2 plotted against latitude. Arrows on error bars in Figures 7.4b and 7.4c indicate that the upper bound is outside the plot range. (d) Strike of seafloor isochrons to the trench axis, plotted against latitude. The grey shade marks the transition in the style of bend-faulting from abyssal hill fault reactivation (< 25–$30°$) to newly formed, trench-parallel faults (> 25–$30°$). 124

7.5 Segment-bin T_e estimates from the Japan and Kuril trenches. (a) Free-air gravity anomaly map (Sandwell et al., 2014, v23.1); the white lines show seafloor isochrons at 5 Ma intervals (Müller et al., 2008, v3.2). The solid black boxes show the segment-bins, and the black arrows show plate convergence vectors from the MORVEL plate motion model (DeMets et al., 2010). (b) T_e from Inversion A1, and the ensemble-averaged seafloor age 100 km from the trench axis, plotted against latitude. (c) T_e from Inversion A2 plotted against latitude. Arrows on error bars in Figures 7.5b and 7.5c indicate that the upper bound is outside the plot range. (d) Strike of seafloor isochrons to the trench axis, plotted against latitude. The grey shade marks the transition in the style of bend-faulting from abyssal hill fault reactivation (< 25–$30°$) to newly formed, trench-parallel faults (> 25–$30°$). 125

7.6 Segment-bin T_e estimates from the Mariana and Izu-Bonin trenches. (a) Free-air gravity anomaly map (Sandwell et al., 2014, v23.1); the white lines show seafloor isochrons at 5 Ma intervals (Müller et al., 2008, v3.2). The solid black boxes show the segment-bins, and the black arrows show plate convergence vectors from the MORVEL plate motion model (DeMets et al., 2010). (b) T_e from Inversion A1, and the ensemble-averaged seafloor age 100 km from the trench axis, plotted against latitude. (c) T_e from Inversion A2 plotted against latitude. Arrows on error bars in Figures 7.6b and 7.6c indicate that the upper bound is outside the plot range. (d) Strike of seafloor isochrons to the trench axis, plotted against latitude. The grey shade marks the transition in the style of bend-faulting from abyssal hill fault reactivation (< 25–$30°$) to newly formed, trench-parallel faults (> 25–$30°$). 126

7.7 Trench-bin T_e from Inversion A2, with two T_e values for the Middle America trench: one for the region to the west of the Tehuantepec Ridge and the other for the region to the east of it (bins shown in dashed red in Figure 7.1a). The plots show that at the Middle America trench, seaward T_e increases with age but landward T_e does not, and that the landward T_e to the west of the Tehuantepec Ridge appears anomalously high. 130

7.8 Ensemble-averaged depth anomalies at the (a) Peru and Chile trenches, and (b) Mariana and Izu-Bonin trenches. 133

7.9 Seafloor age (solid) and effective thermal age (dashed) at the Peru (grey) and Chile (black) trenches. The effective thermal ages were calculated from trench-bin ensemble-averaged seafloor depths using the plate-cooling model of Parsons and Sclater (1977). 134

7.10 T_e from the trench-outer rise system of circum-Pacific subduction zones plotted against effective thermal age, t_{eff}. The top and bottom rows show the trench-bin and segment-bin results respectively. (a,d) shows constant T_e from Inversion A1; (b,e) and (c,f) show landward T_e and seaward T_e respectively from Inversion A2. Best-fitting plate-cooling isotherms are shown in solid black and 95 % confidence intervals in dashed black; the temperatures of these isotherms are labelled in the top right of each plot. 137

7.11 (a) The vertical force resulting from the temperature contrast between slab and mantle, F_v, plotted against the maximum observed curvature at the trench-outer rise of circum-Pacific subduction zones. (b) Plate weakening from Inversion A2 plotted against the maximum observed curvature. The symbols are coloured by seafloor age. 139

7.12 Figure showing the anomalous outer-rise geometry and T_e in regions where the model assumptions (for an elastic plate undergoing cylindrical bending) are violated. (a), (b) and (c) show plots from the Aleutian, Peru-Chile and Middle America trenches respectively. Plots on the left are from segment-bins where the model assumptions are violated, due to either arcuate trench geometry or trench-oblique plate convergence, and adjacent plots on the right are from neighbouring segment-bins where the model assumptions hold. Each pair of plots shows the observed and best-fit gravity from Inversion A2 (the trench, bin number and seafloor age range is labelled) and below that, the best-fit T_e profile from Inversion A2. The figure shows that regions where the model assumptions are violated (plots on left) are characterised by relatively large-amplitude, sharply curved outer rises and by relatively low plate weakening. 144

7.13 (*Figure on next page*) Plots showing seismicity and bend-faulting at the outer trench-slope of the Middle America trench. (a) GEBCO bathymetry overlain with all earthquakes, as of 2013, in the ISC (black dots) and CMT (focal mechanisms) catalogues. Only events seaward of the trench axis and within the trench-bin (black dash) are shown. CMT events have been plotted at their respective EHB positions, as these are more accurate (e.g., Bürgmann et al., 2005; Ranero et al., 2005). (b) Histograms of ISC, EHB and CMT seismicity against distance from the trench, where the bin width is 10 km. This shows the landward increase in seismicity due to outer trench-slope bend-faulting. (c,d) Swath bathymetry, gridded at 200 m resolution, from the boxes shown in Figure 7.13a. This dataset is comprised of all available data in the region, totalling 30 cruises. The dashed red lines in Figure 7.13c show the approximate azimuth of the pre-existing abyssal hill fabric. (e) Swath bathymetry along the profiles shown in Figures 7.13c and 7.13d. 146

7.14 Figure illustrating the correlation between the nature of bend-faulting and the geometry of the outer rise. The plots show ensemble-averaged profiles of bathymetry and gravity from (a,b) the Peru and Chile trenches and (c,d) the western and eastern Middle America trenches. At trenches where abyssal hill faults are reactivated as bend-faults (grey lines), the outer rise is smoothly curved and well defined. At trenches where new, trench-parallel bend-faults are formed (black lines), the outer rise is subdued and the plate bends sharply into the trench. We suggest that this sharply bent section might reflect a 'hinge' (red dash), such that the seaward propagation of bending moments through the plate is inhibited. 150

8.1 The yield strength predicted by the brittle and ductile failure laws used in this study. The shallow, brittle yield strength was calculated with Byerlee's (1978) friction coefficients and hydrostatic PFP. The yield strengths for the LTP flow laws are shown in solid black and labelled a to f. The dot-dashed lines show the yield strengths for the dry and wet PLC laws of Hirth and Kohlstedt (2003). The semi-brittle regime is marked in dashed grey. The yield strengths were calculated for an 80 Ma plate-cooling geotherm and $\dot{\varepsilon} = 10^{-16}$ s^{-1} 160

8.2 The yield strength envelopes used in this study, calculated for a range of plate ages (assuming a plate-cooling geotherm and $\dot{\varepsilon} = 10^{-16}$ s^{-1}). The LTP flow law is labelled on the bottom left of each plot and the water content on the bottom right. 165

8.3 Figure illustrating the calculation of the predicted T_e. An elastic bending stress profile (dashed red line) is calculated for a given curvature, κ, and then truncated by the YSE to give the bending stress in the presence of plastic yielding (solid red line). This stress profile can then be used to calculate the bending moment and predicted T_e. 167

8.4 Schematic illustrating elastic-perfectly plastic behaviour. Below the yield stress, σ_{yield} in the figure, stress increases linearly with strain. When σ_{yield} is reached, strain continues to increase without any further increase in stress. 167

8.5 Predicted T_e vs. plate curvature for each of the YSEs used in this study and for a range of plate ages. The LTP flow law used to construct the YSE is labelled in the top left of each pair of plots. The upper plots show predicted T_e and the lower plots show predicted T_e as a fraction of the initial mechanical thickness, T_m. All YSEs were calculated with $\dot{\varepsilon} = 10^{-16}$ s^{-1}. 169

8.6 Figure illustrating how the strain rate, $\dot{\varepsilon}_{xx}$, was estimated for the circum-Pacific trench-outer rise flexure profiles. The plot shown is for the Kuril trench-bin profile. (a) Observed plate curvatures were used to calculate $\frac{\mathrm{d}\kappa}{\mathrm{d}x}$ as a function of distance from the trench axis. (b) $\frac{\mathrm{d}\kappa}{\mathrm{d}x}$ and the trench-normal subduction velocity were used to calculate $\dot{\varepsilon}_{xx}$ as a function of distance from the trench. The YSE for each profile was calculated using the mean $\dot{\varepsilon}_{xx}$ in the region of plate bending (between x_a and x_c), calculated at distance $|y - y_n| = h_{200}$ from the neutral surface (h_{200} is the depth to the 200 °C isotherm). Also shown are the strain rates calculated for $|y - y_n| = 5$ km and $|y - y_n| = 30$ km. 171

8.7 Figure illustrating the variation in predicted T_e due to depth variations in strain rate. (a) YSEs for the Kuril trench-bin (mean age 115 Ma), calculated using the strain rates shown in dash in Figure 8.6b at a distance 65 km from the trench axis. These strain rates were calculated at a distance $|y-y_n| = 5$ km and $|y - y_n| = 30$ km from the neutral surface respectively, which represents the depth range over which stresses are likely to be supported on geological timescales. (b) Predicted T_e as a function of plate curvature for each of the YSEs shown in Figure 8.7a. 173

8.8 Figure illustrating the variation in predicted T_e due to circum-Pacific variations in strain rate. (a) YSEs for a 115 Ma cooling plate, calculated using the minimum and maximum strain rates that were estimated for our circum-Pacific trench-outer rise profiles. (b) Predicted T_e as a function of plate curvature for each of the YSEs shown in Figure 8.8a. 173

8.9 Figure illustrating the comparison between the predicted T_e and the observed T_e from Inversion A1. The plots shown are for the Kuril trench-bin profile. (a) Following Mueller and Phillips (1995), plate curvatures from the best-fitting elastic plate model were used to calculate the predicted T_e. (b) The predicted T_e (red line) was calculated as a function of distance from the trench axis, and the value at the point of maximum curvature (red arrow) was compared to the observed T_e (black line; grey shade is the uncertainty). The predicted T_e profile shown was calculated with the LTP law of Mei et al. (2010). 175

8.10 For the circum-Pacific segment-bins, the predicted T_e (red diamonds) and the observed T_e from Inversion A1 (black dots) plotted against seafloor age. The LTP flow law used to calculate the predicted T_e is labelled on the bottom left of each plot; in all cases, the brittle regime was calculated with Byerlee's (1978) friction coefficients and hydrostatic PFP. The grey curves show the depths to the 300, 600, 900 and 1200 °C plate-cooling isotherms. The isotherms that best fit the observed T_e and predicted T_e are shown in black and red respectively. 177

8.11 For the circum-Pacific trench-bins, the predicted T_e (red diamonds) and the observed T_e from Inversion A1 (black dots) plotted against seafloor age. The LTP flow law used to calculate the predicted T_e is labelled on the bottom left of each plot; in all cases, the brittle regime was calculated with Byerlee's (1978) friction coefficients and hydrostatic PFP. The grey curves show the depths to the 300, 600, 900 and 1200 °C plate-cooling isotherms. The isotherms that best fit the observed T_e and predicted T_e are shown in black and red respectively. 178

8.12 Statistics comparing the observed T_e from Inversion A1 to the predicted T_e calculated assuming Byerlee's (1978) friction coefficients and hydrostatic PFP. The top row is for the segment-bins (Figure 8.10) and the bottom row is for the trench-bins (Figure 8.11). The left plots show the RMS error between the observed T_e and the predicted T_e for each LTP flow law. The right plots show the best-fit isotherm to the observed T_e (black line, where the grey shade is the 95 % confidence interval), and the best-fit isotherm to the predicted T_e for each LTP flow law (red diamonds). The LTP flow laws are numbered as in Figure 8.10. 179

8.13 YSE showing the effect of the friction coefficient, μ_f, on the brittle yield strength. The solid lines show the brittle yield strength calculated with Byerlee's (1978) friction coefficients and the dashed lines show that calculated with $\mu_f = 0.3$. Hydrostatic PFP was assumed in both cases. 181

8.14 Statistics comparing the observed T_e from Inversion A1 to the predicted T_e calculated assuming $\mu_f = 0.3$ and hydrostatic PFP. The top row is for the segment-bins and the bottom row is for the trench-bins. The left plots show the RMS error between the observed T_e and the predicted T_e for each LTP flow law. The right plots show the best-fit isotherm to the observed T_e (black line, where the grey shade is the 95 % confidence interval), and the best-fit isotherm to the predicted T_e for each LTP flow law (red diamonds). The LTP flow laws are numbered as in Figure 8.10. 181

8.15 For the circum-Pacific segment-bins, the predicted T_e (red diamonds) and the observed T_e from Inversion A1 (black dots) plotted against the effective thermal age. The LTP flow law used to calculate the predicted T_e is labelled on the bottom left of each plot; in all cases, the brittle regime was calculated with Byerlee's (1978) friction coefficients and hydrostatic PFP, and the geotherm was calculated using the effective thermal age. The grey curves show the depths to the 300, 600, 900 and 1200 °C plate-cooling isotherms. The isotherms that best fit the observed T_e and predicted T_e are shown in black and red respectively. 184

8.16 For the circum-Pacific trench-bins, the predicted T_e (red diamonds) and the observed T_e from Inversion A1 (black dots) plotted against the effective thermal age. The LTP flow law used to calculate the predicted T_e is labelled on the bottom left of each plot; in all cases, the brittle regime was calculated with Byerlee's (1978) friction coefficients and hydrostatic PFP, and the geotherm was calculated using the effective thermal age. The grey curves show the depths to the 300, 600, 900 and 1200 °C plate-cooling isotherms. The isotherms that best fit the observed T_e and predicted T_e are shown in black and red respectively. 185

8.17 Gridded datasets for the Hawaiian Islands region. (a) Bathymetry map (GEBCO_08 30 × 30 second, Ioc et al., 2003). The islands are outlined in black, and the white points are the locations of seismically constrained crustal deflections collected along three ship transects by Watts and Ten Brink (1989). In Figure 8.18b, these data points are projected along the great circle path shown in red. (b) Seafloor age (Müller et al., 2008, v3.2); the major islands and fracture zones are labelled. (c) The surface load that was used to calculate the elastic plate flexure; this was obtained by masking the bathymetry using the 4500 m isobath and then adding 4500 m to the remaining bathymetry. 186

8.18 The surface load and observed crustal deflections in the Hawaiian Islands region. (a) The surface load that was used to calculate the elastic plate deflections, sampled along the great circle path shown in red in Figure 8.17c. (b) Seismically constrained depths to the top of oceanic crust (Watts and Ten Brink, 1989) from the three transects that are shown as white points in Figure 8.17c; these data have been projected along the same great circle path. 188

8.19 Illustration of the continuous elastic plate model that was used to model the flexure of the lithosphere beneath the Hawaiian volcanic chain. 189

8.20 Results from inversion of flexural observations in the Hawaiian Island region. (a) The RMS error between the calculated elastic plate deflections and the observed crustal deflections plotted against T_e and load density, ρ_l. The contours are at 50 m intervals. (b) The RMS error plotted against T_e. The dashed grey line corresponds to 1.25 times the minimum RMS error, which was used to estimate the T_e uncertainty. 191

8.21 The best-fit elastic plate solution for the Hawaiian Islands, obtained for $T_e = 26$ km and $\rho_l = 2600$ kg/m^3. (a) A grid of the elastic plate flexure that best fits the observed crustal deflections. The contours are at 500 m intervals. (b) The top plot shows the surface load that was used to calculate the elastic plate deflections, sampled along the great circle path shown in red in Figure 8.21a. The lower three plots show the observed (black) and best-fit calculated (red) crustal deflections along each of the three ship transects (shown as black points in Figure 8.21a); these data have been projected along the same great circle path. The calculated deflections for $T_e = 10$ km and $T_e = 50$ km are also shown (grey crosses). 192

8.22 The plate curvature, κ, of the best-fit elastic plate model (Figure 8.21a) in the (a) chain-normal and (b) chain-parallel direction. The black dots are the locations of the seismically constrained crustal deflections and the grey line is the great circle path along which the curvature in Figure 8.23b was calculated. The contours are intervals of 1×10^{-7}m^{-1}. 194

8.23 Figure illustrating the plate curvature that was used to calculate the predicted T_e for the Hawaiian Islands region. (a) The black line shows the best-fit elastic plate deflection along the profile shown in red in Figure 8.21a. The blue, red and orange points show the observed crustal deflections projected along this profile. (b) The chain-normal and chain-parallel curvature calculated from the best-fit elastic plate model along the profile shown in red in Figure 8.21a. The predicted T_e was calculated using the maximum chain-normal curvature in the regions where we have observed data, $\kappa = 1.6 \times 10^{-7}$ m^{-1}. 194

8.24 Comparison between the results of the YSE-curvature method and those of Zhong and Watts (2013) at the Hawaiian Islands. All results were calculated assuming $\mu_f = 0.7$ and zero PFP. (a,b) The predicted T_e for each LTP flow law (red squares) compared to the observed T_e (black line). The upper end of the error bar on the predicted T_e is the predicted mechanical thickness, T_m. Also shown for comparison is the RMS error between the observed and calculated crustal deflections from the study of Zhong and Watts (2013) (grey circles). To calculate the predicted T_e shown Figure 8.24a, the YSEs for the LTP laws of Evans and Goetze (1979) and Raterron et al. (2004) were constructed by interpolating between the LTP and PLC curves (solid grey in Figure 8.25). To calculate the predicted T_e shown in Figure 8.24b, the YSEs for these two laws were constructed using only the LTP flow strength (dashed black in Figure 8.25). (c) The YSE (black) and stress distribution (red) that were used to calculate the predicted T_e for the LTP law of Mei et al. (2010). 197

8.25 The YSEs used to calculate the predicted T_e for the flow law of (a) Evans and Goetze (1979) and (b) Raterron et al. (2004). The YSEs shown in solid grey were constructed by interpolating between the points at which the LTP strength is 200 MPa and the PLC strength is 100 MPa, so that there is no depth-discontinuity in the yield strength. These were used to calculate the predicted T_e shown in Figure 8.24a. The YSEs shown in dashed black were constructed using only the LTP flow strength, defining the mechanical thickness as the point at which the LTP strength falls below 1 % of the overburden pressure. These were used to calculate the predicted T_e shown in Figure 8.24b. 199

8.26 For the Hawaiian Islands, the predicted T_e for each LTP flow law (red squares) compared to the observed T_e (black line). (a) The predicted T_e was calculated assuming Byerlee's (1978) friction coefficients and hydrostatic PFP. (b) The predicted T_e was calculated assuming $\mu_f = 0.3$ and hydrostatic PFP. The upper end of the error bar on the predicted T_e is the predicted mechanical thickness. 200

9.1 Schematic of the stress-strain (σ-ϵ) path for loading and unloading of an elastic-perfectly plastic material. Loading initially occurs elastically, such that stress increases linearly with strain. When the plastic yield stress, σ_{yield}, is reached, loading occurs plastically, such that strain increases without any further increase in stress. When the stress is reduced, unloading occurs elastically, such that when the stress has decreased to zero, there is a residual strain, ε_r. Thus, the material has 'memory' of its previous failure; this is known as strain hysteresis. 205

9.2 The response of a continuous elastic-plastic plate to loading by a submarine seamount load. (a) The elastic-plastic plate. The white dashed areas show the depth-extent of plastic yielding, the dashed black line shows the depth of the neutral surface, and the double arrows indicate tension or compression. The plate has depth-dependent yield strength, defined by the YSE shown on the right. The YSE was calculated for a 60 Ma cooling plate and $\dot{\varepsilon} = 10^{-16}$ s^{-1}, and was constructed with the LTP flow law of Mei et al. (2010), the dry PLC law of Hirth and Kohlstedt (2003), and Byerlee's (1978) friction coefficients with hydrostatic PFP. (b) The dashed grey shows the mechanical thickness of the plate, $T_m(x)$, and the solid grey shows the final $T_e^{yield}(x)$. The dashed black shows the initial deflection of the elastic-plastic plate, calculated using an elastic plate with $T_e(x) = T_m(x)$, and the solid black shows the final deflection, calculated with the final $T_e^{yield}(x)$. (c) The dashed grey shows the initial plate curvature and the solid grey shows the final curvature. The dashed black shows the initial bending moment and the solid black shows the final moment. . . . 207

9.3 The response of a broken elastic-plastic plate to loading by end-loads, as calculated using the iterative method. The plate was loaded with end-loads $M_0 = 8 \times 10^{16}$ N and $V_0 = 0.5 \times 10^{12}$ Nm^{-1}. (a) The elastic-plastic plate. The white dashed areas show the depth-extent of plastic yielding, the dashed black line shows the depth of the neutral surface, and the double arrows indicate tension or compression. The plate has depth-dependent yield strength, defined by the YSE shown on the right. The YSE was calculated as in Figure 9.2. (b) The dashed grey shows the mechanical thickness of the plate, $T_m(x)$, and the solid grey shows the final $T_e^{yield}(x)$. The dashed black shows the initial deflection of the elastic-plastic plate, calculated using an elastic plate with $T_e(x) = T_m(x)$, and the solid black shows the final deflection, calculated with the final $T_e^{yield}(x)$. (c) The dashed grey line shows the initial plate curvature and the solid grey line shows the final curvature. The dashed black line shows the initial bending moment and the solid black shows the final moment. . . . 208

9.4 Figure illustrating the stress and bending moment in an elastic-plastic plate during unbending. (a) The grey line shows the stress distribution in a plate bent to a curvature of $\kappa = 4 \times 10^{-7}$ m^{-1}, and the red and blue lines show the stress after the plate has subsequently been unbent to $\kappa = 2 \times 10^{-7}$ m^{-1} and $\kappa = 0$ respectively. The yield strength in the plate is defined by the laboratory-derived YSE shown in black. The YSE was calculated for an 80 Ma cooling plate and $\dot{\varepsilon} = 10^{-16}$ s^{-1}, and the flow laws are labelled on the figure. (b) The solid line shows the moment-curvature path that corresponds to the bending and subsequent unbending illustrated in Figure 9.4a. The dashed line shows the moment-curvature path if bending were to continue to higher curvature. . 210

9.5 The response of a broken elastic-plastic plate to loading by end-loads, as calculated using the Runge-Kutta method. (a) The elastic-plastic plate. The white dashed areas show the depth-extent of plastic yielding, and the double arrows indicate tensional or compressional yielding. The plate has depth-dependent yield strength, defined by the YSE shown on the right. The YSE was calculated as in Figure 9.2. (b) The dashed grey line shows the mechanical rigidity, D_m, that corresponds to the mechanical thickness of the plate, and the solid grey line shows the incremental rigidity of the final elastic-plastic plate, D_{inc}. The dashed black line shows the initial elastic plate deflection, calculated for an elastic plate with $D = D_m$, and the solid black line shows the final elastic-plastic plate deflection, calculated via a landward, step-by-step integration from x_c. (c) The dashed grey line shows the initial elastic plate curvature and the solid grey line shows the final elastic-plastic plate curvature. The dashed black line shows the bending moment in the initial elastic plate and the solid black line shows the moment in the final elastic-plastic plate. 213

9.6 Comparison between the broken elastic-plastic plate solutions calculated using the iterative and Runge-Kutta methods. These solutions are also compared to the solution for a variable T_e elastic plate akin to that used in Inversion A2. (a) Plate deflection. (b) Plate curvature. (c) Bending moment. (d) T_e, where the equivalent T_e for the elastic-plastic models was calculated from the final solution using Equations 3.17 and 3.16. 215

9.7 The blue, red and yellow points show seismically constrained depths to the top of oceanic crust (Watts and Ten Brink, 1989) from the three transects that are shown as black points in Figure 8.17a. These data have been projected along the great circle path shown in red in Figure 8.17a. We calculated an average profile of the observed depths (shown as a black line) by interpolating the data from each transect to 1 km spacing and then averaging the interpolated profiles over the intervals covered by all three transects. 217

9.8 Figure illustrating the calculation of ensemble-averaged profiles of (a) the volcanic load and (b) the seafloor age in the Hawaiian Islands region. The grids (shown in Figures 8.17c and 8.17b respectively) were sampled along a series of chain-normal profiles (black) that encompass the region where we have observed data, and these profiles were then arithmetically averaged (red). 217

9.9 Results from elastic-plastic plate modelling of the Hawaiian Islands data, where the brittle regime was calculated with $\mu_f = 0.7$ and zero PFP. (a) For each LTP flow law, a comparison between the observed crustal deflections and the calculated elastic-plastic plate deflections. The flow law is labelled on each plot. (b) The black diamonds show the RMSE between the observed and calculated deflections for each flow law, and the grey circles show the RMSE from the study of Zhong and Watts (2013). 220

9.10 Results from elastic-plastic plate modelling of the Hawaiian Islands data, where the brittle regime was calculated with Byerlee's (1978) friction coefficients and hydrostatic PFP. (a) For each LTP flow law, a comparison between the observed crustal deflections and the calculated elastic-plastic plate deflections. The flow law is labelled on each plot. (b) The RMSE between the observed and calculated deflections for each flow law. 222

9.11 Results from elastic-plastic plate modelling of the Hawaiian Islands data, where the brittle regime was calculated with $\mu_f = 0.3$ and hydrostatic PFP. (a) For each LTP flow law, a comparison between the observed crustal deflections and the calculated elastic-plastic plate deflections. The flow law is labelled on each plot. (b) The RMSE between the observed and calculated deflections for each flow law. 223

9.12 Results from Inversion C1, in which circum-Pacific gravity profiles were modelled using an elastic-plastic plate with brittle regime defined by Byerlee's (1978) friction coefficients and hydrostatic PFP. (a) Observed trench-bin gravity anomalies (solid grey) and best-fit anomalies calculated with the LTP flow laws of Mei et al. (2010) (dashed black) and M(10^6) (dotted red). (b) For each LTP flow law, the mean RMSE for all the circum-Pacific profiles, where the trench-bins and segment-bins have been given equal weighting. 227

9.13 Results from Inversion C2, in which circum-Pacific gravity profiles were modelled using an elastic-plastic plate with brittle regime defined by $\mu_f = 0.3$ and hydrostatic PFP. (a) Observed trench-bin gravity anomalies (solid grey) and best-fit anomalies calculated with the LTP flow laws of Mei et al. (2010) (dashed black) and M(10^4) (dotted red). (b) For each LTP flow law, the mean RMSE for all the circum-Pacific profiles, where the trench-bins and segment-bins have been given equal weighting. 228

9.14 Figure illustrating the stress distribution in an elastic-plastic plate subjected first to axial loading and then to bending. The solid blue line is the initial stress distribution when the plate subjected to an axial force, F. The dashed red line is the final stress distribution when the plate is subsequently bent to a curvature of $\kappa = 1.5 \times 10^{-7}$ m^{-1}. The dotted black line is the stress distribution that would exist if the plate were bent to the same curvature in the absence of axial loading. (a) shows the stress distribution for a compressional axial load, and (b) shows that for a tensional load. 230

9.15 Figure illustrating the stress distribution in an elastic-plastic plate subjected first to bending and then to axial loading. The solid blue line is the initial stress distribution when the plate is bent to a curvature of $\kappa = 1.5 \times 10^{-7}$ m^{-1}. The dashed red line is the final stress distribution when the plate is subsequently subjected to an axial force, F. (a) shows the stress distribution for a compressional axial load, and (b) shows that for a tensional load. 231

9.16 Figure illustrating the effect of axial loading on the deflection of, and stress distribution in, a broken elastic-plastic plate. The left and right plots illustrate the effect of axial compression and tension respectively. The top row of plots shows the deflection of three broken elastic-plastic plates with end-loads, M_0 and V_0, applied at the plate-break: one with no axial loading, one with an axial force applied before bending, and one with an axial force applied after bending. The bottom three rows of plots show the corresponding deviatoric stress distributions in the flexed plates, where the thick and thin contours are at 100 and 50 MPa intervals respectively. The plate has YSE-defined yield strength as shown in Figure 9.14. The end-loads are $M_0 = 4 \times 10^{16}$ N and $V_0 = 1 \times 10^{12}$ Nm^{-1}. The compressional and tensional axial force is $F = -1.1 \times 10^{13}$ Nm^{-1} and $F = 5.5 \times 10^{12}$ Nm^{-1} respectively, which is equal to half the total compressional and tensional strength of the plate respectively. . 234

9.17 Results from Inversion D1. Here, circum-Pacific gravity profiles were modelled using an elastic-plastic plate, where an axial force was applied before bending and the brittle regime was defined with Byerlee's (1978) friction coefficients and hydrostatic PFP. (a) Observed trench-bin gravity anomalies (solid grey) and best-fit anomalies calculated with the LTP flow laws of Mei et al. (2010) (dashed black) and M(10^6) (dotted red). (b) For each LTP flow law, the mean RMSE for all the circum-Pacific profiles, where the trench-bins and segment-bins have been given equal weighting. 238

9.18 Results from Inversion D2. Here, circum-Pacific gravity profiles were modelled using an elastic-plastic plate, where an axial force was applied before bending and the brittle regime was defined with $\mu_f = 0.3$ and hydrostatic PFP. (a) Observed trench-bin gravity anomalies (solid grey) and best-fit anomalies calculated with the LTP flow laws of Mei et al. (2010) (dashed black) and M(10^4) (dotted red). (b) For each LTP flow law, the mean RMSE for all the circum-Pacific profiles, where the trench-bins and segment-bins have been given equal weighting. 239

9.19 Results from Inversion D3. Here, circum-Pacific gravity profiles were modelled using an elastic-plastic plate, where an axial force was applied after bending and the brittle regime was defined with Byerlee's (1978) friction coefficients and hydrostatic PFP. (a) Observed trench-bin gravity anomalies (solid grey) and best-fit anomalies calculated with the LTP flow laws of Mei et al. (2010) (dashed black) and M(10^6) (dotted red). (b) For each LTP flow law, the mean RMSE for all the circum-Pacific profiles, where the trench-bins and segment-bins have been given equal weighting. 240

9.20 Results from Inversion D4. Here, circum-Pacific gravity profiles were modelled using an elastic-plastic plate, where an axial force was applied after bending and the brittle regime was defined with $\mu_f = 0.3$ and hydrostatic PFP. (a) Observed trench-bin gravity anomalies (solid grey) and best-fit anomalies calculated with the LTP flow laws of Mei et al. (2010) (dashed black) and M(10^4) (dotted red). (b) For each LTP flow law, the mean RMSE for all the circum-Pacific profiles, where the trench-bins and segment-bins have been given equal weighting. . . 241

9.21 For the trench-bins, the best-fitting axial force from Inversions D1, D3 and D4. The line colour/pattern denotes the LTP flow law used to define the elastic-plate; the best and worst fitting laws are plotted in black and red respectively. The results are ordered from left to right with increasing plate age. 243

9.22 For the trench-bins, the best-fitting axial stress from Inversions D1, D3 and D4, which corresponds to the axial force shown in Figure 9.21. The line colour/pattern denotes the LTP flow law used to define the elastic-plate; the best and worst fitting laws are plotted in black and red respectively. The results are ordered from left to right with increasing plate age. 243

10.1 Analogue model of a Bingham-Maxwell, or elastic-perfectly viscoplastic, material. 254

10.2 Schematic of the variation of stress with time in an elastic-plastic and a Bingham-Maxwell material respectively. At time t_1, a step strain ε_1 is applied. The induced elastic stress, σ_0^1, is less than the yield stress, σ_{yield}, and therefore both materials behave elastically. At time t_2, a step strain ε_2 is applied and this time the induced elastic stress, σ_0^2, is greater than σ_{yield}. This causes the elastic-plastic material to behave perfectly plastically, such that it deforms at the yield stress. In contrast, the Bingham-Maxwell material behaves as a Maxwell viscoelastic material such that the stress relaxes from its initial elastic value to the yield stress with relaxation time $\tau = \frac{\eta}{E}$. 255

10.3 Comparison between the Bingham-Maxwell and elastic-plastic YSE models. (a) The variation in stress with time following a step change in curvature for a Bingham-Maxwell (red dash) and elastic-plastic (solid blue) plate respectively. The YSE (solid black) was calculated using laboratory derived flow laws as labelled on the figure; the age and strain rate are also labelled. (b) Black shows the effective viscosity corresponding to the YSE shown in Figure 10.3a. Grey shows the geotherm used to calculate the YSE. (d) The change in T_e with time following three step changes in curvature (Figure 10.3c), as calculated using the YSE shown in Figure 10.3a. 256

10.4 Figure illustrating the calculation of the predicted T_e at the trench-outer rise of circum-Pacific subduction zones (the profile shown is the Kuril trench-bin). (a) The plate curvature calculated from the best-fitting elastic plate model from Inversion A1. (b) For the Bingham-Maxwell and elastic-plastic model respectively, the predicted T_e that was calculated using the curvature in Figure 10.4a and the YSE in Figure 10.4c. (c) The stress distribution that was used to calculate the predicted T_e at the point x_a in Figure 10.4b. The YSE was calculated assuming a plate-cooling geotherm for the ensemble-averaged seafloor age 100 km from the trench axis. 258

10.5 For the circum-Pacific segment-bins, the observed T_e from Inversion A1 (black dots) and the predicted T_e calculated assuming a Bingham-Maxwell (red squares) and elastic-plastic (blue diamonds) rheology respectively, plotted against seafloor age. The LTP flow law used to calculate the predicted T_e is labelled on the bottom left of each plot; in all cases, the brittle regime was calculated with Byerlee's (1978) friction coefficients and hydrostatic PFP. The grey curves show the depths to the 300, 600, 900 and 1200 °C plate-cooling isotherms. The black, red and blue isotherms are the best-fits to the observed, Bingham-Maxwell and elastic-plastic T_e respectively. 262

10.6 For the circum-Pacific trench-bins, the observed T_e from Inversion A1 (black dots) and the predicted T_e calculated assuming a Bingham-Maxwell (red squares) and elastic-plastic (blue diamonds) rheology respectively, plotted against seafloor age. The LTP flow law used to calculate the predicted T_e is labelled on the bottom left of each plot; in all cases, the brittle regime was calculated with Byerlee's (1978) friction coefficients and hydrostatic PFP. The grey curves show the depths to the 300, 600, 900 and 1200 °C plate-cooling isotherms. The black, red and blue isotherms are the best-fits to the observed, Bingham-Maxwell and elastic-plastic T_e respectively. 263

10.7 Statistics comparing the observed T_e from Inversion A1 to the predicted T_e calculated assuming a Bingham-Maxwell (red squares) and elastic-plastic (blue diamonds) rheology respectively. Byerlee's (1978) friction coefficients and hydrostatic PFP were assumed in both cases. The top row is for the segment-bins (Figure 10.5) and the bottom row is for the trench-bins (Figure 10.6). The left plots show the RMS error between the observed T_e and the predicted T_e for each LTP flow law. The right plots show the best-fit isotherm to the observed T_e (black line, where the grey shade is the 95 % confidence interval), and the best-fit isotherm to the predicted T_e for each LTP flow law. The LTP flow laws are numbered as in Figure 10.5. 264

10.8 The observed T_e (black line) at the Hawaiian Islands compared to the predicted T_e calculated assuming an elastic-plastic (blue diamonds) and Bingham-Maxwell (red squares) rheology respectively. Byerlee's friction coefficients and hydrostatic PFP were assumed in both cases. The upper end of the error bar on the predicted T_e is the predicted mechanical thickness. (b) The YSE used to calculate the predicted T_e shown in Figure 10.8a for the LTP law of Mei et al. (2010). The blue curve is the elastic-plastic bending stress distribution and the dashed red curve is the final, present-day Bingham-Maxwell stress distribution. 266

10.9 The observed T_e (black line) at the Hawaiian Islands compared to the predicted T_e calculated assuming moderate thermal rejuvenation of the lower lithosphere. The rejuvenation was simulated by increasing the temperature in the lower half of the mechanical lithosphere by an amount that increases with depth from 0 to 200 °C. Byerlee's friction coefficients and hydrostatic PFP were assumed. The upper end of the error bar on the predicted T_e is the predicted mechanical thickness. 268

A.1 Bathymetry map of the Middle America trench (GEBCO_08 30 × 30 second, Ioc et al., 2003). The solid white lines show seafloor isochrons at 5 Ma intervals (Müller et al., 2008, v3.2), and the dashed black line marks the East Pacific Rise (EPR). The segment-bins are shown and numbered in solid black, and plate convergence vectors from the MORVEL plate motion model (DeMets et al., 2010) are shown as black arrows. 288

A.2 Bathymetry map of the Peru-Chile trench (GEBCO_08 30 × 30 second, Ioc et al., 2003). The solid white lines show seafloor isochrons at 5 Ma intervals (Müller et al., 2008, v3.2). The segment-bins are shown and numbered in solid black, and plate convergence vectors from the MORVEL plate motion model (DeMets et al., 2010) are shown as black arrows. The dashed red lines mark aseismic ridges and the black stars mark hotspot locations. 290

A.3 Bathymetry map of the Aleutian trench (GEBCO_08 30×30 second, Ioc et al., 2003). The solid white lines show seafloor isochrons at 5 Ma intervals (Müller et al., 2008, v3.2). The segment-bins are shown and numbered in solid black, and plate convergence vectors from the MORVEL plate motion model (DeMets et al., 2010) are shown as black arrows. 291

A.4 Bathymetry map of the Tonga-Kermadec trench (GEBCO_08 30 × 30 second, Ioc et al., 2003). The solid white lines show seafloor isochrons at 5 Ma intervals (Müller et al., 2008, v3.2). The segment-bins are shown and numbered in solid black, and plate convergence vectors from the MORVEL plate motion model (DeMets et al., 2010) are shown as black arrows. 293

A.5 Bathymetry map of the Kuril-Japan trench (GEBCO_08 30 × 30 second, Ioc et al., 2003). The solid white lines show seafloor isochrons at 5 Ma intervals (Müller et al., 2008, v3.2). The segment-bins are shown and numbered in solid black, and plate convergence vectors from the MORVEL plate motion model (DeMets et al., 2010) are shown as black arrows. 294

A.6 Bathymetry map of the Izu-Bonin-Mariana trench (GEBCO_08 30×30 second, Ioc et al., 2003). The solid white lines show seafloor isochrons at 5 Ma intervals (Müller et al., 2008, v3.2). The segment-bins are shown and numbered in solid black, and plate convergence vectors from the MORVEL plate motion model (DeMets et al., 2010) are shown as black arrows. 296

List of Tables

2.1 Age of the subducting seafloor at circum-Pacific subduction zones. The ages were sampled from the seafloor age grid of Müller et al. (2008, v3.2) at a distance 100 km seaward of the trench axis. 22

3.1 The densities and gravitational, elastic and thermal constants that were assumed in this study. The thermal constants are from the plate cooling model of Parsons and Sclater (1977). 50

8.1 Parameters for the Low-Temperature Plasticity (LTP) olivine flow laws that were tested in this study, applicable to Equation 8.4. The flow laws listed as M(10^4), M(10^6) and M(10^8) are weakened modifications of Mei et al. (2010), where A_m has been increased by 4, 6 and 8 orders of magnitude respectively. 162

8.2 Parameters for the Power-Law Creep (PLC) olivine flow laws used in this study, applicable to Equation 8.5. Note that for wet olivine, B_m was calculated for a water concentration of 1000 H/10^6Si. 162

List of Abbrevations

Abbrevation	**Meaning**
FFT	Fast Fourier Transform
GBS	Grain-Boundary Sliding
LTP	Low-Temperature Plasticity
LPO	Lattice-Preferred Orientation
MAD	Mean Absolute Difference
MOR	Mid-Ocean Ridge
PFP	Pore-Fluid Pressure
PLC	Power-Law Creep
RMS	Root Mean Squared
RMSE	Root Mean Squared Error
SNR	Signal-to-Noise Ratio
YSE	Yield Strength Envelope

Acknowledgements

First and foremost, I must thank my supervisor, Tony Watts. This thesis is built upon his ideas, and has benefitted greatly from his advice, enthusiasm, knowledge and wisdom. I thank him especially for his kindness and for believing in me even when I didn't believe in myself.

I extend my sincerest thanks to Christine Pierce, whose planning and organisation ensured that research cruise SO215 was an experience I'll never forget. Thanks also to the crew of R/V Sonne, and to the scientists and technicians who helped to make the cruise such a success. I also note, with thanks, the funding received from NERC that facilitated the cruise and my DPhil.

My thesis examiners, Michel Diament and Lars Hansen, are thanked for their time and effort in reading my thesis, and for a very interesting discussion in my viva voce.

With sadness, I pay tribute to the late Evgueni Burov. His body of work has been instrumental in shaping my ideas on the strength and rheology of the lithosphere, and I also had the pleasure of attending several of his sessions at EGU. He will be greatly missed in the geodynamic community.

During my time in Oxford, my work has beneffited from many fruitful discussions with members of the Marine Lab. So thanks to: Brook K, Brook T, Clara, Dan, Dirk, James, Lara, Lily, Michele, Rebecca and Tristan. In particular, I thank Dan Bassett for his friendship, his silliness, his scientific advice and insight, and for the use of his ensemble-averaging code. In addition, a special mention must go to those Marine Lab members who helped with the proof-reading of this thesis.

The technical and administrative staff in the Department of Earth Sciences are warmly

acknowledged. In particular, thanks to Steve Usher for ensuring that the computing systems in the Marine Lab always ran smoothly, to Yasuko and Elaine for keeping my finances and academic progress in order, and to Alice and Milly for dealing with my countless record deliveries.

My time in Oxford wouldn't have been half as much fun without the wonderful people I lived with: Conor, Emre, Maria, Martin, Matt, Michael and Nadine. Thanks to you all for the laughs and for keeping me (almost) sane. And thanks to the many lovely people I danced with over the years, especially to Kamil and the JSP crew.

Last but not least, I am eternally grateful to my family—Mum, Dad and Chris—for their love and support over the past few years and beyond. I genuinely couldn't have done it without them.

Chapter 1

Introduction

1.1 Early ideas on flexural isostasy

The theory of plate tectonics is based on the assumption of rigid lithospheric plates that are capable of transmitting stresses over thousands of kilometres. However, the idea of a rigid lithosphere was postulated long before the advent of plate tectonics. The pioneering studies of Gilbert (1890) and Barrell (1914) were the first to suggest that surface and buried loads might be regionally compensated by the flexure (bending) of a strong lithosphere, rather than locally compensated by Airy or Pratt isostasy (Watts, 2001). Gilbert (1890) observed that uplift following the removal of Lake Bonneville is less than predicted by Airy isostasy and therefore suggested that the crust resists uplift due to it intrinsic strength. Barrell (1914) calculated that observed gravity anomalies can be explained by regional compensation at least equally as well as by local isostasy, and that the long-wavelength pattern of residual anomalies indicates significant departures from Pratt isostasy. In the following decades, several authors sought to explain observations of regional compensation by modelling the lithosphere as an elastic plate overlying an inviscid substrate. For example, Jeffreys (1926) invoked this model to explain the crust's response to folding and to erosion and re-deposition, and Meinesz (1941) used it to explain oceanic gravity anomalies, in particular those surrounding ocean islands such as the Hawaiian island of Oahu. Gunn (1943) modelled the deformation of the lithosphere at a number of geological features such as mountain ranges, trenches and river

deltas, and calculated that the mode of compensation depends not only on the strength of the lithosphere, but also on the wavelength of the load. Walcott (1970) was the first to investigate the spatial and temporal variation of lithospheric rigidity, where he measured the amplitude and wavelength of the flexural response to loading by mountains, seamounts, ice sheets and sediments. He found that cratonic lithosphere appears more rigid than oceanic lithosphere, and that the lithosphere appears stronger in its response to short-term loads than to long-term loads.

1.2 Elastic plate models of oceanic lithosphere

In the decade following the study of Walcott (1970), there were many studies that used the elastic plate model to investigate spatial variations in the rigidity of oceanic lithosphere. In these studies and those since, the flexural rigidity—a measure of the resistance offered by an elastic plate undergoing bending—is commonly expressed through the effective elastic thickness, T_e. The T_e is the thickness of an elastic plate, overlying an inviscid substrate, that responds to loading in the same manner as the lithosphere. It is important to note that T_e is not necessarily the depth to any physical boundary; it is simply a proxy that reflects the depth-integrated stress in the lithosphere.

In the oceans, T_e is generally constrained from observations of flexure at one of four geological features: the trench-outer rise system seaward of subduction zones (Figure 1.1); seamounts and ocean islands; fracture zones; or Mid-Ocean Ridges (MOR). One of two techniques is generally used to constrain T_e at these features, and these are often termed 'forward' and 'spectral' methods respectively. In forward methods, elastic plate deflections are calculated for a range of T_e values and compared to observed bathymetric, gravimetric, or crustal deflections. We note that although these are dubbed 'forward' methods, inversion procedures are often incorporated, for example, to constrain the loads acting at subduction zones. In spectral methods, the relationship between the Fourier spectra of observed bathymetry and gravity is calculated as a function of wavelength, and then compared with theoretical functions for different T_e values. In the oceans, the free-air admittance function is generally used, producing robust results in the case that the coherence between free-air gravity and topography is high (Kalnins and Watts, 2009).

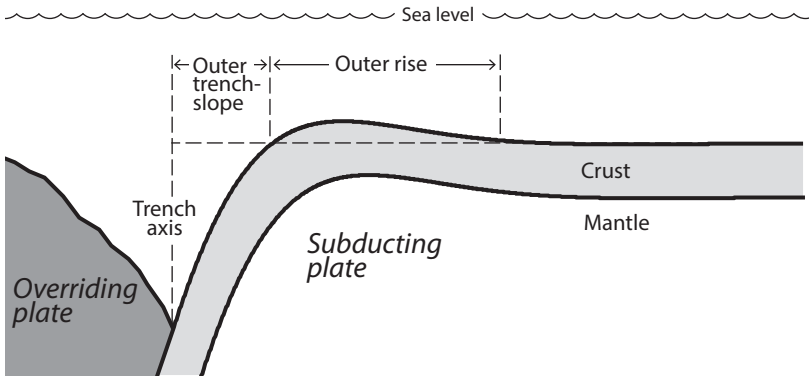

Figure 1.1: Cartoon illustrating the trench-outer rise system of a subduction zone. The trench-outer rise system is the flexural feature immediately seaward of the trench axis, which forms as the subducting plate descends beneath the overriding plate. It comprises the flexural depression known as the outer trench-slope, and the flexural bulge known as the outer rise.

One of the first applications of forward methods was made by Hanks (1971), who used a broken (semi-infinite) elastic plate to model ship-track bathymetry at the Kuril-Hokkaido trench-outer rise system. Applying a vertical shear force at the trench axis, where the force was constrained using the trench depth, he found a best-fit T_e of 27 km and that a large horizontal compressive force was required to fit the observations. Watts and Talwani (1974) used Hanks' (1971) T_e value to forward model ship-track bathymetry and gravity seaward of northern and western Pacific subduction zones, and obtained reasonably good fits by varying the applied horizontal and vertical shear forces. Watts and Cochran (1974) and Watts et al. (1975) used an elastic plate to model ship-track bathymetry and gravity profiles across the Hawaiian-Emperor seamount chain and Great Meteor seamount respectively. They found flexural rigidities of the same order of magnitude as at oceanic trenches, suggesting that some portion of the lithosphere must behave elastically on the timescale of 10^s Myr. Caldwell et al. (1976) modelled trench-outer rise bathymetry in the northern and western Pacific, incorporating an applied bending moment as well as a vertical shear force. They devised a method in which the T_e and end-loads are estimated by measuring the height and width of the outer rise respectively, and resolved T_e of 20–29 km. This study, as well as that of Parsons and Molnar (1978), showed that when an applied bending moment is considered, large horizontal stresses are not required to fit flexural observations at subduction zones.

A series of studies then employed spectral methods to estimate T_e along the Hawaiian-Emperor chain (Watts, 1978), at the Mid-Atlantic Ridge and East Pacific Rise (Cochran, 1979) and at aseismic ridges (McKenzie and Bowin, 1976; Detrick and Watts, 1979). Variations in T_e along the Hawaiian-Emperor chain, and the low T_e at MORs and aseismic ridges, led to the suggestion that oceanic T_e depends on the age of the lithosphere at the time of loading and does not change appreciably with time after loading (Watts, 1978). This idea was corroborated by Caldwell and Turcotte (1979), who used the method of Caldwell et al. (1976) to estimate T_e from ship-track bathymetry at the trench-outer rise system of circum-Pacific subduction zones. They found that the young lithosphere at the Middle America trench is much weaker than older lithosphere at western Pacific trenches, and suggested that T_e reflects the depth at which elastic stresses are relaxed by creep on geological timescales.

1.2.1 T_e vs. the age of oceanic lithosphere at the time of loading

Watts (1978) and Caldwell and Turcotte (1979) suggested that oceanic T_e is, to first order, controlled by the age of the lithosphere at the time of loading, and more recent studies have have substantiated this result. For example, Levitt and Sandwell (1995) performed a joint inversion of ship-track bathymetry and satellite-derived gravity profiles seaward of global subduction zones, inverting for parameters such as flexural wavelength, flexural amplitude, trench axis location, and an applied bending moment. They found that younger (< 80 Ma) lithosphere is clearly weaker than older (> 80 Ma) lithosphere, but that there is scatter in the relationship between T_e and plate age, which they attributed to bathymetric noise and inelastic yielding of the lithosphere. Watts and Zhong (2000) presented a compilation of T_e estimates from seamounts and ocean islands, trenches, fracture zones and MORs, which clearly increase with the plate age at the time of loading (Figure 1.2). This compilation shows that T_e estimates from seamounts and ocean islands generally fall between the depths to the 300 °C and 600 °C isotherms, based on a plate cooling model (Parsons and Sclater, 1977), and that mechanical thickness[1] estimates from trenches generally fall between the 500 °C and 800 °C isotherms.

[1]The mechanical thickness, T_m, is the depth in the lithosphere to which non-negligible stresses can be supported on geological timescales. T_m is always larger than T_e

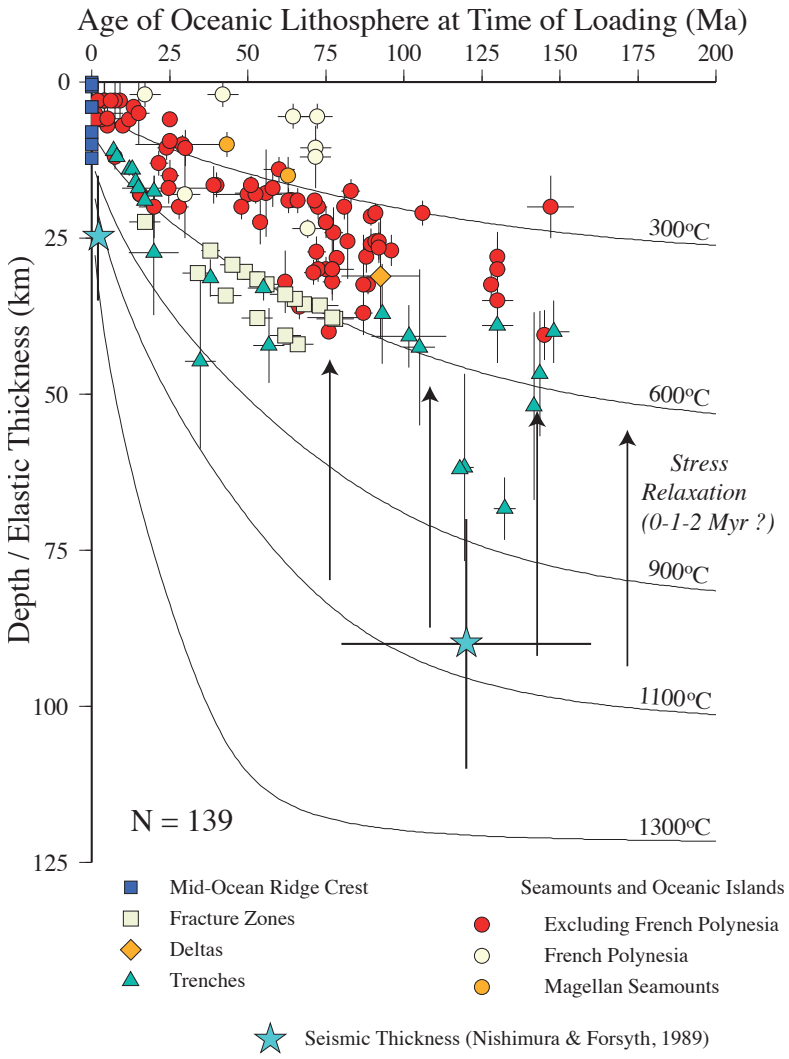

Figure 1.2: Oceanic T_e estimates plotted against the age of lithosphere at the time of loading, from Watts and Zhong (2000). Note that the majority of the values from trenches (blue triangles) have been corrected for the effects of plate curvature, and thus are actually mechanical thickness estimates, not T_e estimates. The figure also shows two estimates of the seismic thickness of oceanic lithosphere (blue stars).

The observed increase in oceanic T_e with the age of the lithosphere at the time of loading is not surprising. Variations in heat flow and seafloor depth suggest that the thermal oceanic lithosphere behaves as a conductive plate that cools as it moves away from the MOR (Langseth et al., 1966; McKenzie, 1967; Parsons and Sclater, 1977). Laboratory deformation studies of mantle minerals, such as olivine, show that at relatively high temperatures, they deform via temperature-dependent creep, where the flow strength increases with decreasing temperature. It follows from these observations that oceanic lithosphere should strengthen with age as it moves away from the MOR. It was somewhat surprising, therefore, that the recent study of

Bry and White (2007) found no relationship between T_e and plate age at the trench-outer rise system of global subduction zones. They suggested that either there is no relationship between the strength of the lithosphere and plate age, or that T_e is the wrong parameter to reveal such a relationship.

1.2.2 Plate weakening at oceanic subduction zones

It has been demonstrated by several studies that at subduction zones, an elastic plate of constant T_e cannot simultaneously fit the steepness of the outer trench-slope and the amplitude and wavelength of the outer rise. This suggests that the subducting plate is weakened as it bends into the trench. For example, Contreras-Reyes and Osses (2010) and Manríquez et al. (2014) found that plate weakening is required to fit flexural observations seaward of the Chile trench, and Zhang et al. (2014) reached the same conclusion at the Mariana trench. In addition, Billen and Gurnis (2005) used a spectral admittance technique to show that the Pacific plate is weakened as it is subducted at the Kermadec trench. Weakening of the subducting plate is likely to be caused primarily by bending-induced inelastic yielding, which occurs due to a combination of shallow, brittle and deeper, ductile failure (e.g., Goetze and Evans, 1979; Brace and Kohlstedt, 1980; McNutt and Menard, 1982). This is evidenced by observations of bend-faulting on the outer trench-slope (e.g., Jones et al., 1978; Masson, 1991; Ranero et al., 2003). Further weakening might occur if these bend-faults provide a pathway for seawater to penetrate and serpentinize the uppermost mantle. This is evidenced by observations of anomalously low seismic velocity and anomalously high Poisson's ratio in the crust and uppermost mantle at the outer trench-slope (e.g., Ranero and Sallares, 2004; Grevemeyer et al., 2007; Contreras-Reyes et al., 2008b).

1.3 Elastic plate models of continental lithosphere

The elastic plate model has also been used to investigate variations in the flexural rigidity of continental lithosphere. For example, T_e has been estimated at foreland basins by forward modelling the flexure of the lithosphere beneath advancing fold and thrust loads (e.g., Karner

and Watts, 1983; Lyon-Caen and Molnar, 1983; Burov et al., 1990; Stewart and Watts, 1997; Jordan and Watts, 2005), and in cratonic interiors by using spectral methods to measure the flexural response to surficial and buried loads that have accrued during a craton's long history (e.g., Forsyth, 1985; Lowry and Smith, 1994; Swain and Kirby, 2006; Pérez-Gussinyé et al., 2009). It has emerged from these studies that plate age also has an influence on the flexural rigidity in continental regions. For example, foreland basins formed on Archean/Proterozoic lithosphere appear to be associated with a higher T_e ($\sim$ 40–100 km) than those formed on Phanerozoic lithosphere ($\sim$ 5–30 km), and T_e estimates from stable cratonic interiors are generally high ($\gtrsim$ 70 km) (e.g., Watts, 1992; Burov and Diament, 1995; Burov and Watts, 2006; Watts et al., 2013). However, due to the complex structure and thermotectonic history of continental lithosphere, the relationship between T_e and plate age is not as simple as it is in the oceans. In addition, the idea that Archean/Proterozoic lithosphere has high T_e has been subject to some controversy, as some authors have used forward (Maggi et al., 2000; Jackson, 2002) and spectral (McKenzie and Fairhead, 1997; McKenzie, 2003) modelling to resolve low T_e in these regions. The elastic plate model has also been used in the continents to model the evolution of rifted sedimentary basins. For example, the stratigraphic 'architecture' of rifted margins (e.g., East Coast USA, NE Brazil) suggests that T_e increases with time after basin formation as the margin increases in distance from the MOR and the lithosphere cools (Watts et al., 1982; Watts and Thorne, 1984).

1.4 Elastic-plastic and viscoelastic plate models of the lithosphere

Although the elastic plate model provides a good fit to many observations of long-term lithospheric flexure, at some subduction zones it cannot simultaneously explain the wavelength of the outer rise and the steepness of the outer trench-slope. Furthermore, it predicts unreasonably high bending stresses in the outermost portions of the flexed lithosphere. This led De Bremaecker (1977) to suggest that trench-outer rise observations could be explained by the advection of a viscous lithosphere; however, this model cannot explain the support of seamounts and ocean islands for 10^s Myr. On the other hand, several authors proposed that

subducting lithosphere behaves as an elastic-perfectly plastic plate, where they arbitrarily defined a depth-independent or linearly-varying yield stress (McAdoo et al., 1978; Turcotte et al., 1978; Bodine and Watts, 1979). Soon after this, Goetze and Evans (1979) formulated the Yield Strength Envelope (YSE), which defines the variation of yield stress with depth based on laboratory-derived failure criteria for frictional sliding and ductile creep. This allowed Bodine et al. (1981) and McAdoo and Sandwell (1985) to model lithospheric flexure using an elastic-plastic plate with laboratory-derived, depth-dependent yield stress.

Another limitation of the elastic plate model is that it cannot account for the observed time-dependence of lithospheric flexure. For example, it cannot explain the decrease with time in the portion of the lithosphere that appears to behave elastically: from the short-term seismic thickness associated with seismic waves, to the medium-term (10^3–10^4 yr) elastic thickness associated with post-glacial rebound, to the long-term ($>$ 1–2 Myr) elastic thickness associated with seamount and orogenic loading (Figure 1.2) (e.g., Walcott, 1970; Anderson, 1980; Watts and Zhong, 2000). The elastic plate model also cannot explain the stratigraphic patterns observed in the moats that flank ocean islands (Watts and Zhong, 2000), the coastal plain of the East Coast USA (Sleep and Snell, 1976), and a number of cratonic and foreland basins (Sleep and Snell, 1976; Beaumont, 1981; Quinlan and Beaumont, 1984). This led these authors and others to model the lithosphere using a thin viscoelastic plate of uniform viscosity, as this model predicts a decrease in rigidity with time.

However, there are two main problems with the thin viscoelastic plate model. First, it predicts that bending stresses relax to zero after long periods of time, which is inconsistent with the observation of long-term strength in the oceans ($>$ 10 Myr) and continents ($>$ 100 Myr) (Kusznir and Karner, 1985; Watts and Zhong, 2000). Second, it does not account for the decrease in viscosity with depth that should occur due to the temperature-dependent nature of ductile creep. To account for these deficiencies, Courtney and Beaumont (1983) and Watts and Zhong (2000) modelled the lithosphere as a multilayered viscoelastic plate, with the effective viscosity of each layer prescribed by an assumed geotherm and a flow law for linear diffusion creep. This model predicts a rapid decrease in rigidity in the first 1–2 Myr after loading, as the stresses in the relatively hot lower lithosphere relax and stresses migrate upwards into the relatively cold upper lithosphere. At later times, there is very little

stress relaxation, as the high viscosities in the relatively cold upper lithosphere mean that it behaves essentially elastically on the timescale of 2–10^s Myr. Zhong and Watts (2013) developed these ideas further using a 3-D finite-element Maxwell viscoelastic model in which the effective viscosity is prescribed by failure criteria for frictional sliding, low-temperature plasticity and power-law creep. They used this to model lithospheric deformation induced by Hawaiian Island loading, which will be discussed further in Section 1.7.

1.5 Laboratory-derived flow laws for the upper mantle

The flexural rigidity, or T_e, of the lithosphere is a reflection of the depth-integrated strength across the brittle, elastic and ductile deformation regimes. Thus, T_e is a reflection of the lithosphere's rheology. The rheology of the upper mantle is thought to be dominated by that of polycrystalline olivine, as olivine is the most abundant, and probably weakest, mineral (Karato et al., 1993; Kohlstedt et al., 1995). Flow laws for diffusion (e.g., Karato et al., 1986; Mei and Kohlstedt, 2000b; Faul and Jackson, 2007) and dislocation (e.g., Goetze, 1978; Hirth and Kohlstedt, 2003; Mei et al., 2010) creep in olivine have been derived via rock mechanics experiments. These laws aim to provide insight into how the upper mantle deforms and they are often used as inputs in geodynamic models (e.g., Cloetingh et al., 2004; Burov and Watts, 2006; Burov and Gerya, 2014).

However, inferring the plastic deformation processes that occur in the mantle requires extrapolation of flow laws from the laboratory to geological conditions, which involves huge extrapolations in timescale and spatial scale (Brace and Kohlstedt, 1980; Kohlstedt et al., 1995; Karato, 2010). For example, laboratory strain rates, typically of the order 10^{-6}–10^{-3} s^{-1}, are ~ 10 orders of magnitude faster than the strain rates associated with lithospheric flexure, 10^{-18}–10^{-14} s^{-1} (Karato, 2010; Burov, 2011). In addition, the high differential stresses in the laboratory mean that elevated pressures and/or temperatures, higher than those found in nature, are required to prevent brittle failure (e.g., Raterron et al., 2004; Mei et al., 2010). Laboratory experiments are usually conducted on small ($\sim$ 10–20 mm long), monomineralic samples of polycrystalline olivine or on single olivine crystals. These are obtained either from synthetic minerals (e.g. Karato et al., 1986) or from a rock that is representative of the man-

tle, such as the olivine bearing peridotite xenoliths from San Carlos, Arizona (e.g., Mei and Kohlstedt, 2000a; Katayama and Karato, 2008). Real rock aggregates, on the other hand, are polymineralic and may have large-scale structure that effects their deformation, such as localized shear zones (e.g., Warren and Hirth, 2006). Moreover, the grain size of polycrystalline samples used in the laboratory is typically 5–20 µm, whilst the grain size in the upper mantle is typically 1–10 mm, but may be as small as 10 µm in ductile shear zones (Karato et al., 1986; Karato, 2008). Finally, laboratory experiments are conducted under simple loading conditions such as triaxial compression or simple shear, whilst geological deformation is generally much more complex.

The numerous differences between laboratory and geological conditions mean that there are uncertainties in the extrapolation of flow laws to upper mantle conditions. For example, flow laws may not scale as predicted by laboratory experiments, or there may be a complete change in the deformation mechanism with the extrapolation to geological conditions (Karato, 2010). Thus, it is important to use geological and geophysical observations to constrain mantle rheology and to test the predictions of laboratory-derived flow laws. In the following sections, we will discuss some studies that have attempted to do this.

1.6 Constraining the rheology of the sub-lithospheric upper mantle

There have been many efforts to constrain the rheology of the sub-lithospheric upper mantle, where temperatures are high (> 1350 °C) and deviatoric stresses are low (< 10 MPa). For example, by modelling observations of post-glacial rebound, the average viscosity of the upper mantle has been well constrained at $\sim 10^{21}$ Pa s (e.g., Haskell, 1935; Mitrovica, 1996). In addition, studies of post-glacial relaxation times at different spatial scales have been used to constrain the variation of mantle viscosity with depth, constraining a low viscosity (10^{19}–10^{20} Pa s) layer at $\sim$ 100–300 km depth and a lower mantle viscosity that is 10–100 times higher than that of the upper mantle (McConnell, 1968; Nakada and Lambeck, 1987; Mitrovica, 1996). Whilst post-glacial rebound studies provide most information on the asthenosphere

and underlying mantle, there is also evidence that a thick (70–145 km), effectively elastic lithosphere is required to fully explain observations, especially in the near field (McConnell, 1968; Mitrovica and Peltier, 1993). The variation in mantle viscosity with depth has also been constrained by modelling the long-wavelength geoid anomaly highs associated with oceanic subduction zones. For example, Hager (1984) suggested that these observations require that sinking slabs are partially compensated by a viscosity contrast at the upper/lower mantle transition, and that the lower mantle is 30–100 times more viscous than the upper mantle.

The studies discussed above all assumed a Newtonian (linear) viscosity of the upper mantle, which implies that deformation occurs predominantly by diffusion creep. Indeed, early theoretical studies suggested that diffusion creep might be the dominant deformation mechanism in the upper mantle, as it occurs under high temperature and low stress conditions (e.g., Nabarro, 1948; Gordon, 1965). This idea was supported by Karato et al. (1993), who showed that the upper mantle must have a predominantly linear rheology in order to explain observations of post-glacial rebound. However, Karato et al. (1993) also noted that observations of seismic anisotropy at shallow depths ($<$ 200 km) suggest Lattice-Preferred Orientation (LPO), which until recently was considered to form via non-linear dislocation creep but not via diffusion creep. They therefore suggested a layered rheological structure for the upper mantle, where the shallow ($<$ 200 km) mantle deforms via non-linear dislocation creep and the deeper mantle via linear diffusion creep. However, Miyazaki et al. (2013) showed in laboratory experiments that LPO can form in the diffusion creep regime as a result of grain rotation caused by diffusion-accommodated Grain-Boundary Sliding (GBS). They therefore suggested that diffusion creep is the dominant deformation mechanism throughout all of the sub-lithospheric upper mantle, in agreement with post-glacial rebound observations.

On the other hand, it has been argued that observations of post-glacial rebound do not accurately reflect the long-term, steady-state rheology associated with mantle convection. For example, Turcotte and Schubert (1982, p. 326) pointed out that the flow associated with post-glacial rebound is superimposed on, and involves smaller stresses than, the flow associated with mantle convection. They suggested, therefore, that the mantle may appear to have linear viscosity during glacial rebound, even if it actually has non-linear rheology. It has also been argued that because of the very small strains involved in post-glacial rebound,

viscosity estimates deduced from such observations may actually reflect transient creep and not the steady-state creep that facilitates mantle convection (e.g., Weertman et al., 1978; Peltier, 1985). Weertman et al. (1978) therefore proposed that on the basis of the predicted stress levels and grain size in the upper mantle, dislocation creep is likely to be the dominant deformation mechanism throughout. Behn et al. (2009) reached the same conclusion based on a 1-D steady-state flow model for grain size evolution in the oceanic upper mantle. Asaadi et al. (2011) also suggested that non-linear dislocation creep is required to explain the rate at which the Hawaiian seafloor swell decays after it moves over the Hawaiian plume. In contrast, by extrapolating their laboratory-derived flow law to mantle conditions, Hansen et al. (2011) suggested that non-Newtonian dislocation-accommodated GBS could be the dominant deformation mechanism throughout most of the upper mantle. This idea is also supported by the agreement between the LPO measured in their experiments and the observed seismic anisotropy in the upper mantle.

1.7 Constraining the rheology of oceanic lithosphere

There have been many efforts to constrain the rheology of the olivine-rich oceanic lithosphere, where temperatures are relatively low (< 1350 °C) and deviatoric stresses are relatively high (> 10 MPa). In the shallowest portions of the lithosphere, deformation occurs via brittle processes such as frictional sliding on fault surfaces (e.g., Byerlee, 1978; Goetze and Evans, 1979). However, with increasing depth and temperature, there is a transition to temperature and strain rate dependent ductile processes. Laboratory experiments suggest that in olivine, dislocation creep is the dominant ductile process at lithospheric conditions (e.g., Goetze, 1978; Hirth and Kohlstedt, 2003; Mei et al., 2010), and this is supported by observations of seismic anisotropy (e.g., Nishimura and Forsyth, 1989; Debayle and Ricard, 2013) and LPO in naturally deformed lithospheric rocks (e.g., Kohlstedt et al., 1995; Ismail and Mainprice, 1998).

Laboratory studies suggest that at lower temperature ($\lesssim$ 600–800 °C) and higher stress ($\gtrsim$ 100–200 MPa) lithospheric conditions, dislocation creep in olivine is rate-limited by the glide of dislocations (e.g., Goetze, 1978; Evans and Goetze, 1979; Raterron et al., 2004;

Katayama and Karato, 2008; Mei et al., 2010). This mechanism is commonly referred to as Low-Temperature Plasticity (LTP) or Peierls creep. At higher temperature ($\gtrsim$ 600–800 °C) and lower stress ($\lesssim$ 100–200 MPa) lithospheric conditions, laboratory experiments suggest that dislocation creep is rate-limited by the climb of dislocations (e.g., Chopra and Paterson, 1984; Hirth and Kohlstedt, 1996). This mechanism is commonly known as Power-Law Creep (PLC). The transition from LTP to PLC with increasing temperature is often observed in the laboratory (e.g., Goetze, 1978; Katayama and Karato, 2008).

It is important to test how well laboratory-derived LTP and PLC flow laws extrapolate to geological conditions. One way of doing this is to test them against observations of the flexure of oceanic lithosphere. A breakthrough in this regard came when Goetze and Evans (1979) developed the concept of the Yield Strength Envelope (YSE), which defines the variation of yield stress with depth based on laboratory-derived failure criteria for frictional sliding and ductile creep. Under the assumption of elastic-perfectly plastic behaviour, YSEs can be used to determine the flexural rigidity, or T_e, predicted by a set of brittle and ductile failure criteria and an assumed plate curvature. This can then be compared to the T_e derived by modelling observed bathymetry and gravity anomalies. By this process, elastic plate models of lithospheric flexure can be used to test the predictions of laboratory-derived flow laws. Using this technique, Goetze and Evans (1979) found good agreement between rigidities derived by modelling trench-outer rise observations and rigidities predicted by YSEs constructed with the dry olivine PLC and LTP flow laws of Goetze (1978). In contrast, McNutt and Menard (1982) used this technique to show that the same YSEs are too strong to fit observations of flexure at trench-outer rise systems and seamounts. The discrepancy between these two studies is likely due to the different plate curvatures that were assumed when calculating the YSE-derived T_e (Mueller and Phillips, 1995).

YSEs can also be used to define the yield stress in elastic-plastic plate models of lithospheric flexure, providing another way to test the predictions of laboratory-derived flow laws. For example, Bodine et al. (1981) used a YSE-defined elastic-plastic plate to model flexure at seamounts and trench-outer rises and found that the dry olivine flow laws of Goetze (1978) are too strong to fit the observations. However, McAdoo et al. (1978) used the same elastic-plastic plate formulation to model geoid anomalies over subduction zone outer rises

and found that the laws of Goetze (1978) provide a good fit to observations. They suggested that the discrepancy between the two studies is due to noise in the ship-track bathymetry used by Bodine et al. (1981). More recently, Garcia-Castellanos et al. (2000) used a YSE-defined elastic-plastic plate to model flexure at the Tonga-Kermadec trench and found that a horizontal force is required to fit the observations.

The YSE is based on the assumption that the lithosphere behaves as an elastic-perfectly plastic material. This might be a reasonable approximation to the long-timescale ($>$ 1–2 Myr) behaviour of the lithosphere, but it cannot account for the time-dependent behaviour that is observed at shorter timescales. Therefore, Courtney and Beaumont (1983) and Watts and Zhong (2000) devised another method of constraining lithospheric rheology that does account for time-dependent behaviour. They modelled flexural observations using a temperature-dependent, multi-layered viscoelastic plate model in which the effective viscosity of each layer was prescribed by a flow law for diffusion creep. By comparing their model with observations from seamounts and oceanic trench-outer rise systems, they were able to constrain the best-fit reference asthenospheric viscosity and creep activation energy. However, these models assumed that the lithosphere deforms via diffusion creep, which is inconsistent with the results of rock mechanics experiments and observations of LPO in the lithosphere. Zhong and Watts (2013) therefore developed a 3-D finite-element Maxwell viscoelastic model, with temperature-dependent, non-linear viscosity that incorporates frictional sliding, LTP and PLC. By comparing model predictions to seismically constrained Moho depths and the depth-dependence of seismicity in the Hawaiian Islands region, they were able to constrain lithospheric rheology. They found that deformation is insensitive to PLC, but that laboratory-derived flow laws for LTP, including the recent law of Mei et al. (2010), are too strong to fit the observations.

1.8 Constraining the rheology of continental lithosphere

YSEs and elastic-plastic plate models have also been used to constrain the rheology of continental lithosphere, which has a multi-layered structure consisting of a quartz-rich upper crust, a diabase/diorite/plagioclase-rich lower crust, and an olivine-rich upper mantle (e.g. Burov and Diament, 1995). Multi-layered YSEs have been used to show that the high T_e in

Archean/Proterozoic cratons and observations of seismicity in the uppermost mantle require a strong upper crust and a strong, dry mantle; this has been dubbed the 'jelly sandwich' model (Chen and Molnar, 1983; Burov and Watts, 2006). In contrast, other authors have argued that the continental uppermost mantle is aseismic and that Archaean/Proterozoic cratons have low T_e (e.g., Maggi et al., 2000; Jackson, 2002). These authors used multi-layered YSEs to show that a strong crust overlying a weak, probably-wet upper mantle is required to explain these observations; this has been dubbed the 'crème brûlée' model. However, it has been pointed out that an aseismic upper mantle is not necessarily weak (Watts and Burov, 2003; Burov and Watts, 2006). This is because seismicity reflects not only the strength of the lithosphere, but also the stress level and the deformation mechanism by which plastic failure occurs.

Burov and Diament (1995) used YSEs and elastic-plastic plate models to show that the rigidity of continental lithosphere is dependent not only on its thermal structure, but also on the relative thickness of the quartz-rich upper crust and olivine-rich mantle, and the degree of coupling between them. This, along with the relatively complex thermotectonic history of continental lithosphere, helps to explain why the relationship between T_e and plate age is not as simple in the continents as in the oceans. Viscoelastic-plastic geodynamic models have also been used to constrain the rheology of continental lithosphere, for example, by testing the validity of the jelly sandwich and crème brûlée models (Burov and Watts, 2006; Burov, 2011). This has shown that a strong upper mantle is required to explain stable continental subduction and the persistence of surface topographic features and their compensating roots. Thus, the crème brûlée model seems incompatible with observations.

1.9 Thesis aims

In this chapter, we have described some of the efforts made to constrain the spatial and temporal variation of the lithosphere's flexural rigidity, and the rheology of the lithospheric and sub-lithospheric mantle. In this thesis, we address three main issues that have been raised by these previous studies.

First, the recent study of Bry and White (2007) modelled bathymetry and gravity at the trench-outer rise system of global subduction zones. This was the first such study to use high-resolution grids of bathymetry and satellite-derived gravity, to use averaged profiles to reduce noise, to estimate errors by calculating misfit as a function of T_e, and to use inversion techniques to derive the applied forces at the trench axis. Somewhat surprisingly, therefore, Bry and White (2007) found no relationship between T_e and plate age, which is inconsistent with models for the cooling of oceanic lithosphere and the temperature-dependent creep of lithospheric minerals. Thus, it is important to reassess the relationship between T_e and plate age in the oceans, as it has implications for our understanding of plate cooling and lithospheric rheology.

Second, several recent flexural modelling studies have shown that at the outer trench-slope of oceanic subduction zones, the subducting plate is significantly weakened by bending-induced inelastic yielding (e.g., Billen and Gurnis, 2005; Contreras-Reyes and Osses, 2010; Manríquez et al., 2014; Zhang et al., 2014). However, these studies have focussed only on individual trenches or on small sections of trenches. Therefore, it is important to test if plate weakening occurs ubiquitously at oceanic subduction zones by modelling a large number of observations using a consistent methodology.

Third, Zhong and Watts (2013) constrained the rheology of oceanic lithosphere by using a 3-D viscoelastic model to model flexural observations in the Hawaiian Islands region. They found that laboratory-derived LTP flow laws, including the recent law of Mei et al. (2010), are too strong to fit the observations. This suggests either that these laws do not scale as expected or that the lithosphere deforms by different processes. It is therefore important to test if laboratory-derived LTP flow laws are generally too strong to fit observations of flexure in the oceans, particularly as these laws are often used as an input to geodynamic models. One reason that laboratory-derived flow laws might appear too strong is the hotspot setting of the Hawaiian Islands. Hotspots are associated with both active volcanism and a broad topographic swell, and so they may have an anomalous thermal and mechanical structure. Therefore, it is particularly important to test LTP flow laws in regions that are not affected by active volcanism.

To address these three issues, we have modelled observations of flexure at the trench-outer rise system of all the major circum-Pacific subduction zones. This is an ideal dataset for exploring the relationship between T_e and the age of oceanic lithosphere at the time of loading. It provides a wide range of subducting plate ages, from 2 to 157 Ma, and because the subducting plate is being loaded at the present day, the results are unaffected by variations in T_e with load age (Watts and Zhong, 2000). In addition, the subduction zones that surround the Pacific provide the best examples of trench-outer rise flexure, as they are characterised by: relatively long, linear and continuous trenches; well-defined outer rises; subducting plates that extend a large distance seaward without being affected by other tectonic features; approximately trench-normal plate convergence; and low sediment-fill. The circum-Pacific dataset also allows us to assess if plate weakening occurs ubiquitously at oceanic subduction zones, and to test if there is any variation in weakening with plate age. The trench-outer rise system is also an excellent place to constrain lithospheric rheology, as there is no large-scale present-day magmatic activity and therefore the age of the lithosphere is likely to reflect its background thermal and mechanical structure.

In addressing the issues discussed above, the main aims of this thesis are as follows:

1. To reassess the relationship between T_e and the age of oceanic lithosphere at the time of loading.

We modelled ensemble-averaged, trench-normal profiles of free-air gravity at the trench-outer rise system of circum-Pacific subduction zones. By producing ensemble-averaged profiles, we removed much of the short-wavelength noise that is unrelated to the long-wavelength trench-outer rise flexure, thus improving the accuracy of T_e estimates. The observations were modelled using a broken elastic plate model in which a bending moment and vertical shear force were applied at the trench axis. The best-fit T_e and loading conditions were derived using an inverse procedure that also allowed us to assess the uncertainty in T_e.

In Chapter 2, we describe the preparation of the ensemble-averaged gravity profiles and in Chapter 3, we describe the broken elastic plate model and gravity model that were used to model these observations. In Chapter 4, we describe the inversion technique that was

used to find the best-fit T_e and loading conditions, and how this was tested by inverting a synthetic dataset. In Chapter 5, we present the results from Inversion A1, in which the observed gravity was modelled using a plate of constant T_e, and investigate any discrepancies between our results and those of Bry and White (2007). Finally, in Chapter 7, we discuss our observed relationship between T_e and plate age, and also discuss a range of other factors that may influence the rigidity of oceanic lithosphere and the accuracy of T_e estimates.

2. To assess the amount of plate weakening that occurs at the trench-outer rise system of oceanic subduction zones.

We conducted a second inversion, Inversion A2, in which the circum-Pacific gravity profiles were modelled using a broken elastic plate with variable T_e. We inverted for two T_e values—a 'landward T_e' and a 'seaward T_e'—where prior to inversion, observed plate curvatures were used to define the location of the linear transition between the two values. Inversion A2 is presented in Chapter 6, along with a discussion on the possible causes of plate weakening at the trench-outer rise system.

3. To constrain the rheology of oceanic lithosphere using observations of flexure.

We used two different methods to constrain lithospheric rheology, and in particular the LTP rheology, at the trench-outer rise system of circum-Pacific subduction zones. By testing the predictions of a range of recent laboratory-derived LTP flow laws, these methods provide a link between large-scale, long-timescale geological deformation and small-scale, short-timescale laboratory deformation. In the first method, the T_e derived by inversion of the observed gravity profiles was compared to the T_e predicted by laboratory-derived YSEs, which are based on failure criteria for frictional sliding and dislocation creep. This is presented in Chapter 8. In the second method, the observed gravity profiles were modelled using elastic-plastic plates that have depth-dependent yield stress defined by laboratory-derived YSEs. This is presented in Chapter 9. We tested the validity of both of these methods by using them to constrain the rheology in the Hawaiian Islands region and comparing the results to those of Zhong and Watts (2013). This is also presented in Chapters 8 and 9. Finally, in Chapter 10, we compare the lithospheric rheology at the trench-outer rise system of subduction zones to

that in the Hawaiian Islands region, and discuss the rheological implications of our results.

1.10 Software used in this thesis

Unless stated otherwise, all modelling software used in this thesis was written by the author. Programs were predominantly written in Fortran, but occasionally in MATLAB, and scripts were written in Bash. All of the swath bathymetry data presented in this thesis were processed using the MB-System software package (Caress and Chayes, 2008). All of the figures presented were created using Generic Mapping Tools (Wessel et al., 2013) and finalised in Adobe Illustrator. The thesis itself was written in LaTeX.

Chapter 2

Data preparation

Our first aim was to reassess the relationship between T_e and the age of oceanic lithosphere at the time of loading. To do this, we modelled ensemble-averaged, trench-normal profiles of free-air gravity at the trench-outer rise system of all the major circum-Pacific subduction zones: Middle America; Aleutian; Peru-Chile; Tonga-Kermadec; Kuril; Japan; Izu-Bonin; Mariana. In this chapter, we will describe the preparation of the ensemble-averaged gravity profiles. We will also describe the preparation of ensemble-averaged bathymetry profiles, as these were also utilised in this study.

2.1 Circum-Pacific subduction zones

The trench-outer rise system of circum-Pacific subduction zones is an ideal dataset for investigating the relationship between T_e and the age of oceanic lithosphere at the time of loading. Firstly, as shown in Table 2.1 and Figure 2.1, it provides a wide range of subducting plate ages, from 2 to 157 Ma. Secondly, subducting lithosphere is being loaded at the present day, thus avoiding the added complication of any variation in T_e with load age (Watts and Zhong, 2000). Thirdly, the trench-outer rise system is generally not subject to large-scale magmatic activity and therefore the age of the lithosphere is likely to reflect its background thermal and mechanical structure.

Subduction zone	Subducting seafloor age (Ma)
Middle America	2–27
Peru-Chile	27–53
Aleutian	52–66
Tonga-Kermadec	85–118
Kuril	102–127
Japan	131–136
Izu-Bonin	132–144
Mariana	140–157

Table 2.1: Age of the subducting seafloor at circum-Pacific subduction zones. The ages were sampled from the seafloor age grid of Müller et al. (2008, v3.2) at a distance 100 km seaward of the trench axis.

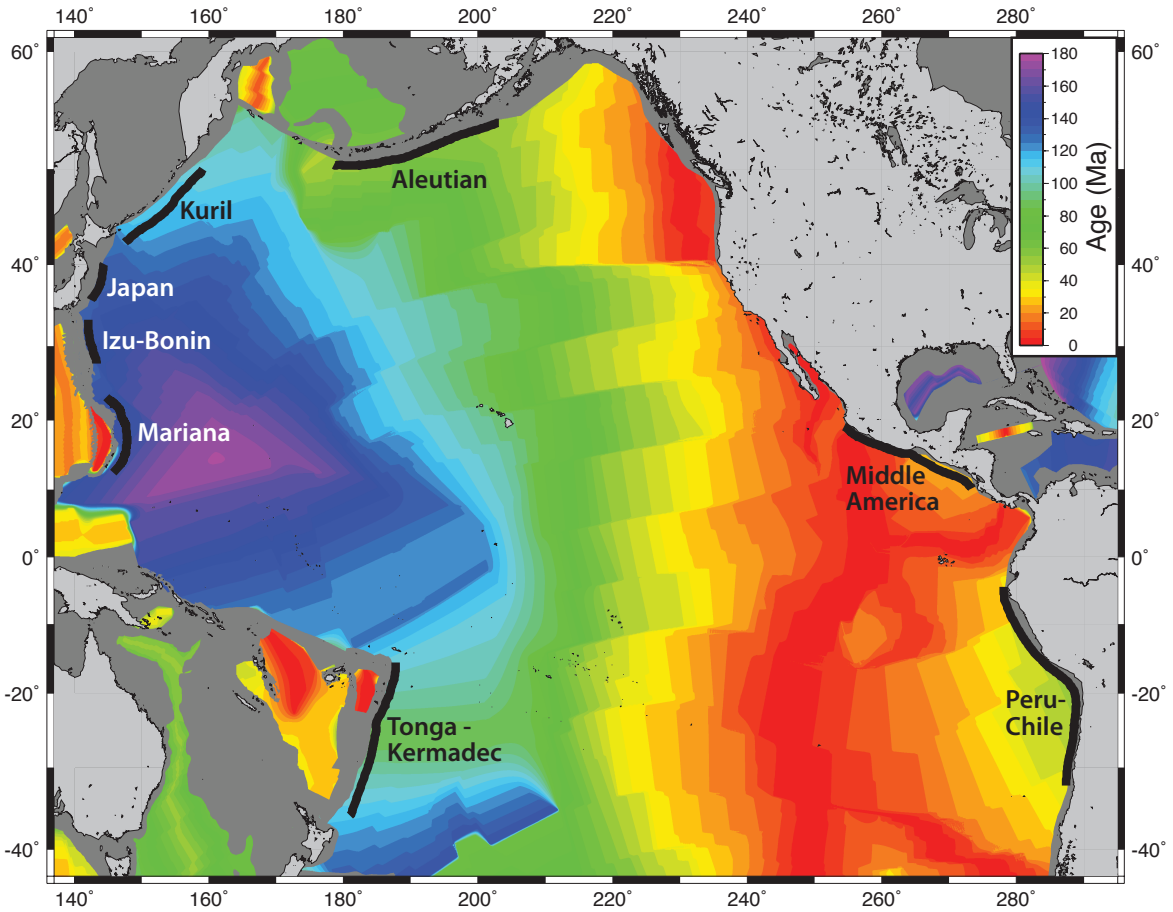

Figure 2.1: Seafloor age in the Pacific from the grid of Müller et al. (2008, v3.2). The trench axes of the subduction zones considered in this study are marked in solid black.

2.2 Gravity and bathymetry data

At subduction zones, the flexure of the subducting plate manifests in bathymetry and free-air gravity as a deep trench ($\sim$ 1–4 km, $\sim$ 100–280 mGal), the seaward side of which is known as the outer trench-slope, and a flexural bulge ($\sim$ 100–500 m, $\sim$ 5–60 mGal) known as the outer rise (Figure 1.1). These features are collectively referred to as the 'trench-outer rise system'. Global, high-resolution grids of bathymetry and free-air gravity are available, which allowed us to model flexure at the trench-outer rise system of all the major circum-Pacific subduction zones using a consistent dataset. We used the satellite-derived free-air gravity anomaly grid of Sandwell et al. (2014, v23.1) and the GEBCO One Minute bathymetry grid (v2.0; Ioc et al., 2003). The gravity grid of Sandwell et al. (2014), shown in Figure 2.2, was constructed from radar altimeter measurements of ocean surface slope from the Geosat/GM, ERS-1, CryoSat-2 and Jason-1 missions, and has $\sim$ 2 mGal accuracy. The GEBCO One Minute bathymetry grid, shown in Figure 2.3, is based only on depth soundings and does not incorporate bathymetry predicted from satellite-derived gravity, which means that our gravity and bathymetry datasets are independent of each other.

2.3 Ensemble-averaging

We aimed to model the relatively long-wavelength ($\sim$ 200–500 km) trench-outer rise flexure associated with plate subduction, and thus wished to remove the relatively short-wavelength ($\sim$ 5–100 km) features such as seamounts, fracture zone ridges and troughs, and abyssal hill fabrics. From here on, these relatively short-wavelength features will be referred to as 'noise'. To this end, we produced ensemble-averaged, trench-normal profiles of gravity and bathymetry within a number of geographic bins. As shown in Figures 2.2 and 2.3, two bin sizes were considered: relatively wide bins that encompass entire trenches (shown in red dash) and narrower ($\sim$ 250–350 km wide) bins that sub-divide each trench into segments (shown in solid black). The wider bins, from here on referred to as 'trench-bins', were used predominantly to investigate the relationship between T_e and plate age. The narrower bins, from here on referred to as 'segment-bins', were additionally used to investigate T_e variations

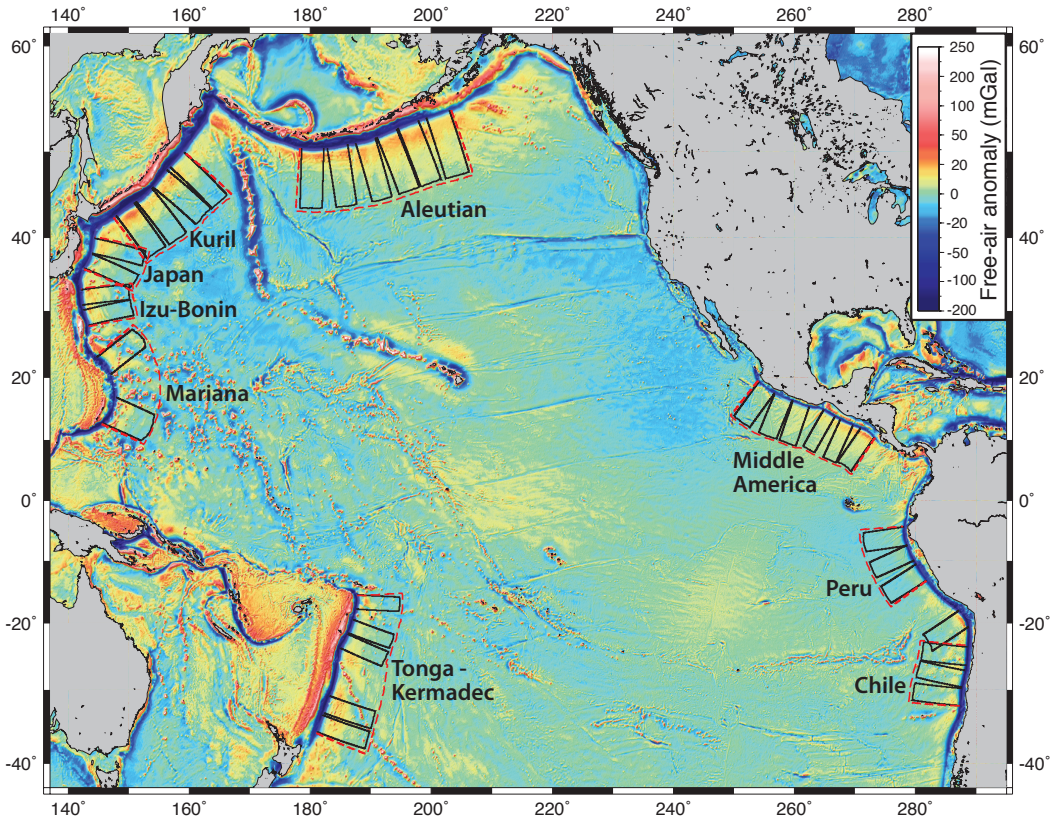

Figure 2.2: Free-air gravity anomaly map of the Pacific Ocean (Sandwell et al., 2014, v23.1), showing the locations of the geographic bins within which the ensemble-averaged profiles were calculated. The red dash shows the 'trench-bins' and the solid black shows the 'segment-bins'.

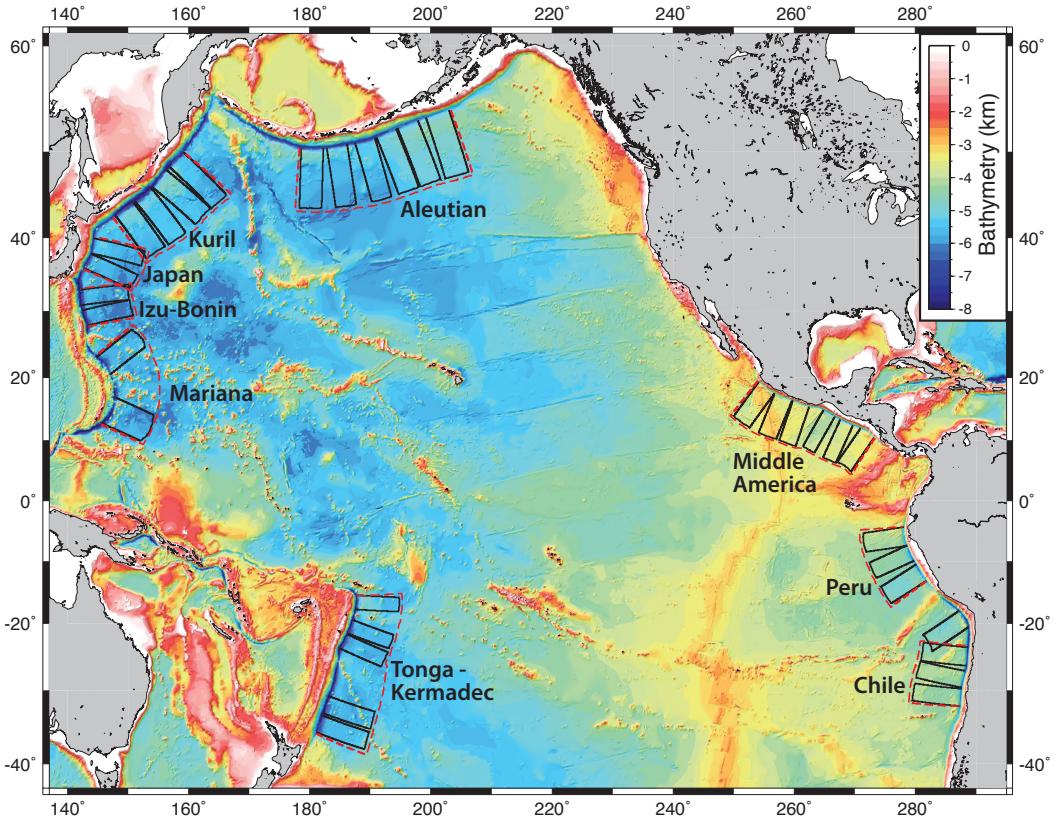

Figure 2.3: Bathymetry map of the Pacific Ocean (GEBCO One Minute, v2.0; Ioc et al., 2003), showing the locations of the geographic bins within which the ensemble-averaged profiles were calculated. The red dash shows the 'trench-bins' and the solid black shows the 'segment-bins'.

along each trench. When choosing the locations of the segment-bins, regions of subducting aseismic ridges or seamounts were avoided, as these features significantly mask the long-wavelength flexural signal. Examples include: the Cocos Ridge (Middle America trench); the Carnegie and Nazca Ridges (Peru trench); the Emperor seamount chain (intersection of the Kuril and Aleutian trenches); the Louisville Ridge (Tonga-Kermadec trench); and the Magellan seamounts (Mariana trench). Sediment-filled trenches such as the Cascadia subduction zone (Davis and Hyndman, 1989) and the southernmost Chile trench (Contreras-Reyes et al., 2007) were also excluded from the study, as the sediments completely obscure the top of the flexed oceanic crust. Figure 2.4 shows the segment-bin numbering system that will be used throughout the thesis.

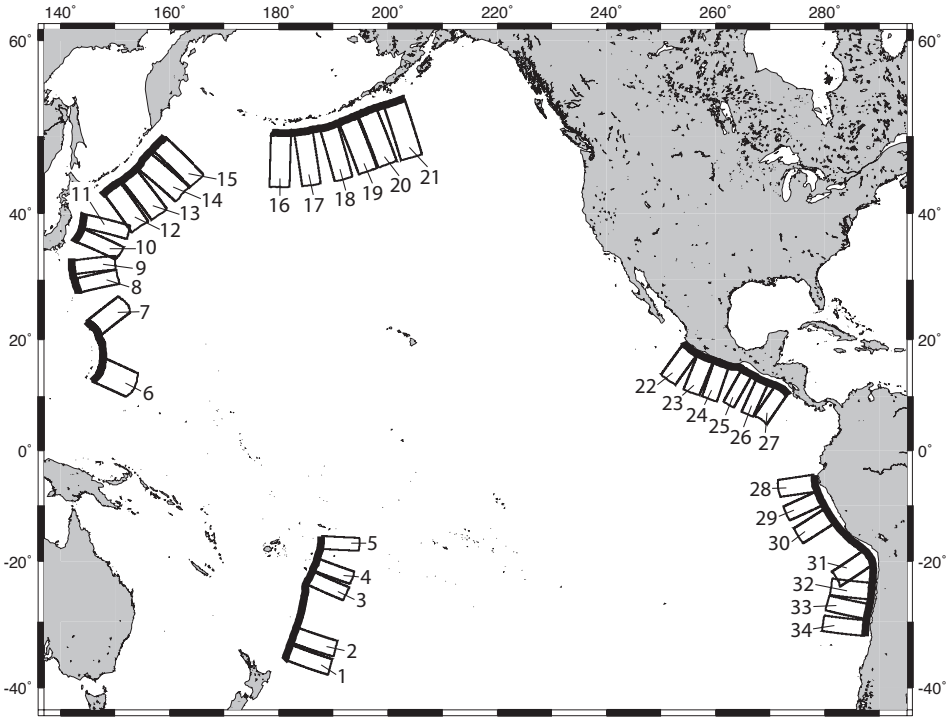

Figure 2.4: The segment-bin numbering system that is used throughout this thesis. The thick black lines show locations of trenches and the thinner black lines show the locations of the segment-bins.

To calculate the ensemble-averaged profiles of gravity and bathymetry, we used the ensemble-averaging code of Bassett (2014), which proceeds as follows. First, as illustrated in Figures 2.5 and 2.6 respectively, a series of trench-normal profiles of free-air gravity or bathymetry are sampled within the bin. Then, the frequency spectrum of each profile is calculated using

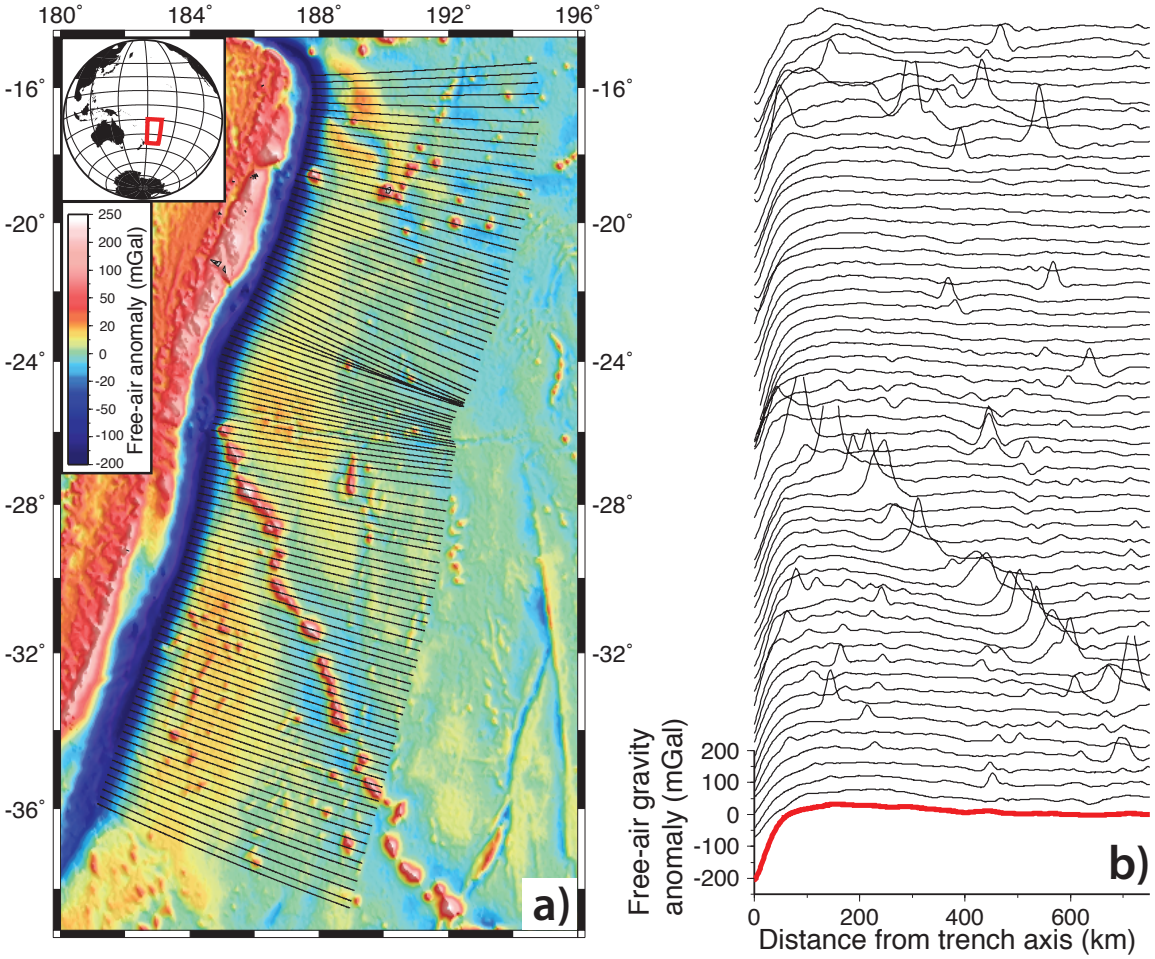

Figure 2.5: Figure illustrating the calculation of the trench-bin ensemble-averaged gravity profile at the Tonga-Kermadec trench. (a) Free-air gravity anomaly map (Sandwell et al., 2014, v23.1) with the locations of the profiles that were ensemble-averaged. (b) The black lines show the free-air gravity along the profiles shown in Figure 2.5a (for clarity, only every other profile is shown), and the red line shows the ensemble-averaged profile.

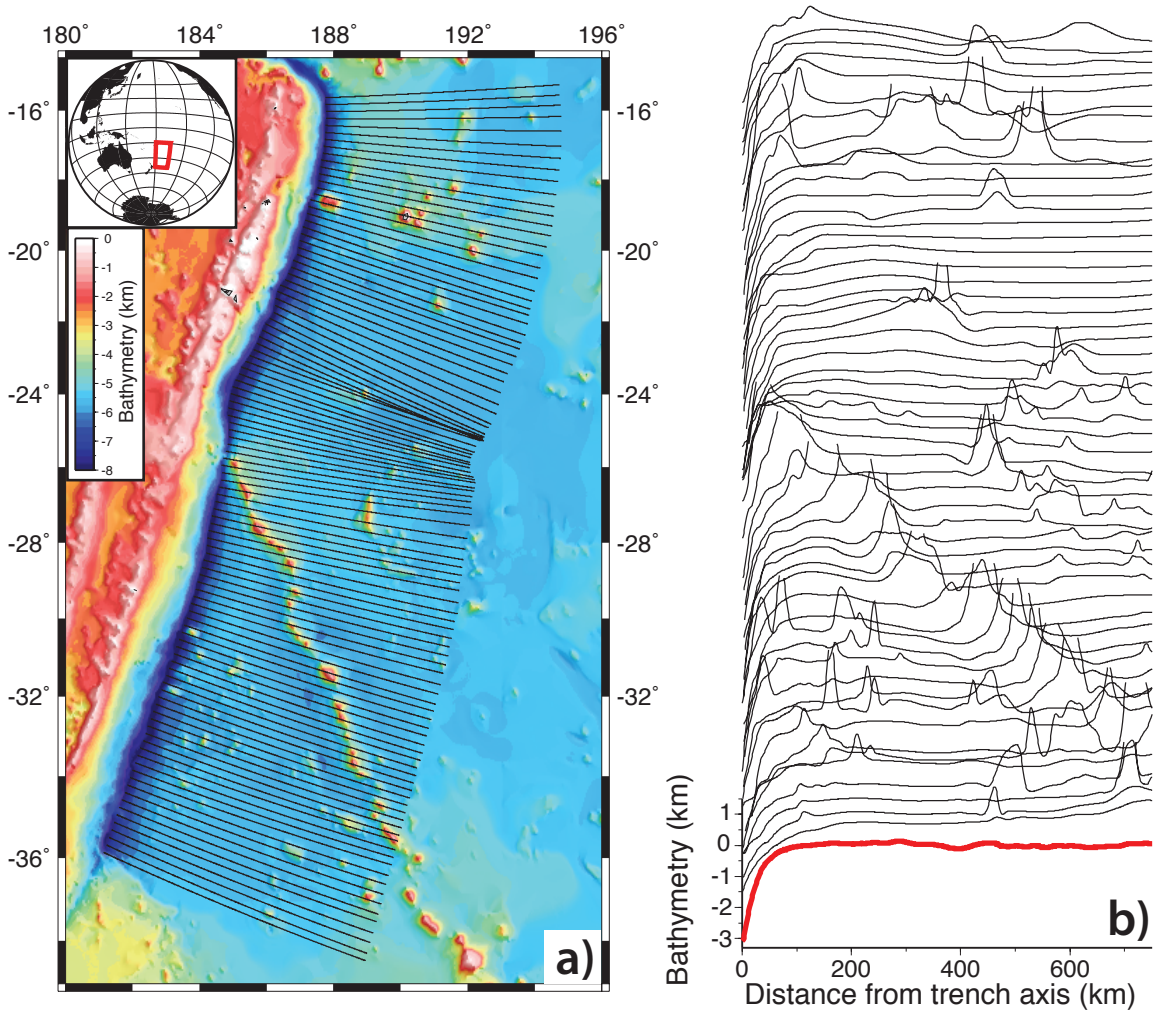

Figure 2.6: Figure illustrating the calculation of the trench-bin ensemble-averaged bathymetry profile at the Tonga-Kermadec trench. (a) Bathymetry map (GEBCO One Minute, v2.0; Ioc et al., 2003) with the locations of the profiles that were ensemble-averaged. (b) The black lines show the bathymetry along the profiles shown in Figure 2.6a (for clarity, only every other profile is shown), and the red line shows the ensemble-averaged profile.

a Fast Fourier Transform (FFT). The individual spectra are then averaged, whereby constructive interference enhances the power of features that are common across the bin and destructive interference reduces the power of uncommon features. An inverse FFT is then used to convert the average frequency spectrum to an average profile in the spatial domain. As illustrated in Figures 2.5b and 2.6b (red profile), the ensemble-averaging process successfully suppresses the short-wavelength features whilst enhancing the long-wavelength flexural signal associated with subduction. Note that the trench-bin ensemble-averaged profiles are relatively noise-free, compared to the segment-bin profiles, as they were averaged over a larger area.

2.4 Data corrections

We were interested in modelling the plate flexure caused by subduction, and thus it was important to correct the observed gravity and bathymetry profiles for any signals that are unrelated to this process.

2.4.1 Plate cooling

Bathymetry data were corrected for the subsidence caused by the thermal cooling of the lithosphere as it moves away from the mid-ocean ridge. We did this using the plate cooling model, which treats the thermal lithosphere as a conductive plate with its base maintained at the temperature of an isothermal asthenosphere and the seafloor at 0 °C (Langseth et al., 1966; McKenzie, 1967; Parsons and Sclater, 1977). Parsons and Sclater (1977) found that in the North Pacific and North Atlantic, the variation in seafloor depth, d, with seafloor age, t_s, is well fit by a 125 ± 10 km thick cooling plate with a basal temperature of 1350 ± 275 °C:

$$\begin{aligned} d(t_s) &= 2500 + 350\sqrt{t_s} \quad \text{if} \quad t_s < 20 \text{ Ma} \\ d(t_s) &= 6400 - 3200\exp(-t_s/62.8) \quad \text{if} \quad t_s \geq 20 \text{ Ma} \end{aligned} \tag{2.1}$$

We corrected the observed bathymetry using this age-depth relationship, where t_s was derived from the seafloor age grid of Müller et al. (2008, v3.2).

Gravity data were corrected for the gravity anomaly caused by plate cooling. This was calculated by first calculating the geoid height-age relationship for the plate cooling model using the formula of Sandwell and Schubert (1980), and then converting this to a gravity anomaly-age relationship using (Chapman, 1979):

$$\mathscr{F}(\Delta g) = g|k|\mathscr{F}(H) \tag{2.2}$$

where $\mathscr{F}$ denotes the Fast Fourier Transform (FFT), Δg is the gravity anomaly, g is the acceleration due to Earth's gravity, k is the wavenumber in the frequency domain, and H is the geoid height.

2.4.2 Long-wavelength gravity anomalies

Gravity data were also corrected for the long-wavelength highs associated with the positive density anomalies of subducted slabs (e.g., McKenzie, 1969; Hager, 1984). To do this, a long-wavelength gravity field was first synthesized from the EGM2008 (Pavlis et al., 2012) spherical harmonic coefficients up to and including degree and order 16. This corresponds to wavelengths $\gtrsim$ 2500 km and, as shown in Figure 2.7, successfully captures the long-wavelength highs associated with subducted slabs. This gravity field was then ensemble-averaged within each profile bin and removed from the ensemble-averaged free-air gravity profile.

2.5 Flexural wavelength vs. plate age

The corrected trench-bin ensemble-averaged gravity and bathymetry profiles are shown in Figures 2.8a and 2.8b respectively. This shows that each trench is characterised by a flexural depression (the outer trench-slope), and seaward of that, a flexural bulge (the outer rise). We note that some outer rises, for example at the Tonga-Kermadec trench, are less pronounced than others; this will be discussed later in this thesis. Figures 2.8a and 2.8b also show that there is a general increase in flexural wavelength with plate age (from top to bottom in the figure). For example, the gravimetric wavelength of the trench-outer rise system is $\sim$ 200 km at the Middle America and Peru-Chile trenches, $\sim$ 300 km at the Aleutian trench, and

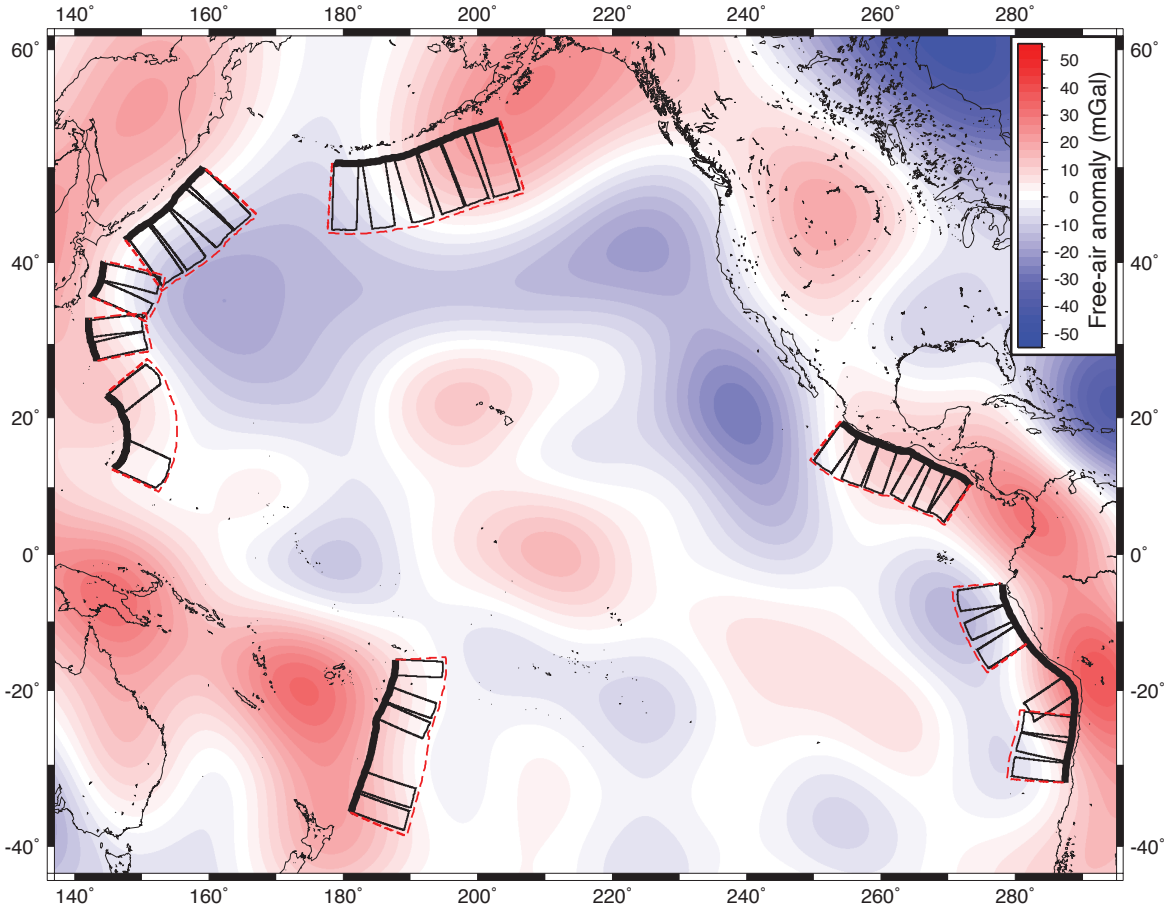

Figure 2.7: Long-wavelength gravity anomalies of the Pacific Ocean, synthesized from EGM2008 spherical harmonic coefficients up to and including degree and order 16. Trench axes are shown in thick black, segment-bins in thin black and trench-bins in red dash.

$\sim$ 400–500 km at older trenches. This suggests that the flexural rigidity of the lithosphere increases with age. Figure 2.8c shows that there is also a general increase with plate age in the distance from the trench axis to the first flexural node, x_0. For example, for lithosphere younger than 80 Ma, the mean x_0 is 55 ± 14 km and 41 ± 6 km from gravity and bathymetry respectively, whilst for older lithosphere, it is 72 ± 7 km and 67 ± 17 km respectively. This is another indication that there is an increase in flexural rigidity with age. However, we note that there is scatter in the increase in x_0 with age; for example, values at the Peru-Chile and Tonga-Kermadec trenches appear anomalously high. This could be because there are factors other than plate age that significantly affect the flexural rigidity and/or that x_0 is also influenced by factors other than the flexural rigidity.

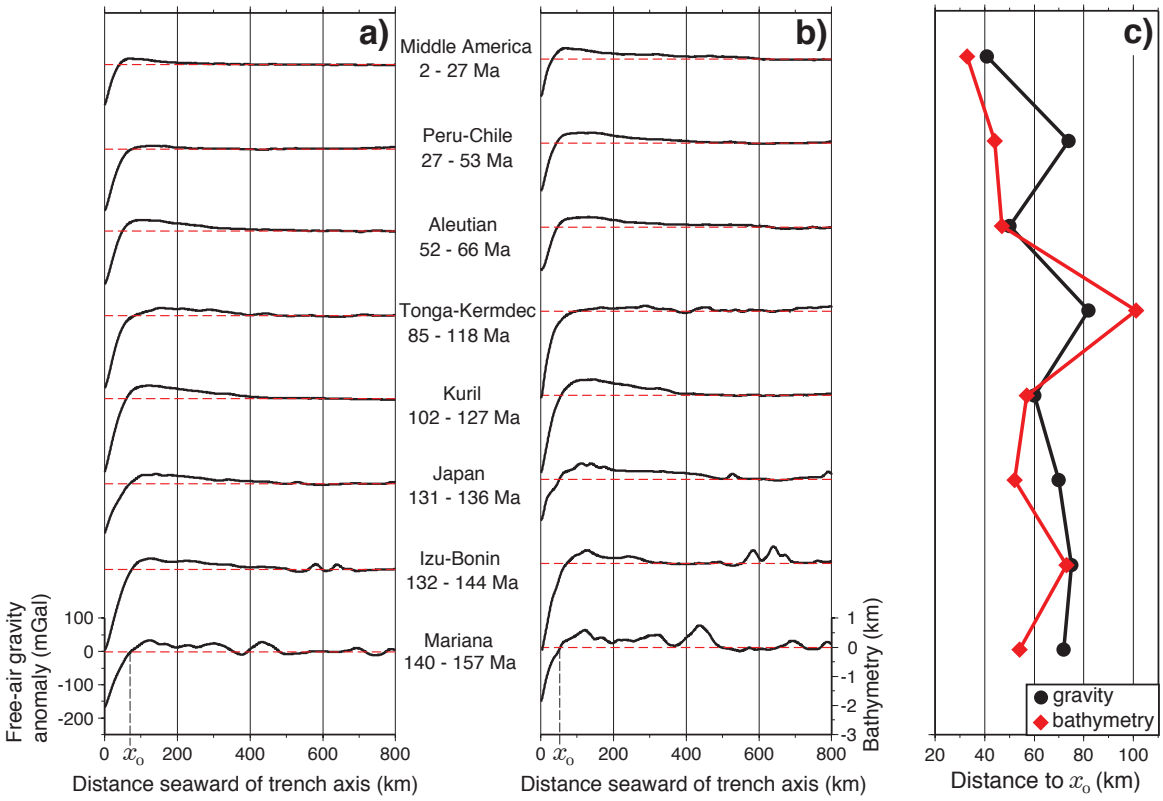

Figure 2.8: Corrected trench-bin ensemble-averaged profiles of (a) free-air gravity and (b) bathymetry, ordered from top to bottom with increasing age of the subducting plate. (c) Distance from the trench axis to the first flexural node, x_0, from the gravity and bathymetry profiles shown in Figures 2.8a and 2.8b respectively.

2.6 Chapter summary

In this chapter, we have described the generation of ensemble-averaged, trench-normal profiles of gravity and bathymetry at the trench-outer rise system of circum-Pacific subduction zones. The key points are as follows:

- Ensemble-averaged profiles were calculated in order to suppress short-wavelength noise, such as seamounts and fracture zones, whilst enhancing the long-wavelength flexural signal associated with plate subduction.

- Ensemble-averaged profiles were calculated for two different bin sizes. The trench-bins encompass entire trenches and were used primarily to investigate the relationship between T_e and plate age. The segment-bins sub-divide each trench into segments and

were additionally used to investigate along-trench T_e variations.

- Gravity and bathymetry data were corrected for the effect of plate cooling, and gravity data also for the long-wavelength highs associated with subducted slabs.

- There is a general increase with plate age in the flexural wavelength of circum-Pacific trench-outer rise systems. This suggests that the flexural rigidity increases with age.

Chapter 3

Flexure and gravity modelling

In the previous chapter, we described the generation of ensemble-averaged profiles of free-air gravity at the trench-outer rise system of circum-Pacific subduction zones. In this chapter, we will describe the elastic plate model and gravity model that were used to model these profiles.

3.1 Elastic plate model

Flexure of the lithosphere is commonly modelled as the flexure of a thin elastic plate overlying an inviscid substrate, where the plate thickness is small compared to the radii of plate curvature and the vertical deflections are small compared to the thickness of the plate (e.g., Turcotte and Schubert, 1982; Watts, 2001). In the theory of thin elastic plates undergoing small deflections, the following assumptions are made (Timoshenko et al., 1959):

1. There is no deformation in the middle plane of the plate, known as the 'neutral surface'.
2. Points initially lying on a normal to the neutral surface remain on this normal after bending. This means that axial (horizontal) shear stresses can be neglected.
3. Normal stresses acting perpendicular to the surface of the plate can be neglected.

As illustrated in Figure 3.1, flexure at the trench-outer rise system of subduction zones is commonly modelled using a broken (semi-infinite) elastic plate undergoing cylindrical (2-D)

bending, where the plate-break is located at the trench axis. This is the approach adopted in this study. In this section, we will first derive the fourth order differential equation for an elastic plate undergoing cylindrical bending and will then describe the solution to this equation for the case of a broken elastic plate. As shown in Figure 3.1, our coordinate system is such that the x direction is normal to the trench axis, z is parallel to it, and y is normal to the surface of the plate.

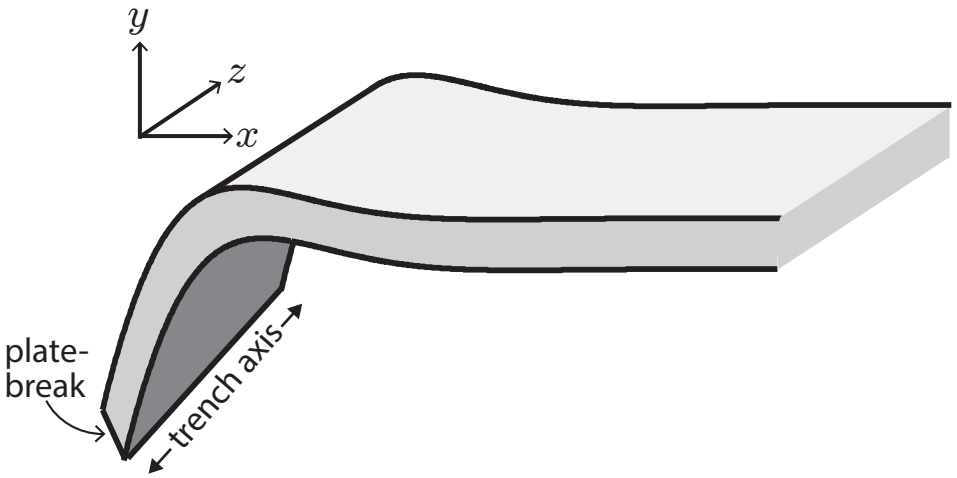

Figure 3.1: Illustration of broken elastic plate undergoing cylindrical bending, and the coordinate system used in this study.

3.1.1 Cylindrical bending model

We note that this section is heavily indebted to the work of Turcotte and Schubert (1982).

The cylindrical bending model assumes that the plate is infinite in the trench-parallel direction and that there is no strain in this direction. This is reasonable because in nature, in general, the magnitude of strain in the trench-parallel direction is very small compared to that in the trench-normal direction. We note that this might not be the case in regions of highly arcuate trench geometry or highly oblique plate convergence, which we will discuss later in this thesis.

When an elastic plate (undergoing cylindrical bending) is loaded with forces and/or

torques, bending moments, $M(x)$, and vertical shear forces, $V(x)$, are created throughout the plate that ensure that it is in equilibrium. As illustrated in Figure 3.2, we adopt the sign convention used by McAdoo et al. (1978), where a positive bending moment acts to extend the top fibres of the plate and a positive shear force acts to rotate an element of the plate clockwise. Let us consider the forces and torques acting on a small element of the plate during cylindrical bending, as shown in Figure 3.2. F is any axial (horizontal) force, which is positive for tension and assumed to be self-equilibrating ($\frac{\mathrm{d}F}{\mathrm{d}x} = 0$), and $q(x)$ is the upwards force per unit area exerted by any distributed vertical load the plate is required to support. Note that $M(x)$, $V(x)$, $q(x)$ and F are all per unit length in the z direction. A balance of forces in the vertical direction yields:

$$q(x)\mathrm{d}x - \mathrm{d}V = 0 \tag{3.1}$$

where $\mathrm{d}x$ is the width of the element. Differentiating with respect to x gives:

$$q(x) - \frac{\mathrm{d}V}{\mathrm{d}x} = 0 \tag{3.2}$$

A balance of the torques acting on the element yields:

$$\mathrm{d}M + F\mathrm{d}w + V\mathrm{d}x = 0 \tag{3.3}$$

where w is the vertical deflection of the plate and is positive upwards, and $\mathrm{d}w$ is the vertical deflection across the small plate element. Differentiating with respect to x gives:

$$\frac{\mathrm{d}M}{\mathrm{d}x} + F\frac{\mathrm{d}w}{\mathrm{d}x} + V = 0 \tag{3.4}$$

Differentiating Equation 3.4 with respect to x and substituting Equation 3.2 gives:

$$\frac{\mathrm{d}^2M}{\mathrm{d}x^2} + F\frac{\mathrm{d}^2w}{\mathrm{d}x^2} + q(x) = 0 \tag{3.5}$$

When this equation is applied to oceanic lithosphere, the distributed load, $q(x)$, is comprised of two components:

$$q(x) = -(\rho_m - \rho_w)gw + q_s(x) \tag{3.6}$$

where: ρ_m is mantle density; ρ_w is seawater density; g is the acceleration due to Earth's gravity; $-(\rho_m - \rho_w)gw$ is the upwards restoring force per unit area that acts on the plate due to the density contrast between mantle and seawater; and $q_s(x)$ is the upwards force per unit area from any distributed load on the surface of the plate, such as sediments. Substituting Equation 3.6 into Equation 3.5 gives:

$$\frac{\mathrm{d}^2 M}{\mathrm{d}x^2} + F\frac{\mathrm{d}^2 w}{\mathrm{d}x^2} - (\rho_m - \rho_w)gw + q_s(x) = 0 \tag{3.7}$$

This is the differential equation for an elastic oceanic lithospheric plate overlying an inviscid mantle substrate.

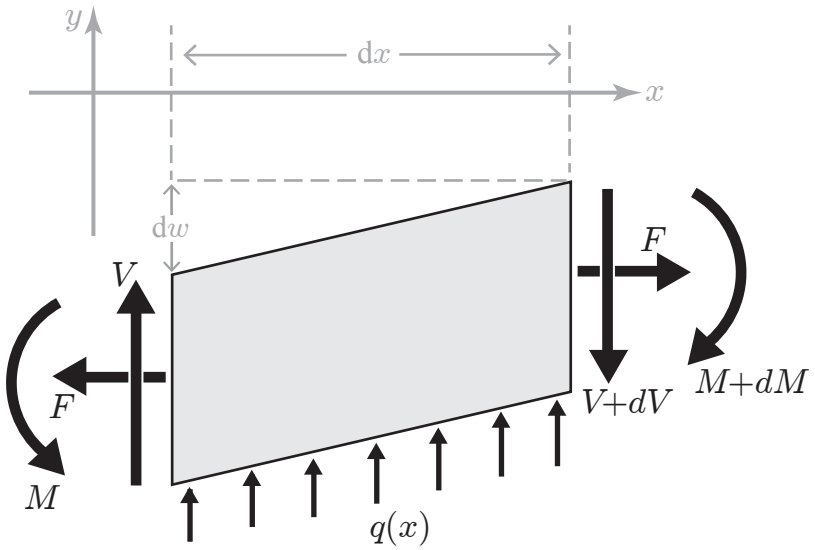

Figure 3.2: Forces and torques acting on a small element of a thin elastic plate during cylindrical bending.

In order to solve Equation 3.7 for the vertical deflection of the plate, w, we must relate the bending moment, M, to w. As illustrated in Figure 3.3, bending creates normal fibre stresses in the plate, σ_{xx}, which for convex upwards bending are tensional in the upper half of the plate and compressional in the lower half. The magnitude of these stresses increases from zero at the neutral surface to a maximum at the top and bottom of the plate. The fibre stress acting on each depth-element of the plate exerts a torque about the neutral surface and

the sum of these torques gives the bending moment:

$$M = \int_0^{T_e} \sigma_{xx}(y - y_n)\,\mathrm{d}y \tag{3.8}$$

where y_n is the depth of the neutral surface and T_e is the thickness of the plate, which is generally termed the 'effective elastic thickness' when applied to lithospheric deformation. At this point, it is important to stress that T_e does not reflect the physical thickness of the lithosphere, or the depth to any physical or petrological boundary. It is simply the thickness of an elastic plate that responds to loading in the same manner as the lithosphere, and reflects the depth-integrated strength across the brittle, elastic and ductile deformation regimes (e.g. Burov, 2011).

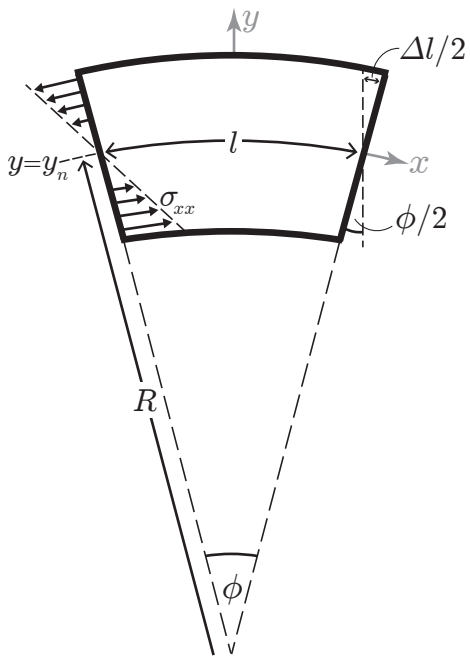

Figure 3.3: Illustration of the normal stresses, σ_{xx}, and strains, $\varepsilon_{xx} = \Delta l/l$, in an element of a thin elastic plate undergoing cylindrical bending.

As illustrated in Figure 3.3, during convex upwards bending, the upper fibres of the plate are extended and the lower fibres contracted with normal strain $\varepsilon_{xx} = \Delta l/l$, where l is the original length of the plate element. Because the plate is thin, we assume $\sigma_{yy} = 0$ and because the bending is cylindrical, $\varepsilon_{zz} = 0$. This is an example of plane stress, so that σ_{xx} and ε_{xx}

are related by:

$$\sigma_{xx} = \frac{E}{1-\nu^2}\varepsilon_{xx} \tag{3.9}$$

where ν is Poisson's ratio and E is Young's modulus. Substituting Equation 3.9 into Equation 3.8 gives:

$$M = \frac{E}{1-\nu^2}\int_0^{T_e} \varepsilon_{xx}(y-y_n)\,\mathrm{d}y \tag{3.10}$$

The normal strain, ε_{xx}, increases with distance from the neutral surface and is dependent on the local radius curvature, R. From Figure 3.3, because ϕ is a small angle, we can write:

$$\begin{gathered}\Delta l = (y-y_n)\phi = (y-y_n)\frac{l}{R} \\ \varepsilon_{xx} = \frac{\Delta l}{l} = \frac{(y-y_n)}{R}\end{gathered} \tag{3.11}$$

The plate curvature, κ, is the inverse of the radius of curvature, so that:

$$\varepsilon_{xx} = (y-y_n)\kappa \tag{3.12}$$

The sign convention adopted here is such that positive curvature implies extension of the top fibres of the beam, i.e. convex upwards bending. For vertical deflections that are small compared to length over which they occur, we can write:

$$\varepsilon_{xx} = (y-y_n)\kappa = -(y-y_n)\frac{\mathrm{d}^2 w}{\mathrm{d}x^2} \tag{3.13}$$

Substituting Equation 3.13 into Equation 3.10 gives:

$$M = \frac{-E}{1-\nu^2}\frac{\mathrm{d}^2 w}{\mathrm{d}x^2}\int_0^{T_e}(y-y_n)^2\,\mathrm{d}y \tag{3.14}$$

For an elastic plate, $y_n = T_e/2$ and therefore:

$$M = \frac{-E\,{T_e}^3}{12(1-\nu^2)}\frac{\mathrm{d}^2 w}{\mathrm{d}x^2} \tag{3.15}$$

We can now define the flexural rigidity, D:

$$D = \frac{E {T_e}^3}{12(1-\nu^2)} \tag{3.16}$$

This is a measure of the resistance offered by the plate during bending, and it gives the bending moment required to flex the plate to a given curvature:

$$M = -D\frac{\mathrm{d}^2 w}{\mathrm{d}x^2} = D\kappa \tag{3.17}$$

Equation 3.17 relates the bending moment, M, to the vertical deflection of the plate, w, and is used to solve Equation 3.7. This will now be described.

3.1.2 Broken elastic plate model

To describe lithospheric flexure at the trench-outer rise system of subduction zones, a broken (semi-infinite) elastic plate model is commonly used, and this is the approach adopted here. In this model, illustrated in Figure 3.4, the plate is infinite is the seaward direction and there is a break in the plate at the trench axis, termed the 'plate-break'. At the plate-break, a bending moment M_0 and vertical shear force V_0 are applied; we will collectively refer to M_0 and V_0 as the 'end-loads'. Physically, M_0 and V_0 are the moment and shear force that exist in the lithospheric plate at the trench axis due to tectonic forces such as slab pull, collision resistance and slab suction. These end-loads account for the fact that we are modelling a continuous lithospheric plate with a broken plate.

In solving Equation 3.7 for the case of a broken plate, the boundary conditions are as follows:

$$\begin{aligned} w &\to 0 \quad \text{as} \quad x \to \infty \\ \frac{\mathrm{d}w}{\mathrm{d}x} &\to 0 \quad \text{as} \quad x \to \infty \\ M|_{x=0} &= M_0 \\ V|_{x=0} &= V_0 \end{aligned} \tag{3.18}$$

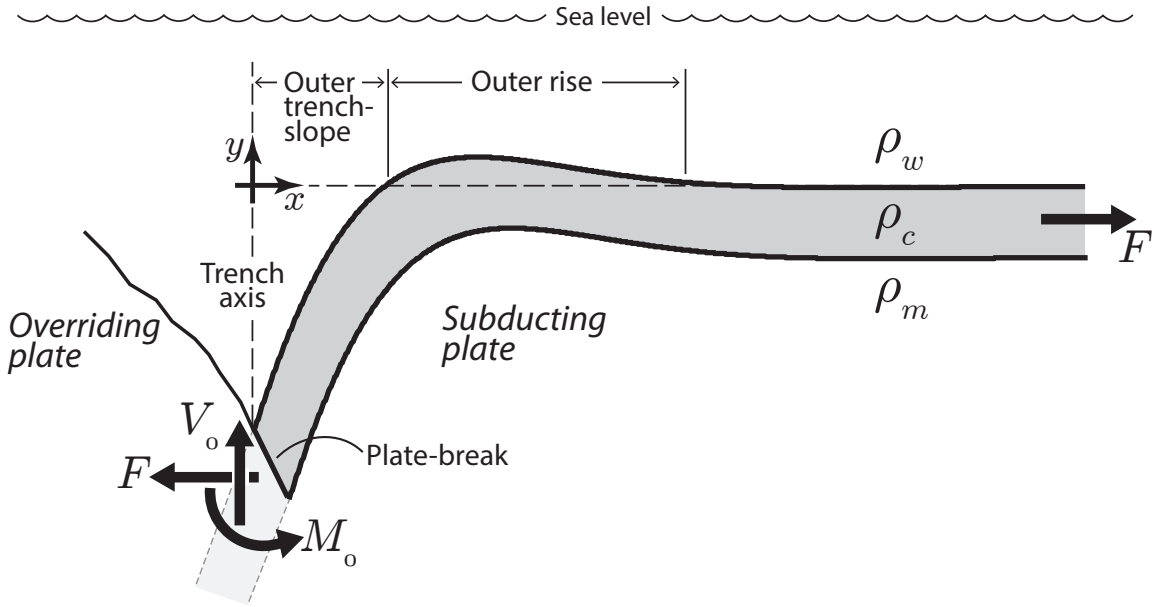

Figure 3.4: Cartoon of the broken elastic plate model that was used to model flexure at the trench-outer rise system. There is a break in the plate at the trench axis, where a bending moment M_0 and vertical shear force V_0 are applied.

If there is no distributed surface load ($q_s(x) = 0$), no axial load ($F = 0$) and the flexural rigidity, D, is constant throughout the plate, an analytical solution to Equation 3.7 can be found (Turcotte and Schubert, 1982):

$$
\begin{aligned}
w(x) &= \frac{\alpha^2 e^{-x/\alpha}}{2D}\left\{M_0 \sin\left(\frac{x}{\alpha}\right) + (\alpha V_0 - M_0)\cos\left(\frac{x}{\alpha}\right)\right\} \\
M(x) &= -e^{-x/\alpha}\left\{(\alpha V_0 - M_0)\sin\left(\frac{x}{\alpha}\right) - M_0 \cos\left(\frac{x}{\alpha}\right)\right\} \\
V(x) &= \frac{e^{-x/\alpha}}{\alpha}\left\{(2M_0 - \alpha V_0)\sin\left(\frac{x}{\alpha}\right) + \alpha V_0 \cos\left(\frac{x}{\alpha}\right)\right\}
\end{aligned}
\tag{3.19}
$$

where α is the flexural parameter:

$$
\alpha = \left[\frac{4D}{(\rho_m - \rho_w)g}\right]^{1/4} \tag{3.20}
$$

However, we solved Equation 3.7 via finite differences, as this allowed us to consider distributed surface loading, axial loading and variations in flexural rigidity. To do this, we used the method presented by Contreras-Reyes and Osses (2010). Here, making use of Equation 3.17, Equation

3.7 is written as a system of first order differential equations:

$$\begin{aligned}
\frac{\mathrm{d}w}{\mathrm{d}x} &= k_1 \\
\frac{\mathrm{d}k_1}{\mathrm{d}x} &= -\frac{M}{D(x)} \\
\frac{dM}{dx} &= k_2 \\
\frac{\mathrm{d}k_2}{\mathrm{d}x} &= \frac{FM}{D(x)} + (\rho_m - \rho_w)gw - q_s(x)
\end{aligned} \tag{3.21}$$

This can be written in condensed form as:

$$\frac{\mathrm{d}S}{\mathrm{d}x} + P(x)S = Q(x) \tag{3.22}$$

where $S = (w,\, k_1,\, M,\, k_2)^{\mathrm{T}}$, $Q(x) = (0,\, 0,\, 0,\, -q_s)^{\mathrm{T}}$ and

$$P(x) = \begin{pmatrix} 0 & -1 & 0 & 0 \\ 0 & 0 & D^{-1}(x) & 0 \\ 0 & 0 & 0 & -1 \\ -(\rho_m - \rho_w)g & 0 & -FD^{-1}(x) & 0 \end{pmatrix} \tag{3.23}$$

Equation 3.22 is discretized using centred finite differences and the finite difference system is written as a tridiagonal block matrix and solved for S using an LU decomposition solver. As illustrated in Figure 3.5, this solution was tested against the analytical solution given in Equation 3.19. For a typical trench-outer rise profile, the RMS error between the two solutions, as a percentage of the maximum deflection (PRMS error), is $< 10^{-4}$ %. As illustrated in Figure 3.6, the finite difference solution was also tested against the analytical solution for a broken elastic plate loaded by a distributed rectangular load (Hetényi, 1946), where the PRMS error between the two solutions is $< 10^{-2}$ %. In addition, the finite difference solution was tested against Hetényi's (1946) solution for a broken elastic plate loaded by a vertical shear force and an axial load, where the PRMS error is $< 10^{-4}$ %.

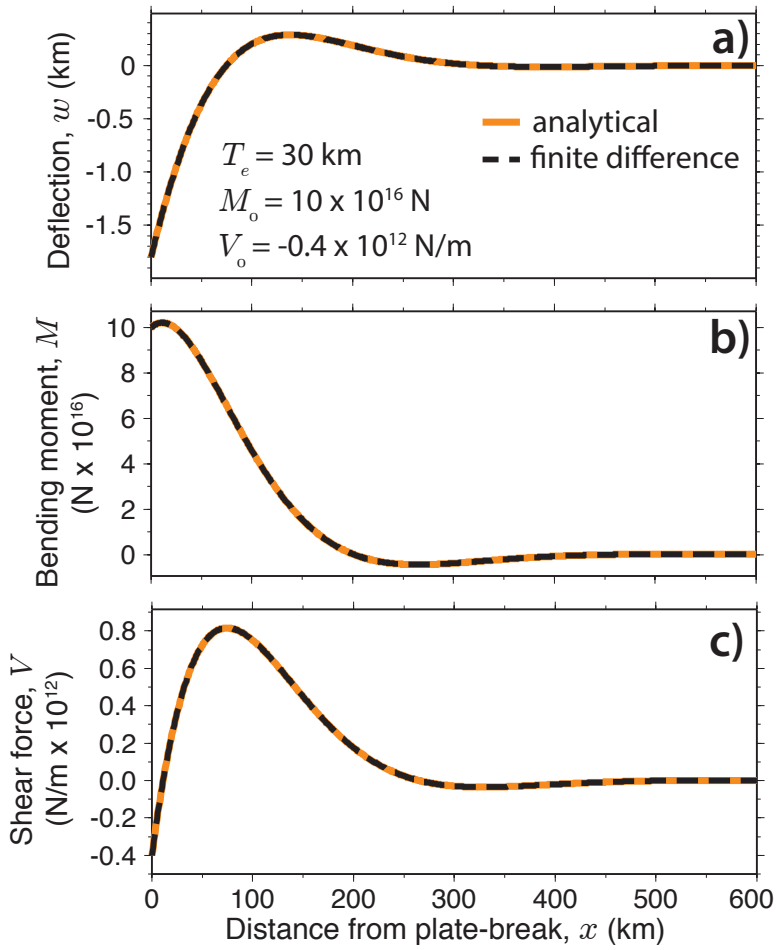

Figure 3.5: Comparison between analytical and finite difference solutions for a broken elastic plate with a bending moment M_0 and vertical shear force V_0 applied at the plate-break. (a) shows the plate deflection, (b) shows the bending moment and (c) shows the vertical shear force.

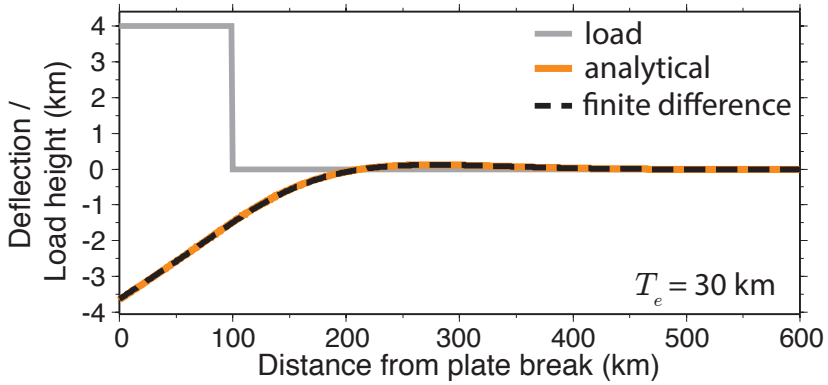

Figure 3.6: Comparison between analytical (Hetényi, 1946) and finite difference solutions for a broken elastic plate loaded by a rectangular end load.

3.1.3 Axial loading

When modelling trench-outer rise flexure, we neglected axial loading (i.e. $F = 0$), as is common in elastic plate modelling studies (e.g., Caldwell et al., 1976; Bodine and Watts, 1979; Contreras-Reyes and Osses, 2010; Zhang et al., 2014). We believe this is a reasonable assumption; our reasoning is as follows. Torque balances (Forsyth and Uyeda, 1975; Chapple and Tullis, 1977; Hager and O'Connell, 1981), plate velocities (Forsyth and Uyeda, 1975) and intraplate stress patterns (Richardson, 1992) suggest that the motion of subducting oceanic plates is governed by the following force balance (e.g., Forsyth and Uyeda, 1975; Liu and McNally, 1993; Schellart, 2004):

$$F_{SP} - F_{SR} - F_{CR} + F_{SS} + F_{RP} - F_{BR} - F_{BD} = 0 \tag{3.24}$$

Here, the driving forces are: slab pull, F_{SP}, due to the weight of the subducted slab; slab suction, F_{SS}, which occurs when descending slabs, particularly detached lower mantle slabs, drive mantle flow that exerts shear tractions on the base of the subducting and overriding plates (Conrad et al., 2004); ridge push, F_{RP}, due to the pressure gradient caused by excess elevation at the mid-ocean ridge. The resisting forces are: slab resistance, F_{SR}, which includes the forces used to bend and unbend the slab, to overcome shear resistance between the slab and mantle, to drive slab suction, and to drive slab roll-back (e.g., Schellart, 2004; Buffett, 2006; Capitanio et al., 2009); collision resistance, F_{CR}, due to coupling between the overriding and subducting plates along the subduction fault; bending resistance, F_{BR}, which is the force required to bend the surface plate at the outer rise; basal drag, F_{BD}, which is the force required to overcome shear resistance between the surface plate and underlying asthenosphere. The net slab pull force, F_{NSP}, is the component of the slab pull force that is transmitted to the surface plate as a tensional axial force after overcoming the slab resistance and collision resistance:

$$F_{NSP} = F_{SP} - F_{SR} - F_{CR} \tag{3.25}$$

Assuming dynamic equilibrium, this must be balanced by the forces acting on the surface plate (Garcia-Castellanos et al., 2000):

$$F_{NSP} = F_{SS} + F_{RP} - F_{BR} - F_{BD} \tag{3.26}$$

Based on the force balance presented above, the maximum tensional axial force that can act on the surface plate is F_{NSP}. Numerical (Capitanio et al., 2009) and analogue (Schellart, 2004) modelling studies suggest that the maximum value of F_{NSP} that might occur in nature is $\sim 6 \times 10^{12}$ Nm^{-1}. This occurs for the thickest, densest, steepest, longest slabs (that do not reach the upper-lower mantle transition), and is an order of magnitude less than F_{SP}. As shown in Figure 3.7a, even for a relatively thin elastic plate ($T_e = 20$ km), this maximum value of F_{NSP} has only a small effect on the plate deflection for a typical trench-outer rise profile. Furthermore, one would expect that the thickest, densest slabs would be attached to the thickest, coldest, strongest surface plates, in which case this value of F_{NSP} would have an even smaller effect on the deformation. For example, Figure 3.7a shows that the effect is negligible for a plate with $T_e = 30$ km. In addition, this maximum value of F_{NSP} may be too large, as the models of Capitanio et al. (2009) and Schellart (2004) did not include the overriding plate and therefore did not account for the force required to overcome the collision resistance, F_{CR}. For example, if we assume that the subduction thrust fault has downdip length of 50–150 km (Pacheco et al., 1993) and supports shear stresses of 15–30 MPa (Zhong and Gurnis, 1994), it would require 0.75–4.5 $\times 10^{12}$ Nm^{-1} to overcome this resistance, which would further reduce F_{NSP}.

Based on the force balance presented above, the maximum compressional axial force that can act on the surface plate is $F_{SS} + F_{RP}$, which would occur in the unlikely scenario that $F_{BE}+F_{BD} = 0$. For the oldest oceanic lithosphere, the ridge push force, F_{RP}, is thought to be $\sim 3 \times 10^{12}$ N m^{-1} (Parsons and Richter, 1980). The slab suction force, F_{SS}, which drives both the subducting and overriding plates towards the trench, is less well constrained than F_{RP} and F_{NSP}, but modelling of plate velocities suggests that it is of comparable magnitude to F_{NSP} (Conrad and Lithgow-Bertelloni, 2002; Conrad et al., 2004). Thus, using the maximum value of F_{NSP} described in the previous paragraph, a reasonable estimate for the maximum compressional axial force that might occur in nature is $\sim 9 \times 10^{12}$ N m^{-1}. Figure 3.7b shows that for a relatively thin elastic plate ($T_e = 20$ km), this force has a significant effect on the plate deflection, and that for a plate with $T_e = 30$ km, the effect is smaller but non-negligible. Therefore, it might seem important to include axial loading when modelling trench-outer rise flexure. However, as suggested previously by Mueller and Phillips (1995) and as we will show

in the next chapter, if an elastic plate model is used to invert for the axial force acting on subducting lithosphere, the results are strongly biased towards tensional axial forces. Thus, any compressional force that might be acting on the lithosphere cannot be reliably constrained using the elastic plate model.

In summary, the maximum tensional axial force that might be expected to occur in nature has little effect on the deflection of a broken elastic plate. The maximum compressional force that might be expected does have a significant effect on plate deflections. However, elastic plate inversions are strongly biased towards tensional axial forces and therefore cannot be used to constrain compressional forces. Therefore, unless otherwise specified, axial loading was neglected in the elastic plate inversions presented in the following chapters.

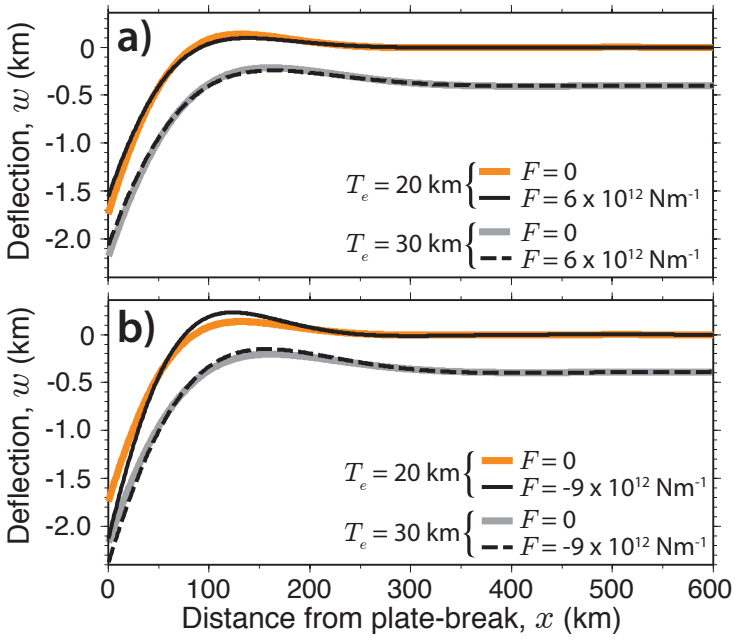

Figure 3.7: Figure showing the effect of an axial force, F, on the deflection of a broken elastic plate. (a) shows the effect of the maximum tensional axial force that might be expected to occur in nature, and (b) shows the effect of the maximum compressional axial force that might be expected to occur. Each plot show deflections for plates with $T_e = 20$ km and $T_e = 30$ km, which were calculated with $M_0 = 1 \times 10^{16}$ N and $M_0 = 5 \times 10^{16}$ N respectively, with $V_0 = 1 \times 10^{12}$ N m^{-1} in both cases.

3.2 Gravity model

In order to model the observed trench-outer rise gravity profiles, calculated elastic plate deflections had to be converted to gravity anomalies. To do this, we used the method of Bott (1969), which is illustrated in Figure 3.8. This is an exact method that calculates the gravity anomaly for a polygon, which extends to infinity into and out of the plane of the figure, by summing the anomalies for a series of semi-infinite slabs, infinite in the positive x direction, with edges defined by the edges of the polygon. The gravity anomaly for each slab is given by (Heiland, 1940, p. 153):

$$\Delta g_i = -2G\Delta\rho \{ - [x_i \sin\theta_i + y_i \cos\theta_i] [\sin\theta_i \log(r_{i+1}/r_i) + \cos\theta_i(\phi_{i+1} - \phi_i)] + y_{i+1}\phi_{i+1} - z_i\phi_i \} \quad (3.27)$$

where G is the gravitational constant; $\Delta\rho$ is the density contrast of the body; x_i and y_i are positions of the polygon's vertices relative to the observation point, P; r_i is the distance between the vertices and P; and the angles, θ_i and ϕ_i, are as shown in Figure 3.8. Going clockwise round the body, this formula takes a negative sign if the depth increases between x_i and x_{i+1}, and a positive sign if the depth decreases. Thus, by summing the anomalies from all of the slabs, the regions outside of the polygon cancel, leaving only the gravity anomaly due to the material inside the polygon:

$$\Delta g = \sum_{i=1}^{N} \Delta g_i \quad (3.28)$$

where N is the number of vertices. As shown in Figure 3.9, we tested this method against the analytical solution for the gravity anomaly over a buried cylinder, and they agree with a PRMS error of $< 10^{-2}$ %.

The method of Bott (1969) is well suited to calculating trench-outer rise gravity anomalies because, unlike the line integral method of Talwani et al. (1959), it does not require a closed polygon. As illustrated in Figure 3.10b, for a trench-outer rise flexure profile, the method of Bott (1969) can be used to sum the anomalies for a series of semi-infinite slabs, with edges

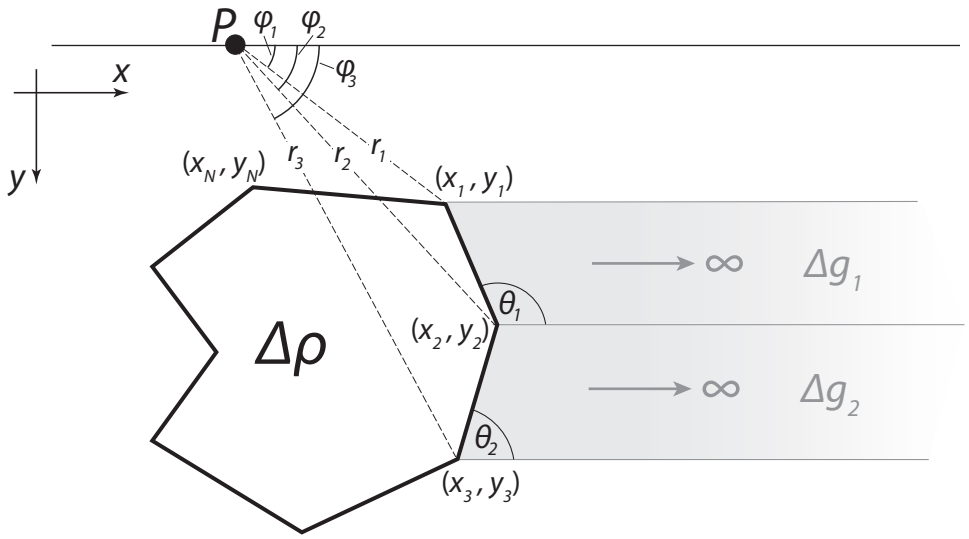

Figure 3.8: Illustration of the gravity calculation method of Bott (1969). The total anomaly is obtained by summing the anomalies due to a series of semi-infinite slabs with edges defined by the edges of the polygon.

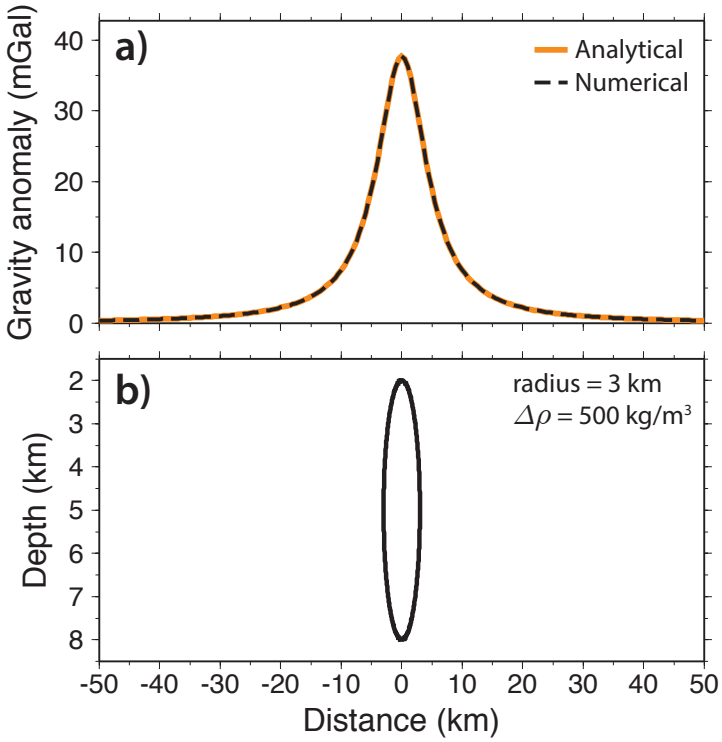

Figure 3.9: (a) Comparison between analytical and numerical gravity anomalies over a buried cylinder, shown in (b).

defined by the seafloor/moho, that extend to infinity in the seaward direction. Then, by vertically shifting the calculated gravity anomaly so that $\Delta g \to 0$ as $x \to \infty$, we obtain the anomaly relative to the abyssal plain. As shown in Figure 3.10, we tested this method against the method of Levitt and Sandwell (1995) for a typical trench-outer rise flexure profile. Their method is based on the first order terms of Parker's (1973) expansion and is equivalent to a Bouguer slab formula with an approximate reduction in amplitude due to the upward continuation of a constant wavelength ($2\pi\alpha$) signal from a mean depth, d:

$$\Delta g = 2\pi G w \Delta\rho \exp\left(\frac{-d}{\alpha}\right) \tag{3.29}$$

As shown in Figure 3.10 the gravity anomalies calculated by the the two methods are in good agreement, with a PRMS error of < 1 %. Note that this error is non-negligible, but this is because the method of Levitt and Sandwell (1995) is an approximate one, whilst the method of Bott (1969) is exact.

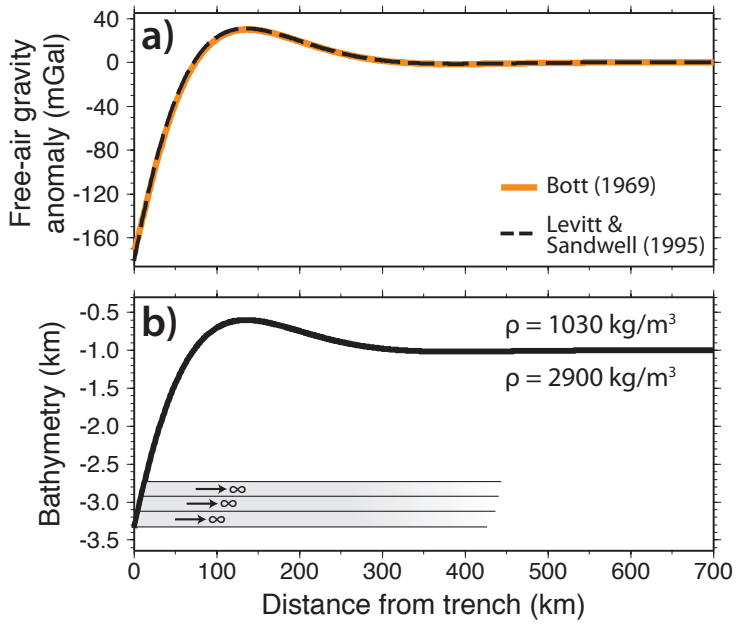

Figure 3.10: Comparison between trench-outer rise gravity anomalies calculated using the methods of Bott (1969) and Levitt and Sandwell (1995). The gravity anomalies, shown in (a), due to the bathymetry shown in (b) were calculated with a density contrast typical of that between oceanic crust and seawater. The grey shade illustrates the semi-infinite slabs that are used to calculate the gravity anomaly in the method of Bott (1969).

3.2.1 Modelling observed trench-outer rise gravity anomalies

When modelling the observed circum-Pacific trench-outer rise gravity anomalies, we accounted for the anomalies arising from the seafloor (sediment/seawater density contrast), the top of the crust (crust/sediment) and the Moho (mantle/crust). As illustrated in Figure 3.11, the gravity anomalies were calculated as follows:

1. The elastic plate deflection due to the end-loads M_0 and V_0 was calculated; the assumed elastic constants are given in Table 3.1. In this calculation, we accounted for seafloor sediments by including a distributed sediment load that was ensemble-averaged from the observed sediment thickness grid of Divins (2003).

2. The gravity anomaly arising from the seafloor and the top of the crust were calculated as follows. The observed sediment thickness was added to the calculated elastic plate deflection. The resultant deflection was then vertically shifted so that the abyssal depth was equal to the observed abyssal seafloor depth, which was taken as the mean ensemble-averaged bathymetry 500–800 km from the trench axis. The gravity anomaly from the top of the sediment (i.e. the seafloor) was then was calculated with $\Delta\rho = \rho_s - \rho_w$, and the anomaly from the top of the elastic plate (i.e. the top of the crust) was calculated with $\Delta\rho = \rho_c - \rho_s$. Here, ρ_c, ρ_s and ρ_w are the density of oceanic crust, sediment and seawater respectively; the assumed densities are given in Table 3.1.

3. The gravity anomaly arising from the Moho was calculated as follows. The calculated elastic plate deflection was vertically shifted so that the abyssal depth was equal to the observed abyssal Moho depth. This observed depth was taken as the sum of the mean ensemble-averaged bathymetry and mean crustal thickness 500–800 km from the trench axis, where the crustal thickness was ensemble-averaged from the CRUST2.0 grid (Bassin, 2000). The gravity anomaly from this interface was then calculated with $\Delta\rho = \rho_m - \rho_c$, where ρ_m is the density of mantle.

4. The calculated anomalies from the seafloor, top of the crust and Moho were summed to give the total calculated gravity anomaly. This could then be compared to the observed ensemble-averaged gravity profile.

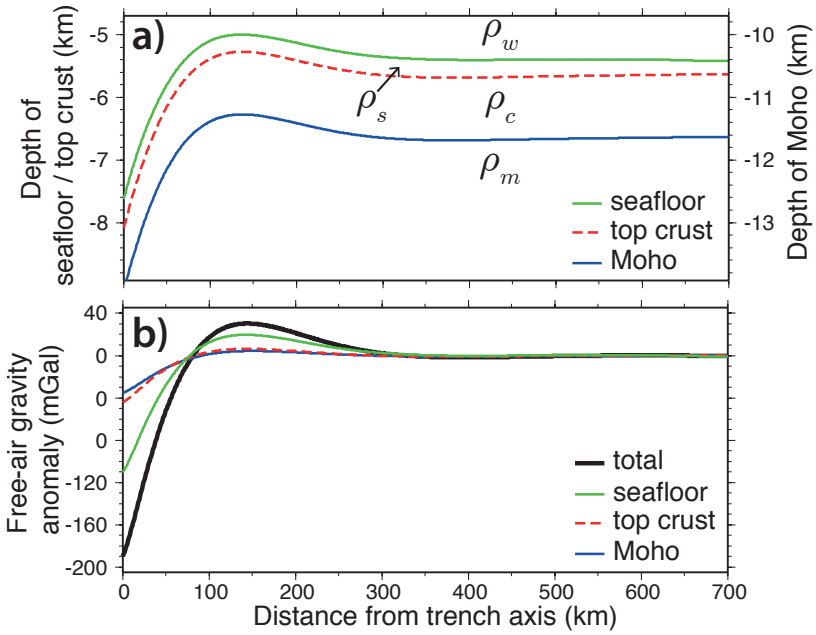

Figure 3.11: Figure illustrating the calculation of gravity anomalies when modelling observed trench-outer rise profiles. (a) shows the density contrasts that were included the calculation—the seafloor, the top of the crust, the Moho—and illustrates the density in each layer. (b) shows the gravity anomalies arising from each of these density contrasts. These anomalies were summed to give the total anomaly, shown in black.

Symbol	Description	Value
g	acceleration due to Earth's gravity	$9.81\ \mathrm{m\,s^{-2}}$
G	gravitational constant	$6.67 \times 10^{-11}\ \mathrm{m^3\,kg^{-1}\,s^{-2}}$
E	Young's modulus	100 GPa
ν	Poisson's ratio	0.25
ρ_w	seawater density	$1030\ \mathrm{kg\,m^{-3}}$
ρ_s	sediment density	$2400\ \mathrm{kg\,m^{-3}}$
ρ_c	oceanic crust density	$2900\ \mathrm{kg\,m^{-3}}$
ρ_m	mantle density	$3330\ \mathrm{kg\,m^{-3}}$
T_t	thermal lithosphere thickness	125 km
M_t	temperature at base of thermal lithosphere	1350 °C
α	thermal diffusivity of the lithosphere	$8 \times 10^{-7}\ \mathrm{m\,s^{-2}}$

Table 3.1: The densities and gravitational, elastic and thermal constants that were assumed in this study. The thermal constants are from the plate cooling model of Parsons and Sclater (1977).

3.3 Chapter summary

In this chapter, we have described the elastic plate model and the gravity model that were used to model the observed free-air gravity at the trench-outer rise system of circum-Pacific subduction zones. The key points are as follows:

- Trench-outer rise flexure was modelled using a broken elastic plate undergoing cylindrical bending, where the plate-break was located at the trench axis. A bending moment M_0 and vertical shear force V_0 were applied at the plate-break. These end-loads account for the moment and shear force that exist in the lithospheric plate at the trench axis due to tectonic forces such as slab pull, collision resistance and slab suction.

- Axial loading was neglected in this study because elastic plate inversions are strongly biased towards tensional axial forces, and the maximum tensional force that might be expected to occur in nature has little effect on elastic plate deflections.

- Gravity anomalies were calculated using the method of Bott (1969). The anomalies arising from the seafloor, top of the crust and Moho were calculated and then summed to give the total anomaly.

Chapter 4

Inversion methodology and synthetic testing

In the previous chapters, we described the generation of ensemble-averaged profiles of free-air gravity at the trench-outer rise system of circum-Pacific subduction zones, and the elastic plate model and gravity model that were used to model these observations. In this chapter, we will first describe the inversion methodology that was used to find the T_e and end-loads, M_0 and V_0, that best fit the observed profiles. We will then describe how this methodology was tested by inverting a synthetic dataset.

4.1 Inversion methodology

The aim of the inversion was to find the T_e and end-loads that best fit the observed ensemble-averaged gravity profiles. We were most interested in investigating the relationship between T_e and plate age and thus required a robust estimate of the uncertainty in T_e. Therefore, T_e was iterated from 2 to 80 km in steps of 1 km, and three parameters were optimized at each iteration: M_0, V_0 and a vertical shift, c. The best-fit optimization parameters were found using *MPFIT* (Markwardt, 2009), a damped least squares algorithm based on the *MINPACK* program (Moré, 1978). This algorithm seeks the parameters that minimise the objective

function:

$$F_{obj}(\beta) = \sum_{n=1}^{N} [\Delta g_n - \Delta \hat{g}_n(\beta)]^2 \tag{4.1}$$

where $\beta = (M_0, V_0, c)$ are the optimization parameters; Δg_n is the observed gravity anomaly at the nth point in the profile; $\Delta \hat{g}_n(\beta)$ is the calculated anomaly at the nth point in the profile; and N is the number of points in the profile. Throughout this thesis, we will present F_{obj} as the RMS error between the observed and calculated gravity anomalies, Δg_{rms}:

$$\Delta g_{rms} = \sqrt{\frac{F_{obj}}{N}} \tag{4.2}$$

The efficiency of the optimization was maximised by scaling the optimization parameters so that their final magnitude was in the range $0 \rightarrow 1$, and by scaling F_{obj} so that its final value was in the range $0 \rightarrow 1$. The optimization requires an initial guess at β, but we carried out tests with a number of different initial guesses and found that it has no effect on results. This suggests that the optimization finds a global, rather than local, minimum and this will be proven further in the next chapter.

4.1.1 Uncertainty in T_e

After iterating over the T_e values and optimizing β at each iteration, the best-fitting T_e is that which gives the minimum Δg_{rms}, as illustrated in Figure 4.1. By iterating over a range of T_e values, the uncertainty in T_e could also be estimated. Following Bry and White (2007), the upper and lower bounds on T_e were defined as the values at which Δg_{rms} exceeds 1.25 times the minimum Δg_{rms}, as illustrated in Figure 4.1. Inversion of synthetic data suggests that this is a reasonable criterion, as will be discussed in Section 4.2.3.

4.1.2 Optimization constraints

We attempted to use geophysical observations and synthetic modelling to place constraints on the optimization parameters, β, prior to inversion, as this would increase the resolution of T_e estimates. We will now review the evidence that was used to place constraints on the bending moment and vertical shear force at the trench axis, M_0 and V_0.

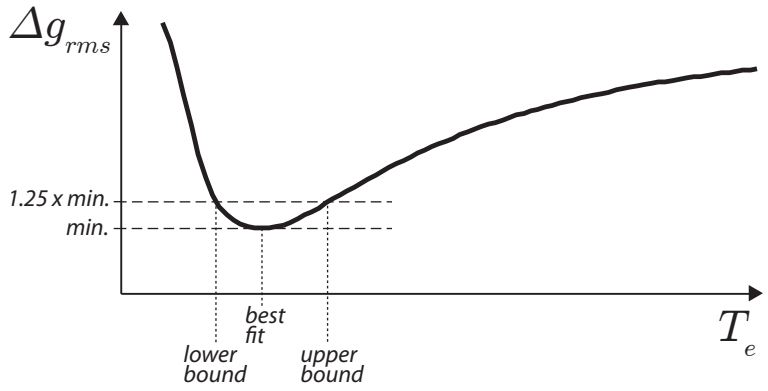

Figure 4.1: Illustration of how the uncertainty in T_e was estimated. The upper and lower bounds on T_e were defined as the values at which Δg_{rms} exceeds 1.25 times the minimum Δg_{rms}.

4.1.2.1 Constraints on M_0

Equation 3.17 shows that for an elastic plate, the bending moment is proportional to the plate curvature. Therefore, observations of the curvature of the subducting plate near the trench axis may be used to constrain M_0. Unfortunately, it is difficult to estimate the plate curvature directly from bathymetry, as it is sensitive to small fluctuations in depth. However, several lines of evidence suggest that the curvature is positive at the trench axis—that is, that the shallow lithosphere is in tension and the plate is bent convex upwards—and therefore that M_0 must be positive. This evidence will now be reviewed.

Outer trench-slope seismicity: Global studies of seismicity reveal that shallow, normal-faulting earthquakes are a ubiquitous feature of the outer trench-slope and outer rise, extending to depths of up to 30 km (Chapple and Forsyth, 1979; Christensen and Ruff, 1988; Craig et al., 2014a). These events are attributed to the convex upwards bending of the lithosphere, which is reflected in the geometry of the outer rise and outer trench-slope. This bending also causes deeper compressional events that are separated from the shallow tensional events by an aseismic elastic core, but the compressional events are less common due to the ductile nature of deformation at these depths. Shallow compressional events are very rare and where they have been observed, they occur very close to the trench axis. It has been suggested that these events are not caused by plate bending, but may be a result of increased axial compression

late in the megathrust seismic cycle in regions of high interplate coupling (Christensen and Ruff, 1988; Mueller et al., 1996b), or reactivation of extensional bend-faults as they encounter the resistance of the overriding plate (Massell, 2002). There are few observations of intraslab seismicity immediately landward of the trench axis, but shallow tensional events at the Middle America (Ranero et al., 2005), southern Chile (Tilmann et al., 2008), central Aleutian (Frohlich et al., 1982), and Japan (Yoshii, 1979) trenches suggest that the shallow lithosphere remains in tension immediately following subduction. All of these observations suggest that the shallow plate is in tension at the trench axis, and therefore that the plate curvature is positive. If the plate had unbent to negative curvature prior to subduction, shallow compressional seismicity would occur frequently, which is not observed.

Outer trench-slope bend-faulting: Outer trench-slopes commonly display normal faulting that is parallel or sub-parallel to the trench axis, whilst thrust faults are very uncommon. This faulting is consistently attributed to the convex upwards bending of the lithosphere (e.g., Masson, 1991; Kobayashi et al., 1998; Massell, 2002; Ranero et al., 2003; Grevemeyer et al., 2005; Ranero et al., 2005). A few thrust faults have been observed at the trench axis of the Chile trench, but it has been suggested that these are horst blocks that are reactivated as thrust faults when they encounter the resistance of the overriding plate (Massell, 2002). Once again, these observations suggest that the shallow plate is in tension at the trench axis, and therefore that the plate curvature is positive.

Intraslab seismicity: Intraslab seismicity provides an image of the subducted slab. Several authors have used these images to show that the dip of the plate increases from a few degrees at the outer trench-slope, to 10–20° along the interplate interface, to 30–65° at depths of 75–100 km (e.g., Engdahl and Scholz, 1977; Isacks and Barazangi, 1977; Bevis, 1986). As the plate curvature is the first derivative of the slope, this indicates that the subducting plate/slab has positive curvature between the outer rise and depths of 75–100 km..

Active-source seismic velocity models: We visually examined the active-source seismic velocity models across subduction zones that were used in the construction of *Slab1.0* (Hayes

et al., 2012, reference list at `http://earthquake.usgs.gov/data/slab/#refs`). These models show that the dip of the subducting plate always increases landward from the outer trench-slope to the interplate interface. This corroborates the findings from intraslab seismicity and once again suggests that the subducting plate has positive curvature at the trench axis. Two examples of these velocity models are shown in Figure 4.2.

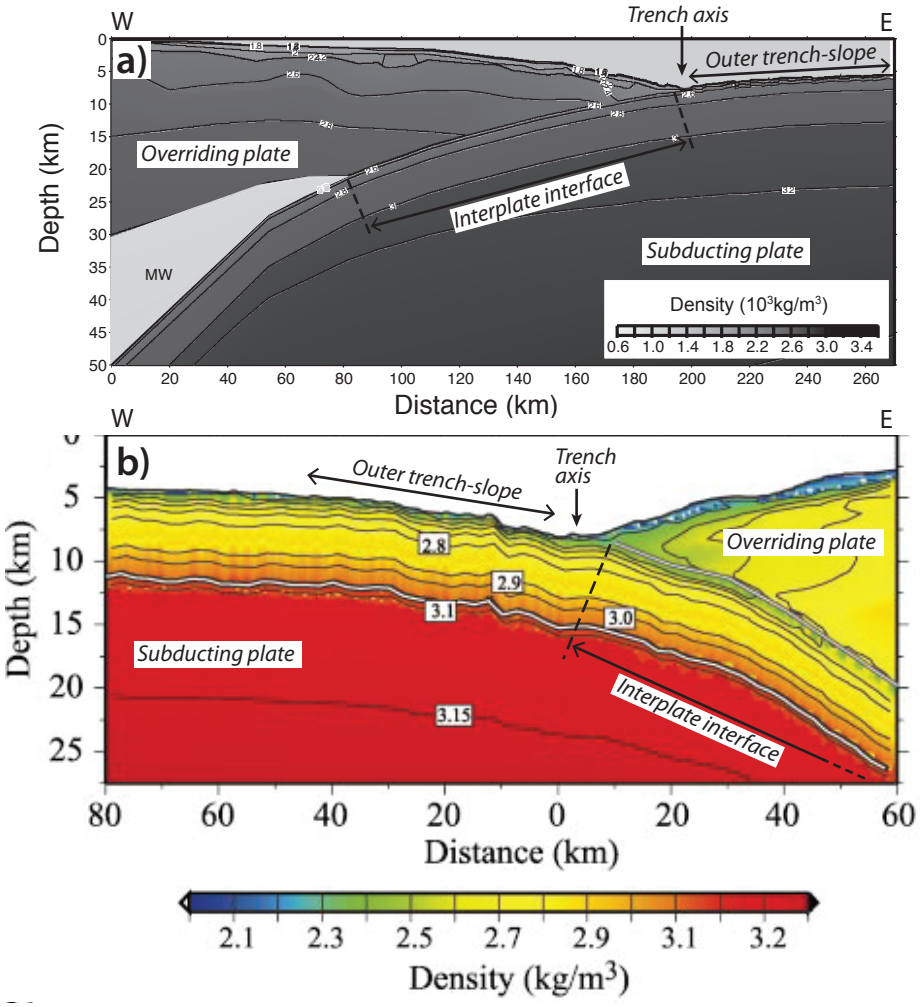

Figure 4.2: Active-source seismic velocity models from the (a) central Japan and (b) north Chile trenches, modified from Miura et al. (2005) and Ranero and Sallares (2004) respectively.

Synthetic modelling: We conducted a series of synthetic models to test if the bending moment at the trench axis, M_0, is likely to be positive. As illustrated in Figure 4.3a, a broken elastic plate was loaded with a trapezoidal end load to simulate the effect of the overriding plate, and a bending moment M_s was applied at the plate-break to simulate the moment that

exists in the subducted slab at depth. As illustrated in Figure 4.3b, the bending moment at the edge of the trapezoidal load, which corresponds to M_0, was then calculated for a range of T_e, M_s, load heights and load widths. We tested load heights from 2–6 km, load widths from 20–100 km, T_e from 10–70 km, and M_s to give plate curvatures ranging from 0 to 5×10^{-6} m^{-1}. Tests were conducted with plates of constant rigidity and also plates with rigidity that decreases landward of the outer rise. In total, 540 tests were run and in all cases M_0 was positive.

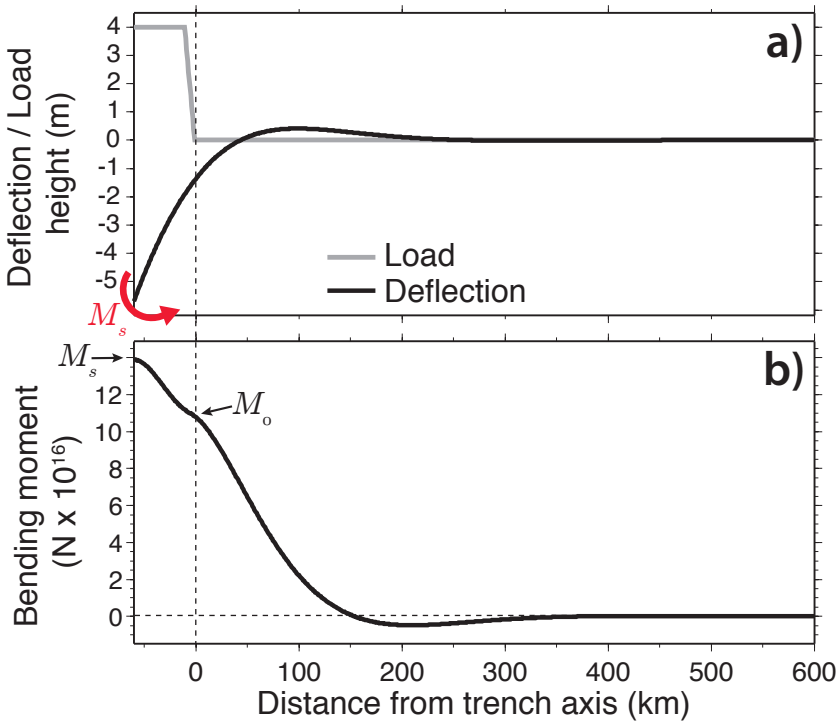

Figure 4.3: An example of the synthetic model used to constrain the bending moment at the trench axis, M_0. See text.

Summary: The evidence presented above suggests that the subducting plate has positive curvature at the trench axis, and therefore M_0 was constrained to be positive ($M_0 > 0$) in all inversions unless stated otherwise.

4.1.2.2 Constraints on V_0

It was not possible to place constraints on V_0 prior to inversion, as the geometries of the observed trench-outer rise bathymetry profiles suggest that V_0 may be either positive or negative; we show this as follows. Substituting equation 3.6 into 3.2 gives:

$$\frac{\mathrm{d}V}{\mathrm{d}x} = -(\rho_m - \rho_w)gw + q_s(x) \tag{4.3}$$

Neglecting sediment loading ($q_s(x) = 0$) and integrating both sides w.r.t. x gives:

$$\int \mathrm{d}V = -(\rho_m - \rho_w)g \int w \, \mathrm{d}x \tag{4.4}$$

Evaluating between $x = 0$ and $x = \infty$ gives:

$$V|_{x=\infty} - V|_{x=0} = -(\rho_m - \rho_w)g \int_0^\infty w \, \mathrm{d}x \tag{4.5}$$

As $\frac{\mathrm{d}w}{\mathrm{d}x}|_{x=\infty} = 0$, $V|_{x=\infty} = 0$, which gives:

$$V|_{x=0} \equiv V_0 = (\rho_m - \rho_w)g \int_0^\infty w \, \mathrm{d}x \tag{4.6}$$

The integral here is simply the area under the deflection curve; if the area bounded by the downward deflection of the outer trench-slope is greater than the area bounded by the upward deflection of the outer rise, V_0 will be negative, and vice-versa. Visual inspection of the ensemble-averaged bathymetry profiles (e.g. Figure 2.8b) shows that at some trenches, for example the Kuril, the area bounded by the outer rise is clearly larger than the area bounded by the outer trench-slope; whilst at other trenches, such as the Tonga-Kermadec, the opposite is true. Thus, the geometries of trench-outer rise bathymetry profiles suggest that V_0 may be either positive or negative.

4.2 Synthetic testing

To test the efficacy of our inversion methodology and the effect of varying profile length, we generated and inverted a suite of synthetic trench-outer rise flexure profiles. This will now be described.

4.2.1 Generating synthetic profiles

When creating the synthetic flexure profiles, the aim was to characterize the long-wavelength ($\sim$ 200–500 km) trench-outer rise flexure associated with plate subduction, as well as the short-wavelength ($\sim$ 5–100 km) noise caused by features such as seamounts, fracture zone ridges and troughs, and abyssal hill fabrics.

4.2.1.1 Trench-outer rise flexure

The first step was to create typical trench-outer rise flexure profiles by loading a broken elastic plate with end-loads. Two sets of profiles were produced. In the first set, the flexure was calculated with plates of constant rigidity; 80 of these profiles were produced with T_e randomly chosen from the range 10–80 km. In the second set, the flexure was calculated with variable rigidity plates that weaken landward of the outer rise, as illustrated in Figure 4.4a. This was to simulate any plate weakening that might occur in nature due to bending-induced inelastic yielding (e.g., Bodine and Watts, 1979; Goetze and Evans, 1979; Brace and Kohlstedt, 1980; McNutt and Menard, 1982) and mantle hydration via bend-faults (e.g., Ranero et al., 2003; Grevemeyer et al., 2005; Ranero et al., 2005; Contreras-Reyes et al., 2007). As illustrated in Figure 4.4a, 80 variable rigidity profiles were produced with plates that weaken linearly from a 'seaward T_e' to a 'landward T_e'. Seaward T_e was randomly chosen from the range 10–80 km and plate weakening from the range 30–70 %. As illustrated in Figure 4.4a, the variable T_e profile was defined so that the plate begins to weaken 100–200 km from the trench axis, which corresponds to the observed position of the outer rise peak at circum-Pacific trenches, and stops weakening close to the trench axis.

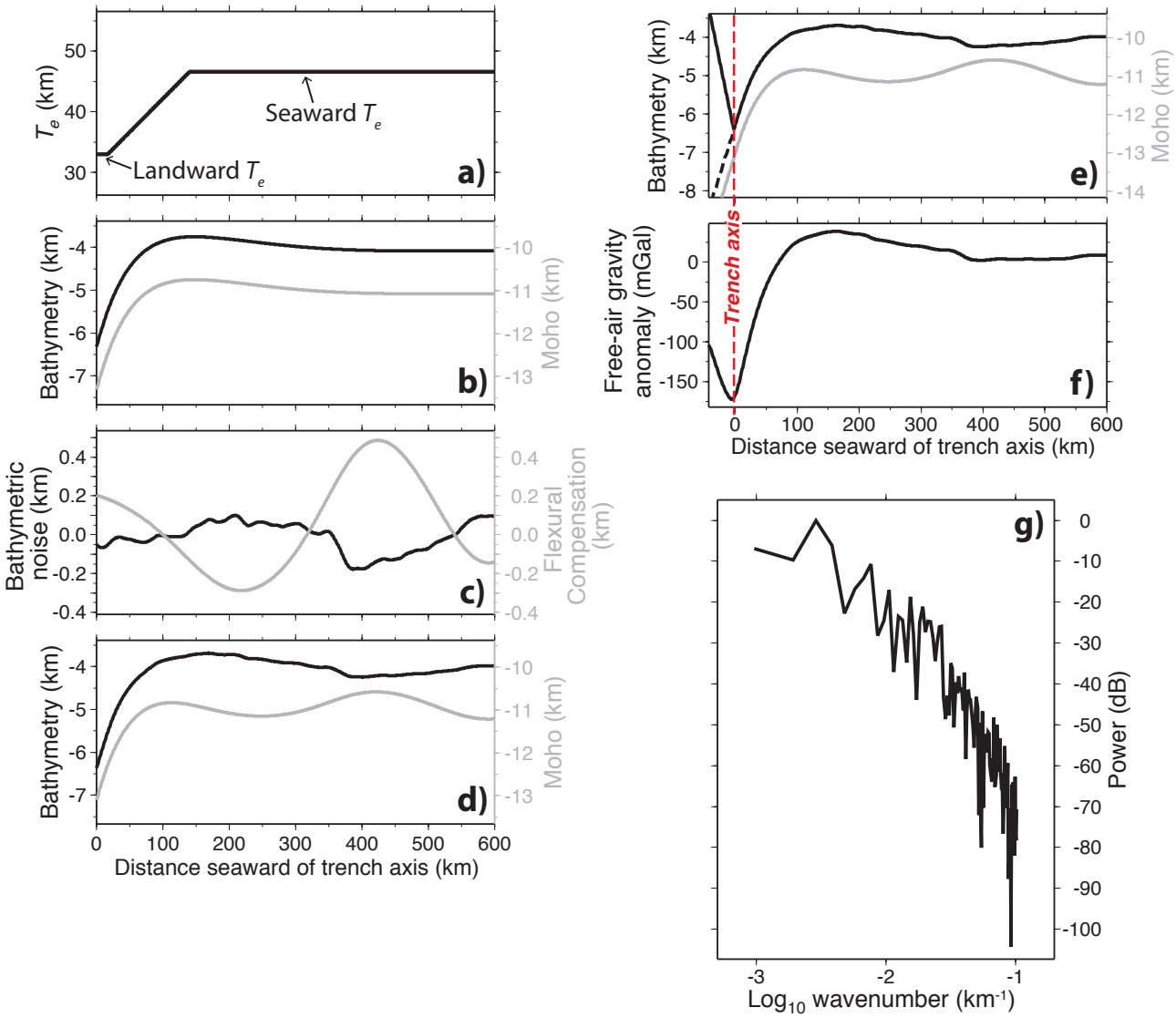

Figure 4.4: Figure illustrating the generation of synthetic gravity anomaly and bathymetry profiles. (a) A broken elastic plate was defined with constant or variable (shown) T_e. (b) A bending moment M_0 and vertical shear force V_0 were applied at the plate-break to produce a long-wavelength trench-outer rise flexure profile. This was then shifted to a typical seafloor depth (black) and Moho depth (grey). (c) Short-wavelength bathymetric noise (black) was generated using a spectral synthesis method; the corresponding synthetic power spectrum is shown in Figure 4.4g. Its flexural compensation (grey) was calculated assuming that the noise was emplaced on hot, weak lithosphere. (d) The bathymetric noise was added to the long-wavelength trench-outer rise bathymetry (black) and its flexural compensation was added to the Moho (grey). (e) The landward wall of the trench and the descent of the subducting plate beneath it were simulated for the 50 km landward of the trench axis. The dashed black line shows the top of the subducting plate, solid grey shows the Moho of the subducting plate, and solid black shows the seafloor bathymetry. (f) The free-air gravity anomalies arising from the synthetic bathymetry and Moho were calculated and then summed to give the final synthetic gravity anomaly. (g) The synthetic power spectrum corresponding to the bathymetry shown in Figure 4.4c.

The end-loads, M_0 and V_0, were chosen to give trench depths that are typical of those observed in nature. V_0 was randomly chosen from the range -1×10^{12} to 1×10^{12} N m^{-1}, as this range is typical of values found in previous trench-outer rise flexure studies (e.g., McQueen and Lambeck, 1989; Contreras-Reyes and Osses, 2010). M_0 was then randomly chosen to produce trench depths (relative to the abyssal depth) from the range 1500–3000 m.

As illustrated in Figure 4.4b, after the flexural profile was calculated, it was shifted to a typical abyssal seafloor depth to give the bathymetric deflection, and shifted again by a typical crustal thickness to give the Moho deflection, which was required to calculate the synthetic gravity anomaly. The abyssal depth was chosen randomly from the range 3500–5500 m and the crustal thickness from the range 6000–7000 m.

4.2.1.2 Short-wavelength noise

The second step was to add noise to the flexural signal to reflect short-wavelength features such as seamounts, fracture zone ridges and troughs, and abyssal hill fabrics. We wished to add synthetic noise that reflects the noise in our observed ensemble-averaged bathymetry profiles. To this end, we conducted a spectral analysis of the observed profiles and then used the results to instruct the generation of the synthetic noise. This process, as well as some of the general spectral characteristics of seafloor bathymetry, will now be described.

Spectral characteristics of bathymetry

At relatively long wavelengths ($>$ 400–500 km), seafloor bathymetry is well described by models of plate-cooling and trench-outer rise flexure, but at shorter wavelengths, it appears more random. However, at the shorter wavelengths, statistically similar bathymetric features are observed at many different length scales; this has led several authors (e.g., Bell, 1975; Barenblatt et al., 1984; Gilbert and Malinverno, 1988; Mareschal, 1989) to describe bathymetry using fractal geometry, such that its power spectrum has the form (Mandelbrot, 1983):

$$P \propto \frac{1}{f^b} \tag{4.7}$$

where P is power, f is frequency and b is a constant related to the fractal dimension, D_f:

$$D_f = \frac{5 - b}{2} \tag{4.8}$$

D_f is a measure of how the complexity of a pattern changes with the scale at which it is measured. It can be seen from Equation 4.7 that fractal geometry is characterised by a linear relationship between logarithmic frequency and logarithmic power, where b is the slope of the log-log power spectrum. Bell (1975) and Mareschal (1989) used this to show that ship track bathymetry in the Eastern Pacific has fractal geometry with a fractal dimension $D_f = 1.5$, and Barenblatt et al. (1984) found the same D_f near the Mid-Atlantic Ridge. Gilbert and Malinverno (1988) analysed a ship track flow-line in the South Atlantic, finding that the bathymetry is only well fit by a fractal geometry at short wavelengths, with a fractal dimension $D_f = 1.1$.

Spectral analysis of ensemble-averaged bathymetry

The profiles used in this study have been ensemble-averaged, so it is not clear that they will exhibit fractal bathymetry as individual ship track data appears to. Therefore, we analysed the power spectra of the segment-bin ensemble-averaged bathymetry profiles so that we could produce representative synthetic noise. As illustrated in Figure 4.5a, 800 km long profiles were analysed, extending from 500 to 1300 km seaward of the trench axis in order to exclude the long-wavelength trench-outer rise flexural signal. The power spectrum for each segment-bin profile (e.g. Figure 4.5b) was estimated using the periodogram, which estimates the power spectral density as the squared magnitude of the Discrete Fourier Transform (DFT). Prior to calculating the DFT using a Fast Fourier transform (FFT), the bathymetry was de-trended, low-pass filtered to remove signal components above the Nyquist frequency, and windowed using a cosine-tapered window (Tukey, 1967). Windowing smooths the ends of the profile to zero, ensuring that it is periodic, thus reducing spectral leakage. After the individual segment-bin spectra were calculated, they were averaged within each subduction zone to reduce the variance of the power spectrum estimates. These averaged spectra are shown in Figure 4.6.

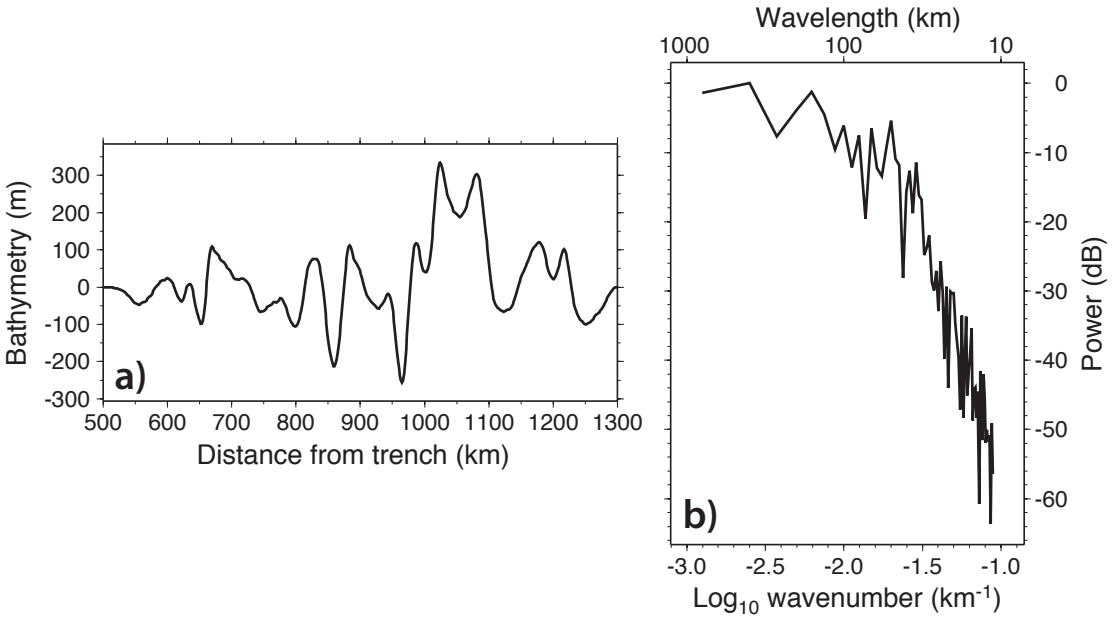

Figure 4.5: Figure illustrating the spectral analysis of ensemble-averaged bathymetry profiles. (a) De-trended, low-pass filtered, windowed ensemble-averaged bathymetry from the abyssal region of segment-bin 22 (Middle America trench). (b) The power spectrum of the bathymetry shown in Figure 4.5a, as estimated using the periodogram.

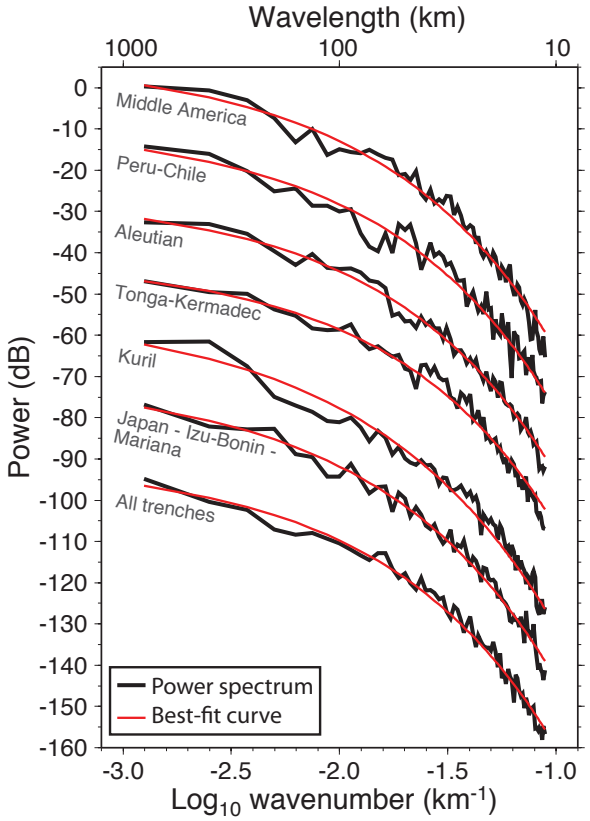

Figure 4.6: Average power spectrum estimates (black lines) for the abyssal ensemble-averaged bathymetry seaward of circum-Pacific subduction zones. Best-fit curves are shown in red; the equation that defines these curves was used in the generation of the synthetic noise profiles.

As shown in Figure 4.6, it is clear that the log-log power spectra are not well fit by a straight line, and thus the ensemble-averaged bathymetry does not have fractal geometry. The rapid falloff in power at lower wavelengths shows the advantage of ensemble-averaging: much of the short-wavelength information has been removed due to destructive interference of the Fourier spectra. Trial and error reveals that the log-log spectra are well fit by an equation of the form (red curves in Figure 4.6):

$$\log(P) \propto A.10^{B\log(f)} \tag{4.9}$$

where P is the power, f is the spatial frequency (wavenumber), and A and B are constants. Note that we do not attach any physical meaning to this equation; it simply fits the data well. The relationship between power and wavenumber is therefore:

$$P \propto 10^{Af^B} \tag{4.10}$$

With A held fixed at -25, least squares regression gives a mean best-fit value for B of 0.55 ± 0.02. Equation 4.10 could then be used with these values to generate synthetic noise that is characteristic of the observed ensemble-averaged bathymetry profiles; this will be described in the next paragraph. So that the amplitude of the synthetic noise could be scaled to be representative of that in nature, we also calculated the mean amplitude of the observed bathymetry in the spatial domain, finding a value of 94 ± 68 m.

Spectral synthesis of bathymetric noise

Synthetic noise profiles were created using a modified version of the spectral synthesis method of Peitgen et al. (1988), which proceeds as follows. First, a smooth power spectrum, P, is calculated using equation 4.10. Then, random fluctuations with Gaussian distribution are added to P to give P_{dft}. This spectrum is then used to calculate the real and imaginary parts of the synthetic DFT coefficients, R_{dft} and I_{dft} respectively, with random phase, ϕ, using the equations:

$$\begin{aligned} R_{dft} &= P_{dft}\cos(\phi) \\ I_{dft} &= P_{dft}\sin(\phi) \end{aligned} \tag{4.11}$$

The inverse transform of this DFT is then calculated to give the synthetic noise profile in the spatial domain. These profiles were then scaled to have mean amplitude randomly chosen within one standard deviation of the mean observed amplitude, 94 ± 68 m. An example of synthetic noise in the spatial and frequency domains is shown in black in Figures 4.4c and Figure 4.4g respectively.

Flexural compensation of bathymetric noise

In nature, short-wavelength features such as seamounts are flexurally compensated, such that the density anomaly of the Moho deflection reduces their gravimetric expression. To simulate this, as illustrated by the grey line in Figure 4.4c, we calculated the Moho deflection beneath the synthetic bathymetric noise by loading it on an elastic plate with T_e randomly chosen from the range 5 and 15 km. These low T_e values were chosen because the majority of seamounts that influence circum-Pacific subduction zones—for example, the Magellan and Marcus-Wake seamounts at the Mariana and Izu-Bonin trenches, the Iquique and Copiapó ridges at the Peru-Chile trench, and the Louisville Ridge at the Tonga-Kermadec trench—were formed on hot, weak lithosphere (e.g. Watts and Zhong, 2000). Furthermore, the same is true of any features that formed at a MOR, such as abyssal hills and crustal thickness variations due to hyper-extension at transform faults or spreading rate variations (e.g. Cochran, 1979).

Adding the noise to the trench-outer rise flexure

After the short-wavelength bathymetric noise and its flexural compensation were calculated, they were added to the long-wavelength trench-outer rise bathymetry and Moho flexure profiles respectively, as shown in Figure 4.4d. The resultant bathymetry and Moho profiles could then be used to calculate the synthetic gravity anomaly profile.

4.2.1.3 Landward of the trench axis

In nature, density variations immediately landward of the trench axis also contribute to outer trench-slope gravity anomalies, particularly the upward bathymetric deflection of the landward wall of the trench and the downward deflection of the subducting plate beneath it.

One limitation of the broken elastic plate model used in this study is that the calculated gravity anomalies do not account for these landward density variations. It was therefore important to use synthetic testing to ascertain the effect that this limitation has on T_e estimates. To this end, as shown in Figure 4.4e, we simulated the 50 km immediately landward of the trench axis so that it could be incorporated in the calculation of the synthetic gravity anomalies. To reflect nature, the gradient of the landward wall was randomly chosen to be 1.5–2.5 times steeper than that of the outer trench-slope, and we assumed that the subducting plate descends beneath the landward wall along the same trajectory as the outer trench-slope.

4.2.1.4 Gravity anomalies

The final synthetic bathymetry and Moho profiles (Figure 4.4e) were generated by combining the long-wavelength trench-outer rise flexure, the short-wavelength noise and its flexural compensation, and the landward wall of the trench and the subducting plate beneath it. These were then used to calculate the synthetic free-air gravity profile (Figure 4.4f). Density contrasts from both seaward and landward of the trench axis were incorporated in this calculation. We assumed that the short-wavelength bathymetric features have the same density as the underlying crust and that there is no sediment cover on the subducting plate. Therefore, seaward of the trench axis, the only density contrasts are the Moho (mantle/crust contrast) and the seafloor (crust/seawater contrast); the assumed densities are given in Table 3.1. As illustrated in Figure 4.4e, landward of the trench axis, the density anomalies are the Moho (solid grey), the top of the subducting plate (dashed black) and the seafloor (solid black); we assumed that the material atop the subducting plate has a density of 2400 $\mathrm{kg\,m^{-3}}$ to simulate low density sediments in the forearc.

The final synthetic gravity and bathymetry profiles could then be inverted to test our inversion methodology, as will be described in the following sections. In all of these inversions, an elastic plate of constant T_e was used to fit the synthetic data.

4.2.2 Synthetic test 1 – gravity vs. bathymetry

In the first synthetic test, we inverted synthetic gravity anomaly and bathymetry profiles in order to test the efficacy of inverting each data type. Here, the input dataset was the constant rigidity synthetic profiles; inversion of the variable rigidity synthetic profiles will be discussed in Section 4.2.4. Figure 4.7 shows that, irrespective of profile length, the inversion of gravity anomalies better recovers the input T_e than does inversion of bathymetry. This is because short-wavelength features, which obscure the long-wavelength trench-outer rise signal that we are interested in modelling, have lower gravimetric amplitude than bathymetric amplitude. There are two reasons for this. Firstly and most significantly, short-wavelength features such as seamounts are flexurally compensated, so that the gravity anomaly caused by the Moho deflection counteracts that caused by the bathymetric deflection. Secondly, gravity anomalies are attenuated due to upward continuation from the seafloor to sea-level, and this attenuation is greater at shorter wavelengths (e.g., Blakely, 1996, p. 287; Sandwell and Smith, 1997). In light of these findings, we focus this study on the inversion of free-air gravity data rather than bathymetry data.

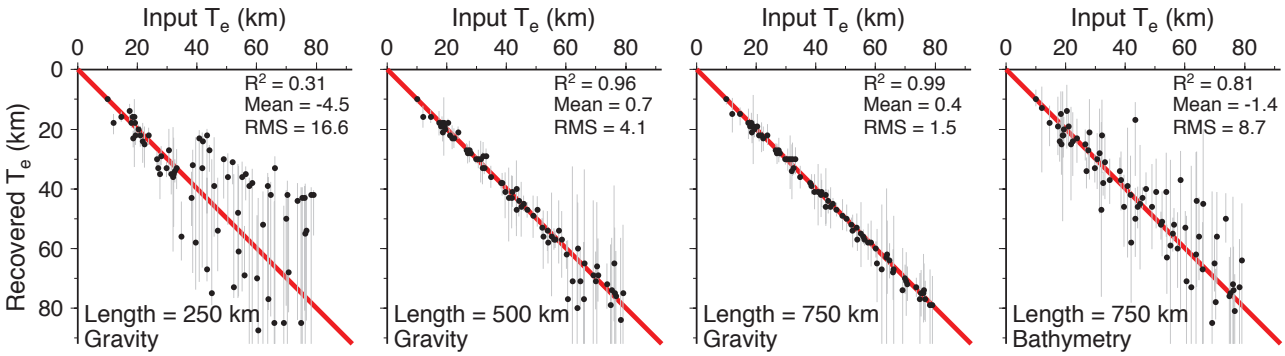

Figure 4.7: Results from inversion of the constant rigidity synthetic profiles, showing the effect of varying profile length and data type (labelled on each plot). Also shown on each plot is the R^2 value, and the mean and RMS difference between the input and recovered T_e.

4.2.3 Synthetic test 2 – profile length

To test the effect of varying the profile length, we inverted synthetic gravity profiles of length 250, 500, 750 and 1000 km. Once again, the input dataset was the constant rigidity synthetic profiles. As shown in Figure 4.7, inversion of 250 km profiles recovers T_e poorly, particularly for higher rigidities. This is because short profiles omit much of the flexural signal, particularly for stronger plates where the flexural wavelength can be > 500 km. Figure 4.7 shows that inversion of 500 km profiles recovers T_e well, but that inversion of 750 km provides better recovery for the highest rigidities. Inversion of 1000 km profiles provides no significant improvement and therefore 750 km profiles were used in this study, unless otherwise stated.

Figure 4.7 also shows that when inverting 750 km gravity profiles, the input T_e is always within error of the recovered T_e. This suggests that the criteria used to estimate the uncertainty in T_e is reasonable. In addition, Figure 4.7 shows that the error bars are larger for stronger input plates. This was to be expected, as Equations 3.20 and 3.16 show that α, which reflects the wavelength of flexure, is proportional to ${T_e}^{3/4}$. Thus, the sensitivity of the flexural wavelength to changes in T_e decreases with increasing rigidity.

As shown in Figure 4.7, when inverting 750 km gravity profiles, the agreement between the input T_e and recovered T_e is excellent. This suggests that T_e recovery is little affected by the failure of the broken elastic plate model to account for gravity anomalies caused by density contrasts landward of the trench axis.

4.2.4 Synthetic test 3 – input profiles with variable rigidity

In the final synthetic test, we inverted the variable rigidity synthetic profiles using a constant T_e plate. This test was to ascertain the meaning of T_e when a variable rigidity lithosphere is modelled with a plate of constant T_e. As shown in Figure 4.8, for 750 km long gravity profiles, the recovered T_e is well fit by a weighted average of the input T_e profile, where the weights are given by the squared magnitude of the input gravity anomaly. This is logical, as the objective function, F_{obj}, is dependent on the squared anomaly. This suggests that if the lithosphere is weakened as it approaches circum-Pacific trenches, as has been suggested by

previous studies (e.g., Bodine and Watts, 1979; Judge and McNutt, 1991; Contreras-Reyes and Osses, 2010; Manríquez et al., 2014), the recovered constant T_e will reflect an average of the lithosphere's spatially varying rigidity. It also suggests that the recovered T_e will be biased towards the low rigidities close to the trench axis, where the amplitude of the gravity anomaly is highest.

A comparison of Figures 4.7 and 4.8 shows that the uncertainty in recovered T_e is larger when inverting variable rigidity input plates than when inverting constant rigidity input plates. Thus, if circum-Pacific subducting lithosphere does indeed weaken as it approaches the trench, we might expect quite large uncertainties in T_e. Figure 4.8 also shows that the uncertainties in T_e are significantly larger for stronger input plates and that T_e recovery is better for gravity than for bathymetry. It also shows that T_e recovery is poor for 250 km long profiles, such that T_e is generally underestimated for stronger input plates.

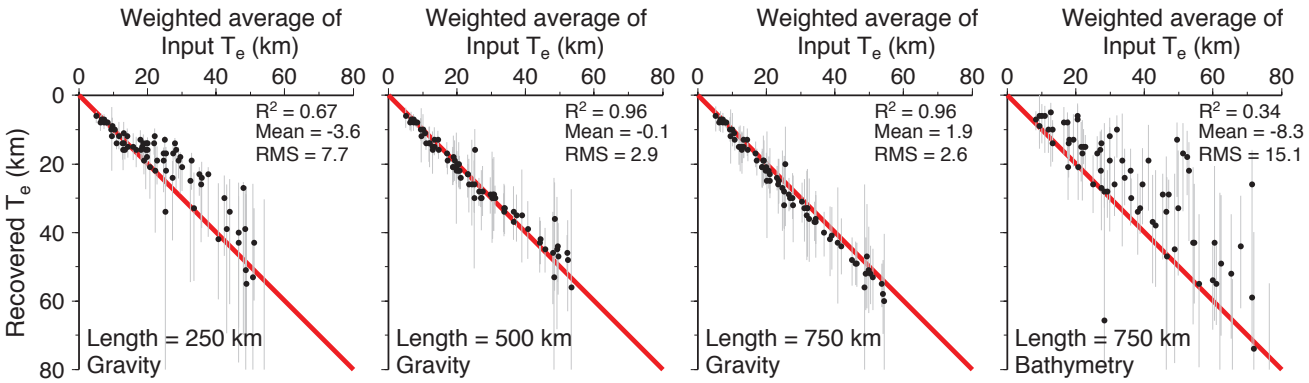

Figure 4.8: Results from inversion of the variable rigidity synthetic profiles, showing the effect of varying profile length and data type (labelled on each plot). Also shown on each plot is the R^2 value, and the mean and RMS difference between the input and recovered T_e.

4.3 Chapter summary

In this chapter, we have described the inversion methodology that was used to find the T_e and end-loads, M_0 and V_0, that best fit the observed gravity at the trench-outer rise of circum-Pacific subduction zones. We have also described the creation and inversion of a synthetic

dataset that was used to test the inversion methodology. The key points are as follows:

- The inversion methodology iterates over T_e values and at each iteration, optimizes for M_0 and V_0 using a damped least squares algorithm.
- Geophysical observations and synthetic modelling were used to show that in nature, the subducting plate curvature is positive at the trench axis. Therefore, M_0 was constrained to be positive in our inversions, unless otherwise stated.
- Synthetic trench-outer rise gravity and bathymetry profiles were created with short-wavelength noise that reflects that in our ensemble-averaged profiles. Two sets of synthetic profiles were produced: the first was calculated with constant rigidity plates; the second was calculated with variable rigidity plates that weaken landward of the outer rise, in order to simulate any lithospheric weakening that may occur in nature.
- The inversion of synthetic profiles shows that T_e is better recovered by the inversion of gravity anomalies than by inversion of bathymetry. This is because the gravimetric expression of short-wavelength features, such as seamounts and abyssal hills, is reduced due to flexural compensation and upward continuation from the seafloor to sea-level. Therefore, we focussed this study on the inversion of free-air gravity anomalies.
- The inversion of synthetic profiles shows that T_e is poorly recovered by inversion of short (250 km long) profiles because much of the flexural signal is omitted. Therefore, throughout this study, we inverted 750 km long profiles unless otherwise stated.
- The inversion of the variable rigidity synthetic profiles suggests that if the lithosphere is weakened as it approaches circum-Pacific trenches: the recovered constant T_e will reflect an average of the lithosphere's spatially varying rigidity; the recovered T_e will be biased towards the low rigidities close to the trench axis; the uncertainty in the recovered T_e will be quite large.

Chapter 5

Inversion A1 - constant T_e

In the previous chapter, we described the inversion methodology that was used to find the best fitting T_e and end-loads, and the synthetic testing used to ensure its efficacy. In this chapter, we will present the results from inversion of the circum-Pacific ensemble-averaged gravity profiles. In this inversion, labelled 'Inversion A1', the observed trench-outer rise gravity anomalies were modelled using an elastic plate of constant T_e. Following the discussions in the previous chapter, 750 km long profiles of free-air gravity were inverted; this is the case throughout this study, unless otherwise stated. The assumed densities and elastic and gravitational constants are given in Table 3.1; these values were used throughout this study, unless otherwise stated.

5.1 Profile fits

Figure 5.1 shows some of the model fits to the segment-bin ensemble-averaged gravity profiles, along with the corresponding best-fit bending moment and plate curvature profiles; all of the profile fits are shown in Appendix B. The figure shows that the fits to the observed gravity are reasonably good, but in general, a constant T_e plate cannot fit the amplitude and wavelength of the outer rise at the same time as fitting the steepness and curvature of the outer trench-slope. This suggests that the lithosphere is weakened as it approaches the trench axis, which agrees with previous studies (e.g., Bodine and Watts, 1979; Contreras-Reyes and Osses, 2010;

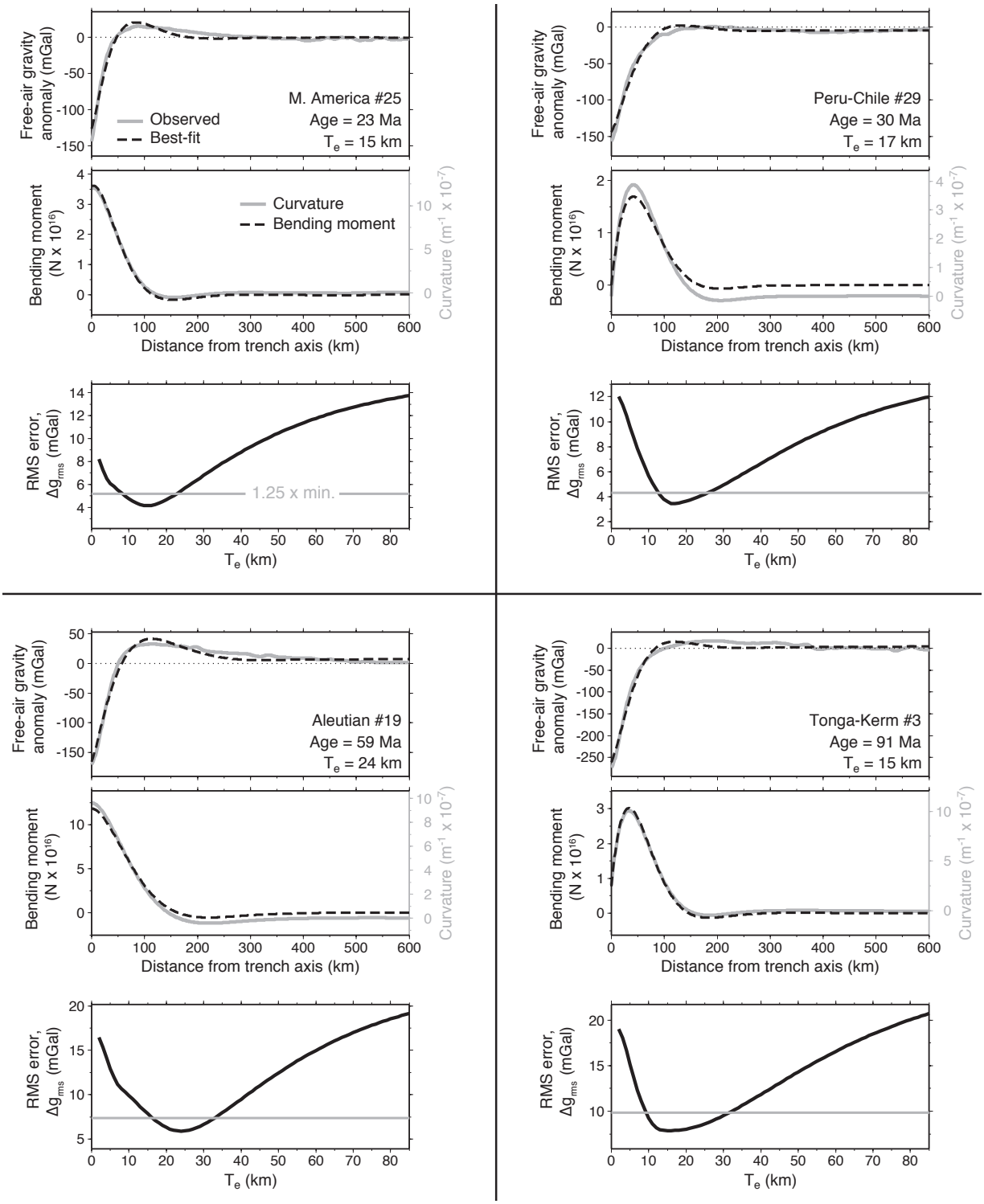

Figure 5.1: Examples of segment-bin profile fits from Inversion A1, in which a constant T_e plate was fitted to circum-Pacific trench-outer rise gravity anomalies. For each bin, the top plot shows the observed and best-fit free-air gravity profile; the trench, bin number, average seafloor age and best-fit T_e are labelled. Beneath each gravity anomaly plot is the corresponding best-fit bending moment and plate curvature profile. Beneath that is the corresponding plot of T_e vs. Δg_{rms}; the grey line shows 1.25 times the minimum Δg_{rms}, which was used to estimate the uncertainty in T_e. For clarity, only the first 600 km of the profile fits are shown, but the inversions were conducted on 750 km profiles. *Figure continued on next page...*

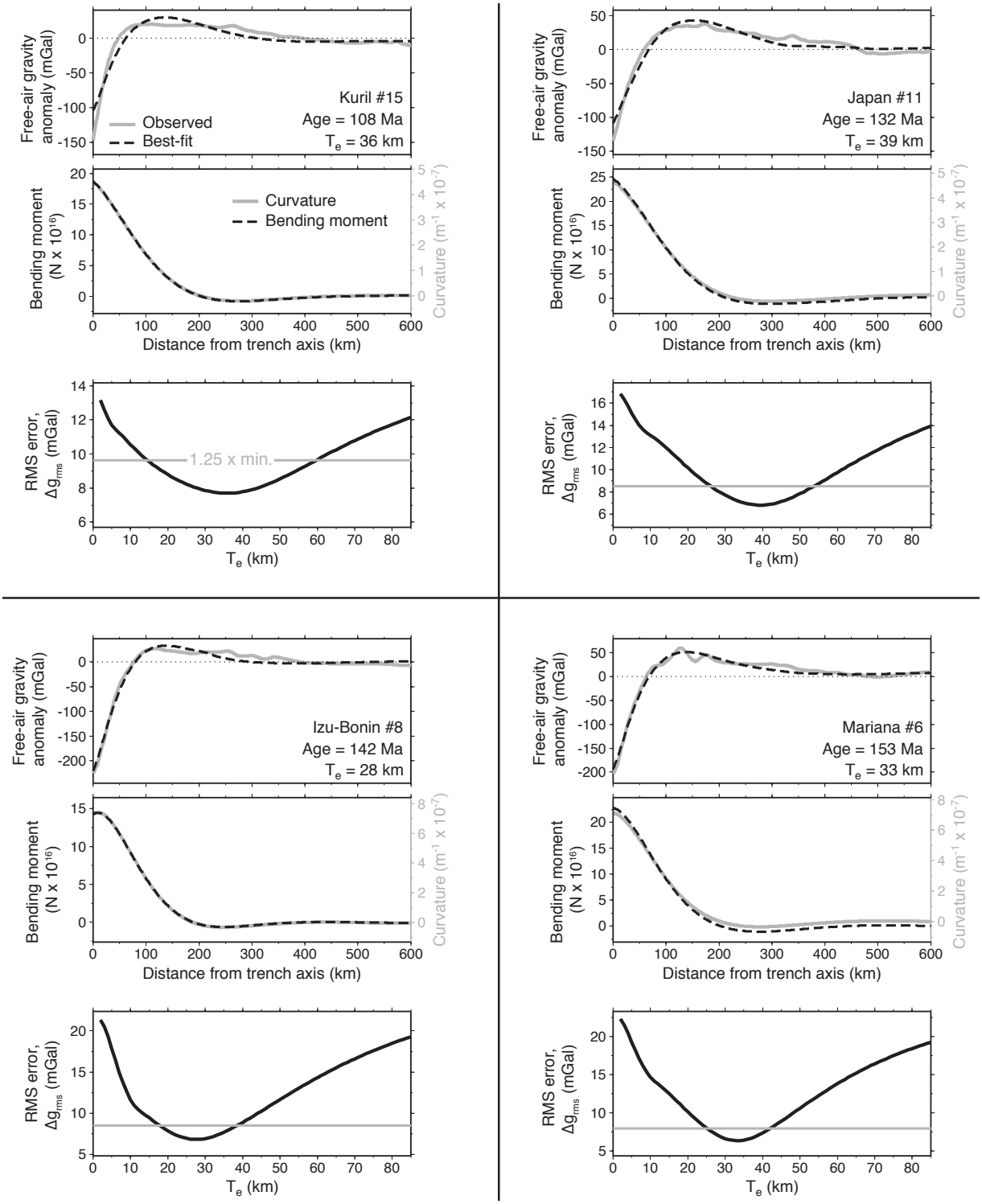

Figure 5.1 continued

Zhang et al., 2014) and will be proven further in the next chapter. Also shown in Figure 5.1 is the RMS error, Δg_{rms}, as a function of T_e. This shows that for all profiles, there is a well defined Δg_{rms} minimum and that, in general, T_e is better constrained for younger lithosphere than for older.

5.2 T_e vs. plate age

Figure 5.2 shows the T_e derived from Inversion A1 plotted against the ensemble-averaged seafloor age 100 km from the trench axis. This shows that for both the segment-bins and trench-bins, there is a general increase in T_e with plate age. For example, for the segment-bins, the Middle America trench (2–27 Ma seafloor) has a mean T_e of 13.7 ± 1.4 km, Peru-Chile (27–53 Ma) 15.1 ± 4.0 km, Aleutian (52–66 Ma) 25.0 ± 2.4 km, Tonga-Kermadec (85–118 Ma) 26.8 ± 9.0 km, Kuril-Japan (102–136 Ma) 30.7 ± 5.2 km, and Izu-Bonin-Mariana (132–157 Ma) 29.5 ± 1.5 km. This is consistent with the ideas that oceanic lithosphere cools as it moves away from the mid-ocean ridge (e.g. Parsons and Sclater, 1977) and that ductile creep processes in lithospheric minerals are strongly temperature-dependent (e.g., Kohlstedt and Goetze, 1974; Goetze, 1978). A weighted least squares regression, where T_e uncertainties were used as weights, reveals that based on a plate cooling model (Parsons and Sclater, 1977; parameters given in Table 3.1), the relationship between T_e and plate age is best fit by the depth to the 400 ± 35 °C and 380 ± 57 °C isotherms for the segment-bins and trench-bins respectively. The similarity of these isotherms shows that the results are robust across different bin widths. Note that we are not suggesting that T_e reflects the depth to these isotherms, or that these isotherms represent the depth to any physical or petrological boundary; they are simply a measure of how T_e varies with age.

Figure 5.2 also shows that although there is a general increase in T_e with plate age, there is some scatter in the T_e values. This suggests that there are factors other than plate age that also affect the rigidity of the lithosphere and/or the accuracy of T_e estimates; this will be discussed in Chapter 7. It is clear that there is an increase in T_e from 10–15 km at the Middle America trench, where the lithosphere is very young, to values generally > 25 km for lithosphere older than 80 Ma. However, for lithosphere older than 80 Ma, T_e is quite scattered

and there is no clear increase with age, and in addition, there is considerable scatter in T_e at the Peru-Chile trench; these points will be discussed in Chapter 7. Figure 5.2 shows that for lithosphere older than 80 Ma, T_e is less scattered for the trench-bin profiles than for the segment-bin profiles. This suggests that some of the scatter in the segment-bin T_e is due to inaccuracies caused by short-wavelength noise in the flexural signal, as the trench-bin profiles were ensemble-averaged over a much larger area and are therefore relatively noise-free.

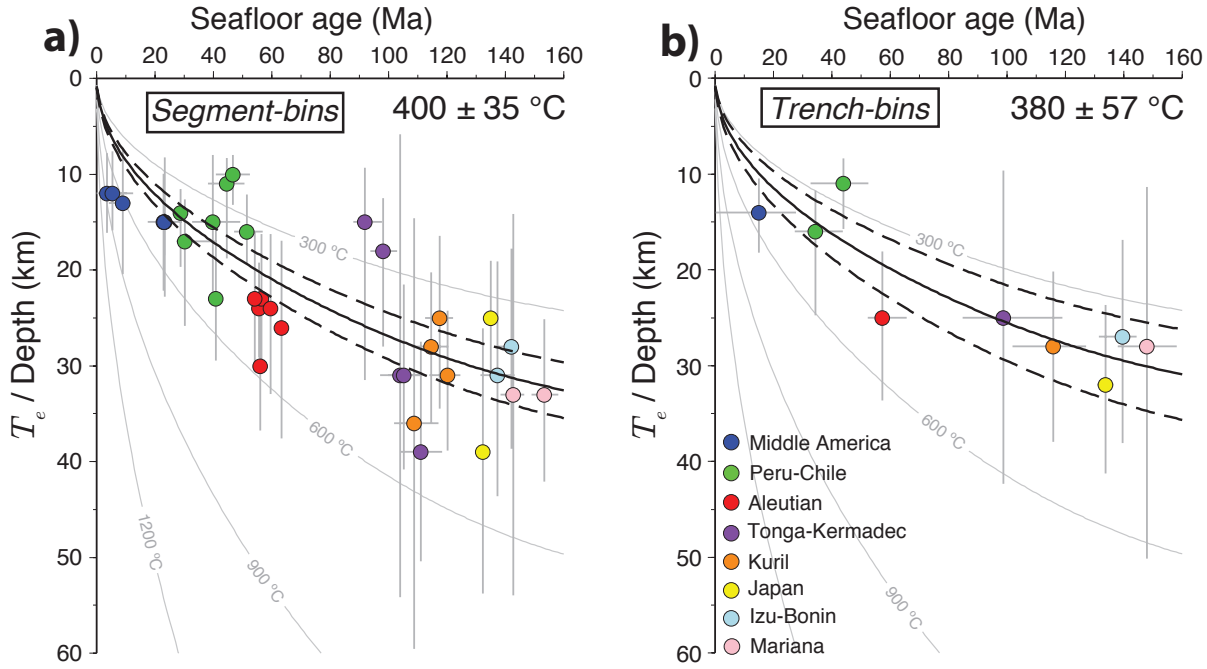

Figure 5.2: T_e from Inversion A1 plotted against seafloor age for the (a) segment-bins and (b) trench-bins. The uncertainties in T_e and age are shown as straight grey lines. The grey curves show the depth to the plate-cooling isotherms of Parsons and Sclater (1977). The isotherms that best fit the T_e-age relationship are shown in solid black and the 95 % confidence intervals in dashed black; the temperatures of these isotherms are labelled in the top right of each plot.

Figure 5.2 also shows that the uncertainties in T_e are quite large, particularly for older, stronger lithosphere. This agrees with the results of synthetic testing, shown in Figure 4.8, which suggest that T_e uncertainties are large when modelling a variable rigidity lithosphere with a constant T_e plate. However, despite the large uncertainties, we are confident that the increase in T_e with plate age is robust, as in fact, the variation in T_e uncertainty also suggests an increase in rigidity with age. This is because synthetic tests (Figures 4.7 and 4.8) show that T_e uncertainties are larger for stronger input plates, and as shown in Figure 5.2, the

uncertainties in circum-Pacific T_e are generally larger for older lithosphere. For example, the average T_e uncertainty for young (< 80 Ma) and old (> 80 Ma) lithosphere is 12 and 25 km respectively.

5.3 Trade-offs between T_e, M_0 and V_0

At a subduction zone, the loads acting on the subducting plate are not well constrained. Our inversion procedure therefore optimizes for end-loads, M_0 and V_0, which represent the bending moment and vertical shear force that exist in the lithospheric plate at the trench axis due to tectonic forces such as slab pull, collision resistance and slab suction. As M_0 and V_0 are unknown, it was important to explore the trade-offs between these parameters and T_e. To this end, a grid search was performed in which M_0 and V_0 were iterated, and at each iteration T_e was optimized using a damped least squares algorithm. M_0 was iterated from $(M_0^{best} - 2M_0^{dev})$ to $(M_0^{best} + 2M_0^{dev})$, where M_0^{best} is the best-fit value from Inversion A1, and M_0^{dev} is the maximum deviation from M_0^{best} within the uncertainty limits from Inversion A1. V_0 was iterated from $(V_0^{best} - 2V_0^{dev})$ to $(V_0^{best} + 2V_0^{dev})$, where V_0^{best} and V_0^{dev} are as described for M_0.

As shown in Figure 5.3, there is a strong trade-off between T_e and M_0, where T_e increases with the magnitude of M_0. This is as expected, because Equation 3.17 shows that to produce a given curvature, a larger rigidity is required for a larger moment. However, although the trade-off is strong, Δg_{rms} increases rapidly away from the best-fit value in the M_0 direction, and therefore T_e is quite well constrained in this direction. In the V_0 direction, Δg_{rms} increases less rapidly away from the best-fit value. However, the trade-off between T_e and V_0 is not as strong and therefore T_e is also well constrained in this direction. Figure 5.3 also shows: that the best-fit solutions from Inversion A1 (red stars) are always situated in a well-defined Δg_{rms} minimum; that Δg_{rms} increases away from this minimum in all directions; that within the parameter space explored, there is no indication of any other Δg_{rms} minima. This suggests that our inversion methodology has found a global, rather than local, minimum in Δg_{rms}.

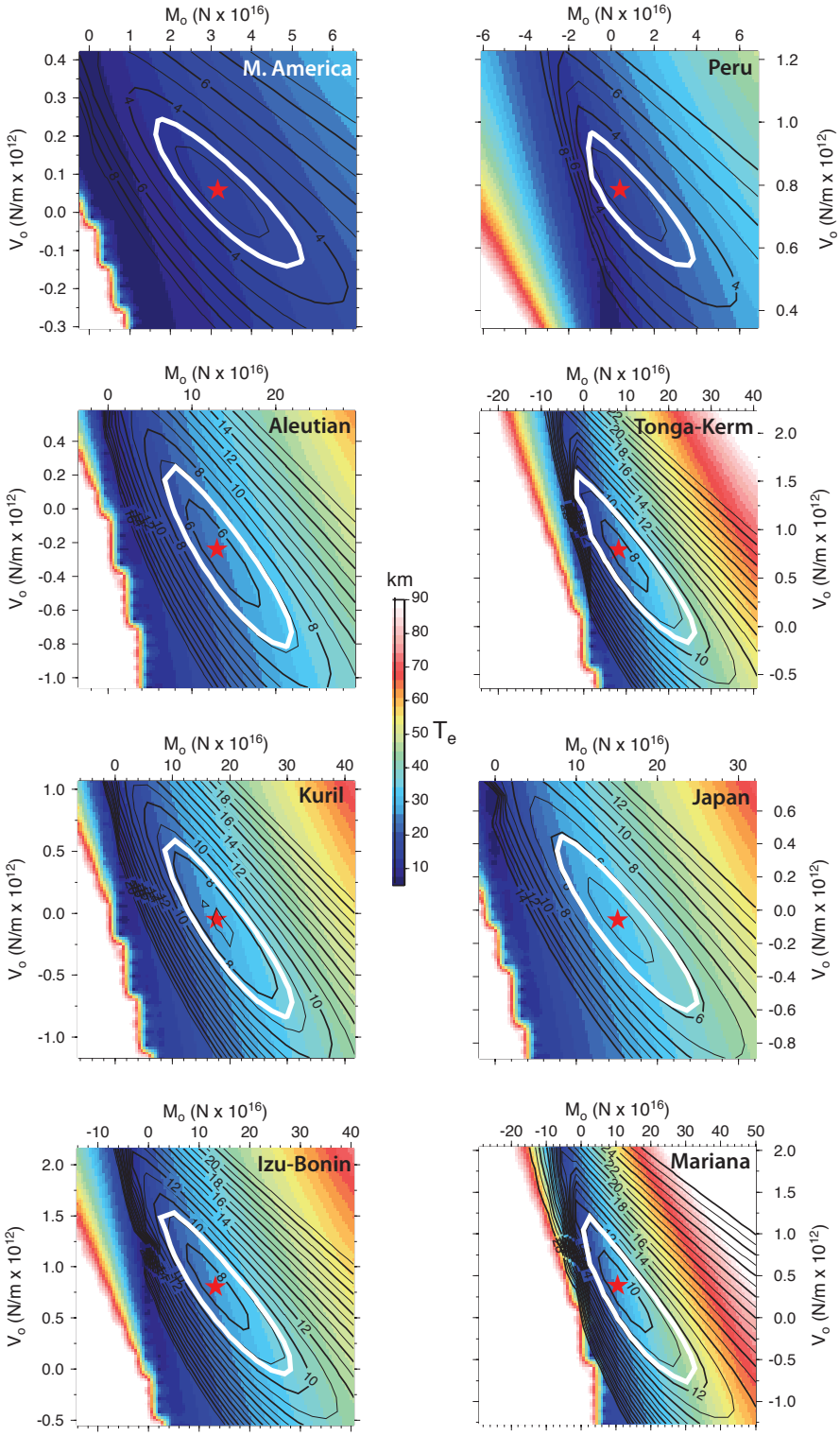

Figure 5.3: Plots showing the trade-offs between M_0, V_0, and T_e for the trench-bin profiles; the trench is labelled on the top right of each plot. To calculate this, M_0 and V_0 were iterated and T_e was optimized at each iteration using a damped least squares algorithm. The colour map shows the best-fit T_e. The RMS error between the observed and calculated gravity, Δg_{rms}, is contoured every 1 mGal up to a maximum of 3 times the minimum Δg_{rms}. The white contour is 1.25 times the minimum Δg_{rms}, which was used to estimate the T_e uncertainty in Inversion A1. The red star shows the best-fit solution from Inversion A1.

5.4 Sensitivity tests

To check that the relationship between T_e and plate age is robust, we conducted a series of inversions to test the sensitivity of results to: profile length; the wavelength of the spherical harmonic anomaly removed prior to inversion; the constraint placed on M_0; the assumed physical properties (e.g., Young's modulus and mantle, crust and sediment densities); axial loading. Unless stated otherwise, all inversions were conducted on 750 km long free-air gravity profiles. All statistics quoted in this section refer to the segment-bin T_e results, but the trench-bin results are qualitatively similar and are shown in the figures.

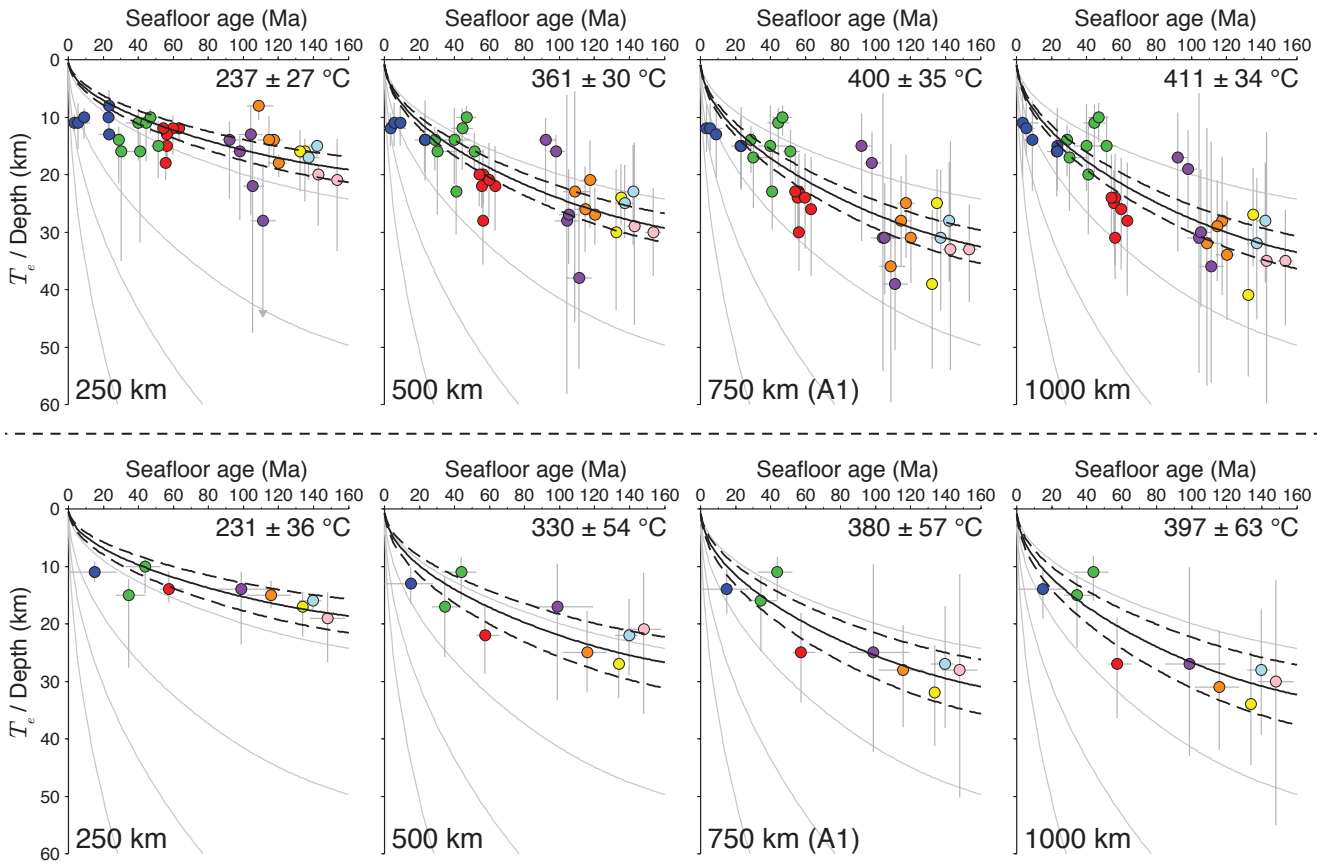

Figure 5.4: T_e plotted against seafloor age from inversion of different profile lengths. The profile length is labelled on the bottom left of each plot, where '(A1)' indicates the results from our preferred inversion, Inversion A1. The top and bottom rows show the segment-bin and trench-bin results respectively. The grey curves show the depths to the 300, 600, 900 and 1200 °C plate-cooling isotherms. The isotherms that best fit the T_e-age relationship are shown in solid black and the 95 % confidence intervals in dashed black; the temperatures of these isotherms are labelled in the top right of each plot. The T_e estimates are coloured by trench as in Figure 5.2.

5.4.1 Profile length

To test the effect of varying profile length, we conducted inversions on 250 km, 500 km and 1000 km long profiles. As shown in Figure 5.4, T_e estimates generally decrease with decreasing profile length. Relative to Inversion A1, in which the profile length was 750 km, T_e is reduced by an average of 8.6 ± 6.9 km and 2.5 ± 2.7 km for 250 km and 500 km profiles respectively. T_e is reduced by greater amounts for older, stronger lithosphere, such that with decreasing profile length, the T_e-age relationship becomes less clear and is best fit by colder isotherms than in Inversion A1. For example, relative to Inversion A1, T_e estimated from 250 km profiles is reduced by an average of 12.8 ± 6.6 km and 5.3 ± 5.0 km for old (> 80 Ma) and young (< 80 Ma) lithosphere respectively. These results mirror those from the inversion of the variable rigidity synthetic profiles (Figure 4.8), which show that inversion of short profiles underestimates T_e for stronger input plates. This suggests that short profiles provide an inaccurate picture of the relationship between rigidity and age; this is because they cannot cover the entire flexural wavelength of the outer rise, which can be > 500 km for old, strong lithosphere. Figure 5.4 shows that relative to inversion A1, T_e estimates from inversion of 1000 km profiles are increased by an average of only 0.5 ± 1.5 km and the best-fit isotherm by only 11 °C. This agrees with the results from the inversion of synthetic data, which show that there is little difference in T_e recovery between 750 km and 1000 km profiles; this is because even for the strongest lithosphere, the outer rise never has wavelength > 600 km.

5.4.2 Wavelength of the removed spherical harmonic anomaly

In Inversion A1, a long-wavelength gravity anomaly was removed from the observed profiles prior to inversion; this anomaly was synthesized from EGM2008 (Pavlis et al., 2012) spherical harmonic coefficients up to and including degree and order 16. To test the sensitivity of T_e to the wavelength of the removed signal, we conducted inversions where harmonics up to and including degree and order 10, 22 and 30 respectively were removed prior to inversion. These long-wavelength gravity anomalies are shown in map view in Figure 5.5 and the corresponding trench-bin ensemble-averaged profiles are shown in Figure 5.6. Harmonics higher than degree and order 30 were not considered because they introduce short-wavelength (400–700 km)

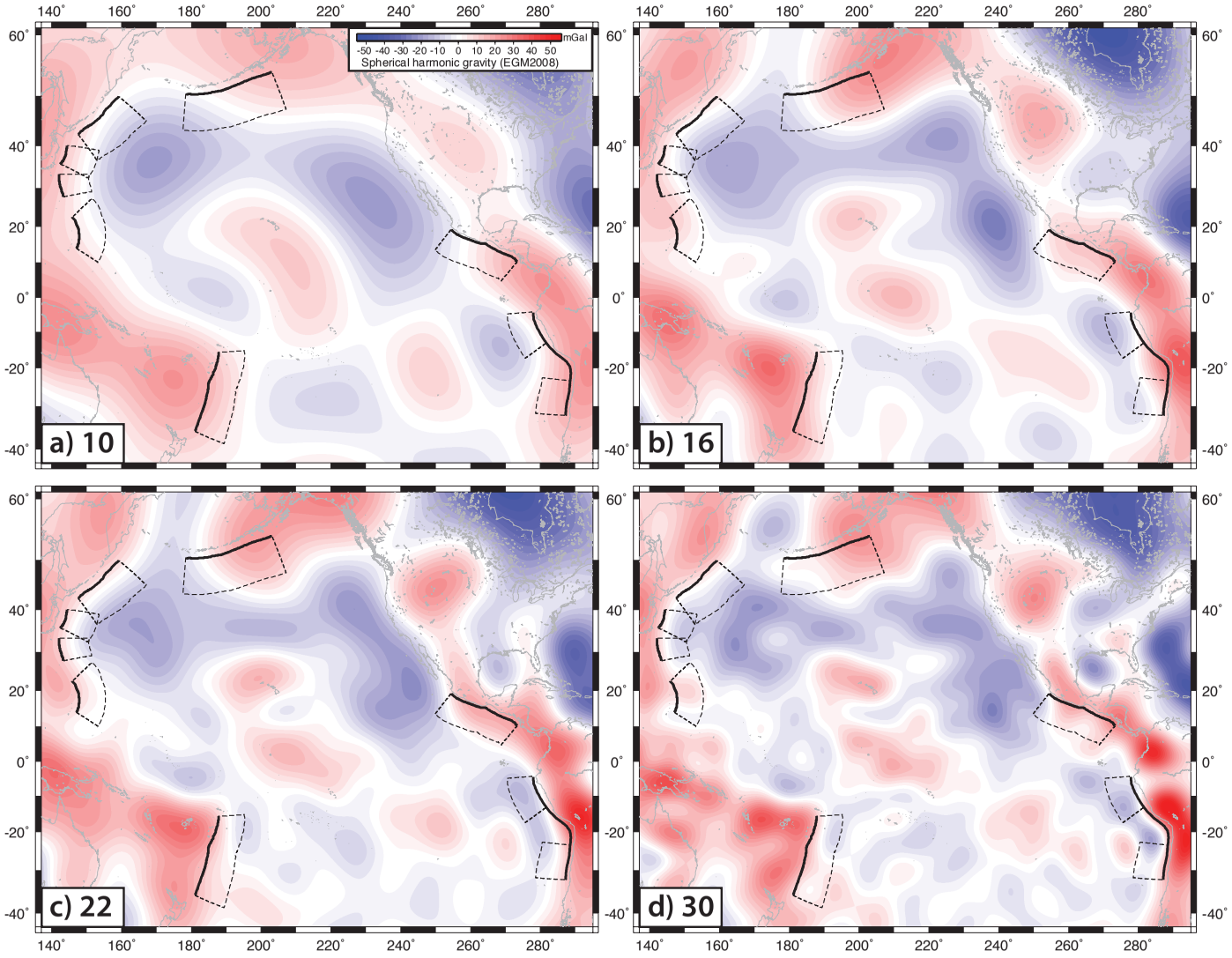

Figure 5.5: Long-wavelength gravity anomalies of the Pacific Ocean, synthesized from the EGM2008 spherical harmonic coefficients (Pavlis et al., 2012). The maximum degree and order of the harmonics used in the synthesis is labelled at the bottom left of each plot. Solid black lines mark the trenches modelled in this study and dashed black lines show the trench-bin locations.

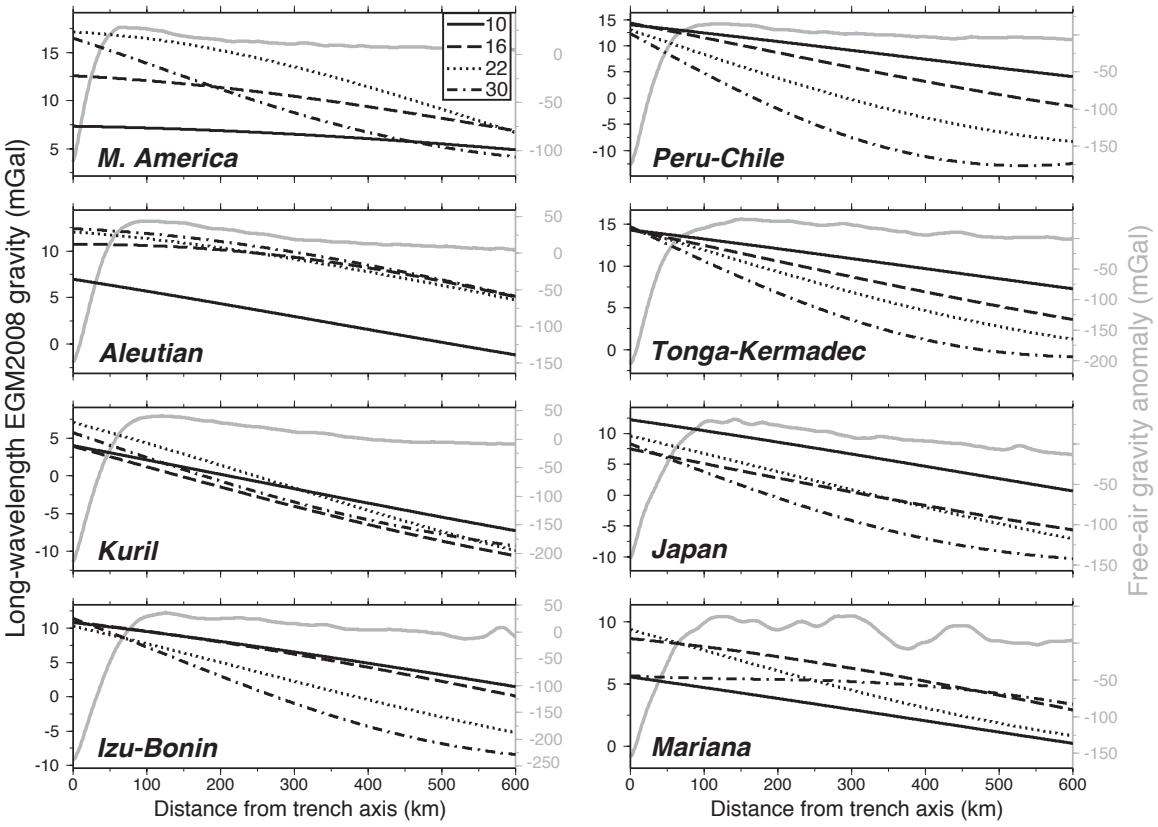

Figure 5.6: Trench-bin ensemble-averaged profiles of long-wavelength gravity anomalies. The black lines show the long-wavelength anomalies, where the pattern (legend on the top left plot) indicates the maximum degree and order of the spherical harmonics used in the synthesis. The observed free-air gravity anomalies are shown in grey; these profiles have not had any long-wavelength signal removed. Note that we have shown an ensemble-averaged profile for the entire Peru-Chile trench.

sinusoidal fluctuations that are clearly unrelated to the long-wavelength high associated with subducted slabs. As shown in Figure 5.7, variation in the removed spherical harmonic does have some effect on the results, particularly at the Peru-Chile and Tonga-Kermadec trenches. However, the general pattern of increasing T_e with age is unaffected. For example, relative to Inversion A1, the best-fit isotherm differs by a maximum of only 15 °C, and the Mean Absolute Difference (MAD) in T_e relative to Inversion A1 is < 2 km in all cases.

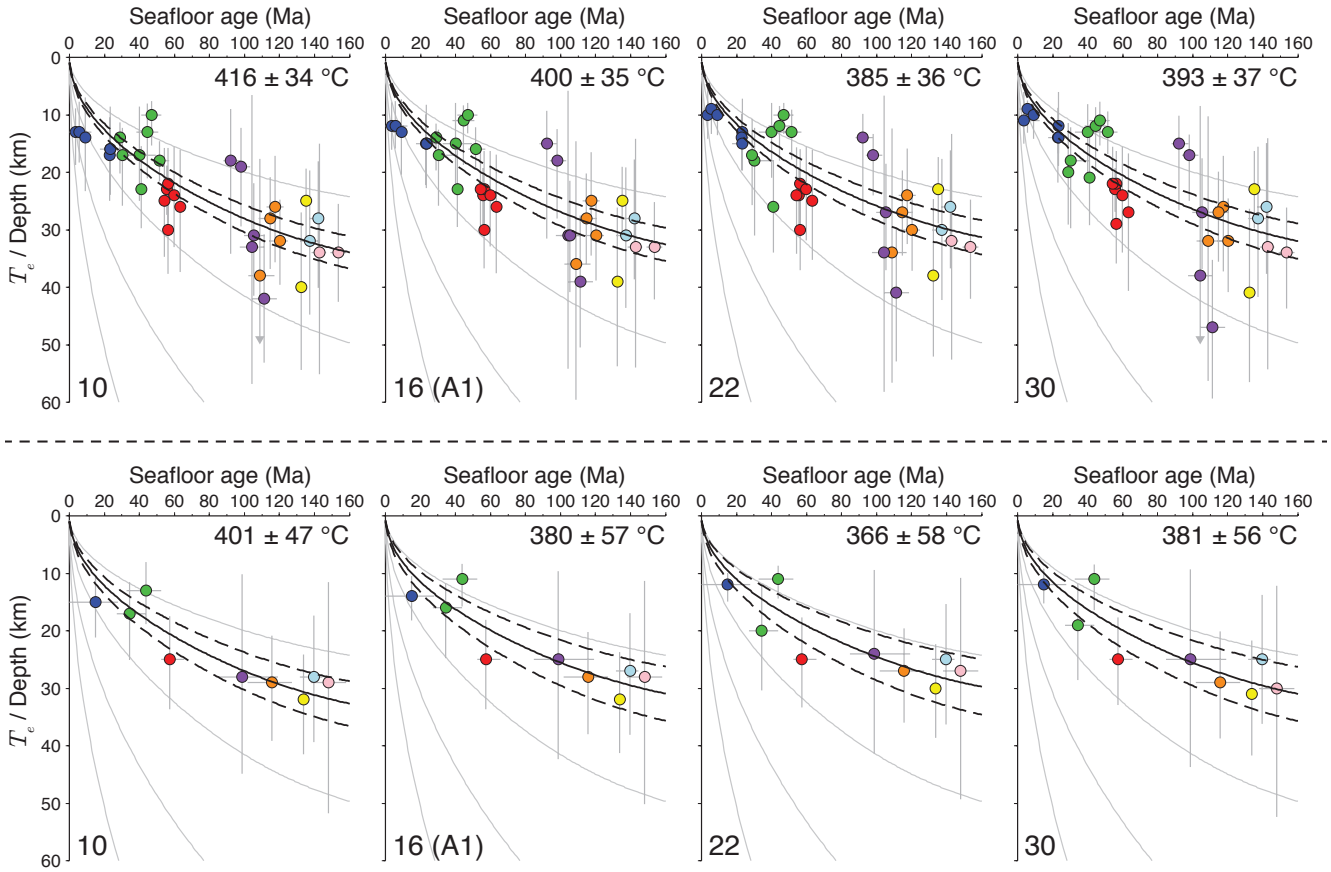

Figure 5.7: T_e plotted against seafloor age from inversion of profiles that have had different wavelength gravity anomalies removed prior to inversion. The maximum degree and order of the removed spherical harmonic anomaly is shown on the bottom left of each plot, where '(A1)' indicates the results from our preferred inversion, Inversion A1. The top and bottom rows show the segment-bin and trench-bin results respectively. The curves show plate-cooling isotherms as described in Figure 5.4.

5.4.3 Constraint on M_0

In Inversion A1, M_0 was constrained to be positive, as geophysical observations and synthetic modelling suggest that the plate curvature is positive at the trench axis. To test the effect that this has on T_e estimates, an inversion was conducted without any constraint on M_0. As shown in Figure 5.8, this has little effect on results, as only 3 out of the 36 segment-bin profiles have negative best-fit M_0, all of which are at the Peru-Chile trench. Furthermore, the best-fit T_e for these bins only differs from Inversion A1 by an average of 2 km.

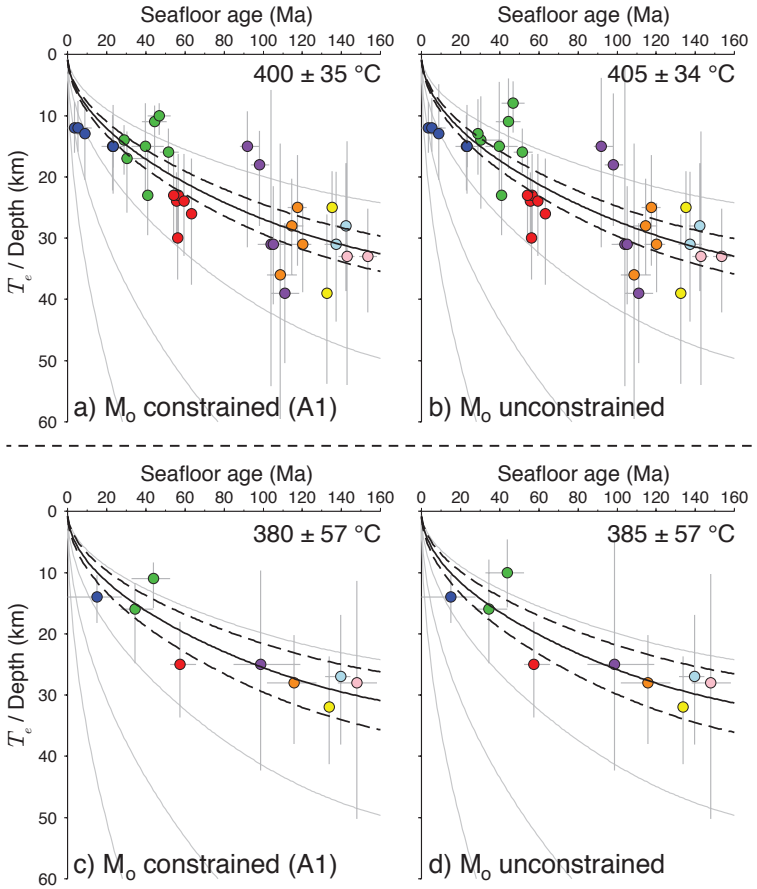

Figure 5.8: T_e plotted against seafloor age from inversions where (a,c) M_0 was constrained to be positive (Inversion A1), and (b,d) M_0 was unconstrained. The top and bottom rows show the segment-bin and trench-bin results respectively. The curves show plate-cooling isotherms as described in Figure 5.4.

5.4.4 Young's modulus

To test the effect of varying Young's modulus, E, inversions were conducted with $E = 75$ GPa and $E = 125$ GPa respectively ($E = 100$ GPa in Inversion A1). As shown in Figure 5.9, T_e estimates decrease with increasing E, such that T_e is an average of 3.8 ± 1 km larger for $E = 75$ GPa than for $E = 125$ GPa. This was to be expected because Equation 3.16 shows that for a given flexural rigidity, larger T_e is required for smaller E.

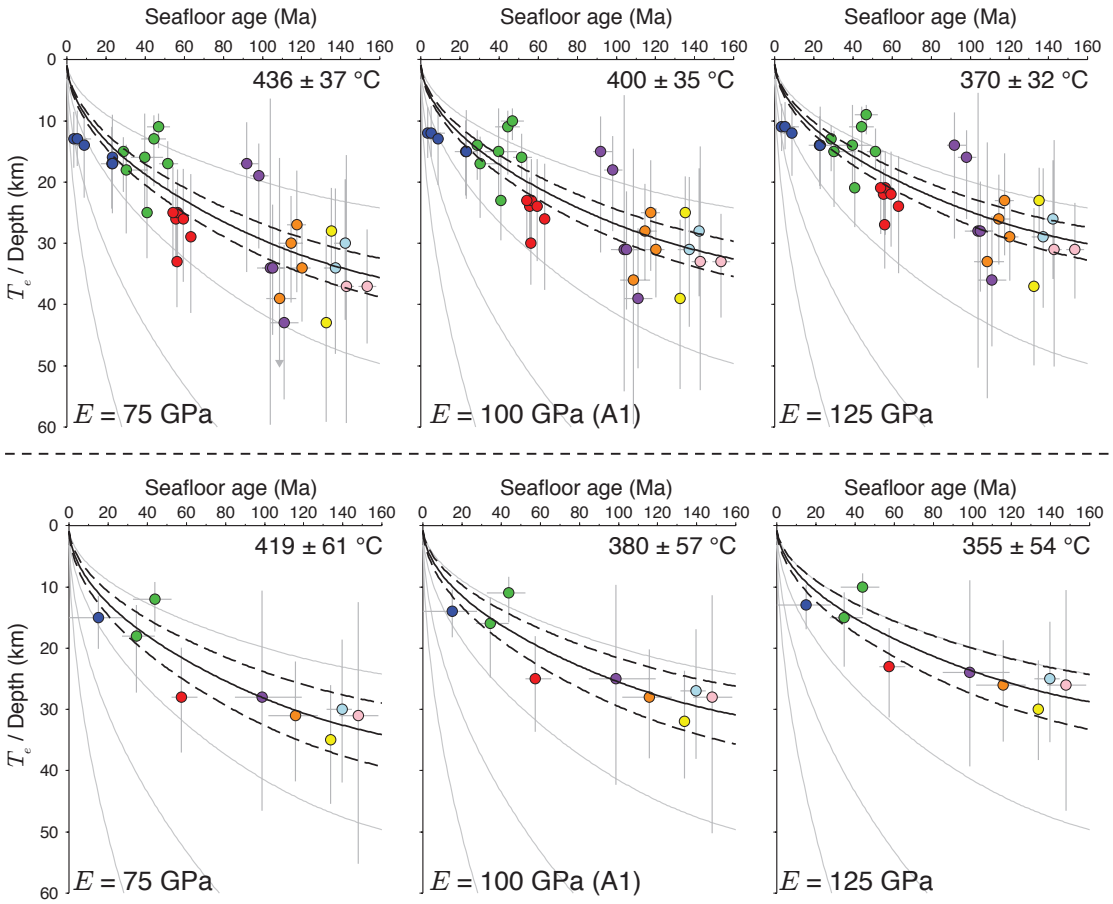

Figure 5.9: T_e plotted against seafloor age from inversions where different values for Young's modulus, E, were assumed. The assumed E is labelled on the bottom left of each plot, where '(A1)' indicates the results from our preferred inversion, Inversion A1. The top and bottom rows show the segment-bin and trench-bin results respectively. The curves show plate-cooling isotherms as described in Figure 5.4.

5.4.5 Densities

To test the sensitivity of T_e to the assumed densities, inversions were conducted with mantle densities of 3230 and 3430 kg/m^3 (3330 kg/m^3 in Inversion A1), crust densities of 2700 and 3000 kg/m^3 (2900 kg/m^3 in Inversion A1), and sediment densities of 2000 and 2600 kg/m^3 (2400 kg/m^3 in Inversion A1). As shown in Figure 5.10, variation in mantle density has only a small effect on results, with the best-fit isotherm varying by only 11 °C over the values considered. Variations in crustal and sediment densities have almost zero effect on T_e estimates and therefore the results are not plotted. An inversion was also conducted where sediment loading was not considered, which also has negligible effect on the results.

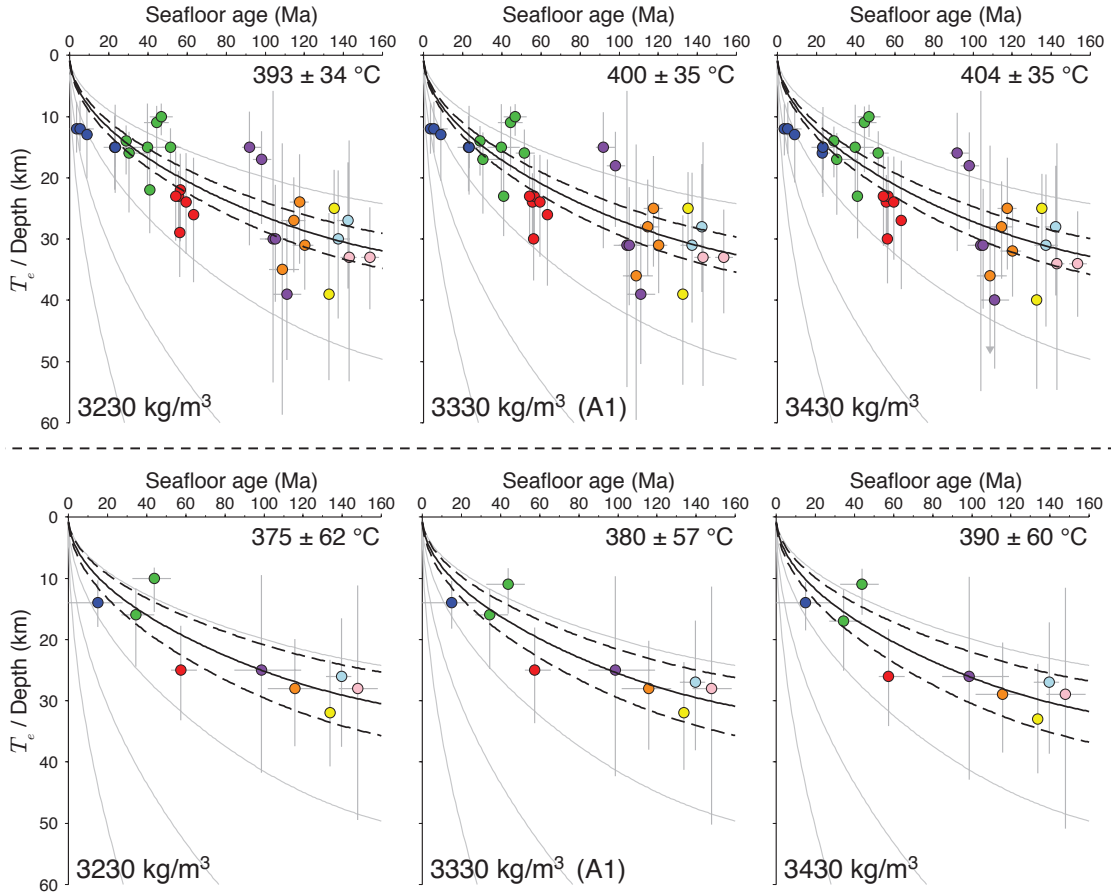

Figure 5.10: T_e plotted against seafloor age from inversions where different mantle densities were assumed. The density is labelled on the bottom left of each plot, where '(A1)' indicates the results from our preferred inversion, Inversion A1. The top and bottom rows show the segment-bin and trench-bin results respectively. The curves show plate-cooling isotherms as described in Figure 5.4.

5.4.6 Axial loading

As discussed in the previous chapter, we neglected axial loading in our elastic plate inversions. To test the effect that this has on T_e estimates, we conducted an inversion where we optimized for an axial force, F, in addition to the end-loads, M_0 and V_0. This inversion was subject to the constraint that -9×10^{12} Nm^{-1} $\leq F \leq 6 \times 10^{12}$ Nm^{-1}, which is the range of axial forces that might be expected to occur in nature, as discussed in Section 3.1.3. As shown in Figure 5.11, optimizing for an axial force has little effect on T_e estimates. Interestingly, the best fitting F for all profiles is the maximum permissible tensional value, 6×10^{12} Nm^{-1}. This finding agrees with the study of Mueller and Phillips (1995), who used an elastic-plastic

plate model—with laboratory-derived, depth-dependent yield strength—to compute synthetic trench-outer rise flexure profiles for a range of axial forces. They then inverted these profiles using an elastic plate model and found that the results are strongly biased towards tensional F, to the extent that the best fitting elastic plate solutions imply tensional F even for synthetic profiles that were computed with compressional F. Furthermore, the results of their inversions imply tensional axial forces in excess of the total tensional strength of their synthetic elastic-plastic plates. Indeed, we also conducted inversions where no constraint was placed on F, and the results imply tensional axial forces in excess of the total tensional strength of oceanic lithosphere ($\gtrsim 3 \times 10^{13}$ Nm^{-1}). The reason for this bias towards large, tensional (positive) forces can be seen by substituting Equation 3.17 into Equation 3.4, which gives:

$$D\frac{\mathrm{d}\kappa}{\mathrm{d}x} = -F\frac{\mathrm{d}w}{\mathrm{d}x} - V \tag{5.1}$$

This shows that if $\frac{\mathrm{d}w}{\mathrm{d}x}$ is positive—as is the case at the outer trench-slope—relatively large, positive F gives relatively large, negative $\frac{\mathrm{d}\kappa}{\mathrm{d}x}$. This allows the curvature, κ, to decrease seaward from a large value to a small value over a relatively short distance, which allows the constant T_e elastic plate to fit the high curvature and short wavelength of the outer trench-slope at the same time as fitting the relatively low curvature and long wavelength of the outer rise, without the need for any plate weakening.

5.4.7 Summary

In this section, we have shown that the relationship between T_e and plate age is robust. T_e is fairly insensitive to: the assumed densities; the constraint place on M_0; the wavelength of the spherical harmonic signal removed prior to inversion; and axial loading. It is sensitive to profile length, such that the relationship between T_e and age is not clear for short profiles, but synthetic tests show that this is because short profiles omit much of the long-wavelength flexural signal, causing T_e to be underestimated for stronger lithosphere.

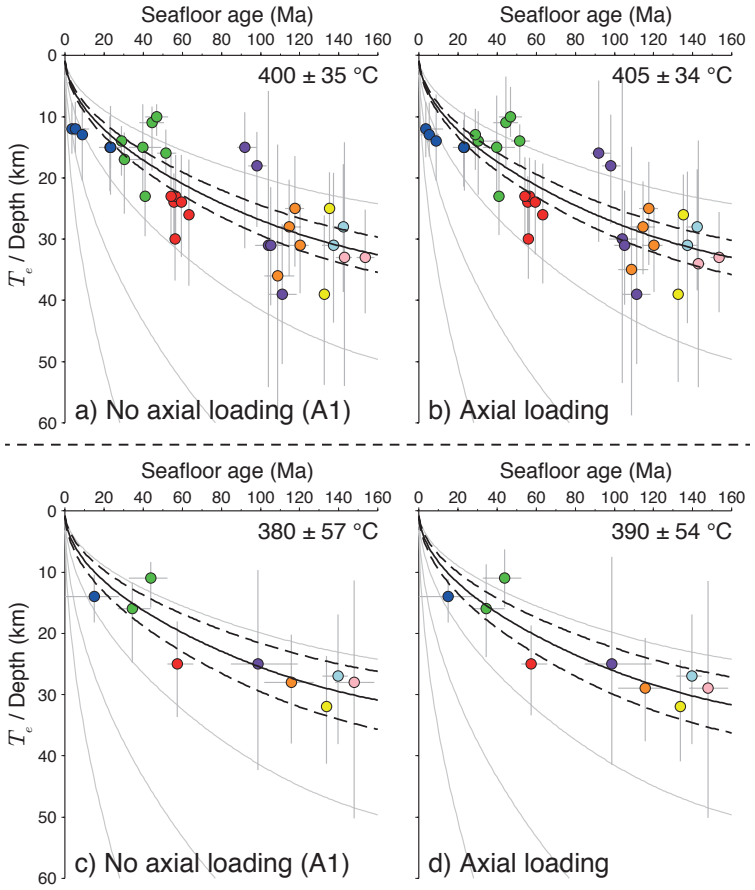

Figure 5.11: T_e plotted against seafloor age from inversions where (a,c) axial loading was neglected (Inversion A1) and (b,d) an axial force was inverted for. The top and bottom rows show the segment-bin and trench-bin results respectively. The curves show plate-cooling isotherms as described in Figure 5.4.

5.5 Comparison with the results of Bry and White (2007)

Our results from Inversion A1 show that, to first order, T_e increases with plate age. As shown in Figure 5.12, this result contrasts strongly with the results of Bry and White (2007). They modelled 700 km long free-air gravity profiles at the trench-outer rise of global subduction zones and, despite using a similar approach to that used here, found no clear relationship between T_e and age. They therefore suggested either that the lithosphere does not strengthen with age or that T_e is not the correct parameter to reveal such a relationship. It is important to understand why such a discrepancy exists between the two studies and to ascertain which study better reflects the true variation in lithospheric rigidity, as the results have implications for our understanding of lithospheric rheology, plate thermal structure and flexural modelling.

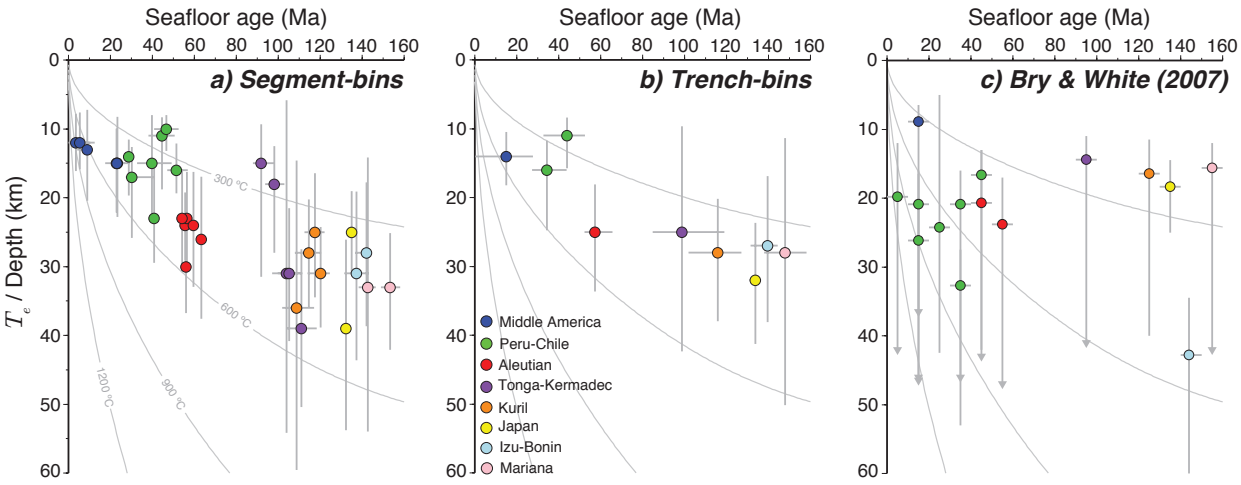

Figure 5.12: Figure comparing the results of this study to those of Bry and White (2007). (a) Segment-bin T_e and (b) trench-bin T_e from Inversion A1 plotted against seafloor age. (c) Circum-Pacific T_e estimates digitized from Bry and White (2007), which were obtained by inversion of 700 km-long, averaged profiles of free-air gravity; arrows on error bars indicate an unconstrained upper bound on T_e. The figure shows that in contrast to this study, Bry and White (2007) found no relationship between T_e and plate age.

5.5.1 Profile binning

Before discussing the discrepancy in T_e between the two studies, we will briefly describe the differences in profile binning. Similarly to this study, Bry and White (2007) produced averaged profiles for a series of bins. However, whilst we split each trench into a number of equally spaced segment-bins, they divided them into 10 Ma seafloor age bins, which explains why their study has fewer circum-Pacific T_e estimates than ours. However, as evidenced by the similarity between our segment-bin and trench-bin results, bin width should not affect the general pattern of results.

We note that this study also differs from that of Bry and White (2007) in that they modelled three profiles with plate age < 20 Ma at the Peru-Chile trench, as shown in Figure 5.12c. Two of these profiles are from bins that coincide with subducting ridges—the Carnegie Ridge and the Chile Rise—which we do not include because these features obscure the flexural signal. The third is from south of the Juan Fernandez Ridge, which we do not include because the trench is sediment-filled and therefore the top of the flexed oceanic crust is obscured.

5.5.2 Understanding the discrepancy between the two studies

Similarly to this study, Bry and White (2007) modelled trench-outer rise flexure using a broken elastic plate model with constant T_e, and found the best-fit parameters by iterating over T_e and optimizing for the end-loads. However, there are small differences between the two studies, which will be described in the following sections. To explore the effects that these differences have on circum-Pacific T_e estimates, we conducted two modified inversions—Inversions B1 and B2—of our segment-bin and trench-bin gravity profiles. By comparing the results of these modified inversions to those of Bry and White (2007) and to our preferred inversion (Inversion A1), we can gain an understanding of the discrepancy between the two studies.

Furthermore, to test the efficacy of each of these modified inversions, we also inverted the synthetic gravity profiles described in Section 4.2.1. The success of these modified inversions in recovering T_e should allow us to ascertain which of the two studies better reflects the true variation of lithospheric rigidity with age. Here, we focus on inversion of the variable rigidity synthetic profiles, which weaken landward of the outer rise, rather than the constant rigidity synthetic profiles. This is because the variable rigidity profiles better reflect nature, as the profile fits from Inversion A1, as well as previous studies (e.g., Bodine and Watts, 1979; Contreras-Reyes and Osses, 2010; Manríquez et al., 2014), suggest that the lithosphere is weakened as it approaches the trench axis; this will also be proven further in the next chapter.

In the following sections, we will describe the differences between this study and that of Bry and White (2007), and the modified inversions used to test their effects. We will also discuss the results of these inversions and how they help us to understand the discrepancy in T_e between the two studies. Results from inversion of the circum-Pacific segment-bin and trench-bin profiles are shown in Figures 5.13a and 5.13b respectively, and results from inversion of the synthetic profiles are shown in Figure 5.13c. In all cases, 750 km long gravity profiles were inverted with a plate of constant T_e; Bry and White (2007) inverted 700 km long profiles, but tests show that this small difference in profile length has negligible effect on results.

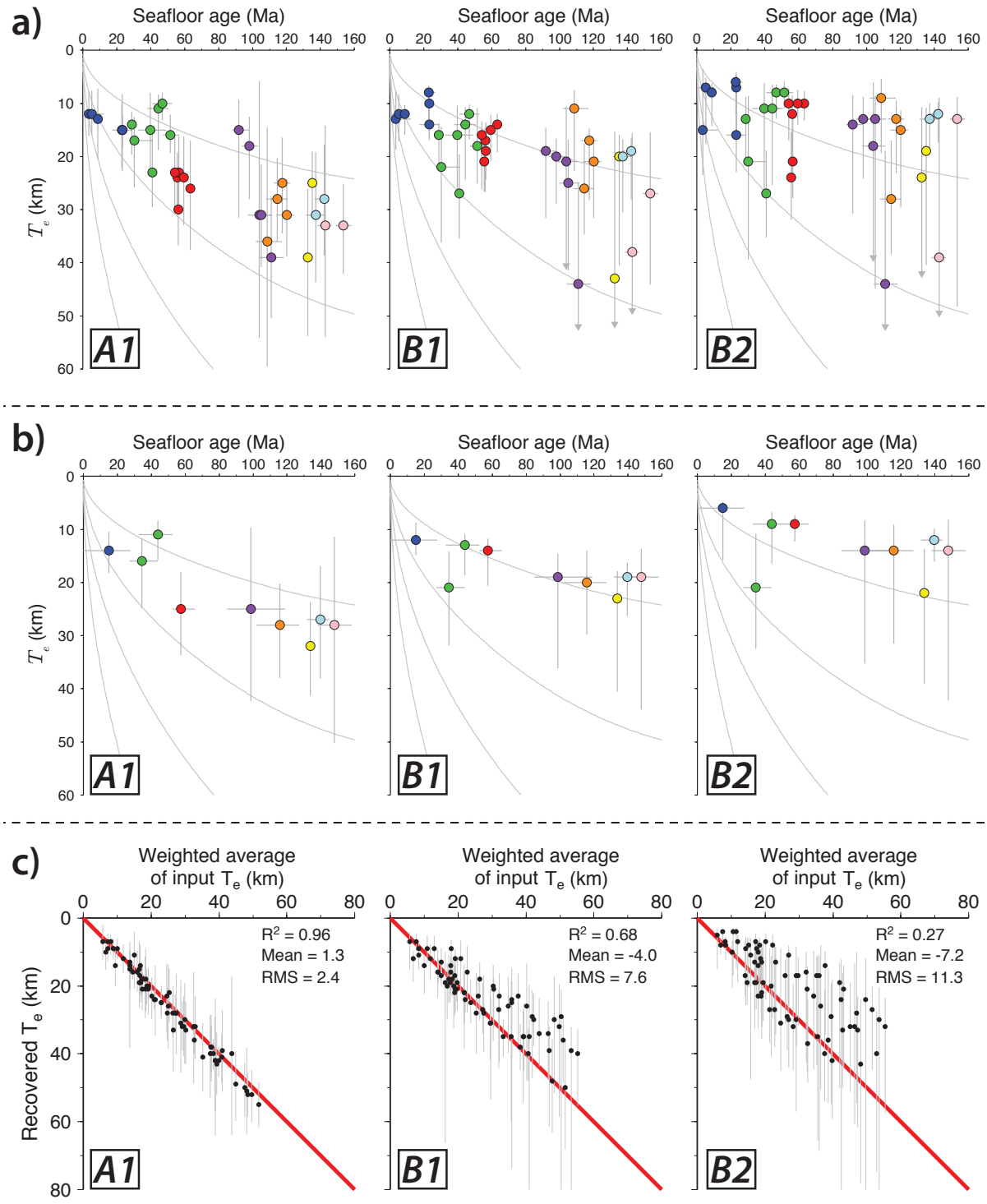

Figure 5.13: Results from our preferred inversion, Inversion A1, compared to Inversions B1 and B2. The inversion name is labelled on the bottom left of each plot. (a) and (b) show T_e against seafloor age, as derived from inversion of the circum-Pacific segment-bin and trench-bin profiles respectively. Arrows on error bars indicate an unconstrained upper bound on T_e. (c) shows recovered T_e against input T_e, as derived from inversion of the variable rigidity synthetic profiles. The input T_e is given as a weighted average of the input T_e profile, where the weights are given by the squared magnitude of the input gravity anomaly.

5.5.2.1 Inversion B1

There are two differences between this study and that of Bry and White (2007) that are explicitly clear. Firstly, to account for any long-wavelength gravity anomalies that are not related to the flexure of the subducting plate, we removed a low order spherical harmonic signal from the observed profiles prior to inversion. In contrast, Bry and White (2007) did not remove any long-wavelength signal prior to inversion; instead, they optimized for a linear gravimetric slope, which means that their inversion could add a long-wavelength tilt to the calculated anomalies. Secondly, in this study, calculated elastic plate deflections were converted to gravity anomalies using an exact method (Bott, 1969), taking into account the seafloor, top crust and Moho density contrasts and their respective undeflected depths. In contrast, Bry and White (2007) used a Bouguer slab approximation that accounts for only a single density contrast and does not take into account the undeflected depth of this contrast.

Inversion B1 was used to test the effect of the two differences described above. In this inversion, a low order spherical harmonic signal was not removed prior to inversion; instead, a linear gravimetric slope was optimized for, as in the study of Bry and White (2007). In addition, calculated flexural deflections were converted to gravity anomalies using the Bouguer slab approximation used by Bry and White (2007). Figures 5.13a and 5.13b show that Inversion B1 generally produces lower circum-Pacific T_e than Inversion A1. The reduction in T_e relative to Inversion A1 is greater for older lithosphere; for example, the mean reduction in segment-bin T_e for young (< 80 Ma) and old (> 80 Ma) lithosphere is 2.2 km and 4.8 km respectively. As a result, the relationship between T_e and plate age is significantly flattened relative to Inversion A1, such that the increase in T_e with age is much less clear and the results are quite similar to those of Bry and White (2007) (shown in Figure 5.12c). Note also that as in the study of Bry and White (2007), Inversion B1 produces circum-Pacific T_e that has a tightly constrained lower bound, but a poorly constrained upper bound. The similarity between the circum-Pacific T_e estimates from Inversion B1 and those of Bry and White (2007) suggests that much of the discrepancy between the two studies can be explained by differences in the treatment of the long-wavelength anomalies and the gravity calculation method. We

also carried out inversions to test both of these factors separately and the results show that the treatment of the long-wavelength anomalies is the most important factor. In general, the gravity calculation method makes only a small difference to the results, where the Bouguer slab approximation generally produces T_e estimates that are 1–2 km higher, and slightly more scattered, than those obtained by Inversion A1.

Figure 5.13c shows the results from inversion of the synthetic profiles. This shows that, in concordance with the circum-Pacific T_e results, Inversion B1 generally produces lower recovered T_e than Inversion A1, where the largest reduction in T_e occurs for stronger synthetic input plates. As a result, the input T_e is generally underestimated and the underestimation is generally greater for stronger input plates. This suggests that Inversion B1 underestimates the rigidity of circum-Pacific lithosphere, where the underestimation is greater for older, stronger plates; therefore, the increase in T_e with plate age is significantly masked.

5.5.2.2 Inversion B2

In addition to the differences described above, the observed and modelled gravity profiles presented by Bry and White (2007) suggest two other differences from this study. Firstly, in some of the observed profiles modelled by Bry and White (2007), there is a landward, upward deflection in free-air gravity close to the trench axis. It is not made explicit why this is, but it suggests that the trench axis was inaccurately located—specifically, that it was placed landward of the bathymetric minimum, where the bathymetric deflection of the landward trench wall causes a landward, upward deflection in the gravity anomaly (illustrated in Figures 5.14a and 5.14b). In contrast, in this study the trench axis was located using an automated algorithm (Bassett, 2014). Secondly, in the study of Bry and White (2007), some of the best-fit model profiles also have a landward, upward deflection at the trench axis so that they fit the deflection in the observed gravity. This means that the plate curvature is negative at the trench axis and therefore suggests that they did not place any constraint on M_0 prior to inversion. In contrast, in this study, we used geophysical observations and synthetic modelling to suggest that in nature, the plate curvature at the trench axis is positive and therefore we constrained M_0 to be positive.

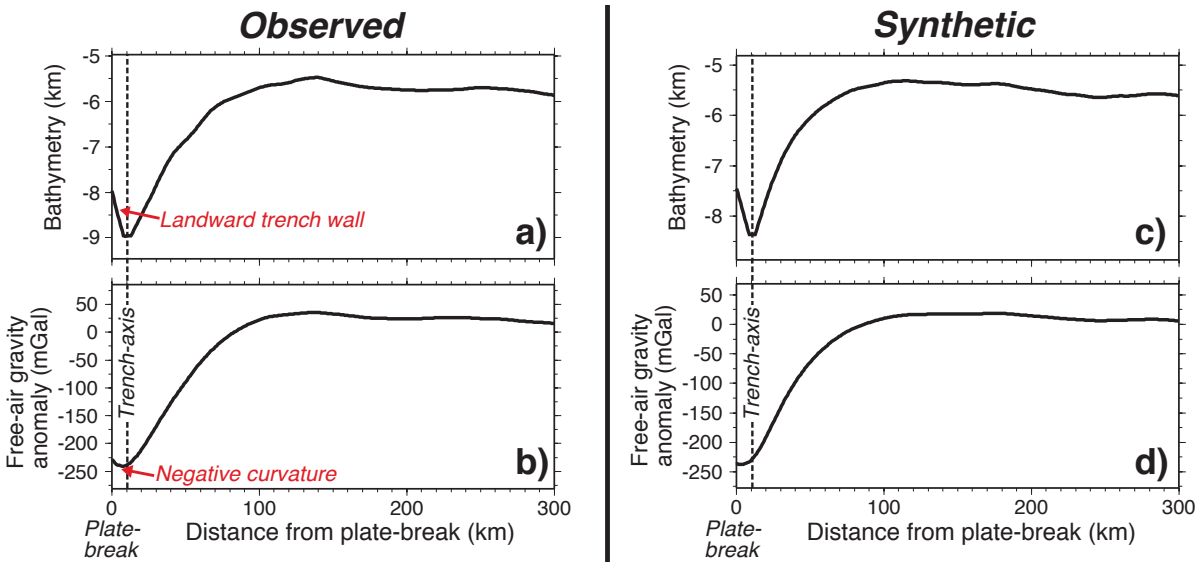

Figure 5.14: Plots showing the position of the plate-break in Inversion B2. The plate-break was placed 10 km landward of the bathymetrically defined trench axis. (a) and (b) show observed ensemble-averaged bathymetry and gravity respectively from the Izu-Bonin trench-bin. (c) and (d) show bathymetry and gravity from a synthetic profile.

Inversion B2 was used to test the additional effect of the two differences presented in the previous paragraph. This inversion was like Inversion B1—in that a gravimetric slope was optimized for and a Bouguer slab approximation was used to calculate the gravity—but with two modifications. Firstly, the plate-break ($x = 0$) was placed 10 km landward of the bathymetrically defined trench axis, as illustrated in Figure 5.14. As illustrated in Figures 5.14c and 5.14d, the synthetic input profiles account for the landward trench wall and the descent of the subducting plate beneath it (see Section 4.2.1.3). Secondly, there was no constraint placed on the applied bending moment, M_0.

Figures 5.13a and 5.13b show that Inversion B2 generally produces lower circum-Pacific T_e than Inversion B1, and that the relationship between T_e and plate age is further flattened. As a result, there is no perceivable increase in T_e with age, as is the case in the study of Bry and White (2007) (shown in Figure 5.12c). Thus, we suggest that differences in the location of the trench axis and the constraint placed on M_0 may also contribute to the discrepancy between the two studies. Figure 5.13c shows the results from inversion of the synthetic profiles. This shows that, in concordance with the circum-Pacific T_e results, Inversion B2 generally produces lower recovered T_e than Inversion B1 and the relationship between input T_e and recovered T_e

is further flattened. This suggests that Inversion B2 even further underestimates the rigidity of circum-Pacific lithosphere and further masks the relationship between T_e and plate age.

5.5.2.3 Summary

The results of Inversion B1 suggest that much of the discrepancy between this study and that of Bry and White (2007) can be explained by differences in the treatment of the long-wavelength gravity anomalies and the gravity calculation method, where the former difference is the most important factor. The inversion of synthetic profiles suggests that by inverting for a linear gravimetric slope, Bry and White (2007) have underestimated circum-Pacific T_e, where the underestimation is greater for older, stronger lithosphere; therefore, they have not detected the increase in rigidity with plate age. In addition, it seems that Bry and White (2007) inaccurately located the trench axis at some trenches and did not place any constraint on M_0. The results of Inversion B2 suggest that this may also contribute to the discrepancy between the two studies and may have caused further inaccuracies in the T_e estimates of Bry and White (2007). The results presented in this section show that, where possible, it is important to use geophysical and geological observations to limit the number of, or place constraints on, free parameters in flexural inversions. Ideally, the only unknowns in flexural inversions should be T_e and the loading conditions, unless the load is already known, such as at seamounts and ocean islands.

5.6 Chapter summary

In this chapter, we have described Inversion A1, in which circum-Pacific trench-outer rise gravity anomalies were modelled using a constant T_e plate. The key points are as follows:

- Model fits to the observed gravity profiles are reasonably good, but in general, a constant T_e plate cannot fit the amplitude and wavelength of the outer rise at the same time as fitting the steepness and curvature of the outer trench-slope. This suggests that the lithosphere is weakened as it approaches the trench axis.

- For both the segment-bins and trench-bins, there is a general increase in T_e with plate age from 10–15 km at the Middle America trench to generally > 25 km for lithosphere older than 80 Ma. The increase in segment-bin and trench-bin T_e with age is best fit by the depth to the 400 ± 35 °C and 380 ± 57 °C plate-cooling isotherms respectively. However, we note that there is some scatter in the T_e values and that for lithosphere older than 80 Ma, there is no clear increase with age.

- T_e uncertainties are quite large, but synthetic inversions suggest that this is because we have used a constant T_e plate to model the variable rigidity subducting lithosphere. T_e uncertainties increase with plate age, which, based on the results of synthetic inversions, is another indication that T_e increases with age.

- We performed a grid search of the parameter space around the best-fit solutions from Inversion A1. The results suggest that our inversion methodology finds a global, rather than local, minimum in Δg_{rms}.

- The relationship between flexural rigidity and plate age is fairly insensitive to: the assumed densities; the constraint place on M_0; the wavelength of the spherical harmonic signal removed prior to inversion; the assumed E; axial loading. It is sensitive to profile length because short profiles omit much of the flexural signal.

- Inversions B1 and B2 suggest that the discrepancy between this study and that of Bry and White (2007) can be explained by differences in: the treatment of the long-wavelength gravity anomalies; the gravity calculation method; the constraint placed on M_0; the trench axis location. Results from inversion of synthetic profiles suggest that Bry and White (2007) have underestimated the rigidity of older, stronger lithosphere, thus masking the relationship between T_e and plate age.

Chapter 6

Inversion A2 - variable T_e

In the previous chapter, we described Inversion A1, in which a constant T_e elastic plate was used to model ensemble-averaged gravity profiles at the trench-outer rise system of circum-Pacific subduction zones. The results of this inversion show that for most profiles, a constant T_e plate cannot fit the amplitude and wavelength of the outer rise at the same time as fitting the steepness and curvature of the outer trench-slope. This confirms that the subducting lithosphere is weakened as it is flexed at the outer tench-slope and outer rise. Therefore, to assess the extent of plate weakening at circum-Pacific subduction zones, we conducted a second inversion, Inversion A2, in which the flexed plate was allowed to weaken landward of the outer rise. In this chapter, we will describe Inversion A2 and its results, and will also discuss some of the possible causes of plate weakening at the trench-outer rise of subduction zones.

6.1 Defining the location of weakening

We aimed to model the trench-outer rise flexure using a variable T_e elastic plate that weakens as it approaches the trench. The first step was to define where, and over what distance, the plate weakening occurs; we will now review how previous authors have approached this, before describing the method used in this study. Contreras-Reyes and Osses (2010) and Manríquez et al. (2014) modelled flexure seaward of the Peru-Chile trench using a 2-D and 3-D elastic

plate respectively. They considered lithospheric weakening by arbitrarily defining 3 or 4 constant T_e segments landward of the outer rise peak, using forward modelling and a Monte Carlo optimization technique respectively to find the best-fit T_e for each segment. Zhang et al. (2014) modelled flexure at the Mariana trench using an elastic plate with 2 constant T_e segments, where the width of the segments was found using an inverse approach.

The approach of Contreras-Reyes and Osses (2010) and Manríquez et al. (2014) entails defining the peak of the outer rise, which is often difficult in the presence of seamounts or other short-wavelength bathymetric features, or in regions without a pronounced outer rise. The method of Zhang et al. (2014), on the other hand, adds another free parameter to the inversion, which introduces additional trade-offs and reduces resolution of other parameters such as T_e. In light of these considerations, we chose to use the observed plate curvature to define the location of plate weakening prior to inversion, as the curvature is likely to exert first-order control on strength evolution through bending-induced inelastic yielding. Furthermore, as the curvature can be estimated from the observed surfaces of flexure, the weakening in our model should reflect that in nature.

6.1.1 Estimating plate curvature

In order to define the location of plate weakening, we required estimates of the plate curvature at the outer trench-slope. The curvature, κ, of oceanic lithosphere cannot easily be calculated directly from observed bathymetry or free-air gravity, as it is very sensitive to small fluctuations. Therefore, we fitted a constant T_e elastic plate to 170 km long ensemble-averaged gravity profiles, using the same procedure as in Inversion A1, and then calculated the curvature from the best-fit models. The short profile length used here allowed the inversion to fit the steepness and curvature of the outer trench-slope without having to fit the long-wavelength outer rise, therefore providing a more accurate estimate of the plate curvature than the results from Inversion A1.

To check that the method described above provides a reasonable estimate of the actual plate curvature, we directly estimated the curvature of the trench-bin bathymetry profiles, which are relatively smooth owing to the large area over which they were ensemble-averaged.

To do this, we estimated $\frac{\mathrm{d}w}{\mathrm{d}x}$ using a linear regression in a 40 km wide moving-window. This was then median filtered with a 10 km filter width to remove short-wavelength fluctuations, and then differentiated to give κ (Equation 3.13). As shown in Figure 6.1, the curvature estimates from both methods show generally good agreement, suggesting that the 170 km elastic plate model provides a reliable estimate of the actual plate curvature at the outer trench-slope. From here on, the term 'observed curvature' will be used to refer to the curvature estimated by fitting a constant T_e elastic plate to 170 km long ensemble-averaged gravity profiles.

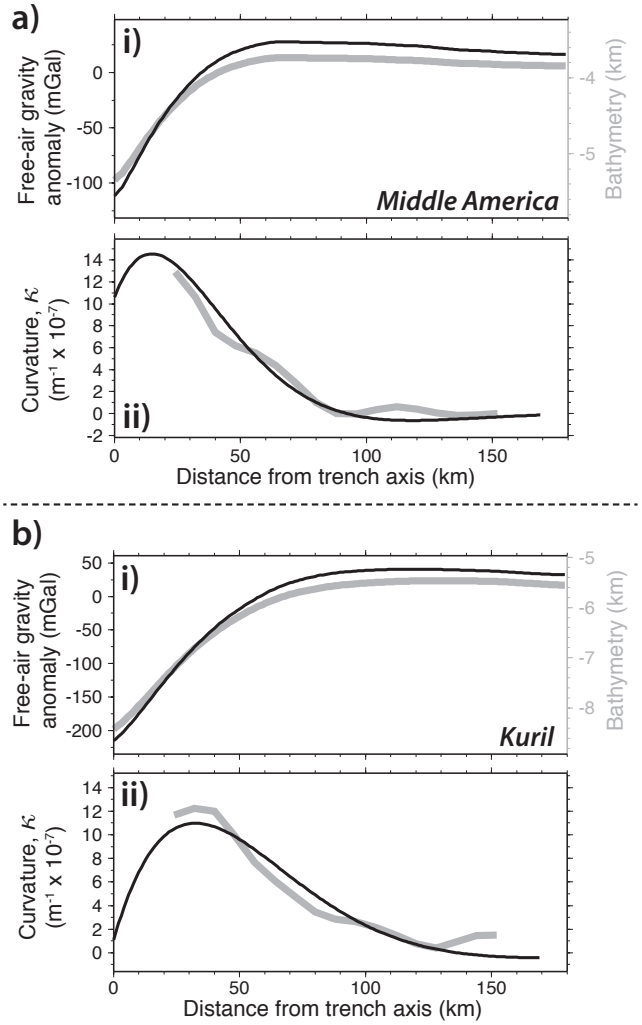

Figure 6.1: Plots illustrating how the plate curvature was estimated at the outer trench-slope of circum-Pacific subduction zones. (a) is from the Middle America trench-bin and (b) is from the Kuril trench-bin. (i) The observed ensemble-averaged bathymetry and free-air gravity. (ii) The black line shows the curvature estimated by fitting an elastic plate to 170 km long gravity profiles (the 'observed curvature'), and the grey line shows the curvature estimated from the bathymetry using a moving window regression.

6.1.2 Using the observed curvature to define the location of plate weakening

After the observed curvature was derived, the next step was to use it to define where, and over what distance, the plate weakening occurs. Whilst previous authors allowed abrupt changes in rigidity (Contreras-Reyes and Osses, 2010; Manríquez et al., 2014; Zhang et al., 2014), we chose to let it decrease linearly from a 'seaward T_e' to a 'landward T_e', as illustrated by the grey line in Figure 6.2. Our reasoning is that when flexure is calculated using elastic-plastic plates with laboratory-derived, depth-dependent yield strength, an approximately linear decrease in rigidity is found; this will be described in Chapter 9. As shown in Figure 6.2, T_e was allowed to decrease landward of the point x_b, at which $\kappa = 1 \times 10^{-7}$ m^{-1}. In reality, the rigidity will begin to decrease as soon as the plate begins to bend (i.e. landward of the point at which $\kappa = 0$), but if this point were chosen as x_b, there would be very little deflection in the gravity anomaly with which to constrain the seaward T_e. As shown in Figure 6.2, we stipulated that the linear, landward decrease in T_e terminates at the point of maximum curvature, x_a. This point generally occurs close to the trench axis; the mean distance from the axis is 23 ± 10 km and the range is 0–42 km.

Landward of x_a, the decrease in the observed curvature suggests that the subducting plate begins to unbend. For a realistic elastic-plastic or viscoelastic-plastic rheology, unbending occurs along a different stress-strain path than the preceding bending, resulting in strain hysteresis (e.g., McAdoo et al., 1978; Bodine and Watts, 1979; Bodine et al., 1981; Mueller et al., 1996a). This process cannot be modelled with a static elastic plate, and we note that this is a limitation of this study. However, we will show in Section 9.1.5 that the variable T_e profile illustrated in Figure 6.2 provides a close approximation to the flexure calculated using an elastic-plastic plate model that accounts for unbending. In addition, we suggest that the landward decrease in observed curvature close to the trench axis is not actually a reflection of the curvature of the subducting plate. Instead, it may reflect: gravity anomalies caused by the upward deflection of the landward wall of the trench and low density sediments in the forearc; smoothing of the trench axis by the ensemble-averaging process; turbiditic deposits at the bottom of the trench; crustal fragments from the subducting plate that are thrust

upwards into the trench upon meeting the resistance of the overriding plate (Massell, 2002). Therefore, we feel that unbending is unlikely to be an important process in the trench-outer rise system.

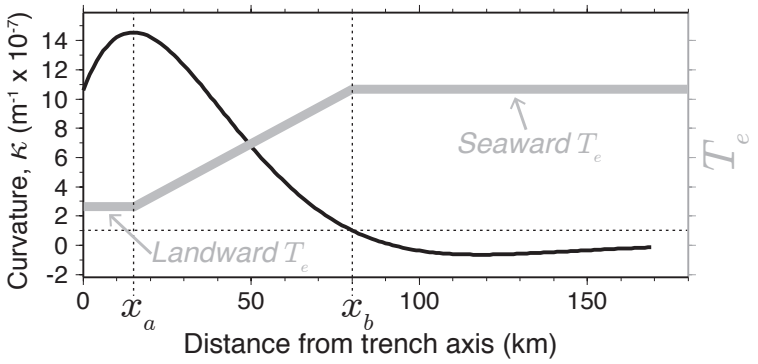

Figure 6.2: Figure showing how the observed curvature (black) was used to define the location of plate weakening (grey) in Inversion A2.

6.1.3 Summary

In summary, we used the observed plate curvature to define the location of plate weakening prior to inversion. As shown in Figure 6.2, T_e was allowed to decrease linearly from what we define as a seaward T_e to a landward T_e, with the linear decrease occurring between the point at which $\kappa = 1 \times 10^{-7}$ m^{-1}, x_b, and the point of maximum κ, x_a. We note that this neglects any additional plate weakening that may occur in the back-bulge, which is the concave upwards flexural depression immediately seaward of the outer rise. However, the curvature is relatively small in this region (generally $|\kappa| < 0.5 \times 10^{-7}$ m^{-1}) and therefore the amount of weakening will be small compared to that which occurs landward of the outer rise.

After the locations of the landward T_e and seaward T_e were defined, an inversion (Inversion A2) was used to find the best-fit value for each. This will be described in the following section.

6.2 Inversion methodology

In Inversion A2, the methodology was as follows. First, landward T_e was iterated from 2 to 85 km in steps of 1 km and at each iteration, four parameters were optimized using damped

least squares: seaward T_e, M_0, V_0 and a vertical shift, c. Then, to estimate the uncertainty in seaward T_e, landward T_e was held fixed at its best-fit value and seaward T_e was iterated upward of this to 130 km; at each iteration, three parameters were optimized: M_0, V_0 and c. We chose to iterate over landward T_e first because this is better constrained than seaward T_e due to the relatively high Signal-to-Noise Ratio (SNR) close to the trench axis. Note that this inversion methodology does not *force* the plate to weaken; it is possible for the best-fit values of landward T_e and seaward T_e to be equal.

6.3 Profile fits

Figure 6.3 shows some of the segment-bin profile fits from Inversion A2, along with the best-fit T_e, bending moment and curvature profiles; all of the profile fits are shown in Appendix C. Comparison with the results from the constant T_e inversion (Inversion A1, Figure 5.1) shows that the fits to the observed gravity are significantly improved by the variable T_e inversion, as models now fit the both the steepness and curvature of the outer trench-slope and the wavelength and amplitude of the outer rise. Relative to Inversion A1, the best-fit RMS error, Δg_{rms}, is improved by an average of 39 % and by up to 73 %. This is quite a substantial improvement given that the calculated anomalies seaward of the outer rise are changed little relative to Inversion A1. The plate weakens in 42 out of 43 best-fit models; the average reduction in T_e between the seaward and landward values is 51 ± 11 % and the range is 20–72 %. Also shown in Figure 6.3 is Δg_{rms} as a function of landward T_e and seaward T_e respectively. Landward T_e is very well constrained, but seaward T_e less so; this is because the SNR is significantly higher closer to the trench axis.

The improvement in the fits to the observed gravity suggests that the lithosphere is weakened significantly landward of the outer rise. This has been suggested by several authors in relation to individual trenches (e.g., Turcotte et al., 1978; Bodine and Watts, 1979; Contreras-Reyes and Osses, 2010; Manríquez et al., 2014; Zhang et al., 2014), but these results show that this is a ubiquitous feature of circum-Pacific subduction zones.

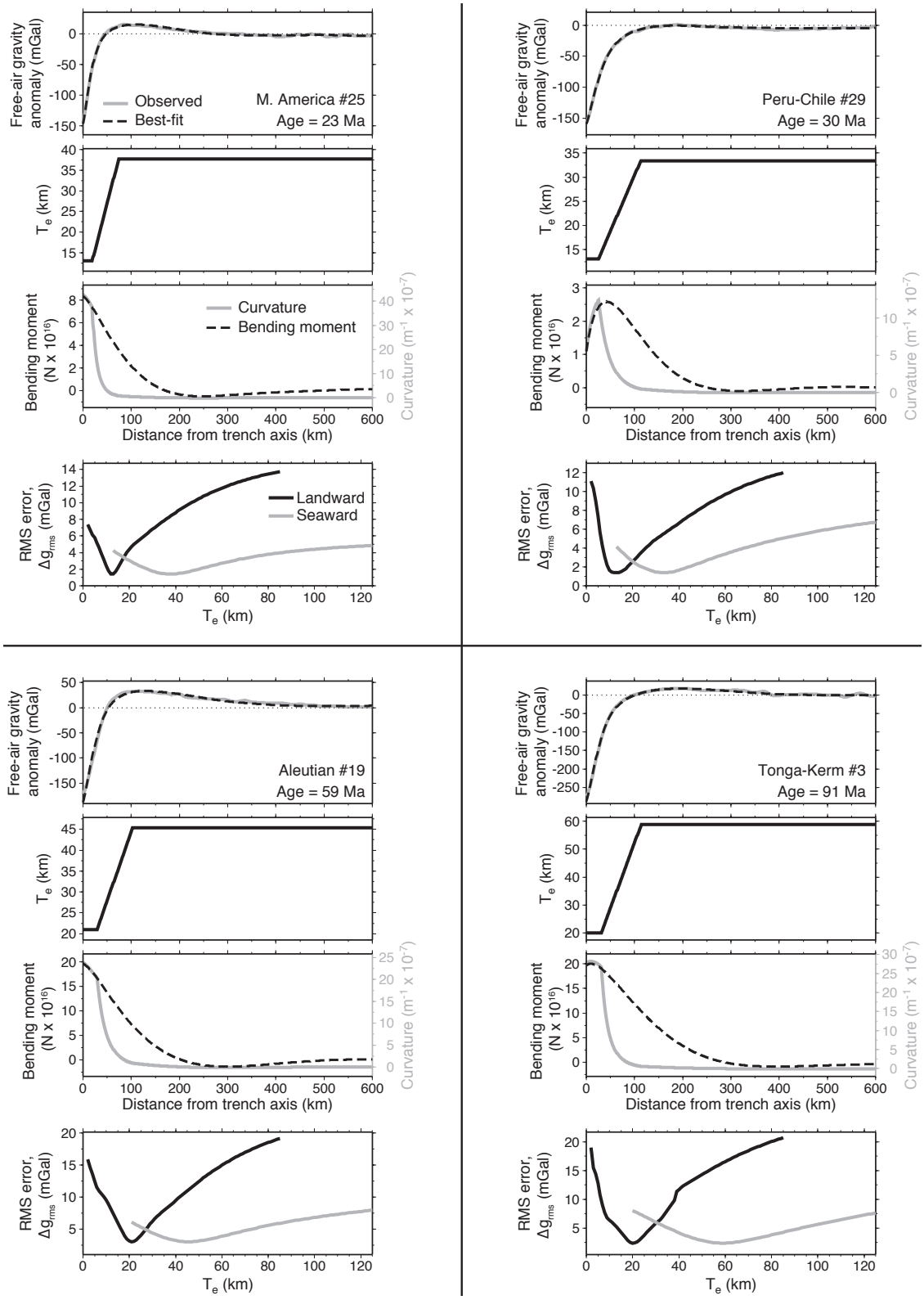

Figure 6.3: Examples of segment-bin profile fits from Inversion A2, in which a variable T_e plate was fitted to circum-Pacific trench-outer rise gravity anomalies. For each bin, the top plot shows the observed and best-fit free-air gravity profile; the trench, bin number and average seafloor age are labelled. Note that these are the same bins as shown in Figure 5.1.
Figure and caption continued on next page...

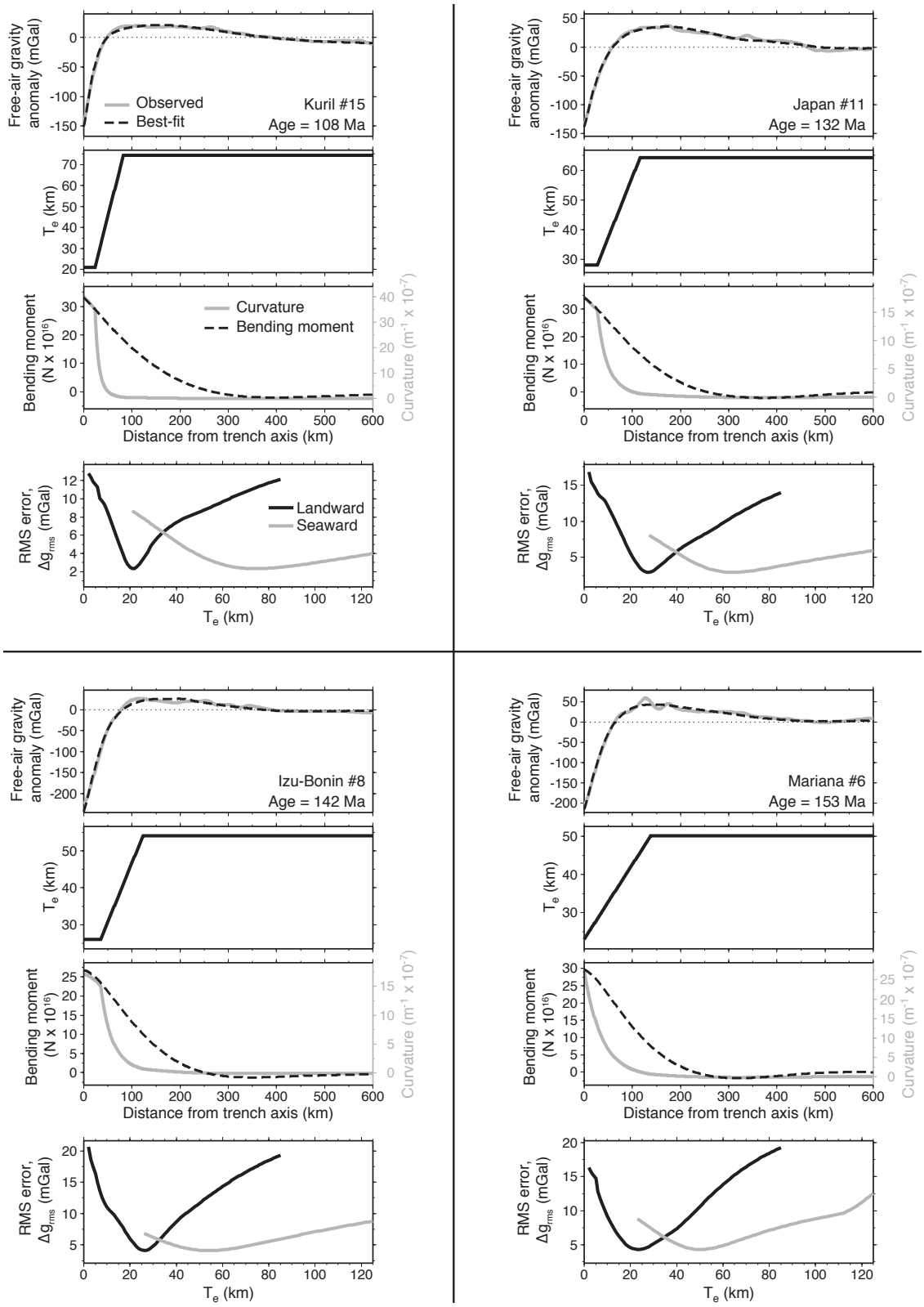

Figure 6.3 continued: Beneath each gravity anomaly plot is the corresponding best-fit T_e profile, and beneath that, the corresponding bending moment and curvature profile. Beneath that is the corresponding plot of landward T_e (black line) and seaward T_e (grey line) vs. Δg_{rms}. For clarity, only the first 600 km of the profile fits are shown, but the inversions were conducted on 750 km profiles.

6.4 T_e vs. plate age

6.4.1 Landward T_e

Figure 6.4 (a and c) shows the landward T_e derived from Inversion A2 plotted against the ensemble-averaged seafloor age 100 km from the trench axis. This shows that for both the segment-bins and trench-bins, there is a general increase in landward T_e with plate age. For example, for the segment-bins, the Middle America trench (2–27 Ma seafloor) has a mean landward T_e of 12.0 ± 1.2 km, Peru-Chile (27–53 Ma) 13.7 ± 2.7 km, Aleutian (52–66 Ma) 20.8 ± 2.3 km, Tonga-Kermadec (85–118 Ma) 22.8 ± 3.5 km, Kuril-Japan (102–136 Ma) 23.7 ± 2.3 km, and Izu-Bonin-Mariana (132–157 Ma) 27.5 ± 3.2 km. The variation in landward T_e is best fit by the depth to the 349 ± 22 °C and 342 ± 35 °C plate-cooling isotherm for the segment-bins and trench-bins respectively; the similarity between these isotherms shows that the results are robust across different bin widths. It is clear that there is an increase in landward T_e from 11–14 km at the Middle America trench, where the lithosphere is very young, to values generally > 20 km for lithosphere older than 80 Ma. However, Figure 6.4 (a and c) shows that for lithosphere older than 80 Ma, there is no clear increase in landward T_e with age, and in general, there is some scatter in the T_e-age relationship.

Figure 6.4 (a and c) shows that there is less scatter in the landward T_e values from Inversion A2 than in the constant T_e values from Inversion A1 (Figure 5.2). This suggests that some of the scatter in Inversion A1 is a result of modelling the variable rigidity lithosphere with a constant T_e plate and/or a result of the relatively low SNR in the observed gravity seaward of the outer trench-slope. Figure 6.4 (a and c) also shows that the uncertainties in landward T_e from Inversion A2 are generally smaller than the uncertainties in constant T_e from Inversion A1 (Figure 5.2). This suggests that the relatively large T_e uncertainties in Inversion A1 are due to modelling the variable rigidity lithosphere with a constant T_e plate and/or due to the relatively low SNR seaward of the outer trench-slope. This agrees with the results of synthetic testing (Figure 4.8), which show that T_e uncertainties are quite large when modelling a variable rigidity input plate with a constant T_e plate. As the uncertainty and scatter in landward T_e is quite low, this gives us further confidence that the first-order increase in T_e with plate age is a robust result.

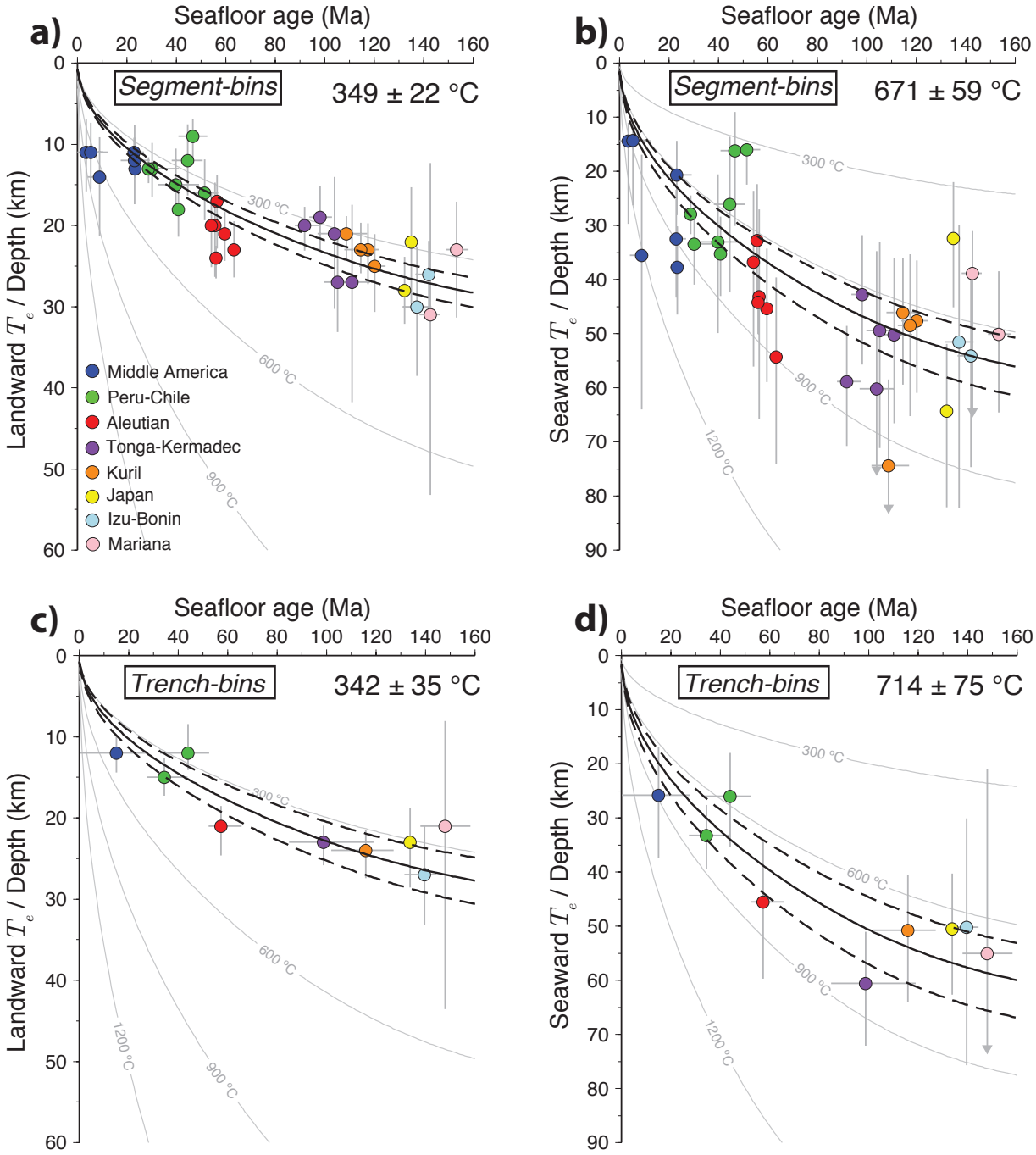

Figure 6.4: T_e from Inversion A2 plotted against seafloor age for the (a,b) segment-bins and (c,d) trench-bins. (a,c) shows the landward T_e and (b,d) shows the seaward T_e. The uncertainties in T_e and age are shown as straight grey lines; arrows on error bars indicate an unconstrained upper bound on T_e. The grey curves show the depth to the plate-cooling isotherms of Parsons and Sclater (1977). The isotherms that best fit the T_e-age relationship are shown in solid black and the 95 % confidence intervals in dashed black; the temperatures of these isotherms are labelled in the top right of each plot.

6.4.2 Seaward T_e

Figure 6.4 (b and d) shows the seaward T_e derived from Inversion A2 plotted against seafloor age. This shows that the relationship between seaward T_e and plate age is more scattered than that for landward T_e; this is because the SNR in the observed gravity is relatively low seaward of the outer trench-slope. However, it is clear that for both the segment-bins and trench-bins, there is general increase in seaward T_e with age. For example, for the segment-bins, the Middle America trench (2–27 Ma seafloor) has a mean seaward T_e of 25.8 ± 9.8 km, Peru-Chile (27–53 Ma) 26.8 ± 7.4 km, Aleutian (52–66 Ma) 42.8 ± 6.8 km, Tonga-Kermadec (85–118 Ma) 52.3 ± 6.5 km, Kuril-Japan (102–136 Ma) 52.2 ± 13.5 km, and Izu-Bonin-Mariana (132–157 Ma) 48.6 ± 5.8 km. The variation in seaward T_e is best fit by the depth to the 671 ± 59 °C and 714 ± 75 °C isotherm for the segment-bins and trench-bins respectively. As both landward T_e and seaward T_e show a general increase with plate age, this suggests to us that the first-order increase in rigidity with age is a robust result.

6.4.3 Comparison to Inversion A1

The best-fit isotherms to the seaward T_e and landward T_e from Inversion A2 are higher and lower respectively than those obtained in Inversion A1. This is as expected, as the constant T_e estimates from Inversion A1 reflect an average of the lithosphere's decreasing rigidity as it travels over the outer rise and descends into the trench. Seaward T_e, however, reflects an average of only the relatively strong (unweakened) region seaward of the outer rise and landward T_e reflects only the relatively weak region landward of this. Landward T_e is an average of 3.5 km lower than the constant T_e from Inversion A1, whilst seaward T_e is an average of 18.1 km higher. This shows that the constant T_e estimates from Inversion A1 are biased towards the low rigidities close to the trench axis, where the amplitude of the gravity anomaly is highest; this is in agreement with the results from inversion of synthetic profiles.

6.4.4 Plate weakening vs. plate age

Figure 6.5 shows plate weakening, i.e. the reduction in T_e between the seaward and landward values, plotted against plate age. The shows that, irrespective of bin size, there is no correlation between plate weakening and plate age, and that for the majority of bins, the best-fit weakening is between 40 % and 65 %.

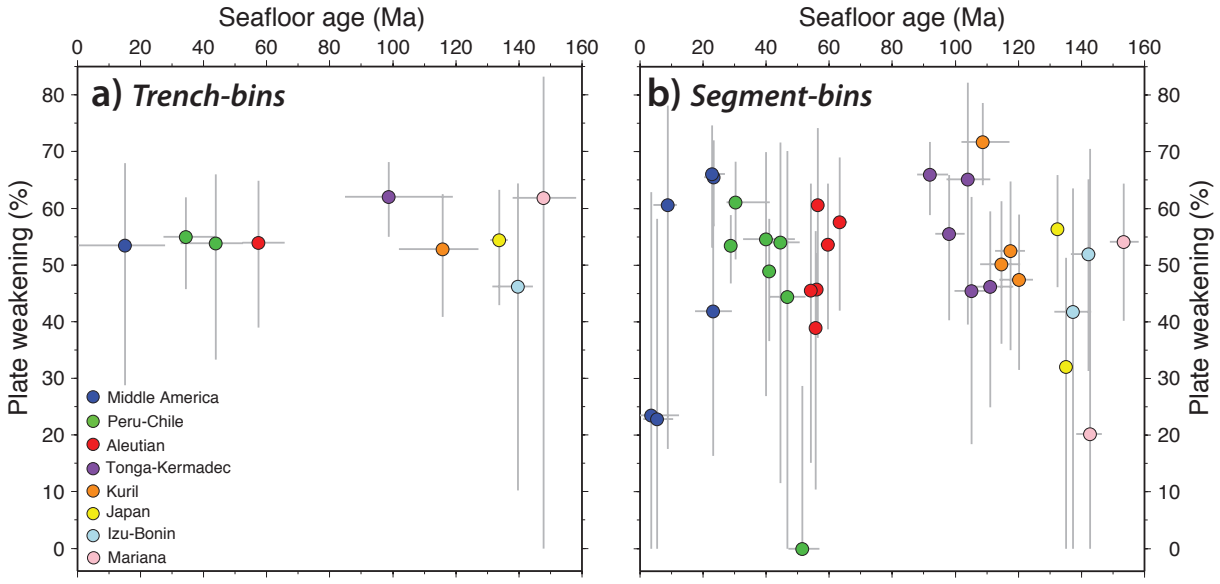

Figure 6.5: Plate weakening from Inversion A2 plotted against seafloor age, for the (a) trench-bins and (b) segment-bins.

6.5 Causes of plate weakening

As described in the previous section, the fit to almost all of the observed free-air gravity profiles is improved by a plate that weakens landward of the outer rise, where the average reduction in T_e between seaward and landward values is 51 ± 11 % and the maximum is 72 %. This suggests that the lithosphere undergoes significant weakening as it approaches the trench axis and that this is a ubiquitous feature of circum-Pacific subduction zones. This corroborates previous flexural studies that suggested plate weakening at individual trenches (e.g., Turcotte et al., 1978; Bodine and Watts, 1979; Billen and Gurnis, 2005; Contreras-Reyes and Osses, 2010; Manríquez et al., 2014; Zhang et al., 2014). This plate weakening is likely to be caused

primarily by bending-induced inelastic yielding (e.g., Goetze and Evans, 1979; Brace and Kohlstedt, 1980; McNutt and Menard, 1982; Contreras-Reyes and Osses, 2010), and perhaps also by mantle hydration and serpentinization via bend-faults on the outer trench-slope (e.g., Escartin et al., 2001; Ranero and Sallares, 2004; Grevemeyer et al., 2007). In this section, we will discuss these weakening mechanisms and the observational evidence for them.

6.5.1 Bending-induced inelastic yielding

Experimental rock mechanics (e.g., Byerlee, 1978; Goetze, 1978) predicts that upon bending at the outer trench-slope and outer rise, the lithosphere should yield via shallow, brittle processes such as faulting and deep, ductile processes such as dislocation creep. This is illustrated in Figure 6.6, which shows an example of a Yield Strength Envelope (YSE)—a plot of the laboratory-derived yield strength of olivine as a function of depth. The solid red curve shows the calculated deviatoric bending stress, $\Delta\sigma_{xx}$, for a plate curvature of $\kappa = 5\times10^{-7}$ m^{-1}. The figure shows that at shallow depths, $\Delta\sigma_{xx}$ exceeds the yield strength predicted by a Coulomb-Navier failure criterion for frictional sliding (Byerlee, 1978) and therefore brittle faulting is predicted. At greater depths, $\Delta\sigma_{xx}$ exceeds the yield strength predicted by dislocation creep laws for olivine (Hirth and Kohlstedt, 2003; Mei et al., 2010) and therefore ductile flow is predicted. As a result of this brittle and ductile yielding, the relationship between the bending moment, M, and plate curvature, κ, is non-linear, where $\frac{\mathrm{d}M}{\mathrm{d}\kappa}$ decreases with increasing κ. This means that the flexural rigidity, $D = \frac{M}{\kappa}$, decreases with increasing plate curvature. Note that YSEs and their relationship to T_e will be discussed in more detail in Chapter 8; here, we have only given a brief explanation.

6.5.2 Observational evidence for inelastic yielding

There is abundant observational evidence of shallow, brittle failure at the outer trench-slope of subduction zones. Firstly, swath bathymetry reveals that the majority of outer trench-slopes are pervasively fractured by extensional bend-faults (e.g., Jones et al., 1978; Masson, 1991; Massell, 2002; Ranero et al., 2003; Grevemeyer et al., 2005; Ranero et al., 2005; Billen et al., 2007). This is illustrated in Figure 6.7 (c to e), which shows bend-faulting at the

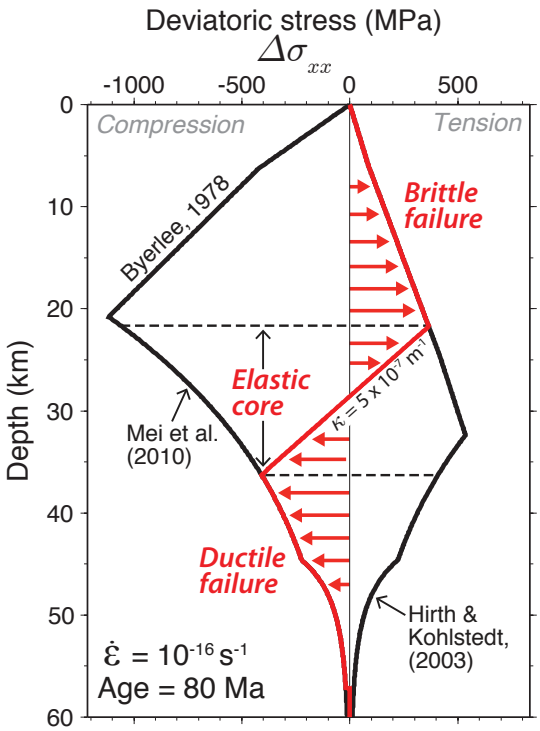

Figure 6.6: Figure illustrating bending-induced inelastic yielding. The black curves show a yield strength envelope for 80 Ma oceanic lithosphere, and the red curve shows the stress distribution induced when the plate is bent to a curvature of $\kappa = 5 \times 10^{-7}\,\mathrm{m}^{-1}$ (assuming an elastic-perfectly plastic rheology). The flow laws are labelled on the plot; the brittle regime was calculated assuming hydrostatic pore fluid pressure.

Tonga-Kermadec trench as imaged by a newly compiled, cleaned swath bathymetry dataset comprised of all available data in the region, totalling 36 cruises. Here, the incoming tectonic fabric of oceanic crust strikes roughly perpendicular to the trench. As a result, it is difficult to reactivate this fabric and so new, trench-parallel, large-offset (up to $>$ 1.5 km), widely spaced ($\sim$ 5–10 km) normal faults are formed as the plate bends. Both landward-dipping and seaward-dipping faults are formed such that they bound horst and graben structures. At subduction zones where the fabric of oceanic crust strikes at low angles to the trench ($<$ 25–30°), this fabric is reactivated as a series of small-offset (150–500 m), closely spaced (a few km), landward-dipping faults (e.g., Massell, 2002; Ranero et al., 2003; Billen et al., 2007); this will be discussed further in the next chapter. Seismic reflection profile data, for example at the Middle America trench, have also imaged bend-faults that offset the seafloor and penetrate the uppermost mantle to depths of $\sim$ 20 km (Ranero et al., 2003).

Bend-faulting is also reflected in outer trench-slope seismicity (e.g., Chapple and Forsyth,

1979; Forsyth, 1982; Christensen and Ruff, 1988; Craig et al., 2014a). This is illustrated in Figure 6.7 (a and b), which shows ISC (International Seismological Centre, 2013), EHB (Engdahl et al., 1998) and CMT (Dziewonski et al., 1981; Ekström et al., 2012) seismicity seaward of the Tonga-Kermadec trench axis. These events are predominantly tensional and occur at shallow depths (< 30 km); deeper compressional earthquakes occur less frequently and are separated from shallow events by an aseismic core, which reflects the region where stresses are not high enough to cause yielding (e.g., Chapple and Forsyth, 1979; Craig et al., 2014a). The relative infrequency of these deeper events indicates the transition to predominantly ductile deformation; indeed, it is likely that these occur via semi-brittle, rather than purely brittle processes.

6.5.3 Mantle hydration and serpentinization

Bend-faults may further contribute to lithospheric weakening by providing a pathway for seawater to enter, either by thermal convection or seismic pumping, and subsequently alter the crust and upper mantle (e.g., Yamano and Uyeda, 1990; Peacock, 2001; Ranero et al., 2003; Grevemeyer et al., 2007). Indeed, a growing body of evidence suggests that the crust and uppermost mantle undergo significant hydration at the outer trench-slope. For example, active source seismic studies show anomalously low P-wave velocities at the outer trench-slope of the Chile trench (e.g., Ranero and Sallares, 2004; Contreras-Reyes et al., 2008a; Contreras-Reyes et al., 2008b), the Middle America trench (Grevemeyer et al., 2007), and the Kermadec trench (Bassett, 2014). Further evidence comes from 2-D travel time tomography offshore Southern Central Chile, which reveals anomalously high Poisson's ratio and low seismic anisotropy at the outer trench-slope (Contreras-Reyes et al., 2008b). Moreover, hydrothermal circulation is indicated by heat flow surveys offshore Nicaragua, Central Chile and Peru, which show that heat flow landward of the outer rise is lower than expected for conductive heat loss and lower than the global mean for crust of that age (Yamano and Uyeda, 1990; Grevemeyer et al., 2005).

Hydration of mantle peridotite at temperatures < 400–500 °C results in serpentinization, where olivine is altered to the serpentine minerals lizardite, chrysolite and antigorite (e.g., Wicks, 1969; Coleman and Keith, 1971; Moody, 1976). Serpentinite has a very different

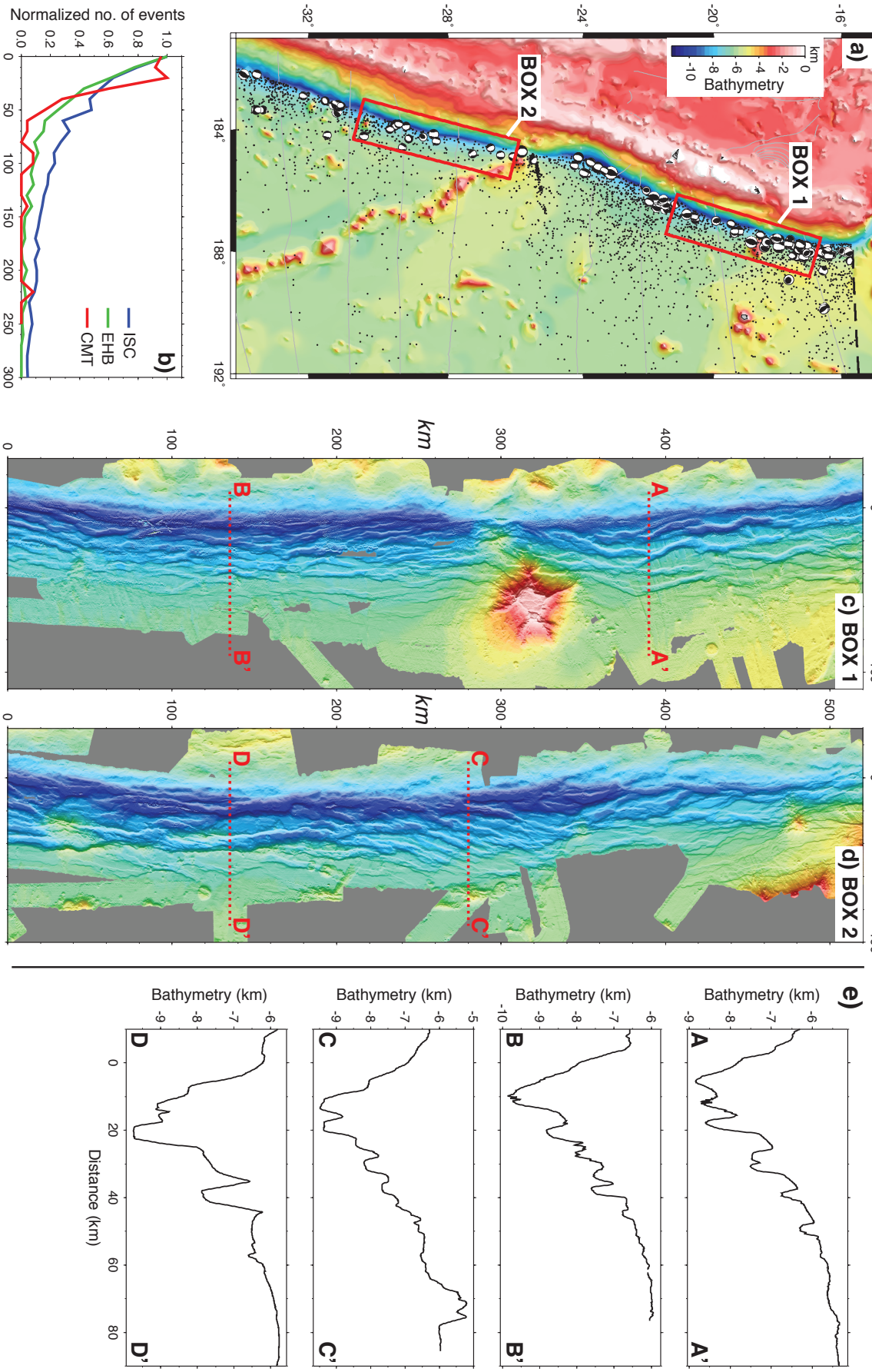

Figure 6.7: *Caption on next page*

Figure 6.7: (*Figure on previous page*) Plots showing seismicity and bend-faulting at the outer trench-slope of the Tonga-Kermadec trench. (a) GEBCO bathymetry overlain with all earthquakes, as of 2013, in the ISC (black dots) and CMT (focal mechanisms) catalogues. Only events seaward of the trench axis and within the trench-bin (black dash) are shown. CMT events have been plotted at their respective EHB positions, as these are more accurate (e.g., Bürgmann et al., 2005; Ranero et al., 2005). (b) Histograms of ISC, EHB and CMT seismicity against distance from the trench, where the bin width is 10 km. This shows the landward increase in seismicity due to outer trench-slope bend-faulting. (c,d) Swath bathymetry, gridded at 200 m resolution, from the boxes shown in Figure 6.7a. This is from a newly compiled, cleaned dataset comprised of all available data in the region, totalling 36 cruises. The incoming fabric of oceanic crust strikes at high angles to the trench and therefore new, large-offset, horst-and-graben style faults are formed. (e) Swath bathymetry along the profiles shown in Figures 6.7c and 6.7d. This shows the horst and graben structures, which are bounded by bend-faults with offsets up to > 1.5 km.

rheology to that of olivine and therefore mantle serpentinization at the outer trench-slope may influence lithospheric strength; this will be discussed in the following paragraphs.

In the brittle regime, laboratory experiments show that lizardite, the most abundant polymorph in serpentinized peridotite, has lower frictional strength than most lithospheric rocks (Dengo and Logan, 1981; Moore et al., 1997). Furthermore, the fracture strength of serpentinite is lower than that of other common lithospheric rocks, with lizardite being particularly weak (Raleigh and Paterson, 1965; Escartin et al., 1997). This low fracture strength results in a transition from localized brittle deformation to distributed cataclastic flow with increasing pressure, which may cause further weakening. Escartin et al. (1997) also suggested that the geometry of micro-cracking may confine fluids within serpentinized shear zones, further reducing their strength relative to the surrounding rock and potentially leading to strain localization.

Experiments on peridotite cores with 10–15 % serpentine show that the strength and style of brittle deformation is comparable to that of pure serpentinite, which suggests that the deformation of partially serpentinized peridotite is primarily accommodated by serpentine minerals (Escartin et al., 2001). Active source seismic studies of outer trench-slopes reveal that at Moho depths, upper mantle P-wave velocities are reduced from 8.1–8.3 km/s to 7.4–7.6 km/s, indicating serpentinization of 20–25 % (Ranero and Sallares, 2004; Grevemeyer et al., 2007; Contreras-Reyes et al., 2008a). Thus, it is likely that significant weakening has occurred

in the brittle regime, with rock behaviour perhaps approaching that of pure serpentinite.

Deformation studies also show that serpentine is weaker than olivine in the dislocation creep regime (Hilairet et al., 2007). Thus, ductile weakening could occur if the deeper mantle is hydrated and partially serpentinized. Indeed, it has been suggested that the lower planes of intermediate-depth double seismic zones are caused by serpentine dehydration embrittlement (e.g., Peacock, 2001; Wang, 2002); if this is the case, the lithosphere must have been hydrated to these depths (up to 50 km) prior to subduction. It is unlikely that outer trench-slope bend-faults could facilitate hydration this deep, as this would require them penetrating from the shallow tensional regime, through the neutral surface, into the deeper compressional regime. However, it has been suggested that thermal cracking to depths of 30–50 km could provide fluid pathways that are pervasive throughout the sub-crustal mantle lithosphere (Korenaga, 2007). If this was the case, serpentinized cracks might localize deformation, perhaps leading to further weakening via grain size reduction and a subsequent transition from dislocation to diffusion creep (e.g., Karato et al., 1986; Warren and Hirth, 2006). Indeed, the (infrequent) occurrence of relatively deep, compressional outer rise earthquakes at the Japan (Gamage et al., 2009; Hino et al., 2009), Tonga, Kuril, Chile and Middle America trenches (Craig et al., 2014a) suggests that some kind of strain localization is occurring in the ductile deformation regime.

6.6 Chapter summary

In this chapter, we have described Inversion A2, in which circum-Pacific trench-outer rise gravity anomalies were modelled using a variable T_e elastic plate. The key points are as follows:

- Inversion A2 seeks two best-fitting T_e values—a landward T_e and a seaward T_e—where prior to inversion, the observed plate curvature was used to define the location of the linear transition between the two values.
- Model fits to observed gravity anomalies are significantly improved relative to the constant T_e inversion (Inversion A1), as the variable T_e plates fit both the steepness and

curvature of the outer trench-slope and the wavelength and amplitude of the outer rise. The best-fit Δg_{rms} is improved by an average of 39 % and by up to 73 %.

- The plate weakens in 42 out of 43 best-fit models, where the average reduction in T_e between the seaward and landward values is 51 ± 11 % and the range is 20–72 %. This suggests that significant plate weakening is a ubiquitous feature of the outer trench-slope and outer rise of circum-Pacific subduction zones.

- Irrespective of bin size, there is a general increase in both landward T_e and seaward T_e with plate age, which gives us further confidence that the increase in flexural rigidity with age is a robust result. For example, for the trench-bins, the increase in landward T_e and seaward T_e with age is best fit by the depth to the 342 ± 35 °C and 714 ± 75 °C plate-cooling isotherm respectively. However, we note that there is some scatter in the T_e values and that for lithosphere older than 80 Ma, there is no clear increase with age.

- Landward T_e is better constrained and less scattered than seaward T_e; this is due to the relatively high SNR in the observed gravity landward of the outer rise. Landward T_e is also better constrained and less scattered than the constant T_e derived from Inversion A1. This suggests that some of the scatter and uncertainty in T_e from Inversion A1 is due modelling the variable rigidity lithosphere with a constant T_e plate and/or the relatively low SNR seaward of the outer trench-slope.

- The plate weakening that occurs landward of the outer rise is caused primarily by bending-induced inelastic yielding—a combination of shallow, brittle and deep, ductile failure—and perhaps also by mantle hydration and serpentinization via bend-faults.

- Bending-induced inelastic yielding is evidenced by observations of seismicity and bend-faulting on the outer trench-slope. For example, we have presented a newly compiled, processed swath bathymetry dataset for the outer trench-slope of the Tonga-Kermadec trench. Mantle hydration and serpentinization is evidenced by, for example, reduced P-wave velocities and reduced heat flow at the outer trench-slope.

Chapter 7

Discussion on circum-Pacific T_e variations

In the previous two chapters, we showed that there is a first-order increase in T_e with plate age at circum-Pacific subduction zones (Figures 5.2 and 6.4). This finding is consistent with models for the cooling of oceanic lithosphere and the ductile creep of lithospheric minerals; our reasoning is as follows. Variations in seafloor depth and heat flow show that oceanic lithosphere cools with age as it moves away from the mid-ocean ridge (e.g., Langseth et al., 1966; McKenzie, 1967; Parsons and Sclater, 1977). Rock mechanics experiments show that the ductile deformation of lithospheric minerals occurs via temperature-dependent creep, where the flow stress increases with decreasing temperature (e.g., Goetze, 1978; Brace and Kohlstedt, 1980; Chopra and Paterson, 1984; Karato et al., 1986). The flexural rigidity of the lithosphere reflects the depth-integrated strength across the elastic, brittle and ductile deformation regimes. We see therefore that oceanic lithosphere cools with age, the ductile flow stress increases with decreasing temperature, and the flexural rigidity is dependent on this flow stress. Therefore, the T_e of oceanic lithosphere is expected to increase with age, as we have found at the trench-outer rise system of circum-Pacific subduction zones.

However, although we have found a first-order increase in T_e with plate age, there is certainly some scatter in the relationship. This suggests that there are factors other than

plate age that also affect the flexural rigidity of oceanic lithosphere and/or that there are inaccuracies in our T_e estimates. In this chapter, we will discuss both of these possibilities with reference to our results from Inversions A1 and A2, which are shown plotted along each trench in the following six pages (Figures 7.1–7.6) and are plotted against age in Figures 5.2 and 6.4. These figures will be referred to throughout this chapter, where T_e estimates from Inversion A1 will be referred to as 'constant T_e' and estimates from Inversion A2 will continue to be referred to as 'landward T_e' and 'seaward T_e'. Unless otherwise stated, plate ages quoted in this chapter refer to the ensemble-averaged seafloor age (Müller et al., 2008, v3.2) 100 km seaward of the trench axis (plotted in part b of Figures 7.1–7.6). For a description of the tectonic setting of each of the subduction zones shown in Figures 7.1–7.6, see Appendix A.

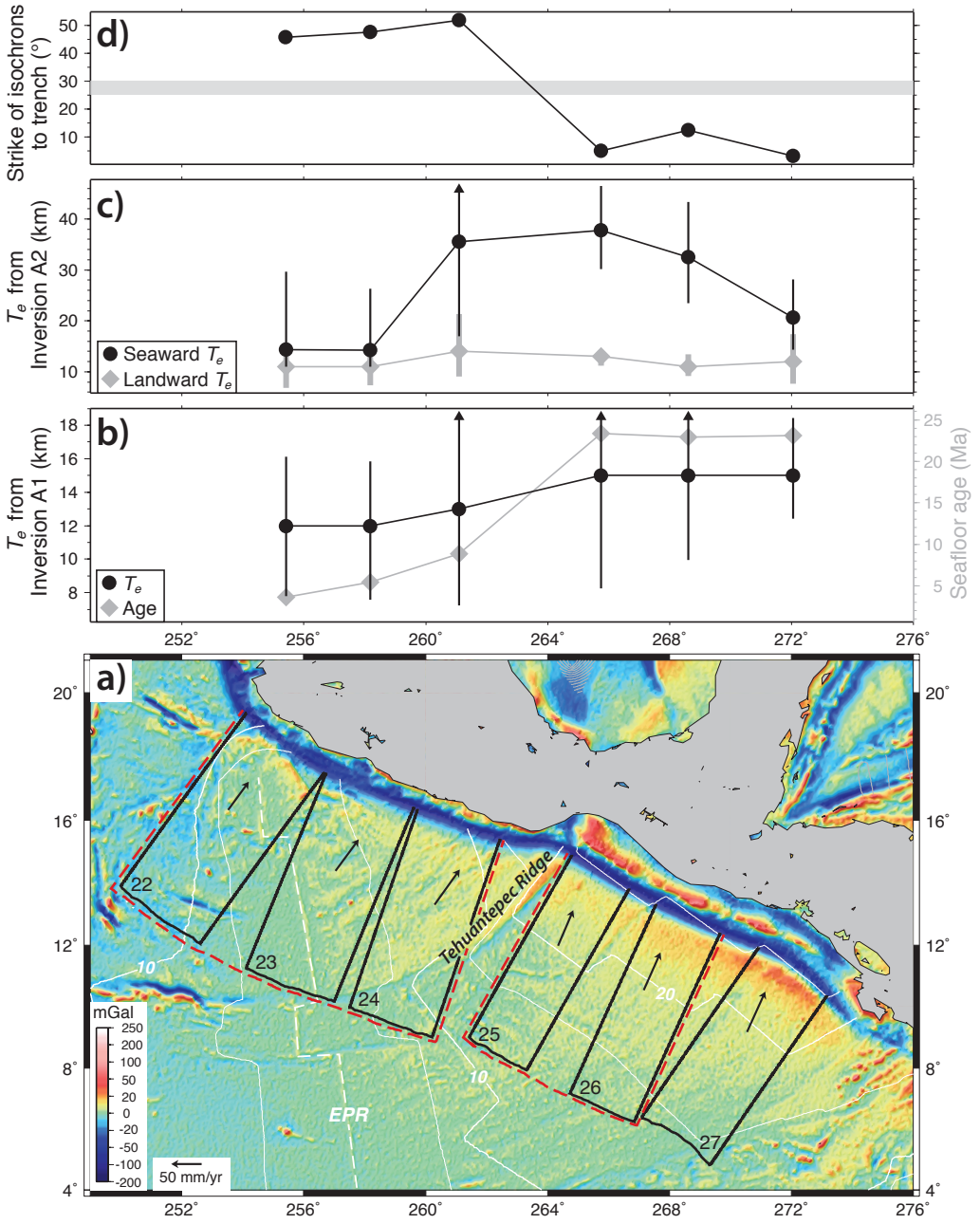

Figure 7.1: Segment-bin T_e estimates from the Middle America trench. (a) Free-air gravity anomaly map (Sandwell et al., 2014, v23.1); the white lines show seafloor isochrons at 5 Ma intervals (Müller et al., 2008, v3.2) and the dashed white line marks the East Pacific Rise (EPR). The solid black boxes show the segment-bins and the dashed red boxes show the bins described in Section 7.1.3. The black arrows show plate convergence vectors from the MORVEL plate motion model (DeMets et al., 2010). (b) T_e from Inversion A1, and the ensemble-averaged seafloor age 100 km from the trench axis, plotted against longitude. (c) T_e from Inversion A2 plotted against longitude. Arrows on error bars in Figures 7.1b and 7.1c indicate that the upper bound is outside the plot range. (d) Strike of seafloor isochrons to the trench axis, plotted against longitude. The grey shade marks the transition in the style of bend-faulting from abyssal hill fault reactivation ($<$ 25–30°) to newly formed, trench-parallel faults ($>$ 25–30°).

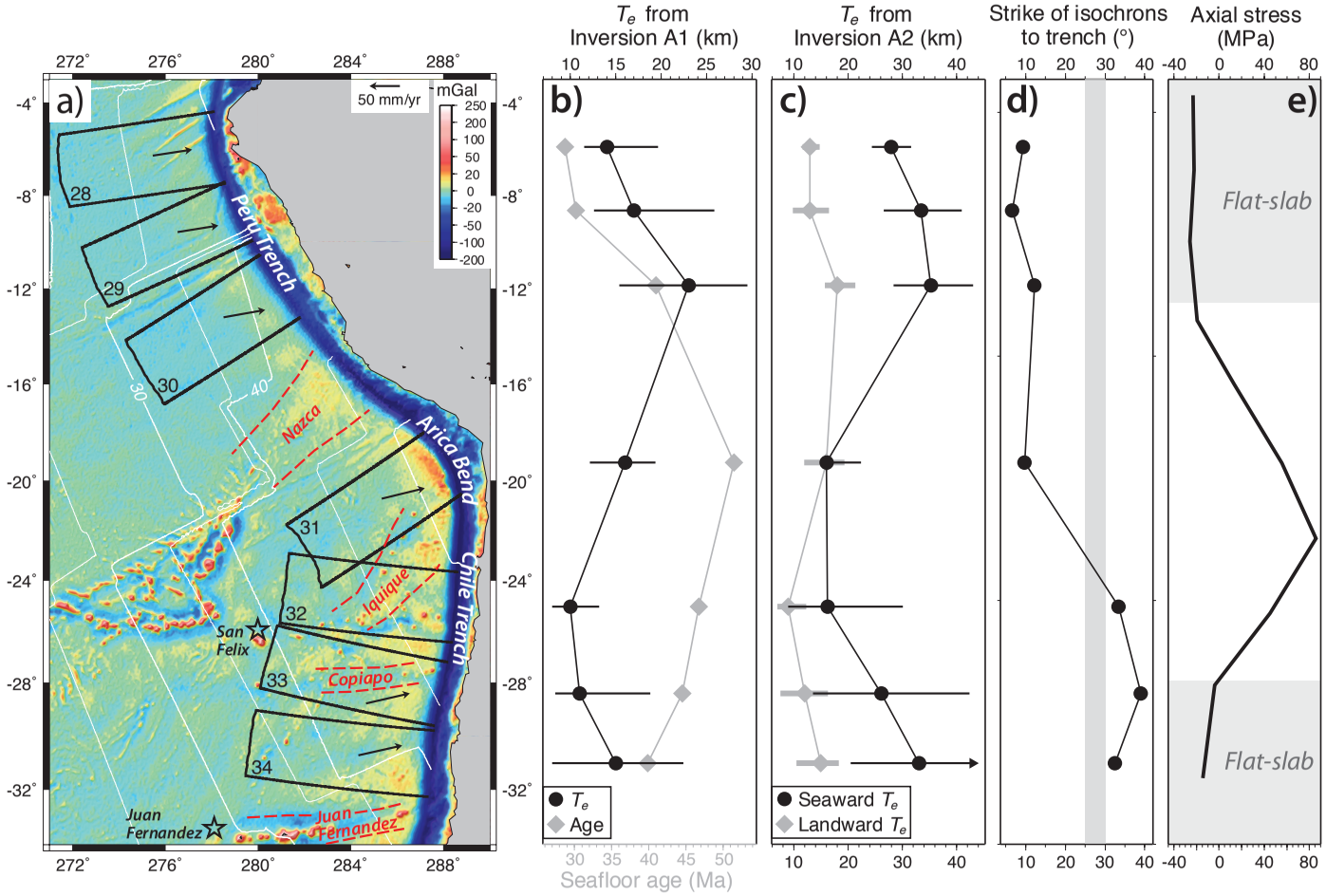

Figure 7.2: Segment-bin T_e estimates from the Peru-Chile trench. (a) Free-air gravity anomaly map (Sandwell et al., 2014, v23.1); the white lines show seafloor isochrons at 5 Ma intervals (Müller et al., 2008, v3.2). The solid black boxes show the segment-bins, and the black arrows show plate convergence vectors from the MORVEL plate motion model (DeMets et al., 2010). The dashed red lines mark aseismic ridges and the black stars mark hotspot locations (Zhao, 2007). (b) T_e from Inversion A1, and the ensemble-averaged seafloor age 100 km from the trench axis, plotted against latitude. (c) T_e from Inversion A2 plotted against latitude. Arrows on error bars in Figures 7.2b and 7.2c indicate that the upper bound is outside the plot range. (d) Strike of seafloor isochrons to the trench axis, plotted against latitude. The grey shade marks the transition in the style of bend-faulting from abyssal hill fault reactivation (< 25–$30°$) to newly formed, trench-parallel faults (> 25–$30°$). (e) Black line shows trench-normal axial stresses digitized from Wortel and Cloetingh (1985) and the grey shade shows regions of flat-slab subduction (from Manea et al., 2012).

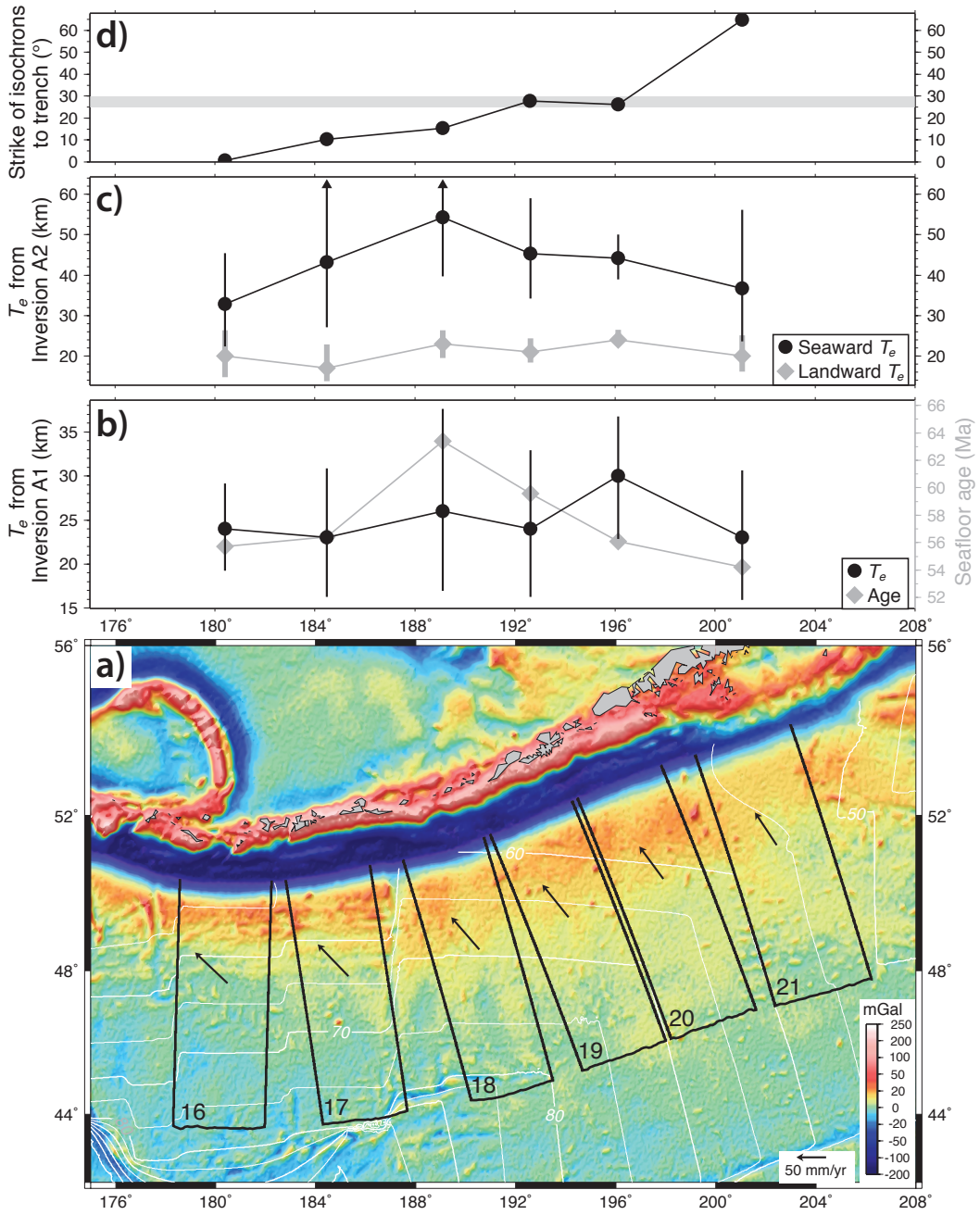

Figure 7.3: Segment-bin T_e estimates from the Aleutian trench. (a) Free-air gravity anomaly map (Sandwell et al., 2014, v23.1); the white lines show seafloor isochrons at 5 Ma intervals (Müller et al., 2008, v3.2). The solid black boxes show the segment-bins, and the black arrows show plate convergence vectors from the MORVEL plate motion model (DeMets et al., 2010). (b) T_e from Inversion A1, and the ensemble-averaged seafloor age 100 km from the trench axis, plotted against longitude. (c) T_e from Inversion A2 plotted against longitude. Arrows on error bars in Figures 7.3b and 7.3c indicate that the upper bound is outside the plot range. (d) Strike of seafloor isochrons to the trench axis, plotted against longitude. The grey shade marks the transition in the style of bend-faulting from abyssal hill fault reactivation (< 25–$30°$) to newly formed, trench-parallel faults (> 25–$30°$).

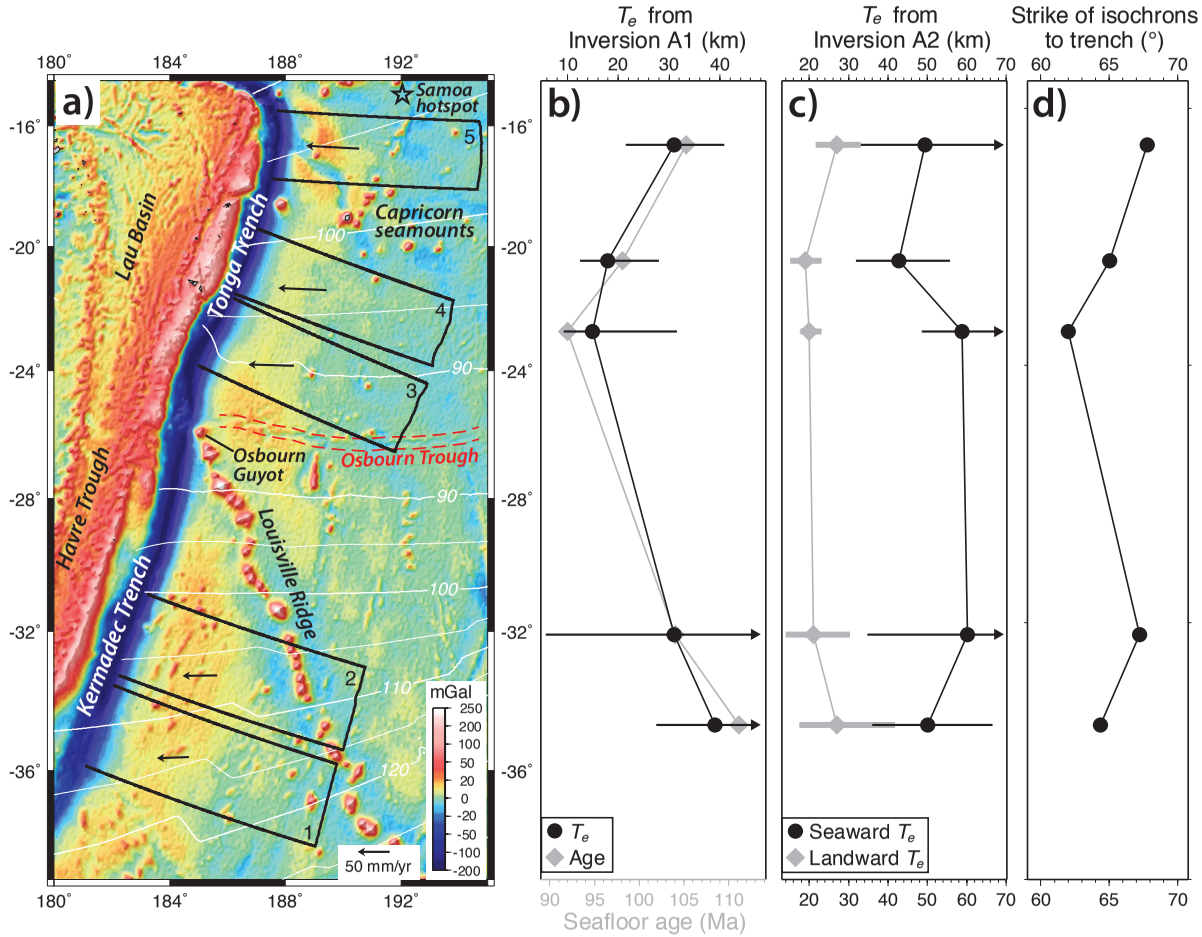

Figure 7.4: Segment-bin T_e estimates from the Tonga-Kermadec trench. (a) Free-air gravity anomaly map (Sandwell et al., 2014, v23.1); the white lines show seafloor isochrons at 5 Ma intervals (Müller et al., 2008, v3.2). The solid black boxes show the segment-bins, and the black arrows show plate convergence vectors from the MORVEL plate motion model (DeMets et al., 2010). (b) T_e from Inversion A1, and the ensemble-averaged seafloor age 100 km from the trench axis, plotted against latitude. (c) T_e from Inversion A2 plotted against latitude. Arrows on error bars in Figures 7.4b and 7.4c indicate that the upper bound is outside the plot range. (d) Strike of seafloor isochrons to the trench axis, plotted against latitude. The grey shade marks the transition in the style of bend-faulting from abyssal hill fault reactivation (< 25–$30°$) to newly formed, trench-parallel faults (> 25–$30°$).

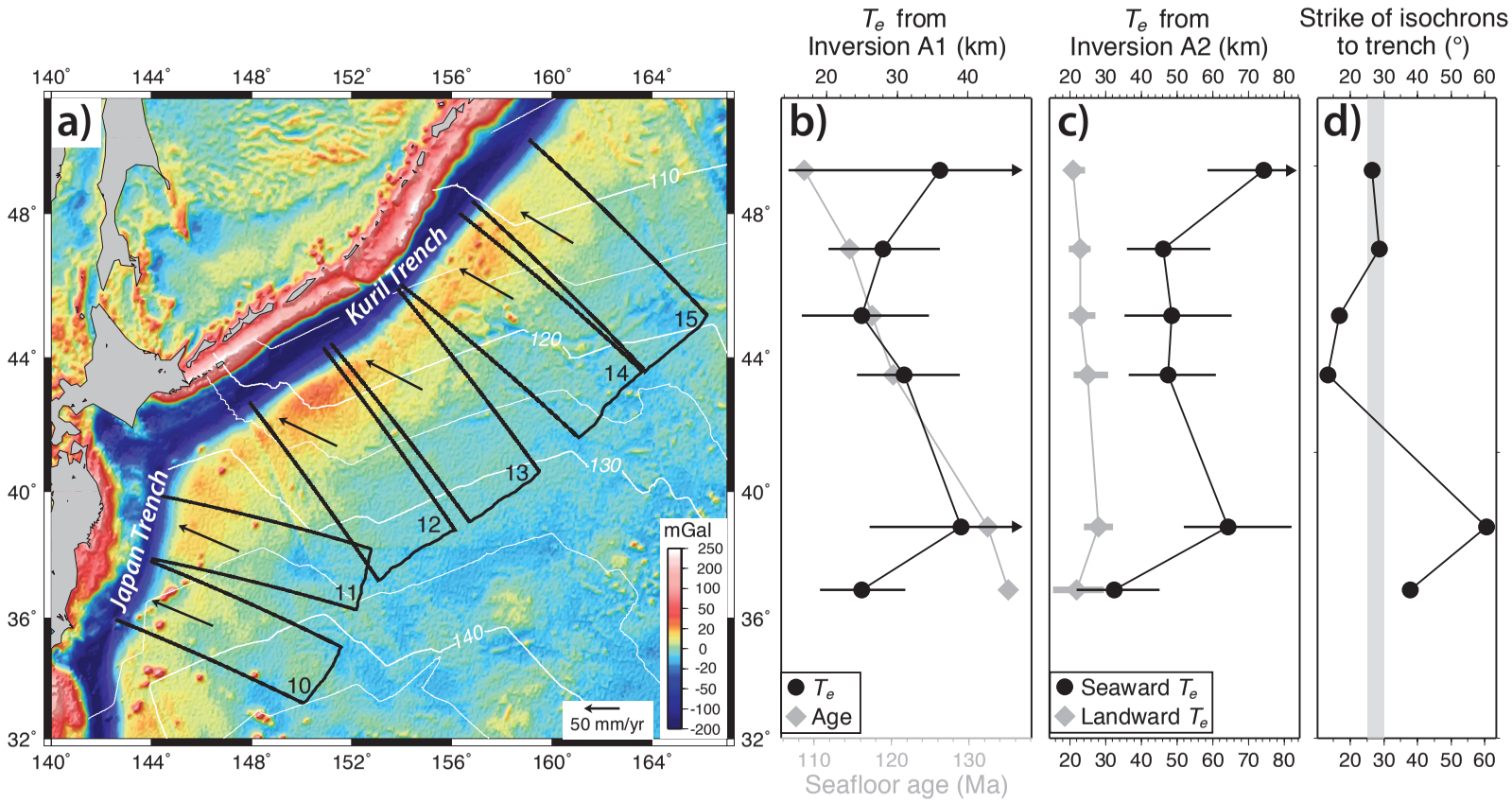

Figure 7.5: Segment-bin T_e estimates from the Japan and Kuril trenches. (a) Free-air gravity anomaly map (Sandwell et al., 2014, v23.1); the white lines show seafloor isochrons at 5 Ma intervals (Müller et al., 2008, v3.2). The solid black boxes show the segment-bins, and the black arrows show plate convergence vectors from the MORVEL plate motion model (DeMets et al., 2010). (b) T_e from Inversion A1, and the ensemble-averaged seafloor age 100 km from the trench axis, plotted against latitude. (c) T_e from Inversion A2 plotted against latitude. Arrows on error bars in Figures 7.5b and 7.5c indicate that the upper bound is outside the plot range. (d) Strike of seafloor isochrons to the trench axis, plotted against latitude. The grey shade marks the transition in the style of bend-faulting from abyssal hill fault reactivation ($<$ 25–30°) to newly formed, trench-parallel faults ($>$ 25–30°).

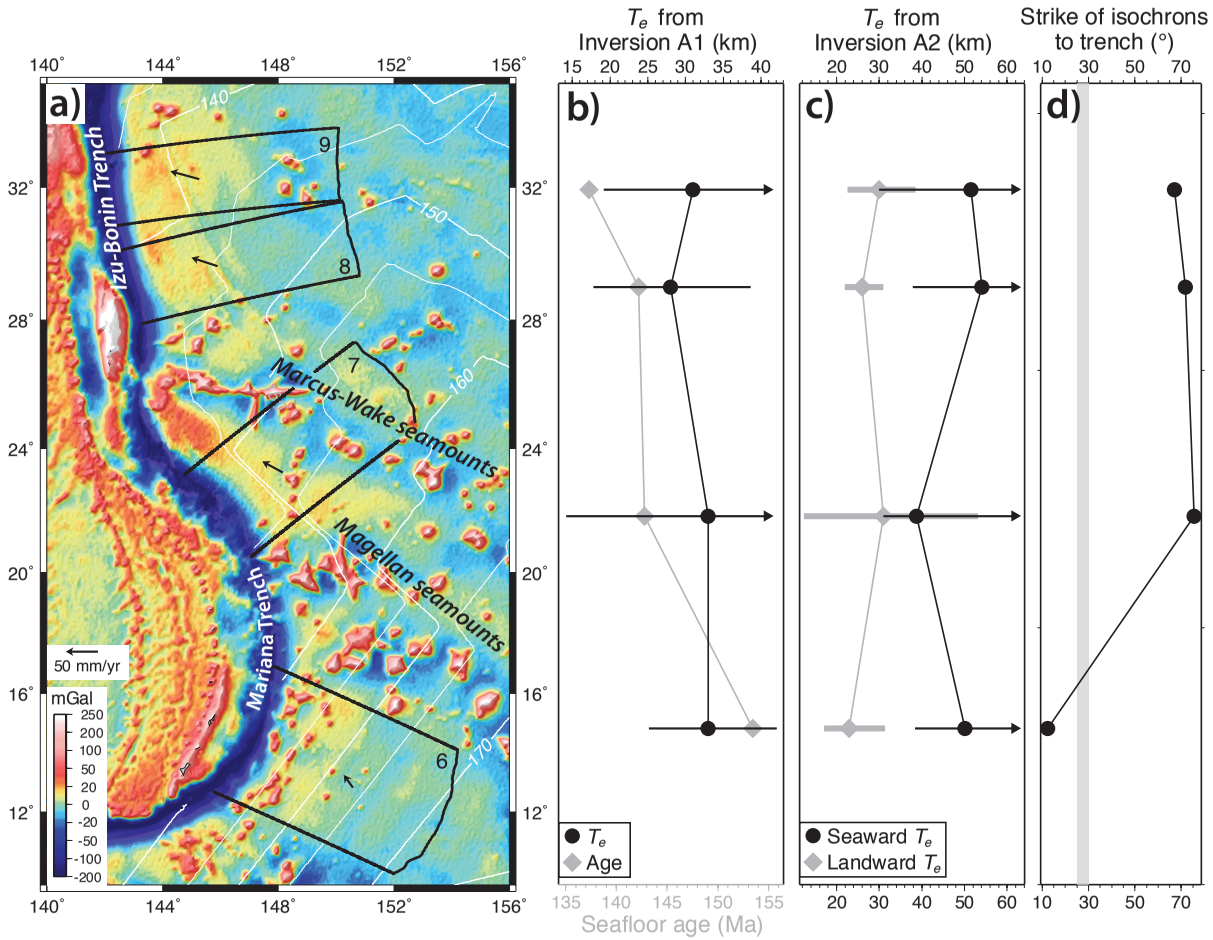

Figure 7.6: Segment-bin T_e estimates from the Mariana and Izu-Bonin trenches. (a) Free-air gravity anomaly map (Sandwell et al., 2014, v23.1); the white lines show seafloor isochrons at 5 Ma intervals (Müller et al., 2008, v3.2). The solid black boxes show the segment-bins, and the black arrows show plate convergence vectors from the MORVEL plate motion model (DeMets et al., 2010). (b) T_e from Inversion A1, and the ensemble-averaged seafloor age 100 km from the trench axis, plotted against latitude. (c) T_e from Inversion A2 plotted against latitude. Arrows on error bars in Figures 7.6b and 7.6c indicate that the upper bound is outside the plot range. (d) Strike of seafloor isochrons to the trench axis, plotted against latitude. The grey shade marks the transition in the style of bend-faulting from abyssal hill fault reactivation (< 25–$30°$) to newly formed, trench-parallel faults (> 25–$30°$).

7.1 Regions at variance with a simple relationship between T_e and plate age

To aid our discussions in this chapter, we will first describe three regions where the results of Inversions A1 and A2 are at variance with a simple relationship between T_e and plate age, and where other factors may therefore have a significant effect on the flexural rigidity and/or the accuracy of T_e estimates. These regions will then be referred to at various points throughout this chapter. Note that we are not implying that these are the *only* regions where the results deviate from a simple T_e-age relationship; these are just regions where the deviation is particularly evident and that serve to illustrate many of the discussion points in this chapter.

7.1.1 Old lithosphere

As shown in Figures 5.2 and 6.4, for lithosphere older than 80 Ma, there is no clear increase in T_e with plate age. In addition to some of the points that will be discussed later in this chapter, there are two theoretical reasons why this might be the case. Firstly, because plate-cooling is a diffusive process, the rate of cooling slows with age, and because heat is supplied at the base of the plate, the rate of cooling is particularly slow for lithosphere older than $\sim$ 70 Ma, as the thermal structure begins to 'feel' the influence of the bottom boundary condition (Parsons and Sclater, 1977). This means that for older lithosphere, the thermal structure, and therefore the ductile flow strength, changes relatively little with plate age. For example, the depth to the 600 °C plate-cooling isotherm increases by only 11 km from 80 to 150 Ma, compared to an increase of 24 km from 10 to 80 Ma. Secondly, the flexural parameter, α, which reflects the wavelength of flexure, is proportional to ${T_e}^{3/4}$ (Equations 3.20 and 3.16); this means that the sensitivity of the flexural wavelength to T_e decreases with increasing rigidity. As a result, changes in T_e are more difficult to detect for older, stronger lithosphere—particularly in the presence of short-wavelength noise such as seamounts—and thus T_e estimates are more uncertain. This is reflected in the results from inversion of synthetic profiles (Figures 4.7 and 4.8), which show that T_e is less well constrained for stronger input plates than for weaker.

7.1.2 Peru-Chile

North of the Nazca Ridge, at the Peru trench (Figure 7.2), T_e increases with plate age. Plate age increases southwards (bins 28 to 30) from 28 to 41 Ma, which is coincident with an increase in: constant T_e from 14 to 23 km, landward T_e from 13 to 18 km, and seaward T_e from 28 to 35 km. This is as expected from thermal cooling models, because young lithosphere cools rapidly and therefore plate age should have a strong effect on rigidity. Moving south of the Nazca Ridge to the Chile trench, however, there is a sudden decrease in T_e despite an increase in plate age. Figure 7.2 shows that plate age increases from 41 Ma in bin 30 to 47 Ma in bin 32, which is coincident with a drop in: constant T_e from 23 to 10 km, landward T_e from 18 to 9 km, and seaward T_e from 35 to 16 km. Furthermore, T_e then increases southwards from bin 32 to bin 34, despite a decrease in plate age. Plate age decreases from 47 Ma in bin 32 to 40 Ma in bin 34, which is coincident with an increase in: constant T_e from 10 to 15 km, landward T_e from 9 to 15 km, and seaward T_e from 16 to 33 km. Here, we have not discussed the T_e in bin 31, because the arcuate trench geometry of the Arica Bend causes the outer rise to have anomalous geometry, which will be discussed in Section 7.6.

From the description above, it is clear that the results at the Chile trench are at variance with a simple increase in T_e with plate age; in fact, the opposite seems to be true. This is further illustrated by the plots of T_e against plate age (Figures 5.2 and 6.4), which show that the segment-bin T_e in bins 32 and 33 appears anomalously low for the age and that the Chile trench-bin T_e also appears anomalously low. These anomalous values are quite surprising, because the lithosphere is relatively young and therefore cooling relatively quickly, such that plate age should have a strong effect on the flexural rigidity. Note that Judge and McNutt (1991) also found anomalously low T_e values the the trench-outer rise system of the Chile trench, which suggests that this is a robust result.

7.1.3 Middle America

At the Middle America trench (Figure 7.1), the plate age increases eastwards across the Tehuantepec Ridge from 9 Ma in bin 25 to 23 Ma in bin 26. As the lithosphere is very young,

rapid plate-cooling should mean that the lithosphere to the east of the ridge is significantly colder, and therefore stronger, than that to the west. Surprisingly therefore, there is no significant change in either landward T_e or constant T_e across the ridge. Landward T_e decreases eastwards from 14 km in bin 25 to 13 km in bin 26, and constant T_e increases from 13 km to 15 km. Seaward T_e is poorly constrained in bin 24, but there is an increase from 14 km in bins 22 and 23 to 33–38 km in bins 25 and 26. Here, we have not discussed the T_e in bin 27, because the outer rise appears to have anomalous geometry, which will be discussed in Section 7.6.

From the description above, it is clear that the results at the Middle America trench are at variance with a simple increase in T_e with plate age. Despite there being a 14 Ma eastwards increase in age across the Tehuantepec Ridge, there is little change in either landward T_e or constant T_e. However, it appears that there might be an eastwards increase in seaward T_e across the ridge, but the large uncertainties in these values make it difficult to be conclusive. Therefore, in an attempt to reduce this uncertainty, we inverted ensemble-averaged profiles from the two bins shown in dashed red in Figure 7.1a. One of these bins encompasses the region to the west of the Tehuantepec Ridge and the other encompasses the region to the east, not including bin 27, where the outer rise appears to have anomalous geometry. As shown in Figure 7.7a, landward T_e to the west and east of the ridge is 12 km and 11 km respectively, despite a 17 Ma difference in plate age. Furthermore, it is clear that the landward T_e to the west of the ridge is anomalously high for the age. However, as shown in Figure 7.7b, seaward T_e does increase with age across the Tehuantepec Ridge, from 17 to 33 km, with both of these values falling on the $\sim$ 900 °C isotherm. This interesting observation—that seaward T_e increases with age at the Middle America trench, but landward T_e does not—may offer clues as to the cause of the anomalously high landward T_e to the west of the Tehuantepec Ridge.

We will now begin our discussion of factors other than plate age that may affect the flexural rigidity of oceanic lithosphere and/or the accuracy of our circum-Pacific T_e estimates.

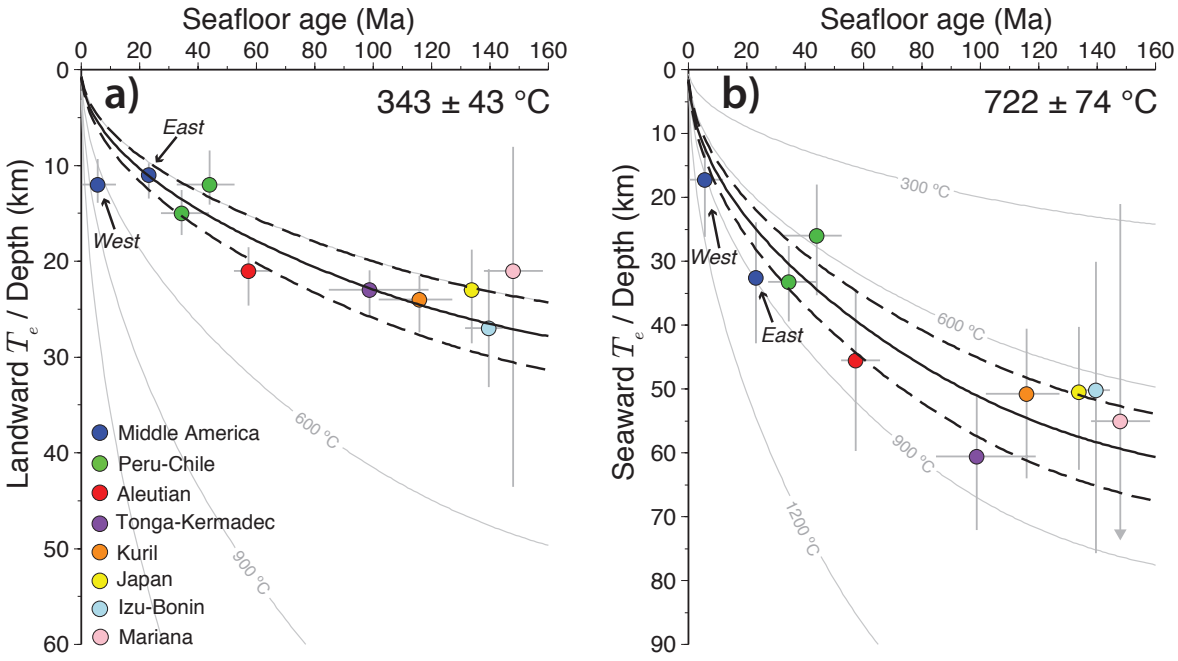

Figure 7.7: Trench-bin T_e from Inversion A2, with two T_e values for the Middle America trench: one for the region to the west of the Tehuantepec Ridge and the other for the region to the east of it (bins shown in dashed red in Figure 7.1a). The plots show that at the Middle America trench, seaward T_e increases with age but landward T_e does not, and that the landward T_e to the west of the Tehuantepec Ridge appears anomalously high.

7.2 Short-wavelength noise

Even after ensemble-averaging, trench-outer rise gravity profiles retain some short-wavelength noise that is unrelated to the long-wavelength flexure caused by plate subduction. This noise is likely to cause inaccuracies in T_e estimates. The trench-bin profiles are less noisy than the segment-bins, as they were ensemble-averaged over a larger area. We suggest that this explains why the trench-bin T_e is less scattered than the segment-bin T_e, as shown in Figures 5.2 and 6.4. In particular, as shown in Figure 6.4 (c and d), seaward T_e is much more scattered for the segment-bins than for the trench-bins. This is because seaward of the outer trench-slope, the amplitude of the flexural deflection is relatively low and therefore the signal-to-noise ratio in the observed gravity is relatively low.

Short-wavelength noise is predominantly in the form of seamounts and aseismic ridges created by hotspot volcanism. There are many hotspot tracks on older, western Pacific lithosphere and this might contribute to the scatter in segment-bin T_e for lithosphere older than 80

Ma. For example, the Izu-Bonin, and in particular the Mariana, trenches are affected by the Cretaceous seamounts that make up the Darwin Rise, such as the Magellan and Marcus-Wake groups (Figure 7.6a) (e.g., Duncan and Clague, 1985; Smith et al., 1989; Smoot, 1989). As shown in Figure 7.4a, the Tonga-Kermadec trench is subducting the Louisville Ridge seamount chain, which formed over a hotspot presently located near the intersection of the Eltanin fracture zone and the East Pacific Rise (Watts et al., 1988; Koppers et al., 2004). The northern Tonga trench is also affected by the Capricorn seamount group, which is thought to be be part of a partially subducted seamount chain that extends eastwards to Niue Island (Brodie, 1965; Crawford et al., 2003). As shown in Figure 7.2a, the Peru-Chile trench is intersected by a number of aseismic ridges: the Nazca Ridge, formed by the Easter-Salas hotspot (Ray et al., 2012); the Juan Fernández Ridge, formed by the Juan Fernández hotspot (Yáñez et al., 2001); and the Iquique and Copiapó Ridges (Contreras-Reyes and Carrizo, 2011; Manea et al., 2012), which likely formed above the San Felix hotspot.

7.3 Thermal rejuvenation

As well as introducing short-wavelength noise into the flexural signal, hotspot volcanism might also have thermally rejuvenated the lithosphere (Menard and McNutt, 1982; McNutt, 1984). 'Thermal rejuvenation' is when the lithosphere is reheated by a mantle hotspot so that its thermal structure is significantly altered, and perhaps 'reset' to that of younger lithosphere. As the ductile flow strength of lithospheric minerals, such as olivine, is temperature dependent, this thermal rejuvenation might weaken the lithosphere and cause a reduction in T_e (e.g., McNutt, 1984; Smith et al., 1989). In this section, we will discuss two circum-Pacific regions where hotspot-induced thermal rejuvenation might have an effect on the T_e of the subducting plate. Before beginning this discussion, we will introduce two concepts that will be referred to throughout: 'depth anomalies' and the 'effective thermal age', t_{eff}.

7.3.1 Depth anomalies

One simple method of detecting thermal anomalies in the lithosphere is by calculating depth anomalies—these are deviations in the observed seafloor depth from the depth predicted by the plate-cooling subsidence model of Parsons and Sclater (1977). Positive depth anomalies mean that the observed seafloor is shallower than predicted and therefore that the lithosphere might be hotter than its seafloor age suggests, whilst the opposite is true for negative depth anomalies. We note, however, that there are other potential causes of depth anomalies, such as dynamically supported topography, crustal thickness variations, and volcanic features such as large igneous provinces and seamounts. Therefore, the geological setting must be considered when interpreting them.

We calculated trench-outer rise depth anomalies in order to test for thermal rejuvenation of the lithosphere in regions affected by hotspot volcanism. Following Hillier and Watts (2005), prior to calculating the depth anomalies, the ensemble-averaged seafloor depths were isostatically corrected for sediment loading. The sediment thickness was ensemble-averaged from the grid of Divins (2003) and the isostatic correction was calculated using (Schroeder, 1984):

$$s = 0.224S + 900\left[1 - \exp\left(\frac{-S}{1800}\right)\right] \tag{7.1}$$

where s is the isostatic correction and S is the sediment thickness, both in metres. This correction accounts for the variation in sediment density with sediment thickness. In Figure 7.8, some of the trench-bin depth anomaly profiles are shown; these plots will be discussed later in this section. Note that the large depth anomalies close to the trench axis are due to the flexure induced by plate subduction; it is only the abyssal anomalies (i.e. seaward of the outer rise) that may reflect the lithosphere's thermal structure.

7.3.2 Effective thermal age, t_{eff}

Another concept related to thermal rejuvenation is the effective thermal age, t_{eff} (McNutt, 1984). This is the age that corresponds to the observed seafloor depth, d, based on the plate-cooling model of Parsons and Sclater (1977), and is given by a rearrangement of their

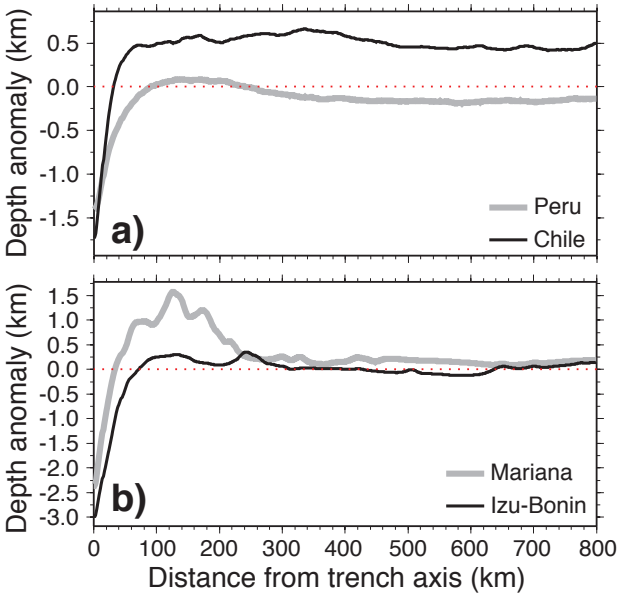

Figure 7.8: Ensemble-averaged depth anomalies at the (a) Peru and Chile trenches, and (b) Mariana and Izu-Bonin trenches.

depth-age curve:

$$\begin{aligned} t_{eff} &= \left(\frac{d - 2500}{350}\right)^2 \quad \text{if} \quad d < 4065 \text{ m} \\ t_{eff} &= -62.8 \log\left(\frac{6400 - d}{3200}\right) \quad \text{if} \quad d \geq 4065 \text{ m} \end{aligned} \tag{7.2}$$

The effective thermal age might better reflect the thermal structure of lithosphere than the seafloor age, and thus might better reveal correlations between T_e and thermal structure. Therefore, we calculated t_{eff} from our ensemble-averaged bathymetry profiles. To do this, we first fitted a straight line to the abyssal (500–800 km from trench axis) bathymetry, in order to remove the effect of short-wavelength fluctuations in depth, and then used this best-fit line as d in Equation 7.2. We only considered the abyssal region when calculating t_{eff} because the seafloor depths landward of this reflect the subduction-induced flexure of the outer rise and outer trench-slope, rather than the thermal structure of the lithosphere. In Figure 7.9, we show a comparison between the seafloor age and t_{eff} for the Peru and Chile trench-bins; this will be discussed later in this section. We note that in calculating t_{eff}, it is assumed that the seafloor depth reflects a plate-cooling geotherm, but that in reality, the thermal structure may be more complex. For example, hotspot-driven thermal rejuvenation might only reheat the lower part of the lithosphere, leaving the shallow thermal structure unchanged (McNutt, 1984).

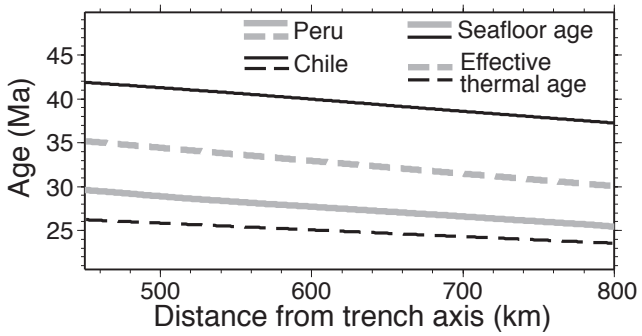

Figure 7.9: Seafloor age (solid) and effective thermal age (dashed) at the Peru (grey) and Chile (black) trenches. The effective thermal ages were calculated from trench-bin ensemble-averaged seafloor depths using the plate-cooling model of Parsons and Sclater (1977).

We will now discuss two regions where the subducting plate has been affected by hotspot volcanism, and the effect that this appears to have on T_e. We are not suggesting that these are the only hotspot-affected regions in our study; they are just regions that illustrate some interesting points.

7.3.3 Peru-Chile

The Nazca Ridge (Figure 7.2a), which is presently subducting at the Peru trench, has been dated at 30 Ma $\sim$ 350 km seaward of the trench, which suggests that it was emplaced on $\sim$ 9 Ma lithosphere (Ray et al., 2012). Therefore, because the subducting plate was so young ($\sim$ 9 Ma) when it was above the hotspot, it is unlikely that the hotspot could have rejuvenated it (reduced t_{eff}) by more than a few Myr. Furthermore, as the lithosphere was above the hotspot $\sim$ 30 Ma, any associated thermal perturbation is likely to have significantly dissipated with age. However, the hotspot volcanism that formed the Juan Fernández, Iquique and Copiapó Ridges, which are all subducting at the Chile trench, may have significantly rejuvenated the lithosphere.

The Juan Fernández Ridge (Figure 7.2a), which formed above the Juan Fernández hotspot, has been dated at 8.5 Ma $\sim$ 100 km seaward of the trench, and therefore formed on $\sim$ 30 Ma lithosphere (Yáñez et al., 2001). The geometry of the Iquique and Copiapó Ridges suggests to us that they formed above the San Felix hotspot (Figure 7.2a). As the Juan Fernández

and San Felix hotspots are a similar distance from the trench, these ridges likely formed at around the same time as the Juan Fernández Ridge. Thus, as the trench-proximal sections of the Iquique and Copiapó Ridges are underlain by ∼ 43–50 Ma seafloor, they were probably emplaced on ∼ 35–42 Ma lithosphere.

The evidence presented above suggests that much of the lithosphere in the Chile trench-outer rise system was above the Juan Fernández and San Felix hotspots only ∼ 8.5 Ma. Therefore, any thermal rejuvenation that might have occurred is unlikely to have fully dissipated with age. Furthermore, as the lithosphere was reasonably old (∼ 30–42 Ma) when it was above the hotspots, there was potential for significant thermal rejuvenation. Indeed, rejuvenation is suggested by the positive abyssal depth anomaly of 420–500 m at the Chile trench (Figure 7.8a), which is indicative of anomalously hot lithosphere and is ∼ 600 m shallower than the depth anomaly at the Peru trench. This suggests that the lithosphere subducting at the Chile trench may be hotter than predicted by its seafloor age. Indeed, as shown in Figure 7.9, the abyssal seafloor depths seaward of the Chile trench give an effective thermal age of 23–26 Ma, which is much younger than the seafloor age of 37–41 Ma. In contrast, the abyssal effective thermal age at the Peru trench is 30–34 Ma, which is slightly older than its seafloor age of 25–29 Ma. Thus, we suggest that thermal rejuvenation is a possible contributor to the anomalously low T_e at the Chile trench (as described in Section 7.1.2). Indeed the most anomalous T_e values are those in bins 32 and 33 (Figures 7.2, 5.2, 6.4), which are directly on top of the Iquique and Copiapó Ridges, where any hotspot-induced thermal rejuvenation would likely have been at its most intense.

7.3.4 Mariana-Izu-Bonin

The Izu-Bonin, and in particular the Mariana, trenches are affected by the Cretaceous seamounts that make up the Darwin Rise, such as the Magellan and Marcus-Wake groups (Figure 7.6a) (e.g., Duncan and Clague, 1985; Smith et al., 1989; Smoot, 1989). These seamounts are thought to have formed above the South Pacific Superswell (e.g., Duncan and Clague, 1985; McNutt and Fischer, 1987), and anomalously low T_e values (for the seamount loading) suggest that the lithosphere was anomalously hot (i.e. rejuvenated) at their time of formation

(e.g., Smith et al., 1989; Wolfe and McNutt, 1991). However, a lack of present day heat flow (Stein and Abbott, 1991) or surface wave velocity (Nishimura and Forsyth, 1985) anomalies along the Darwin Rise suggests that the lithosphere has since cooled sufficiently that there is no significant present day thermal anomaly (McNutt and Judge, 1990). This is supported by the absence of large abyssal depth anomalies seaward of the Izu-Bonin ($\sim$ 0 m) and Mariana ($<$ 160 m) trenches (Figure 7.8b). This explains why, despite being affect by hotspot-volcanism in the past, the subducting lithosphere at these trenches does not appear anomalously weak for its age.

7.3.5 T_e vs. effective thermal age

The effective thermal age, t_{eff}, might better reflect the thermal structure of the lithosphere than the seafloor age. Therefore, in Figure 7.10, we have plotted T_e estimates from Inversions A1 and A2 against t_{eff}. Note that in keeping with the plots of T_e vs. seafloor age (Figures 5.2 and 6.4), the t_{eff} in this plot is the ensemble-averaged value 100 km seaward of the trench. To calculate this, we added m_{diff} to the ensemble-averaged seafloor age 100 km seaward of the trench, where m_{diff} is the mean difference between the seafloor age and t_{eff} in the abyssal region (500–800 km seaward of the trench axis).

Figure 7.10 shows that the best-fit isotherms (solid black curves) for T_e vs. t_{eff} are very similar to those for T_e vs. seafloor age (Figures 5.2 and 6.4). However, for the trench-bins, the scatter around the best-fit isotherm is lower in the plots of T_e vs. t_{eff}; this is evidenced by the smaller 95 % confidence intervals on the best-fit isotherms. We suggest therefore that some of the scatter in the relationship between T_e and seafloor age could be due to departures in lithospheric thermal structure from that predicted by a plate-cooling model, for example due to hotspot-induced rejuvenation. We note, however, that the calculation of t_{eff} assumes that the seafloor depth is dependent only on the thermal structure, whilst in reality the depth may be affected by other factors such as, for example, dynamically supported topography and crustal thickness variations. Figure 7.10 also shows that the T_e values at the Chile trench do not appear as anomalously low when plotted against t_{eff}, which suggests that thermal rejuvenation could explain the anomalously low flexural rigidity in this region.

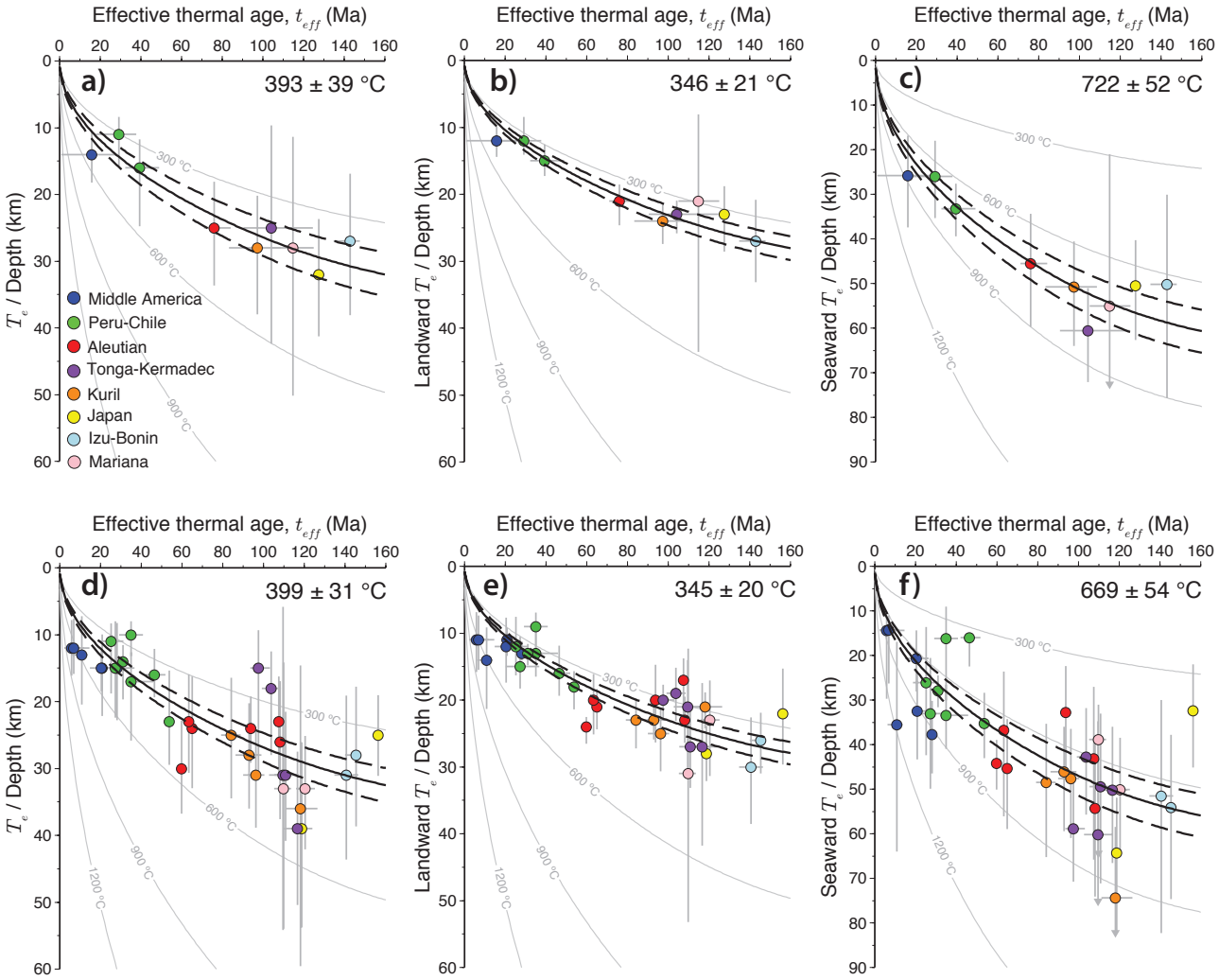

Figure 7.10: T_e from the trench-outer rise system of circum-Pacific subduction zones plotted against effective thermal age, t_{eff}. The top and bottom rows show the trench-bin and segment-bin results respectively. (a,d) shows constant T_e from Inversion A1; (b,e) and (c,f) show landward T_e and seaward T_e respectively from Inversion A2. Best-fitting plate-cooling isotherms are shown in solid black and 95 % confidence intervals in dashed black; the temperatures of these isotherms are labelled in the top right of each plot.

7.4 Plate weakening

As described in the previous chapter, the lithosphere is weakened as it travels over the outer rise and into the trench due to a combination of bending-induced inelastic yielding and mantle hydration via bend-faults. As T_e estimates reflect an average of this strength evolution, variations in the magnitude of weakening, resulting from variations in plate curvature and mantle hydration, may cause scatter in the relationship between T_e and plate age. In this section, we will discuss some possible causes of variations in plate curvature and mantle hydration.

7.4.1 Plate curvature

Variations in plate curvature should lead to variations in the amount of bending-induced inelastic yielding that occurs at the outer trench-slope. For a given flexural rigidity, the curvature of the lithosphere is controlled by the vertical load acting on it, where a larger load gives larger curvature. The vertical load on the subducting plate is primarily provided by the downgoing slab: either by slab-pull or slab-suction, or a combination of both (Conrad and Lithgow-Bertelloni, 2002). Force balances (Richter and McKenzie, 1978; England and Wortel, 1980) and viscous flow models (Zhong and Gurnis, 1994) show that the vertical component of the slab-derived force is primarily governed by the age, dip and descent velocity of the slab, where older, steeper, faster descending slabs exert a greater force.

To test if there is any relationship between the observed plate curvature and the slab-derived vertical force, F_v, at circum-Pacific subduction zones, we calculated F_v for our ensemble-averaged profiles using the equation of England and Wortel (1980). This equation assumes that F_v is caused only by the temperature contrast between the subducting slab and the surrounding mantle, and it takes into account the subduction velocity, dip and thickness of the slab. We estimated the subduction velocity as the sum of the trench-normal plate convergence velocity (MORVEL plate motion model, DeMets et al., 2010) and the backarc deformation rate (from Heuret and Lallemand, 2005). The dip of the slab was estimated via linear regression to slab depths that were ensemble-averaged from the *Slab1.0* slab model

(Hayes et al., 2012). The thickness of the lithosphere was estimated as the depth to the 930 °C plate-cooling isotherm, as this best fits the Pacific variation in the depth to the seismically imaged lithosphere-asthenosphere boundary (Rychert and Shearer, 2011).

Figure 7.11a shows F_v plotted against the maximum observed curvature for each circum-Pacific ensemble-averaged profile (see Section 6.1.1 for description of the curvature estimation), where the symbols are coloured by seafloor age. This shows that F_v is strongly correlated with plate age, but that there is no correlation between F_v and the observed curvature. This is because, although F_v is greater for older lithosphere, older lithosphere is generally more rigid and therefore flexes over a longer wavelength. Figure 7.11b shows the maximum observed curvature plotted against the plate weakening derived from Inversion A2 (i.e. the % reduction in T_e between the seaward and landward values). This shows that there is no correlation between plate weakening and plate curvature, which might seem surprising. However, laboratory-derived YSEs predict that plate weakening varies by only $\sim$ 20 % over the entire range of observed curvatures (the method used to calculate this will be described in the next chapter). It is unlikely that Inversion A2 could resolve such small variations in plate weakening, due to the high uncertainty in the seaward T_e values, which explains the lack of correlation between weakening and curvature

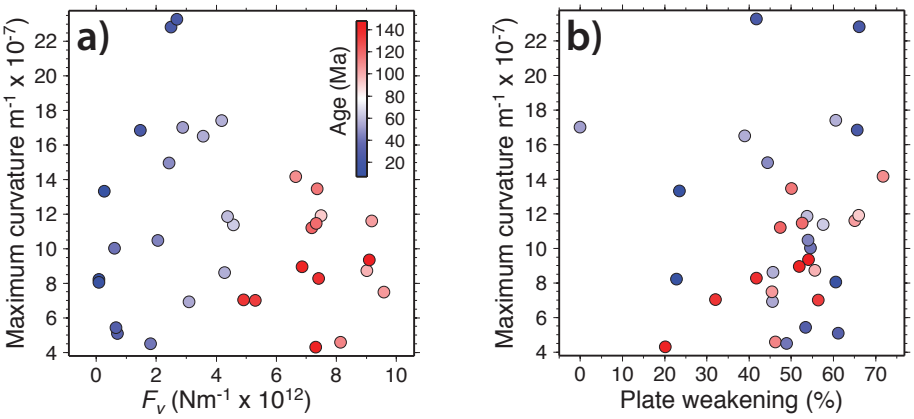

Figure 7.11: (a) The vertical force resulting from the temperature contrast between slab and mantle, F_v, plotted against the maximum observed curvature at the trench-outer rise of circum-Pacific subduction zones. (b) Plate weakening from Inversion A2 plotted against the maximum observed curvature. The symbols are coloured by seafloor age.

7.4.2 Mantle hydration and bend-faulting

Variations in the amount of mantle hydration, and therefore serpentinization, that occurs landward of the outer rise might cause variations in plate weakening. This hydration occurs primarily via bend-faults on the outer trench-slope (e.g., Ranero and Sallares, 2004; Grevemeyer et al., 2007), and therefore plate weakening might be affected by variations in the spatial extent, nature and density of these faults. For example, the penetration depth of bend-faults should vary with plate curvature, where the depth increases with curvature. In addition, Naliboff et al. (2013) used thermo-mechanical numerical modelling to show that bend-faulting patterns are significantly affected by downgoing plate age and velocity, downgoing-overriding plate coupling and slab-pull. Moreover, the spacing, offset, style (e.g., Masson, 1991; Massell, 2002) and perhaps permeability of bend-faults is dependent on whether or not they form via reactivation of abyssal hill faults, as discussed further in Section 7.7.

In addition to causing plate weakening, serpentinization might also affect the gravity anomaly in the region of bend-faulting, which might influence T_e estimates. This is because partially serpentinized peridotite has a lower density than normal peridotite: $\sim$ 3.1 kg/m^3 for 20 % serpentinization compared to a normal density of $\sim$ 3.3 kg/m^3 (Escartin et al., 2001). Thus, it should produce a gravity low, which would increase the magnitude of the outer trench-slope anomaly.

7.5 Axial loading

Axial loading was neglected in this study because elastic plate inversions are strongly biased towards tensional axial forces, and the maximum tensional force that might be expected to occur in nature has little effect on elastic plate deflections (Section 3.1.3). However, laboratory-derived YSEs predict that even reasonably small levels of axial normal stress ($\gtrsim$ 100 MPa) can have a significant effect on the rigidity, and therefore flexure, of a lithosphere with realistic elastic-plastic or viscoelastic-plastic rheology (e.g., McNutt, 1984; Mueller et al., 1996a; Garcia-Castellanos et al., 2000). A tensional axial force acting on the lithosphere shifts the flexural bending stresses into the tensional regime. As the frictional strength of rock is lower

in tension, this deepens the neutral axis and can substantially decrease the bending moment and therefore rigidity (McNutt, 1984). In contrast, a compressional axial force shifts the bending stresses into the frictionally stronger compressional regime, which can cause a slight increase in moment and rigidity.

Axial normal stresses $\gtrsim$ 100 MPa might occur at the trench-outer rise system of circum-Pacific subduction zones, depending on the balance between the driving and resisting forces that act on the subducting plate. These stresses might therefore affect the rigidity of the subducting plate and contribute to the scatter in the relationship between T_e and plate age. For example, a net slab pull force, F_{NSP}, of $\sim 6 \times 10^{12}$ Nm^{-1} (Schellart, 2004; Capitanio et al., 2009) would produce tensional normal stresses of $\sim$ 100–150 MPa if distributed across a 40–60 km thick mechanical lithosphere. The axial forces that act on the subducting plate at circum-Pacific trenches are generally not well constrained and therefore we make no effort to correlate them with T_e estimates. However, in the following paragraph, we will discuss how axial stresses may have an influence on the anomalously low T_e at the Chile trench (as described in Section 7.1.2).

Numerical modelling of tectonic forces at the Peru-Chile trench suggests that the central section is characterized by relatively large tensional axial stresses, whilst the peripheral regions are subjected to smaller compressional stresses (Wortel and Cloetingh, 1985); this has been digitized and plotted in Figure 7.2e. Note that these stresses were calculated assuming that they are distributed across a 100 km thick elastic plate and therefore may be 2 or 3 times higher if they are only distributed across the mechanical thickness of the lithosphere (Wortel and Cloetingh, 1985). The region of high tensional axial stress occurs the where the slab dips relatively steeply and interplate coupling is relatively low, whilst the peripheral regions are characterized by flat slab subduction and relatively high interplate coupling (Gutscher, 2002; Manea et al., 2012), as illustrated in Figure 7.2e. As shown in Figure 7.2 (b and c), the region of tensional axial stress roughly corresponds to the region of anomalously low T_e seaward of the Chile trench. Thus, tensional axial loading might also contribute to the anomalous weakness of the subducting plate in this region.

7.6 Model assumptions

In this study, trench-outer rise flexure was modelled as a thin elastic plate undergoing cylindrical (2-D) bending. This model assumes that there is no strain in the trench-parallel direction and that axial (horizontal) shear stresses can be neglected. Therefore, if either of these assumptions is violated at circum-Pacific subduction zones, our estimates of the lithosphere's rigidity might be inaccurate. These model assumptions might be violated in regions of highly arcuate trench geometry, as this would introduce bending stresses that have a significant trench-parallel component (Judge and McNutt, 1991; Garcia et al., 2015). In addition, the assumptions might be violated in regions where plate convergence is highly oblique to the trench, as this might introduce trench-oblique, axial shear stresses (Dolan and Mann, 1998; Mortera-Gutiérrez et al., 2003). For example, Mortera-Gutiérrez et al. (2003) showed that the rotation of bend-faults at the westernmost Aleutian trench, where plate convergence is highly trench-oblique, requires a model of dextral shear stresses superimposed on the stresses caused by subduction-induced flexure.

In this section, we will describe three regions that are characterised by either arcuate trench geometry or trench-oblique plate convergence, and will discuss the effect that this may have on T_e estimates and the geometry of the outer rise. In this section, the 'convergence angle' is defined as the angle between the strike of the trench and the plate convergence vector (convergence vectors are shown as arrows in part a of Figures 7.1–7.6). The 'gravimetric amplitude' of the outer rise is defined as the difference between the maximum gravity anomaly and the mean anomaly observed on the abyssal seafloor seaward of the outer rise, between 500 and 800 km from the trench axis. This was measured from best-fit profiles from Inversion A2, so as to avoid the influence of short-wavelength features, such as seamounts, that might be present in the observed profiles.

7.6.1 Observations

As shown in Figure 7.3a, plate convergence at the westernmost Aleutian trench is highly oblique to the trench, with convergence angles $< 40°$. Figure 7.12a (left) shows that this

coincides with a sharply curved, high-amplitude outer rise (gravimetric amplitude of 50 mGal in bin 16 and 40 mGal in bin 17; bin locations shown in Figure 7.3a). This contrasts with the central and eastern sections of the trench (bins 18–21), where the convergence angles are $> 70°$, and the outer rise is more smoothly curved and has a lower amplitude of 18–30 mGal, as illustrated in Figure 7.12a (right).

As shown in Figure 7.2a, at the central Peru-Chile trench, there is a highly arcuate, concave trench segment known as the Arica Bend (bin 31). A least squares regression reveals that the minimum radius of curvature of the trench in this region is ~ 300 km. As observed by Judge and McNutt (1991) and as shown in Figure 7.12b (left), the outer rise here is also sharply curved and has an anomalously high gravimetric amplitude of 28 mGal, compared with 4–12 mGal elsewhere along the trench, as illustrated in Figure 7.12b (right).

As shown in Figure 7.1a, there is a highly arcuate, concave trench segment at the eastern-most end of the Middle America trench (bin 27), where the minimum radius of curvature is ~ 350 km. As shown in Figure 7.12c (left), this region also has a sharply curved, pronounced outer rise with a gravimetric amplitude of 36 mGal, compared with 7–24 mGal elsewhere along the trench, as illustrated in Figure 7.12c (right).

7.6.2 Discussion

The observations described above suggest that in regions where the model assumptions are violated, due to either arcuate trench geometry or trench-oblique plate convergence, the outer rise is relatively sharply curved and has relatively high amplitude. This observation is in agreement with 3-D elastic plate models of highly concave trenches, which produce a very pronounced outer rise because the trench-normal bending stresses associated with plate subduction are superimposed on the trench-oblique bending stresses associated with the curvature of the trench (Garcia et al., 2015). To our knowledge, there have been no modelling studies investigating the effect of trench-oblique plate convergence on outer-rise geometry, and this is beyond the scope of this study.

It might be expected that these regions where the model assumptions are violated, and

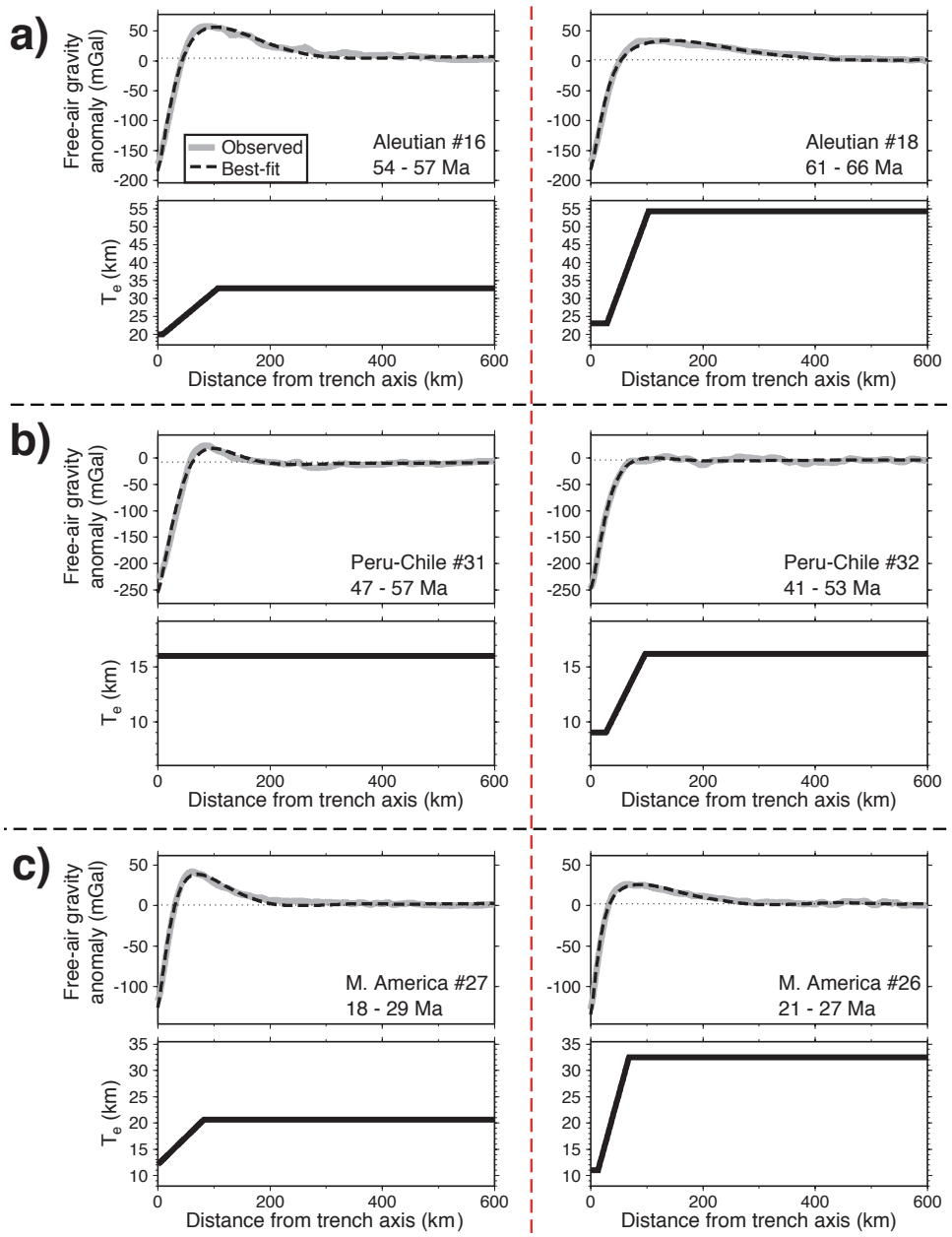

Figure 7.12: Figure showing the anomalous outer-rise geometry and T_e in regions where the model assumptions (for an elastic plate undergoing cylindrical bending) are violated. (a), (b) and (c) show plots from the Aleutian, Peru-Chile and Middle America trenches respectively. Plots on the left are from segment-bins where the model assumptions are violated, due to either arcuate trench geometry or trench-oblique plate convergence, and adjacent plots on the right are from neighbouring segment-bins where the model assumptions hold. Each pair of plots shows the observed and best-fit gravity from Inversion A2 (the trench, bin number and seafloor age range is labelled) and below that, the best-fit T_e profile from Inversion A2. The figure shows that regions where the model assumptions are violated (plots on left) are characterised by relatively large-amplitude, sharply curved outer rises and by relatively low plate weakening.

where the outer rise has anomalous geometry, would produce anomalous T_e estimates. Surprisingly therefore, in none of these regions do constant T_e estimates (from Inversion A1) differ significantly from neighbouring bins, which agrees with the findings of Judge and McNutt (1991) at the Peru-Chile trench. However, as shown in Figure 7.12, variable T_e estimates (from Inversion A2) do differ somewhat: the bins where the model assumptions are violated (left plots) require less plate weakening than neighbouring bins where the model assumptions hold (right plots). For example, at the Peru-Chile trench (Figure 7.12b), the Arica Bend profile (bin 31) has zero weakening, compared to 44–61 % elsewhere along the trench. At the Middle America trench (Figure 7.12c), the easternmost profile (bin 27), where the trench is highly concave, has best-fit weakening of 41 %, compared to 65–66 % in the two neighbouring bins. The westernmost profile (bin 16) at the Aleutian trench (Figure 7.12a), where the plate convergence is at its most trench-oblique, has best-fit weakening of 39 %, compared to 55–61 % in the three neighbouring bins. It seems likely that the apparently low plate weakening in regions of arcuate trench geometry or trench-oblique plate convergence is due to the deficiency of the model used in this study, rather than any true variation in lithospheric weakening. However, further modelling is required to confirm this, but this is beyond the scope of this study.

7.7 Style of bend-faulting

The style of bend-faulting on the outer trench-slope of subduction zones is primarily controlled by the orientation of the pre-existing crustal fabric. This fabric consists of 'abyssal hills', which are horst blocks bounded by normal faults that formed $\sim$ 2–8 km from the Mid-Ocean Ridge (MOR) (e.g., Searle, 1984; Macdonald et al., 1996; Buck and Poliakov, 1998). These abyssal hill faults form sub-parallel to the MOR and are thought to form via stretching, volcanic growth faulting, or a combination of both. Several authors have observed that when the subducting plate is flexed at the outer trench-slope, abyssal hill faults are reactivated as bend-faults when they strike less than 25–30° from trench-parallel (e.g., Masson, 1991; Massell, 2002; Ranero et al., 2005; Billen et al., 2007). Landward-dipping faults are preferentially reactivated, producing a step-down pattern of relatively small-offset (150–500 m), closely spaced (a few

km) faults. In contrast, when the abyssal hill faults strike at greater angles to the trench, it is difficult to reactivate them and therefore new, trench-parallel bend-faults are formed. As shown at the Tonga-Kermadec trench (Figure 6.7), these faults have relatively large offset (up to $>$ 1.5 km) and are relatively widely spaced (5–10 km); both landward-dipping and seaward-dipping faults are formed such that they bound horst and graben structures.

Variations in the style of bend-faulting on the outer trench-slope, as described above, may affect the flexural deformation and/or rigidity of the subducting plate. To investigate this possibility, we will discuss two subduction zones where the strike of the pre-existing abyssal hill fabric changes along-trench from $<$ 25–30° to $>$ 25–30° from trench-parallel. As a proxy for the strike of the abyssal fabric, for each ensemble bin, we measured the angle between the trench and the incoming seafloor isochrons. These angles are plotted in part d of Figures 7.1–7.6, where the grey shaded bar represents the transition from abyssal hill fault reactivation ($<$ 25–30°) to newly formed, trench-parallel faulting ($>$ 25–30°). Figures 7.1 and 7.2 show that at the Middle America and Peru-Chile trenches respectively, the along-trench change in the strike of the pre-existing fabric (relative to the trench) suggests that there should be a change in the style bend-faulting on the outer-trench slope. We will now describe the variation in bend-faulting at these trenches, before discussing the effect that this variation might have on the geometry of the outer rise and/or T_e.

Figure 7.13: (*Figure on next page*) Plots showing seismicity and bend-faulting at the outer trench-slope of the Middle America trench. (a) GEBCO bathymetry overlain with all earthquakes, as of 2013, in the ISC (black dots) and CMT (focal mechanisms) catalogues. Only events seaward of the trench axis and within the trench-bin (black dash) are shown. CMT events have been plotted at their respective EHB positions, as these are more accurate (e.g., Bürgmann et al., 2005; Ranero et al., 2005). (b) Histograms of ISC, EHB and CMT seismicity against distance from the trench, where the bin width is 10 km. This shows the landward increase in seismicity due to outer trench-slope bend-faulting. (c,d) Swath bathymetry, gridded at 200 m resolution, from the boxes shown in Figure 7.13a. This dataset is comprised of all available data in the region, totalling 30 cruises. The dashed red lines in Figure 7.13c show the approximate azimuth of the pre-existing abyssal hill fabric. (e) Swath bathymetry along the profiles shown in Figures 7.13c and 7.13d.

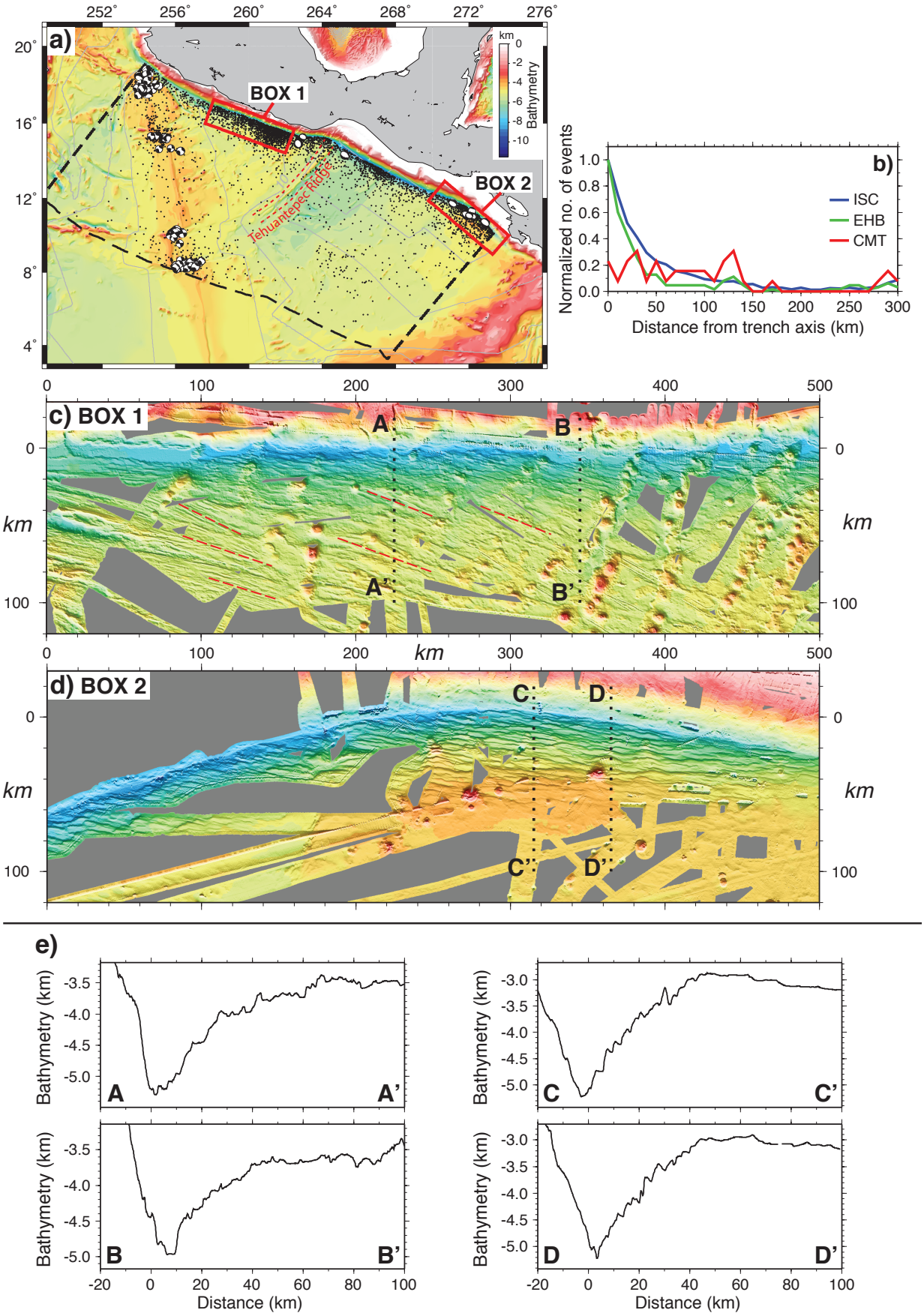

Figure 7.13: *Caption on previous page*

7.7.1 Observations of bend-faulting

Figure 7.2d shows at the Chile trench (bins 32–34), the seafloor isochrons strike $> 30°$ from trench-parallel. Swath bathymetry shows that as a result, new, trench-parallel bend-faults are formed and that these faults bound horst and graben structures (Ranero and Sallares, 2004; Ranero et al., 2005). In contrast, at the Peru trench (bins 28–30), the iscohrons strike $\sim 10°$ from trench-parallel. As far as we are aware, there is no swath data coverage of the outer trench-slope seaward of the Peru trench, but we assume that the incoming abyssal hill faults are reactivated as bend-faults.

Figure 7.1d shows that at the Middle America trench, westwards of the Tehuantepec Ridge (bins 22–24), the seafloor isochrons strike 45–50° from trench-parallel, whilst eastwards of the ridge (bins 25–27), the strike is 4–12°. In Figure 7.13 (c–e), we have shown swath bathymetry at the outer trench-slope of the Middle America trench; this is comprised of all the available data in the MGDS (Marine Geoscience Data System) database, totalling 30 cruises for the region. Figures 7.13d and 7.13e (profiles C and D) show that eastwards of the Tehuantepec Ridge, abyssal hill faults are reactivated as small-offset, closely spaced bend-faults that step down towards the trench, and that the faulting begins $\sim$ 40–50 km from the trench axis. This has been observed by previous authors in both swath bathymetry (Grevemeyer et al., 2005; Ranero et al., 2005; Grevemeyer et al., 2007; Lefeldt et al., 2009) and seismic reflection profiles (Ranero and Sallares, 2004), and Ranero et al. (2005) showed that this style of bend-faulting is consistent across all of the region eastwards of the Tehuantepec Ridge. Figures 7.13c and 7.13e (profiles A and B) show that westwards of the Tehuantepec Ridge, there is an absence of pervasive bend-faulting on the outer trench-slope. In both map view and profile view, the incoming abyssal hill fabric can be seen (strike marked in red dash in Figure 7.13c), but there is no perceivable bend-faulting until perhaps 10–20 km from the trench axis, where faults may just be starting to form. This contrasts with other regions where the incoming abyssal fabric strikes at high angles to the trench—such as the Tonga-Kermadec (Figure 6.7), Japan (Kobayashi et al., 1998) and Chile (Ranero and Sallares, 2004; Ranero et al., 2005) trenches—where new, trench-parallel faults are formed and are pervasive across the outer trench-slope. We note that, as shown by the red dash in Figure 7.13c, the incoming abyssal

fabric westwards of the Tehuantepec Ridge appears to strike at lower angles to the trench than suggested by the seafloor isochrons of Müller et al. (2008) (grey lines in Figure 7.13a). Nonetheless, it appears that the abyssal hill faults are not reactivated as bend-faults.

7.7.2 Bend-faulting and the geometry of the outer rise

Figure 7.14 shows ensemble-averaged bathymetry and gravity from the Peru and Chile trench-bins (a and b), and from the eastern and western sections of the Middle America trench (c and d). The bin locations for the Middle America trench are shown in red dash Figure 7.13; note that the bin for the eastern section excludes the region of arcuate trench geometry (see Section 7.6). Figure 7.14 shows that at the Peru and eastern Middle America trenches (grey lines), where bend-faulting occurs via reactivation of abyssal hill faults, the bathymetric and gravimetric outer rise is smoothly curved, well defined and has an amplitude of $\sim$ 250 m/10 mGal and $\sim$ 220 m/20 mGal respectively. In contrast, at the Chile and western Middle America trenches (black lines), where abyssal hill faults strike too obliquely to the trench to be reactivated, there is no clear expression of the outer rise in either bathymetry or gravity. Moving landwards along these profiles, the plate remains more-or-less undeflected, other than the short-wavelength fluctuations associated with seamounts, until 50–70 km from the trench axis (red dash in Figure 7.14), where it suddenly bends sharply and descends steeply into the trench.

The observations presented above suggest that at the Middle America and Peru-Chile trenches, the outer rise is relatively smoothly curved and well defined in regions where abyssal hill faults can be reactivated as bend-faults. In contrast, in regions where the abyssal fabric strikes too obliquely to the trench to be reactivated, the outer rise is relatively subdued and the plate bends sharply into the trench. Further work is required to confirm that this relationship is causal, which is beyond the scope of this study, but nonetheless, we will offer a tentative explanation for such a causal relationship in the following paragraph.

At subduction zones where the abyssal hill faults can be reactivated, the uppermost, brittle lithosphere can flex relatively easily, as strain can be accommodated by frictional sliding along the pervasive, closely spaced and probably-frictionally weak (e.g., Escartin et al.,

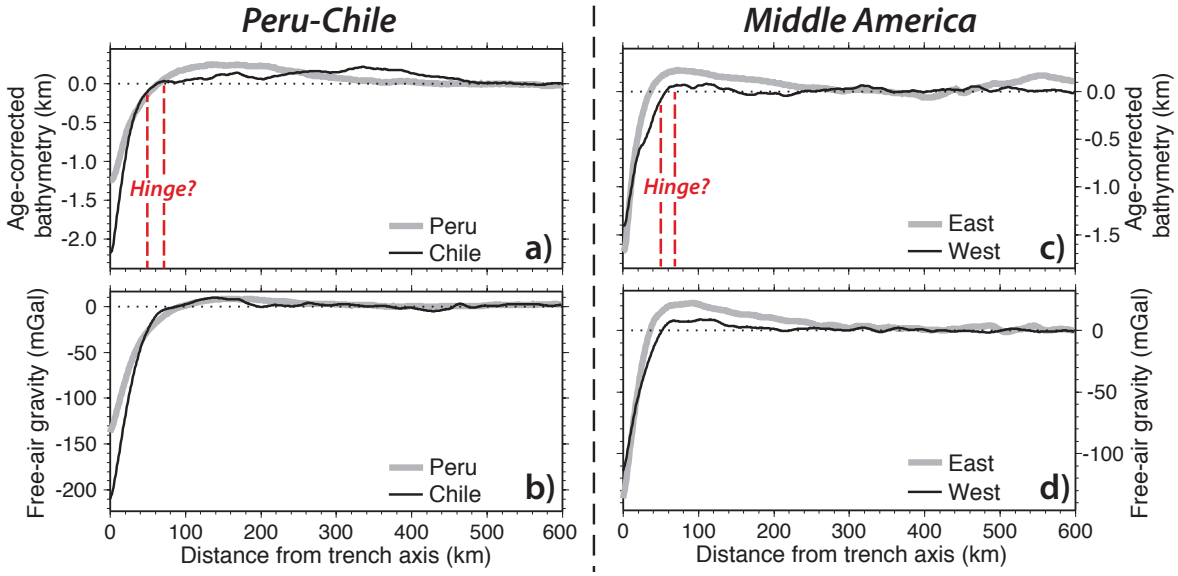

Figure 7.14: Figure illustrating the correlation between the nature of bend-faulting and the geometry of the outer rise. The plots show ensemble-averaged profiles of bathymetry and gravity from (a,b) the Peru and Chile trenches and (c,d) the western and eastern Middle America trenches. At trenches where abyssal hill faults are reactivated as bend-faults (grey lines), the outer rise is smoothly curved and well defined. At trenches where new, trench-parallel bend-faults are formed (black lines), the outer rise is subdued and the plate bends sharply into the trench. We suggest that this sharply bent section might reflect a 'hinge' (red dash), such that the seaward propagation of bending moments through the plate is inhibited.

2001; Craig et al., 2014b) pre-existing faults. This allows the bending moments (due to slab-pull, for example) to propagate a large distance seaward of the trench axis, producing a well-defined outer rise. In contrast, at subduction zones where the abyssal hill faults cannot be reactivated, new bend-faults must be formed via the growth and coalescence of crack arrays and fractures (e.g., Griffith, 1921; Brace, 1960; Scholz, 2002). We suggest that the subdued nature of the outer rise in these regions is due to a sudden change in the mechanical properties the lithosphere upon the formation of these faults, as we will now explain. After new bend-faults have been formed: it is relatively easy to flex the uppermost, brittle lithosphere because strain can be accommodated by frictional sliding along the faults; the lithosphere is relatively weak because the shallow, brittle strength is governed by frictional sliding; the neutral surface of bending is relatively deep because the shallow, brittle lithosphere is relatively weak. In contrast, prior to formation of the bend-faults: it is relatively difficult to flex the uppermost, brittle lithosphere because strain cannot be accommodated along faults; the lithosphere is relatively strong because the shallow, brittle strength is governed by the fracture

of intact rock; the neutral surface of bending is relatively shallow because the shallow, brittle lithosphere is relatively strong. In light of these differences, we suggest that as the lithosphere approaches the trench, it reaches a point where the bending stresses become large enough to form new bend-faults, and that at this point, the mechanical properties of the lithosphere change abruptly as described above. When this occurs, the plate suddenly descends steeply into the trench, as is observed 50–70 km from the western Middle America and Chile trench axes (red dash in Figure 7.14). We suggest that this sudden change in the slope of the plate, combined with the abrupt change in the mechanical properties of the lithosphere, leads to the development of something akin to a mechanical hinge. The outer rise is then subdued for the following reasons. Firstly, a mechanical hinge cannot transmit bending moments (Gere and Goodno, 2009, p. 399), and thus the seaward propagation of bending moments from the trench axis is inhibited. Secondly, any bending moments that are transmitted seaward through the 'hinge' do not cause significant deformation of the shallow lithosphere because, as described above, it has relatively high flexural rigidity, strain cannot be accommodated along faults and the neutral surface is relatively shallow.

We note that the above hypothesis requires the fracture of intact rock in the 'hinge' region, which we suggest occurs 50–70 km from the Chile and western Middle America trench axes (Figure 7.14). This is supported by observations of bend-faulting seaward of the Chile trench, where noticeable horsts and grabens first appear $\sim$ 60 km seaward of the trench axis (Ranero and Sallares, 2004). However, as shown in Figure 7.13c and 7.13e (profiles A and B), there is no noticeable faulting seaward of the western Middle America trench until perhaps 10–20 km from the trench axis. We suggest that the 'hinge' in this region could represent the onset of crack growth or the coalescence of crack arrays and fractures, but that the bending stresses are not great enough to form large faults that rupture to the surface. Indeed, the shallow bending stresses are likely to be significantly smaller at the Middle America trench than at the Chile trench. This is because the lithosphere seaward of the western Middle America trench is very young (2–10 Ma) and hot, and therefore its mechanical thickness should be relatively small. This means that the distance from the neutral surface to the seafloor, and therefore the shallow bending stresses, should be relatively small.

7.7.3 Bend-faulting and T_e

The variations in the geometry of the outer rise described above are likely to contribute to the scatter in the relationship between T_e and plate age. In addition, the nature of bend-faulting might also have a direct effect on the flexural rigidity of the lithosphere. For example, as described in Section 7.1.3, at the Middle America trench, the seaward T_e increases with age across the Tehuantepec Ridge (Figure 7.7b), but the landward T_e does not (Figure 7.7a). We suggest that the anomalously high landward T_e to the west of the Tehuantepec Ridge is due to the absence of bend-faulting on the outer trench-slope in this region. As the subducting plate in this region is so young (2–10 Ma) and therefore hot, the mechanical thickness is likely to be small and therefore the neutral surface is likely to be shallow. This means that the shallow bending stresses are not great enough to rupture large faults, and therefore the amount of bending-induced plate weakening that occurs is anomalously low. This results in the anomalously high flexural rigidity at the outer trench-slope.

7.8 Trade-offs between T_e and the end-loads

As the loads are not well constrained at subduction zones, we inverted for two end-loads, M_0 and V_0, using a damped least squares algorithm. Uncertainties in these end-loads, and trade-offs between them and T_e, may contribute to the scatter in the relationship between T_e and plate age.

7.9 Strain rate

The strain rate associated with plate flexure at the trench-outer rise system should vary with plate convergence rate and plate curvature. This might be expected to cause variations in flexural rigidity and T_e, as the ductile flow strength of lithospheric minerals is dependent on strain rate. As we will describe in the next chapter, we estimated strain rates for our circum-Pacific ensemble-averaged profiles using observed plate curvatures and plate convergence velocities. The calculated strain rates range from $10^{-16.3}\,\mathrm{s}^{-1}$ to $10^{-15.1}\,\mathrm{s}^{-1}$, and laboratory-derived YSEs

predict only 2–3 km variation in T_e across this range. Therefore, although strain rate variations might contribute to the scatter in the relationship between T_e and plate age, the effect is unlikely to be large.

7.10 Strain history

As the lithosphere travels over the outer rise and into the trench, it bends with increasing plate curvature, deforming elastically below the yield stress and plastically above it, which causes its flexural rigidity to decrease. This process is reasonably well approximated by a variable rigidity elastic plate that weakens landward of the outer rise, as was used in Inversion A2. However, if the lithosphere begins to unbend before it is subducted, as suggested by the observed plate curvatures at some trenches (Section 6.1.1) and as suggested by some previous authors, it will undergo unloading that is complex in nature and cannot be modelled by a variable rigidity elastic plate (e.g., McAdoo et al., 1978; Bodine and Watts, 1979; Mueller and Phillips, 1995; Mueller et al., 1996a). For example, if we assume that the lithosphere has an elastic-plastic rheology, the stress decrease associated with plate unbending occurs along a different stress-strain path than the preceding bending, resulting in strain hysteresis. This limitation of the elastic plate model might cause inaccuracies in estimates of the lithosphere's flexural rigidity. However, we believe that these inaccuracies are unlikely to be significant for two reasons. First, the observed plate curvatures, as calculated by fitting an elastic plate to 170 km long gravity profiles, suggest that the point of maximum curvature occurs very close to the trench axis (mean distance 23 ± 10 km). Therefore, if unbending does occur before subduction, it is likely to only affect a small region close to the trench axis. Second, we suggest that the landward decrease in observed curvature that occurs at some trenches might not actually reflect plate unbending, and instead might be an artefact of using gravity data to estimate the curvature. For example, the decrease in observed curvature could reflect: the gravitational effect of the landward wall of the trench and low density sediments in the forearc; turbiditic deposits at the bottom of the trench; crustal fragments from the downgoing plate that are thrust upwards into the trench upon meeting the resistance of the overriding plate (Massell, 2002); smoothing of the trench axis by the ensemble-averaging process.

7.11 Chapter summary

In this chapter, we have discussed the relationship between circum-Pacific T_e and plate age, as well as a range of other factors that may affect T_e estimates. The key points are as follows:

- The first-order increase in T_e with plate age that was found in Inversions A1 and A2 agrees with models for the cooling of oceanic lithosphere and the ductile deformation of lithospheric minerals. However, there is some scatter in the T_e-age relationship, which suggests that there are other factors that affect the flexural rigidity and/or the accuracy of T_e estimates.

- Inaccuracies in T_e estimates may be caused by: short-wavelength bathymetric noise, for example due to hotspot volcanism; failure of the cylindrical bending model to account for arcuate trench geometry or oblique plate convergence; trade-offs between T_e and the end-loads; failure of the elastic plate model to account for complex loading histories, such as 'elastic unloading' or the formation of a lithospheric 'hinge'; the effect of bend-faulting on the geometry of the outer rise.

- Factors other than plate age that may affect the rigidity of oceanic lithosphere include: thermal anomalies in the lithosphere, for example due to hotspot-induced thermal rejuvenation; variations in plate weakening due to variations in plate curvature and mantle hydration; plate weakening by axial normal stresses; variations in the style of bend-faulting on the outer trench-slope .

- T_e values seaward of the Chile trench appear anomalously low for the plate age, which we suggest is due hotspot-induced thermal rejuvenation and/or tensional, axial normal stresses.

- Landward T_e at the western Middle America trench appears anomalously high for the plate age. We suggest that this is because the subducting plate is young, hot and therefore thin, which means that the shallow bending stresses are not large enough to form new bend-faults on the outer trench-slope.

- For lithosphere older than 80 Ma, there is no clear increase in T_e with plate age, which

we attribute to: the decrease in the rate of plate-cooling with plate age; the relatively low sensitivity of the flexural wavelength to T_e for older, stronger plates; bathymetric noise caused by hotspot volcanism, particularly at the Tonga-Kermadec, Izu-Bonin and Mariana trenches.

Chapter 8

Constraining the rheology of oceanic lithosphere using the YSE-curvature method

In the previous chapters, we derived T_e as a function of plate age by modelling gravity anomalies at the trench-outer rise system of circum-Pacific subduction zones. In this chapter, we will describe how these results were used to constrain the rheology of oceanic lithosphere, and in particular the rheology in the Low-Temperature Plasticity (LTP) regime. We tested the predictions of five published LTP flow laws (Goetze, 1978; Evans and Goetze, 1979; Raterron et al., 2004; Katayama and Karato, 2008; Mei et al., 2010) using a method similar to that used by, for example, Goetze and Evans (1979) and McNutt and Menard (1982). To do this, we constructed Yield Strength Envelopes (YSE) with each of the LTP flow laws and then used these, along with plate curvatures, to calculate 'predicted T_e' values for our circum-Pacific trench-outer rise profiles. The validity of each LTP flow law was then tested by comparing the predicted T_e to the 'observed T_e' that was derived by modelling the observed gravity anomalies. We dub this approach to constraining the mantle rheology as the 'YSE-curvature method'. To test the validity of the YSE-curvature method, we then used this approach to constrain the rheology in the Hawaiian Islands region and compared our results with those of Zhong and Watts (2013), who used a 3-D finite-element Maxwell viscoelastic model to

constrain the rheology.

8.1 Constructing the Yield Strength Envelope (YSE)

The first step in the YSE-curvature method was to construct Yield Strength Envelopes (YSE) for each of the Low-Temperature Plasticity (LTP) flow laws that we wished to test. The YSE describes the depth-dependence of lithospheric yield strength—i.e. the deviatoric stress at which plastic failure occurs—as predicted by laboratory-derived failure laws. The YSE can be divided into two major regimes on the basis of the dominant deformation mechanism: the relatively shallow and cold brittle regime, where deformation occurs via brittle faulting; and the relatively deep and hot ductile regime, where deformation occurs via plastic flow (e.g., Kohlstedt et al., 1995; Karato, 2008, p. 115). Other styles of brittle and ductile deformation may occur, such as cataclastic flow and ductile faulting respectively, but when constructing YSEs it is common to only consider brittle faulting and plastic flow. This is because processes such as cataclastic flow and ductile faulting are less well understood and are likely to only occur under specific conditions. For example ductile faulting may occur as a result of thermal runaway instability or grain-size reduction, and cataclastic flow and ductile faulting may both occur in the poorly understood semi-brittle deformation regime (Karato, 2008), which will be discussed in Section 8.1.3.

8.1.1 Brittle faulting

It is common to assume that the shallow lithosphere is pervasively fractured and therefore that the brittle strength can be described by a Coulomb-Navier failure criterion for frictional sliding on pre-existing fault surfaces, known as Amonton's law (e.g., Goetze and Evans, 1979; Brace and Kohlstedt, 1980; Kohlstedt et al., 1995). This criterion assumes that the shear strength of a fault is given by the sum of its frictional strength and its cohesive strength due to chemical bonding across the fault:

$$|\tau| = C_0 + \mu_f(-\sigma_n - P_f) \tag{8.1}$$

where τ is the shear strength, C_0 is the cohesive strength, μ_f is the coefficient of friction, σ_n is the normal stress acting across the fault (note that the minus sign is in keeping with our sign convention that compressional stresses are negative), and P_f is the Pore-Fluid Pressure (PFP). On the basis of a large number of experimental results, Byerlee (1978) found that μ_f and C_0 are nearly independent of temperature and and rock type:

$$\begin{aligned} \tau &= 0.85(-\sigma_n - P_f) \quad , \quad -\sigma_n \leq 200 \text{ MPa} \\ \tau &= 50 + 0.6(-\sigma_n - P_f) \quad , \quad -\sigma_n > 200 \text{ MPa} \end{aligned} \tag{8.2}$$

Anderson's (1905; 1951) theory of faulting uses Equation 8.1 to define the tectonic deviatoric stress, $\Delta\sigma_{xx} = \sigma_{xx} - \sigma_{yy}$, that is required to cause frictional sliding; i.e. the brittle yield strength, $\Delta\sigma_{xx}^{brit}$. This theory assumes that σ_{xx} (trench-normal), σ_{yy} (vertical) and σ_{zz} (trench-parallel) are principal stresses, that there is no strain in the y direction, and that faults form via the coalescence of optimally oriented fractures (Turcotte and Schubert, 1982, pp. 354–355):

$$\Delta\sigma_{xx}^{brit} = \frac{\pm 2\{\mu_f(-\rho g y - P_f) + C_0\}}{(1 + {\mu_f}^2)^{1/2} \pm \mu_f} \tag{8.3}$$

where $\rho g y = \sigma_{yy}$ is the lithostatic pressure, ν is Poisson's ratio, and the upper signs are for normal faults and the lower signs for thrust faults. In Figure 8.1, we show $\Delta\sigma_{xx}^{brit}$ (for thrust faults) calculated with Byerlee's values for μ_f and C_0 (hydrostatic PFP was assumed).

8.1.2 Plastic flow

Olivine is the most abundant and probably the weakest mineral in the upper mantle, and therefore the ductile rheology of the lithosphere is likely to dominated by that of polycrystalline olivine (e.g., Karato et al., 1993; Zimmerman and Kohlstedt, 2004). Beneath the mid-ocean ridge, extensive partial melting of upwelling mantle at $\sim$ 70 km depth partitions water into the melt phase, resulting in a dry, high viscosity residuum (Karato et al., 1986; Hirth and Kohlstedt, 1996; Morgan, 1997). Therefore, when constructing YSEs for oceanic lithosphere, it is common to assume that the ductile yield strength is governed by the plastic flow of dry olivine (e.g., Goetze and Evans, 1979; Brace and Kohlstedt, 1980; McNutt and Menard, 1982; Kohlstedt et al., 1995), and this is the approach used here. Note that the

ductile rheology of the basaltic oceanic crust is unimportant, as the deformation is brittle at these depths. At the moderate temperatures (< 1350 °C) and relatively high deviatoric stresses (> 10 MPa) typical of lithospheric deformation, laboratory studies, as well as observations of seismic anisotropy and microstructures of deformed upper mantle rocks, suggest that dislocation creep is the dominant plastic flow mechanism (e.g., Goetze, 1978; Karato et al., 1993; Kohlstedt et al., 1995). Laboratory studies show that dislocation creep in olivine occurs via two main mechanisms, Low-Temperature Plasticity (LTP) and Power-Law Creep (PLC), which we will describe in the following paragraphs.

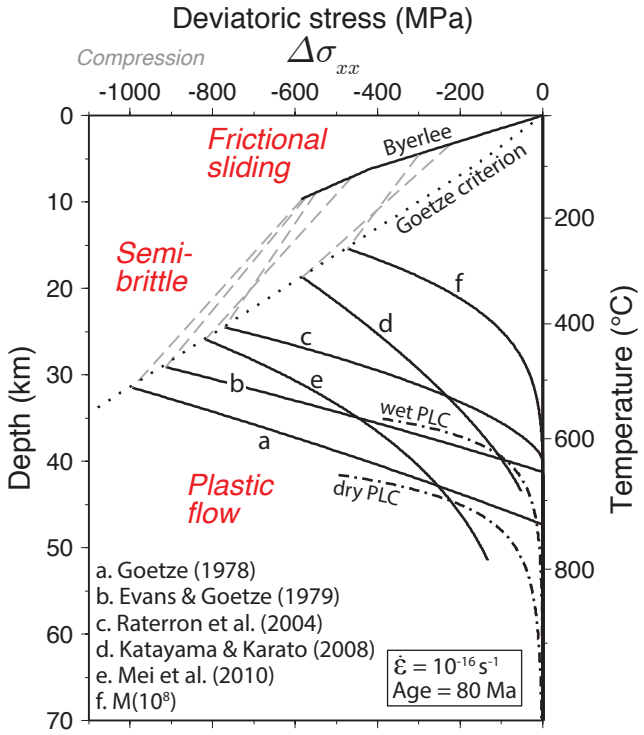

Figure 8.1: The yield strength predicted by the brittle and ductile failure laws used in this study. The shallow, brittle yield strength was calculated with Byerlee's (1978) friction coefficients and hydrostatic PFP. The yield strengths for the LTP flow laws are shown in solid black and labelled a to f. The dot-dashed lines show the yield strengths for the dry and wet PLC laws of Hirth and Kohlstedt (2003). The semi-brittle regime is marked in dashed grey. The yield strengths were calculated for an 80 Ma plate-cooling geotherm and $\dot{\varepsilon} = 10^{-16}$ s^{-1}

At lower temperatures and higher differential stresses ($\lesssim$ 600–800 °C, $\gtrsim$ 100–300 MPa at geological strain rates), dislocation creep in olivine occurs predominantly by the glide of dislocations, which is limited by the intrinsic resistance of the lattice, known as the Peierls

stress (Mei et al., 2010). This mechanism is referred to by various names such as Low-Temperature Plasticity (LTP), exponential creep or Peierls creep, and its constitutive equation is of the form:

$$\dot{\varepsilon} = A_m {\sigma_d}^n \exp\left\{-\frac{H_0^*}{RT}\left(1-\left(\frac{\sigma_d}{\sigma_P}\right)^p\right)^q\right\} \tag{8.4}$$

where: $\dot{\varepsilon}$ is the strain rate; A_m is a material-dependent parameter; $\sigma_d = \sigma_1 - \sigma_3$ is the differential stress, where $\sigma_1 \geq \sigma_2 \geq \sigma_3$ are the principal stresses; n is a non-dimensional parameter that arises from the stress-dependence of dislocation density (Mei et al., 2010); H_0^* is the activation enthalpy at zero stress; R is the gas constant; T is the temperature; σ_P is the Peierls stress; p and q are non-dimensional parameters that depend on the geometry of kinks (Kocks, 1975; Mei et al., 2010). Note that the pressure dependence of LTP is not well constrained, but that it is significantly lower than for other creep processes that occur in the mantle (Karato, 2008, pp. 174-175; Katayama and Karato, 2008). We tested five laboratory-derived LTP flow laws in this study (Goetze, 1978; Evans and Goetze, 1979; Raterron et al., 2004; Katayama and Karato, 2008; Mei et al., 2010), the parameters for which are given in Table 8.1. We also tested three additional flow laws, which are listed in Table 8.1 and throughout this thesis as M(10^4), M(10^6) and M(10^8). These are weakened modifications of the law of Mei et al. (2010), where A_m has been increased by 4, 6 and 8 orders of magnitude respectively. We tested these modifications in light of the study of Zhong and Watts (2013), who used a 3-D finite-element viscoelastic model, with laboratory-derived effective viscosity, to compute predicted crustal deflections beneath the Hawaiian Islands. They found that the law of Mei et al. (2010) is much too strong to fit the observed, seisimically constrained crustal deflections, and that it must be significantly weakened in order to explain the observations.

At higher temperatures and lower differential stresses ($\gtrsim$ 600–800 °C, $\lesssim$ 100–300 MPa at geological strain rates), dislocation creep in olivine occurs via both climb and glide of dislocations (e.g., Goetze, 1978; Chopra and Paterson, 1984; Hirth and Kohlstedt, 1996; Hirth and Kohlstedt, 2003; Karato and Jung, 2003). This mechanism is commonly known as Power-Law Creep (PLC) and its constitutive equation is of the form:

$$\dot{\varepsilon} = B_m {\sigma_d}^n \exp\left(-\frac{E^* + PV^*}{RT}\right) \tag{8.5}$$

where B_m is a material-dependent parameter that can include the influence of water content, n is the stress exponent, E^* is the activation energy, P is pressure, and V^* is the activation volume. We used two published PLC flow laws in this study and the relevant parameters for Equation 8.5 are given in Table 8.2.

LTP flow law	A_m ($s^{-1}\,MPa^{-n}$)	n	H_0^* ($kJ\,mol^{-1}$)	σ_P (GPa)	p	q
Goetze (1978)	5.7×10^{11}	0	536	8.5	1	2
Evans and Goetze (1979)	1.4×10^{12}	0	499	9.1	1	2
Raterron et al. (2004)	2.6×10^{12}	0	564	15.4	2/3	2
Katayama and Karato (2008)	$1.0 \times 10^{7.8}$	2	518	2.87	1	2
Mei et al. (2010)	1.4×10^{-7}	2	320	5.9	1/2	1
M(10^4)	1.4×10^{-3}	2	320	5.9	1/2	1
M(10^6)	1.4×10^{-1}	2	320	5.9	1/2	1
M(10^8)	1.4×10^{1}	2	320	5.9	1/2	1

Table 8.1: Parameters for the Low-Temperature Plasticity (LTP) olivine flow laws that were tested in this study, applicable to Equation 8.4. The flow laws listed as M(10^4), M(10^6) and M(10^8) are weakened modifications of Mei et al. (2010), where A_m has been increased by 4, 6 and 8 orders of magnitude respectively.

PLC flow law	B_m ($s^{-1}\,MPa^{-n}$)	n	E^* ($kJ\,mol^{-1}$)	V^* ($10^{-6}\ m^3\,mol^{-1}$)
Hirth and Kohlstedt (2003) – dry	1.10×10^5	3.5	530	14
Hirth and Kohlstedt (2003) – wet	3.58×10^5	3.5	480	11

Table 8.2: Parameters for the Power-Law Creep (PLC) olivine flow laws used in this study, applicable to Equation 8.5. Note that for wet olivine, B_m was calculated for a water concentration of 1000 H/10^6Si.

For a given strain rate, the LTP and PLC flow laws can be used to define the tectonic deviatoric stress required to cause plastic flow; i.e. the ductile yield strength, $\Delta\sigma_{xx}^{duct}$. For example, the yield strength for PLC is given by:

$$|\Delta\sigma_{xx}^{duct}| = \sigma_d = \left\{ \frac{\dot{\varepsilon}_{xx}}{B} \exp\left(\frac{E^* + PV^*}{RT} \right) \right\}^{1/n} \tag{8.6}$$

In Figure 8.1, we show $\Delta\sigma_{xx}^{duct}$ predicted by each of the LTP (solid lines) and PLC (dot-dashed lines) flow laws used in this study for an 80 Ma plate-cooling geotherm and $\dot{\varepsilon} = 10^{-16}\ s^{-1}$.

Note that to avoid cluttering the figure, we have only shown one weakened modification of Mei et al. (2010), M(10^8).

8.1.3 Semi-brittle regime

Between the brittle faulting and plastic flow deformation regimes, there exists a poorly understood, transitional semi-brittle regime where deformation occurs via a mixture of brittle and ductile processes. Whilst there are no flow laws to describe the semi-brittle regime, deformation experiments on calcite marble (Scholz, 1968; Edmond and Paterson, 1972), halite (Shimamoto, 1986) and granite (Stesky, 1978) suggest that the relatively shallow portion is characterized by localized, stable sliding that is accommodated by a mixture of brittle and ductile processes, whilst the deeper portion is characterized by distributed deformation that involves plastic flow and homogeneously distributed micro-cracks (Scholz, 1988; Kohlstedt et al., 1995; Katayama and Karato, 2008). Thus, with increasing depth, there appears to be a gradual transition from brittle to ductile, and from localized to homogeneous deformation. The transition between the brittle and semi-brittle regimes is known as the brittle-ductile transition (BDT), and observations suggest that this occurs when the ductile yield strength is about five times the brittle yield strength (Kohlstedt et al., 1995). The transition between the semi-brittle and ductile regimes, known as the brittle-plastic transition (BPT), is defined by the Goetze criterion, which states that brittle processes will contribute to deformation for differential stresses larger than the overburden pressure (Kohlstedt et al., 1995). In Figure 8.1, we have marked the semi-brittle region for each LTP flow law in dashed grey.

8.1.4 Yield strength envelope

In Figure 8.2, for each LTP flow law tested in this study, we have shown YSEs for a range of plate ages (assuming a plate-cooling geotherm). Note that to avoid cluttering the figure, we have only shown one weakened modification of Mei et al. (2010), M(10^8). When constructing the YSEs, the semi-brittle regime was neglected, as there are no flow laws to define it. Therefore, the yield strength is governed by the weaker of the brittle (frictional sliding) and ductile (plastic flow) strengths: $\Delta\sigma_{xx}^{yield} = \min(\Delta\sigma_{xx}^{brit}, \Delta\sigma_{xx}^{duct})$. Figure 8.2 shows that with increasing

depth, and therefore increasing pressure and temperature, there is a transition from strongly pressure-dependent brittle deformation to strongly temperature-dependent ductile deformation. The LTP flow laws of Goetze (1978), Evans and Goetze (1979), Raterron et al. (2004), and Mei et al. (2010) and its weakened modifications are for dry olivine (water content < 80 H/10^6Si; Mei and Kohlstedt, 2000a), and therefore were used in conjunction with the dry PLC law of Hirth and Kohlstedt (2003). The LTP flow law of Katayama and Karato (2008) is for wet olivine (810–1220 H/10^6Si) and therefore was used in conjunction with the wet (1000 H/10^6Si) PLC law of Hirth and Kohlstedt (2003). Note that we have also conducted tests using the PLC laws of Karato and Jung (2003), and it makes little difference to the predicted T_e.

As is common when constructing YSEs, we assumed that plastic flow occurs via the easiest mechanism possible, and therefore that $\Delta\sigma_{xx}^{duct}$ is equal to the weaker of the LTP and PLC yield strengths (Goetze and Evans, 1979; Brace and Kohlstedt, 1980). However, as illustrated in Figure 8.1, because $n = 0$ in the LTP flow laws of Goetze (1978), Evans and Goetze (1979) and Raterron et al. (2004), the yield strength disappears to zero and does not intersect the PLC curve. This is problematic because it means there is a depth-discontinuity in the olivine yield strength, which is physically unreasonable. Therefore, for these three LTP laws, we linearly interpolated between the points at which the LTP strength is 200 MPa and the PLC strength is 100 MPa, as shown in Figure 8.2 (a, b, c). We chose these stresses because this is the approximate range over which 'power-law breakdown', or the transition from LTP to PLC, occurred in the studies of Goetze (1978) and Evans and Goetze (1979). Although this breakdown stress range was observed at laboratory strain rates, we would expect it to be similar at geological strain rates. This is because the activation energy in these three LTP laws is very similar to that in the PLC law of Hirth and Kohlstedt (2003) (Tables 8.1, 8.2), and Tsenn and Carter (1987) showed that when this is the case, the breakdown stress is nearly independent of strain rate. Figure 8.2 shows that the ductile yield strength increases with plate age as the oceanic lithosphere cools, but that the rate of increase slows with age because the rate of plate-cooling slows with age.

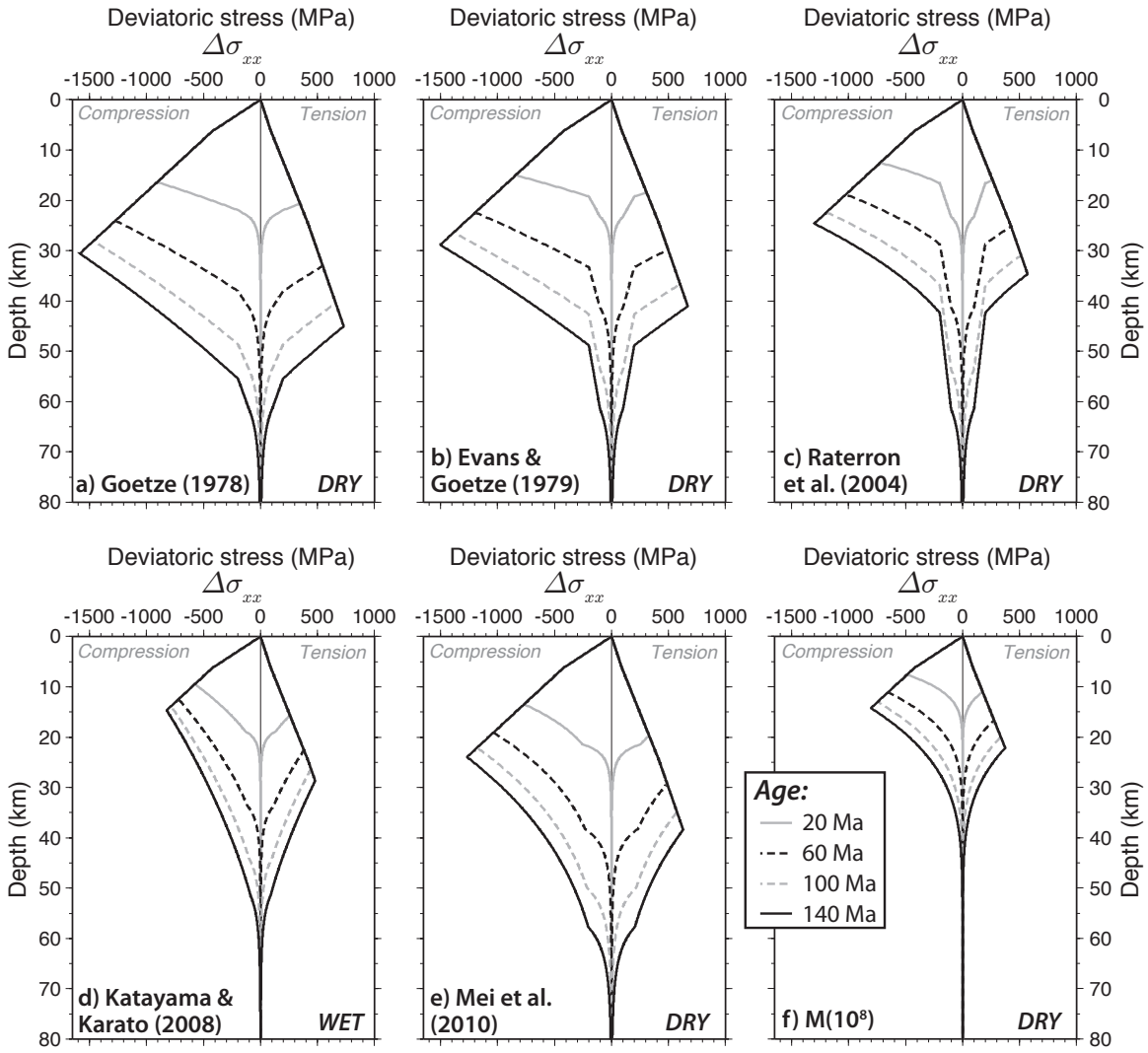

Figure 8.2: The yield strength envelopes used in this study, calculated for a range of plate ages (assuming a plate-cooling geotherm and $\dot{\varepsilon} = 10^{-16}$ s^{-1}). The LTP flow law is labelled on the bottom left of each plot and the water content on the bottom right.

8.2 Calculating the predicted T_e

We used the YSEs illustrated in Figure 8.2, along with plate curvatures, to calculate 'predicted T_e' values for our circum-Pacific trench-outer rise profiles. Then, to test the validity of each LTP flow law, the predicted T_e was compared to the 'observed T_e' that was derived via the inversions described in the previous chapters. In this section, we will describe the calculation of the predicted T_e.

As described in Chapter 3, the flexural rigidity, D, of a thin elastic plate is given by the

ratio of the bending moment, M, and the plate curvature, κ:

$$D = \frac{M}{\kappa} \tag{8.7}$$

and the flexural rigidity is related to T_e by:

$$D = \frac{E\,{T_e}^3}{12(1-\nu^2)} \tag{8.8}$$

where E is Young's modulus and ν is Poisson's ratio. For a given curvature, the YSE can be used to calculate the bending moment in a thin plate that undergoes depth-dependent, laboratory-derived plastic yielding. This bending moment and curvature can then be used to calculate the equivalent T_e, or 'predicted T_e', via Equations 8.7 and 8.8; we will now describe this process in detail.

As shown by Equations 3.9 and 3.12, under the assumptions of thin plate cylindrical bending and in the absence of plastic yielding, the deviatoric elastic bending stress in a plate flexed to curvature κ is given by:

$$\Delta\sigma_{xx}^{elast} = \frac{E(y-y_n)\kappa}{1-\nu^2} \tag{8.9}$$

where y is depth and y_n is the depth of the neutral surface, i.e. the plane along which there is zero strain. An example $\Delta\sigma_{xx}^{elast}$ profile is shown in red dash in Figure 8.3. This can then be used along with the YSE to calculate the stress distribution in the presence of plastic yielding. Here, we assume that the lithosphere behaves as an elastic-perfectly plastic material. This means that stresses below the yield strength are supported elastically, but that when the yield strength is reached, perfectly plastic deformation occurs such that the strain can increase without any further increase in stress (Figure 8.4). In practice, this means that $\Delta\sigma_{xx}^{elast}$ is truncated by the YSE, as illustrated by the solid red stress profile in Figure 8.3:

$$\begin{aligned} \Delta\sigma_{xx} &= \Delta\sigma_{xx}^{elast} \quad \text{if} \quad \Delta\sigma_{xx}^{elast} < \Delta\sigma_{xx}^{yield} \\ \Delta\sigma_{xx} &= \Delta\sigma_{xx}^{yield} \quad \text{if} \quad \Delta\sigma_{xx}^{elast} \geq \Delta\sigma_{xx}^{yield} \end{aligned} \tag{8.10}$$

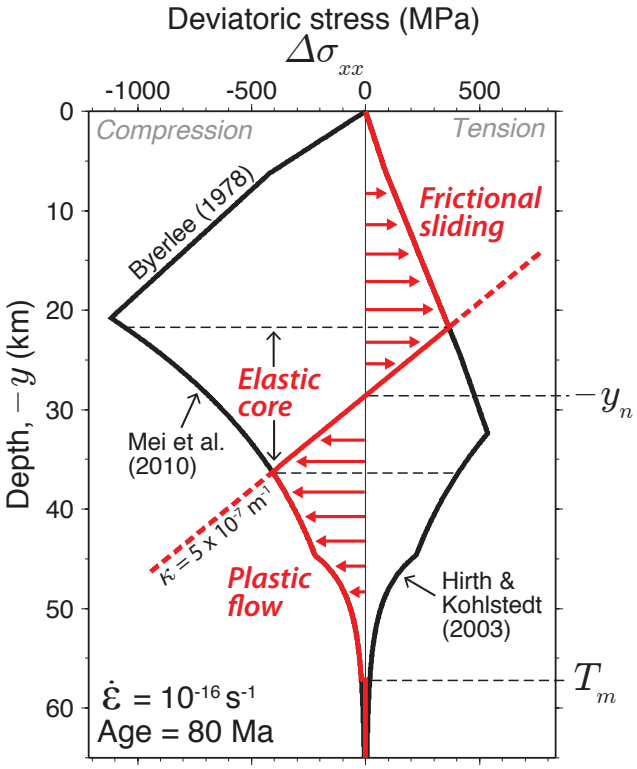

Figure 8.3: Figure illustrating the calculation of the predicted T_e. An elastic bending stress profile (dashed red line) is calculated for a given curvature, κ, and then truncated by the YSE to give the bending stress in the presence of plastic yielding (solid red line). This stress profile can then be used to calculate the bending moment and predicted T_e.

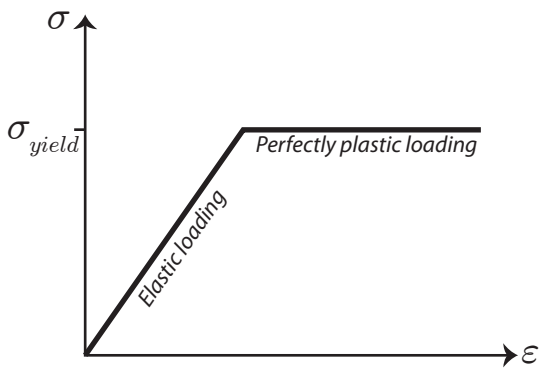

Figure 8.4: Schematic illustrating elastic-perfectly plastic behaviour. Below the yield stress, σ_{yield} in the figure, stress increases linearly with strain. When σ_{yield} is reached, strain continues to increase without any further increase in stress.

When calculating $\Delta\sigma_{xx}$, an optimization was used to find the depth of the neutral surface, y_n, that meets the criterion for pure bending, i.e. bending in the absence of axial loading:

$$\int_0^{T_m} \Delta\sigma_{xx}\,\mathrm{d}y = 0 \tag{8.11}$$

where T_m is the mechanical thickness, defined as the depth to which the lithosphere is capable of supporting non-negligible stresses on geological timescales ($>$ 1 Ma). This was taken as the depth at which the yield strength falls below 1 % of the overburden pressure (Cloetingh and Burov, 1996). Figure 8.3 shows that during lithospheric bending, there are regions of relatively shallow, brittle failure and relatively deep, ductile failure and that these regions are separated by an 'elastic core', where $\Delta\sigma_{xx}$ is below the yield strength and stresses are supported elastically. The deviatoric stress profile described by Equation 8.10 can then be used to calculate the bending moment in the YSE-defined plate:

$$M = \int_0^{T_m} \Delta\sigma_{xx}(y - y_n)\,\mathrm{d}y \tag{8.12}$$

This bending moment can then be used along with the plate curvature to calculate the predicted flexural rigidity and the predicted T_e (Equations 8.7 and 8.8).

8.2.1 Predicted T_e vs. plate curvature

In Figure 8.5, we have shown the predicted T_e as a function of plate curvature, κ, for each of the YSEs used in this study and for a range of plate ages. The figure shows that T_e decreases with $|\kappa|$ due to brittle and ductile failure, and that the rate of decrease slows with increasing $|\kappa|$. The figure also shows that predicted T_e is higher for negative curvatures than for positive. This is because negative curvature implies compression of the uppermost, brittle lithosphere and as shown by Equation 8.3 and Figure 8.2, the brittle yield strength is higher in compression. Figure 8.5 also shows that although the decrease in T_e is larger for older plates (upper plots), the reduction in T_e as a fraction of the initial mechanical thickness, T_m, is nearly independent of plate age (lower plots). This is in agreement with our finding from Inversion A2 that there is no correlation between plate weakening and plate age (Figure 6.5).

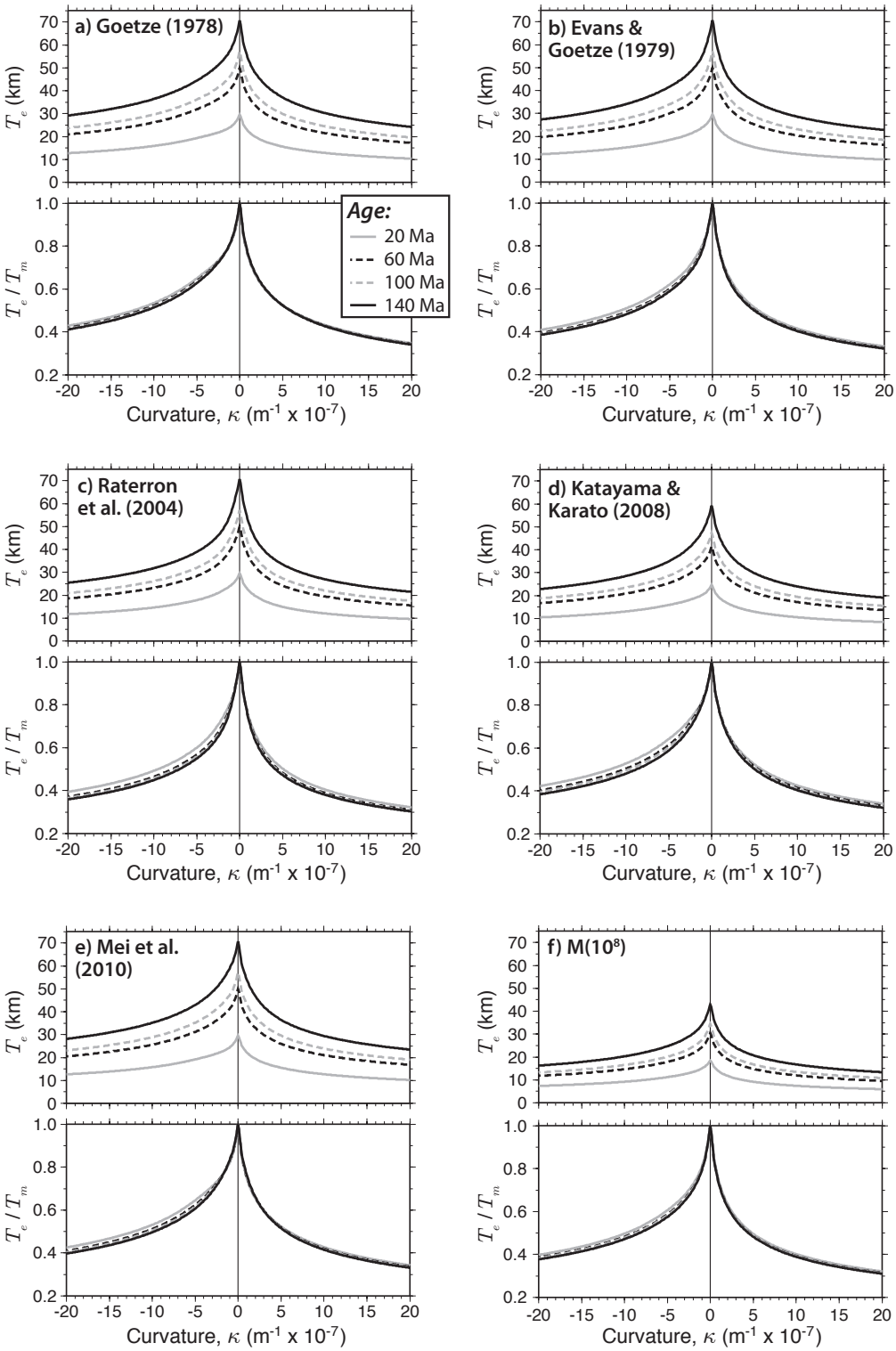

Figure 8.5: Predicted T_e vs. plate curvature for each of the YSEs used in this study and for a range of plate ages. The LTP flow law used to construct the YSE is labelled in the top left of each pair of plots. The upper plots show predicted T_e and the lower plots show predicted T_e as a fraction of the initial mechanical thickness, T_m. All YSEs were calculated with $\dot{\varepsilon} = 10^{-16}$ s^{-1}.

8.3 Constraining LTP flow laws at circum-Pacific subduction zones

In the previous sections, we described the construction of lithospheric YSEs and how these can be used to calculate the predicted T_e as a function of plate curvature, assuming that the lithosphere behaves as an elastic-perfectly plastic material. In this section, we will describe how this technique was used to calculate the predicted T_e at circum-Pacific subduction zones and how, in an effort to constrain mantle rheology, this was compared to the observed T_e that was derived via Inversion A1. We dub this approach to constraining mantle rheology as the 'YSE-curvature method'.

8.3.1 Strain rate

Before calculating the predicted T_e for our circum-Pacific profiles, an appropriate strain rate, $\dot{\varepsilon}_{xx}$, was required to calculate the ductile region of the YSEs (Equations 8.4, 8.5, 8.6). As discussed in Chapter 3, the elastic strain that is induced in the subducting plate by flexure is related to the plate curvature, κ, by $\varepsilon_{xx} = (y - y_n)\kappa$, where y is depth and y_n is the depth of the neutral surface. Therefore the strain rate is given by:

$$\dot{\varepsilon}_{xx} = (y - y_n)\frac{\mathrm{d}\kappa}{\mathrm{d}t} \tag{8.13}$$

where t is time. As we have estimates of κ as a function of distance from the trench, $\dot{\varepsilon}_{xx}$ could be calculated using:

$$\dot{\varepsilon}_{xx} = (y - y_n)V_s\frac{\mathrm{d}\kappa}{\mathrm{d}x} \tag{8.14}$$

where V_s is the subduction velocity and $\frac{\mathrm{d}\kappa}{\mathrm{d}x}$ is the change in κ with distance from the trench. As illustrated in Figure 8.6b, for each circum-Pacific trench-outer rise profile, we used Equation 8.14 to calculate $\dot{\varepsilon}_{xx}$ as a function of distance from the trench axis. Here, $\frac{\mathrm{d}\kappa}{\mathrm{d}x}$ was calculated from the 'observed curvature' profiles (Figure 8.6a), which were obtained by fitting an elastic plate to 170 km-long observed ensemble-averaged gravity profiles (see Section 6.1.1 for more details). V_s was calculated as the sum of the trench-normal plate convergence velocity

(*MORVEL* plate motion model, DeMets et al., 2010) and the backarc deformation rate (from Heuret and Lallemand, 2005). Figure 8.6b shows that $\dot{\varepsilon}_{xx}$ varies both with distance from the trench and with distance from the neutral surface, $|y - y_n|$. In the following paragraphs, we will discuss these variations and will describe which value of $\dot{\varepsilon}_{xx}$ was used to construct the circum-Pacific YSEs.

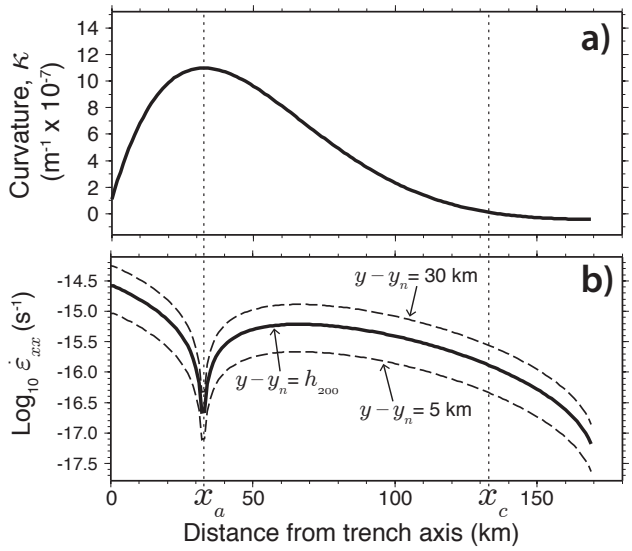

Figure 8.6: Figure illustrating how the strain rate, $\dot{\varepsilon}_{xx}$, was estimated for the circum-Pacific trench-outer rise flexure profiles. The plot shown is for the Kuril trench-bin profile. (a) Observed plate curvatures were used to calculate $\frac{\mathrm{d}\kappa}{\mathrm{d}x}$ as a function of distance from the trench axis. (b) $\frac{\mathrm{d}\kappa}{\mathrm{d}x}$ and the trench-normal subduction velocity were used to calculate $\dot{\varepsilon}_{xx}$ as a function of distance from the trench. The YSE for each profile was calculated using the mean $\dot{\varepsilon}_{xx}$ in the region of plate bending (between x_a and x_c), calculated at distance $|y - y_n| = h_{200}$ from the neutral surface (h_{200} is the depth to the 200 °C isotherm). Also shown are the strain rates calculated for $|y - y_n| = 5$ km and $|y - y_n| = 30$ km.

Equation 8.14 and Figure 8.6b show that $\dot{\varepsilon}_{xx}$ varies with $|y - y_n|$. One limitation of the YSE is that it assumes that $\dot{\varepsilon}_{xx}$ is constant with depth and thus does not account for this variation. However, we do not believe that this limitation has a large effect on the accuracy of the predicted T_e; our reasoning is as follows. The dashed lines in Figure 8.6b show $\dot{\varepsilon}_{xx}$ calculated at two distances from the neutral surface: $|y - y_n| = 5$ km (lower line) and $|y - y_n| = 30$ km (upper line). This represents the depth range over which stresses are likely to be supported on geological timescales, as the mechanical thickness, T_m, of oceanic lithosphere is generally less than half the thermal thickness, $T_t = 125$ km (Watts et al., 1980). The strain rate for $|y - y_n| < 5$ km (i.e. very close to the neutral surface) is unimportant

because this is where the ductile and brittle strength is at a maximum and the bending stress is at a minimum, so that the stresses will be supported elastically no matter what the strain rate. Figure 8.6b shows that $\dot{\varepsilon}_{xx}$ varies by almost an order of magnitude between $|y - y_n| = 5$ km and $|y - y_n| = 30$ km, but Figure 8.7 shows that for this range of strain rates, the predicted T_e varies by only 1–2 km. Thus, if we choose a strain rate intermediate between these values, the maximum error in the predicted T_e due to depth variations in $\dot{\varepsilon}_{xx}$ is likely to be < 1 km. When calculating the YSEs for circum-Pacific subduction zones, we used the strain rate calculated at $|y - y_n| = h_{200}$ (solid black line in Figure 8.6b), where h_{200} is the depth to the 200 °C plate-cooling isotherm for the ensemble-averaged seafloor age 100 km from the trench axis. This isotherm provides an intermediate strain rate and also accounts for the increase in mechanical thickness with plate age.

Figure 8.6b shows that $\dot{\varepsilon}_{xx}$ also varies with distance from the trench axis. For the region of plate bending (between x_a and x_c), $\dot{\varepsilon}_{xx}$ varies by greater than an order of magnitude for any given $|y - y_n|$. Tests shows that the variation in the predicted T_e for this range of strain rates is 2–3 km and therefore if we choose an average strain rate between x_a and x_c, the maximum error in the predicted T_e caused by lateral variations in $\dot{\varepsilon}_{xx}$ is likely to be < 1.5 km. Thus, for each circum-Pacific profile, we calculated the mean $\dot{\varepsilon}_{xx}$ for the region of plate bending (between x_a and x_c) at a distance $|y - y_n| = h_{200}$ from the neutral surface; this value was then used to calculate the YSE. We did not consider the region landward of x_a (Figure 8.6a) when calculating $\dot{\varepsilon}_{xx}$ because, as discussed in Section 7.10, we are not confident of the accuracy of the observed curvatures in this region. We also did not consider the region of concave upwards bending immediately seaward of x_c because the magnitudes of bending are small here (generally $|\kappa| < 0.5 \times 10^{-7}$ m^{-1}). For our circum-Pacific profiles, the mean $\dot{\varepsilon}_{xx}$ value ranges from $10^{-16.3}$ s^{-1} to $10^{-15.1}$ s^{-1} and the average is $10^{-15.7 \pm 0.3}$ s^{-1}. Figure 8.8 shows that for this range of strain rates, the predicted T_e varies by up to 2–3 km. Therefore, as discussed in Section 7.9, strain rate variations might contribute to the scatter in our circum-Pacific observed T_e estimates.

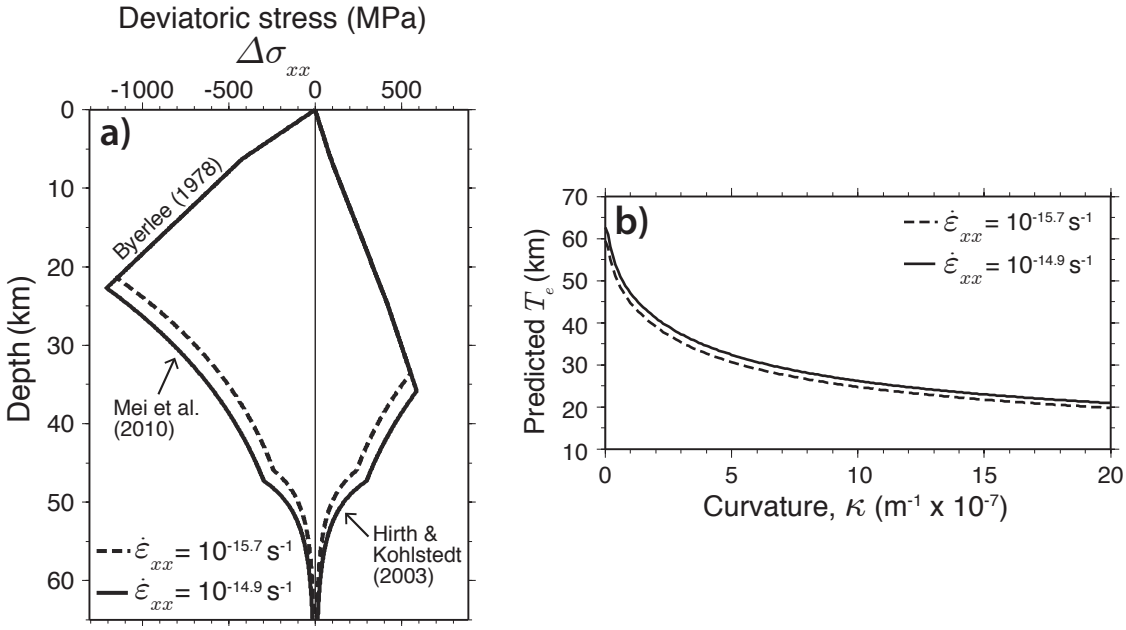

Figure 8.7: Figure illustrating the variation in predicted T_e due to depth variations in strain rate. (a) YSEs for the Kuril trench-bin (mean age 115 Ma), calculated using the strain rates shown in dash in Figure 8.6b at a distance 65 km from the trench axis. These strain rates were calculated at a distance $|y - y_n| = 5$ km and $|y - y_n| = 30$ km from the neutral surface respectively, which represents the depth range over which stresses are likely to be supported on geological timescales. (b) Predicted T_e as a function of plate curvature for each of the YSEs shown in Figure 8.7a.

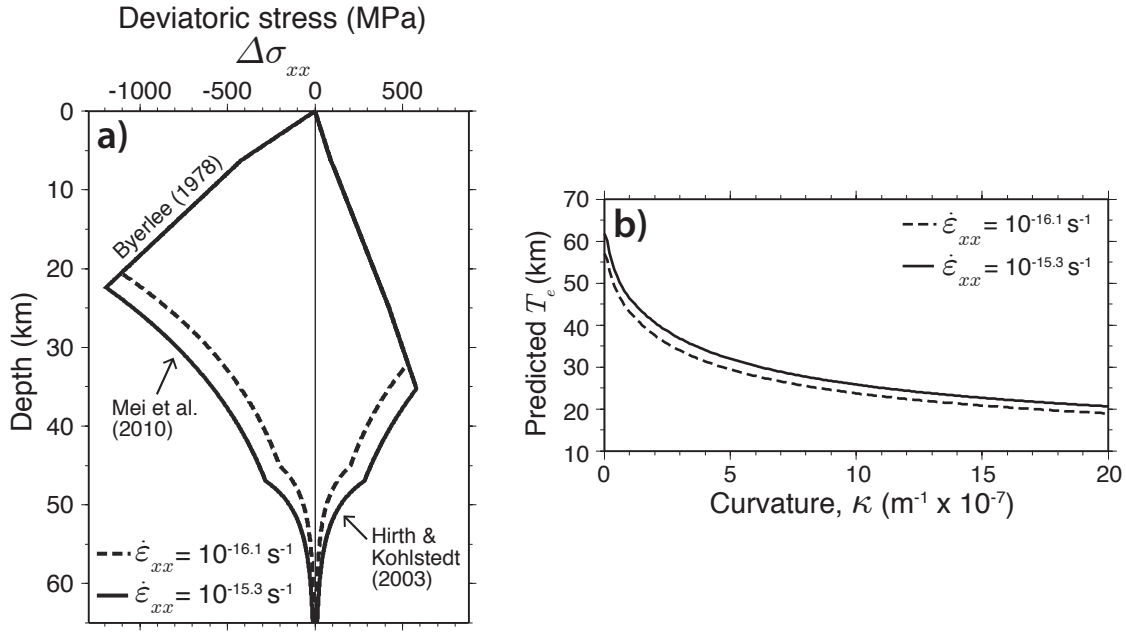

Figure 8.8: Figure illustrating the variation in predicted T_e due to circum-Pacific variations in strain rate. (a) YSEs for a 115 Ma cooling plate, calculated using the minimum and maximum strain rates that were estimated for our circum-Pacific trench-outer rise profiles. (b) Predicted T_e as a function of plate curvature for each of the YSEs shown in Figure 8.8a.

8.3.2 Geotherm

When calculating the YSEs for our circum-Pacific trench-outer rise profiles, we assumed a plate-cooling geotherm (Parsons and Sclater, 1977; parameters given in Table 3.1), calculated for the ensemble-averaged seafloor age 100 km seaward of the trench axis. We note that this does not account for any variation in seafloor age and thermal structure with distance from the trench. However, the age varies by only 1–5 Ma in the region we were interested in ($<$ 200 km from the trench axis) and tests show that there is little variation in the predicted T_e for this age range.

8.3.3 Comparing the predicted T_e to the observed T_e

We wished to compare the T_e predicted by laboratory-derived YSEs to the observed T_e derived via the elastic plate inversions presented in the previous chapters. We concentrated on the results from Inversion A1, in which a constant T_e plate was fitted to the observed gravity profiles (Chapter 5; Figure 5.2), rather than the results from Inversion A2, in which a variable T_e plate was used. We did this because Mueller and Phillips (1995) conducted a synthetic modelling study to test the YSE-curvature method, where they used a constant T_e inversion to derive their observed T_e. The results of their study could therefore be used to instruct our study, as we will now describe.

In order to compare the predictions of the YSEs to the observed T_e, an appropriate value of plate curvature, κ, had to be chosen with which to calculate the predicted T_e (Equation 8.9). As shown in Figure 8.9a, the curvature, and therefore the calculated T_e (red in Figure 8.9b), varies with distance from the trench axis and as a result, it is not immediately obvious which value of κ should be used. This has led to discrepancies between previous studies that used the YSE-curvature method at subduction zone trench-outer rises. For example, Goetze and Evans (1979) used the maximum curvature from the best-fitting elastic plate model to calculate the predicted T_e, and found that YSEs constructed with the LTP flow law of Goetze (1978) provide a good fit to the observed T_e. In contrast, McNutt and Menard (1982) used the curvature at the first zero-crossing (first flexural node) of the best-fitting elastic plate model,

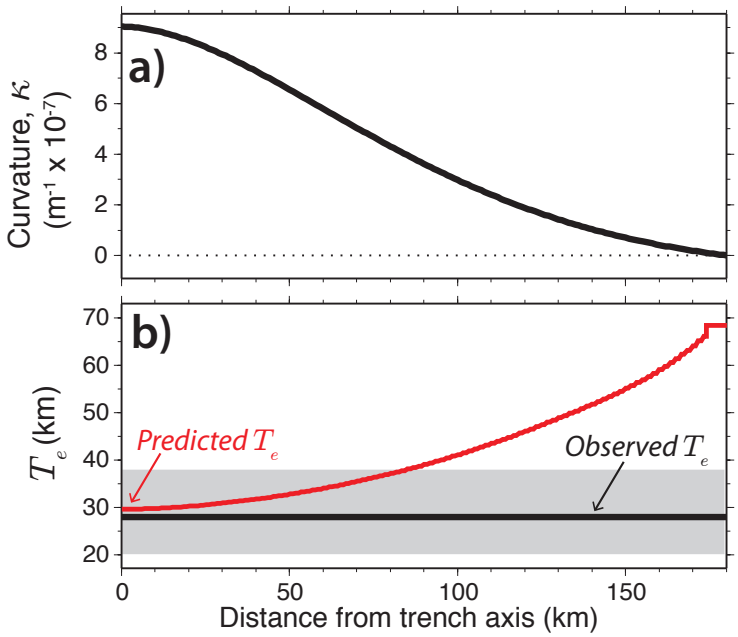

Figure 8.9: Figure illustrating the comparison between the predicted T_e and the observed T_e from Inversion A1. The plots shown are for the Kuril trench-bin profile. (a) Following Mueller and Phillips (1995), plate curvatures from the best-fitting elastic plate model were used to calculate the predicted T_e. (b) The predicted T_e (red line) was calculated as a function of distance from the trench axis, and the value at the point of maximum curvature (red arrow) was compared to the observed T_e (black line; grey shade is the uncertainty). The predicted T_e profile shown was calculated with the LTP law of Mei et al. (2010).

and found that the same LTP flow law is too strong to fit the observed T_e. In an effort to clear up this discrepancy, Mueller and Phillips (1995) created synthetic trench-outer rise flexure profiles using elastic-plastic plates with laboratory-derived, depth-dependent yield strength, and then used the YSE-curvature method to attempt to recover the input rheology. They found that the input rheology was best recovered when the predicted T_e was calculated using the maximum curvature, rather than the curvature at the first zero-crossing, in agreement with Goetze and Evans (1979). They also found that the input rheology was best recovered when the predicted T_e was calculated using the maximum curvature of the best-fitting elastic plate model (i.e. the model used to derive the observed T_e), rather than the maximum curvature of the synthetic elastic-plastic flexure profile. Thus, rather than using the 'observed curvature' (see Section 6.1.1 and Figure 6.1 for description), which we feel better reflects the actual curvature of the lithosphere, we calculated the predicted T_e using the maximum curvature of the best-fitting elastic plate model, as derived via Inversion A1 (illustrated in Figure 8.9).

8.3.4 Results – Byerlee's friction coefficients

In the first test, the brittle regime for all YSEs was calculated with Byerlee's (1978) friction coefficients (Equation 8.2) and hydrostatic PFP, as illustrated in Figure 8.2. We assumed hydrostatic PFP because there is abundant evidence that bend-faults on the outer trench-slope facilitate significant hydration of the crust and uppermost mantle (e.g., Yamano and Uyeda, 1990; Peacock, 2001; Ranero et al., 2003; Grevemeyer et al., 2007). In Figures 8.10 and 8.11, for the segment-bins and trench-bins respectively, the observed T_e (black circles) and predicted T_e (red diamonds) are plotted against seafloor age for each of the LTP flow laws. Following the discussions in Section 8.3.1, we have assigned an uncertainty of 6 km to the predicted T_e values—2 km for depth variations in strain rate, 3 km for lateral variations in strain rate and 1 km for lateral variations in plate age—but this does not account for uncertainties in the assumed value of plate curvature. Figure 8.12 shows the RMS error (RMSE) between the observed and predicted T_e (left plots), and a comparison between the best-fit isotherms to the observed and predicted T_e (right plots); the top row is for the segment-bins and the bottom row is for the trench-bins. The LTP flow laws in Figure 8.12 are numbered as in Figure 8.10.

Figures 8.10, 8.11 and 8.12 show that for both the segment-bins and trench-bins, the LTP flow laws that provide the worst fit to the observed T_e are M(10^6) and M(10^8)—weakened modifications of Mei et al. (2010) where A_m has been increased by 6 and 8 orders of magnitude respectively. These laws produce the highest RMSE between the predicted T_e and observed T_e (> 8.3 km and > 6.5 km for the segment-bins and trench-bins respectively). The best-fit isotherms to the predicted T_e for M(10^6) and M(10^8) (< 290 °C for both the segment-bins and trench-bins) are much too low to fit the best-fit to the observed T_e (400 °C and 380 °C for the segment-bins and trench-bins respectively), which suggests that these laws are too weak to fit the observations. For the segment-bins (Figure 8.10 and top row in Figure 8.12), the LTP laws that best fit the observed T_e are Evans and Goetze (1979) and Raterron et al. (2004), with RMSE < 4.6 km and a best-fit isotherm of 414 °C and 398 °C respectively. The laws of Goetze (1978) and Mei et al. (2010) also provide a good fit to the observed T_e, with RMSE < 5.1 km and best-fit isotherms that are within the 95 % confidence interval of the

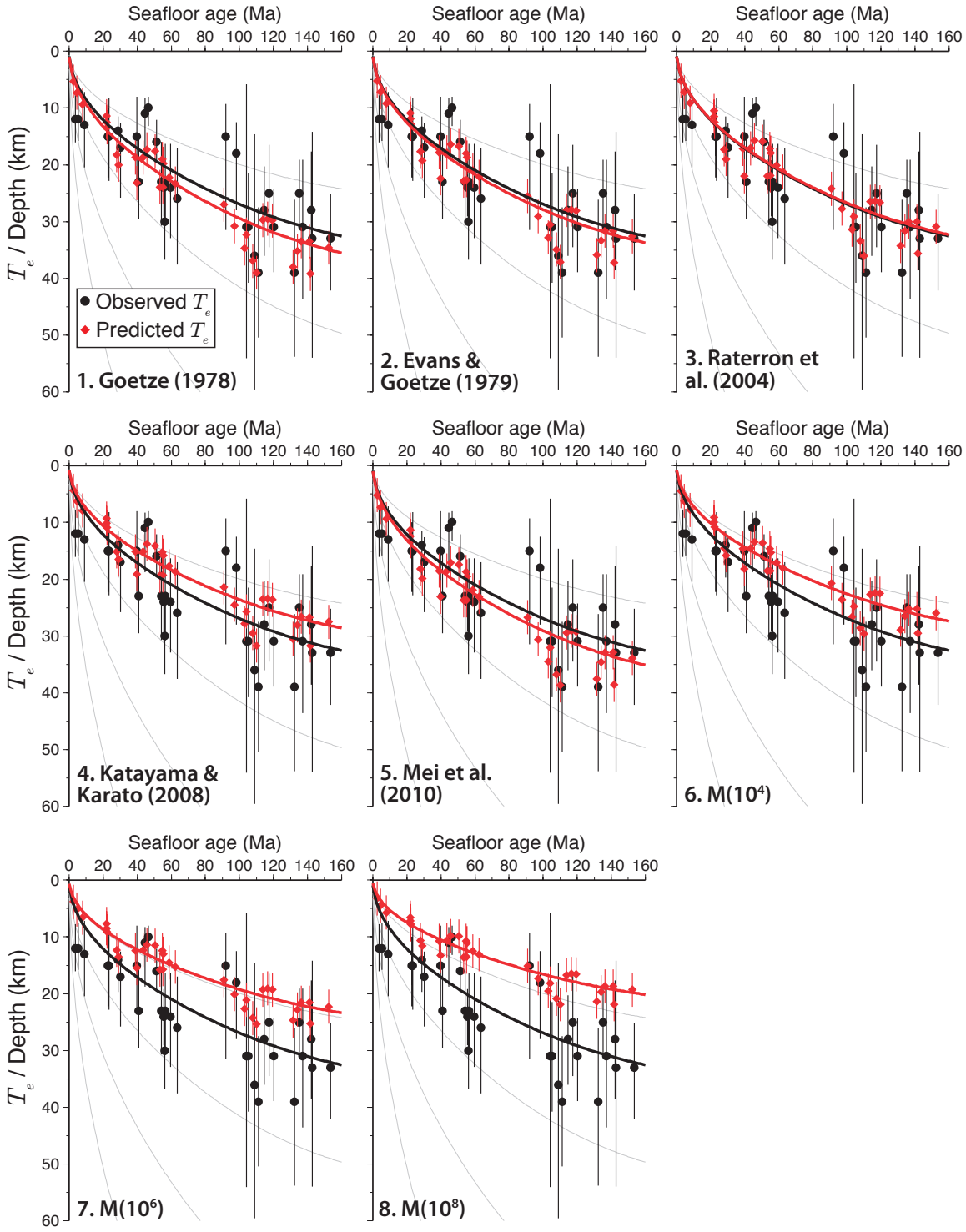

Figure 8.10: For the circum-Pacific segment-bins, the predicted T_e (red diamonds) and the observed T_e from Inversion A1 (black dots) plotted against seafloor age. The LTP flow law used to calculate the predicted T_e is labelled on the bottom left of each plot; in all cases, the brittle regime was calculated with Byerlee's (1978) friction coefficients and hydrostatic PFP. The grey curves show the depths to the 300, 600, 900 and 1200 °C plate-cooling isotherms. The isotherms that best fit the observed T_e and predicted T_e are shown in black and red respectively.

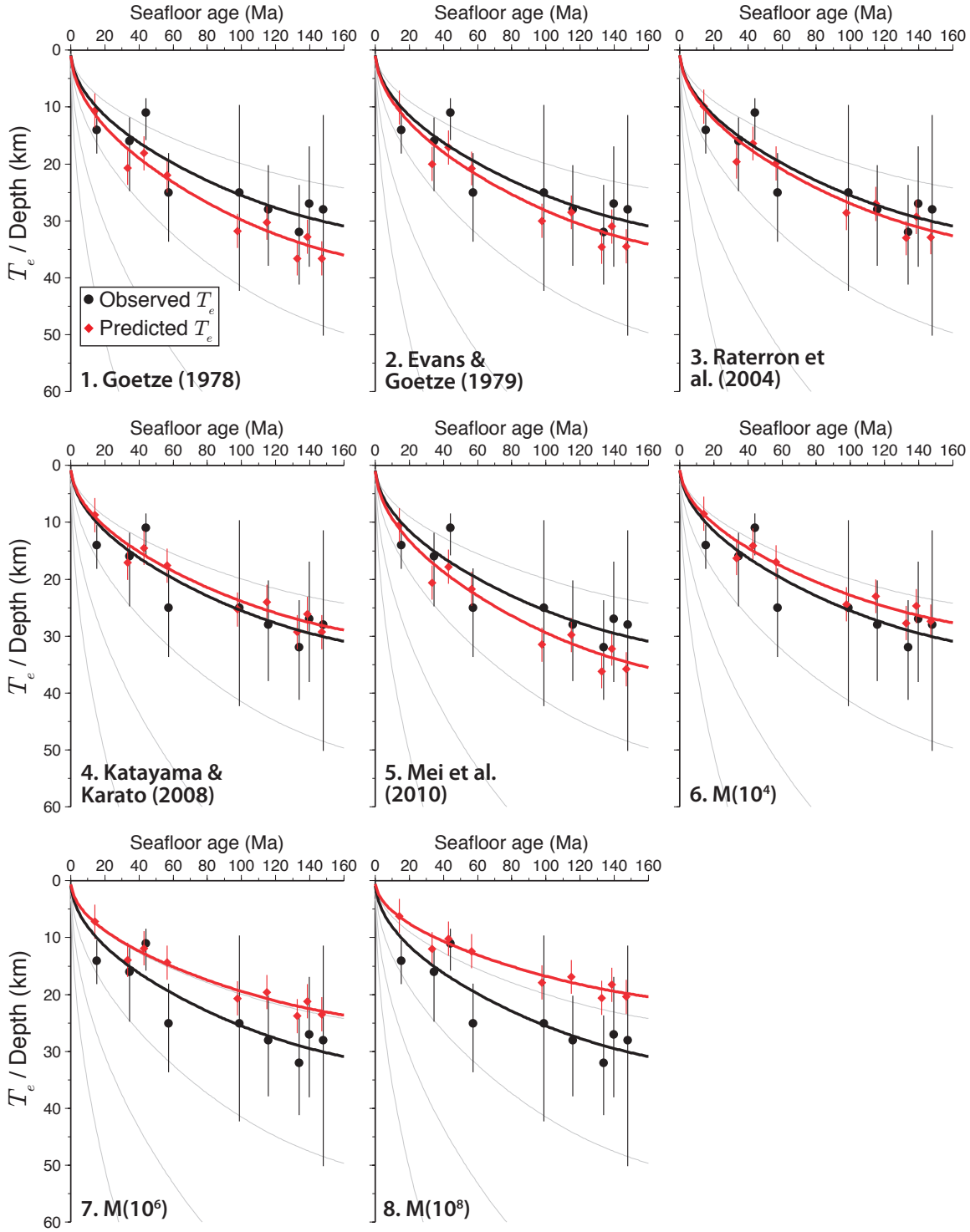

Figure 8.11: For the circum-Pacific trench-bins, the predicted T_e (red diamonds) and the observed T_e from Inversion A1 (black dots) plotted against seafloor age. The LTP flow law used to calculate the predicted T_e is labelled on the bottom left of each plot; in all cases, the brittle regime was calculated with Byerlee's (1978) friction coefficients and hydrostatic PFP. The grey curves show the depths to the 300, 600, 900 and 1200 °C plate-cooling isotherms. The isotherms that best fit the observed T_e and predicted T_e are shown in black and red respectively.

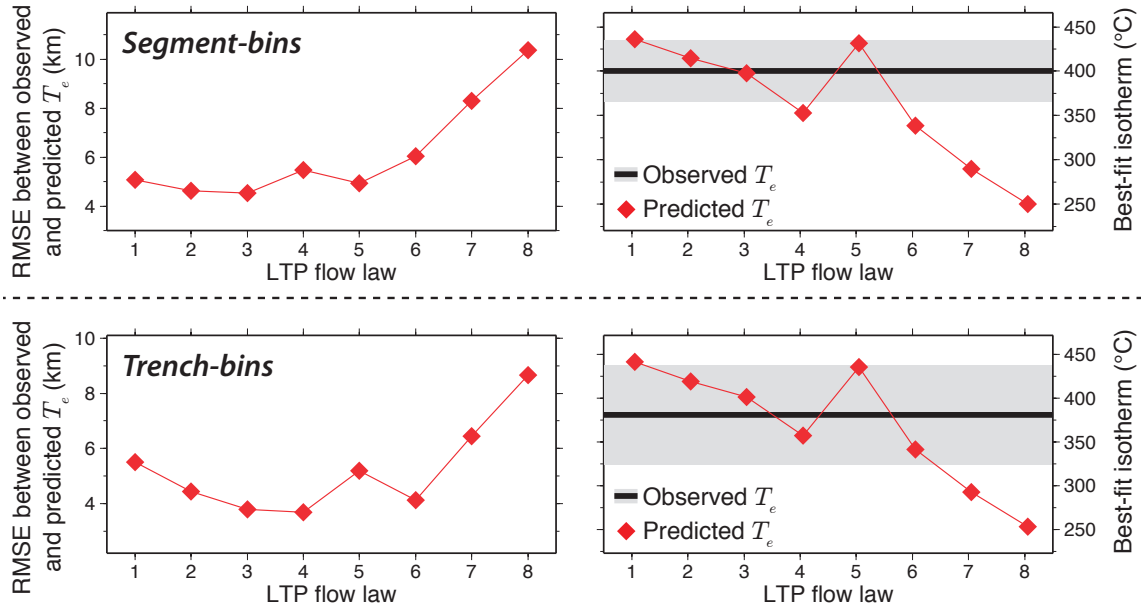

Figure 8.12: Statistics comparing the observed T_e from Inversion A1 to the predicted T_e calculated assuming Byerlee's (1978) friction coefficients and hydrostatic PFP. The top row is for the segment-bins (Figure 8.10) and the bottom row is for the trench-bins (Figure 8.11). The left plots show the RMS error between the observed T_e and the predicted T_e for each LTP flow law. The right plots show the best-fit isotherm to the observed T_e (black line, where the grey shade is the 95 % confidence interval), and the best-fit isotherm to the predicted T_e for each LTP flow law (red diamonds). The LTP flow laws are numbered as in Figure 8.10.

observed best-fit isotherm. The laws of Katayama and Karato (2008) and M(10^4) also provide a reasonably good fit to the observed T_e, with RMSE < 6 km, but their best-fit isotherms are just below the 95 % confidence interval of the observed best-fit isotherm. For the trench-bins (Figure 8.11 and bottom row in Figure 8.12), the LTP laws that best fit the observed T_e are Raterron et al. (2004) and Katayama and Karato (2008), with RMSE < 3.8 km and best-fit isotherms of 401 °C and 360 °C respectively. The laws of Evans and Goetze (1979), Mei et al. (2010) and M(10^4) also provide quite a good fit to the observed T_e, with RMSE < 5.2 km and best-fit isotherms that are within the 95 % confidence interval of the observed best-fit isotherm.

8.3.5 Results – $\mu_f = 0.3$

The pioneering study of Byerlee (1978) found that the friction coefficient, μ_f, and cohesive strength, C_0, of rocks is nearly independent of rock type (Equation 8.2). However, several authors have suggested that faults are much weaker in nature than predicted by rock friction experiments. For example, Craig et al. (2014b) recently used earthquake focal mechanisms from the outer trench-slope of oceanic subduction zones to suggest that for newly formed, trench-parallel bend-faults, $\mu_f \lesssim 0.3$. They suggested that this may be due to the formation of weak clay minerals by hydrothermal alteration at the mid-ocean ridge. Another possible weakening mechanism is serpentinization in the olivine-rich upper mantle by fluids that penetrate bend-faults (e.g., Escartin et al., 1997; Ranero and Sallares, 2004; Grevemeyer et al., 2007). In light of the findings of Craig et al. (2014b), we conducted a second test where the brittle regime of the YSEs was calculated assuming $\mu_f = 0.3$, $C_0 = 0$ and hydrostatic PFP, as illustrated in Figure 8.13. Figure 8.14 shows the statistics for the results of this test.

Figure 8.14 shows that for both the segment-bins (top row) and trench-bins (bottom row), the weakened modifications of Mei et al. (2010) provide the worst fit to the observed T_e. These laws produce the highest RMSE between the observed and predicted T_e, 7.4–11.6 km for the segment-bins and 5.5–10.0 km for the trench-bins. The best-fit isotherms to the predicted T_e for these laws, which range from 230 to 310 °C, are much too low to fit the best-fit to the observed T_e, 400 °C and 380 °C for the segment-bins and trench-bins respectively. This suggests that these laws are too weak to fit the observations. The laws that best fit the observed T_e are Goetze (1978), Evans and Goetze (1979), Raterron et al. (2004) and Mei et al. (2010), with RMSE < 5.1 km and < 3.8 km for the segment-bins and trench-bins respectively, and best-fit isotherms that are within the 95 % confidence interval of the observed best-fit isotherm

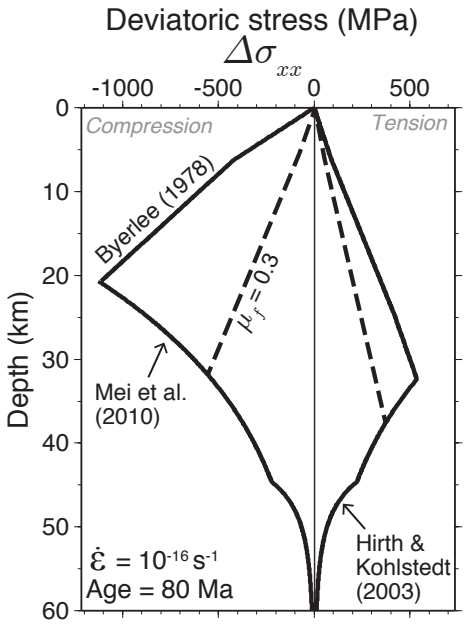

Figure 8.13: YSE showing the effect of the friction coefficient, μ_f, on the brittle yield strength. The solid lines show the brittle yield strength calculated with Byerlee's (1978) friction coefficients and the dashed lines show that calculated with $\mu_f = 0.3$. Hydrostatic PFP was assumed in both cases.

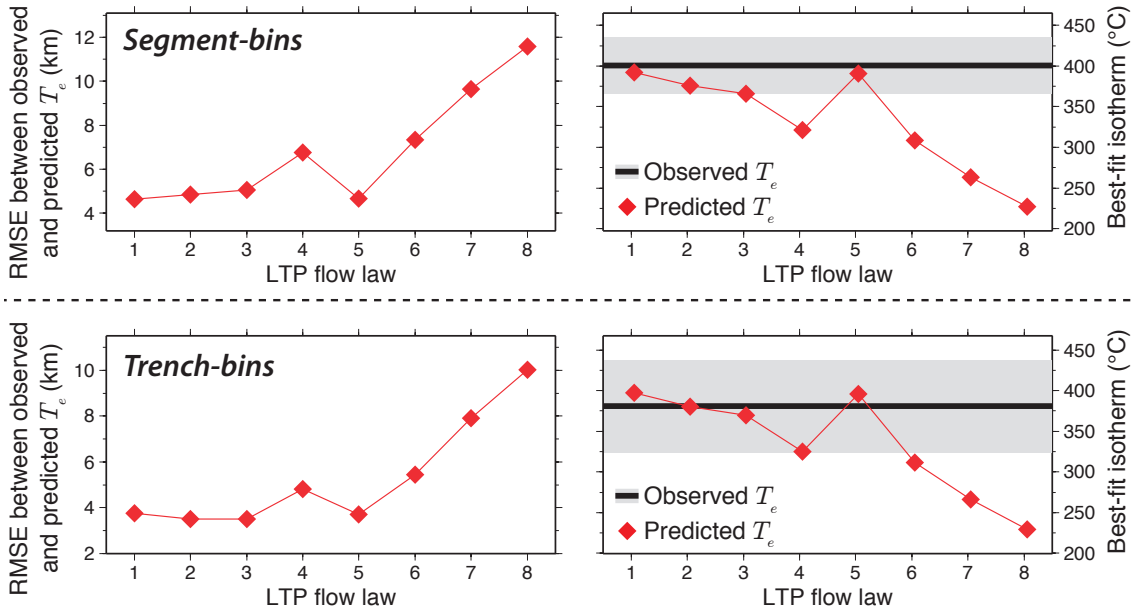

Figure 8.14: Statistics comparing the observed T_e from Inversion A1 to the predicted T_e calculated assuming $\mu_f = 0.3$ and hydrostatic PFP. The top row is for the segment-bins and the bottom row is for the trench-bins. The left plots show the RMS error between the observed T_e and the predicted T_e for each LTP flow law. The right plots show the best-fit isotherm to the observed T_e (black line, where the grey shade is the 95 % confidence interval), and the best-fit isotherm to the predicted T_e for each LTP flow law (red diamonds). The LTP flow laws are numbered as in Figure 8.10.

8.3.6 Results – effective thermal age

As discussed in Section 7.3.2, the effective thermal age, t_{eff}, might better reflect the lithosphere's thermal structure than the seafloor age. Therefore, we conducted a test where the ductile regime for all YSEs was calculated assuming a plate-cooling geotherm for the ensemble-averaged t_{eff} 100 km seaward of the trench axis (see Section 7.3.2 for details of t_{eff} calculation). The brittle regime for all YSEs was calculated assuming Byerlee's (1978) friction coefficients and hydrostatic PFP. The observed and predicted T_e for the segment-bins and the trench-bins are shown in Figures 8.15 and 8.16 respectively. These figures show that the results are very similar to those obtained using the seafloor age (Figures 8.10 and 8.11). However, regardless of the LTP flow law, the fit between the observed and predicted T_e is improved, particularly for the trench-bins. The RMSE is improved by up to 7 % for the segment-bins and up to 18 % for the trench-bins. This perhaps suggests that t_{eff} better reflects the lithosphere's thermal structure than the seafloor age; however, the improvement is not large enough to make a definitive statement.

8.3.7 Discussion

In this section, we have used the YSE-curvature method to constrain the mantle rheology at the trench-outer rise system of circum-Pacific subduction zones, and in particular the rheology in the Low-Temperature Plasticity (LTP) regime. In this approach, laboratory-derived YSEs and plate curvatures were used to calculate the predicted T_e, which was then compared to the observed T_e derived from Inversion A1. Regardless of the assumed friction coefficient, the LTP flow laws of Goetze (1978), Evans and Goetze (1979), Raterron et al. (2004) and Mei et al. (2010) all provide quite a good fit to the observed T_e. This is somewhat surprising, as Zhong and Watts (2013) found that these laws are much too strong to fit flexural observations at the Hawaiian Islands. They calculated the deformation due to volcano loading using a 3-D finite-element viscoelastic model, where the effective viscosity was prescribed by failure laws for frictional sliding, LTP and PLC. By isolating the load of the Hawaiian islands and comparing calculated deflections and stresses to observations of seismically constrained crustal deflections and the depth-dependence of seismicity respectively, they were able to constrain upper mantle

rheology. Zhong and Watts (2013) found that results are insensitive to the PLC regime and fairly insensitive to the friction coefficient, and that published LTP flow laws, including that of Mei et al. (2010), are much too strong to fit the observed crustal deflections. They therefore weakened the law of Mei et al. (2010) by increasing A_m (Equation 8.4), finding that in order to fit the observations, A_m must be increased by 8 orders of magnitude if $\mu_f = 0.7$ or $\mu_f = 0.25$ is assumed, or by 6 orders of magnitude if $\mu_f = 0.1$ is assumed (they assumed zero PFP in all cases). This contrasts with our results from circum-Pacific subduction zones, which suggest that M(10^6) and M(10^8) are much too weak to fit the observations, as the T_e predicted by these laws is much too low to fit the observed T_e.

The discussion above suggests that there is a discrepancy between the lithospheric mantle rheology at the trench-outer rise of circum-Pacific subduction zones and that at the Hawaiian Islands. Based on the YSE-curvature method, the flow law of Mei et al. (2010) provides a good fit the the observed T_e at subduction zones, but based on 3-D finite-element viscoelastic modelling, this law is much too strong to fit the observed flexure at the Hawaiian Islands (Zhong and Watts, 2013). One possible cause of this discrepancy is the difference in approach between this study and that of Zhong and Watts (2013). Indeed, there are potential problems with the YSE-curvature method, such that it assumes plane stress and constant strain rate with depth, and it does not take into account the loading history. Therefore, it was important to validate the YSE-curvature method by using it to constrain the rheology at the Hawaiian Islands and then comparing the results to those of Zhong and Watts (2013). This will be described in the following section.

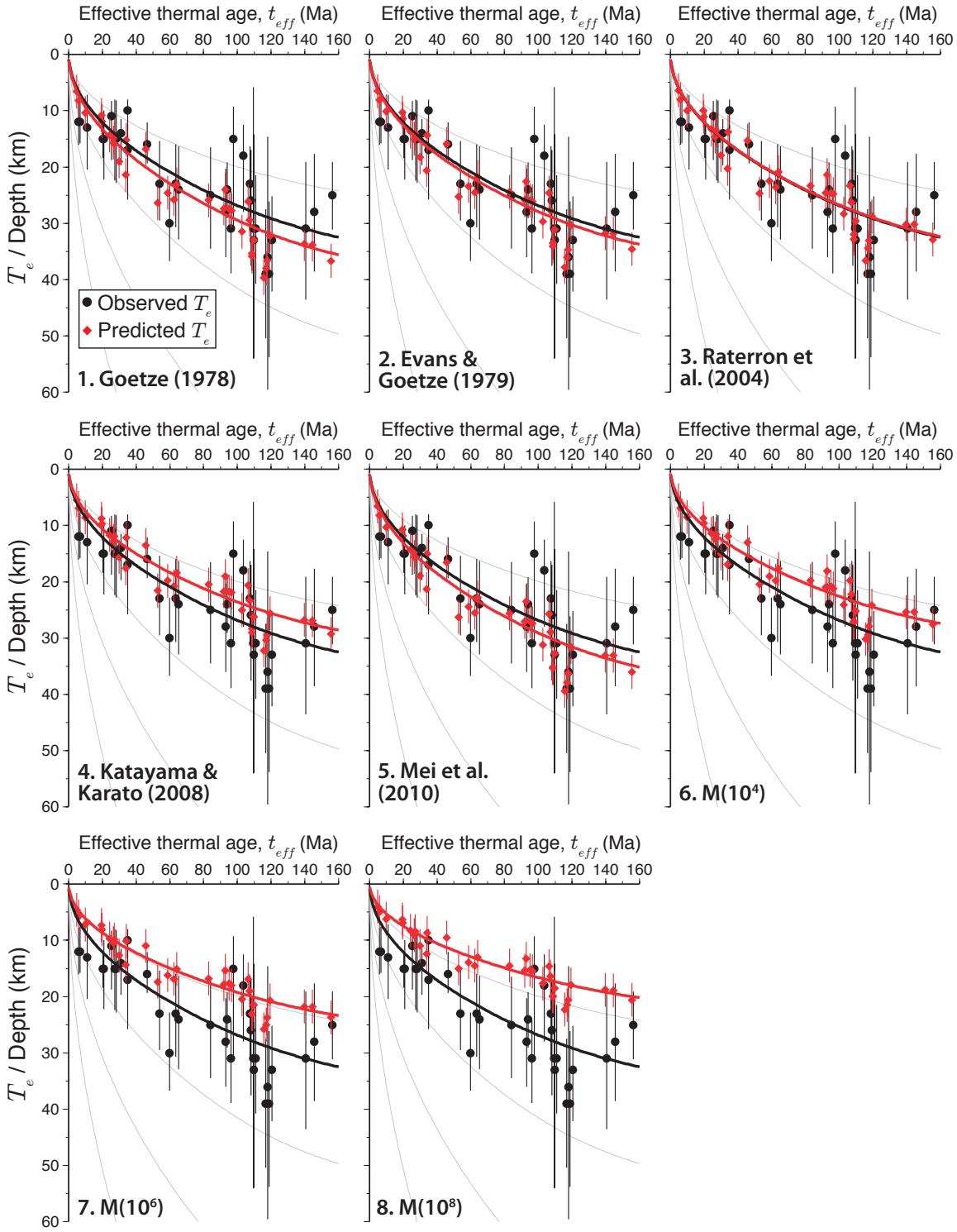

Figure 8.15: For the circum-Pacific segment-bins, the predicted T_e (red diamonds) and the observed T_e from Inversion A1 (black dots) plotted against the effective thermal age. The LTP flow law used to calculate the predicted T_e is labelled on the bottom left of each plot; in all cases, the brittle regime was calculated with Byerlee's (1978) friction coefficients and hydrostatic PFP, and the geotherm was calculated using the effective thermal age. The grey curves show the depths to the 300, 600, 900 and 1200 °C plate-cooling isotherms. The isotherms that best fit the observed T_e and predicted T_e are shown in black and red respectively.

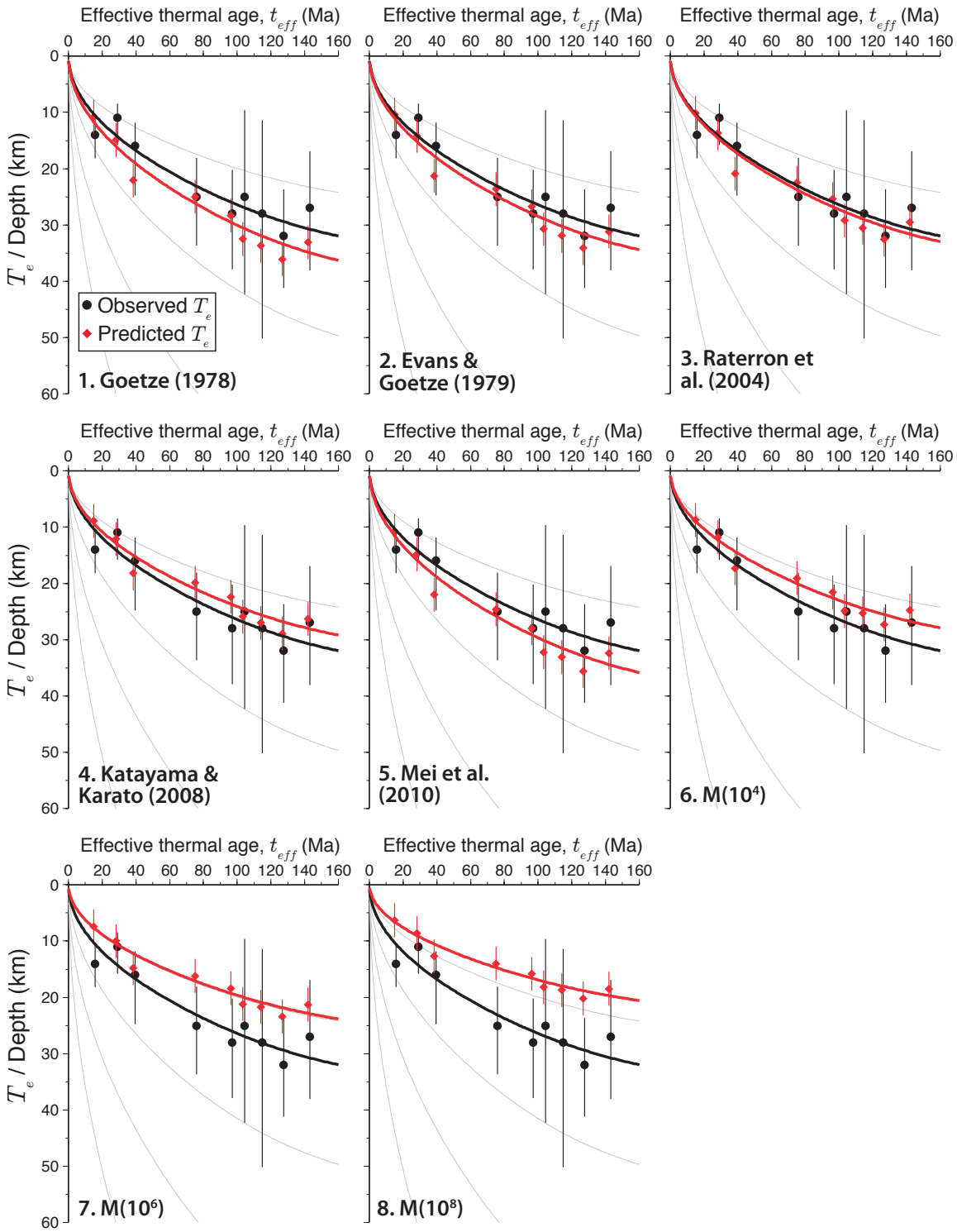

Figure 8.16: For the circum-Pacific trench-bins, the predicted T_e (red diamonds) and the observed T_e from Inversion A1 (black dots) plotted against the effective thermal age. The LTP flow law used to calculate the predicted T_e is labelled on the bottom left of each plot; in all cases, the brittle regime was calculated with Byerlee's (1978) friction coefficients and hydrostatic PFP, and the geotherm was calculated using the effective thermal age. The grey curves show the depths to the 300, 600, 900 and 1200 °C plate-cooling isotherms. The isotherms that best fit the observed T_e and predicted T_e are shown in black and red respectively.

8.4 Constraining LTP flow laws in the Hawaiian Islands region

In this section, we will describe how the YSE-curvature method was used to constrain the mantle rheology in the Hawaiian Islands region, and how these results were compared to those of Zhong and Watts (2013) in order to validate the method.

8.4.1 Tectonic setting

The Hawaiian Island volcanic chain (Figure 8.17a) formed progressively over the last 10^s of Ma as the Pacific plate moved westwards over a mantle plume (Morgan, 1971). Seismic (Li et al., 2000; Wolfe et al., 2009) and geochemical (Hauri et al., 1996) observations suggest that at asthenospheric depths, the plume conduit is presently located beneath the island of Hawaii. Moving eastward along the Hawaiian chain, the islands get progressively younger (Jarrard and Clague, 1977), such that Hawaii is the youngest, having formed over the last 1 Ma (Moore and Clague, 1992) on $\sim$ 90 Ma seafloor (Figure 8.17b). The islands of Molokai and Oahu formed 2–1 Ma and 4–2 Ma respectively (Clague and Dalrymple, 1988).

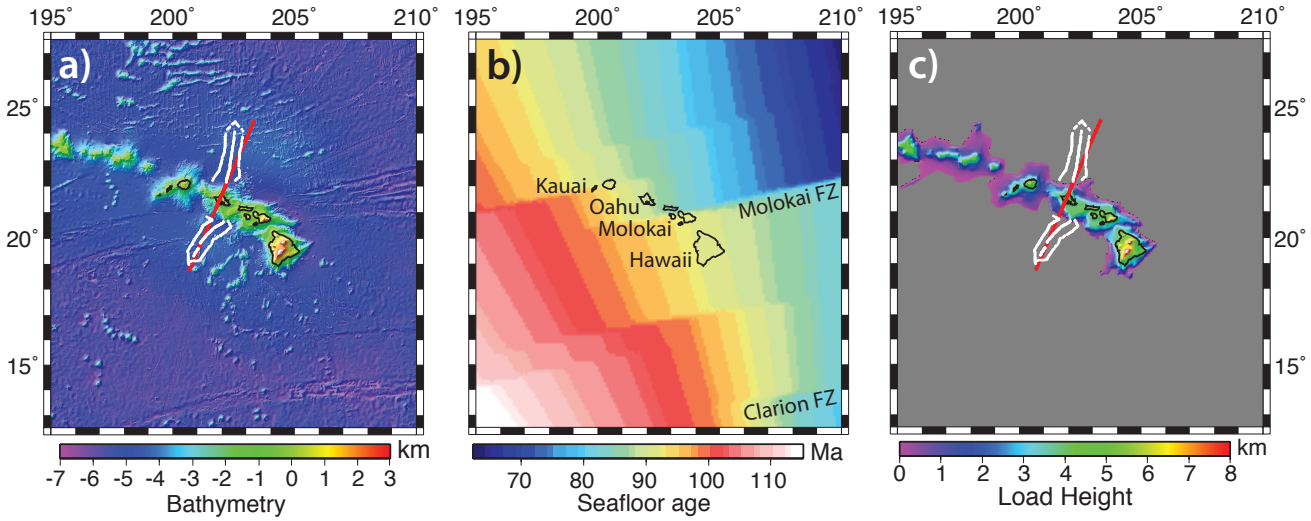

Figure 8.17: Gridded datasets for the Hawaiian Islands region. (a) Bathymetry map (GEBCO_08 30 × 30 second, Ioc et al., 2003). The islands are outlined in black, and the white points are the locations of seismically constrained crustal deflections collected along three ship transects by Watts and Ten Brink (1989). In Figure 8.18b, these data points are projected along the great circle path shown in red. (b) Seafloor age (Müller et al., 2008, v3.2); the major islands and fracture zones are labelled. (c) The surface load that was used to calculate the elastic plate flexure; this was obtained by masking the bathymetry using the 4500 m isobath and then adding 4500 m to the remaining bathymetry.

8.4.2 Deriving the observed T_e

In order to use the YSE-curvature method to constrain the mantle rheology at the Hawaiian Islands, we first required an estimate of the T_e of the lithosphere, i.e. the 'observed T_e'. This will now be described.

8.4.2.1 Data

We modelled the same observed data as Zhong and Watts (2013), which consists of seismically constrained depths to the top of the oceanic crust (from the study of Watts and Ten Brink, 1989). These data were collected along three approximately ridge-normal ship-tracks that intersect the Hawaiian chain at the island of Oahu (white points in Figure 8.17a). Prior to inversion, the data were corrected for swell topography, thermal age and local changes in crustal thickness (e.g. at the Molokai Fracture Zone, Figure 8.17b). In Figure 8.18b, the corrected crustal deflections are plotted; these data have been projected along the great circle path shown in red in Figure 8.17a. The figure shows that the top of the crust is flexed downwards beneath the weight of the volcanic surface load (Figure 8.18a). This produces relatively large amplitude depressions that flank the load, known as 'flexural moats', and relatively small amplitude upward deflections known as 'flexural bulges'.

8.4.2.2 Model

As illustrated in Figure 8.19, we modelled the deflection of the lithosphere beneath the Hawaiian volcanic chain as the flexure of a thin elastic plate overlying an inviscid substrate. At seamounts and ocean islands, the loads acting on the surface of the plate are relatively well known, as they can be isolated from the observed bathymetry. This contrasts with subduction zones outer-rises, where the loads acting on the plate are not well known and therefore have to be inverted for. As shown in Figure 8.17c, we isolated the loads of the Hawaiian volcanic chain by masking the observed bathymetry (GEBCO_08 30×30 second, Ioc et al., 2003; shown in Figure 8.17a) using the 4500 m isobath and then adding 4500 m to the remaining bathymetry. We calculated the 3-D flexure beneath these loads using the code of Cardozo

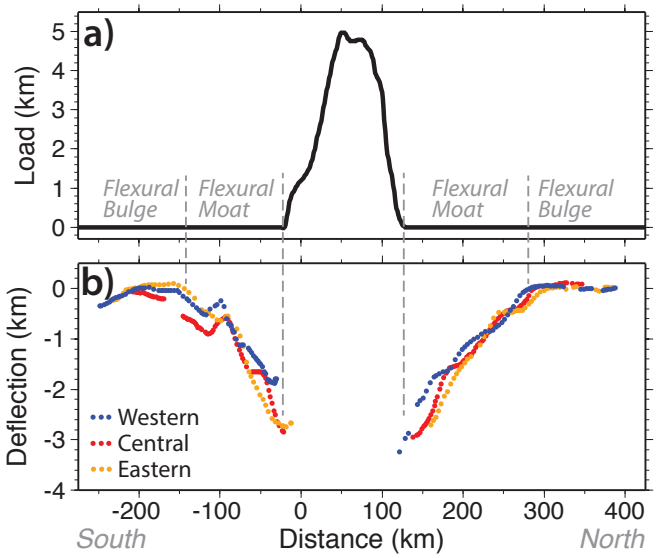

Figure 8.18: The surface load and observed crustal deflections in the Hawaiian Islands region. (a) The surface load that was used to calculate the elastic plate deflections, sampled along the great circle path shown in red in Figure 8.17c. (b) Seismically constrained depths to the top of oceanic crust (Watts and Ten Brink, 1989) from the three transects that are shown as white points in Figure 8.17c; these data have been projected along the same great circle path.

(2009), which uses finite differences to solve the 3-D flexure equation, which in the absence of any horizontal loading is given by (Timoshenko et al., 1959):

$$\nabla^2 \left(D \nabla^2 w \right) - (1-\nu) \left(\frac{\partial^2 D}{\partial x^2} \frac{\partial^2 w}{\partial z^2} + 2 \frac{\partial^2 D}{\partial x \partial z} \frac{\partial^2 w}{\partial x \partial z} + \frac{\partial^2 D}{\partial z^2} \frac{\partial^2 w}{\partial x^2} \right) + (\rho_m - \rho_i) g w = q \quad (8.15)$$

where D is the flexural rigidity, w is the vertical deflection of the plate, (x,z) are horizontal Cartesian coordinates, $\nabla^2 = \frac{\partial^2}{\partial x^2} + \frac{\partial^2}{\partial z^2}$ is the Laplace operator, ν is Poisson's ratio, $q(x,z)$ is the distributed vertical surface load (per unit area), g is the acceleration due to gravity, ρ_m and ρ_i are the density of the mantle and the material that infills the flexure respectively, and $(\rho_m - \rho_i)gw$ is the restoring force due to the density difference between the mantle and the infill. As the Hawaiian volcanic chain is an intraplate feature, we assumed that the elastic plate is continuous in all directions, such that the boundary conditions at each x boundary are $w = 0$ and $\frac{\partial w}{\partial x} = 0$, and at each z boundary are $w = 0$ and $\frac{\partial w}{\partial z} = 0$. This contrasts with our model of trench-outer rise flexure, where there is a break in the plate at the trench axis.

We used the simplified model of a constant T_e plate, as this is sufficient to test the

YSE-curvature method and also makes it relatively easy to find the best-fitting T_e via an inversion. As illustrated in Figure 8.19, we assumed that directly beneath the surface load, the infill density, ρ_i, is equal to the density of the load, ρ_l. This accounts for the fact that the volcanoes extend downwards from the sea surface to the top of the flexed crust. The material that infills the flexural moats (Figure 8.19) is likely to be a mixture of volcanoclastic and pelagic sediments, for which we assumed an average density, $\rho_s = 2300$ kg/m^3. Note that we have conducted tests with different assumed sediment densities—$\rho_s = 2200$ kg/m^3 and $\rho_s = 2400$ kg/m^3—and it makes little difference to the results. As illustrated in Figure 8.19, the surface load per unit area was calculated using $q(x,z) = (\rho_l - \rho_w)gh_b + \rho_l g h_a$, where h_b is the height of the load below sea level, h_a is the height above sea level, and ρ_w is the seawater density. The geographic extent of our model is as shown in Figure 8.17, extending from 195°E to 210°E and from 12.5°N to 27.5°N. We used the following equirectangular coordinate transformation to map from geographic to Cartesian coordinates:

$$\begin{aligned} x &= (\phi - \phi_1)\frac{\pi R \cos\theta_2}{180} \\ z &= (\theta - \theta_1)\frac{\pi R}{180} \end{aligned} \tag{8.16}$$

where ϕ_1 is 195°E, θ_1 is 12.5°N, θ_2 is 20°N, and $R = 6371$ km. This transformation gives Cartesian dimensions of 1569 km in the x (east-west) direction and 1668 km in the z (north-south) direction.

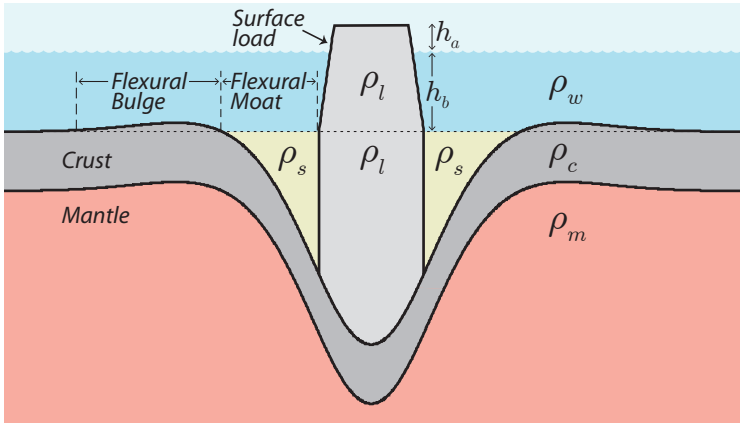

Figure 8.19: Illustration of the continuous elastic plate model that was used to model the flexure of the lithosphere beneath the Hawaiian volcanic chain.

8.4.2.3 Inversion methodology

We used an inverse method to find the T_e and load density, ρ_l, that best fit the observed crustal deflections. We cycled over T_e in steps of 1 km and over ρ_l in steps of 50 kg/m^3, and for each (T_e, ρ_l) parameter pair, the elastic plate flexure was calculated. Then, to account for uncertainties in the undeflected seafloor depth, a damped least squares optimization was used to find the vertical shift, c, that when added to the calculated flexure, best fits the observed deflections. The best-fitting (T_e, ρ_l) parameter pair is that which produces the lowest RMS Error (RMSE) between the observed and calculated deflections.

8.4.2.4 Inversion results

Figure 8.20a shows the RMSE plotted against T_e and ρ_l, and Figure 8.20b shows the RMSE plotted against T_e. The figure shows that there is a well defined RMSE minimum, such that the T_e and ρ_l are well constrained at 26^{48}_{19} km and 2600 kg/m^3 respectively. The superscript and subscript on the T_e estimate are the upper bound and lower bound respectively, which as illustrated in Figure 8.20b, were estimated using 1.25 times the minimum RMSE. Figure 8.20a shows that for $\rho_l < 2750$ kg/m^3, there is little trade-off between T_e and ρ_l, with the best-fit T_e ranging from 26 to 29 km, regardless of the density. However, for $\rho_l > 2750$ kg/m^3, there is a trade-off, where a higher load density requires a higher T_e plate. This is because a heavier load requires a stronger plate to support it.

Our best-fit T_e estimate is similar to those from previous studies of Hawaiian seamount loading. For example, Watts (1978) used the admittance between gravity and bathymetry to derive T_e estimates along the chain in the range 20–30 km, and Wessel (1993) used a 3-D elastic plate to model seismically constrained crustal deflections and found a best-fit T_e of 25 km. Our best-fit ρ_l estimate also agrees with Wessel (1993), who also found a best-fit load density of 2600 kg/m^3. This value is also compatible with density measurements from Hilo drill hole on Hawaii (Moore, 2001), where subaerially erupted lavas have an average density of 2550 kg/m^3 and submarine lavas have an average density of 2680 kg/m^3. These drill hole measurements suggest that it is unlikely that the bulk density of the Hawaiian volcanoes, ρ_l, is greater than 2750 kg/m^3; therefore, the T_e is unlikely to be greater than 29 km.

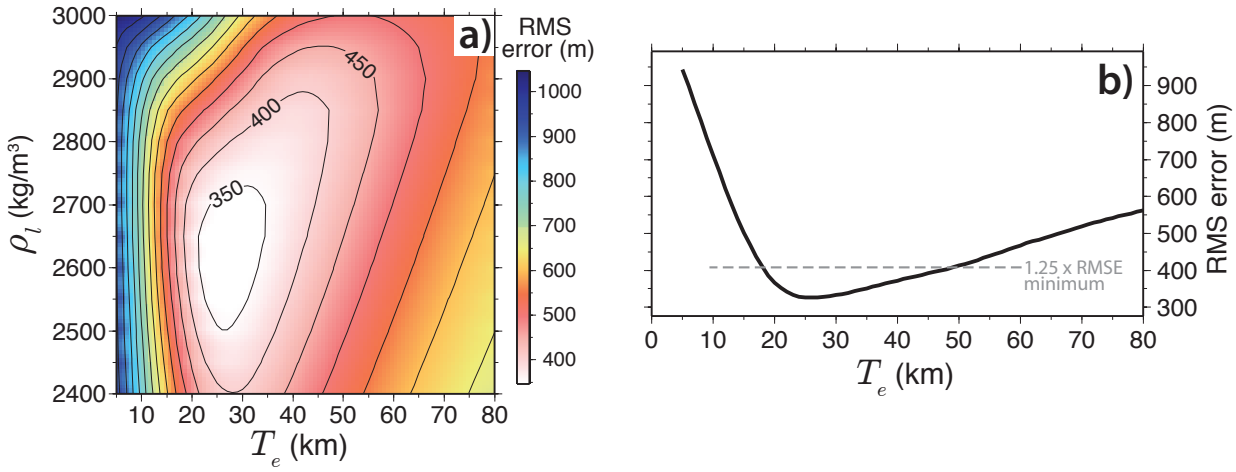

Figure 8.20: Results from inversion of flexural observations in the Hawaiian Island region. (a) The RMS error between the calculated elastic plate deflections and the observed crustal deflections plotted against T_e and load density, ρ_l. The contours are at 50 m intervals. (b) The RMS error plotted against T_e. The dashed grey line corresponds to 1.25 times the minimum RMS error, which was used to estimate the T_e uncertainty.

Figure 8.21a shows a grid of the elastic plate flexure that best fits the observed crustal deflections. This shows the downward flexure of the plate beneath the volcanic surface loads, with amplitude up to 5.3 km beneath Hawaii and up to 3.3 km beneath Oahu. The figure also shows the flexural bulge that surrounds the surface loads, which has amplitude of up to 190 m. Figure 8.21b shows the observed (black) and best-fit calculated (red) crustal deflections along each of the three ship transects. This shows that the best-fit elastic plate model provides a fairly good fit to the observations in the southern section of each transect, but tends to underestimate the deflection in the northern sections. This was also found with the finite-element viscoelastic model of Zhong and Watts (2013), so it is not a result of our using a simple elastic plate model. It has been suggested that it may be a result of a crack in the plate (Wessel, 1993) and/or flexural deformation (Watts and Ten Brink, 1989) at the Molokai fracture zone, but such complexities are beyond the scope of this study. We note, however, that the best-fit viscoelastic model of Zhong and Watts (2013) produced a slightly better overall fit to the observed data (RMSE = 291 m) than our elastic plate model (RMSE = 326 m). This is likely due to the inability of the elastic plate model to account for plastic yielding and the time-dependence of loading. Figure 8.21b also shows the calculated deflections for $T_e = 10$ km and $T_e = 50$ km (grey crosses). It is clear that $T_e = 10$ km is much too weak to fit the observations, as the wavelength of the flexural bulges is too short and the amplitude

too high. In contrast, $T_e = 50$ km is much too strong, as the wavelength of the flexural bulges is too long and the amplitude too low; this suggests that the upper bound on our T_e estimate (48 km) is very conservative.

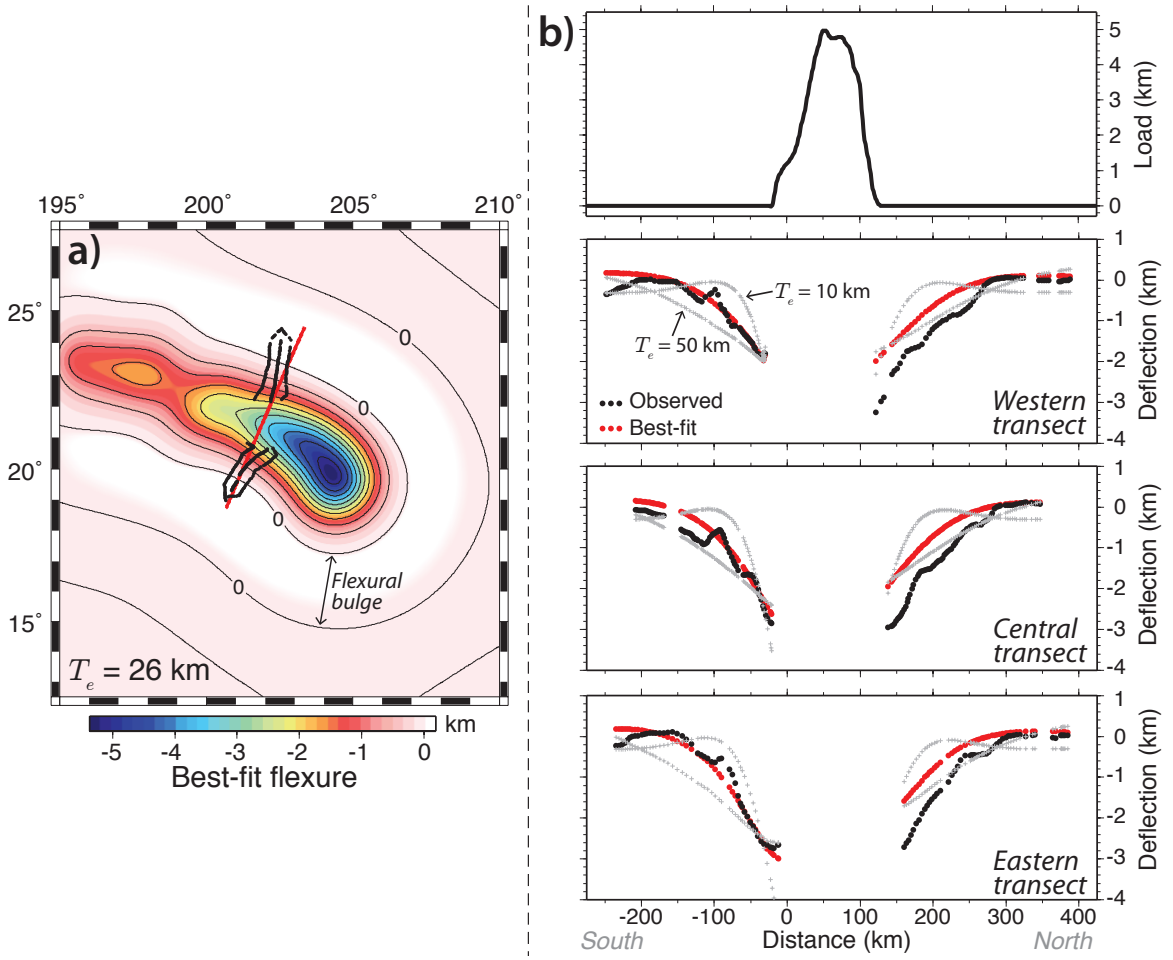

Figure 8.21: The best-fit elastic plate solution for the Hawaiian Islands, obtained for $T_e = 26$ km and $\rho_l = 2600$ kg/m^3. (a) A grid of the elastic plate flexure that best fits the observed crustal deflections. The contours are at 500 m intervals. (b) The top plot shows the surface load that was used to calculate the elastic plate deflections, sampled along the great circle path shown in red in Figure 8.21a. The lower three plots show the observed (black) and best-fit calculated (red) crustal deflections along each of the three ship transects (shown as black points in Figure 8.21a); these data have been projected along the same great circle path. The calculated deflections for $T_e = 10$ km and $T_e = 50$ km are also shown (grey crosses).

8.4.3 Calculating the predicted T_e

After having found the observed T_e by modelling observed crustal deflections, the next step was to use laboratory-derived YSEs to calculate the predicted T_e for the Hawaiian Islands region. This would allow us to test the predictions of LTP flow laws and to test the YSE-curvature method by comparing the results to those of Zhong and Watts (2013). To calculate the predicted T_e, we made the simplifying assumption of plane strain, where two of the principal stresses are directed normal and parallel to the Hawaiian volcanic chain respectively, and the strain is zero in the direction parallel to the chain. This assumption is based on the fact that the Hawaiian chain is an approximately linear and continuous feature and therefore, other than perhaps directly beneath the volcanoes, there should be little deflection of the plate in the chain-parallel direction. We suggest that this assumption is fairly reasonable because as shown in Figure 8.22b, the plate curvature of the best-fit elastic plate model in the chain-parallel direction is relatively small ($|\kappa| \leq 0.3 \times 10^{-7}$ m^{-1}) in the regions where we have observed data (black points). The plane strain assumption means that the predicted T_e can be calculated in the same way as at the trench-outer rise of subduction zones, where the strike of the Hawaiian volcanic chain is analogous to the strike of the trench axis.

8.4.3.1 Plate curvature

To calculate the predicted T_e, we required an appropriate value of plate curvature, κ, with which to calculate the bending stress profile (Equation 8.9). As shown in Figure 8.23b (solid line), we calculated the chain-normal curvature of the best-fit elastic plate model along the great circle path shown in red in Figure 8.21a. Figure 8.23a shows that the calculated deflection along this path provides a fairly good a fit to each of the observed transects, and therefore it seems reasonable to use these curvatures to calculate the predicted T_e. Figure 8.23b (dashed line) also shows that the chain-normal plate curvature along the same great circle path is relatively low ($|\kappa| \leq 0.3 \times 10^{-7}$ m^{-1}), which suggests that the assumption of plane strain is fairly reasonable. Figure 8.23b shows that the curvature in the chain-normal direction is negative beneath the volcanic load, with magnitude up to 4.6×10^{-7} m^{-1}, and is positive in the flexural bulges, with magnitude up to 1.6×10^{-7} m^{-1}. That is to say that the

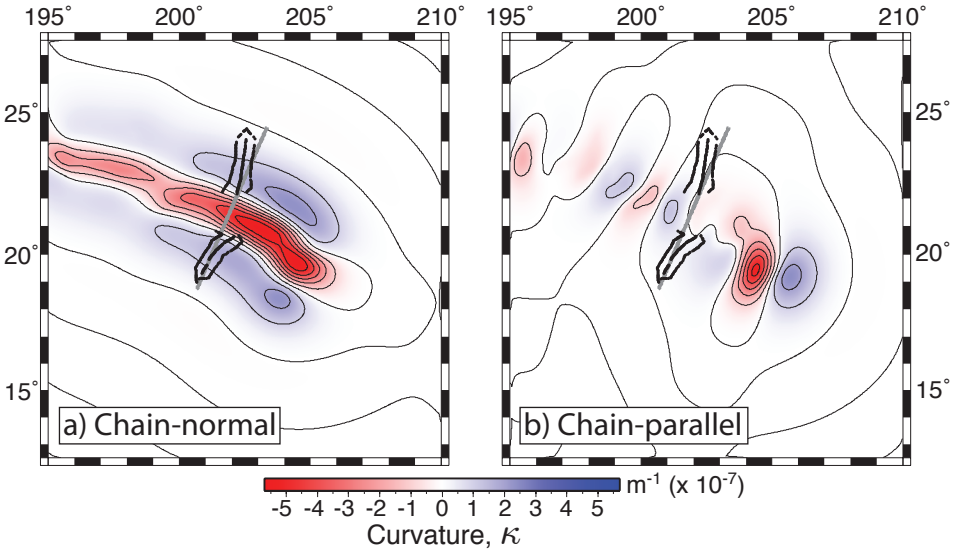

Figure 8.22: The plate curvature, κ, of the best-fit elastic plate model (Figure 8.21a) in the (a) chain-normal and (b) chain-parallel direction. The black dots are the locations of the seismically constrained crustal deflections and the grey line is the great circle path along which the curvature in Figure 8.23b was calculated. The contours are intervals of $1 \times 10^{-7}\mathrm{m}^{-1}$.

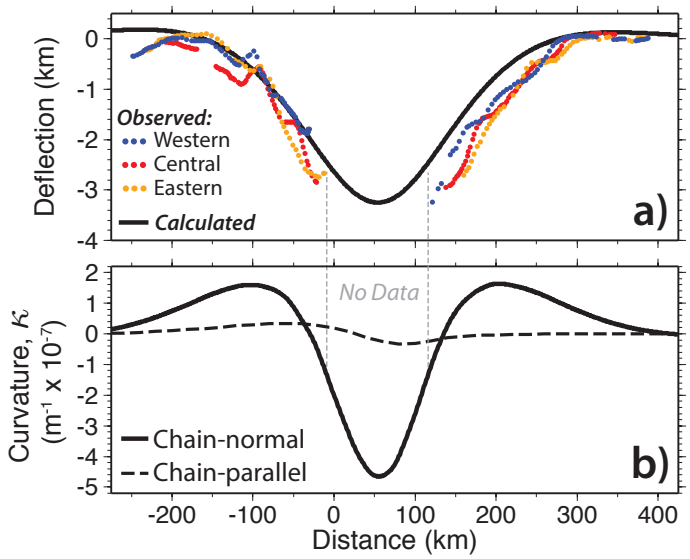

Figure 8.23: Figure illustrating the plate curvature that was used to calculate the predicted T_e for the Hawaiian Islands region. (a) The black line shows the best-fit elastic plate deflection along the profile shown in red in Figure 8.21a. The blue, red and orange points show the observed crustal deflections projected along this profile. (b) The chain-normal and chain-parallel curvature calculated from the best-fit elastic plate model along the profile shown in red in Figure 8.21a. The predicted T_e was calculated using the maximum chain-normal curvature in the regions where we have observed data, $\kappa = 1.6 \times 10^{-7}$ m^{-1}.

plate is bent concave upwards beneath the load and convex upwards in the flexural bulges. We calculated the predicted T_e using the maximum chain-normal curvature in the regions where we have observed data, $\kappa = 1.6 \times 10^{-7}$ m^{-1}. This follows from the synthetic modelling study of Mueller and Phillips (1995), which found that the input rheology of synthetic flexure profiles was best recovered when the predicted T_e was calculated using the maximum curvature of the best-fitting elastic plate model (see Section 8.3.3 for more details). Note that we have also conducted tests using the maximum curvature in the region of no data coverage, -4.6×10^{-7} m^{-1}. This lowers the predicted T_e by 1–3 km, depending on the LTP flow law, but does not significantly affect the general pattern of results.

8.4.3.2 Geotherm

For each LTP flow law, the YSE was calculated with a plate-cooling geotherm for a 90 Ma plate, which is a representative age for the oceanic lithosphere that underlies the Hawaiian Islands in the vicinity of Oahu, as shown in Figure 8.17b. Note that we have also repeated the study using an 80 Ma and 100 Ma geotherm respectively, and it has negligible effect on the results.

8.4.3.3 Strain rate

An appropriate strain rate, $\dot{\varepsilon}$, was required to calculate the ductile regime of the YSEs (Equations 8.4 and 8.5). To estimate $\dot{\varepsilon}$, we assumed that the maximum plate curvature, $\kappa = 1.6 \times 10^{-7}$ m^{-1}, accrued linearly over the shield to post-shield building phase on Oahu, which occurred over 2 Myr (4–2 Ma) (Clague and Dalrymple, 1988). As at the trench-outer rise system, we calculated $\dot{\varepsilon}$ at a distance h_{200} from the neutral surface, where h_{200} is the depth to the 200 °C isotherm for a 90 Ma plate. This gives a strain rate of $\dot{\varepsilon} = 10^{-16.5}$ s^{-1}. Note that we have also repeated the study where the strain rate was calculated for a volcanic building phase of 1 and 4 Myr respectively, and it has negligible effect on the results.

8.4.3.4 LTP flow laws

The strain rate and geotherm described above were used to construct the YSE for each of the LTP flow laws (illustrated in Figure 8.2). These were then used along with the maximum elastic plate curvature, $\kappa = 1.6 \times 10^{-7}$ m^{-1}, to calculate the predicted T_e for each flow law. As at circum-Pacific subduction zones, we tested five laboratory-derived LTP flow laws (Goetze, 1978; Evans and Goetze, 1979; Raterron et al., 2004; Katayama and Karato, 2008; Mei et al., 2010), and three weakened modifications of Mei et al. (2010) where A_m has been increased by 4, 6 and 8 orders of magnitude respectively (Table 8.1). These are referred to as M(10^4), M(10^6) and M(10^8) respectively.

8.4.4 Results – comparison with Zhong and Watts (2013)

We first wished to directly compare our results to those of Zhong and Watts (2013), who constrained the LTP rheology using a 3-D finite-element viscoelastic model, as this would allow us to test the validity of the YSE-curvature method. Therefore, in the first set of tests, the brittle regime of the YSEs was calculated with a friction coefficient of $\mu_f = 0.7$ and zero Pore Fluid Pressure (PFP), as these were the values assumed by Zhong and Watts (2013). Figure 8.24a shows the predicted T_e from the YSE-curvature method (red squares) and the observed T_e derived by modelling observed crustal deflections (black line). The figure shows that the laws of Goetze (1978), Evans and Goetze (1979), Raterron et al. (2004) and Mei et al. (2010) all produce similar predicted T_e values of 40–42 km, which are much too high to fit the observed T_e of 26 km. The predicted T_e is so similar between these laws because the relatively low curvature, and therefore bending stress, means that only a small amount of LTP flow is predicted by these YSEs (Figure 8.24c), and therefore that the ductile strength is predominantly governed by the dry PLC flow law of Hirth and Kohlstedt (2003). Figure 8.24a shows that M(10^4) and the wet LTP law of Katayama and Karato (2008) are also too strong to fit the observed T_e, as they produce a predicted T_e of 32 and 34 km respectively. However, M(10^6) and M(10^8) provide quite a good fit to the observed T_e, with a predicted T_e of 28 and 24 km respectively, which suggests that M(10^7) would provide the best fit to the observed value of 26 km.

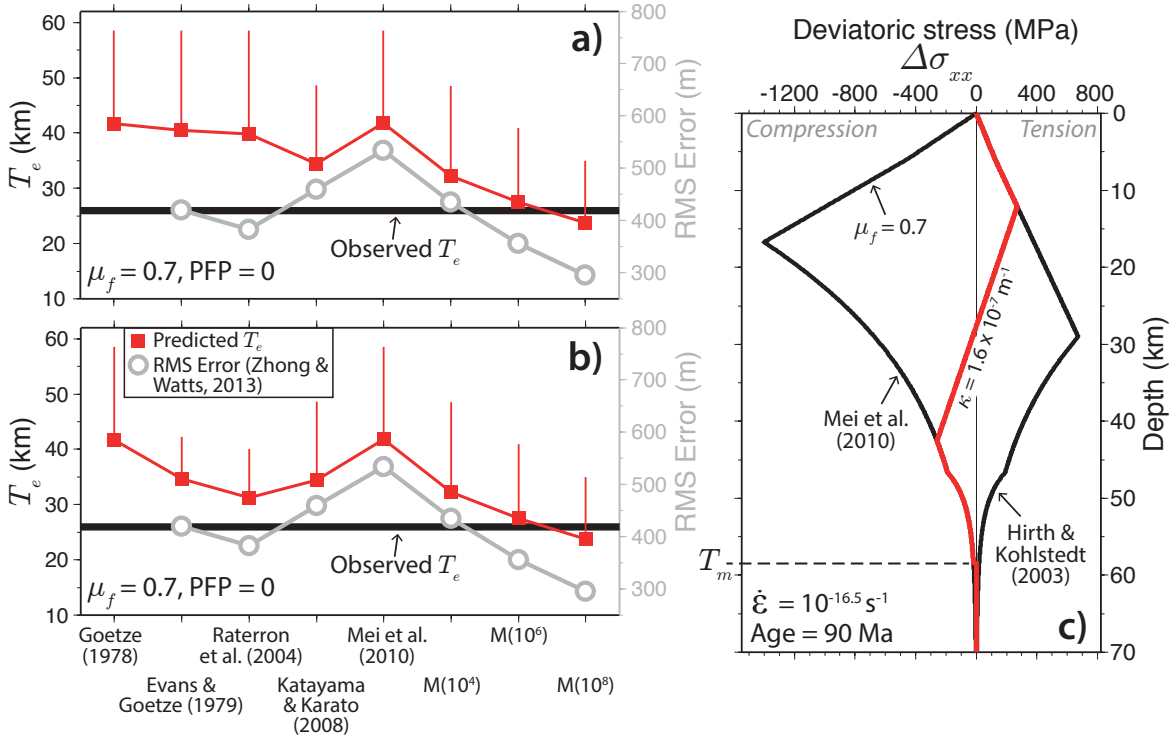

Figure 8.24: Comparison between the results of the YSE-curvature method and those of Zhong and Watts (2013) at the Hawaiian Islands. All results were calculated assuming $\mu_f = 0.7$ and zero PFP. (a,b) The predicted T_e for each LTP flow law (red squares) compared to the observed T_e (black line). The upper end of the error bar on the predicted T_e is the predicted mechanical thickness, T_m. Also shown for comparison is the RMS error between the observed and calculated crustal deflections from the study of Zhong and Watts (2013) (grey circles). To calculate the predicted T_e shown Figure 8.24a, the YSEs for the LTP laws of Evans and Goetze (1979) and Raterron et al. (2004) were constructed by interpolating between the LTP and PLC curves (solid grey in Figure 8.25). To calculate the predicted T_e shown in Figure 8.24b, the YSEs for these two laws were constructed using only the LTP flow strength (dashed black in Figure 8.25). (c) The YSE (black) and stress distribution (red) that were used to calculate the predicted T_e for the LTP law of Mei et al. (2010).

Figure 8.24a also shows the RMS Error (RMSE) between the observed and calculated crustal deflections from the study of Zhong and Watts (2013) (grey circles). This shows that for the LTP laws of Katayama and Karato (2008), Mei et al. (2010) and modifications thereof, the pattern of results from this study (red squares) is very similar to that of Zhong and Watts (2013): Mei et al. (2010) is much too strong to fit the observations; M(10^6) and M(10^8) provide the best fit; and M(10^4) and Katayama and Karato (2008) are intermediate between these results. However, Figure 8.24a shows that for the LTP laws of Evans and Goetze (1979) and Raterron et al. (2004), the results of this study are different to those of Zhong and

Watts (2013). From this study, the T_e predicted by these two laws is greater than that of Katayama and Karato (2008); but from the study of Zhong and Watts (2013), these laws are weaker than, and therefore have a lower RMSE than, Katayama and Karato (2008). This difference arises because when constructing the YSEs for the laws of Evans and Goetze (1979) and Raterron et al. (2004), we interpolated between the points at which the LTP strength is 200 MPa and the PLC strength is 100 MPa, so that there is no depth-discontinuity in the yield strength (illustrated by the solid grey YSEs in Figure 8.25). In contrast, because the finite-element viscoelastic model of Zhong and Watts (2013) solves for both stress and strain rate, they did not have to perform this interpolation, and instead stipulated that the transition from LTP to PLC occurred at a threshold temperature of 800 °C. However, Zhong and Watts (2013) also reported a problem with the laws of Evans and Goetze (1979) and Raterron et al. (2004): because $n = 0$ in these laws (Equation 8.4), the strain rate is nearly stress-independent for stresses less than ∼200 MPa. In effect, this allows the LTP and PLC deformation regimes in the model of Zhong and Watts (2013) to become decoupled by a low viscosity channel at the base of the LTP regime. The closest approximation to this behaviour that can be implemented in the YSE-curvature method is to construct the YSEs for these laws using only the LTP flow strength (illustrated by the dashed black YSEs in Figure 8.25), defining the mechanical thickness, T_m, as the point at which the LTP strength falls below 1 % of the overburden pressure. As shown in Figure 8.24b, when we do this, the results of the YSE-curvature method (red squares) and those of Zhong and Watts (2013) (grey circles) are very similar for all of the flow laws, including those of Evans and Goetze (1979) and Raterron et al. (2004).

The results described above suggest that the YSE-curvature method is a valid technique for constraining mantle rheology. For the LTP flow laws of Katayama and Karato (2008), Mei et al. (2010) and modifications thereof, the results of this method compare well with the study of Zhong and Watts (2013); and when decoupling of the LTP and PLC deformation regimes is accounted for, the results also compare well for the flow laws of Evans and Goetze (1979) and Raterron et al. (2004). The results of both studies suggest that if $\mu_f = 0.7$ and zero PFP is assumed, the law of Mei et al. (2010) is much too strong to fit flexural observations in the Hawaiian Islands region, and that A_m must be increased by 6–8 orders of magnitude in order to fit the observations.

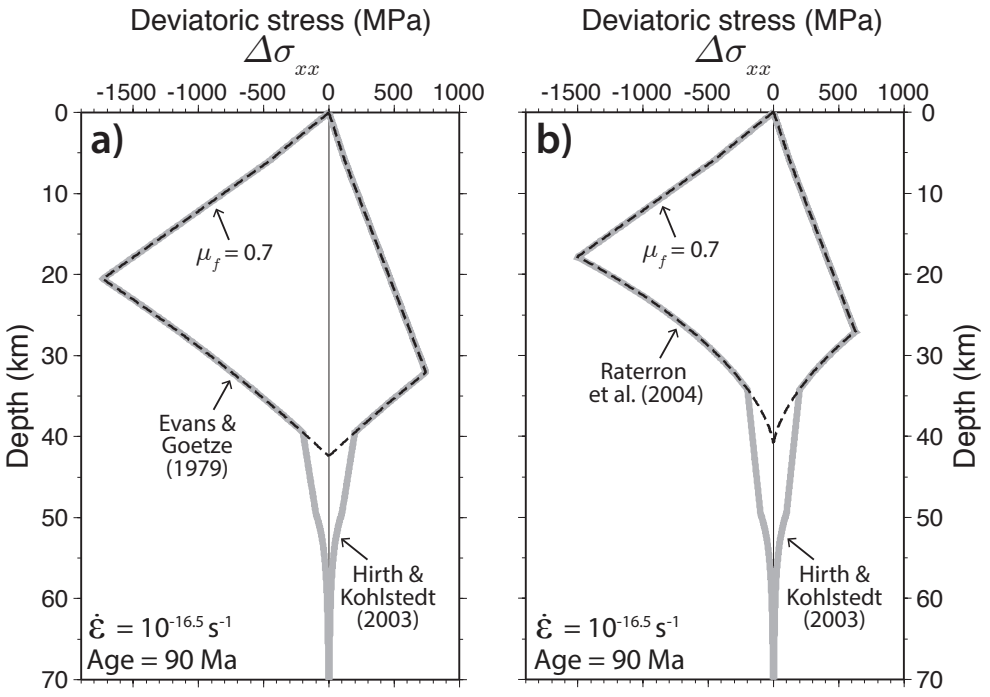

Figure 8.25: The YSEs used to calculate the predicted T_e for the flow law of (a) Evans and Goetze (1979) and (b) Raterron et al. (2004). The YSEs shown in solid grey were constructed by interpolating between the points at which the LTP strength is 200 MPa and the PLC strength is 100 MPa, so that there is no depth-discontinuity in the yield strength. These were used to calculate the predicted T_e shown in Figure 8.24a. The YSEs shown in dashed black were constructed using only the LTP flow strength, defining the mechanical thickness as the point at which the LTP strength falls below 1 % of the overburden pressure. These were used to calculate the predicted T_e shown in Figure 8.24b.

8.4.5 Results – comparison with circum-Pacific subduction zones

Having validated the YSE-curvature method by comparison with the study of Zhong and Watts (2013), we next wished to compare the results from the Hawaiian Islands with those from circum-Pacific trench-outer rise systems. As discussed previously, we calculated the predicted T_e for circum-Pacific subduction zones using two different friction conditions: Byerlee's (1978) empirically derived coefficients and $\mu_f = 0.3$, where hydrostatic PFP was assumed in both case. Therefore, we also tested these same friction coefficients at the Hawaiian Islands, as we will describe below. Here, we will focus on the LTP flow law of Mei et al. (2010) and the weakened modifications of this law.

Figure 8.26a shows the predicted T_e calculated assuming Byerlee's (1978) coeffcients and hydrostatic PFP (red squares). Note that for the LTP laws of Evans and Goetze (1979) and

Raterron et al. (2004), we have not accounted for decoupling of the LTP and PLC deformation regimes (i.e. the predicted T_e was calculated using the YSEs illustrated in solid grey in Figure 8.25). The figure shows that the results are very similar to those calculated with $\mu_f = 0.7$ and zero PFP (Figure 8.24a), but with slightly lower (by 1–2 km) predicted T_e. The law of Mei et al. (2010) predicts a T_e of 40 km, which is much too strong to fit the observed T_e of 26 km. The modification that best fits the observed T_e is M(10^6), where A_m has been increased by 6 orders of magnitude, as this gives a predicted T_e of 27 km.

Figure 8.26b shows the predicted T_e calculated assuming $\mu_f = 0.3$ and hydrostatic PFP. The figure shows that the predicted T_e is less (by 2–3 km) than that calculated assuming Byerlee's (1978) coefficients, but that the flow law of Mei et al. (2010), with a predicted T_e of 37 km, is still too strong to fit the observed T_e. The modification that best fits the observed T_e is M(10^6), which gives a predicted T_e of 25 km.

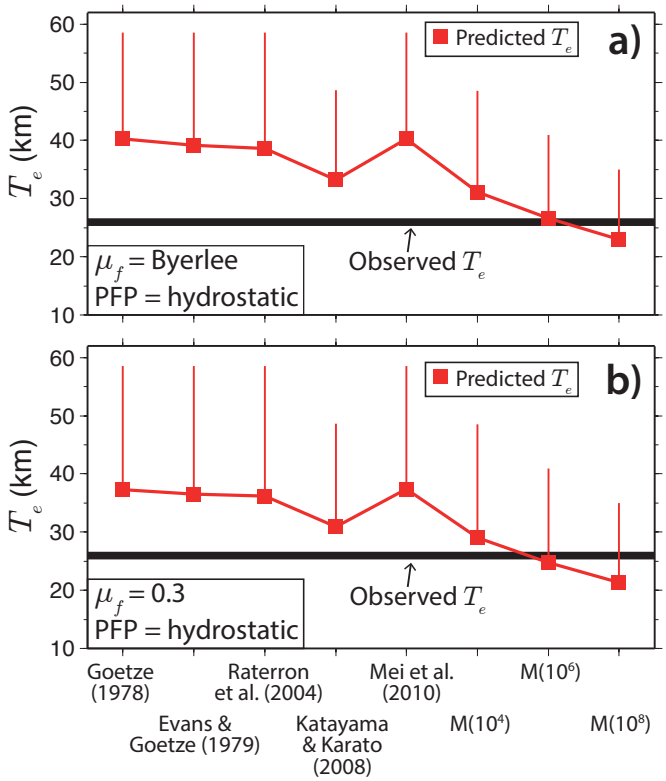

Figure 8.26: For the Hawaiian Islands, the predicted T_e for each LTP flow law (red squares) compared to the observed T_e (black line). (a) The predicted T_e was calculated assuming Byerlee's (1978) friction coefficients and hydrostatic PFP. (b) The predicted T_e was calculated assuming $\mu_f = 0.3$ and hydrostatic PFP. The upper end of the error bar on the predicted T_e is the predicted mechanical thickness.

8.4.6 Summary

We have validated the YSE-curvature method by using it to constrain the mantle rheology in the Hawaiian Islands region and comparing the results to those of Zhong and Watts (2013). The results of this method reveal an apparent discrepancy between the rheology at the Hawaiian Islands and that at the trench-outer rise system of circum-Pacific subduction zones. The LTP flow laws of Goetze (1978), Evans and Goetze (1979), Raterron et al. (2004), Katayama and Karato (2008) and Mei et al. (2010) all provide a reasonably good fit to the observed T_e at circum-Pacific subduction zones, whilst M(10^6) and M(10^8) are much too weak. In contrast, the laws of Goetze (1978), Evans and Goetze (1979), Raterron et al. (2004), Katayama and Karato (2008) and Mei et al. (2010) are all much too strong to fit the observed T_e at the Hawaiian Islands. In this region, assuming Byerlee's friction coefficients or $\mu_f = 0.3$ (and hydostratic PFP), M(10^6) provides the best fit to the observed T_e; i.e. the law of Mei et al. (2010) must be weakened by increasing A_m by 6 orders of magnitude.

8.5 Chapter summary

In this chapter, we have used the YSE-curvature method to constrain the mantle rheology, and in particular the Low-Temperature Plasticity (LTP) rheology, at circum-Pacific trench-outer rise systems and in the Hawaiian Islands region. The key points are as follows:

- The YSE-curvature method is an attempt to constrain mantle rheology by comparing the predictions of laboratory-derived YSEs to T_e estimates derived via the inversion of observed data. YSEs are constructed for each LTP flow law, which are then used to calculate the 'predicted T_e' for an assumed plate curvature. These values are then compared to the 'observed T_e' in order to test the validity of each flow law.

- The YSE-curvature method was validated by using it to constrain the mantle rheology in the Hawaiian Islands region and comparing the results to those of Zhong and Watts (2013), who modelled the observed crustal deflections using a 3-D finite-element viscoelastic model.

- At the trench-outer rise system of circum-Pacific subduction zones, regardless of the assumed friction coefficient, the LTP flow laws of Goetze (1978), Evans and Goetze (1979), Raterron et al. (2004), Katayama and Karato (2008) and Mei et al. (2010) all provide a reasonably good fit to the observed T_e.

- In the Hawaiian Islands region, the laws of Goetze (1978), Evans and Goetze (1979), Raterron et al. (2004), Katayama and Karato (2008) and Mei et al. (2010) are all too strong to fit the observed T_e. In order to fit the observed T_e, the law of Mei et al. (2010) must be weakened by increasing A_m by 6–8 orders of magnitude.

- There is an apparent discrepancy between the mantle rheology in the Hawaiian Islands region and that at circum-Pacific trench-outer rise systems. This discrepancy can be summarised by stating that the recent LTP law of Mei et al. (2010) provides a reasonably good fit to the observed T_e at circum-Pacific subduction zones, but appears much too strong to fit the observed T_e at the Hawaiian Islands.

Chapter 9

Constraining the rheology of oceanic lithosphere using elastic-plastic plate models

In the previous chapter, we used the YSE-curvature method to constrain the mantle rheology, and in particular the Low-Temperature Plasticity (LTP) rheology, at the trench-outer rise system of circum-Pacific subduction zones and at the Hawaiian Islands. In this method, the observed T_e, which was derived by using an elastic plate to model observations of flexure, was compared to the predicted T_e, which was calculated using laboratory-derived Yield Strength Envelopes (YSE) and chosen values of plate curvature. In this chapter, we will describe a second approach that we used to constrain the mantle rheology. In this approach, we computed the deflections of elastic-perfectly plastic plates that have laboratory-derived, depth-dependent yield strength, and compared this to the observed flexural deflections. This approach has a number of advantages over the YSE-curvature method. Firstly, in the YSE-curvature method, the observed T_e is derived by modelling the lithosphere as an elastic plate. Whilst this provides a reasonable fit to the data and a first order estimate of the average rigidity of the lithosphere, it cannot account for bending-induced plastic yielding and the resultant spatial variation in rigidity. By modelling the lithosphere using an elastic-perfectly plastic plate, these factors are accounted for. Secondly, in the YSE-curvature method, an

appropriate value of plate curvature has to be chosen to calculate the predicted T_e, which, as discussed in the previous chapter, is subject to some uncertainty. By directly comparing the deflections of an elastic-plastic plate to the observed deflections of the lithosphere, this issue is avoided. In this chapter, we will describe the calculation of elastic-plastic plate deflections, before describing how this model was used to constrain the mantle rheology at circum-Pacific subduction zones and the Hawaiian Islands.

As discussed in Chapter 1, the elastic-plastic plate model has previously been used to describe the deformation of oceanic lithosphere. However, it has not been used to test a range of recent, laboratory-derived flow laws; this was the aim of the analysis presented in this chapter. In addition, with the exception of the study of Garcia-Castellanos et al. (2000), previous elastic-plastic studies of trench-outer rise flexure have used a forward modelling approach to find the end-loads. In this study, an inverse approach was used, which provides a more robust test of the laboratory-derived flow laws.

9.1 Elastic-plastic plate model

In the elastic-perfectly plastic (from here on abbreviated to 'elastic-plastic') plate model, the plate deforms elastically until some pre-defined yield strength is reached, at which point it deforms plastically with no strain hardening (Figure 9.1). There are two methods of calculating the deflections of an elastic-plastic plate, which we dub the 'iterative method' and the 'Runge-Kutta method' respectively; these will be described in this section. In both methods, we used a cylindrical (2-D) bending model, which assumes plane strain. This is a reasonable assumption for the trench-outer rise system of subduction zones because the magnitude of plate bending in the trench-parallel direction is very small compared to that in the trench-normal direction. This assumption is also fairly reasonable for the Hawaiian Islands region because the Hawaiian volcanic chain is an approximately linear and continuous feature and therefore, other than perhaps directly beneath the volcanoes, there should be little deflection of the plate in the chain-parallel direction.

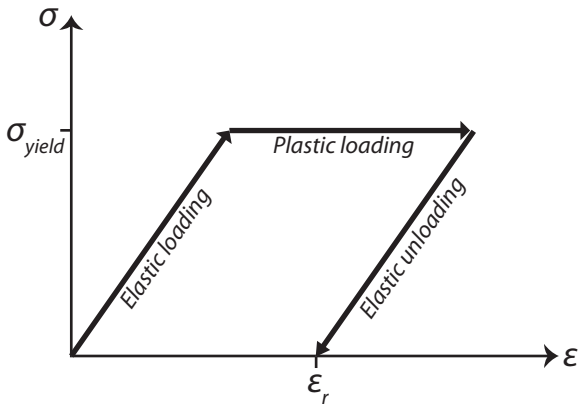

Figure 9.1: Schematic of the stress-strain (σ-ϵ) path for loading and unloading of an elastic-perfectly plastic material. Loading initially occurs elastically, such that stress increases linearly with strain. When the plastic yield stress, σ_{yield}, is reached, loading occurs plastically, such that strain increases without any further increase in stress. When the stress is reduced, unloading occurs elastically, such that when the stress has decreased to zero, there is a residual strain, ε_r. Thus, the material has 'memory' of its previous failure; this is known as strain hysteresis.

9.1.1 Yield strength

The first step in calculating the deflection of an elastic-plastic plate is to pre-define the yield strength as a function of depth. As illustrated in Figures 9.2a and 9.3a (right plots), we defined a depth-dependent yield strength using the laboratory-derived YSEs that were described in the previous chapter. These YSEs consist of a shallow brittle regime, which is defined by a Coulomb-Navier failure criterion for frictional sliding on pre-existing fault surfaces, and a deeper ductile regime, which is defined by flow laws for LTP and Power Law Creep (PLC). After the depth-dependent yield strength is defined, the plate deflections can be calculated. This can be done for a broken plate with end-loads (a bending moment M_0 and vertical shear force V_0) applied at the plate-break, which is applicable to trenches, or for a continuous plate subjected to a distributed load such as a seamount or ocean island.

9.1.2 Iterative method

In the iterative method, a variable T_e elastic plate is used to calculate the elastic-plastic plate deflections, where the T_e represents the rigidity of the elastic-plastic plate as calculated using

the YSE and calculated plate curvatures. First, the deflections are calculated using an elastic plate with $T_e(x) = T_m(x)$, where $T_m(x)$ is the mechanical thickness of the elastic-plastic plate. $T_m(x)$ is taken as the depth at which the yield strength, as defined by the YSE, falls below 1 % of the overburden pressure (Cloetingh and Burov, 1996). The calculated plate curvature, $\kappa(x)$, is then used along with the YSE to calculate the equivalent T_e of the elastic-plastic plate after the initial plastic yielding has occurred, $T_{e,\ i=1}^{yield}(x)$. Here, the calculation of $T_e^{yield}(x)$ is identical to the calculation of the 'predicted T_e' in the YSE-curvature method (see Section 8.2). The deflections are then calculated using an elastic plate with $T_e(x) = T_{e,\ i=1}^{yield}(x)$, and the calculated plate curvature is then used to calculate the equivalent T_e of the elastic-plastic plate after further yielding has occurred, $T_{e,\ i=2}^{yield}(x)$. This process is repeated iteratively (i is the iteration number) until the solution converges to give the final elastic-plastic plate deflection. Upon convergence, the bending moment in the elastic plate defined by $T_e^{yield}(x)$ is equal to the moment calculated using the YSE and the calculated plate curvature. Our convergence criteria is that the maximum change in plate deflection relative to the previous iteration is < 1 %. This generally occurs in ≤ 6 iterations for continuous plates and ≤ 10 iterations for broken plates.

In Figures 9.2a and 9.3a, the white dashed areas show the depth-extent of yielding in a continuous and broken elastic-plastic plate respectively after the solution has converged. The figures show that for a continuous plate, there is plastic yielding directly beneath the load and in the regions flanking the load, and for a broken plate, there is yielding landward of the outer rise in the region close to the plate-break. Figures 9.2b and 9.3b show that as a result of this yielding, the final $T_e^{yield}(x)$ of the elastic-plastic plate (solid grey) is less than the initial mechanical thickness, $T_m(x)$ (dashed grey). Figures 9.2b and 9.3b show that, therefore, the final elastic-plastic plate deflection (solid black) is of higher amplitude and shorter wavelength than the initial deflection calculated with $T_m(x)$ (dashed black). Figures 9.2c and 9.3c show that the final elastic-plastic plate curvature (solid grey) is of higher amplitude than the initial curvature (dashed grey); and that the final bending moment (solid black) is of lower amplitude than the initial moment (dashed black).

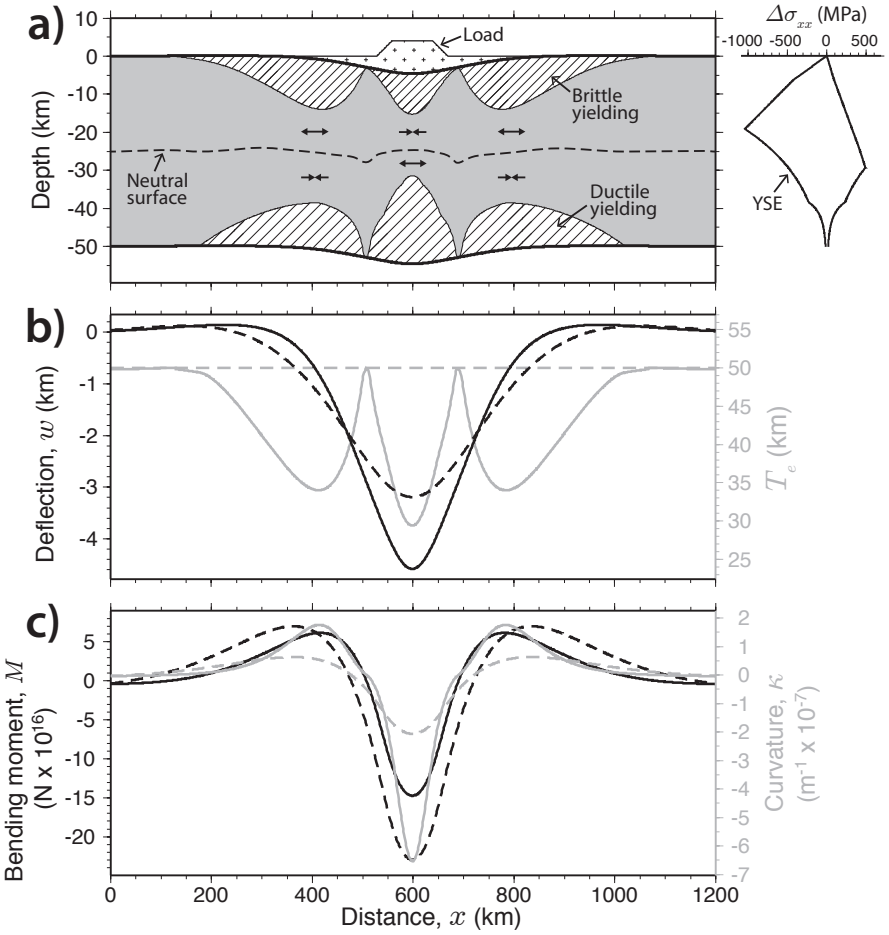

Figure 9.2: The response of a continuous elastic-plastic plate to loading by a submarine seamount load. (a) The elastic-plastic plate. The white dashed areas show the depth-extent of plastic yielding, the dashed black line shows the depth of the neutral surface, and the double arrows indicate tension or compression. The plate has depth-dependent yield strength, defined by the YSE shown on the right. The YSE was calculated for a 60 Ma cooling plate and $\dot{\varepsilon} = 10^{-16}$ s^{-1}, and was constructed with the LTP flow law of Mei et al. (2010), the dry PLC law of Hirth and Kohlstedt (2003), and Byerlee's (1978) friction coefficients with hydrostatic PFP. (b) The dashed grey shows the mechanical thickness of the plate, $T_m(x)$, and the solid grey shows the final $T_e^{yield}(x)$. The dashed black shows the initial deflection of the elastic-plastic plate, calculated using an elastic plate with $T_e(x) = T_m(x)$, and the solid black shows the final deflection, calculated with the final $T_e^{yield}(x)$. (c) The dashed grey shows the initial plate curvature and the solid grey shows the final curvature. The dashed black shows the initial bending moment and the solid black shows the final moment.

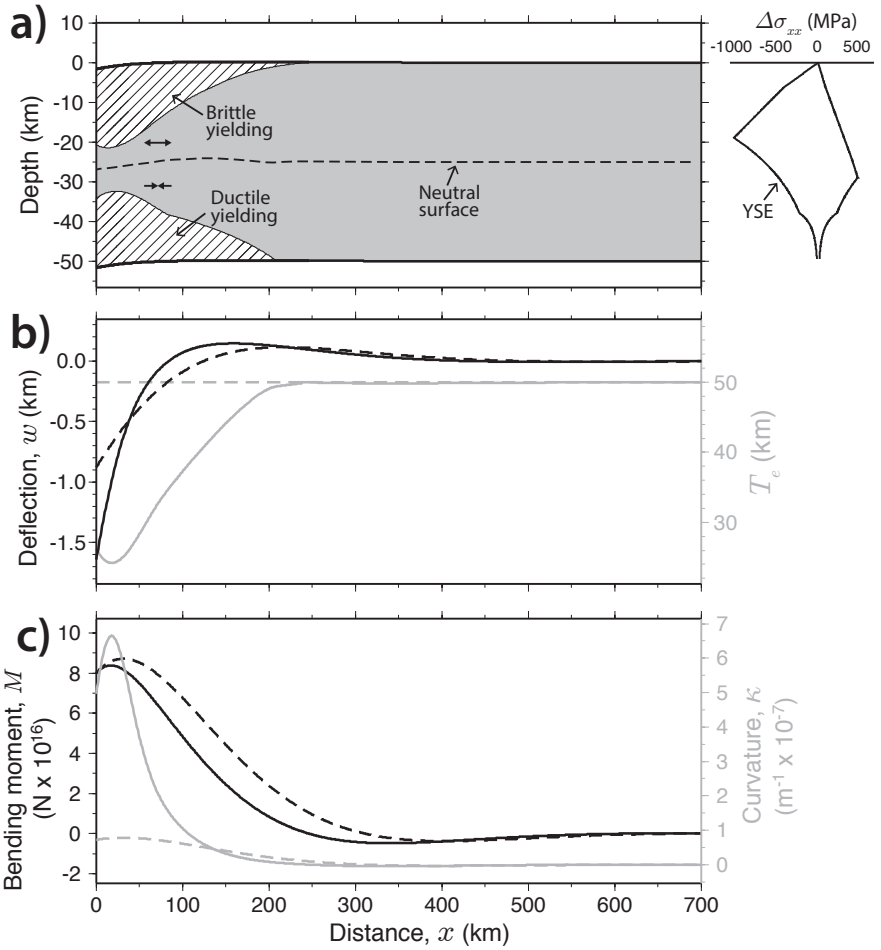

Figure 9.3: The response of a broken elastic-plastic plate to loading by end-loads, as calculated using the iterative method. The plate was loaded with end-loads $M_0 = 8 \times 10^{16}$ N and $V_0 = 0.5 \times 10^{12}$ Nm^{-1}. (a) The elastic-plastic plate. The white dashed areas show the depth-extent of plastic yielding, the dashed black line shows the depth of the neutral surface, and the double arrows indicate tension or compression. The plate has depth-dependent yield strength, defined by the YSE shown on the right. The YSE was calculated as in Figure 9.2. (b) The dashed grey shows the mechanical thickness of the plate, $T_m(x)$, and the solid grey shows the final $T_e^{yield}(x)$. The dashed black shows the initial deflection of the elastic-plastic plate, calculated using an elastic plate with $T_e(x) = T_m(x)$, and the solid black shows the final deflection, calculated with the final $T_e^{yield}(x)$. (c) The dashed grey line shows the initial plate curvature and the solid grey line shows the final curvature. The dashed black line shows the initial bending moment and the solid black shows the final moment.

9.1.3 Runge-Kutta method

In an elastic-plastic material, unloading occurs elastically along a different stress-strain path than the preceding loading, resulting in strain hysteresis. This process is known as 'elastic unloading' (Figure 9.1). Several authors have observed that at a subduction zone, if the downgoing plate begins to unbend before it is subducted, this will induce elastic unloading in the plate that may result in a complex stress distribution (e.g., McAdoo et al., 1978; Bodine and Watts, 1979; Bodine et al., 1981; Mueller and Phillips, 1995; Mueller et al., 1996a). The grey line in Figure 9.4a shows the stress in a YSE-defined elastic-plastic plate bent to a curvature of $\kappa = 4 \times 10^{-7}$ m^{-1}, and the red and blue lines show the stress after the plate has subsequently been unbent to $\kappa = 2 \times 10^{-7}$ m^{-1} and $\kappa = 0$ respectively. The stress distribution that results from unbending was calculated as follows:

1. The initial stress distribution due to bending (grey line in Figure 9.4a) was calculated as described in the previous chapter (Section 8.2, Equations 8.9 and 8.10).

2. The change in stress due to unbending, $\Delta\sigma_{xx}^{unbend}$, was calculated using $\Delta\sigma_{xx}^{unbend} = \frac{E(y-y_n)\Delta\kappa}{1-\nu^2}$; where $\Delta\kappa$ is the reduction in curvature and all other symbols are as in Equation 8.9. We see from this equation that the unbending occurs entirely elastically.

3. $\Delta\sigma_{xx}^{unbend}$ was added to the initial bending stress, and the resultant stress distribution was truncated where it exceeds the YSE. This gives the final stress distribution after unbending by an amount $\Delta\kappa$ (red and blue lines in Figure 9.4a). Note that when calculating $\Delta\sigma_{xx}^{unbend}$, an optimization was used to find the neutral surface depth, y_n, so that the final stress distribution meets the criterion for pure bending (Equation 8.2).

Figure 9.4a shows that the elastic unloading associated with unbending produces a complex stress distribution: during unbending, there is a 'zig-zag' stress pattern (red line) and after complete unbending ($\kappa = 0$), there are residual tensional stresses in the middle and lower part of the plate and compressional stresses in the upper part of the plate (blue line). Thus the plate has 'memory' of its previous failure. The solid line in Figure 9.4b shows the moment-curvature path that corresponds to the bending and subsequent unbending illustrated in

Figure 9.4a. This shows that because the unloading occurs along a different stress-strain path to the preceding loading, the unbending occurs along a different moment-curvature path to the preceding bending. This means that when the bending moment has returned to zero, there is a residual curvature of the plate (i.e. strain hysteresis), and that to completely unbend the plate (i.e. return the curvature to zero), a negative bending moment must be applied.

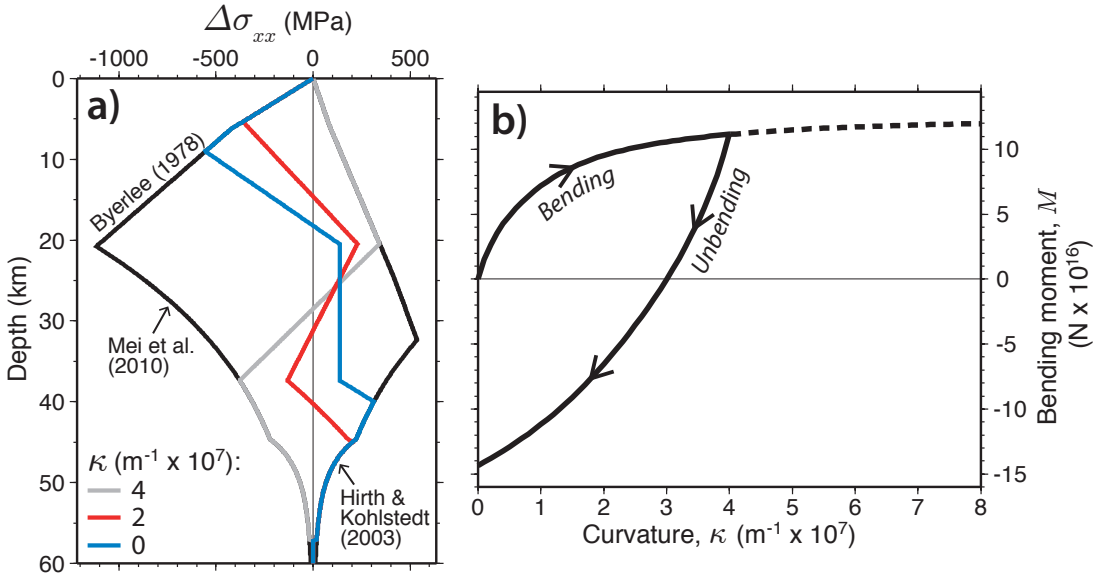

Figure 9.4: Figure illustrating the stress and bending moment in an elastic-plastic plate during unbending. (a) The grey line shows the stress distribution in a plate bent to a curvature of $\kappa = 4 \times 10^{-7}$ m^{-1}, and the red and blue lines show the stress after the plate has subsequently been unbent to $\kappa = 2 \times 10^{-7}$ m^{-1} and $\kappa = 0$ respectively. The yield strength in the plate is defined by the laboratory-derived YSE shown in black. The YSE was calculated for an 80 Ma cooling plate and $\dot{\varepsilon} = 10^{-16}$ s^{-1}, and the flow laws are labelled on the figure. (b) The solid line shows the moment-curvature path that corresponds to the bending and subsequent unbending illustrated in Figure 9.4a. The dashed line shows the moment-curvature path if bending were to continue to higher curvature.

The 'iterative method' of calculating elastic-plastic plate deflections, as presented in the previous section, cannot account for the elastic unloading associated with plate unbending. Therefore, to account for this behaviour, previous authors (e.g., McAdoo et al., 1978; Bodine and Watts, 1979) have used what we call the 'Runge-Kutta method', which is summarised as follows. First, the deflection is calculated for an elastic plate with $T_e(x) = T_m(x)$, where $T_m(x)$ is the mechanical thickness of the elastic-plastic plate, as defined by the YSE. Then, starting from this initial solution, the differential equation for an elastic plate is solved via a

landward, step-by-step integration that accounts for the plastic yielding and elastic unloading associated with bending and unbending. This integration will be described in detail in the following paragraph.

As described in Section 3.1.1, in order to solve the differential equation for an elastic plate (Equation 3.7), we must relate the bending moment, M, to the plate deflection, w. However, when considering plate unbending, the relationship $M = D\kappa = -D\frac{\mathrm{d}^2 w}{\mathrm{d}x^2}$ no longer holds (D is the flexural rigidity, κ is curvature, x is distance). This is illustrated in Figure 9.4b, which shows that when the bending moment has returned to zero after unbending, the curvature is non-zero. Therefore, a different equation must be used to relate M to w, for which we relate the change in M to the change in κ (with respect to x):

$$\frac{\mathrm{d}M}{\mathrm{d}x} = D_{inc}\frac{\mathrm{d}\kappa}{\mathrm{d}x} = -D_{inc}\frac{\mathrm{d}^3 w}{\mathrm{d}x^3} \tag{9.1}$$

where D_{inc} is the 'incremental rigidity', which is a measure of the resistance of the plate to a small change in curvature. Making use of Equation 9.1, Equation 3.7 can be written as the following system of first order differential equations:

$$\begin{aligned}
\frac{\mathrm{d}k_1}{\mathrm{d}x} &= k_2 \\
\frac{\mathrm{d}k_2}{\mathrm{d}x} &= k_3 \\
\frac{\mathrm{d}k_3}{\mathrm{d}x} &= -\frac{k_4}{D_{inc}} \\
\frac{\mathrm{d}k_4}{\mathrm{d}x} &= -Fk_3 + (\rho_m - \rho_w)gw - q_s(x)
\end{aligned} \tag{9.2}$$

where the coefficients $k = (k_1,\ k_2,\ k_3,\ k_4) = (w,\ \frac{\mathrm{d}w}{\mathrm{d}x},\ \frac{\mathrm{d}^2 w}{\mathrm{d}x^2},\ \frac{\mathrm{d}M}{\mathrm{d}x})$, and all other; symbols are as in Equation 3.7. Starting from the point x_c (Figure 9.5a), which is where the plate begins to bend with positive curvature, this system of equations is solved via a landward, step-by-step integration performed using a fourth-order Runge-Kutta algorithm. The initial values for k (at the point x_c) are taken from the initial elastic plate solution calculated with $T_e(x) = T_m(x)$. The incremental rigidity, D_{inc}, at each step of the integration is calculated by using the laboratory-derived YSE (right plot in Figure 9.5a) to calculate the change in

M associated with the change in κ at the previous step (Equation 9.1), where the elastic unloading associated with plate unbending is accounted for as illustrated in Figure 9.4. We note that by beginning the integration at x_c, we are neglecting any plate weakening that occurs in the back-bulge (the flexural depression immediately seaward of the outer rise). However, the curvature is almost negligibly small in this region and therefore there is minimal plate weakening.

The white dashed areas in Figure 9.5a show the depth-extent of plastic yielding in a broken elastic-plastic plate, as calculated using the Runge-Kutta method. This shows that as the integration proceeds landward from x_c, the depth-extent of brittle, tensional and ductile, compressional yielding increases as the plate is bent to higher curvature. Figure 9.5b shows that as a result, the incremental rigidity, D_{inc} (solid grey), decreases landward and is less than the initial 'mechanical rigidity', D_m (dashed grey), that corresponds to the initial mechanical thickness, T_m. When the integration reaches the point of maximum curvature, x_a, the plate begins to unbend. As illustrated in Figure 9.5a, at this point, the entire plate deforms elastically due to the elastic unloading associated with unbending, and as shown in Figure 9.5b, D_{inc} is therefore equal to D_m. As the integration proceeds landward from x_a, almost the entire plate continues to deform elastically until enough unbending has occurred to induce plastic yielding in the opposite direction: brittle, compressional and ductile, tensional yielding. Figure 9.5b (solid grey) shows that this causes D_{inc} to decrease again. Figure 9.5b shows that as a result of the bending-induced plate weakening, the final elastic-plastic plate deflection (solid black) is of higher amplitude than the initial elastic plate deflection calculated with $T_e(x) = T_m(x)$ (dashed black). Figure 9.5c shows that the final elastic-plastic plate curvature (solid grey) is of higher amplitude than the initial elastic plate curvature (dashed grey), and that the final bending moment (solid black) is of lower amplitude than the initial moment (dashed black). Note that in the final elastic-plastic plate solution, the bending moment at the plate-break, M_0, is different than in the initial elastic plate solution calculated with $T_e(x) = T_m(x)$. This is because the Runge-Kutta method solves an initial value problem and so only the M_0 in the initial elastic plate can be specified. This contrasts with the iterative method, where M_0 in the final solution is the same as that in the initial solution (Figure 9.3c). This is because in this method, a boundary value problem is solved at each iteration, where M_0 is one of the boundary conditions.

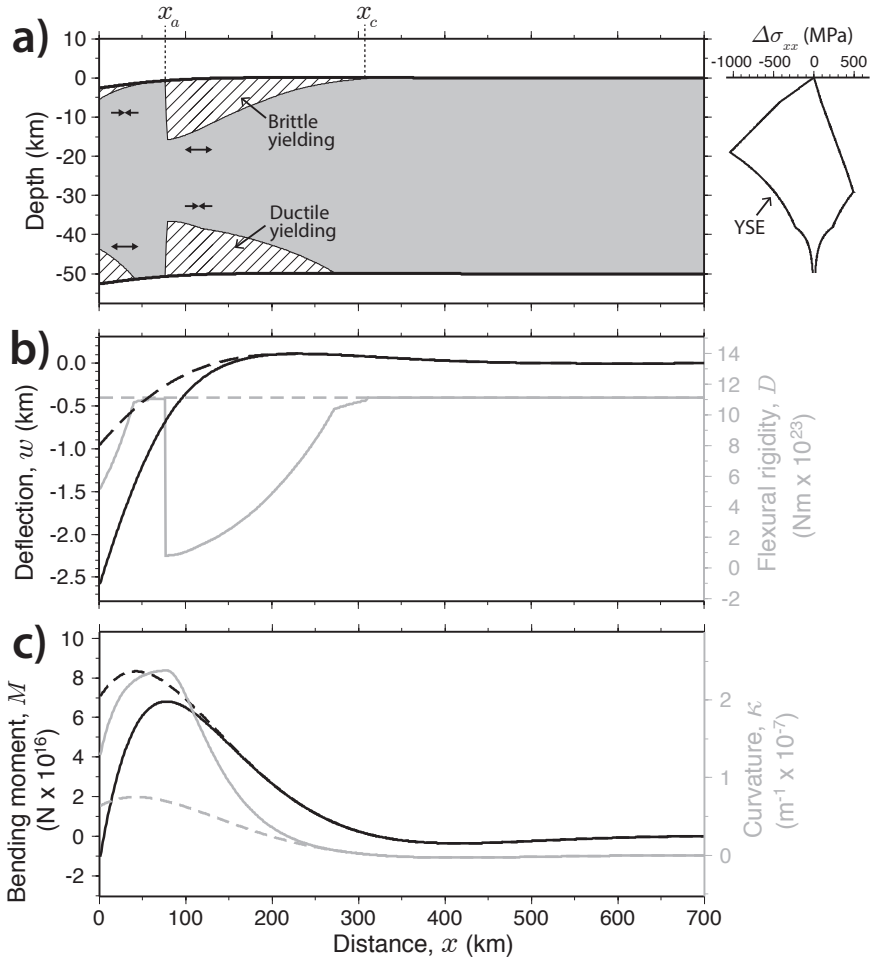

Figure 9.5: The response of a broken elastic-plastic plate to loading by end-loads, as calculated using the Runge-Kutta method. (a) The elastic-plastic plate. The white dashed areas show the depth-extent of plastic yielding, and the double arrows indicate tensional or compressional yielding. The plate has depth-dependent yield strength, defined by the YSE shown on the right. The YSE was calculated as in Figure 9.2. (b) The dashed grey line shows the mechanical rigidity, D_m, that corresponds to the mechanical thickness of the plate, and the solid grey line shows the incremental rigidity of the final elastic-plastic plate, D_{inc}. The dashed black line shows the initial elastic plate deflection, calculated for an elastic plate with $D = D_m$, and the solid black line shows the final elastic-plastic plate deflection, calculated via a landward, step-by-step integration from x_c. (c) The dashed grey line shows the initial elastic plate curvature and the solid grey line shows the final elastic-plastic plate curvature. The dashed black line shows the bending moment in the initial elastic plate and the solid black line shows the moment in the final elastic-plastic plate.

9.1.4 Comparison between the iterative and Runge-Kutta methods

In Figure 9.6, for a typical trench-outer rise profile, we have compared the elastic-plastic plate solutions calculated via the iterative (dashed grey) and Runge-Kutta (solid black) methods. To do this, we first calculated the Runge-Kutta solution, then used the M_0 and V_0 from this solution as boundary conditions for the iterative calculation. The figure shows that although the curvature differs between the two solutions, the deflection and bending moment are almost identical. This suggests that although plate unbending and the associated elastic unloading may have a significant effect on the stress distribution and seismicity at the outer trench-slope of subduction zones (e.g. Bodine and Watts, 1979; Mueller et al., 1996a), it is unlikely to have a significant effect on the plate deflection. Therefore, when modelling our observed trench-outer rise gravity profiles, we used the iterative method to calculate the elastic-plastic plate deflections. We used this method, rather than the Runge-Kutta, because it solves a boundary value problem where M_0 and V_0 are boundary conditions. Therefore, it is better suited to finding the best-fit end-loads via an inverse procedure.

9.1.5 Comparison between the elastic-plastic and variable T_e elastic plate models

In Inversion A2 (Chapter 6), we modelled the trench-outer rise system of subduction zones using a variable T_e elastic plate. In this model, the T_e was allowed to decrease linearly from what we define as a 'seaward T_e' to a 'landward T_e', with the linear decrease occurring between the point x_b, at which $\kappa = 1 \times 10^{-7}$ m^{-1}, and the point of maximum κ, x_a (Figure 6.2). As shown in Figure 9.6, in order to test the validity of this model, we compared it to the elastic-plastic plate model. Figure 9.6d shows that in the elastic-plastic plate model (grey and dashed black), the equivalent T_e (calculated from the final solution using Equations 3.17 and 3.16) decreases linearly seaward of the outer rise, which suggests that the linear decrease used in Inversion A2 (dotted red) is reasonable. Figure 9.6d shows that the equivalent T_e of the elastic-plastic model differs from the variable T_e elastic model in the regions landward of x_a and seaward of x_b, but Figure 9.6a shows that the calculated deflections are very similar. This suggests that the variable T_e elastic plate model that was used in Inversion A2 is reasonable,

and perhaps explains why this inversion produced such good fits to the observed gravity anomalies (Figure 6.3).

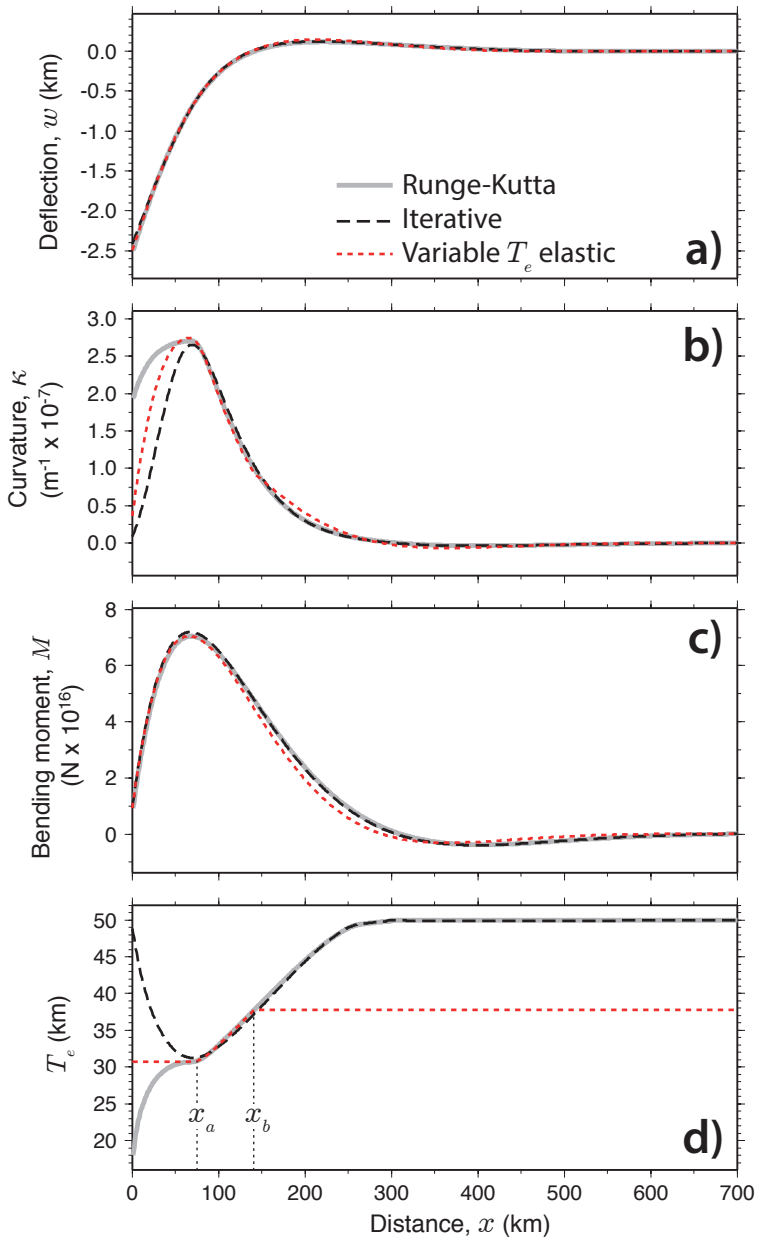

Figure 9.6: Comparison between the broken elastic-plastic plate solutions calculated using the iterative and Runge-Kutta methods. These solutions are also compared to the solution for a variable T_e elastic plate akin to that used in Inversion A2. (a) Plate deflection. (b) Plate curvature. (c) Bending moment. (d) T_e, where the equivalent T_e for the elastic-plastic models was calculated from the final solution using Equations 3.17 and 3.16.

9.2 Constraining LTP flow laws in the Hawaiian Islands region

In the previous section, we described the elastic-plastic plate model, which allows us to calculate the deflection of plates that have laboratory-derived, depth-dependent yield strength. In an effort to constrain LTP flow laws for oceanic lithosphere, we used this model to model observed plate deflections at the trench-outer rise system of circum-Pacific subduction zones and in the Hawaiian Islands region. In this section, we will describe how we modelled the Hawaiian Islands data.

9.2.1 Data

We modelled the seismically constrained depths to the top of the oceanic crust that were described in the previous chapter. These data were collected by Watts and Ten Brink (1989) along three approximately chain-normal ship-tracks that intersect the Hawaiian chain at the island of Oahu (black points in Figure 8.17a). Our elastic-plastic plate model assumes cylindrical (2-D) bending—which we suggest is fairly reasonable for the Hawaiian Islands region because the volcanic chain is an approximately linear and continuous feature—and we therefore required a 2-D profile of observed crustal deflections. To do this, as shown in Figure 9.7 (blue, red and yellow points), we first projected the data from each transect onto the chain-normal great circle path shown in red in Figure 8.17a. Then, we interpolated the data from each transect to 1 km spacing and averaged the interpolated profiles over the intervals covered by all three transects; the average profile is shown as a black line in Figure 9.7. We also required a 2-D profile of the volcanic load, for which we computed an ensemble-averaged, chain-normal profile of the load grid described in the previous chapter (grid shown in Figure 8.17c). To do this, we sampled the grid along a series of chain-normal profiles (black in Figure 9.8a) that encompass the region where we have observed data, and then calculated an arithmetic average of these profiles (red in Figure 9.8a). As shown in Figure 9.8b, to define the thermal structure of the elastic-plastic plate, we used the same technique to compute an ensemble-averaged profile of the seafloor age grid of Müller et al. (2008, v3.2) (grid shown in Figure 8.17b). This average profile was then used to calculate a plate-cooling thermal structure that varies with age along the plate.

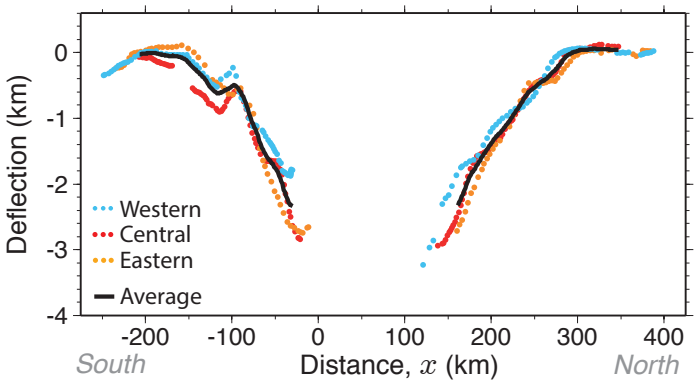

Figure 9.7: The blue, red and yellow points show seismically constrained depths to the top of oceanic crust (Watts and Ten Brink, 1989) from the three transects that are shown as black points in Figure 8.17a. These data have been projected along the great circle path shown in red in Figure 8.17a. We calculated an average profile of the observed depths (shown as a black line) by interpolating the data from each transect to 1 km spacing and then averaging the interpolated profiles over the intervals covered by all three transects.

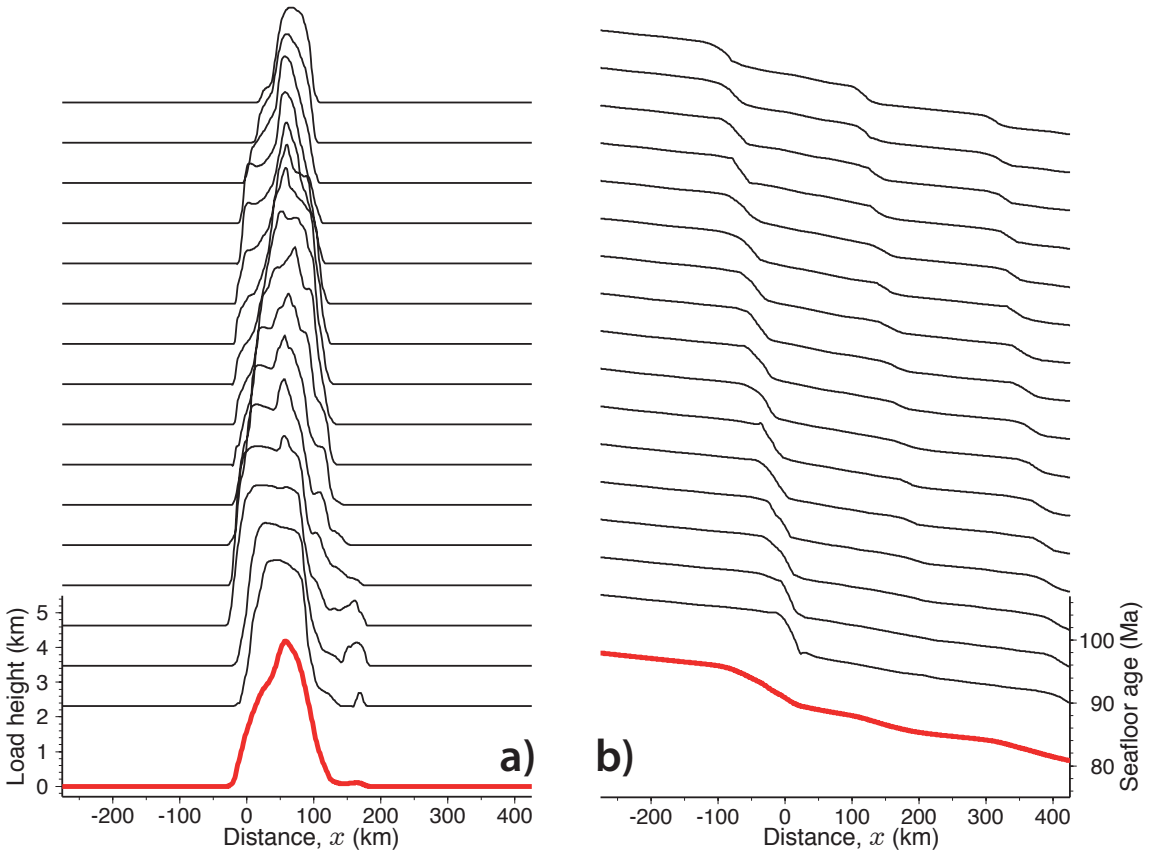

Figure 9.8: Figure illustrating the calculation of ensemble-averaged profiles of (a) the volcanic load and (b) the seafloor age in the Hawaiian Islands region. The grids (shown in Figures 8.17c and 8.17b respectively) were sampled along a series of chain-normal profiles (black) that encompass the region where we have observed data, and these profiles were then arithmetically averaged (red).

9.2.2 Modelling technique

For each LTP flow law, we first constructed the YSEs that define the depth-dependent yield strength in the elastic-plastic plate; these YSEs vary with age (thermal structure) along the plate. As in the previous chapter (Table 8.1), we tested five laboratory-derived LTP flow laws (Goetze, 1978; Evans and Goetze, 1979; Raterron et al., 2004; Katayama and Karato, 2008; Mei et al., 2010) and three weakened modifications of Mei et al. (2010), where A_m (Equation 8.4) has been increased by 4, 6 and 8 orders of magnitude respectively. From here on, these modifications will be referred to as M(10^4), M(10^6) and M(10^8) respectively. When constructing the YSEs, we assumed the same strain rate as in the YSE-curvature method presented in the previous chapter, $\dot{\varepsilon} = 10^{-16.5}$ s^{-1}. For each LTP flow law, we then used the iterative method to calculate the elastic-plastic plate deflections due to the volcanic load. Then, to account for uncertainties in the undeflected seafloor depth, a damped least squares optimization was used to find the vertical shift, c, that when added to the calculated flexure, best fits the observed deflections. The best-fitting LTP flow law is that which produces the lowest RMS Error (RMSE) between the observed and calculated deflections.

When calculating the elastic-plastic plate deflections, we assumed that the density of the volcanic surface load is $\rho_l = 2600$ kg/m^3, which is the best-fit value from the elastic plate inversion presented in the previous chapter. As in the elastic plate inversion (Figure 8.19), we assumed that directly beneath the surface load, the infill density is equal to the load density, and that the material that infills the flexural moats is a mixture of volcanoclastic and pelagic sediments with average density $\rho_s = 2300$ kg/m^3.

9.2.3 Results

9.2.3.1 Comparison with Zhong and Watts (2013)

We first wished to validate the elastic-plastic plate model by comparing the results to those of Zhong and Watts (2013), who modelled the observed crustal deflections using a 3-D finite-element viscoelastic model. They found that in order to explain the observed data, the LTP

law of Mei et al. (2010) must be weakened by increasing A_m by 8 orders of magnitude, where they assumed a friction coefficient, μ_f, of 0.7 and zero Pore Fluid Pressure (PFP). In this first analysis, we assumed the same friction conditions. As discussed in Section 8.4.4 (Figure 8.25), we constructed the YSEs for the laws of Evans and Goetze (1979) and Raterron et al. (2004) using only the LTP flow strength. This was to approximate the decoupling of the LTP and PLC deformation regimes that was observed by Zhong and Watts (2013).

In Figure 9.9a, the fits to the observed crustal deflections are plotted for each LTP law and in Figure 9.9b (black diamonds), the RMSE is plotted for each law. Figure 9.9a shows that the laws of Goetze (1978) and Mei et al. (2010) are much too strong to explain the observed data, as the wavelength of the calculated flexure is too long and the amplitude too low, and Figure 9.9b shows that these laws produce the highest RMSE ($\sim$ 335 m). Of the five laboratory-derived flow laws, Raterron et al. (2004) provides the best fit to the observed data, with an RMSE of 224 m. The laws of Evans and Goetze (1979) and Katayama and Karato (2008) appear slightly too strong, with an RMSE of 252 and 255 m respectively. The modification of Mei et al. (2010) that best fits the observed data is M(10^6), with an RMSE of 212 m. M(10^4) also provides a good fit with an RMSE of 232 m, but M(10^8) appears slightly too weak, with an RMSE of 252 m. Note that, as was the case for the elastic plate model (Figure 8.21), even the best-fitting flow law, M(10^6), underestimates the observed deflections in the northern section of the profille. This was also found by Zhong and Watts (2013), and it has been suggested that it may be a result of a crack in the plate (Wessel, 1993) and/or flexural deformation (Watts and Ten Brink, 1989) at the Molokai fracture zone.

In Figure 9.9b (grey circles), we have also plotted the RMSE from the study of Zhong and Watts (2013). The figure shows that the pattern of results is very similar to that obtained in this study, except that in the study of Zhong and Watts (2013), M(10^8) provides the best fit to the observed data, compared to M(10^6) in this study. There are several possible explanations for this small difference between the two studies. For example, the viscoelastic model used by Zhong and Watts (2013) is 3-D and solves for the strain rate, whilst the elastic-plastic plate model is 2-D and assumes a constant, pre-defined strain rate. In addition, the viscoelastic model is time-dependent as it accounts for stress and strain relaxation, in contrast to the static, time-independent elastic-plastic model. This could explain why Zhong and Watts

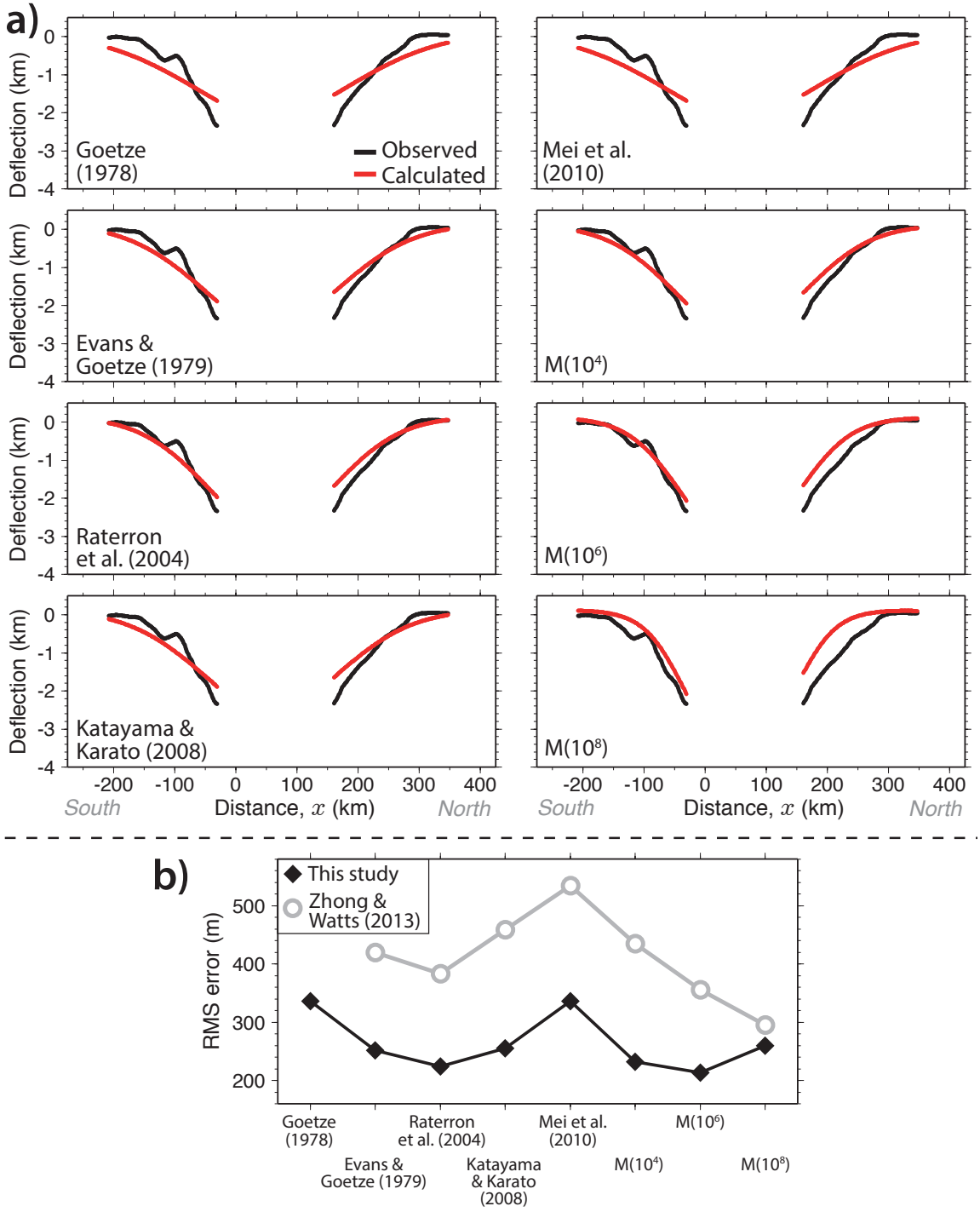

Figure 9.9: Results from elastic-plastic plate modelling of the Hawaiian Islands data, where the brittle regime was calculated with $\mu_f = 0.7$ and zero PFP. (a) For each LTP flow law, a comparison between the observed crustal deflections and the calculated elastic-plastic plate deflections. The flow law is labelled on each plot. (b) The black diamonds show the RMSE between the observed and calculated deflections for each flow law, and the grey circles show the RMSE from the study of Zhong and Watts (2013).

(2013) require greater weakening of the law of Mei et al. (2010) than we do, as the unrelaxed viscoelastic stresses in their model should increase the effective rigidity of the plate; this will be discussed further in the next chapter. Figure 9.9b also shows that the RMSE obtained in this study is consistently lower than that obtained by Zhong and Watts (2013). This is probably because we modelled an average 2-D profile of the observed deflections, whilst Zhong and Watts (2013) modelled the data in 3-D, and in addition, whilst we inverted for a vertical shift, Zhong and Watts (2013) did not.

The results presented above suggest that the elastic-plastic plate model is a valid way to infer mantle rheology, as the results are in general agreement with the study of Zhong and Watts (2013). Both studies suggest that the law of Mei et al. (2010) is much too strong to fit the observed crustal deflections, and that it must be weakened by increasing the material-dependent parameter, A_m, by 6–8 orders of magnitude.

9.2.3.2 Varying the friction coefficient

Having validated the elastic-plastic plate model by comparison with the study of Zhong and Watts (2013), we next tested the effect of varying the friction coefficient, μ_f. As discussed in the previous chapter, we considered two different friction conditions, Byerlee's (1978) empirically derived coefficients (Equation 8.2) and $\mu_f = 0.3$, where hydrostatic PFP was assumed in both cases.

In Figures 9.10a and 9.11a, for Byerlee's (1978) coeffcients and $\mu_f = 0.3$ respectively, the fits to the observed crustal deflections are plotted for each LTP law, and in Figures 9.10b and 9.11b, the RMSE is plotted for each law. Note that for the LTP laws of Evans and Goetze (1979) and Raterron et al. (2004), we interpolated between the LTP and PLC deformation regimes (i.e. we used the YSEs illustrated in solid grey in Figure 8.25). Figures 9.10 and 9.11 show that regardless of the assumed friction coefficient, the dry olivine flow laws of Goetze (1978), Evans and Goetze (1979), Raterron et al. (2004) and Mei et al. (2010) are all too strong to fit the observed crustal deflections, as the wavelength of the calculated flexure is too long and the amplitude too low. The laboratory-derived LTP law that best fits the observations is the wet olivine flow law of Katayama and Karato (2008), with an RMSE of

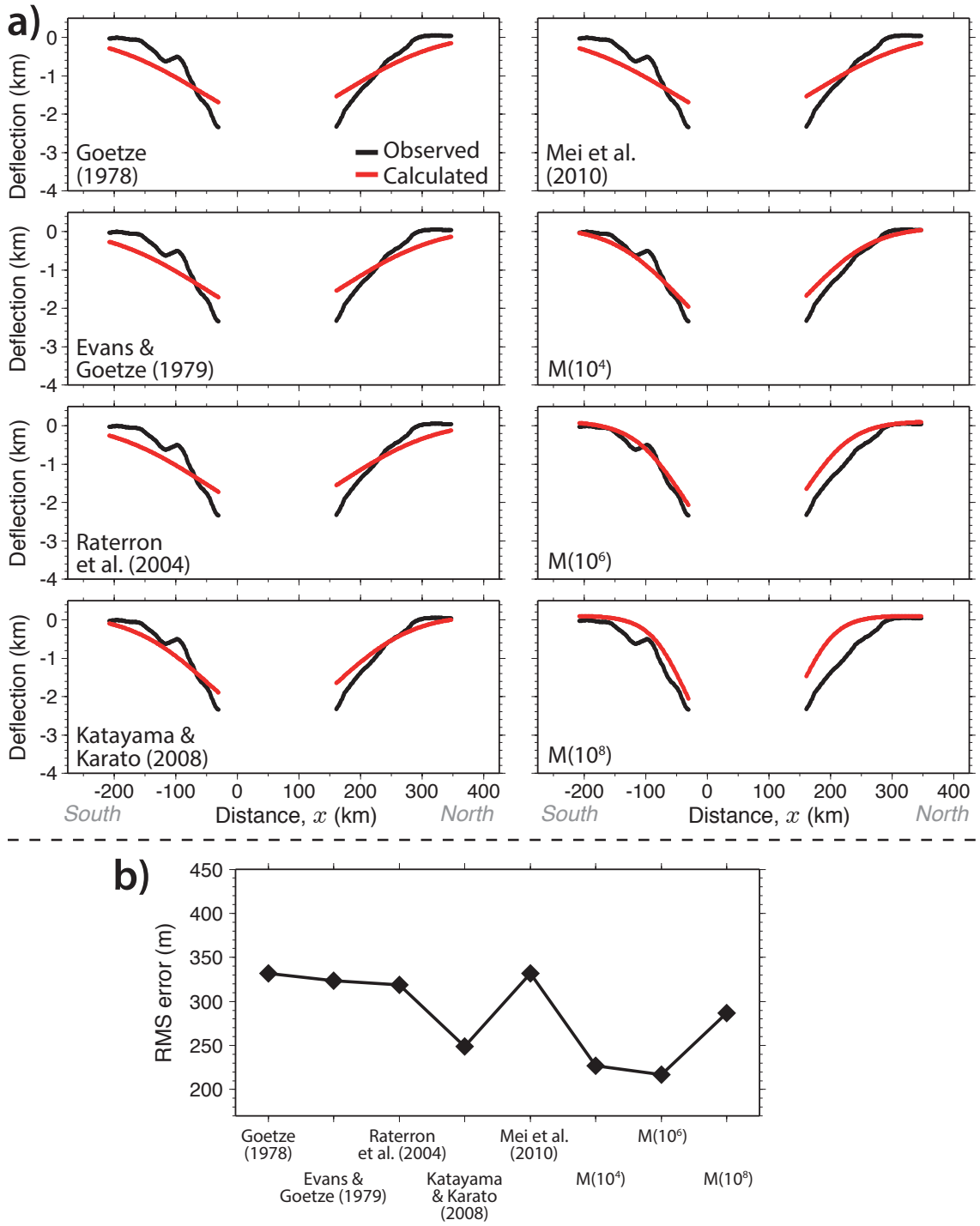

Figure 9.10: Results from elastic-plastic plate modelling of the Hawaiian Islands data, where the brittle regime was calculated with Byerlee's (1978) friction coefficients and hydrostatic PFP. (a) For each LTP flow law, a comparison between the observed crustal deflections and the calculated elastic-plastic plate deflections. The flow law is labelled on each plot. (b) The RMSE between the observed and calculated deflections for each flow law.

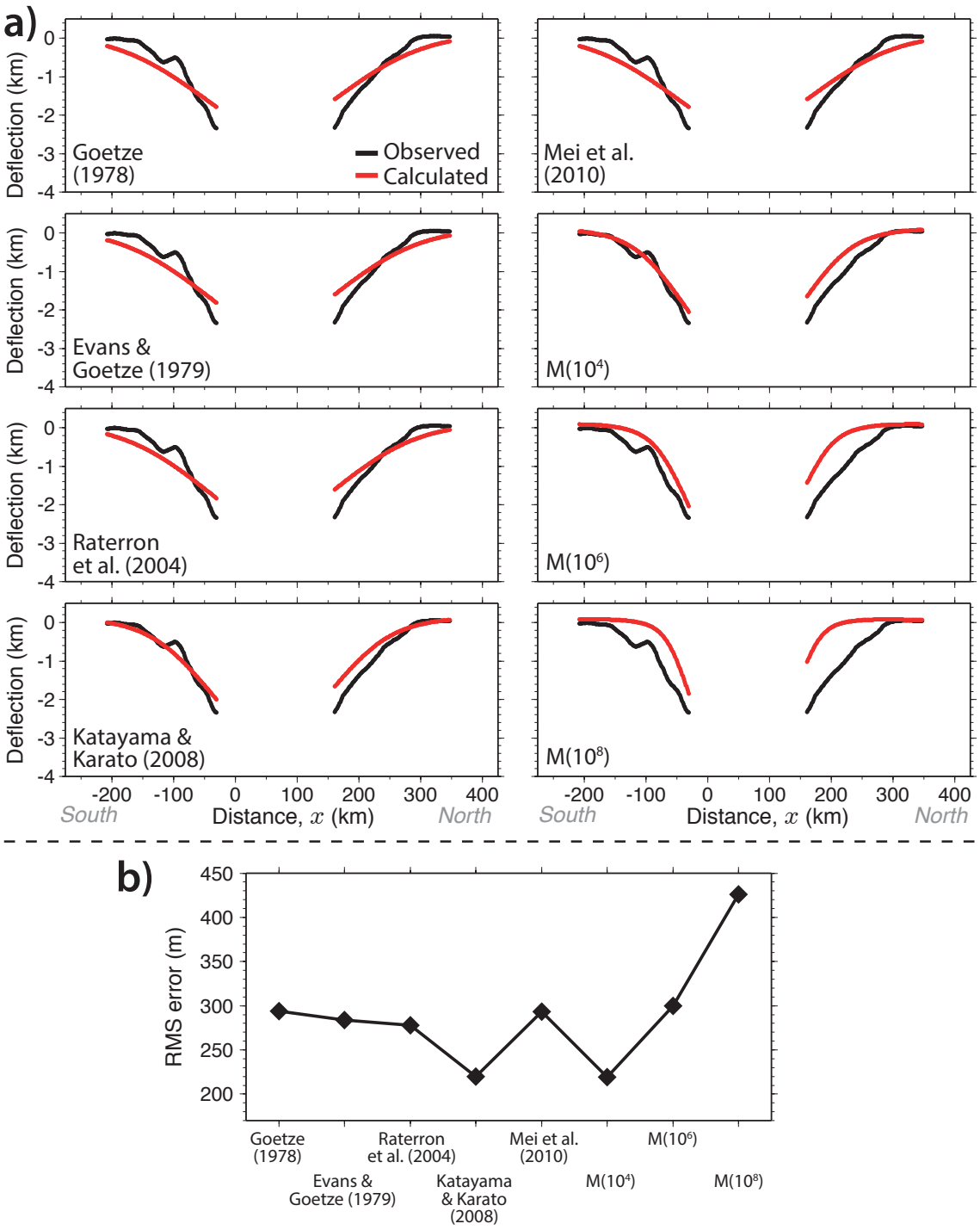

Figure 9.11: Results from elastic-plastic plate modelling of the Hawaiian Islands data, where the brittle regime was calculated with $\mu_f = 0.3$ and hydrostatic PFP. (a) For each LTP flow law, a comparison between the observed crustal deflections and the calculated elastic-plastic plate deflections. The flow law is labelled on each plot. (b) The RMSE between the observed and calculated deflections for each flow law.

250 m if Byerlee's (1978) coefficients are assumed, and 219 m if $\mu_f = 0.3$ is assumed. If Byerlee's (1978) coefficients are assumed (Figure 9.10), the modification of Mei et al. (2010) that best fits the observed deflections is M(10^6), with an RMSE of 217 m, but M(10^8) is too weak, with an RMSE of 287 m. If $\mu_f = 0.3$ is assumed (Figure 9.11), M(10^4) best fits the observed deflections, with an RMSE of 219 m, but M(10^6) is too weak and M(10^8) is much too weak, with an RMSE of 300 and 426 m respectively.

9.2.3.3 Summary

In this section, in an effort to constrain LTP flow laws in the Hawaiian Islands region, we have modelled observed crustal deflections using elastic-plastic plates with laboratory-derived, depth-dependent yield strength. The results from this study are very similar to those of Zhong and Watts (2013), who modelled the same data using a 3-D finite-element viscoelastic model, which suggests that the elastic-plastic plate model is a valid way to infer mantle rheology. The results are also very similar to those from the YSE-curvature method, in that the law of Mei et al. (2010) is much too strong to fit the observed deflections and therefore must be weakened significantly. Based on elastic-plastic plate models, the observed crustal deflections are best fit by increasing the material-dependent parameter of Mei et al. (2010) by: 6 orders of magnitude in the case of $\mu_f = 0.7$ (zero PFP) or Byerlee's (1978) friction coefficients (hydrostatic PFP); or by 4 orders of magnitude in the case of $\mu_f = 0.3$ (hydrostatic PFP). The laboratory-derived LTP law that best fits the observations is the wet olivine law of Katayama and Karato (2008), which provides the best fit overall if $\mu_f = 0.3$ is assumed.

9.3 Constraining LTP flow laws at circum-Pacific subduction zones

In the previous section, we described how the elastic-plastic plate model was used to constrain LTP flow laws in the Hawaiian Islands region. In this section, we will describe how this model was used to constrain LTP flow laws at the trench-outer rise system of circum-Pacific subduction zones.

9.3.1 Data and inversion technique

We modelled the 750 km-long, trench-normal, ensemble-averaged free-air gravity profiles that were described in Chapter 2 (Figures 2.2 and 2.5); for each profile, the inversion procedure was as follows. For each LTP flow law, we first constructed the YSEs that define the depth-dependent yield strength in the elastic-plastic plate, using the average strain rate that was described in Section 8.3.1. The YSEs vary with age (thermal structure) along the profile, where the age was ensemble-averaged from the seafloor age grid of Müller et al. (2008, v3.2). For each LTP flow law, we then iterated over a range of end-loads, M_0 and V_0, and calculated the elastic-plastic plate deflections for each (M_0, V_0) parameter pair. The calculated deflections were then converted to gravity anomalies using the method of Bott (1969), as described in Section 3.2.1. The calculated gravity anomalies were then compared to the observed anomalies by calculating the RMS Error (RMSE) between them, where a damped least squares optimization was used to find the vertical shift, c, that when added to the calculated gravity, best fits the observed gravity. To find the best-fitting (M_0, V_0) parameter pair, we first performed a wide parameter search, where M_0 was varied from zero to the saturation moment (the maximum moment that the elastic-plastic plate can support) and V_0 was varied from -2×10^{12} to 2×10^{12} Nm^{-1}. Then, a second, narrower parameter search was performed in the vicinity of the best-fitting parameter pair from the first search. We tested 169 (M_0, V_0) parameter pairs in the first search and 169 in the second search, giving a total of 338 pairs.

9.3.2 Results

In the first inversion, 'Inversion C1', the brittle regime of the elastic-plastic plates was defined with Byerlee's (1978) friction coefficients and hydrostatic PFP. The results of this inversion are shown in Figure 9.12. Figure 9.12a shows profile fits for the trench-bins (the wide ensemble bins that encompass entire trenches). The observed gravity anomalies are shown in solid grey and the best-fit anomalies for the LTP flow laws of Mei et al. (2010) and M(10^6)—the worst and best fitting laws at the Hawaiian Islands respectively—are shown in dashed black and dotted red respectively. The figure shows that, in general, neither of these laws fits the

observed data well. The law of Mei et al. (2010) cannot fit the wavelength of the outer rise nor the steepness of the outer trench-slope, whilst M(10^6) can fit the steepness of the outer trench-slope, but cannot fit the amplitude and wavelength of the outer rise. For each LTP flow law, Figure 9.12b shows the mean RMSE between the observed and calculated gravity for all the circum-Pacific profiles. The results for the trench-bins and segment-bins (the ensemble bins that split each trench into segments) are very similar, and therefore we have shown a combined RMSE with equal weighting from the trench-bins and segment-bins. This figure shows that none of the flow laws tested provides a good fit to the observed data, as the mean RMSE is > 8.6 mGal in all cases, which compares poorly to the mean RMSE derived from the constant T_e elastic plate inversion, 5.5 mGal (Inversion A1, Chapter 5).

In the second inversion, 'Inversion C2', the brittle regime of the elastic-plastic plates was defined with $\mu_f = 0.3$ and hydrostatic PFP. This is the friction coefficient that was constrained by Craig et al. (2014a) using earthquake focal mechanisms from newly formed, trench-parallel bend-faults. The results of this inversion are shown in Figure 9.13. Figure 9.13a shows that neither Mei et al. (2010) (dashed black) nor M(10^4) (dotted red)—the worst and best fitting laws at the Hawaiian Islands respectively—provides a good fit to the observed free-air gravity. Indeed, Figure 9.13b shows that none of the LTP flow laws tested provides a good fit to the observed data, as the mean RMSE is > 8.9 mGal in all cases.

The results of Inversions C1 and C2 suggest that, regardless of the friction coefficient and LTP flow law, circum-Pacific trench-outer rise gravity anomalies cannot be explained by a broken elastic-plastic plate with a bending moment and vertical shear force applied at the plate-break. However, one possibility that these inversions did not account for is axial (horizontal) loading, which might occur due to a combination of, for example, slab pull, ridge push, slab suction and collision resistance (see Section 3.1.3 for a detailed discussion of the possible sources of axial loading). Therefore, we carried out another set of inversions, where as well as inverting for M_0 and V_0, we also inverted for an axial force, F. In the following sections, we will first describe the effect that axial loading has on the stress distribution, rigidity and deflection of an elastic-plastic plate. Then, we will describe the inversions that were conducted to account for the possible effect of axial loading at circum-Pacific subduction zones.

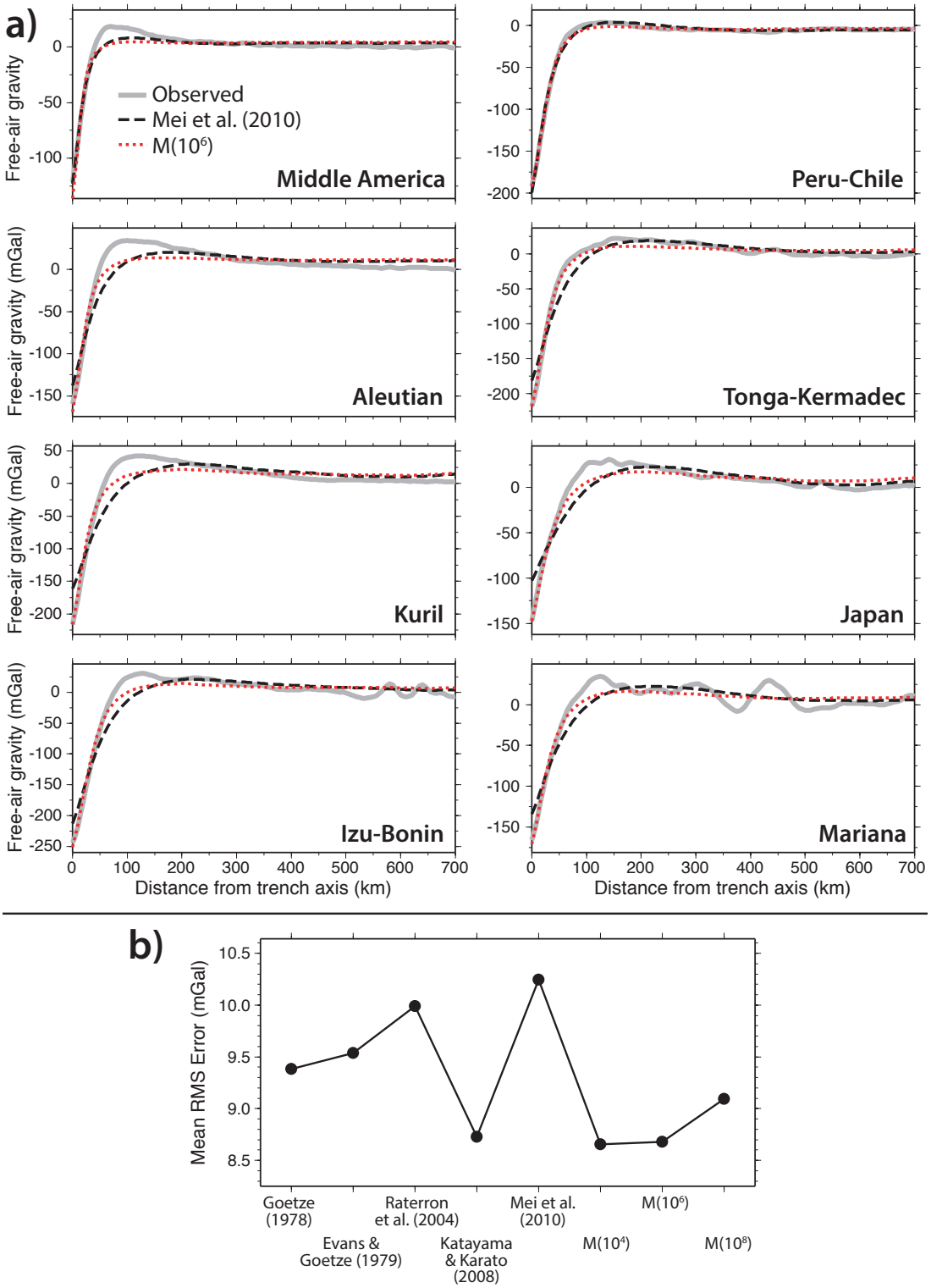

Figure 9.12: Results from Inversion C1, in which circum-Pacific gravity profiles were modelled using an elastic-plastic plate with brittle regime defined by Byerlee's (1978) friction coefficients and hydrostatic PFP. (a) Observed trench-bin gravity anomalies (solid grey) and best-fit anomalies calculated with the LTP flow laws of Mei et al. (2010) (dashed black) and M(10^6) (dotted red). (b) For each LTP flow law, the mean RMSE for all the circum-Pacific profiles, where the trench-bins and segment-bins have been given equal weighting.

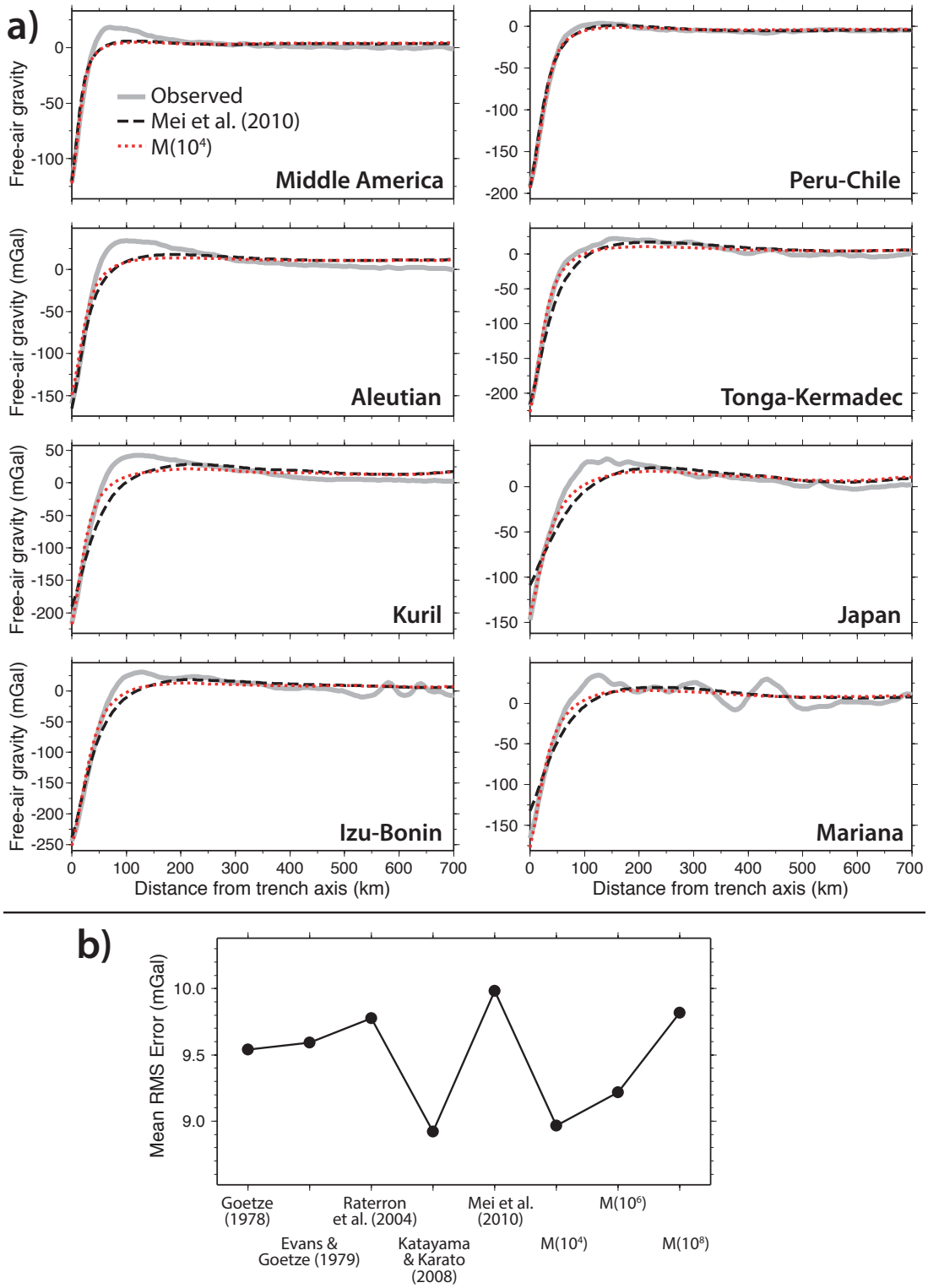

Figure 9.13: Results from Inversion C2, in which circum-Pacific gravity profiles were modelled using an elastic-plastic plate with brittle regime defined by $\mu_f = 0.3$ and hydrostatic PFP. (a) Observed trench-bin gravity anomalies (solid grey) and best-fit anomalies calculated with the LTP flow laws of Mei et al. (2010) (dashed black) and M(10^4) (dotted red). (b) For each LTP flow law, the mean RMSE for all the circum-Pacific profiles, where the trench-bins and segment-bins have been given equal weighting.

9.4 Effect of axial loading on the stress distribution in an elastic-plastic plate

Axial loading affects the stress distribution in a flexed elastic-plastic plate, which in turn affects its rigidity. In addition, due to 'elastic unloading' (Figure 9.1, Section 9.1.3), the stress distribution is also dependent on the timing of axial loading, i.e. whether it occurs before or after plate bending (Mueller and Phillips, 1995; Mueller et al., 1996a).

Figure 9.14 illustrates the stress distribution in an elastic-plastic plate (with depth-dependent, laboratory-derived yield strength) when axial loading occurs before bending. The solid blue line in Figures 9.14a and 9.14b is the initial stress distribution in a 60 Ma plate subjected to a compressional and tensional axial force respectively in the absence of plate bending. The values of these forces, $F = -1.1 \times 10^{13}$ Nm^{-1} and $F = 5.5 \times 10^{12}$ Nm^{-1}, are equal to half the total compressional and tensional strength of the plate respectively (as calculated by integrating $\Delta\sigma_{xx}$ over the compressional/tensional side of the YSE). The dashed red line in Figures 9.14a and 9.14b is the final stress distribution when the plate is then subsequently bent to a curvature of $\kappa = 1.5 \times 10^{-7}$ m^{-1}. For comparison, we have also shown the stress distribution that would exist if the plate were bent to the same curvature in the absence of axial loading (dotted black). The final stress distribution (red dash) in Figure 9.14a shows that, relative to the case of no axial loading (dotted black), compressional axial loading raises the neutral surface, decreases the depth-extent of shallow tensional failure, and increases the depth-extent of deep compressional failure. The final stress distribution in Figure 9.14b shows that, in contrast, tensional axial loading lowers the neutral surface, increases the depth-extent of shallow tensional failure, and decreases the depth-extent of deep compressional failure. Note that in the absence of axial loading, the neutral surface is the depth at which $\Delta\sigma_{xx} = 0$, but in the presence of axial loading, it is the depth at which the initial axial stress (solid blue) and final stress (red dash) intersect. In Figures 9.14a and 9.14b, there is a kink in the final stress distribution: this is due to elastic unloading and shows that the plate has memory of its failure due to the initial axial loading. The T_e that corresponds to the final stress distribution in Figures 9.14a and 9.14b, as given by the ratio of the bending moment and curvature (Equations 3.17

and 3.16), is 30.8 and 30.6 km respectively. This compares to a T_e of 35 km in the absence of axial loading, showing that the initial axial loading weakens the plate. Note that because the brittle lithosphere is weaker in tension than in compression, the amount of weakening per unit axial load is greater for a tensional axial load than for a compressional one.

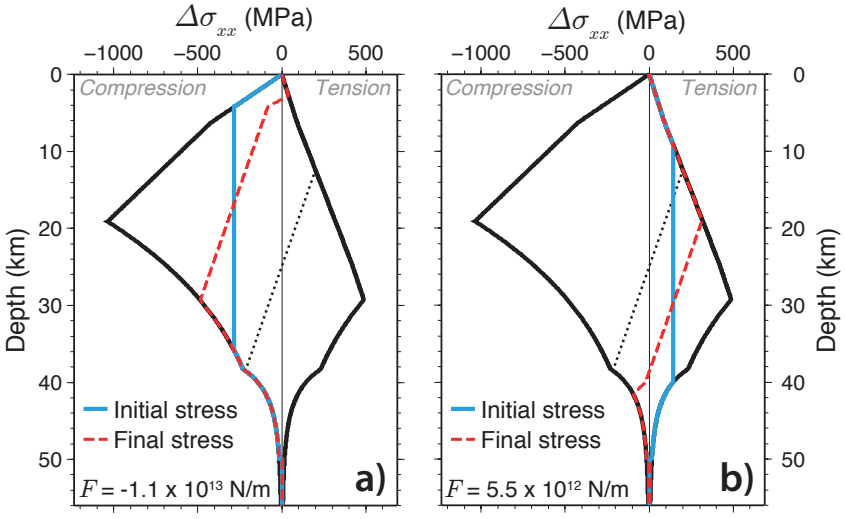

Figure 9.14: Figure illustrating the stress distribution in an elastic-plastic plate subjected first to axial loading and then to bending. The solid blue line is the initial stress distribution when the plate subjected to an axial force, F. The dashed red line is the final stress distribution when the plate is subsequently bent to a curvature of $\kappa = 1.5 \times 10^{-7}$ m^{-1}. The dotted black line is the stress distribution that would exist if the plate were bent to the same curvature in the absence of axial loading. (a) shows the stress distribution for a compressional axial load, and (b) shows that for a tensional load.

Figure 9.15 illustrates the stress distribution that results when axial loading occurs after bending. The solid blue line is the initial stress distribution when the plate is bent to a curvature of $\kappa = 1.5 \times 10^{-7}$ m^{-1} in the absence of axial loading. The dashed red line is the final stress distribution when the plate is subsequently loaded with an axial force with magnitude equal to that in Figure 9.14. Figure 9.15a shows that when a compressional axial load is applied after bending, the shallow lithosphere switches from tensional to compressional failure, and the depth-extent of deep, compressional failure increases. Figure 9.15b shows that when a tensional axial load is applied after bending, the deep lithosphere switches from compressional to tensional failure, and the depth-extent of shallow, tensional failure increases. In both cases, there is a kink in the final stress distribution due to elastic unloading. The T_e is decreased from 35 km before the axial load has been applied to 24.2 km and 26.2 km after

the compressional and tensional load has been applied respectively. This shows that the plate weakening due to axial loading is greater when the load is applied after bending than when it is applied before bending.

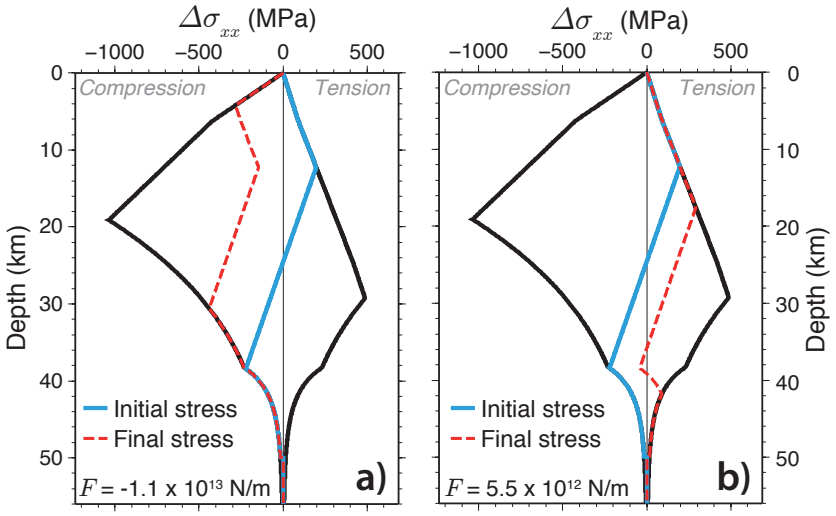

Figure 9.15: Figure illustrating the stress distribution in an elastic-plastic plate subjected first to bending and then to axial loading. The solid blue line is the initial stress distribution when the plate is bent to a curvature of $\kappa = 1.5 \times 10^{-7}$ m^{-1}. The dashed red line is the final stress distribution when the plate is subsequently subjected to an axial force, F. (a) shows the stress distribution for a compressional axial load, and (b) shows that for a tensional load.

It is useful to consider the geological situations in which the two models described above may apply. The first model, in which axial loading occurs before bending, may apply if there are axial stresses that exist in the subducting lithosphere before it enters the trench-outer rise system. The latter model, in which axial loading occurs after bending, may apply if the already-flexed lithosphere in the trench-outer rise system is subject to relatively sudden changes in axial loading. This may occur due to changes in interplate coupling associated with megathrust asperities, or due to the stress accumulation and release associated with the megathrust earthquake cycle (e.g., Christensen and Ruff, 1988; Mueller and Phillips, 1995; Clouard et al., 2007). In reality, a combination of these two end-member models is likely to exist in nature, where some axial stress exists in the lithosphere before it enters the trench-outer rise system, and some is applied after it has been flexed at the outer trench-slope and outer rise. In addition, bending and axial loading may also occur concurrently as the lithosphere approaches the trench axis, as the magnitude of the axial force is likely to increase

as the trench axis is approached. This is because any axial force that is transmitted seaward from the trench axis—either tensional due to slab pull, or compressional due to collision resistance—will be dissipated by the bending of the lithosphere at the outer trench-slope.

9.5 Effect of axial loading on the deflection of an elastic-plastic plate

In the previous section, we described the effect that axial loading has on the stress distribution in, and rigidity of, a flexed elastic-plastic plate. In this section, we will describe the effect that these changes in stress and rigidity have on the deflection of the plate. We will first describe how we calculate elastic-plastic plate deflections in the presence of axial loading:

- To calculate the deflection in the case where an axial force is applied before bending, we use the iterative method as described for the case of no axial loading (Section 9.1.2). The only differences are that the starting stress distribution is that due to the axial load (e.g. blue lines in Figure 9.14), rather than zero, and that the axial force, F, is non-zero in the flexure calculations (Equation 3.7).

- To calculate the deflection in the case where an axial force is applied after bending, we first use the iterative method to calculate the elastic-plastic plate flexure in the absence of axial loading. Then, the stress due to axial loading is added to the resultant bending stress distribution (e.g. dashed red in Figure 9.15), the flexural rigidity is updated accordingly, and the final flexure is calculated using the updated rigidity, where F is non-zero in the flexure calculation. We note that this model cannot account for any evolution in the stress distribution and plate deflection that may occur after this point. This is because the applied axial load greatly reduces the saturation moment of the plate, causing the moment applied at the plate-break, M_0, to exceed the saturation moment. This results in the formation of a 'plastic hinge', whereby the curvature of the plate can increase infinitely without any further increase in moment, and therefore the solution becomes unstable. Clearly, this is a limitation of the simple loading model used here, but we still feel that this model provides a first order insight into the effect of an axial load applied after plate bending.

Figure 9.16 shows the effect of axial loading on the deflection of, and stress distribution in, a broken elastic-plastic plate. The left and right plots show the effect of axial compression and tension respectively. The top row of plots shows the deflection of three broken elastic-plastic plates with end-loads applied at the plate-break: one with no axial loading, one with an axial force applied before bending, and one with an axial force applied after bending. The magnitude of the compressional and tensional axial force, $F = -1.1 \times 10^{13}$ Nm^{-1} and $F = 5.5 \times 10^{12}$ Nm^{-1}, is equal to half the total compressional and tensional strength of the plate respectively. These plots shows that both axial compression and axial tension increase the amplitude of the outer rise, the steepness of the outer trench-slope and the trench depth; this is because the rigidity of the plate is reduced by the axial loading. This effect is greater when axial loading occurs after bending than when it occurs before bending; this is because the former causes the greatest reduction in rigidity. The top plots in Figure 9.16 also show that axial compression has a greater effect on the plate deflection than axial tension, despite the fact that the associated reduction in rigidity is similar in both cases shown. This is because, as well as affecting the stress distribution and rigidity of the plate, the compressional axial force acts mechanically to further increase the amplitude of the flexure, whilst the tensional axial force acts mechanically to decrease the amplitude. The bottom three rows of plots in Figure 9.16 show the deviatoric stress distributions in the flexed plates shown in the top row. This shows that, relative to the case of no axial loading, axial compression raises the neutral surface, whilst axial tension lowers it. It also shows that the compressional bending stresses are larger when axial compression occurs before bending than when it occurs after bending; and that the same is true for the tensional bending stresses in the case of axial tension.

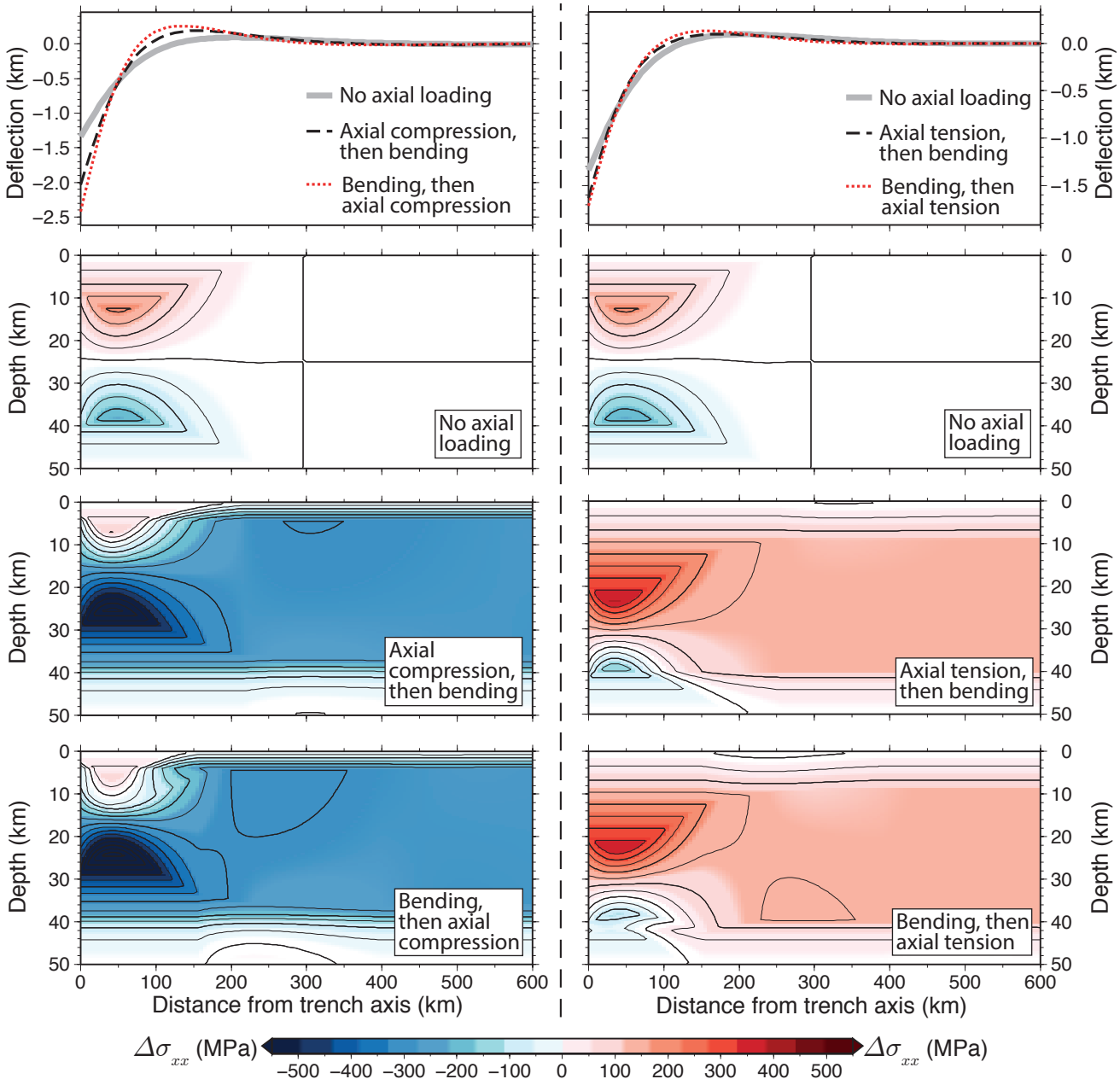

Figure 9.16: Figure illustrating the effect of axial loading on the deflection of, and stress distribution in, a broken elastic-plastic plate. The left and right plots illustrate the effect of axial compression and tension respectively. The top row of plots shows the deflection of three broken elastic-plastic plates with end-loads, M_0 and V_0, applied at the plate-break: one with no axial loading, one with an axial force applied before bending, and one with an axial force applied after bending. The bottom three rows of plots show the corresponding deviatoric stress distributions in the flexed plates, where the thick and thin contours are at 100 and 50 MPa intervals respectively. The plate has YSE-defined yield strength as shown in Figure 9.14. The end-loads are $M_0 = 4 \times 10^{16}$ N and $V_0 = 1 \times 10^{12}$ Nm^{-1}. The compressional and tensional axial force is $F = -1.1 \times 10^{13}$ Nm^{-1} and $F = 5.5 \times 10^{12}$ Nm^{-1} respectively, which is equal to half the total compressional and tensional strength of the plate respectively.

9.6 Axial loading at circum-Pacific subduction zones

The inversions presented in Section 9.3 suggest that in the absence of axial loading, gravity anomalies at the trench-outer rise of circum-Pacific subduction zones cannot be explained by a broken elastic-plastic plate with a bending moment and vertical shear force applied at the plate-break. However, in the previous two sections, we showed that axial loading can have a significant effect on the deflection of an elastic-plastic plate, and therefore it was important to test the effect that this may have at circum-Pacific subduction zones. To do this, we conducted a second set of inversions where, as well as inverting for M_0 and V_0, we also inverted for an axial force, F. These inversions were conducted exactly as described for the case of no axial loading, except that, in addition to iterating over a range of end-loads, we also iterated over a range of axial forces. We first performed a wide parameter search, where M_0 and V_0 were varied as described in Section 9.3, and F was varied from 0.7 times the total compressional strength of the plate to 0.7 times the total tensional strength. Then, a second, narrower parameter search was performed in the vicinity of the best-fitting parameter combination from the first search. We tested 2197 (M_0, V_0, F) parameter combinations in the first search and 2197 in the second search, giving a total of 4396 combinations. We conducted two subsets of inversions: one where the axial force was applied before bending, and one where the axial force was applied after bending. We will now describe the results of these inversions.

9.6.1 Inversion results: axial force applied before bending

In the first set of inversions, the axial force was applied before bending. As in the case of no axial loading, we conducted one inversion where the brittle regime was calculated with Byerlee's (1978) friction coefficients and another where it was calculated with $\mu_f = 0.3$.

In Inversion D1, the brittle regime of the elastic-plastic plates was defined with Byerlee's (1978) friction coefficients and hydrostatic PFP. The results of this inversion are shown in Figure 9.17. Figure 9.17a shows profile fits for the trench-bins. The observed gravity anomalies are shown in solid grey and the best-fit anomalies for the LTP flow laws of Mei et al. (2010) and M(10^6)—the worst and best fitting laws at the Hawaiian Islands respectively—are shown

in dashed black and dotted red respectively. The figure shows that both of these laws fit the steepness of the outer trench-slope well, but that the law of Mei et al. (2010), in general, better fits the amplitude and wavelength of the outer rise. This is further evidenced by Figure 9.17b, which shows the mean RMSE between the observed and calculated gravity for all the circum-Pacific profiles (with equal weighting from the the trench-bins and segment-bins). This shows that the law of Mei et al. (2010) has a mean RMSE of 5.5 mGal, compared to 7.3 mGal for M(10^6). Figure 9.17b also shows that for all of the flow laws, the mean RMSE is significantly improved relative to the case of no axial loading (Figure 9.12), and that the best-fitting laws are those of Evans and Goetze (1979) and Raterron et al. (2004), with a mean RMSE of 5.1 and 5.3 mGal respectively.

In Inversion D2, the brittle regime of the elastic-plastic plates was defined with $\mu_f = 0.3$ and hydrostatic PFP. The results of this inversion are shown in Figure 9.18. Figure 9.18a shows that neither Mei et al. (2010) nor M(10^4)—the worst and best fitting laws at the Hawaiian Islands respectively—provides a good fit to the observed free-air gravity, as neither captures both the steepness of the outer trench-slope and the amplitude and wavelength of the outer rise. Indeed, Figure 9.18b shows that none of the flow laws tested provide a particularly good fit the observed data, as the mean RMSE is > 7.8 mGal in all cases.

9.6.2 Inversion results: axial force applied after bending

In the next set of inversions, the axial force was applied after bending. In Inversion D3, the brittle regime of the elastic-plastic plates was defined with Byerlee's (1978) friction coefficients and hydrostatic PFP. The results of this inversion are shown in Figure 9.19. Figure 9.19a shows that both Mei et al. (2010) and M(10^6) can fit the steepness of the outer trench-slope, but that the law of Mei et al. (2010), in general, better fits the amplitude and wavelength of the outer rise. This is further evidenced in Figure 9.19b, which shows that the laws of Goetze (1978), Evans and Goetze (1979), Raterron et al. (2004) and Mei et al. (2010) all have a mean RMSE < 4.8 mGal, compared to 6.9 mGal for M(10^6).

In Inversion D4, the brittle regime of the elastic-plastic plates was defined with $\mu_f = 0.3$ and hydrostatic PFP. The results of this inversion are shown in Figure 9.20. These results

are very similar to those from Inversion D3, in that the LTP laws that best fit the observed gravity are those of Goetze (1978), Evans and Goetze (1979), Raterron et al. (2004) and Mei et al. (2010), which all have a mean RMSE < 5.3 mGal. M(10^4), which is the best-fitting law at the Hawaiian Islands, provides a worse fit to the amplitude and wavelength of the outer rise, with a mean RMSE of 6.5 mGal.

9.6.3 Summary of inversion results

The elastic-plastic plate inversions presented in this section show that by inverting for an axial force, the fits to circum-Pacific trench-outer rise gravity profiles are significantly improved. The best fits were obtained via Inversion D3, where the brittle regime was defined with Byerlee's (1978) friction coefficients and the axial load was applied after bending (Figure 9.19). However, good fits were also obtained via Inversion D1, where the brittle regime was defined with Byerlee's (1978) friction coefficients and the axial load was applied before bending (Figure 9.17), and via Inversion D4, where the brittle regime was defined by $\mu_f = 0.3$ and the axial load was applied after bending (Figure 9.20). The best-fitting LTP flow laws are those of Goetze (1978), Evans and Goetze (1979), Raterron et al. (2004) and Mei et al. (2010), which provide a good fit to the high curvature and steepness of the outer trench-slope, as well as the amplitude and wavelength of the outer rise. The worst-fitting laws are M(10^8) and M(10^6)—both weakened modifications of Mei et al. (2010)—which cannot fit the amplitude or wavelength of the outer rise. This suggests that these laws are too weak to explain the observed gravity anomalies.

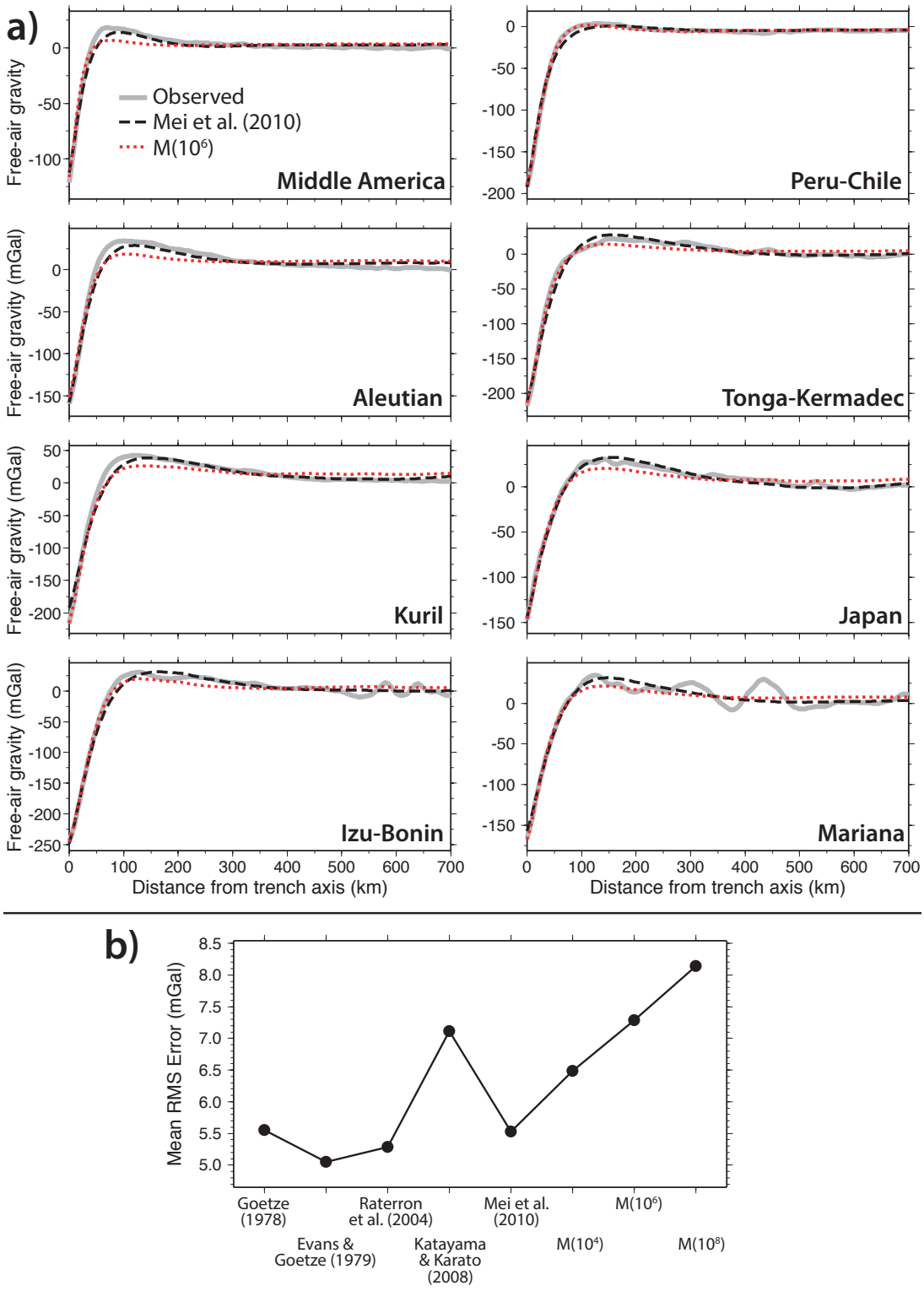

Figure 9.17: Results from Inversion D1. Here, circum-Pacific gravity profiles were modelled using an elastic-plastic plate, where an axial force was applied before bending and the brittle regime was defined with Byerlee's (1978) friction coefficients and hydrostatic PFP. (a) Observed trench-bin gravity anomalies (solid grey) and best-fit anomalies calculated with the LTP flow laws of Mei et al. (2010) (dashed black) and M(10^6) (dotted red). (b) For each LTP flow law, the mean RMSE for all the circum-Pacific profiles, where the trench-bins and segment-bins have been given equal weighting.

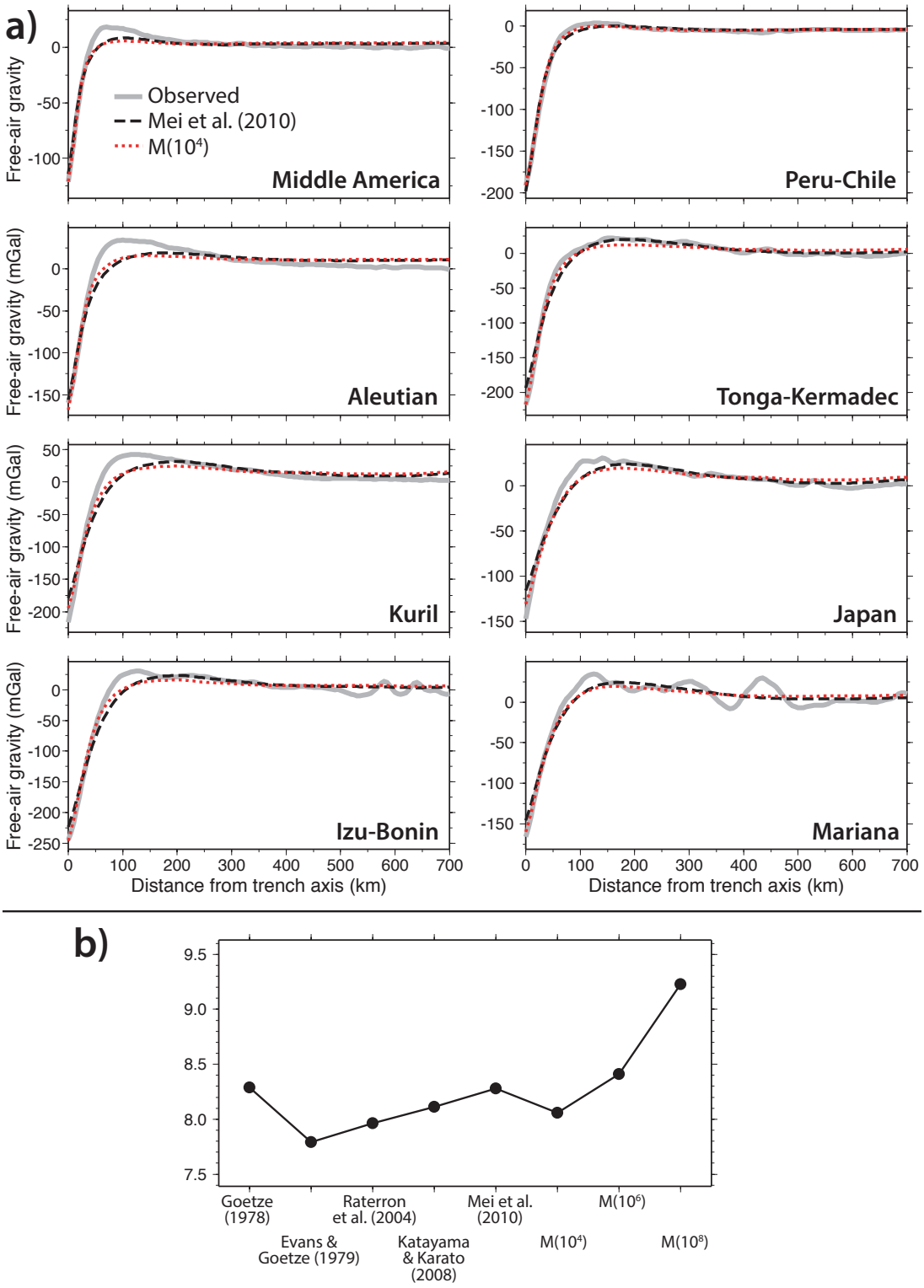

Figure 9.18: Results from Inversion D2. Here, circum-Pacific gravity profiles were modelled using an elastic-plastic plate, where an axial force was applied before bending and the brittle regime was defined with $\mu_f = 0.3$ and hydrostatic PFP. (a) Observed trench-bin gravity anomalies (solid grey) and best-fit anomalies calculated with the LTP flow laws of Mei et al. (2010) (dashed black) and M(10^4) (dotted red). (b) For each LTP flow law, the mean RMSE for all the circum-Pacific profiles, where the trench-bins and segment-bins have been given equal weighting.

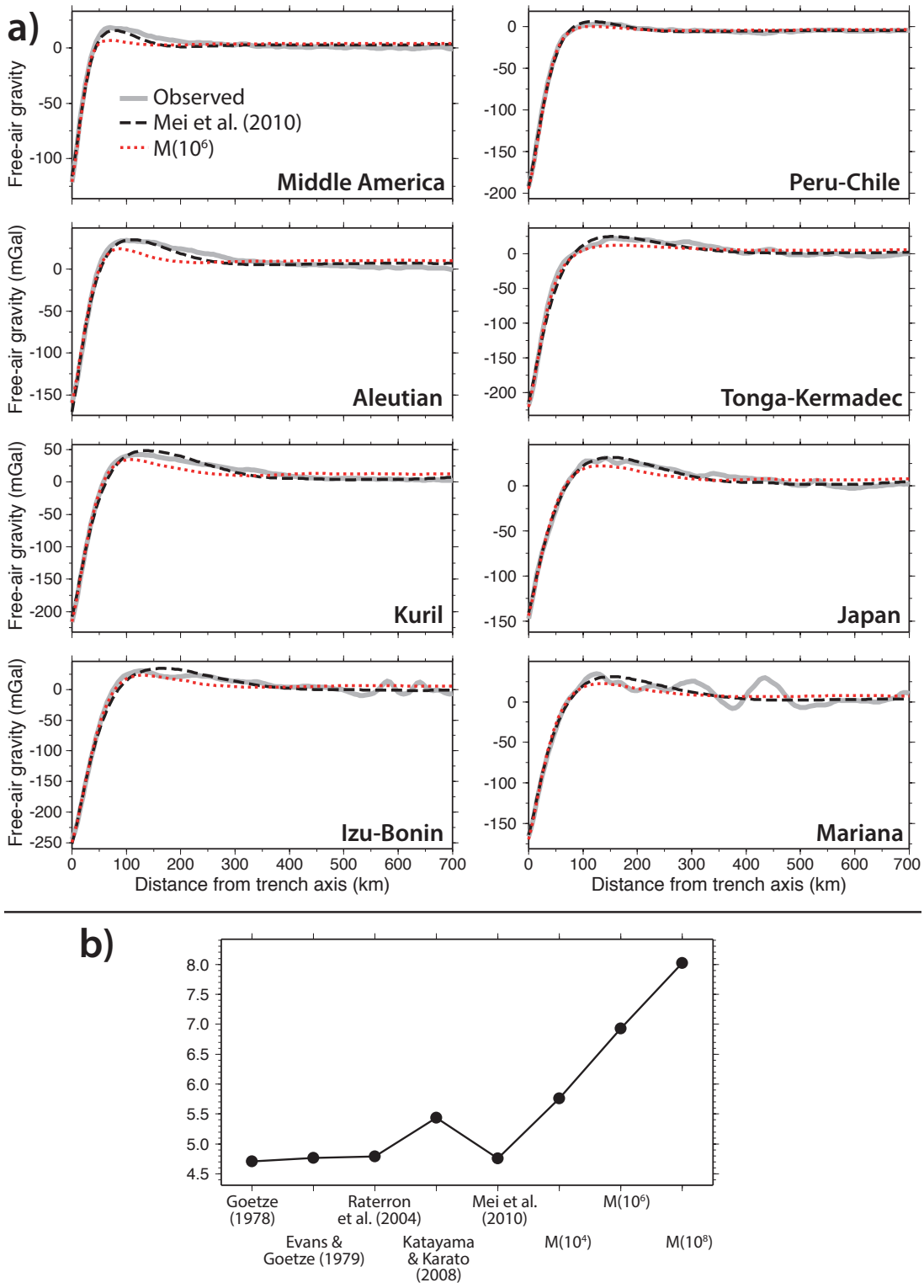

Figure 9.19: Results from Inversion D3. Here, circum-Pacific gravity profiles were modelled using an elastic-plastic plate, where an axial force was applied after bending and the brittle regime was defined with Byerlee's (1978) friction coefficients and hydrostatic PFP. (a) Observed trench-bin gravity anomalies (solid grey) and best-fit anomalies calculated with the LTP flow laws of Mei et al. (2010) (dashed black) and M(10^6) (dotted red). (b) For each LTP flow law, the mean RMSE for all the circum-Pacific profiles, where the trench-bins and segment-bins have been given equal weighting.

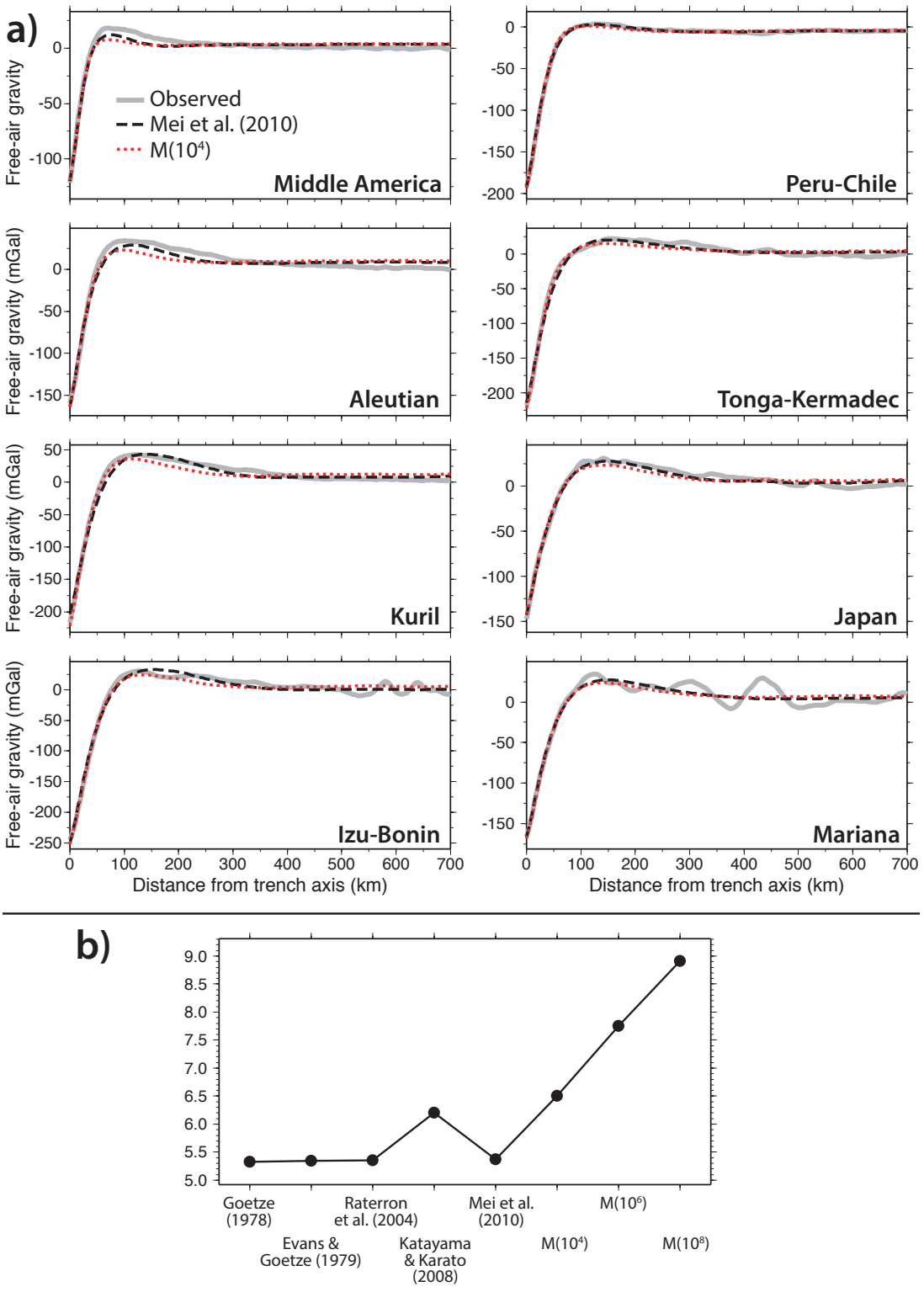

Figure 9.20: Results from Inversion D4. Here, circum-Pacific gravity profiles were modelled using an elastic-plastic plate, where an axial force was applied after bending and the brittle regime was defined with $\mu_f = 0.3$ and hydrostatic PFP. (a) Observed trench-bin gravity anomalies (solid grey) and best-fit anomalies calculated with the LTP flow laws of Mei et al. (2010) (dashed black) and M(10^4) (dotted red). (b) For each LTP flow law, the mean RMSE for all the circum-Pacific profiles, where the trench-bins and segment-bins have been given equal weighting.

9.6.4 Best-fitting axial force

The best-fitting axial force, F, from the inversions presented in this section might provide further insight into the most valid LTP flow laws and also into the forces acting on subducting lithosphere. For the trench-bin profiles, Figure 9.21 shows the best-fitting axial force for each flow law, and Figure 9.22 shows the corresponding axial stress (in the un-yielded portion of the plate). The four flow laws that provide the best fit to the observed gravity anomalies are plotted in black, and those that provide the worst fit are plotted in red; we will concentrate the following discussion on the best-fitting laws. We have not shown the results from Inversion D2, as this inversion provides quite a poor fit to the observed gravity (Figure 9.18).

Figure 9.21 shows that for all three inversions, there is a general increase in the magnitude of the axial force with plate age (from left to right). This is as expected, because the magnitude of tectonic driving forces—for example slab pull, slab suction and ridge push—should be larger for older, colder, thicker plates (e.g., Forsyth and Uyeda, 1975; Parsons and Richter, 1980; Conrad et al., 2004; Schellart, 2004).

As shown in Figure 9.22 (top plot), the results of Inversion D1 imply that compressional axial stresses of up to > 400 MPa are applied before plate bending, which suggests that the subducting lithosphere is subject to large compressional stresses before it enters the trench-outer rise system. If this were the case, shallow, compressional seismicity would occur frequently seaward of the outer rise. This contrasts with the observation that oceanic intraplate seismicity is rare (Wiens and Stein, 1983; Ioc et al., 2003) and is characterised by shallow compression and deeper tension (Wiens and Stein, 1984), which suggests that it is caused by (small magnitude) thermal bending stresses (Wessel, 1992). Therefore, we suggest that the model used in Inversion D1, where the axial force is applied before bending, is not compatible with observations and that the model used in Inversions D3 and D4 is likely to more closely reflect nature.

In Inversions D3 and D4, the axial force was applied after plate bending. This model would apply if the already-flexed lithosphere in the trench-outer rise system is subject to geologically sudden changes in axial loading. It has been suggested that this may occur due to changes in

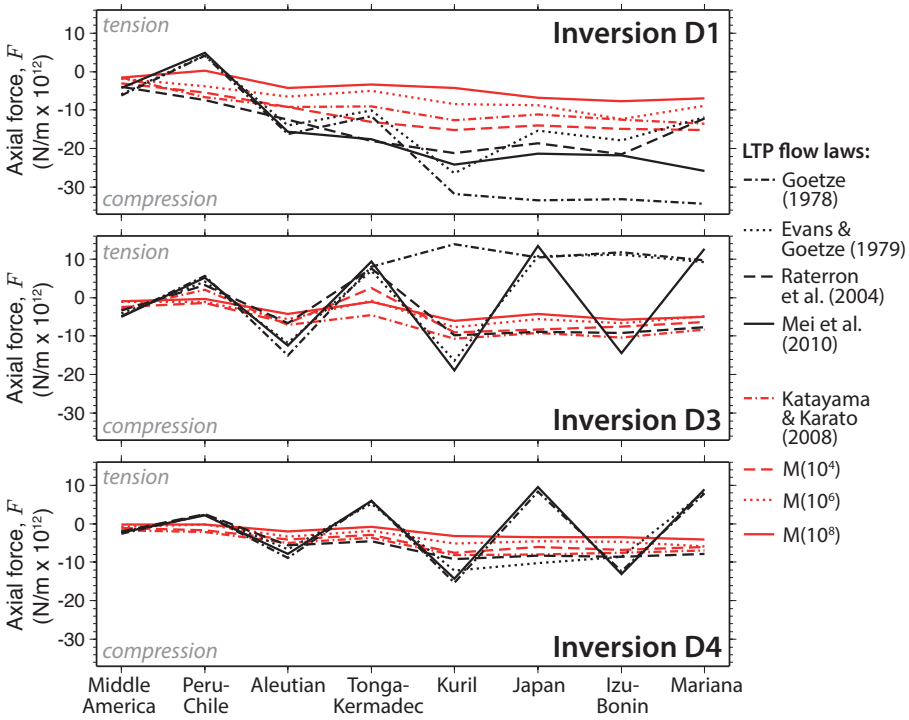

Figure 9.21: For the trench-bins, the best-fitting axial force from Inversions D1, D3 and D4. The line colour/pattern denotes the LTP flow law used to define the elastic-plate; the best and worst fitting laws are plotted in black and red respectively. The results are ordered from left to right with increasing plate age.

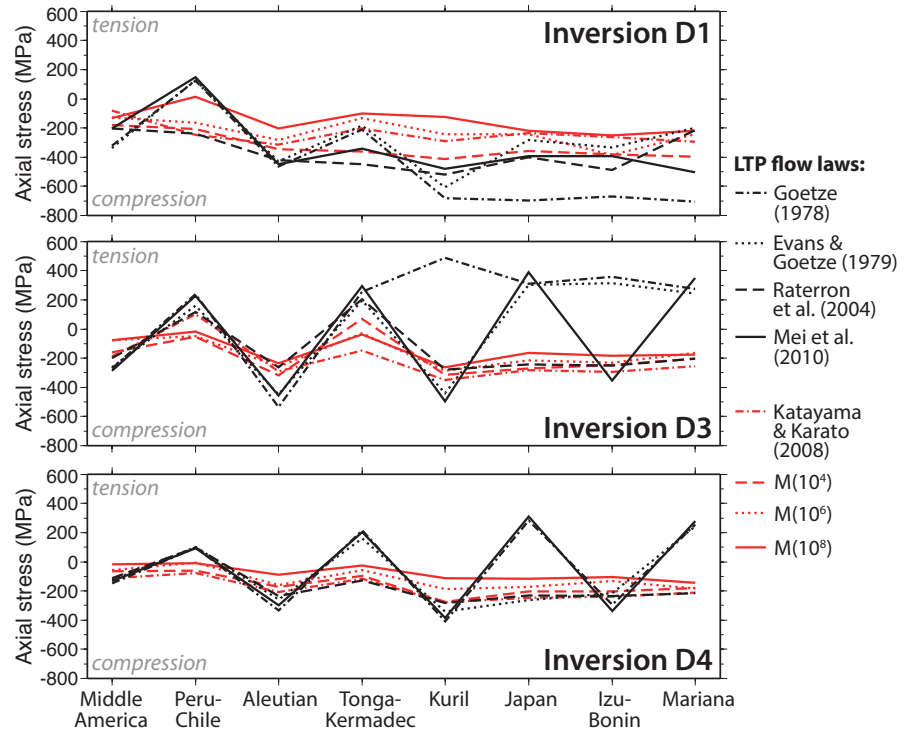

Figure 9.22: For the trench-bins, the best-fitting axial stress from Inversions D1, D3 and D4, which corresponds to the axial force shown in Figure 9.21. The line colour/pattern denotes the LTP flow law used to define the elastic-plate; the best and worst fitting laws are plotted in black and red respectively. The results are ordered from left to right with increasing plate age.

interplate coupling associated with megathrust asperities, or due to the stress accumulation and release associated with the megathrust earthquake cycle (Mueller and Phillips, 1995). For example, the temporal variation of outer rise seismicity suggests that the early part of the megathrust earthquake cycle is characterized by axial tension in the subducting plate, whilst the latter part is characterized by axial compression (e.g., Christensen and Ruff, 1988; Dmowska and Lovison, 1988; Clouard et al., 2007). Another way to think of this is that the subducting plate is subject to a background tensional axial force due to the net slab pull force, but that this is overprinted by an increasing compressional axial force as stress accumulates during each megathrust earthquake cycle (Clouard et al., 2007). Clearly, the static elastic-plastic plate model used here cannot fully capture this temporal variation in axial stress, but nonetheless, we believe that it provides useful first order insight. The model of axial loading after plate bending might also apply if the subducting lithosphere encounters an increased axial force after it has travelled through the outer rise, where the majority of the bending occurs. This would occur if the force transmitted seaward from the trench axis is significantly dissipated by the bending of the plate at the outer rise, as has been suggested by Buffett (2006) and Buffett and Becker (2012). However, the model used here provides only a crude approximation to such a scenario, as it assumes that the axial force is constant throughout the plate.

Figure 9.21 shows that the best-fitting axial force from Inversions D3 and D4 varies with the LTP flow law, which precludes us from making any definitive statement about the forces acting at circum-Pacific subduction zones. Interestingly, for many of the profiles, the observed gravity can be fit almost as well by an axial force of opposite sign, but of similar magnitude, to the best-fitting force shown in the figure. For example, for Inversion D3 and the flow law of Mei et al. (2010), the difference between the RMSE corresponding to the best-fitting tensional and compressional axial force is < 0.5 mGal for the following trench-bins: Middle America, Tonga, Japan, Izu-Bonin and Mariana. This might reflect the fact the lithosphere is subject to both compressional and tensional axial forces during the megathrust earthquake cycle, and that the plate deflection reflects an average of the temporally varying axial load. However, it is more likely that it simply reflects the fact that a tensional and compressional axial force of similar magnitude have a similar effect on the deflection of an elastic-plastic plate. This is

because, although a compressional force causes less plate weakening than a tensional force, the compressional force acts mechanically to increase the amplitude and decrease the wavelength of the outer rise.

Figure 9.21 shows that a larger axial force is required for plates defined by Byerlee's (1978) friction coefficients (Inversion D3) than for those defined by $\mu_f = 0.3$ (Inversion D4). This is because a weaker plate requires a smaller axial force to significantly alter its deflection. Figure 9.21 also shows that of the best-fitting LTP laws (black lines), Raterron et al. (2004) generally requires the smallest magnitude axial force, whilst the laws of Goetze (1978), Evans and Goetze (1979) and Mei et al. (2010) all require similar magnitude forces, but sometimes of differing sign. The latter three laws require tensional axial forces of up to 1.3×10^{13} Nm^{-1} and 1.0×10^{13} Nm^{-1} in the case of Inversion D3 and D4 respectively. This is greater than the maximum net slab pull force predicted by the modelling studies of Schellart (2004) and Capitanio et al. (2009), 6×10^{12} Nm^{-1}. This perhaps suggests that a more appropriate LTP flow law is that of Raterron et al. (2004), which requires tensional axial forces up to 7.5×10^{12} Nm^{-1} and 5×10^{12} Nm^{-1} in the case of Inversion D3 and D4 respectively. In addition, Figure 9.22 shows that the laws of Goetze (1978), Evans and Goetze (1979) and Mei et al. (2010) require compressional axial stresses up to -500 MPa and -400 MPa in the case of Inversion D3 and D4 respectively. If compressional stresses of this magnitude did accumulate during the megathrust earthquake cycle, shallow, compressional outer trench-slope earthquakes would occur frequently, which contradicts the observation that such events are rare (e.g. Craig et al., 2014a). This again might suggest that the the law of Raterron et al. (2004) is a more appropriate flow law, as it requires more moderate stresses of up to -270 MPa. However, we are reluctant to draw a definitive conclusion on the most appropriate LTP flow law on the basis of the resolved axial forces. This is because the large forces required by the laws of Goetze (1978), Evans and Goetze (1979) and Mei et al. (2010) might be due to failings of the elastic-plastic plate model used here. For example, this model is static and therefore cannot capture the temporal variation in axial loading associated with the megathrust earthquake cycle. Due to the effect of elastic unloading, this temporal variation in axial stress would cause additional plate weakening, thus reducing the axial force required to fit the observed gravity. In addition, the model used here assumes that the axial force

is constant throughout the plate. In reality, the force is likely to decrease with distance seaward of the trench, as it is dissipated by the bending of the subducting plate (Buffett, 2006; Buffett and Becker, 2012). Furthermore, the model used here does not account for the plate weakening that might occur due to mantle hydration and serpentinization via outer trench-slope bend-faults (e.g., Escartin et al., 1997; Ranero et al., 2003; Grevemeyer et al., 2007), which would further reduce the axial force required to fit the observations. Note that these model failings are unlikely to affect the conclusion that the weakened modifications of Mei et al. (2010) provide a poor fit to the observed gravity. This is because these laws fail to fit the wavelength and amplitude of the outer rise, which suggests that they are too weak, and thus any additional source of plate weakening is unlikely to improve their fit to the observed data.

In summary, the model most compatible with observations of seismicity is one where an axial force is applied after plate bending. This model might reflect temporal variations in axial stress associated with the megathrust earthquake cycle and/or the dissipation of the axial force by plate bending at the outer rise. However, we note that the static elastic-plastic plate model provides only a crude approximation to these scenarios. The best-fitting axial force varies with the LTP flow law, which precludes us from making any definitive statements about the forces acting at circum-Pacific subduction zones. For many profiles, the observed gravity can be fit almost equally well by a compressional or tensional axial force of similar magnitude, which likely reflects the fact the elastic-plastic plate deflection is similar in both cases. Although the axial forces and stresses required by some flow laws are larger than might be expected, we cannot use this to discriminate between flow laws due to failings of the elastic-plastic plate model.

9.7 Chapter summary

In this chapter, in an effort to constrain mantle rheology, we have used YSE-defined elastic-plastic plates to model observations of flexure at the Hawaiian Islands and at the trench-outer rise system of circum-Pacific subduction zones. Our findings are summarised as follows:

- The dry olivine LTP flow laws of Goetze (1978), Evans and Goetze (1979), Raterron et al. (2004) and Mei et al. (2010) are all too strong to fit the observations at the Hawaiian Islands. The published flow law that best fits the observations is the wet olivine law of Katayama and Karato (2008).

- The recent LTP flow law of Mei et al. (2010) must be significantly weakened to fit the observations at the Hawaiian Islands. The observed crustal deflections are best fit by increasing A_m by: 6 orders of magnitude assuming $\mu_f = 0.7$ (zero PFP) or Byerlee's friction coefficients (hydrostatic PFP); or by 4 orders of magnitude assuming $\mu_f = 0.3$ (hydrostatic PFP). This is in general agreement with the 3-D viscoelastic modelling study of Zhong and Watts (2013), although their model requires slightly greater weakening, which likely reflects the failure of the elastic-plastic model to account for viscoelastic stress relaxation.

- Regardless of the friction coefficient or LTP flow law, in the absence of axial loading, circum-Pacific trench-outer rise gravity anomalies cannot be explained by a broken elastic-plastic plate model. The LTP flow law of Mei et al. (2010) cannot fit the wavelength of the outer rise nor the steepness of the outer trench-slope. The weakened modifications of Mei et al. (2010) can fit the steepness of the outer trench-slope, but they cannot fit the amplitude and wavelength of the outer rise.

- When axial loading is incorporated in the elastic-plastic plate model, the LTP flow laws that best fit the circum-Pacific trench-outer rise observations are those of Goetze (1978), Evans and Goetze (1979), Raterron et al. (2004) and Mei et al. (2010). The worst-fitting laws are M(10^8) and M(10^6)— both weakened modifications of Mei et al. (2010)—which cannot fit the amplitude or wavelength of the outer rise. This suggests that these laws are too weak to explain the observed gravity anomalies.

- The model most compatible with observations of seismicity is one where an axial force is applied after, rather than before, plate bending. This model might reflect temporal variations in axial stress associated with the megathrust earthquake cycle and/or the dissipation of the axial force by plate bending at the outer rise.

Chapter 10

Reconciling mantle rheology at circum-Pacific subduction zones and the Hawaiian Islands

In the previous two chapters, we used two different methods to constrain the mantle rheology, and in particularly the Low-Temperature Plasticity (LTP) rheology, at the trench-outer rise system of circum-Pacific subduction zones and at the Hawaiian Islands. In Chapter 8, we used the YSE-curvature method, in which the T_e derived by inversion of observed gravimetric/crustal deflections was compared to the T_e predicted by laboratory-derived YSEs and observed plate curvatures. In Chapter 9, we directly modelled the observed deflections using elastic-plastic plates with laboratory-derived, depth-dependent yield strength. Both of these methods suggest that at the Hawaiian Islands, the dry olivine LTP flow laws of Goetze (1978), Evans and Goetze (1979), Raterron et al. (2004) and Mei et al. (2010) are too strong to fit the observations. The laboratory-derived LTP law that best fits the observations in this region is the wet olivine law of Katayama and Karato (2008), which provides a particularly good fit if a low friction coefficient is assumed in the elastic-plastic plate model. These methods also suggest that to fit the observations at the Hawaiian Islands, the law of Mei et al. (2010) must be weakened by increasing the material-dependent parameter, A_m, by 4–8 orders of magnitude, depending on the method and the assumed friction coefficient. This is in general

agreement with the study of Zhong and Watts (2013), who modelled the crustal deflections using a 3-D finite-element viscoelastic model and found that A_m must be increased by 6–8 orders of magnitude. In contrast to the Hawaiian Islands, the LTP flow laws that best fit the observations at circum-Pacific subduction zones are those of Goetze (1978), Evans and Goetze (1979), Raterron et al. (2004) and Mei et al. (2010); whilst the law of Katayama and Karato (2008) and the weakened modifications of Mei et al. (2010) are generally too weak to fit the observations. Thus, the results of the YSE-curvature method and elastic-plastic plate modelling suggest that there is a discrepancy between the LTP rheology at the Hawaiian Islands and at circum-Pacific subduction zones. This discrepancy can be expressed by stating that the lithospheric rocks at the Hawaiian Islands appear weaker than those at circum-Pacific subduction zones. In this chapter, we will discuss some possible causes of this discrepancy, before discussing some of the uncertainties involved with extrapolating laboratory-derived flow laws to geological conditions.

10.1 Thermal rejuvenation

It has been suggested that thermal rejuvenation of the lithosphere (i.e. reheating by a mantle hotspot) can significantly reduce its flexural rigidity (e.g., Menard and McNutt, 1982; McNutt, 1984). For example, the anomalously low T_e of the lithosphere beneath the Darwin Rise seamounts has been attributed to thermal rejuvenation at the South Pacific Superswell (e.g., Smith et al., 1989; Wolfe and McNutt, 1991). Thus, one plausible cause of the relative weakness of Hawaiian lithosphere is thermal rejuvenation by the Hawaiian plume. Early field studies of surface heat flow along the Hawaiian swell suggested anomalously high values that increased from the Big Island of Hawaii towards Midway (Detrick et al., 1981; Von Herzen et al., 1982). This led to the suggestion that the Hawaiian swell is supported by anomalously hot lithosphere that has been reheated by the Hawaiian plume to asthenospheric temperatures at depths $>$ 40–50 km. However, subsequent studies showed that there is no systematic increase in heat flow along or across the swell, suggesting predominantly dynamic support and only small temperature anomalies ($<$ 100–200 °C) in the lower lithosphere (Von Herzen et al., 1989).

Two end-member models have been suggested for the effect that thermal rejuvenation has on the temperature structure of oceanic lithosphere (McNutt, 1984). In the first model, the entire lithosphere is reheated such that it has the thermal structure of younger lithosphere; i.e. its effective thermal age, t_{eff}, is reduced. If this model is assumed, tests (based on the YSE-curvature method and elastic-plastic plate model) show that t_{eff} at the Hawaiian Islands must be reduced by 40–50 Ma in order to match the rheology at circum-Pacific subduction zones. In the second thermal rejuvenation model, all lithosphere below a depth y_t is reheated to the temperature of the asthenosphere, leaving the shallower lithosphere unaltered. If this model is assumed, tests show that y_t must be shallower than 35 km in order to match the subduction zone rheology. In light of the findings of Von Herzen et al. (1989), the values required by both of these thermal rejuvenation models seem unlikely. Hence, thermal rejuvenation might contribute to the weakness of Hawaiian Island lithosphere relative to that at circum-Pacific subduction zones, but it is unlikely to be the sole cause of the discrepancy.

10.2 Thermal stresses

Wessel (1992) suggested that thermal stresses might cause the lithosphere beneath seamounts and ocean islands to appear weaker than that at the trench-outer rise of subduction zones. These stresses accrue as the lithosphere cools, producing moderate tensional stresses in the lower mechanical lithosphere and moderate compressional stresses in the shallow lithosphere. This stress pattern would interfere constructively with the bending stresses caused by concave-upward plate bending, and destructively with the stresses caused by convex-downward bending. Wessel (1992) argued that this would cause the lithosphere beneath seamounts and ocean islands to appear relatively weak, as the plate is bent concave-upward directly beneath the volcanic load. In contrast, the lithosphere at the trench-outer rise system would appear relatively strong, as the plate is bent convex-upward.

10.3 Magma-assisted flexure

In response to the study of Zhong and Watts (2013), Buck et al. (2015) suggested that 'magma-assisted flexure' might explain the relative weakness of Hawaiian Island lithosphere. Because the lithosphere is flexed concave-upwards directly beneath the island loads, the flexural stresses in the deeper, ductile regime are extensional. Magma can accommodate lithospheric extension at smaller differential stresses than ductile rock yielding and therefore magmatic dikes would allow the lithosphere to flex more easily beneath the islands. As Hawaii has the highest contemporary magma flux on Earth, magmatic dikes beneath the Hawaiian Island might assist the flexure of the lithosphere, causing it to be relatively weak.

10.4 Viscoelasticity

An alternative explanation for the discrepancy in rheology is differences in the timescales of loading. There is a contrast, for example, between the relatively short-timescale, continuous nature of loading seaward of subduction zones and the relatively long-timescale, discrete nature of loading at seamounts and ocean islands.

There is evidence that during loading, the lithosphere behaves more as a viscoelastic material than a purely elastic or elastic-plastic one, such that it is more rigid on short timescales than on long timescales. For example, there is a decrease in elastic thickness from the short-timescale seismic thickness, to the intermediate-timescale associated with glacial rebound, to the long-timescale associated with seamount loading (e.g., Walcott, 1970; Anderson, 1980; Watts and Zhong, 2000). Further evidence comes from the uplift/subsidence and associated stratigraphic patterns observed in the flexural moats that flank seamounts and ocean islands (Watts and Zhong, 2000), the margins of continental interior basins (Beaumont, 1981) and the coastal plain of rifted continental margins (Sleep and Snell, 1976). Watts and Zhong (2000) used observations of seamount and ocean island loading to show that following loading, it takes 1–2 Myr for the oceanic lithosphere to viscoelastically relax to its long-term elastic thickness.

It seems intuitive that there should also be some form of time-dependent, viscoelastic deformation at oceanic subduction zones. As the subducting plate travels through the outer rise and bends into the trench, it is continuously being strained, where most of the plate curvature, and thus strain, accumulates within 150 km of the trench axis. The range of subduction velocities at circum-Pacific subduction zones is $\sim$ 30–220 mm/yr and thus most of the strain accumulates gradually over a time span of $\sim$ 0.5–3.3 Myr. Furthermore, the continuous nature of the strain accumulation means that at any point on the outer trench-slope, a significant portion of the strain will have accumulated within 10^s–100^s ka. Thus, it is clear that at the outer trench-slope, at least some of the viscoelastic stresses caused by plate flexure may not have had enough time to fully relax. Indeed, Farrington et al. (2014) recently used a viscoelastic plate model to show that viscoelasticity is important during bending and unbending of the subducting plate/slab, and that it affects the geometry of the outer rise.

In contrast to the trench-outer rise system, seamounts and ocean islands are loaded in discrete bursts of volcanism that punctuate long periods of quiescence, after which the lithosphere can creep and relax to its long-term, asymptotic effective elastic thickness. At the Hawaiian Islands, for example, the shield to post-shield building phase on Oahu was between 4 and 2 Ma, and on Molokai between 2 and 1 Ma. Thus, most of the viscoelastic stresses in the Hawaiian region modelled in this study are likely to have fully relaxed in the time since loading, as is suggested by the 3-D finite-element viscoelastic model of Zhong and Watts (2013). This contrasts with the trench-outer rise of subduction zones, where less stress relaxation is likely to have occurred. This disparity might contribute to the the apparent strength of the trench-outer rise lithosphere relative to that in the Hawaiian Islands region.

10.4.1 Accounting for viscoelasticity in the YSE-curvature method

The elastic-perfectly plastic rheology that was assumed in the YSE-curvature method (Chapter 8) and the elastic-plastic plate model (Chapter 9) is time-independent and assumes that all stresses above the yield stress are fully relaxed. Therefore, these models may only place a lower bound on the rigidity of the lithosphere. To explore the possible time-dependence of lithospheric rigidity in our study regions, we developed a modified YSE-curvature method

that accounts for viscoelastic stress relaxation. In this method, the plate is assumed to behave as a Bingham-Maxwell, or elastic-perfectly viscoplastic, material such that below the yield stress it behaves elastically and above the yield stress it behaves as a Maxwell viscoelastic material.

As illustrated in Figure 10.1, the analogue model for a Bingham-Maxwell material consists of an elastic spring element (modulus E) in series with a viscoplastic element, which itself consists of a plastic element (yield stress σ_{yield}) in parallel with a viscous dashpot element (viscosity η). If a strain ε is suddenly applied to such a material at time $t = 0$ and then held constant, the uniaxial stress relaxation with time is given by (Ranalli, 1995, p. 109):

$$\begin{aligned} \sigma(t) &= \sigma_0 \quad \text{if} \quad \sigma_0 \leq \sigma_{yield} \\ \sigma(t) &= \sigma_{yield} + (\sigma_0 - \sigma_{yield}) \exp\left(\frac{-Et}{\eta}\right) \quad \text{if} \quad \sigma_0 > \sigma^{yield} \end{aligned} \tag{10.1}$$

where $\sigma_0 = \varepsilon E$ is the initial elastic stress at time $t = 0$. It can be seen that if σ_0 exceeds the yield stress, the stress relaxes from its initial elastic value to the yield stress with relaxation time $\tau = \frac{\eta}{E}$, such that the asymptotic final stress state is equal to that of the elastic-perfectly plastic model (Figure 10.2).

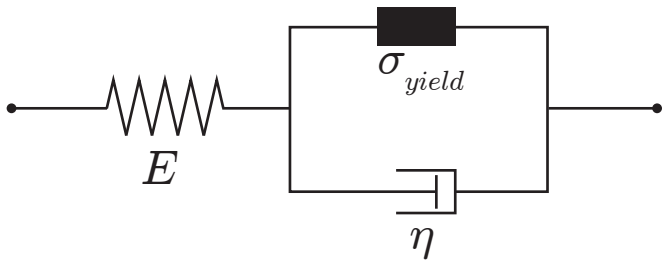

Figure 10.1: Analogue model of a Bingham-Maxwell, or elastic-perfectly viscoplastic, material.

In the YSE-curvature method presented in Chapter 8, the plate curvature and laboratory-derived YSEs are used to calculate the 'predicted T_e' under the assumption that the plate behaves as an elastic-plastic material. In contrast, in the modified YSE-curvature method presented here, the predicted T_e is calculated assuming that the plate behaves as Bingham-Maxwell material. Using Equation 10.1, if the plate is suddenly flexed to a constant curvature

κ at time $t = 0$, the stress distribution in the plate as a function of time is given by:

$$\begin{aligned} \Delta\sigma_{xx}(t) &= \Delta\sigma_{xx}^{elast} \quad \text{if} \quad \Delta\sigma_{xx}^{elast} \leq \Delta\sigma_{xx}^{yield} \\ \Delta\sigma_{xx}(t) &= \Delta\sigma_{xx}^{yield} + \left(\Delta\sigma_{xx}^{elast} - \Delta\sigma_{xx}^{yield}\right) \exp\left(\frac{-Et}{(1-\nu^2)\eta_{eff}}\right) \quad \text{if} \quad \Delta\sigma_{xx}^{elast} > \Delta\sigma_{xx}^{yield} \end{aligned} \tag{10.2}$$

where:

$$\Delta\sigma_{xx}^{elast} = \frac{E(y - y_n)\kappa}{1 - \nu^2} \tag{10.3}$$

Here, $\Delta\sigma_{xx}^{elast}$ is the initial elastic bending stress, $\Delta\sigma_{xx}^{yield}$ is the yield stress as defined by the YSE, y is depth, y_n is the depth of the neutral surface, E is Young's modulus, and ν is Poisson's ratio. The effective viscosity, η_{eff}, is defined as $\eta_{eff} = \Delta\sigma_{xx}^{yield}/\dot{\varepsilon}_{xx}$, where $\dot{\varepsilon}_{xx}$ is the strain rate used to calculate the YSE. Note that in Equation 10.2, we have made the simplifying assumption that the stress relaxation occurs uniaxially.

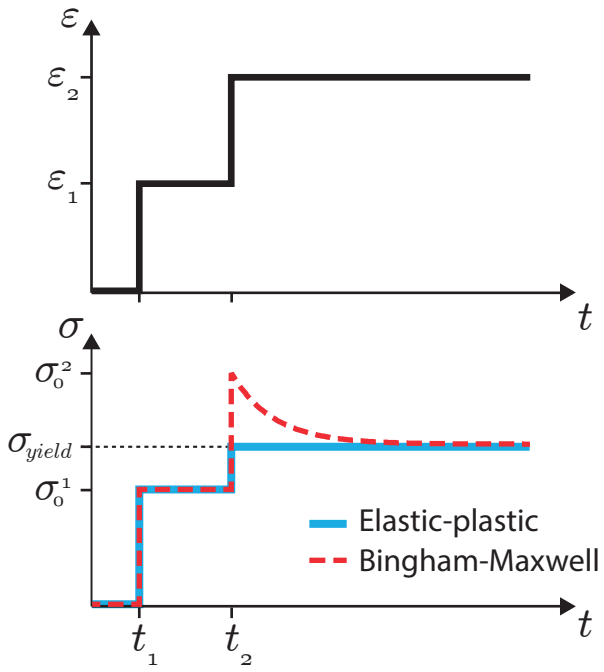

Figure 10.2: Schematic of the variation of stress with time in an elastic-plastic and a Bingham-Maxwell material respectively. At time t_1, a step strain ε_1 is applied. The induced elastic stress, σ_0^1, is less than the yield stress, σ_{yield}, and therefore both materials behave elastically. At time t_2, a step strain ε_2 is applied and this time the induced elastic stress, σ_0^2, is greater than σ_{yield}. This causes the elastic-plastic material to behave perfectly plastically, such that it deforms at the yield stress. In contrast, the Bingham-Maxwell material behaves as a Maxwell viscoelastic material such that the stress relaxes from its initial elastic value to the yield stress with relaxation time $\tau = \frac{\eta}{E}$.

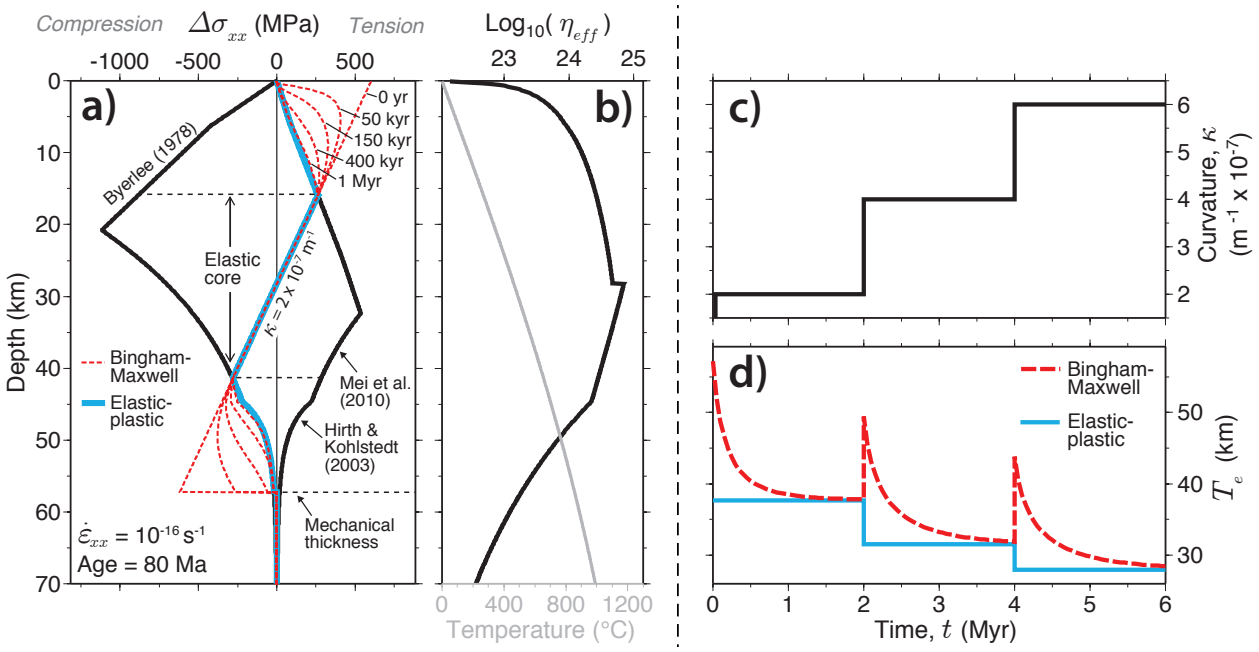

Figure 10.3: Comparison between the Bingham-Maxwell and elastic-plastic YSE models. (a) The variation in stress with time following a step change in curvature for a Bingham-Maxwell (red dash) and elastic-plastic (solid blue) plate respectively. The YSE (solid black) was calculated using laboratory derived flow laws as labelled on the figure; the age and strain rate are also labelled. (b) Black shows the effective viscosity corresponding to the YSE shown in Figure 10.3a. Grey shows the geotherm used to calculate the YSE. (d) The change in T_e with time following three step changes in curvature (Figure 10.3c), as calculated using the YSE shown in Figure 10.3a.

The red dash in Figure 10.3a illustrates the change in stress with time in following a step change in curvature, assuming a Bingham-Maxwell rheology. This shows that the bending stresses below the yield stress are supported elastically and do not change with time, whilst the bending stresses above the yield stress relax from their initial elastic value to the yield stress over a period of just over 1 Myr. This contrasts with the elastic-plastic model (solid blue), in which the stress is time-independent. Figure 10.3a also shows that in the Bingham-Maxwell model, the stresses at the top and bottom of the plate relax quicker than those in the middle of the plate, because the effective viscosity (black in Figure 10.3b) is greatest in the middle of the plate. Figure 10.3d shows the change in T_e with time following three step changes in curvature (Figure 10.3c). Here, the T_e is calculated using the ratio of the bending moment and curvature (Equations 3.17 and 3.16), where the bending moment is calculated using the stress distribution illustrated in Figure 10.3a (Equation 8.12). Figure 10.3d shows that in the elastic-plastic model, each step in curvature induces an immediate decrease in T_e, which

then remains constant. In contrast, in the Bingham-Maxwell model, each step in curvature induces an immediate increase in T_e, because the stresses are initially supported elastically, after which the T_e relaxes with time and asymptotically approaches the elastic-plastic T_e. The figure shows that it takes 1–2 Myr for the T_e to relax to its long-term, asymptotic value, which agrees with the relaxation time found by Watts and Zhong (2000) for seamounts and ocean islands.

10.4.2 Circum-Pacific subduction zones

10.4.2.1 Method

In the YSE-curvature method presented in Chapter 8, we used YSEs and best-fitting elastic plate curvatures to calculate the 'predicted T_e' as a function of distance from the trench at circum-Pacific subduction zones, assuming an elastic-plastic rheology (blue line in Figure 10.4b). We then compared the predicted T_e at the point of maximum curvature, x_a, to the 'observed T_e' that was derived by inversion of the observed gravity profiles (black line in Figure 10.4b). In the modified YSE-curvature method presented here, we repeated this procedure assuming a Bingham-Maxwell rheology (red line in Figure 10.4b). To incorporate this rheology, we modelled the bending of the plate as it approaches the trench as a series of small, incremental step changes in plate curvature. We calculated the stress relaxation function for each increment of curvature (as illustrated in red dash in Figure 10.3a) and then summed all of these functions to give the total stress distribution in the plate as a function of distance from the trench. This stress distribution could then be used to calculate the predicted T_e as a function of distance from the trench. This will be described in detail in the following paragraph.

As shown in Figure 10.4a, we first converted the curvature, κ, from a function of distance to a function of time using the trench-normal subduction velocity (Heuret and Lallemand, 2005; DeMets et al., 2010). Following Mueller and Phillips (1995) (Section 8.3.3), we used the curvature of the best-fitting elastic plate model from Inversion A1, in which a constant T_e elastic plate was fitted to the observed gravity. This function, $\kappa(t)$, provides an estimate of the

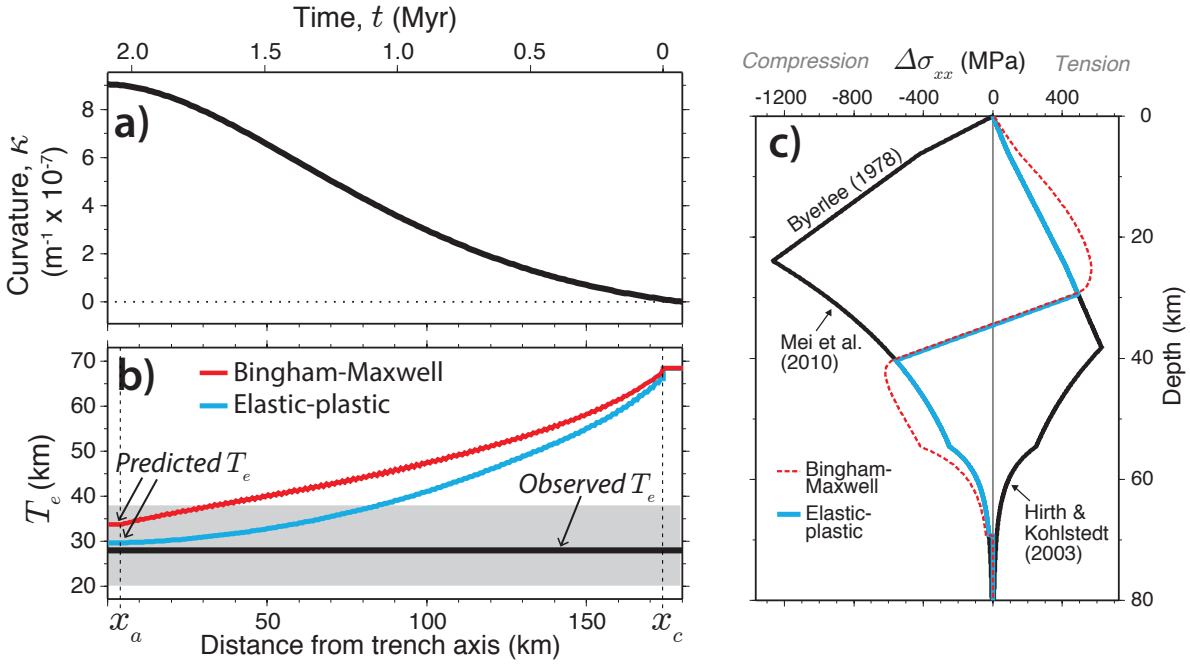

Figure 10.4: Figure illustrating the calculation of the predicted T_e at the trench-outer rise of circum-Pacific subduction zones (the profile shown is the Kuril trench-bin). (a) The plate curvature calculated from the best-fitting elastic plate model from Inversion A1. (b) For the Bingham-Maxwell and elastic-plastic model respectively, the predicted T_e that was calculated using the curvature in Figure 10.4a and the YSE in Figure 10.4c. (c) The stress distribution that was used to calculate the predicted T_e at the point x_a in Figure 10.4b. The YSE was calculated assuming a plate-cooling geotherm for the ensemble-averaged seafloor age 100 km from the trench axis.

curvature (strain) history for each point on the outer trench-slope, assuming that the shape of the trench-outer rise profile has remained fixed over time such that each point has travelled through a path described by the present day deflection seaward of that point. We set $t = 0$ at the point x_c, where the plate begins to bend with positive curvature, and $t = t_{final}$ at the point of maximum curvature, x_a (Figure 10.4a). By setting $t = 0$ at x_c, we have ignored any bending stresses that might be induced by the concave-upwards flexure that occurs seaward of the outer rise, but this is reasonable as the curvatures are of small magnitude in this region. By setting $t = t_{final}$ at x_a, we have ignored any plate unbending that might occur close to the trench axis, as the model used here cannot account for viscoelastic unloading. We then discretized $\kappa(t)$ at 10 kyr intervals and calculated the increment of curvature added at each interval, $\mathrm{d}\kappa_i$, where i is the increment number. The stress relaxation with time induced by each increment of curvature, $\Delta\sigma_{xx,i}(t-t_i)$, was then calculated using Equations 10.2 and 10.3, where t_i is the time at which the increment is applied. The total stress, $\Delta\sigma_{xx}(t)$, was then

calculated using the Boltzmann superposition principle, which for stress relaxation states that the total stress resulting from a series of step strains is equal to the sum of the stresses caused by each individual strain (Lakes, 2009, pp. 14-17):

$$\Delta\sigma_{xx}(t) = \sum_{i=1}^{i=N} \Delta\sigma_{xx,i}(t - t_i) \quad t > t_N \tag{10.4}$$

where N is the number of curvature increments that have been added prior to time t. The Boltzmann superposition principle assumes linear viscoelasticity, which is a fairly reasonable assumption as each increment in strain is small (< 0.005) and the total strain is also fairly small (< 0.05). However, we note that the assumption of linearity means that the model does not account for the possible effect of strain hardening/softening or transient relaxation. Equation 10.4 gives the total stress distribution in the plate as a function of time and therefore as a function of distance from the trench. This stress distribution was then used to calculate the bending moment as a function of distance from the trench (Equation 8.12), which was then used along with the plate curvature to calculate the predicted T_e as a function of distance from the trench (Equations 8.7 and 8.8).

Figure 10.4c shows an example of the final stress distribution at time $t = t_{final}$ ($x = x_a$) for both the Bingham-Maxwell and elastic-plastic model. This shows that for the Bingham-Maxwell model, there are unrelaxed viscoelastic stresses in the plate and therefore, as shown in Figure 10.4b, the predicted T_e is greater than that calculated using the elastic-plastic model. As the predicted T_e varies with distance from the trench, we had to choose a value to compare with the observed T_e. As in the elastic-plastic YSE-curvature method (Section 8.3.3), following Mueller and Phillips (1995), we compared the predicted T_e at the point of maximum curvature, x_a, to the observed T_e derived via Inversion A1, in which a constant T_e plate was fitted to the observed gravity profiles (Chapter 5).

10.4.2.2 Results

In Figures 10.5 and 10.6, for the segment-bins and trench-bins respectively, the observed and predicted T_e are plotted against seafloor age, where the predicted T_e was calculated assuming Byerlee's (1978) friction coefficients and hydrostatic PFP. The predicted T_e calculated assuming a Bingham-Maxwell rheology is shown as red squares, and the predicted T_e calculated assuming an elastic-plastic rheology is shown as blue diamonds. As in the previous chapters (Table 8.1), we tested five laboratory-derived LTP flow laws (Goetze, 1978; Evans and Goetze, 1979; Raterron et al., 2004; Katayama and Karato, 2008; Mei et al., 2010) and three weakened modifications of Mei et al. (2010)—M(10^4), M(10^6) and M(10^8)—where A_m (Equation 8.4) has been increased by 4, 6 and 8 orders of magnitude respectively. Figure 10.7 shows the RMS error (RMSE) between the observed and predicted T_e (left plots), and a comparison between the best-fit isotherms to the observed and predicted T_e (right plots); the top row is for the segment-bins and the bottom row is for the trench-bins. The LTP flow laws in Figure 10.7 are numbered as in Figure 10.5.

Figures 10.5 and 10.7 (top row) show that for the segment-bins, if an elastic-plastic rheology is assumed, the LTP flow laws that best fit the observed T_e are those of Evans and Goetze (1979) and Raterron et al. (2004), with RMSE < 4.6 km and best-fit isotherms that are within 15 °C of the observed best-fit isotherm. The laws of Goetze (1978) and Mei et al. (2010) also provide a good fit to the observed T_e, with RMSE < 5.1 km and best-fit isotherms that are within the 95 % confidence interval of the observed best-fit isotherm. In contrast, Figures 10.5 and 10.7 (top row) show that if a Bingham-Maxwell rheology is assumed, the laws of Goetze (1978), Evans and Goetze (1979), Raterron et al. (2004) and Mei et al. (2010) are all too strong to fit the observed T_e, with RMSE up to 7.8 km and best-fit isotherms that are above the 95 % confidence interval of the observed best-fit isotherm. If a Bingham-Maxwell rheology is assumed, the LTP laws that best fit the observed T_e are those of Katayama and Karato (2008) and M(10^4), a weakened modification of Mei et al. (2010) where A_m has been increased by 4 orders of magnitude. These laws produce RMSE < 5.2 km and best-fit isotherms that are within 21 °C of the observed best-fit isotherm. For both the elastic-plastic and Bingham-Maxwell rheology, M(10^6) and M(10^8) are too weak to fit the observed T_e. In

fact, for these flow laws, there is little difference between the predicted T_e calculated assuming a Bingham-Maxwell rheology and that calculated assuming an elastic-plastic rheology. This is because the low yield strength predicted by these laws results in a low effective viscosity ($\eta_{eff} = \Delta\sigma_{xx}^{yield}/\dot{\varepsilon}_{xx}$). This means that the Maxwell relaxation time is relatively short and therefore that the majority of the viscoelastic stresses have relaxed by the time the lithosphere reaches the trench axis.

Figures 10.6 and 10.7 (bottom row) show that for the trench-bins, if an elastic-plastic rheology is assumed, the LTP flow laws that best fit the observed T_e are those of Raterron et al. (2004) and Katayama and Karato (2008), with RMSE < 3.8 km and best-fit isotherms that are within 23 °C of the observed best-fit isotherm. The laws of Evans and Goetze (1979), Mei et al. (2010) and M(10^4) also provide quite a good fit to the observed T_e, with RMSE < 5.2 km and best-fit isotherms that are within the 95 % confidence interval of the observed best-fit isotherm. In contrast, Figures 10.5 and 10.7 (bottom row) show that if a Bingham-Maxwell rheology is assumed, the laws of Evans and Goetze (1979), Raterron et al. (2004) and Mei et al. (2010) are all too strong to fit the observed T_e, with RMSE up to 9.2 km and best-fit isotherms that are above the 95 % confidence interval of the observed best-fit isotherm. If a Bingham-Maxwell rheology is assumed, the LTP laws that best fit the observed T_e are those of Katayama and Karato (2008) and M(10^4), with RMSE < 4.1 km and best-fit isotherms that are within 19 °C of the observed best-fit isotherm.

In summary, if we assume an elastic-plastic rheology (and Byerlee's friction coefficients), the LTP laws of Goetze (1978), Evans and Goetze (1979), Raterron et al. (2004) and Mei et al. (2010) all provide a reasonably good fit to the observed T_e at circum-Pacific subduction zones. In contrast, if we assume a Bingham-Maxwell rheology, all of these laws appear too strong to fit the observed T_e, and for the law of Mei et al. (2010) to fit the observations, A_m must be increased by ~ 4 orders of magnitude.

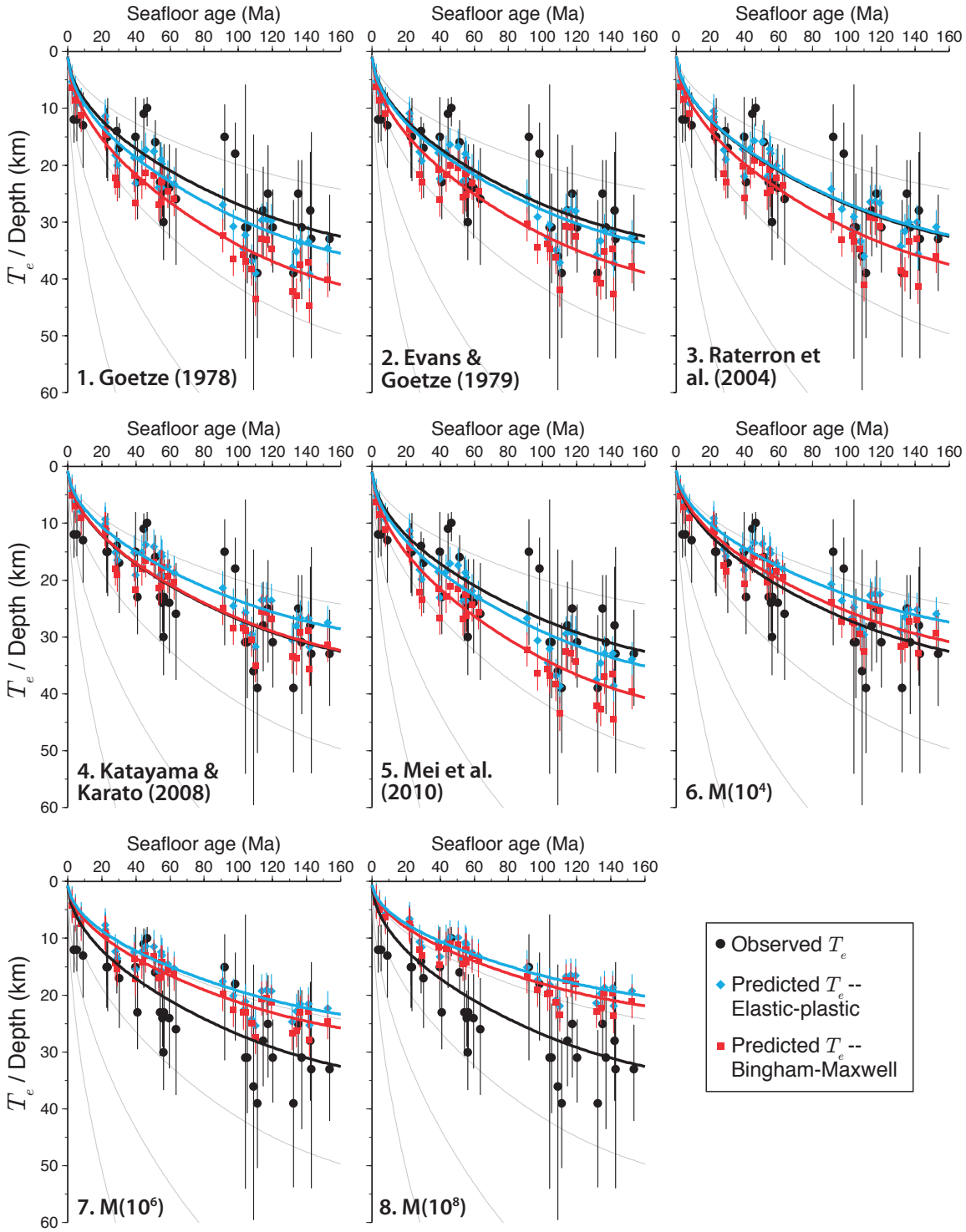

Figure 10.5: For the circum-Pacific segment-bins, the observed T_e from Inversion A1 (black dots) and the predicted T_e calculated assuming a Bingham-Maxwell (red squares) and elastic-plastic (blue diamonds) rheology respectively, plotted against seafloor age. The LTP flow law used to calculate the predicted T_e is labelled on the bottom left of each plot; in all cases, the brittle regime was calculated with Byerlee's (1978) friction coefficients and hydrostatic PFP. The grey curves show the depths to the 300, 600, 900 and 1200 °C plate-cooling isotherms. The black, red and blue isotherms are the best-fits to the observed, Bingham-Maxwell and elastic-plastic T_e respectively.

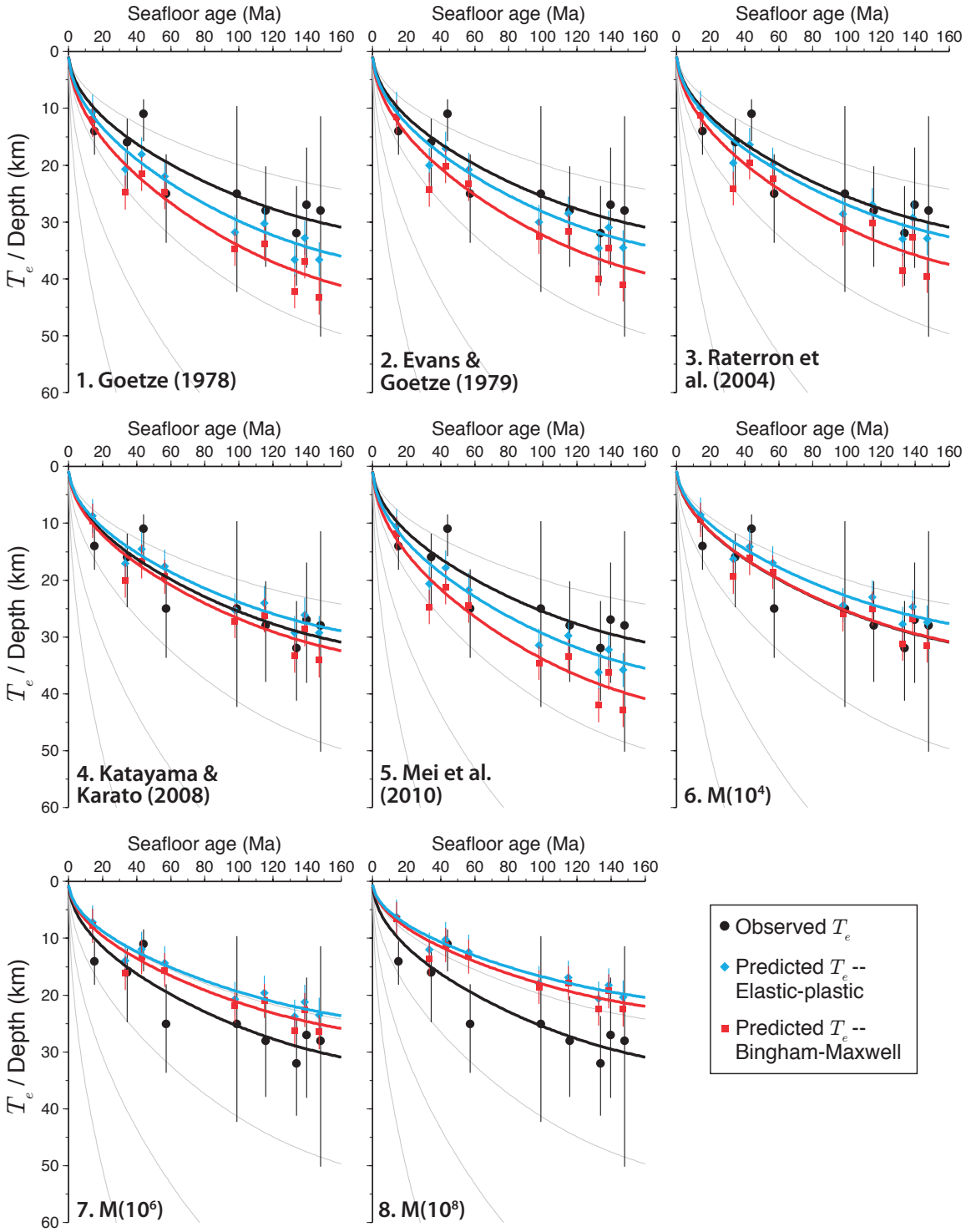

Figure 10.6: For the circum-Pacific trench-bins, the observed T_e from Inversion A1 (black dots) and the predicted T_e calculated assuming a Bingham-Maxwell (red squares) and elastic-plastic (blue diamonds) rheology respectively, plotted against seafloor age. The LTP flow law used to calculate the predicted T_e is labelled on the bottom left of each plot; in all cases, the brittle regime was calculated with Byerlee's (1978) friction coefficients and hydrostatic PFP. The grey curves show the depths to the 300, 600, 900 and 1200 °C plate-cooling isotherms. The black, red and blue isotherms are the best-fits to the observed, Bingham-Maxwell and elastic-plastic T_e respectively.

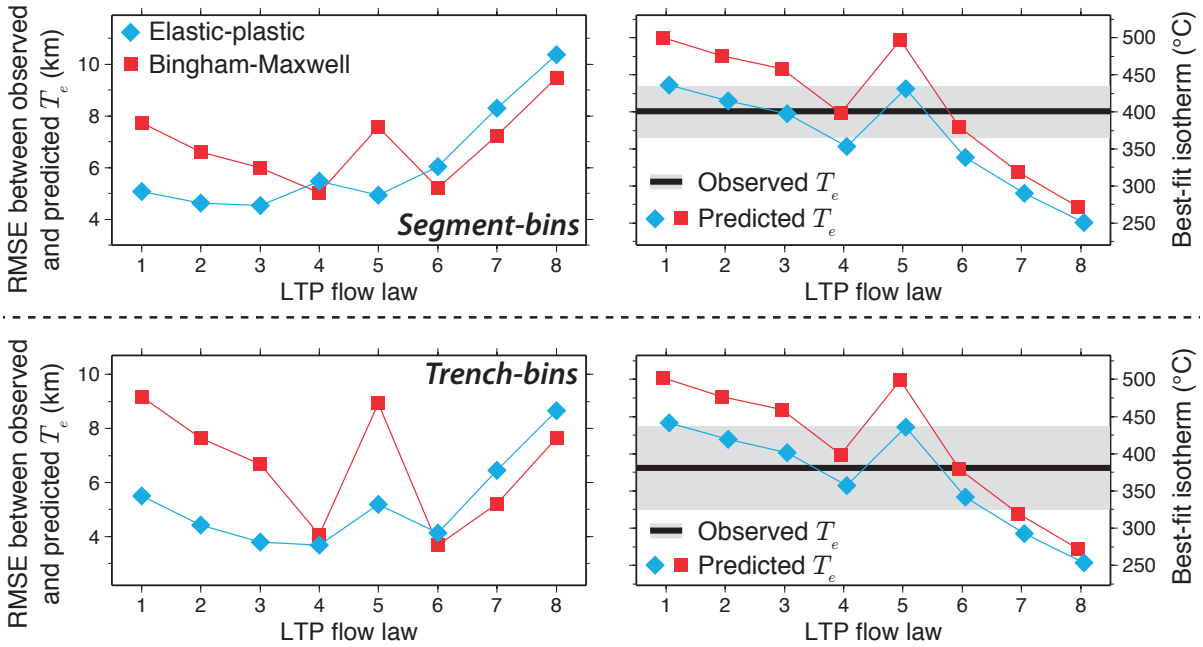

Figure 10.7: Statistics comparing the observed T_e from Inversion A1 to the predicted T_e calculated assuming a Bingham-Maxwell (red squares) and elastic-plastic (blue diamonds) rheology respectively. Byerlee's (1978) friction coefficients and hydrostatic PFP were assumed in both cases. The top row is for the segment-bins (Figure 10.5) and the bottom row is for the trench-bins (Figure 10.6). The left plots show the RMS error between the observed T_e and the predicted T_e for each LTP flow law. The right plots show the best-fit isotherm to the observed T_e (black line, where the grey shade is the 95 % confidence interval), and the best-fit isotherm to the predicted T_e for each LTP flow law. The LTP flow laws are numbered as in Figure 10.5.

10.4.3 Hawaiian Islands

10.4.3.1 Method

In the YSE-curvature method presented in Chapter 8, we derived the 'observed T_e' for the Hawaiian Islands region using a 3-D elastic plate inversion, where the volcanic surface load was estimated from observed bathymetry. Then, assuming an elastic-plastic rheology, we used the maximum chain-normal curvature of the best-fitting elastic plate model to calculate the predicted T_e, and compared this to the observed T_e. In the modified YSE-curvature method presented here, we followed the same procedure, but assumed a Bingham-Maxwell rheology when calculating the predicted T_e. To do this, we estimated the curvature history, $\kappa(t)$, by assuming that the plate curvature accrued linearly from the beginning of the shield

to post-shield building phase on Oahu (Figure 8.17), which occurred 4–2 Ma (Clague and Dalrymple, 1988), until 1 Myr afterwards (i.e from 4–1 Ma). We assumed this because the subsidence and uplift history of ocean islands, the stratigraphic patterns in the moats that surround them, and the results of viscoelastic modelling suggest that oceanic lithosphere has almost completely relaxed to its long-term flexural state within 1 Myr of loading (Watts and Zhong, 2000). However, our model of linearly accruing curvature is only an approximation, as in reality, the curvature would have accrued in an exponentially decaying fashion due to the viscoelastic nature of the lithosphere's response to loading. We then discretized $\kappa(t)$ at 10 kyr intervals and calculated the increment of curvature added at each interval, $\mathrm{d}\kappa_i$, where i is the increment number. The stress relaxation with time induced by each increment of curvature, $\Delta\sigma_{xx,i}(t - t_i)$, was then calculated using Equations 10.2 and 10.3, and the total stress, $\Delta\sigma_{xx}(t)$, was calculated using Equation 10.4. The final, present-day stress distribution (e.g. red dash in Figure 10.8b) was then used to calculated the predicted T_e for comparison to the observed T_e.

10.4.3.2 Results

In Figure 10.8a, the observed T_e (black line) is compared to the predicted T_e calculated assuming an elastic-plastic (blue diamonds) and Bingham-Maxwell (red squares) rheology respectively, where Byerlee's friction coefficients and hydrostatic PFP were assumed in both cases. This shows that because there are unrelaxed viscoelastic stresses in the Bingham-Maxwell model (e.g. red dash in Figure 10.8b), the predicted T_e is greater than that calculated assuming an elastic-plastic rheology. The difference between the two models is greatest for the strongest LTP flow laws (up to 3 km), as these predict the highest effective viscosity and therefore longest relaxation time, whilst the difference is only 1 km for the weakest law, M(10^8). The difference between the elastic-plastic and Bingham-Maxwell models is not as large at the Hawaiian Islands as at circum-Pacific subduction zones, where the difference in predicted T_e is up to 7 km for the strongest LTP flow laws. This is because at the Hawaiian Islands, the plate curvature accrued > 1 Ma, allowing more time for the viscoelastic stresses to relax than at the subduction zones, where the curvature accrued up to the present-day. Figure 10.8a shows that for both the Bingham-Maxwell and elastic-plastic model, the LTP

flow laws of Goetze (1978), Evans and Goetze (1979), Raterron et al. (2004), Katayama and Karato (2008) and Mei et al. (2010) are too strong to fit the observed T_e. For both models, in order for the law of Mei et al. (2010) to fit the observed T_e, A_m must be increased by ~ 6 orders of magnitude.

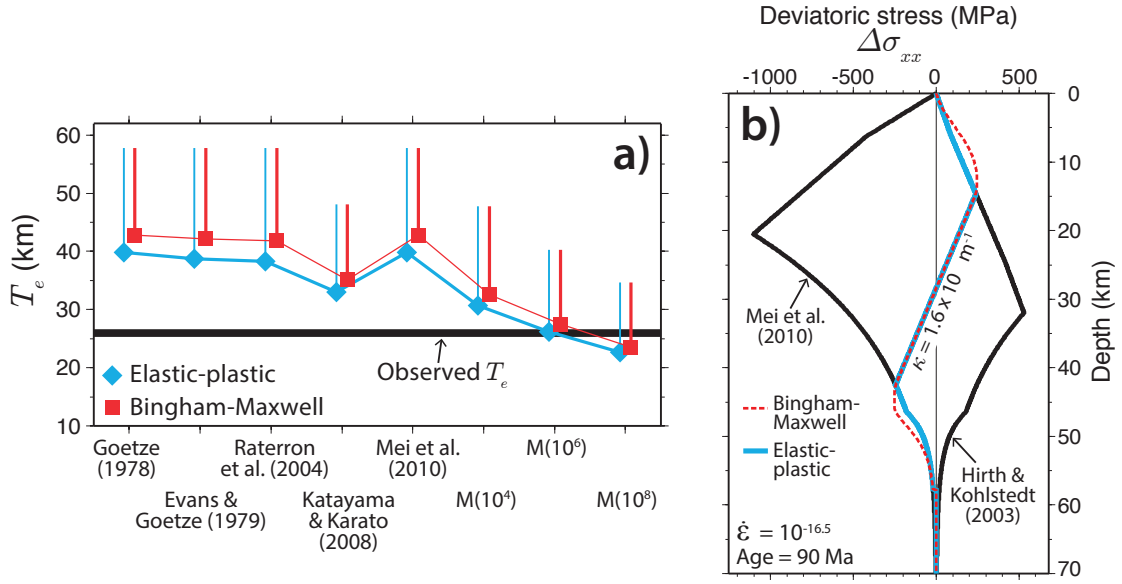

Figure 10.8: The observed T_e (black line) at the Hawaiian Islands compared to the predicted T_e calculated assuming an elastic-plastic (blue diamonds) and Bingham-Maxwell (red squares) rheology respectively. Byerlee's friction coefficients and hydrostatic PFP were assumed in both cases. The upper end of the error bar on the predicted T_e is the predicted mechanical thickness. (b) The YSE used to calculate the predicted T_e shown in Figure 10.8a for the LTP law of Mei et al. (2010). The blue curve is the elastic-plastic bending stress distribution and the dashed red curve is the final, present-day Bingham-Maxwell stress distribution.

10.4.4 Discussion

The results of the modified YSE-curvature method, in which a Bingham-Maxwell rheology was assumed, suggest that viscoelasticity can account for at least some of the discrepancy between the mantle rheology at the Hawaiian Islands and that at circum-Pacific subduction zones. At the trench-outer rise system of subduction zones, the subducting plate is continuously bending as it approaches the trench and thus much of the plate curvature has accrued over the past 100^s kyr. This means that if a Bingham-Maxwell rheology is assumed, there are significant

unrelaxed viscoelastic stresses in the plate, and therefore the predicted T_e is larger than if an elastic-plastic rheology is assumed. Consequently, the LTP laws of Goetze (1978), Evans and Goetze (1979), Raterron et al. (2004) and Mei et al. (2010) all appear too strong to fit the observed T_e at circum-Pacific subduction zones, and Mei et al. (2010) must be weakened by increasing A_m by ~ 4 orders of magnitude (assuming Byerlee's (1978) friction coefficients and hydrostatic PFP). This contrasts with the results from the elastic-plastic YSE-curvature method, where these laws provide a good fit to the observed T_e at the subduction zones. At the Hawaiian Islands, viscoelasticity has less of an effect on the predicted T_e than at the subduction zones. This is because the island of Oahu, which is primarily responsible for our observed crustal deflections, was emplaced 4–2 Ma, allowing more time for the viscoelastic stresses to relax than at the subduction zones. The effect of viscoelasticity on the predicted T_e is particularly small for the weakened modifications of Mei et al. (2010), as these predict a low effective viscosity and therefore short relaxation time. As a result, the law of Mei et al. (2010) must be weakened by ~ 6 orders magnitude whether an elastic-plastic or Bingham-Maxwell rheology is assumed.

So, we see that when viscoelasticity is taken into account, laboratory-derived flow laws for dry olivine, including that of Mei et al. (2010), appear too strong to fit the observed T_e at both circum-Pacific subduction zones and the Hawaiian Islands. However, the flow law of Mei et al. (2010) must be weakened by more at the Hawaiian Islands (A_m increased by 6 orders of magnitude) than at the subduction zones (A_m increased by 4 orders of magnitude). In addition, the wet LTP flow law of Katayama and Karato (2008) provides a good fit to the observed T_e at the subduction zones, but is too strong at the Hawaiian Islands. This suggests that some, but not all, of the discrepancy in mantle rheology between these two regions can be explained by the effects of viscoelasticity. Thus, additional weakening of the Hawaiian lithosphere is also required; as discussed above, this may occur due to thermal rejuvenation, thermal bending stresses, or magma-assisted flexure. For example, we conducted a test where we simulated thermal rejuvenation at Hawaii by increasing the temperature in the lower half of the mechanical lithosphere by an amount that increases with depth from 0 to 200 °C, which is consistent with heat flow observations (Von Herzen et al., 1989). As shown in Figure 10.9, this decreases the predicted T_e such that the law of Katayama and Karato (2008) provides

a good fit to the observed T_e and Mei et al. (2010) must be weakened by increasing A_m by $\sim$ 4 orders of magnitude. This suggests that a combination of viscoelasticity and moderate thermal rejuvenation of Hawaiian lithosphere can account for most of the apparent discrepancy between the rheology at Hawaii and that at the subduction zones.

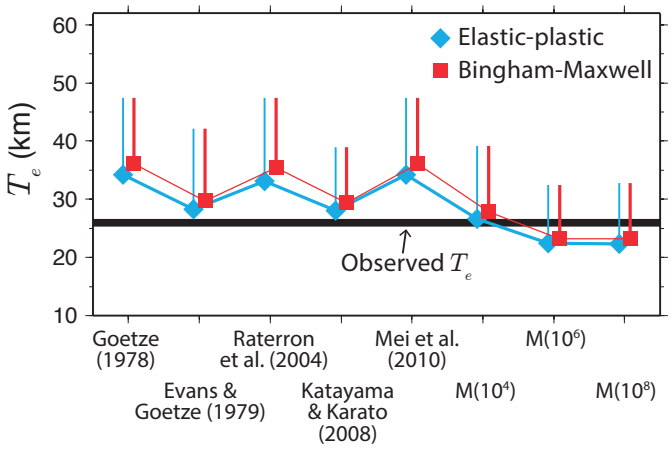

Figure 10.9: The observed T_e (black line) at the Hawaiian Islands compared to the predicted T_e calculated assuming moderate thermal rejuvenation of the lower lithosphere. The rejuvenation was simulated by increasing the temperature in the lower half of the mechanical lithosphere by an amount that increases with depth from 0 to 200 °C. Byerlee's friction coefficients and hydrostatic PFP were assumed. The upper end of the error bar on the predicted T_e is the predicted mechanical thickness.

We note that the above discussion points are reliant on the validity of the modified YSE-curvature method, in which a Bingham-Maxwell rheology is assumed. We are fairly confident of the validity of this method for the Hawaiian Islands region, as if we assume a friction coefficient of 0.7, we find that M(10^8) provides the best fit to the observations, in exact agreement with the results of Zhong and Watts (2013). However, there are several limitations of the Bingham-Maxwell YSE-curvature method. First, it assumes stress relaxation at constant strain and thus does not account for the effects of viscoelastic creep. Second, it assumes constant strain rate with time, depth and with distance from the trench at subduction zones, whilst in reality the strain rate will vary with all of these parameters. Third, the YSE-curvature method relies on assumed values of plate curvature to calculate the predicted T_e, which is subject to some uncertainty (Mueller and Phillips, 1995). The 3-D finite-element viscoelastic model that Zhong and Watts (2013) used at the Hawaiian Islands overcomes all of these shortcomings, as it accounts for creep, solves for the strain rate, and directly mod-

els the observed deflections. However, this model would be more difficult to implement at circum-Pacific subduction zones. This is because the loads and loading history are not well known at subduction zones, making it difficult to forward model the observed data as Zhong and Watts (2013) did at Hawaii. It might be possible to use an optimization or Monte-Carlo technique to invert for simple loading parameters, such as a vertical load and/or bending moment applied at the trench, but this would be very time consuming, as the 3-D finite-element model is relatively computationally-expensive.

10.5 Weakening mechanisms in the LTP regime

When viscoelasticity is accounted for in the YSE-curvature method (by assuming a Bingham-Maxwell rheology), laboratory-derived LTP flow laws for dry olivine are too strong to fit the observed T_e at both the Hawaiian Islands and circum-Pacific subduction zones. In this section, we will consider possible reasons why the olivine-rich oceanic lithosphere might be weaker than predicted by rock mechanics experiments.

10.5.1 Transient creep

At strains of less than a few percent, transient dislocation creep is commonly observed in olivine deformation experiments, where the strain rate is initially high, but then decreases with strain until it reaches a steady state (e.g., Chopra, 1997; Mei et al., 2010). Another way of saying this is that the rock is initially very weak, but then strengthens with strain until it reaches a steady state. This occurs because the dislocation structures, and therefore the dislocation velocity, evolve with strain (Karato, 2008, pp. 145-146). Based on our estimated plate curvatures, the maximum strain at circum-Pacific subduction zones is everywhere < 0.05 and at the Hawaiian Islands, the maximum strain is < 0.005. Thus the majority, if not all, of the deformation in these two regions may have occurred in the transient dislocation creep regime. Laboratory-derived LTP flow laws are generally formulated from the steady state part of deformation experiments, which may explain why they over-predict the strength of the lithosphere. The effects of transient creep might also explain why Hawaiian lithosphere

appears weaker than subducting plate lithosphere. This is because the relatively smaller strains at the Hawaiian Islands might mean that the deformation is occurring in the relatively earlier stages of transient creep, when the strain rate is at its highest and strength is at its lowest.

10.5.2 Water

It is common to assume a dry rheology for oceanic lithosphere, because beneath the mid-ocean ridge, partial melting of the upwelling mantle at depths of 70–115 km is thought to strongly partition water into the melt phase, leaving a dry (< 0.001 wt%) residuum (Karato et al., 1986; Hirth and Kohlstedt, 1996; Morgan, 1997; Karato, 2011). Accordingly, YSEs for oceanic lithosphere are generally constructed using LTP and PLC flow laws that were obtained from experiments on 'dry' olivine ($\lesssim 80$ H/10^6Si; Mei and Kohlstedt, 2000a). Indeed, except for the law of Katayama and Karato (2008), all of the LTP flow laws tested in this study are for dry olivine. However, analysis of mantle rocks and hydrothermal laboratory experiments have shown that water can be stored as hydroxyl in nominally anhydrous minerals such as olivine and pyroxene (e.g., Bai and Kohlstedt, 1992; Bell and Rossman, 1992). Deformation studies show that this water can significantly weaken olivine in the LTP regime by decreasing the Peierls stress (Katayama and Karato, 2008), and in the PLC regime by changing the charge neutrality condition and increasing the concentration of silicon point defects, thus enhancing diffusion-accommodated dislocation climb (Chopra and Paterson, 1981; Chopra and Paterson, 1984; Hirth and Kohlstedt, 1996; Karato and Jung, 2003; Karato et al., 1986; Mei and Kohlstedt, 2000a). Water may also weaken the olivine-rich mantle lithosphere via serpentinization, as serpentine has been shown to be significantly weaker than olivine in the ductile (Hilairet et al., 2007) and brittle (Escartin et al., 1997) regimes.

The discussion above suggests that if oceanic lithosphere is wetter than predicted by mid-ocean ridge melting models, this could explain why it is weaker than predicted by LTP flow laws for dry olivine. This could also explain why the LTP law of Katayama and Karato (2008), which was obtained under water saturated conditions, provides a good fit to the observed T_e at circum-Pacific subduction zones when a Bingham-Maxwell rheology is assumed (Figure

10.7). This law also provides a good fit to the observed T_e at the Hawaiian Islands when we include moderate thermal rejuvenation of the lower mechanical lithosphere (Figure 10.9).

Subducting lithosphere could be hydrated and weakened by seawater that enters the uppermost mantle via bend-faults on the outer trench-slope (e.g. Masson, 1991). These faults have been imaged cutting at least 20 km into the upper mantle and reduced P-wave velocities suggest hydration to similar depths (e.g., Ranero and Sallares, 2004; Grevemeyer et al., 2007; Contreras-Reyes et al., 2008a). However, in the Hawaiian Islands region, bend-faults are unlikely to be as pervasive or penetrate as deep, owing to the relatively lower plate curvatures in the flexural moats/bulges that surround the islands. Warren and Hauri (2014) found that water contents in abyssal peridotites, including samples from the Tonga trench, are higher than expected for residues of melting, which might indicate that oceanic lithosphere is generally wetter than predicted. They found olivine water concentrations of 140–550 H/10^6Si, which is much higher than the concentrations in deformation experiments on dry olivine ($\lesssim$ 80 H/10^6Si). Warren and Hauri (2014) suggested that the high water contents in abyssal peridotites could be explained by the addition of water by late-stage melts trapped in the shallow ($<$ 20–30 km) mantle, which would limit the depths to which water weakening might occur. Another possible explanation is that thermal cracking to depths of 30–50 km provides fluid (seawater) pathways that are pervasive throughout the oceanic lithosphere (Korenaga, 2007).

10.5.3 Grain size

Dislocation creep in olivine is generally considered to be grain-size insensitive (e.g., Karato et al., 1986; Karato, 2010). However, in experiments conducted under 'wet' conditions by Chopra and Paterson (1981) and Chopra (1986), the dislocation creep strength of fine-grained (7 µm) olivine samples was found to be greater than that of coarser-grained natural dunites (100–900 µm). They suggested this could be explained by the Hall-Petch effect (Hall, 1951; Petch, 1953), whereby the flow strength increases with decreasing grain size because grain boundaries impede the motion of dislocations. Perhaps, therefore, naturally occurring lithospheric rock is weaker than found in the laboratory due to the relatively larger grain size (1–10 mm in nature vs. 5–20 µm in the laboratory).

Laboratory studies (e.g. Karato et al., 1986) and observations of mylonites in shear zones (e.g. Warren and Hirth, 2006) suggest that grain size reduction during localized deformation can lead to a transition from dislocation to diffusion creep, resulting in long-term weakening of the lithosphere. This process could reduce the flexural rigidity of oceanic lithosphere, particularly if the bend-faults associated with plate flexure localize deformation (e.g. Ranero et al., 2003), or if thermal cracking provides localized zones of weakness that are pervasive throughout the oceans (Korenaga, 2007).

10.5.4 Pyroxenes

In this study, we have approximated the rheology of oceanic lithosphere as that of pure olivine. This a common assumption, as olivine is the most abundant lithospheric mineral and was also thought to be the weakest (Zimmerman and Kohlstedt, 2004). However, the results of a recent laboratory deformation study suggest that the strength of orthopyroxene is much lower than that of olivine if the grains are favourably oriented (Ohuchi et al., 2011). Thus, small inclusions of orthopyroxene could weaken the mantle lithosphere. Furthermore, the water solubility of orthopyroxene and clinopyroxene is much higher than that of olivine (Bell and Rossman, 1992; Warren and Hauri, 2014), and deformation studies show that the water-weakening effect is greater for clinopyroxene than for olivine (Chen et al., 2006). Thus, inclusions of pyroxene might further weaken the lithosphere if water is present.

10.5.5 Extrapolation from the laboratory to geological conditions

Inferring the plastic deformation processes that occur during lithospheric deformation involves extrapolation of flow laws from the laboratory to geological conditions. This includes a ~ 10 orders of magnitude decrease in strain rate and a 2–3 orders of magnitude increase in grain size, as well as extrapolations in pressure and length-scale. It is possible that with these extrapolations there is a change in deformation mechanism (Karato, 2010), or that the flow laws do not scale as predicted by laboratory studies. It is important, therefore, to continue to investigate lithospheric deformation mechanisms via observations of seismic anisotropy and dislocation microstructures in naturally deformed rocks.

10.5.6 Semi-brittle deformation

The YSEs used in this study were constructed under the assumption that brittle and ductile processes occur independently. However, in reality, there exists a poorly understood, transitional semi-brittle regime where deformation occurs via a mixture of brittle and ductile processes (e.g. Kohlstedt et al., 1995). In this regime, the individual brittle or ductile failure laws are likely to provide only an upper bound on the yield strength, and thus semi-brittle processes could explain why the lithosphere appears weaker than predicted by laboratory-derived flow laws. To test if this is likely to be an important factor in our study regions, we checked if our calculated flexural bending stresses are large enough to cause failure in the semi-brittle deformation regime. To do this, we assumed that the transition between the brittle and semi-brittle regimes (the brittle-ductile transition) occurs when the ductile yield strength is five times the brittle yield strength (Kohlstedt et al., 1995). We assumed that the transition between the semi-brittle and ductile regimes (the brittle-plastic transition) is defined by the Goetze criterion, which states that brittle processes will contribute to deformation for deviatoric stresses larger than the overburden pressure (Kohlstedt et al., 1995). We found that in both study regions, the relatively deep, compressional flexural stresses never exceed the overburden pressure and therefore semi-brittle deformation is unlikely to be important at these depths. At the subduction zones, the relatively shallow, tensional flexural stresses are large enough that semi-brittle deformation is predicted. However, this occurs over a depth interval of only 0–10 km, depending on the profile and on the LTP law, and thus is unlikely to have a large effect on the flexural rigidity. Furthermore, in the Hawaiian Islands region the relatively low curvature means that the shallow flexural stresses are not large enough to cause semi-brittle behaviour. It is therefore unlikely that semi-brittle deformation can account for the apparent weakness of the lithosphere in both study regions.

10.6 Implications for plate tectonics

Geodynamicists have done much work to determine the conditions that allow plate tectonics to occur on Earth (Bercovici, 2003). Numerical convection models have consistently shown

that for plate-style convection to occur, the average yield stress in the lithosphere must be $\lesssim 200$ MPa (e.g., Tackley, 2000; Richards et al., 2001; Foley and Becker, 2009). This is much less than the maximum yield stress predicted by laboratory-derived YSEs for dry olivine. For example, for old lithosphere, the dry olivine LTP flow laws tested in this study predict yield stresses of up to 1200–1500 MPa if Byerlee's friction coefficients are assumed, or 600–800 MPa if $\mu_f = 0.3$ is assumed. This has led to the suggestion that for plate tectonics to occur, oceanic lithosphere must be weaker than predicted by experimental rock mechanics. This is in agreement with our findings at the Hawaiian Islands and, if a Bingham-Maxwell rheology is assumed, the trench-outer rise of circum-Pacific subduction zones. However, the maximum yield stresses predicted by the weakened modifications of Mei et al. (2010)—M(10^4), M(10^6) and M(10^8)—are also greater than predicted by convection models. For old lithosphere, these laws predict stresses up to 700–1000 MPa if Byerlee's friction coefficients are assumed, or 350–500 MPa if $\mu_f = 0.3$ is assumed. However, convection modelling studies have generally assumed a constant yield stress with depth, so it is not immediately clear how this should compare with the depth-dependent yield stress used in this study. In addition, it has been pointed out that the yield stress predicted by convection models is more likely to represent the strength of localized, weak fault zones at plate boundaries, rather than the strength of the plate interiors (e.g., Richards et al., 2001; Karato, 2010). Thus, these values might be unsuitable for comparison with our estimates of the lithosphere's yield strength.

10.7 Chapter summary

The results of the elastic-plastic YSE-curvature method (Chapter 8) and elastic-plastic plate modelling (Chapter 9) reveal an apparent discrepancy between the mantle rheology at the trench-outer rise of circum-Pacific subduction zones and that at the Hawaiian Islands. This discrepancy can be summarised by stating that the lithospheric rocks at the Hawaiian Islands appear weaker than at circum-Pacific subduction zones. In this chapter, we have discussed some possible reasons for this discrepancy. The key points are as follows:

- We used a modified YSE-curvature method, in which a Bingham-Maxwell rheology was

assumed, to show that viscoelasticity can account for at least some of the discrepancy. At subduction zones, the subducting plate is continuously bending such that much of the strain has accumulated within the past 100^s kyr, and thus there are significant unrelaxed viscoelastic stresses. In contrast, the island of Oahu was emplaced in a discrete burst of volcanism 4–2 Ma, allowing enough time for most of the viscoelastic stresses to have relaxed.

- The results of the Bingham-Maxwell YSE-curvature method suggest that laboratory derived LTP flow laws for dry olivine, including that of Mei et al. (2010), are too strong to fit the observed T_e at both circum-Pacific subduction zones and the Hawaiian Islands. If we assume Byerlee's friction coefficients and hydrostatic PFP, Mei et al. (2010) must be weakened by increasing A_m by ~ 4 and ~ 6 orders of magnitude in these regions respectively.

- As an alternative to, or in addition to, the effects of viscoelasticity, the relative weakness of the Hawaiian lithosphere could also be explained by: thermal rejuvenation by the Hawaiian plume; constructive interference between thermal stresses and concave-upwards bending stresses; magma-assisted flexure.

- A combination of viscoelasticity and moderate thermal rejuvenation of the Hawaiian lithosphere can explain almost all of the discrepancy in rheology between the two study regions. When both of these factors are accounted for, the wet LTP flow law of Katayama and Karato (2008) provides a good fit to the observed T_e at both the Hawaiian Islands and circum-Pacific subduction zones. In addition, for both study regions, the law Mei et al. (2010) must be weakened by increasing A_m by ~ 4 orders of magnitude.

- There are many factors that might cause oceanic lithosphere to be weaker than predicted by laboratory-derived LTP flow laws for dry olivine. For example: flexural deformation might occur in the transient creep regime; the lithosphere might be wetter than is predicted by mid-ocean ridge melting models; weakening by strain localization and grain size reduction; the weakening effect of small inclusions of pyroxene; problems with the extrapolation from laboratory conditions to geological conditions; semi-brittle deformation.

Chapter 11

Conclusions and future work

11.1 Conclusions

In this thesis, we have modelled flexural observations with the aim of better understanding spatial variations in the rigidity of oceanic lithosphere and how they relate to plate age, thermal structure and subduction-related processes. In addition, we have also used these observations to test the predictions of laboratory-derived flow laws for olivine, thus providing a link between large-scale, long-timescale geological deformation and small-scale, short-timescale laboratory deformation. In concluding, we will address the three main aims that were set out in the introduction, before providing a brief summary:

1. To re-assess the relationship between T_e and the age of oceanic lithosphere at the time of loading.

In light of the recent study of Bry and White (2007), who found no relationship between T_e and plate age at global subduction zones, we have modelled ensemble-averaged, trench-normal profiles of free-air gravity at the trench-outer rise system of circum-Pacific subduction zones. The observations were modelled using a broken elastic plate model in which a bending moment M_0 and vertical shear force V_0 were applied at the plate-break (trench axis). An inversion procedure was used to find the best-fitting T_e and end-loads, where T_e was iterated over a range of values and M_0 and V_0 were optimized using a damped least squares algorithm.

The results from Inversion A1, in which a constant T_e plate was fitted to the observations, show that there is a first-order increase in T_e with the age of the subducting plate. The T_e increases from 10–15 km at the Middle America trench to generally > 25 km for lithosphere older than 80 Ma, and is best fit by the depth to the 400 ± 35 °C and 380 ± 57 °C plate-cooling isotherm for the segment-bins and trench-bins respectively. The results from Inversion A2, in which a variable T_e plate was fitted to the observations, also show a general increase in T_e with plate age. This is particularly true for the landward T_e, which is well constrained due to the relatively high signal-to-noise ratio in the observed gravity at the outer trench-slope. For example, for the segment-bins, the landward T_e increases from 11–14 km at the Middle America trench to 19–31 km for lithosphere older than 80 Ma, and is best fit by the depth to the 349 ± 22 °C isotherm.

Our finding that there is a general increase in T_e with plate age, and that it is reasonably well fit by the depth to a plate-cooling isotherm, suggests that thermal structure exerts first-order control over the lithosphere's rigidity. This is consistent with the ideas that oceanic lithosphere cools as it moves away from the mid-ocean ridge and that ductile creep processes in lithospheric minerals are strongly temperature-dependent. However, we are not suggesting that the best-fit isotherms to the T_e-age relationship reflect the depth to any physical boundary in the lithosphere. This is because T_e reflects the depth-integrated stress across the brittle, elastic and ductile deformation regimes, rather than any physical thickness.

Although there is a general increase in T_e with plate age at circum-Pacific subduction zones, there is some scatter. We suggest that this is due to a combination of inaccuracies in the T_e estimates and the influence of factors other than plate age on the lithosphere's rigidity. Inaccuracies in T_e estimates may be caused by: short-wavelength bathymetric noise, for example due to hotspot volcanism; failure of the 2-D elastic plate model model to account for arcuate trench geometry or oblique plate convergence; trade-offs between T_e and the end-loads, M_0 and V_0; failure of the elastic plate model to account for complex loading histories, such as 'elastic unloading' or the formation of a lithospheric 'hinge'. Factors other than plate age that may affect the rigidity of oceanic lithosphere include: thermal anomalies, for example due to hotspot-induced thermal rejuvenation; variations in plate weakening due to variations in plate curvature and mantle hydration; plate weakening by axial normal stresses; variations

in the style of bend-faulting on the outer trench-slope.

Our finding that there is a general increase in T_e with the age of subducting lithosphere is not consistent with the results of Bry and White (2007). In order to understand this discrepancy, we conducted a series of modified inversions, where we inverted both the observed circum-Pacific gravity profiles and a suite of synthetic profiles. The results suggest that the discrepancy can be explained by differences in: the treatment of the long-wavelength gravity anomalies, the gravity calculation method, the optimization constraint placed on M_0, and the trench axis location. Of these differences, the treatment of the long-wavelength anomalies is the most important factor: whilst we removed a long-wavelength spherical harmonic gravity signal prior to inversion, Bry and White (2007) inverted for a linear gravimetric slope. Results from inversion of the synthetic profiles suggest that this has caused Bry and White (2007) to underestimate the rigidity of older, stronger lithosphere, thus masking the relationship between T_e and plate age. This shows that, where possible, it is important to use observations to limit the number of free parameters in flexural inversions. Ideally, the only unknowns should be T_e and the loading conditions (unless the loads are already known, such as at seamounts and ocean islands).

2. To assess the amount of plate weakening that occurs at the trench-outer rise system of oceanic subduction zones.

Several studies of individual oceanic subduction zones have suggested that the subducting plate is weakened as it bends into the trench. Indeed, our inversion results show that in general, an elastic plate of constant T_e cannot simultaneously fit the steepness of the outer trench-slope and the wavelength and amplitude of the outer rise. Therefore, in order to assess the extent of plate weakening at circum-Pacific subduction zones, in Inversion A2, we modelled the observed gravity profiles using a variable T_e elastic plate. We inverted for two T_e values—a 'landward T_e' and a 'seaward T_e'—where prior to inversion, observed plate curvatures were used to define the location of the linear transition between the two values. Results show that the variable T_e elastic plate significantly improves the fits to the observed gravity, where the RMS error is improved by a mean of 39 % and by up to 73 %. The plate weakens in 42 out of 43 best-fit models, where the average reduction in T_e between the seaward and

landward values is 51 ± 11 % and the range is 20–72 %.

The results of Inversion A2 suggest that significant plate weakening is a ubiquitous feature of the outer trench-slope and outer rise seaward of subduction zones. This plate weakening is caused primarily by bending-induced inelastic yielding—a combination of shallow, brittle and deep, ductile failure—which is evidenced by observations of seismicity and bend-faulting on the outer trench-slope. In addition, these bend-faults may cause further weakening by providing a pathway for seawater to hydrate and serpentinize the uppermost mantle. This is evidenced by, for example, reduced P-wave velocities and reduced heat flow at the outer trench-slope.

3. To constrain the mantle rheology of oceanic lithosphere using observations of flexure.

Zhong and Watts (2013) used a 3-D finite-element viscoelastic model to show that laboratory-derived LTP flow laws for olivine are too strong to fit observations of flexure in the Hawaiian Islands region. To test if this is generally true of oceanic lithosphere, we used two methods to constrain the LTP rheology at the trench-outer rise system of circum-Pacific subduction zones, where we tested four flow laws for dry olivine (Goetze, 1978; Evans and Goetze, 1979; Raterron et al., 2004; Mei et al., 2010) and one for wet olivine (Katayama and Karato, 2008). In the first method, dubbed the 'YSE-curvature method', the T_e derived by inversion of observed ensemble-averaged gravity profiles was compared to the T_e predicted by elastic-plastic Yield Strength Envelopes (YSE) based on laboratory-derived failure criteria for frictional sliding and ductile creep. In the second approach, the observed ensemble-averaged gravity profiles were modelled using a broken elastic-plastic plate model in which the depth-dependent yield stress was defined by laboratory-derived YSEs.

The results of both methods show that regardless of the assumed friction coefficient, all of the laboratory-derived LTP flow laws provide a reasonably good fit to the observations at circum-Pacific subduction zones. However, it is not possible to reliably distinguish between the laws due to a combination of factors: they all predict fairly similar flexural rigidities; there is uncertainty in the assumed friction coefficient; there is uncertainty in the assumed thermal structure, as there may be thermal anomalies in the lithosphere; there is scatter in

the observed T_e estimates and noise in the observed gravity, as discussed above.

The results described above contrast strongly with the findings of Zhong and Watts (2013) at the Hawaiian Islands. Therefore, to test the validity of the of the YSE-curvature method and the elastic-plastic plate model, we also used these approaches to constrain the rheology in the Hawaiian Islands region. The results of both methods show that regardless of the assumed friction coefficient, all of the laboratory-derived LTP laws for dry olivine are much too strong to fit the observations in this region. In order for the law of Mei et al. (2010) to fit the observations, the pre-exponential factor, A_m, must be increased by 4–8 orders of magnitude, depending on the method and the assumed friction coefficient. This is in general agreement with Zhong and Watts (2013), who found that A_m must be increased by 6–8 orders of magnitude; the slight discrepancy is probably because they assumed a viscoelastic rheology, whilst we assumed an elastic-plastic one. The results also show that the laboratory-derived LTP law that best fits the Hawaiian observations is the wet olivine law of Katayama and Karato (2008), which provides a particularly good fit if a low friction coefficient is assumed in the elastic-plastic plate model.

The results of the YSE-curvature method and elastic-plastic plate modelling suggest that there is a discrepancy between the LTP rheology at the Hawaiian Islands and that at the trench-outer rise system of circum-Pacific subduction zones. Laboratory-derived flow laws for dry olivine are much too strong to fit the observations at the Hawaiian Islands, but provide a reasonably good fit to the observations at subduction zones. Another way of saying this is that the lithospheric rocks in the Hawaiian Islands region appear weaker than those seaward of subduction zones.

One possible cause of this discrepancy is the difference in the timescale of loading and the implications that this has for the viscoelastic behaviour of the lithosphere. Previous studies have shown that on relatively short timescales, oceanic lithosphere exhibits viscoelastic behaviour, such that following loading, it takes 1–2 Myr to relax from the initial seismic thickness to the long-term elastic thickness. At the trench-outer rise system of subduction zones, the subducting plate is continuously bending, such that much of the strain has accumulated within the past 100^{s} kyr. In contrast, the Hawaiian island of Oahu was emplaced in a dis-

crete burst of volcanism 4–2 Ma. Thus, it is likely that there are more unrelaxed viscoelastic stresses at the subduction zones than at the Hawaiian Islands, which could explain why the subducting lithosphere appears stronger.

To explore the effects of viscoelasticity, we developed a modified YSE-curvature method in which a Bingham-Maxwell rheology is assumed, and used it to constrain the rheology in both regions. The results show that viscoelasticity can account for at least some of the discrepancy in rheology between the trenches and Hawaiian islands, as the laboratory-derived LTP laws for dry olivine are too strong to fit the observed T_e in both regions. However, the flow law of Mei et al. (2010) must be weakened by more at the Hawaiian Islands than at the subduction zones, which could be due to the effects of thermal rejuvenation, magma-assisted flexure, or concave-upwards bending in the former region. For example, tests show that a combination of viscoelasticity and moderate thermal rejuvenation of the Hawaiian lithosphere can explain almost all of the discrepancy. When both of these factors are accounted for and Byerlee's friction coefficients are assumed, the dry olivine LTP laws are too strong to fit the observed T_e at both the Hawaiian Islands and circum-Pacific subduction zones, and the law of Mei et al. (2010) must be weakened by increasing A_m by ~ 4 orders of magnitude in both regions. In addition, the wet LTP law of Katayama and Karato (2008) provides a good fit to the observed T_e in both regions.

The results of the modified YSE-curvature method, in which a Bingham-Maxwell rheology was assumed, suggest that oceanic lithosphere is generally weaker than predicted by laboratory-derived LTP flow laws for dry olivine. There are many reasons why this might be the case. For example: flexural deformation might occur in the transient creep regime; the lithosphere might be wetter than is predicted by mid-ocean ridge melting models; weakening by strain localization and grain size reduction; the weakening effect of small inclusions of pyroxene; problems with the extrapolation from laboratory conditions to geological conditions; semi-brittle deformation. It has been suggested from geodynamic convection models that a relatively weak lithosphere, much weaker than predicted by experimental rock mechanics, is required for plate tectonics to occur on Earth. Thus, our finding that LTP flow laws for dry olivine are generally too strong to fit flexural observations (if a Bingham-Maxwell rheology is assumed) may have implications for the existence of plate tectonics.

4. Summary

- There is a general increase in T_e with plate age at circum-Pacific subduction zones, in agreement with plate-cooling models and models for temperature-dependent creep in lithospheric minerals. However, there is scatter in the T_e-age relationship due to a combination of inaccuracies in the T_e estimates and the influence of factors other than plate age on the lithosphere's rigidity.

- The subducting plate is significantly weakened at the outer trench-slope of circum-Pacific subduction zones due to bending-induced inelastic yielding, and mantle hydration and serpentinization via bend-faults.

- Elastic-plastic YSEs and elastic-plastic plate models reveal an apparent discrepancy between the mantle rheology at the Hawaiian Islands and that at the trench-outer rise system of circum-Pacific subduction zones. Laboratory-derived flow laws for dry olivine are much too strong to fit the observations at the Hawaiian Islands, but provide a reasonably good fit to the observations at subduction zones.

- Bingham-Maxwell YSEs suggest that viscoelasticity can account for at least some of the discrepancy in rheology between the two study regions, and that laboratory-derived LTP laws for dry olivine are too strong to fit the observed T_e in both regions. The remaining discrepancy can be explained by moderate thermal rejuvenation of the Hawaiian lithosphere.

11.2 Future work

In this section, we will address some of the limitations of, and questions raised by, this thesis, and will suggest avenues for future research that might address these issues.

We suggest that the increase in T_e with the age of oceanic lithosphere at the time of loading is robust, as it has also been resolved by several previous authors (e.g., Watts, 1978; Caldwell and Turcotte, 1979; Watts and Zhong, 2000). However, with the advent of satellite-derived

grids of bathymetry and gravity, our ability to constrain T_e accurately has greatly improved because, for example, these datasets allow us to produce ensemble-averaged 2-D profiles and to model 3-D data. In addition, modern computation techniques allow us to invert large numbers of observations with relative ease. Therefore, we can improve our understanding of the T_e-age relationship by modelling large, consistent datasets using a consistent methodology. This would overcome one of the problems inherent in the T_e compilation of Watts and Zhong (2000): that the T_e estimates were all derived from different datasets using different techniques. For example, the inversion methodology used in this thesis could be extended to global subduction zones, and could also be modified to constrain the T_e at global seamounts, ocean islands and fracture zones. Spectral methods could also be used to constrain the T_e at these features. For example, Kalnins and Watts (2009) recently used a moving window admittance technique to show that T_e in the Western Pacific ocean is, to first order, controlled by plate age at the time of loading.

We have found that there is scatter in the relationship between T_e and plate age, and thus it is important to better understand how other factors affect the flexural rigidity and deformation at the trench-outer rise system. For example, recent studies have used numerical models to investigate the dynamics and mechanisms of bend-faulting on the outer trench-slope (Naliboff et al., 2013; Zhou et al., 2015). It would be interesting to use these models to better understand how the style of bend-faulting affects the geometry of the outer rise and the flexural rigidity.

We have shown that plate weakening is a ubiquitous feature of the outer trench-slope of circum-Pacific subduction zones, and that it is coincident with bend-faulting. It would also be interesting to investigate how the nature of bend-faulting is affected by plate age, flexural rigidity and plate curvature, and how these submarine faults compare to those on land. For example, we have begun a study that aims to do this by using swath bathymetry to map the length, offset and geometry of bend-faults at the Tonga-Kermadec and Chile trenches.

The elastic and elastic-plastic plate models used in this study are static. This is not a problem as far as constraining T_e is concerned, as T_e estimates are implicitly derived from a static elastic plate model. However, this may be a problem for constraining mantle rheology,

particularly at the trench-outer rise system, where the subducting plate is moving towards the trench. The elastic and elastic-plastic plate models fail to capture the dynamics of this system and therefore fail to account for, for example, viscoelasticity and strain history. Therefore, we tried to account for viscoelasticity by using the Bingham-Maxwell YSE-curvature method. However, this is a fairly crude method, as it does not account for, for example, the motion of the subducting plate, viscous creep and depth-variations in strain rate. Therefore, it is important to use more advanced models to constrain the mantle rheology at subduction zones. For example, the 3-D finite-element viscoelastic model of Zhong and Watts (2013) could be applied to the trench-outer rise system. In addition, Farrington et al. (2014) recently used a viscoelastic plate model to show that viscoelasticity is important during bending and unbending of the subducting slab, and that it affects the geometry of the outer rise. Their model could be adapted to use laboratory-derived flow laws to prescribe the effective viscosity. However, one difficulty with viscoelastic modelling of trench-outer rise observations is that, unlike at seamounts and ocean islands, the loads and loading history are not known. An inversion procedure might therefore be used to constrain simple end-loads, such as a vertical shear force and bending moment, but this would be very computationally expensive owing to the complexity of viscoelastic models.

The elastic-plastic plate model used here and the viscoelastic model used by Zhong and Watts (2013) assume that the shallow, brittle deformation of the lithosphere is continuous; whilst in reality, deformation occurs along localized faults. In addition, the use of frictional sliding laws is based on the assumption that optimally oriented faults pre-exist everywhere, which is obviously not the case. These limitations might have implications for constraining mantle rheology in the ductile regime. Therefore, it would be interesting to incorporate models for fault initiation and growth (e.g. Zhou et al., 2015) into elastic-plastic and viscoelastic models of lithospheric deformation. The elastic-plastic and viscoelastic models also assume that ductile deformation occurs continuously, whilst in nature, it may be localized along ductile shear zones (e.g., Karato et al., 1986, Warren and Hirth, 2006). Thus, future models of lithospheric deformation could incorporate ductile strain localization and the subsequent transition to diffusion creep. In addition, strain localization models could also be incorporated into numerical convection models (e.g., Tackley, 2000; Richards et al., 2001; Foley and Becker,

2009), as this would generate more accurate constraints on the lithospheric strength required for plate tectonics to occur on Earth. Furthermore, it would be useful for these convection models to incorporate depth-dependent, laboratory-derived yield stress, as this could be used to directly test if laboratory flow laws are consistent with the existence of plate tectonics.

In general, it is important to continue to use geophysical and geological observations to test the predictions of laboratory-derived flow laws, thus providing a feedback between the lab and nature. In nature, it would be useful to better constrain the water content of oceanic lithosphere, and to use more observations of flexure to constrain rheology. In the laboratory, it would be beneficial to: further study transient creep in lithospheric minerals and to think about what role this may play in lithospheric deformation; to further investigate the rheology of polymineralic rocks; and to constrain the rheology in the semi-brittle deformation regime.

Appendix A

Tectonic setting of circum-Pacific subduction zones

This appendix contains a description of the tectonic setting of each of the circum-Pacific subduction zones that were modelled in this study. Throughout this appendix, unless stated otherwise, quoted seafloor ages refer to the (segment-bin) bin-averaged age 100 km seaward of the trench axis. Quoted trench depths refer to the 'relative trench depth' — the trench depth relative to the abyssal seafloor depth —, which we calculated from age-corrected, sediment-corrected, ensemble-averaged bathymetry profiles.

A.1 Middle America

At the Middle America trench (Figure A.1), the Cocos plate is subducting beneath the Caribbean plate at a trench-normal convergence rate that increases from 50 mm/yr in the east to 80 mm/yr in the west. In the region considered in this study, the lithosphere was formed at the East Pacific Rise, whilst SW of the study area, the lithosphere was formed at the Cocos-Nazca spreading centre—this area is not considered in this study due to the morphological influence of the Cocos Ridge, which is generally considered to be a trace of the Galápagos Hotspot (Walther, 2003). The trench is segmented by the Tehuantepec Ridge,

which is thought to be a fracture zone that formed as a transform fault on the Guadalupe plate prior to 15 Ma (Manea et al., 2005). West of the Tehuantepec Ridge, there is an east to west increase in seafloor age from 4 Ma to 9 Ma, whilst there is a 14 Ma increase in age across the ridge. East of the ridge, there are two fracture zones with left-lateral offsets, but the of strike of the trench means that the age of the subducting seafloor remains approximately constant at $\sim$ 23 Ma. West of the Tehuantepec Ridge, the incoming isochrons strike $\sim 50°$ from trench-parallel, whilst to the east, the isochrons strike $< 15°$ from trench-parallel. There is an eastwards increase in trench depth from 900 m in segment-bin 22 to 1800 m in bin 26; the depth then decreases to 1100 m in bin 27.

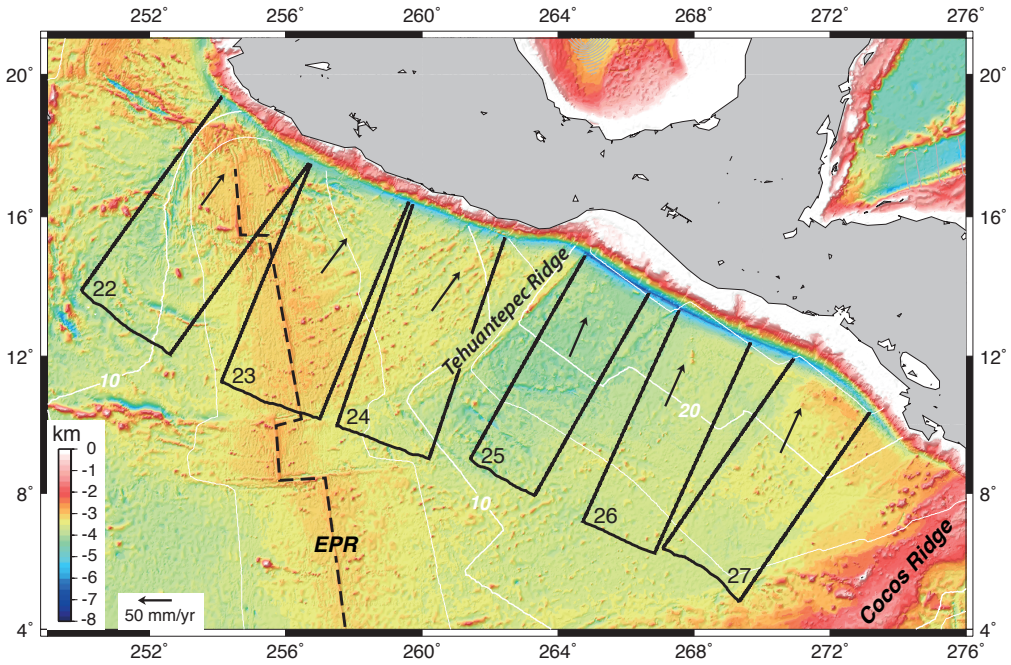

Figure A.1: Bathymetry map of the Middle America trench (GEBCO_08 30 $\times$ 30 second, Ioc et al., 2003). The solid white lines show seafloor isochrons at 5 Ma intervals (Müller et al., 2008, v3.2), and the dashed black line marks the East Pacific Rise (EPR). The segment-bins are shown and numbered in solid black, and plate convergence vectors from the MORVEL plate motion model (DeMets et al., 2010) are shown as black arrows.

A.2 Peru-Chile

At the Peru-Chile trench (Figure A.2), the Nazca plate is subducting beneath South America at a trench-normal convergence rate of 55–71 mm/yr. North of the Juan Fernández Ridge, the Nazca lithosphere was formed at the East Pacific Rise, whilst to the south, the lithosphere was formed at the Chile Rise. Between 18°S and 22°S, there is a southwards change in the strike of the trench from NW to NNE — a feature known as the Arica Bend (Contreras-Reyes and Osses, 2010). One result of this is that north of the ridge, the incoming abyssal hill fabric strikes $< 25°$ from trench-parallel, whilst to the south, the fabric strikes $> 30°$ from trench-parallel. This manifests in a southwards change in the style of bend-faulting on the outer trench-slope: from reactivated abyssal hill faults in the north to new, trench-parallel faults in the south (Massell, 2002; Ranero et al., 2005). Another consequence of this trench geometry is that the subducting lithosphere is oldest (53 Ma) in the Arica Bend region, decreasing to 29 Ma in the north of the study area and 39 Ma in the south. The trench is intersected by a number of right-lateral offset fracture zones and a number of aseismic ridges: the Nazca Ridge, formed by the Easter-Salas hotspot (Ray et al., 2012); the Juan Fernández Ridge, formed by the Juan Fernández hotspot (Yáñez et al., 2001); and the Iquique Ridge (Manea et al., 2005). The trench depth is greatest in the central region of the Peru-Chile trench, with a maximum of 2500 m in segment-bin 32, and decreases to 900–1400 m in the north of study area and 1800 m in the southernmost bin. The relatively shallow trench depths in the north and south of the study area correspond to regions of flat slab subduction (e.g., Barazangi and Isacks, 1976; Gutscher et al., 1999; Manea et al., 2005). The region south of the Juan Fernández Ridge is not considered in this study as the trench is sediment-filled (Contreras-Reyes et al., 2007). The northern end of the Peru trench is not considered due to the morphological influence of the Carnegie Ridge — an aseismic ridge resulting from the interaction between the GalÃąpagos hotspot and the Cocos-Nazca spreading centre. Similarly, the region where the Nazca Ridge is being subducted is not considered.

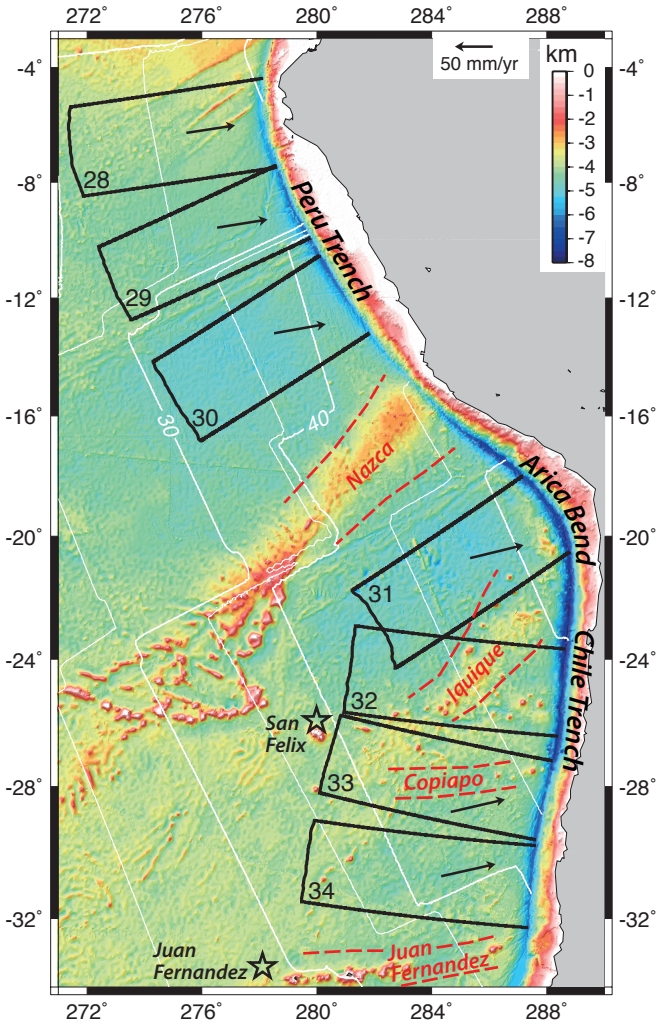

Figure A.2: Bathymetry map of the Peru-Chile trench (GEBCO_08 30 × 30 second, Ioc et al., 2003). The solid white lines show seafloor isochrons at 5 Ma intervals (Müller et al., 2008, v3.2). The segment-bins are shown and numbered in solid black, and plate convergence vectors from the MORVEL plate motion model (DeMets et al., 2010) are shown as black arrows. The dashed red lines mark aseismic ridges and the black stars mark hotspot locations.

A.3 Aleutian

At the Aleutian trench (Figure A.3), the Pacific Plate is subducting beneath the North American Plate. The trench-normal convergence rate increases from 63 mm/yr in the east, where the convergence direction is trench-normal, to 30 mm/yr in the west, where the convergence is highly oblique to the trench. East of 200°E, the incoming lithosphere was formed at the Kula-Pacific spreading centre, so that isochrons strike roughly trench-parallel; west of 200°E,

the lithosphere was formed at the Pacific-Farallon spreading centre (Byrne, 1979), so that isochrons strike > 45° from trench-parallel. The seafloor age peaks at 63 Ma in segment-bin 18, and decreases to ∼ 55 Ma at either end of the study area. The trench is intersected by a series of north-south trending, left-lateral offset fracture zones such as the Rat, Amlia and Adiak fracture zones (Grim and Erickson, 1969; Rea and Dixon, 1983). In segment-bins 16–19, the trench depth is 1500–1700 m. East of these bins, there is an eastwards decrease in trench depth to 900 m in bin 21, which coincides with an eastwards decrease in slab dip and a transition from ocean-ocean to ocean-continent subduction at ∼ 192°E. The region west of 174°E is not considered in this study due to the influence of the subducting Emperor seamount chain, nor the region east of 208°E because of the influence of the Kodiak-Bowie seamount chain (Dalrymple et al., 1987).

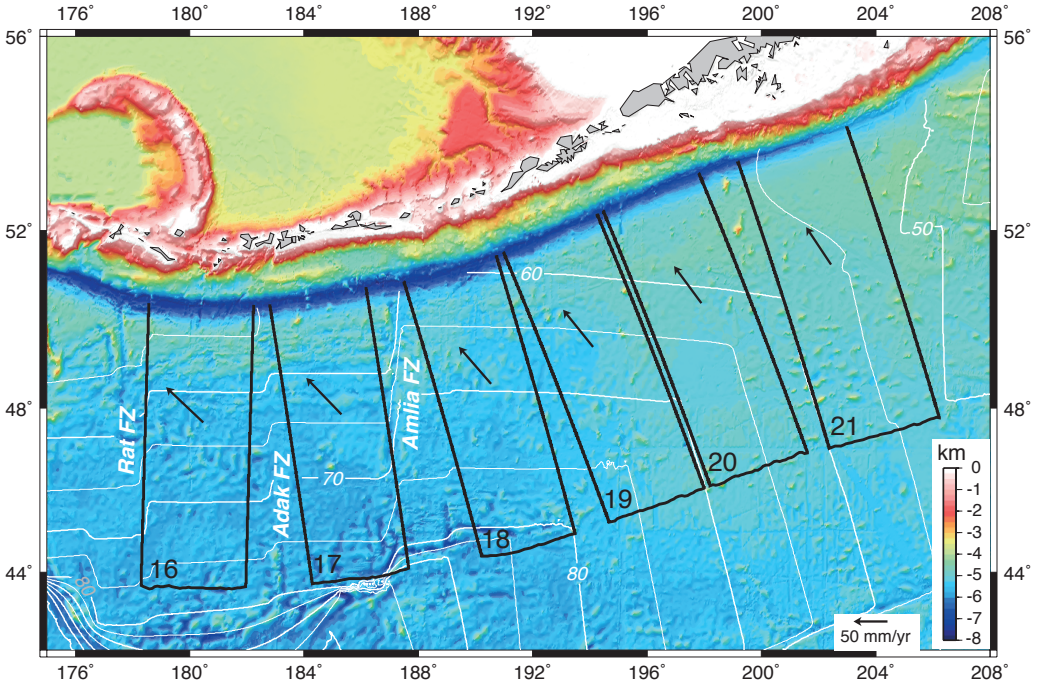

Figure A.3: Bathymetry map of the Aleutian trench (GEBCO_08 30 × 30 second, Ioc et al., 2003). The solid white lines show seafloor isochrons at 5 Ma intervals (Müller et al., 2008, v3.2). The segment-bins are shown and numbered in solid black, and plate convergence vectors from the MORVEL plate motion model (DeMets et al., 2010) are shown as black arrows.

A.4 Tonga-Kermadec

At the Tonga-Kermadec trench (Figure A.4), the Pacific plate is subducting beneath the Indo-Australian plate at a trench-normal convergence rate that increases from 46 mm/yr in the south to 83 mm/yr in the north. However, back-arc spreading rates increase northwards from 15 mm/yr in the southern Havre trough to 120 mm/yr in the northern Lau basin (Heuret and Lallemand, 2005), resulting in subduction velocities that increase northwards from 60 to 240 mm/yr. The downgoing lithosphere was formed at the Osbourn trough, an east-west trending fossil spreading centre that stopped spreading in the late Cretaceous (Billen and Stock, 2000). This results in seafloor ages that range from 87 Ma at the Osbourn Trough to 105 and 111 Ma in the northern and southern ends of the study area respectively. Due to the orientation of the Osbourn trough, the abyssal hill fabric strikes at angles everywhere $> 60°$ from trench-parallel. Thus, new trench-parallel faults are formed as the lithosphere bends into the trench. A swath bathymetry grid comprised of all data available in the MGDS database, as well as from all of the recent Sonne cruises to the region, reveals that the outer trench-slope is pervasively fractured by long (up to > 100 km), large offset (up to 1.5 km) faults that bound horst and graben structures. The Tonga and Kermadec sections of the trench are separated by the subducting Louisville Ridge, a 3500 km long seamount chain that formed over a hotspot presently located near the intersection of the Eltanin fracture zone and the East Pacific Rise (Watts et al., 1988). Osbourn Guyot, the oldest extant seamount in the chain, is currently being subducted and has an age of ~ 78 Ma (Koppers et al., 2004); it was therefore loaded on ~ 10 Ma lithosphere and is unlikely to have had a large effect on the lithosphereâĂŹs thermal structure. At $\sim 19°$S, Capricorn Guyot, a probably Miocene seamount that may be part of a hotspot chain that includes Niue Island, is being subducted (Brodie, 1965; Lonsdale, 1986). Trench depths are 3400–3600 m in segment-bins 3 and 4, decreasing to 2800 m and 1800 m in the northernmost and southernmost bin respectively. The regions of Louisville Ridge and Capricorn seamount subduction are not included in this study due to the morphological influence of these features; the northernmost end of the trench is also not included because convergence here is almost strike-slip and the Western Samoa seamount province strongly masks the flexural signal.

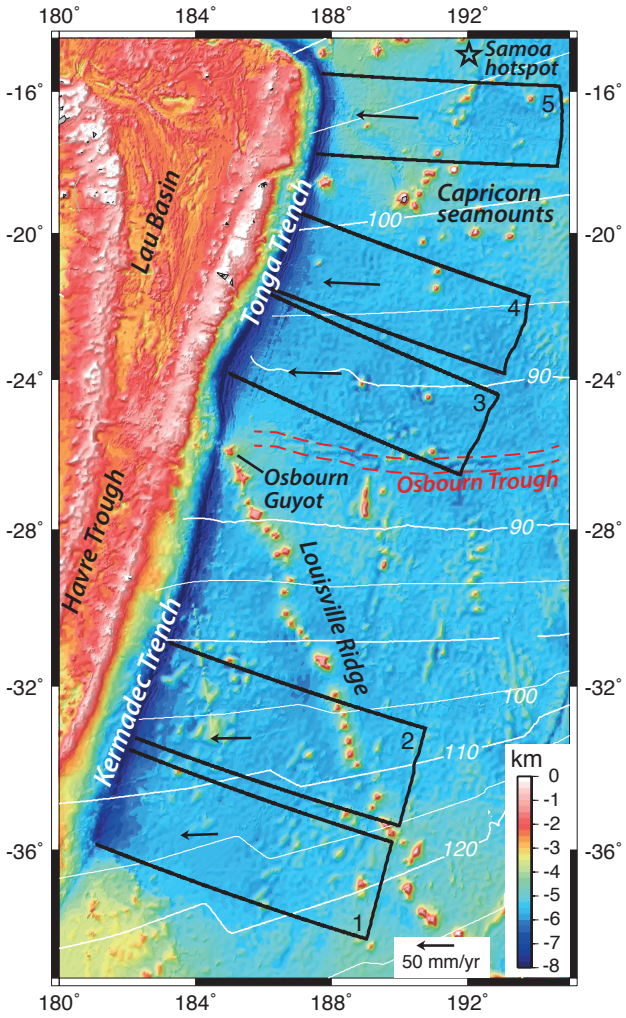

Figure A.4: Bathymetry map of the Tonga-Kermadec trench (GEBCO_08 30 × 30 second, Ioc et al., 2003). The solid white lines show seafloor isochrons at 5 Ma intervals (Müller et al., 2008, v3.2). The segment-bins are shown and numbered in solid black, and plate convergence vectors from the MORVEL plate motion model (DeMets et al., 2010) are shown as black arrows.

A.5 Kuril-Japan

At the Kuril-Japan trench (Figure A.5), the Pacific plate is subducting beneath the Okhotsk plate at a trench-normal convergence rate of 80–90 mm/yr. The age of the subducting seafloor decreases northwards from 135 to 109 Ma, and the Kuril trench is intersected by a number of right-lateral offset fracture zones. At the Japan trench, the abyssal hill fabric strikes $> 30°$ from trench-parallel; this means that abyssal faults cannot be reactivated as bend-faults, and therefore that new, trench-parallel, horst and graben faults are formed on the outer trench-

slope (Kobayashi et al., 1998). At the Kuril trench, in segment-bins 12 and 13, isochrons strike $< 20^{\circ}$ from trench-parallel; thus, abyssal hill faults are reactivated as bend faults on the outer trench-slope (Kobayashi et al., 1998). In bins 14 and 15, isochrons strike 25–30° from trench-parallel, so that bend-faulting may occur via a mixture of abyssal hill fault reactivation and new, trench-parallel faulting (Masson, 1991). The trench depth is 1400–1500 m in the Japan trench, and increases northwards from 3300 to 1600 m in the Kuril trench. At the southern end of the Japan trench, the Cretaceous Joban seamount chain is being subducted (Nishizawa et al., 2009)

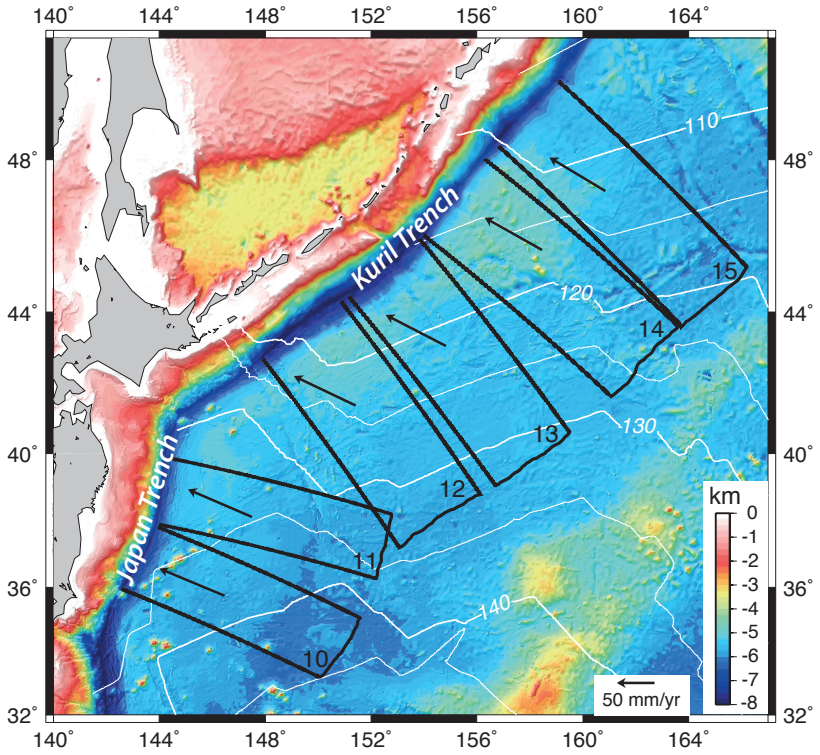

Figure A.5: Bathymetry map of the Kuril-Japan trench (GEBCO_08 30 × 30 second, Ioc et al., 2003). The solid white lines show seafloor isochrons at 5 Ma intervals (Müller et al., 2008, v3.2). The segment-bins are shown and numbered in solid black, and plate convergence vectors from the MORVEL plate motion model (DeMets et al., 2010) are shown as black arrows.

A.6 Izu-Bonin-Mariana

At the Izu-Bonin-Mariana trench (Figure A.6), the Pacific plate is subducting beneath the Philippine Sea plate. Trench-normal convergence rates are 12–21 mm/yr and 36–45 mm/yr at the Mariana and Izu-Bonin trench respectively. However, back-arc spreading rates are high at the Mariana trench — 35 mm/yr — resulting in subduction rates of 40–50 mm/yr (Heuret and Lallemand, 2005). The age of the subducting seafloor decreases northwards from 154 to 137 Ma. Except for the southernmost bin at the Mariana trench, the incoming abyssal fabric strikes everywhere $> 30°$ from trench-parallel. This means that new, trench-parallel, horst and graben faults are formed on the outer trench-slope of the Izu-Bonin (Seta et al., 1991) and central Mariana (Jones et al., 1978) trenches. The trench depth is 3000–3100 m at the Izu-Bonin trench; at the Mariana trench, the trench depth is 2600 m in segment-bin 6 and 1800 m in bin 7. At the Mariana trench, the incoming plate is heavily covered in by a group of predominantly Cretaceous seamounts known as the Magellan seamounts (e.g., Duncan and Clague, 1985; Smith et al., 1989). At the southern end of the Izu-Bonin trench, the Ogasawara Plateau — the large, westernmost seamount on the ~ 80 Ma Michelson Ridge — is currently colliding with the trench (Fryer and Smoot, 1985; Tsuji et al., 2007).

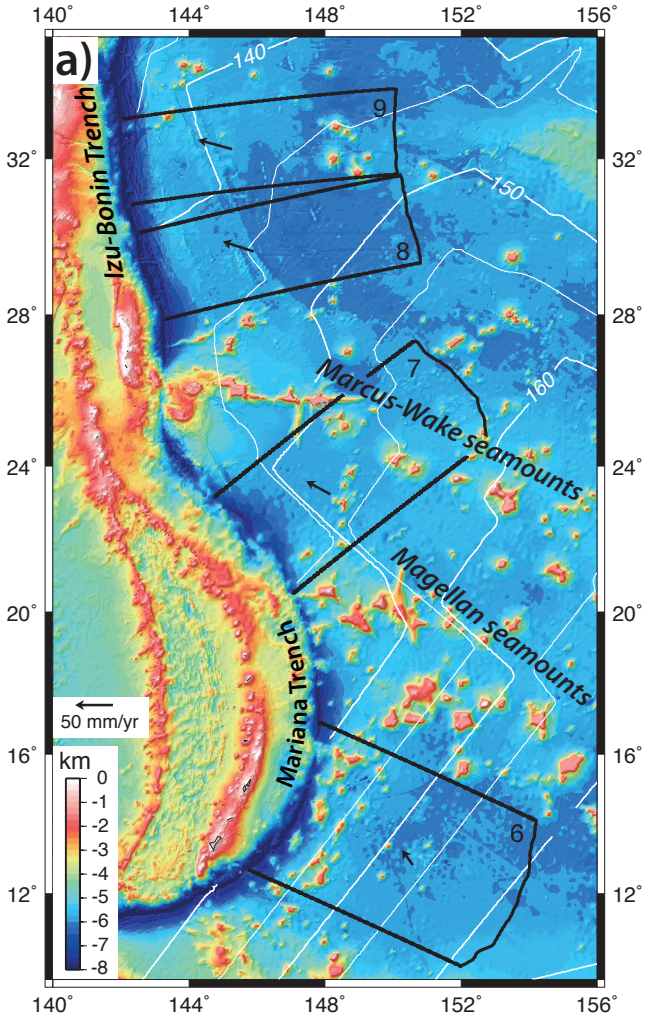

Figure A.6: Bathymetry map of the Izu-Bonin-Mariana trench (GEBCO_08 30 × 30 second, Ioc et al., 2003). The solid white lines show seafloor isochrons at 5 Ma intervals (Müller et al., 2008, v3.2). The segment-bins are shown and numbered in solid black, and plate convergence vectors from the MORVEL plate motion model (DeMets et al., 2010) are shown as black arrows.

Appendix B

Profile fits from Inversion A1

This appendix contains all of the profile fits from Inversion A1, in which circum-Pacific trench-outer rise gravity anomalies were modelled using a constant T_e plate. The segment-bin and trench-bin profile fits are shown in Section B.1 and B.2 respectively; the segment-bins are numbered as in Figure 2.4. Each page contains the results for 4 different profile bins. For each bin, the top plot shows the observed and best-fit free-air gravity profile; the bin number, trench, average seafloor age and best-fit T_e are labelled. Beneath each gravity anomaly plot is the corresponding best-fit bending moment and curvature profile. Beneath that is the corresponding plot of T_e vs. Δg_{rms}; the grey line shows 1.25 times the minimum Δg_{rms}, which was used to estimate the uncertainty in T_e. For clarity, only the first 600 km of the profile fits are shown, but the inversions were conducted on 750 km profiles.

B.1 Segment-bins

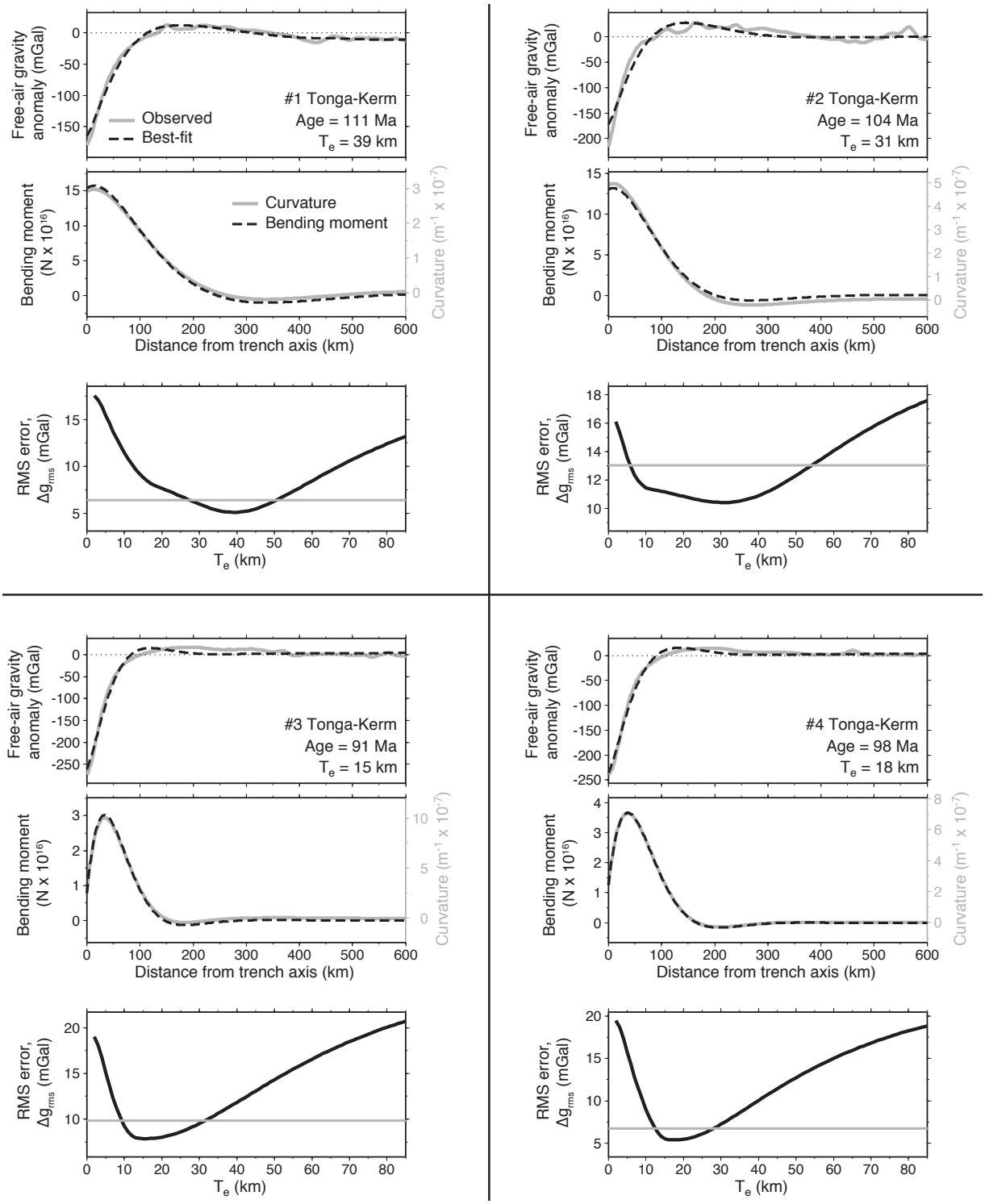

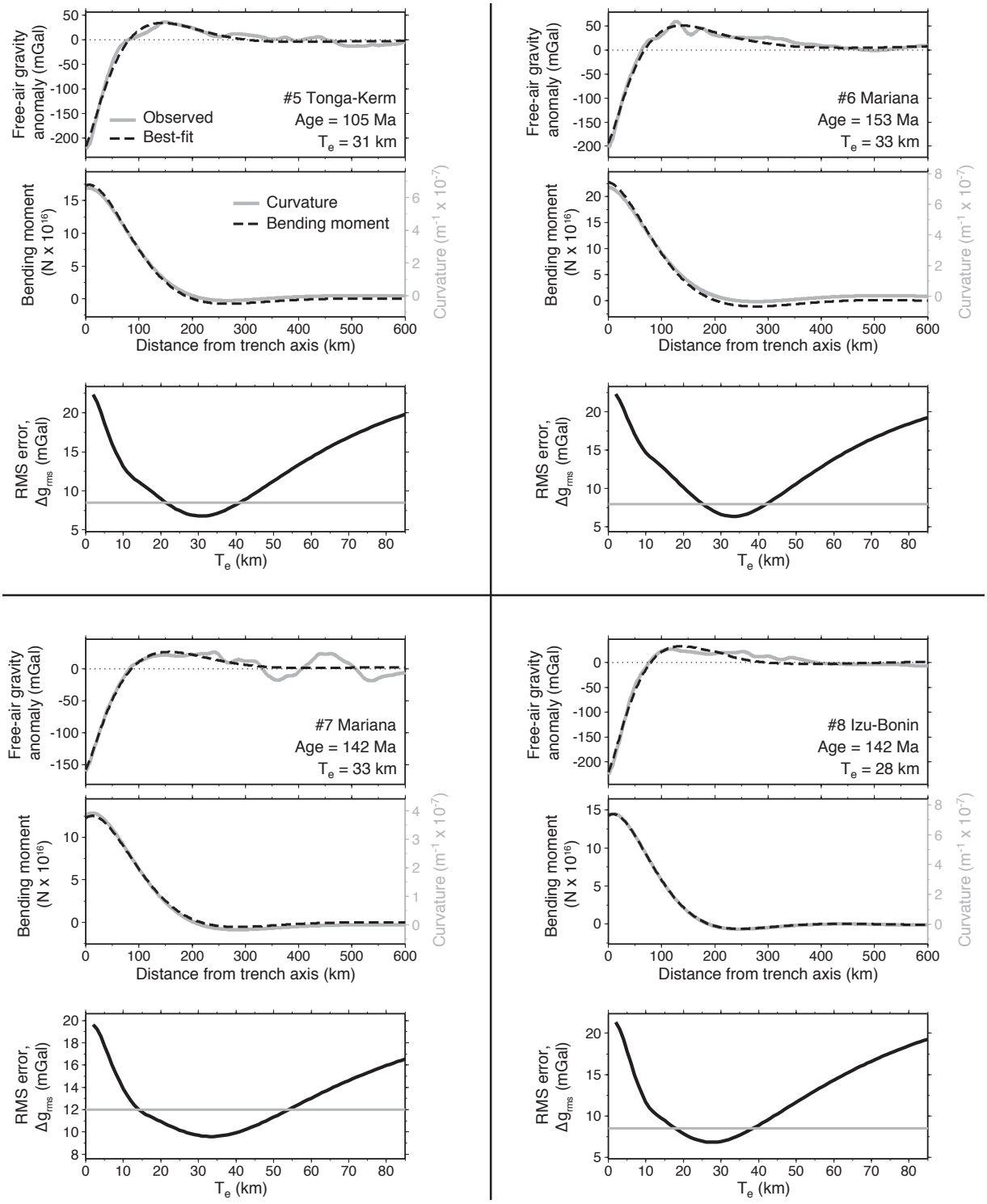
Free-air gravity anomaly (mGal)
Observed
Best-fit
#5 Tonga-Kerm
Age = 105 Ma
T_e = 31 km
Bending moment (N x 10^{16})
Curvature
Bending moment
Curvature (m^{-1} x 10^{-7})
Distance from trench axis (km)
RMS error, Δg_{rms} (mGal)
T_e (km)
#6 Mariana
Age = 153 Ma
T_e = 33 km
#7 Mariana
Age = 142 Ma
T_e = 33 km
#8 Izu-Bonin
Age = 142 Ma
T_e = 28 km

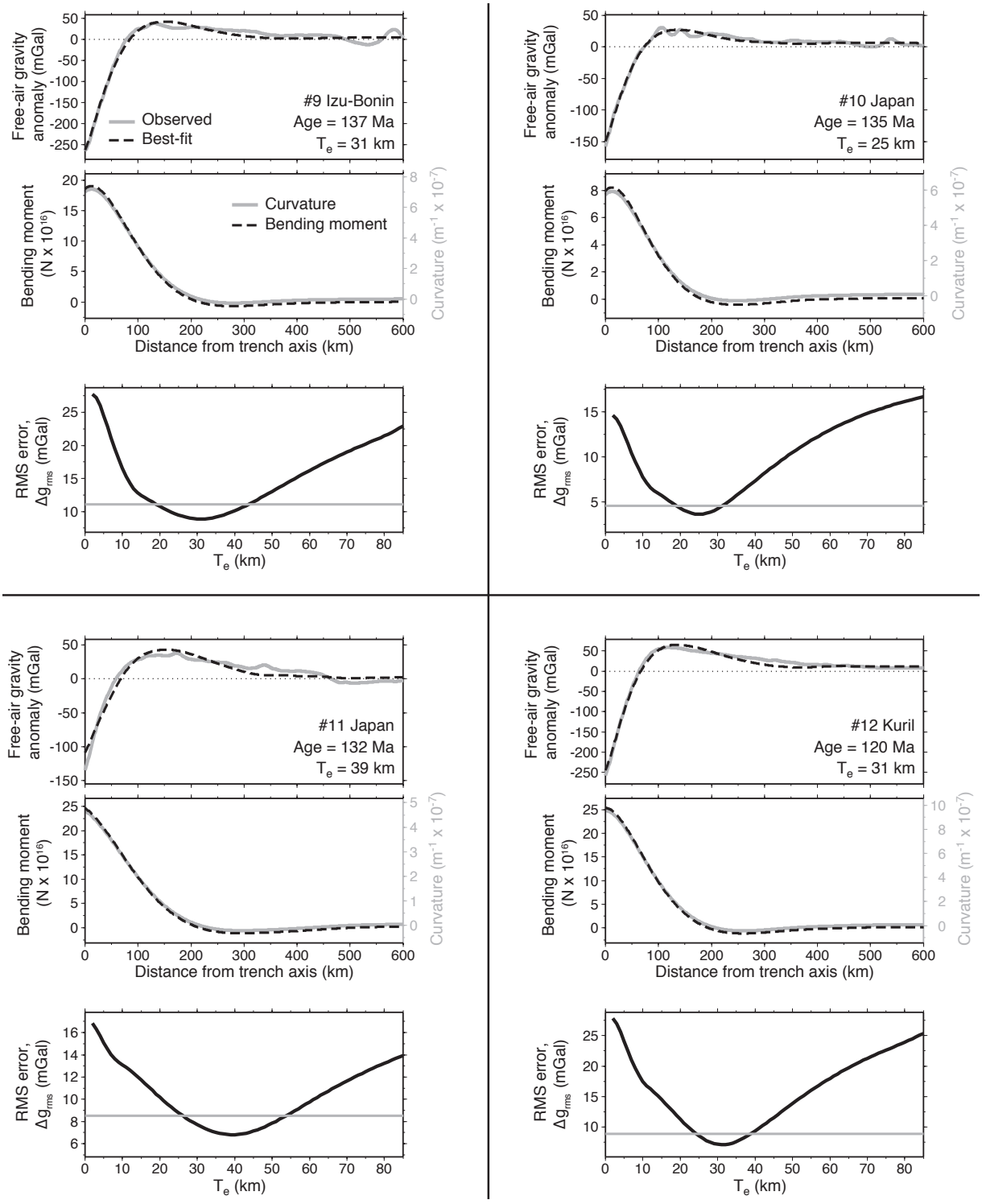
Free-air gravity anomaly (mGal)
Observed
Best-fit
#9 Izu-Bonin
Age = 137 Ma
T_e = 31 km
Bending moment (N x 10^{16})
Curvature
Bending moment
Curvature (m^{-1} x 10^{-7})
Distance from trench axis (km)
RMS error, Δg_{rms} (mGal)
T_e (km)
#10 Japan
Age = 135 Ma
T_e = 25 km
#11 Japan
Age = 132 Ma
T_e = 39 km
#12 Kuril
Age = 120 Ma
T_e = 31 km

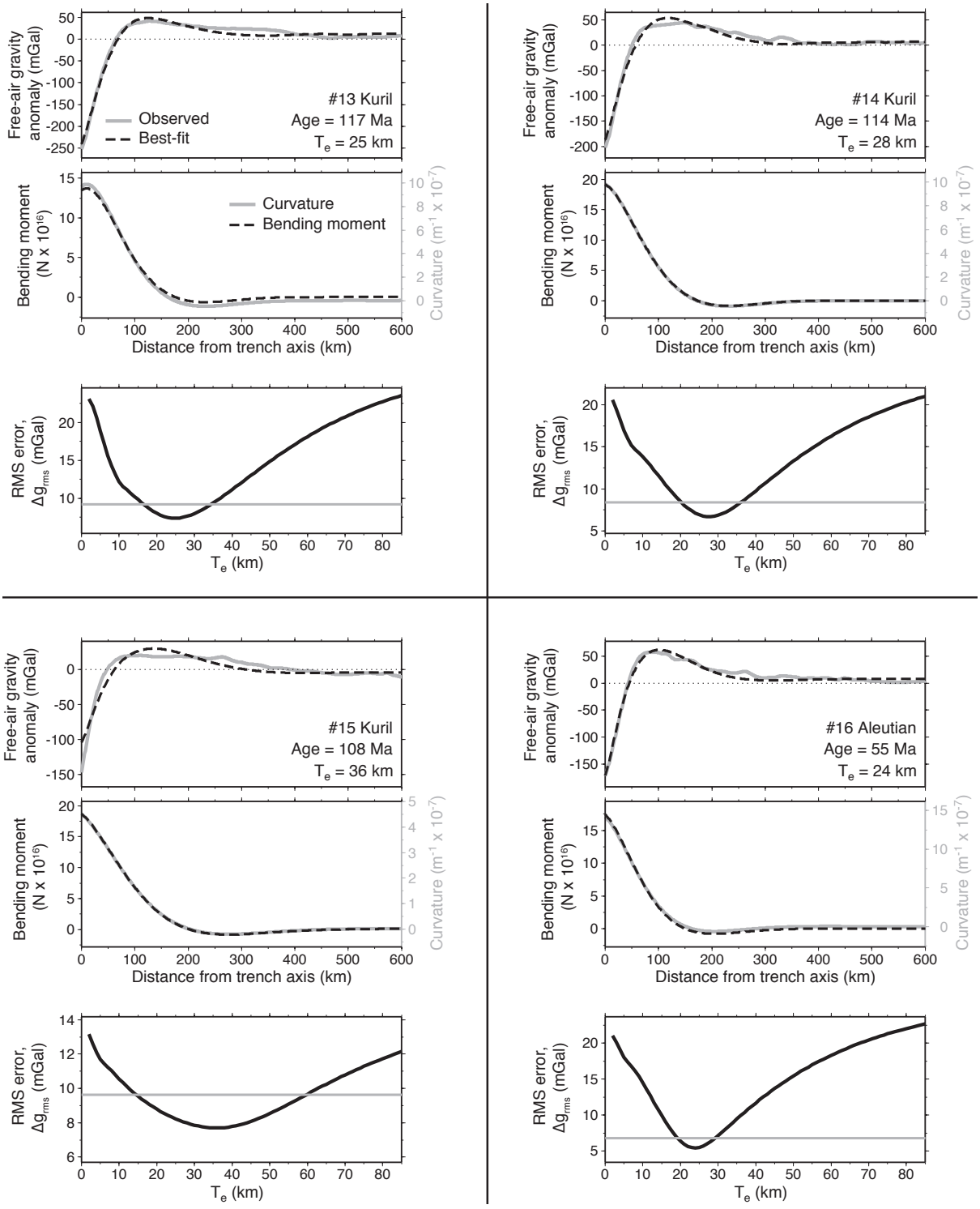
Free-air gravity anomaly (mGal)
Observed
Best-fit
#13 Kuril
Age = 117 Ma
Te = 25 km
Bending moment (N x 10^16)
Curvature
Bending moment
Curvature (m^-1 x 10^-7)
Distance from trench axis (km)
RMS error, Δgrms (mGal)
Te (km)
#14 Kuril
Age = 114 Ma
Te = 28 km
#15 Kuril
Age = 108 Ma
Te = 36 km
#16 Aleutian
Age = 55 Ma
Te = 24 km

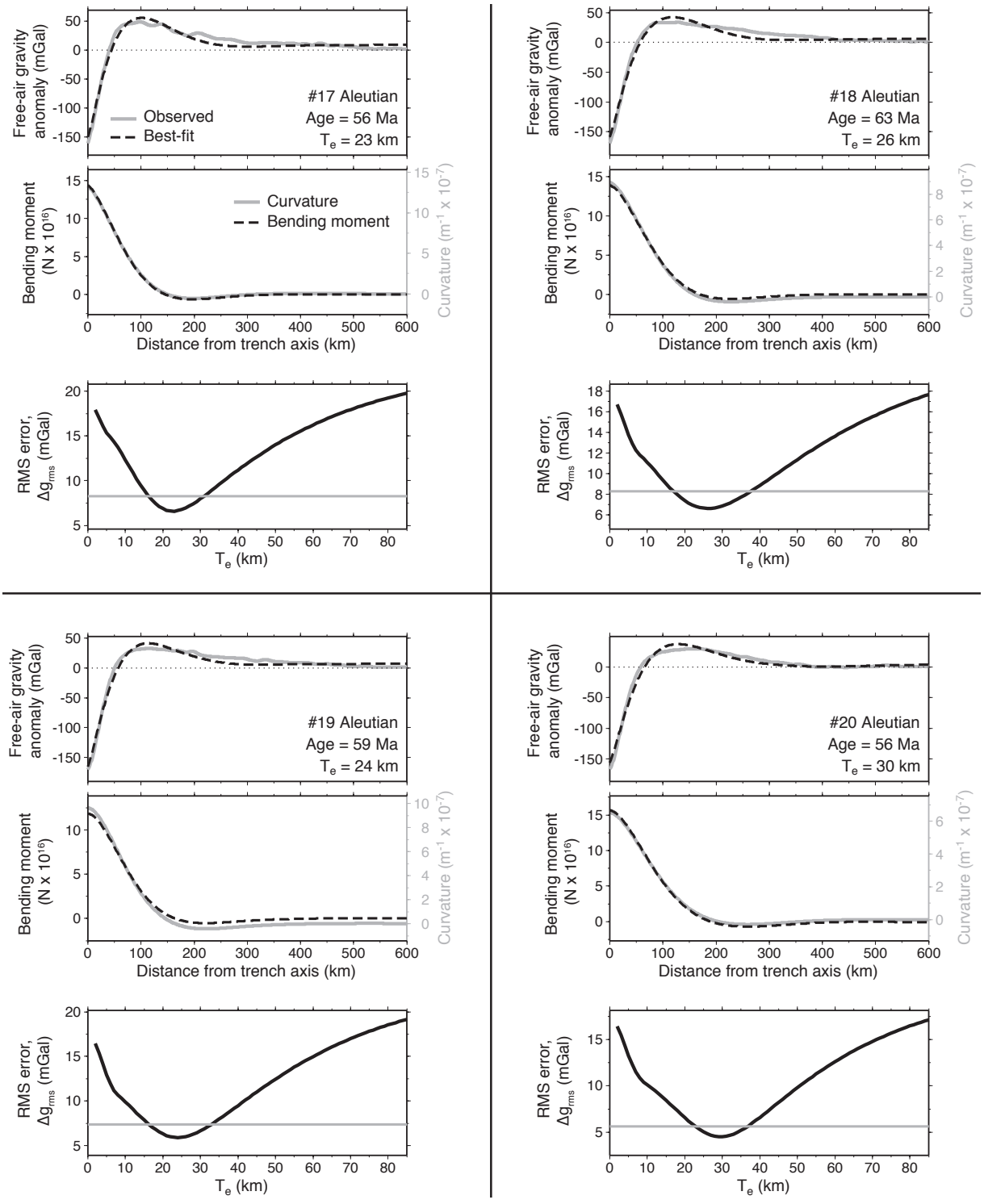
#17 Aleutian
Age = 56 Ma
Te = 23 km
Observed
Best-fit
Curvature
Bending moment
#18 Aleutian
Age = 63 Ma
Te = 26 km
#19 Aleutian
Age = 59 Ma
Te = 24 km
#20 Aleutian
Age = 56 Ma
Te = 30 km
Free-air gravity anomaly (mGal)
Bending moment (N x 10^16)
Curvature (m^-1 x 10^-7)
Distance from trench axis (km)
RMS error, Δg_rms (mGal)
Te (km)

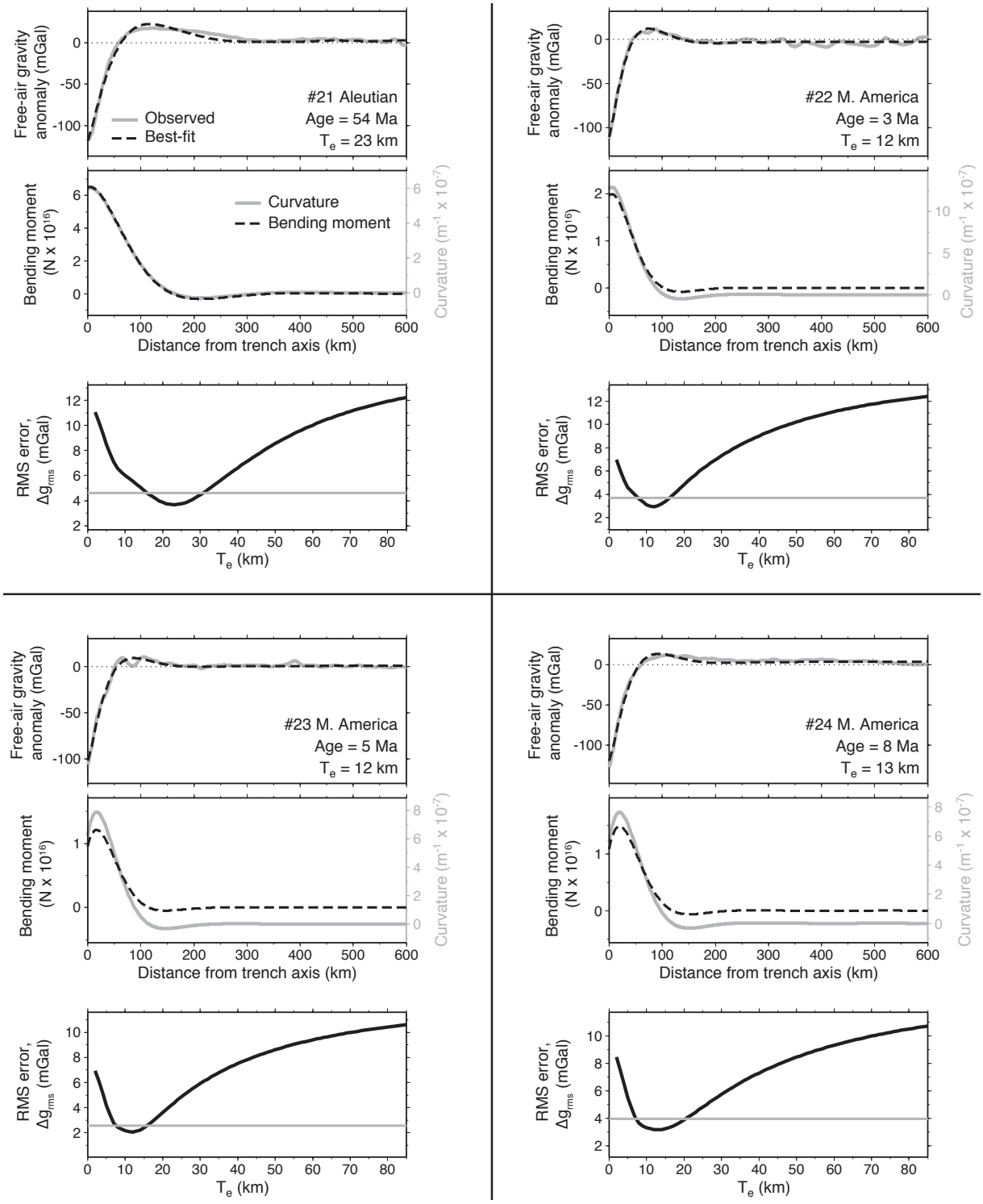
Free-air gravity anomaly (mGal)
Observed
Best-fit
#21 Aleutian
Age = 54 Ma
T_e = 23 km
Bending moment (N x 10^{16})
Curvature
Bending moment
Curvature (m^{-1} x 10^{-7})
Distance from trench axis (km)
RMS error, Δg_{rms} (mGal)
T_e (km)
#22 M. America
Age = 3 Ma
T_e = 12 km
#23 M. America
Age = 5 Ma
T_e = 12 km
#24 M. America
Age = 8 Ma
T_e = 13 km

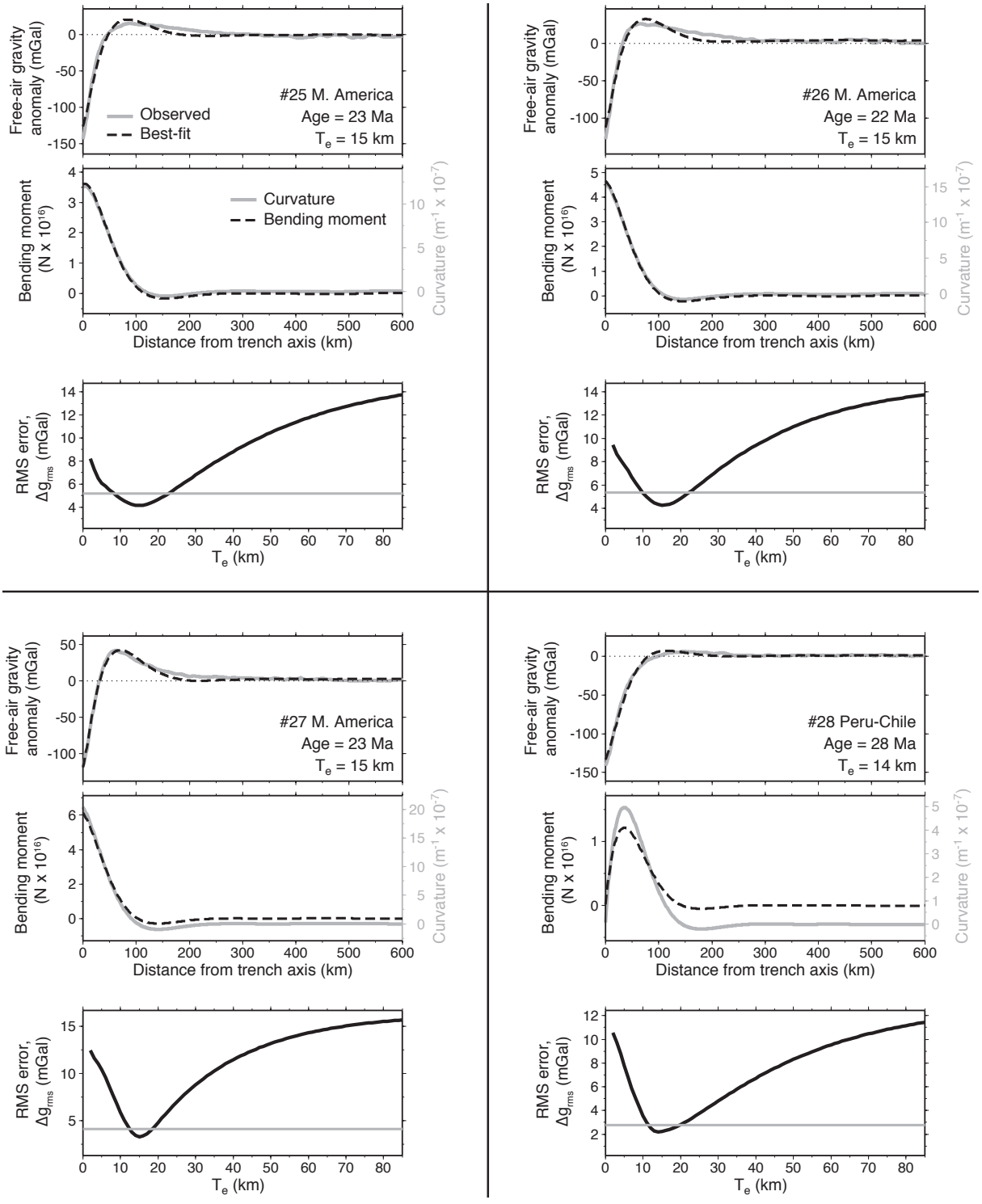
Free-air gravity anomaly (mGal)
Observed
Best-fit
#25 M. America
Age = 23 Ma
Te = 15 km
Bending moment (N x 10^16)
Curvature
Bending moment
Curvature (m^-1 x 10^-7)
Distance from trench axis (km)
RMS error, Δgrms (mGal)
Te (km)
#26 M. America
Age = 22 Ma
Te = 15 km
#27 M. America
Age = 23 Ma
Te = 15 km
#28 Peru-Chile
Age = 28 Ma
Te = 14 km

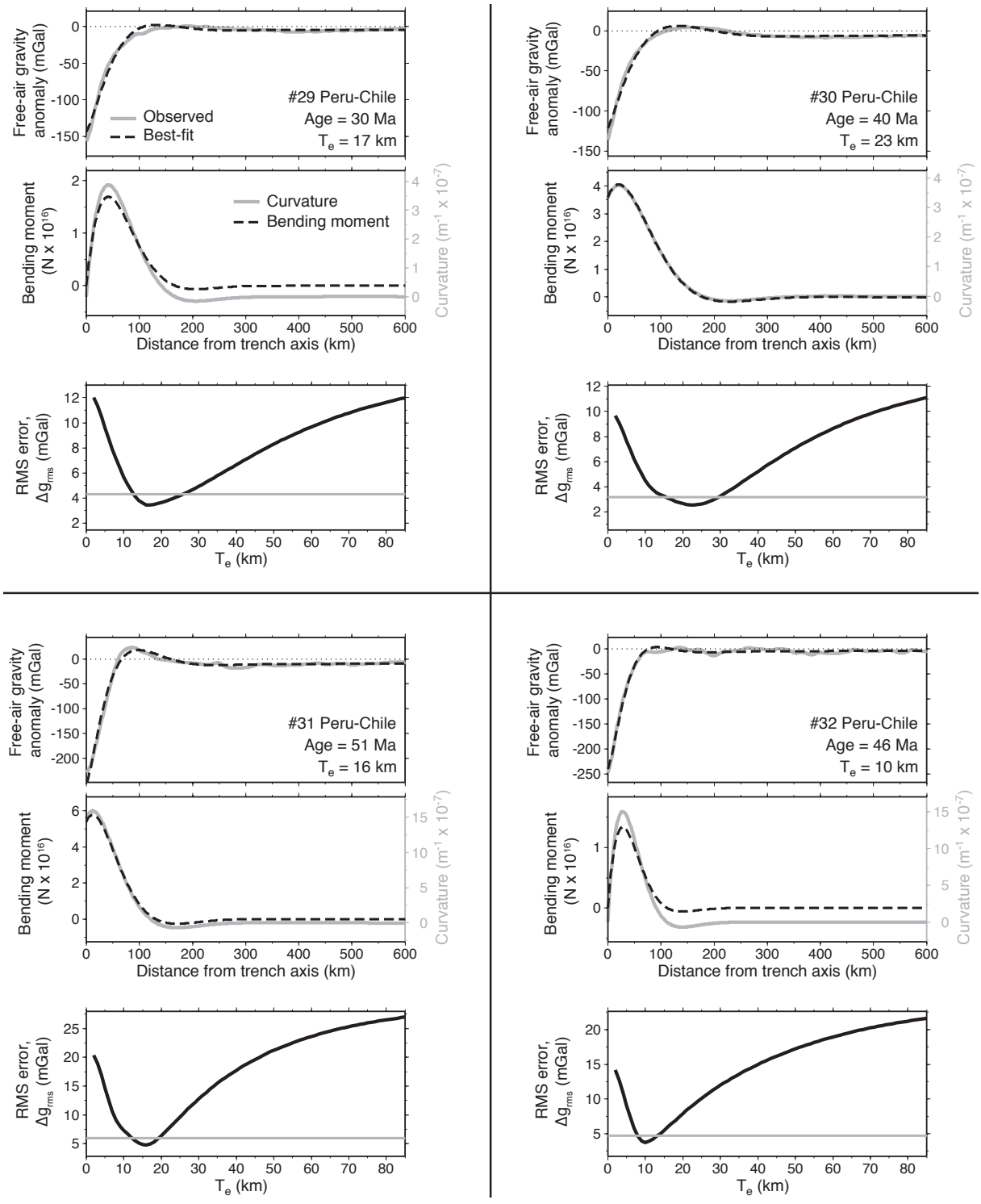
#29 Peru-Chile
Age = 30 Ma
T_e = 17 km
Observed
Best-fit
Curvature
Bending moment
Free-air gravity anomaly (mGal)
Bending moment (N x 10^{16})
Curvature (m^{-1} x 10^{-7})
Distance from trench axis (km)
RMS error, Δg_{rms} (mGal)
T_e (km)
#30 Peru-Chile
Age = 40 Ma
T_e = 23 km
#31 Peru-Chile
Age = 51 Ma
T_e = 16 km
#32 Peru-Chile
Age = 46 Ma
T_e = 10 km

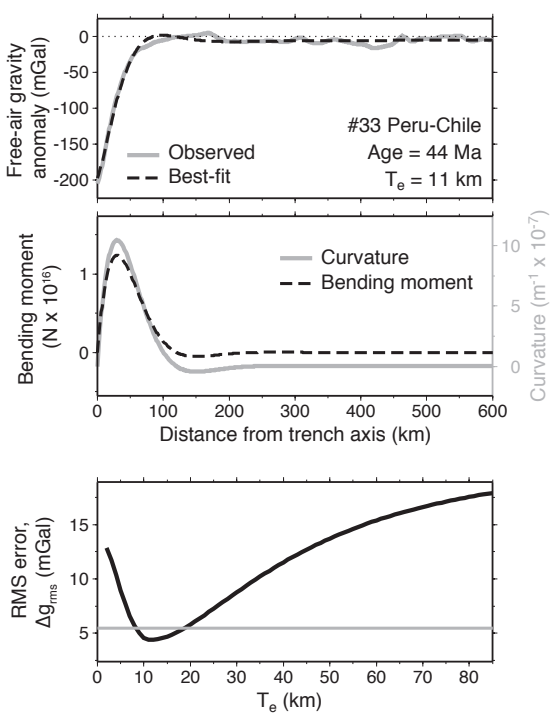
Free-air gravity anomaly (mGal)
0
-50
-100
-150
-200
Observed
Best-fit
#33 Peru-Chile
Age = 44 Ma
T_e = 11 km
Bending moment (N x 10^{16})
1
0
Curvature
Bending moment
Curvature (m^{-1} x 10^{-7})
10
5
0
0
100
200
300
400
500
600
Distance from trench axis (km)
RMS error, Δg_{rms} (mGal)
15
10
5
0
10
20
30
40
50
60
70
80
T_e (km)

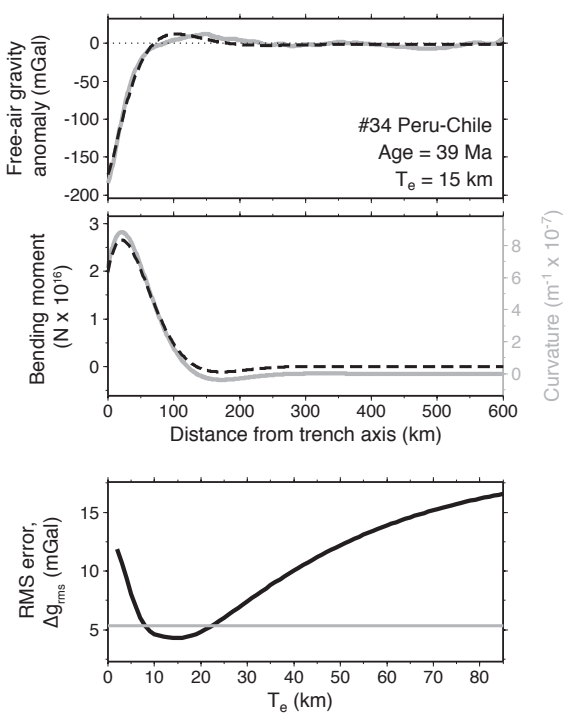
Free-air gravity anomaly (mGal)
0
-50
-100
-150
-200
#34 Peru-Chile
Age = 39 Ma
T_e = 15 km
Bending moment (N x 10^{16})
3
2
1
0
Curvature (m^{-1} x 10^{-7})
8
6
4
2
0
0
100
200
300
400
500
600
Distance from trench axis (km)
RMS error, Δg_{rms} (mGal)
15
10
5
0
10
20
30
40
50
60
70
80
T_e (km)

B.2 Trench-bins

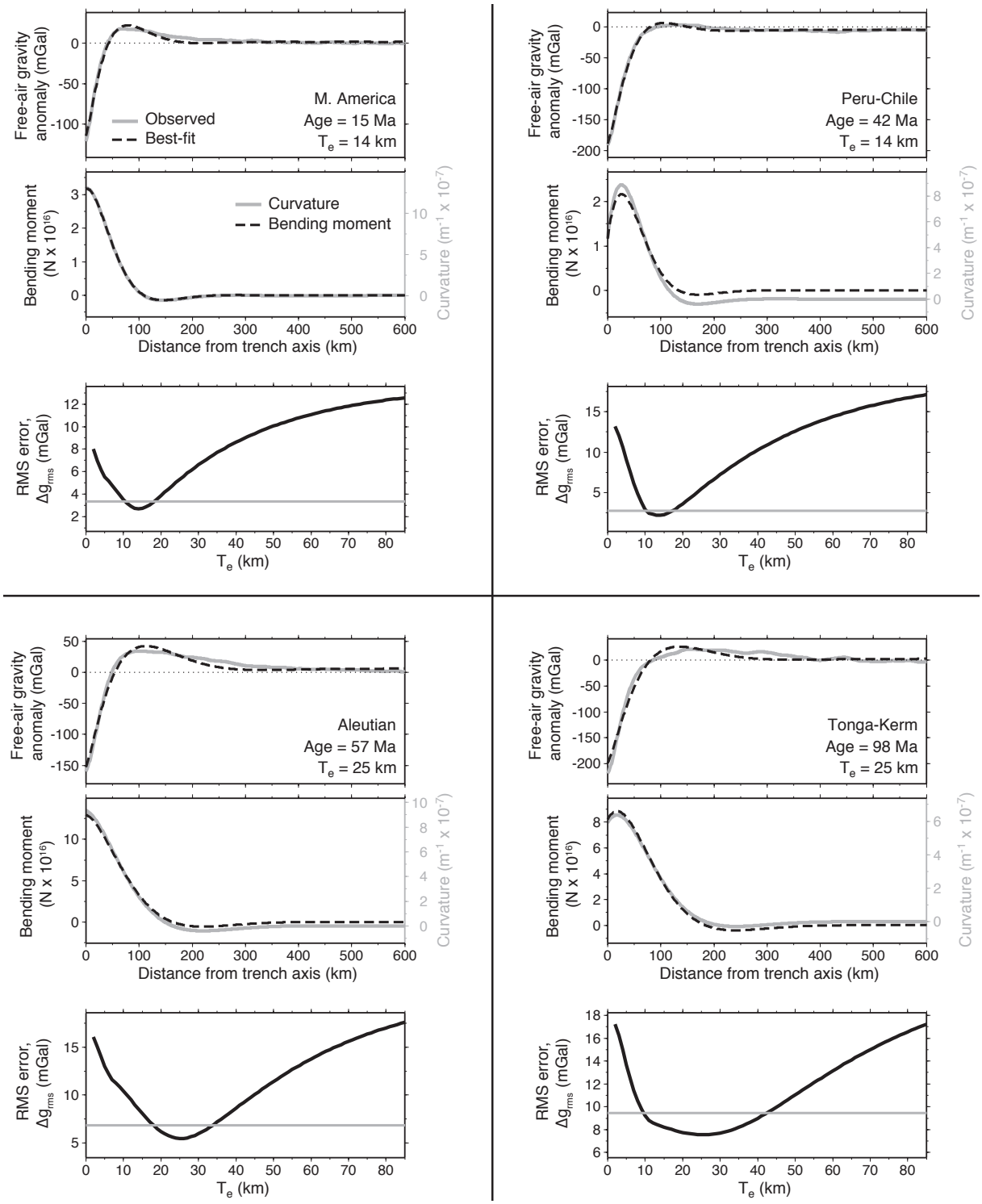

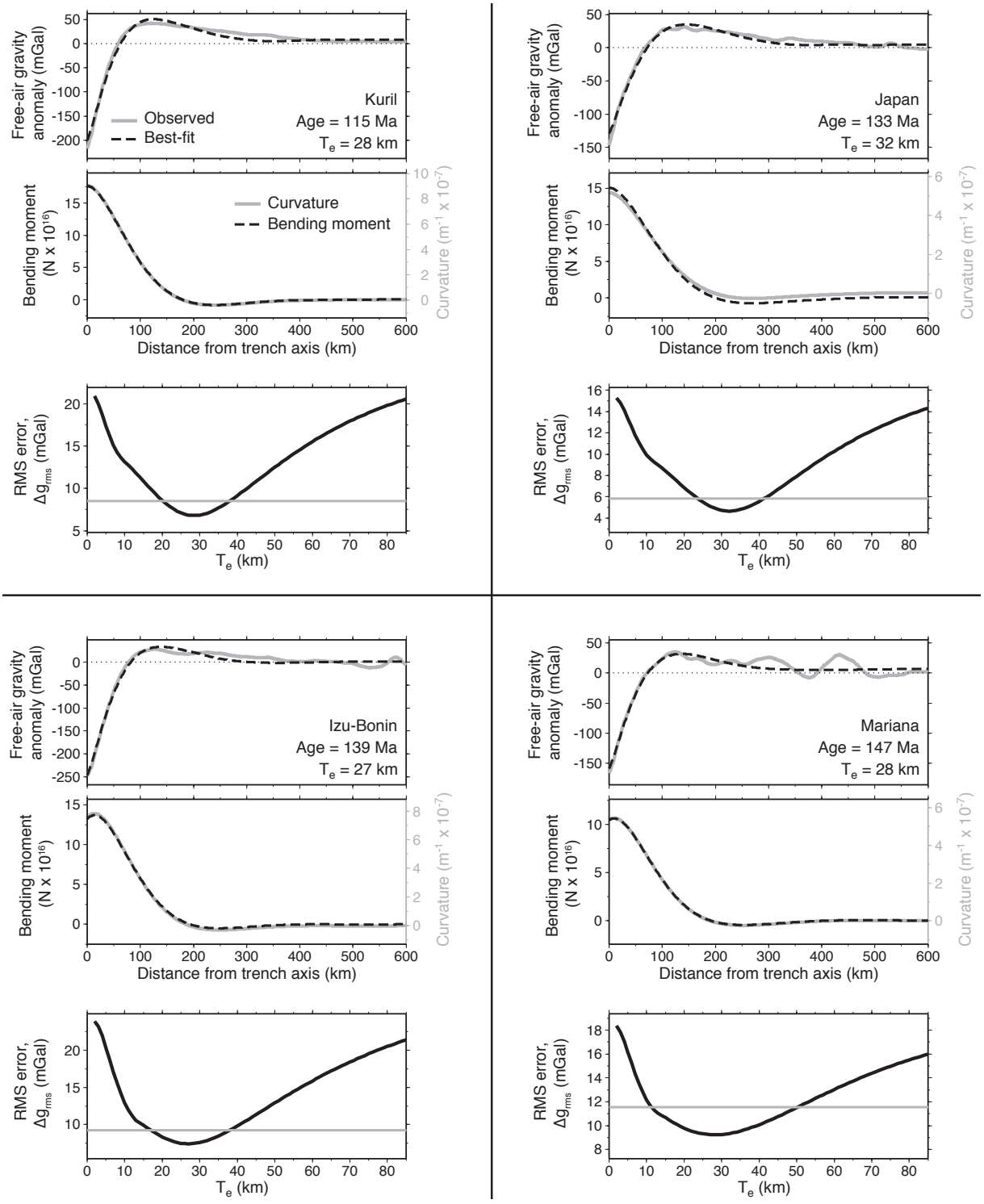
Free-air gravity anomaly (mGal)
Observed
Best-fit
Kuril
Age = 115 Ma
Te = 28 km
Bending moment (N x 10^16)
Curvature
Bending moment
Curvature (m^-1 x 10^-7)
Distance from trench axis (km)
RMS error, Δgrms (mGal)
Te (km)
Japan
Age = 133 Ma
Te = 32 km
Izu-Bonin
Age = 139 Ma
Te = 27 km
Mariana
Age = 147 Ma
Te = 28 km

Appendix C

Profile fits from Inversion A2

This appendix contains all of the profile fits from Inversion A2, in which circum-Pacific trench-outer rise gravity anomalies were modelled using a variable T_e elastic plate. The segment-bin and trench-bin profile fits are shown in Section C.1 and C.2 respectively; the segment-bins are numbered as in Figure 2.4. Each page contains the results for 4 different profile bins. For each bin, the top plot shows the observed and best-fit free-air gravity profile; the bin number, trench and average seafloor age are labelled. Beneath each gravity anomaly plot is the corresponding best-fit T_e profile, and beneath that, the corresponding bending moment and curvature profile. Beneath that is the corresponding plot of landward T_e (black line) and seaward T_e (grey line) vs. Δg_{rms}. For clarity, only the first 600 km of the profile fits are shown, but the inversions were conducted on 750 km profiles.

C.1 Segment-bins

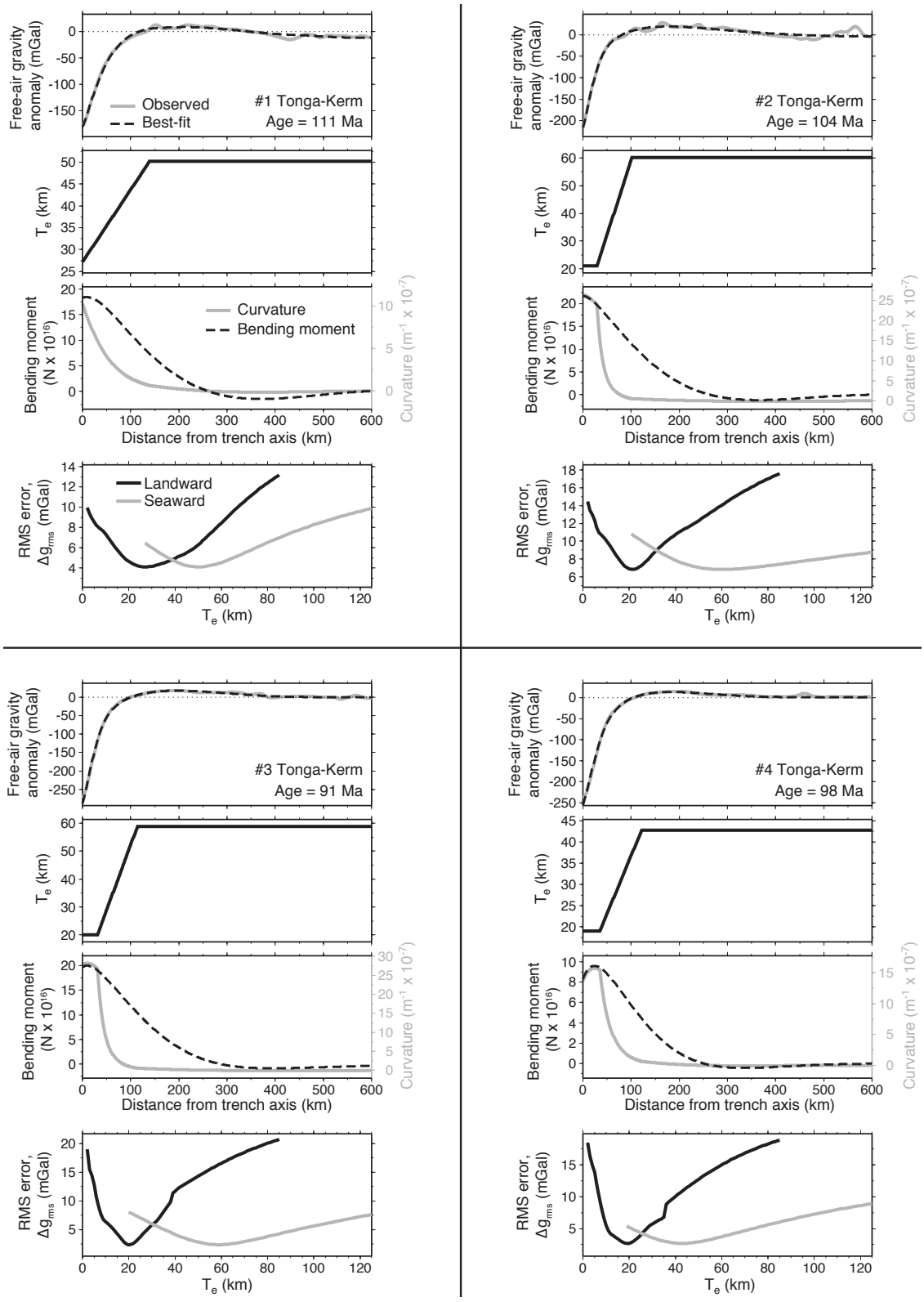

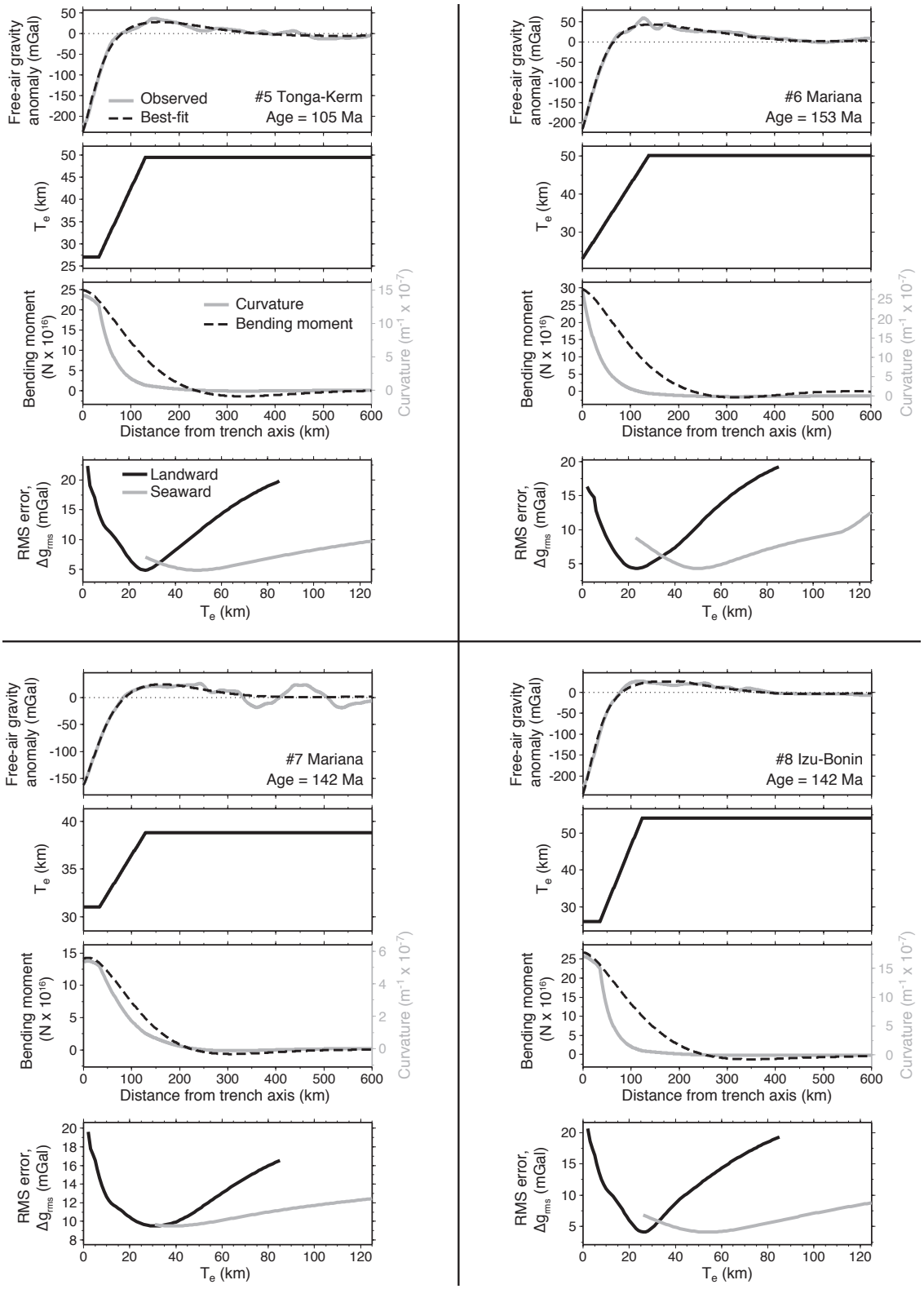
Free-air gravity anomaly (mGal)
Observed
Best-fit
#5 Tonga-Kerm
Age = 105 Ma
#6 Mariana
Age = 153 Ma
#7 Mariana
Age = 142 Ma
#8 Izu-Bonin
Age = 142 Ma
Te (km)
Bending moment (N x 10^16)
Curvature
Bending moment
Curvature (m^-1 x 10^-7)
Distance from trench axis (km)
RMS error, Δgrms (mGal)
Landward
Seaward
Te (km)

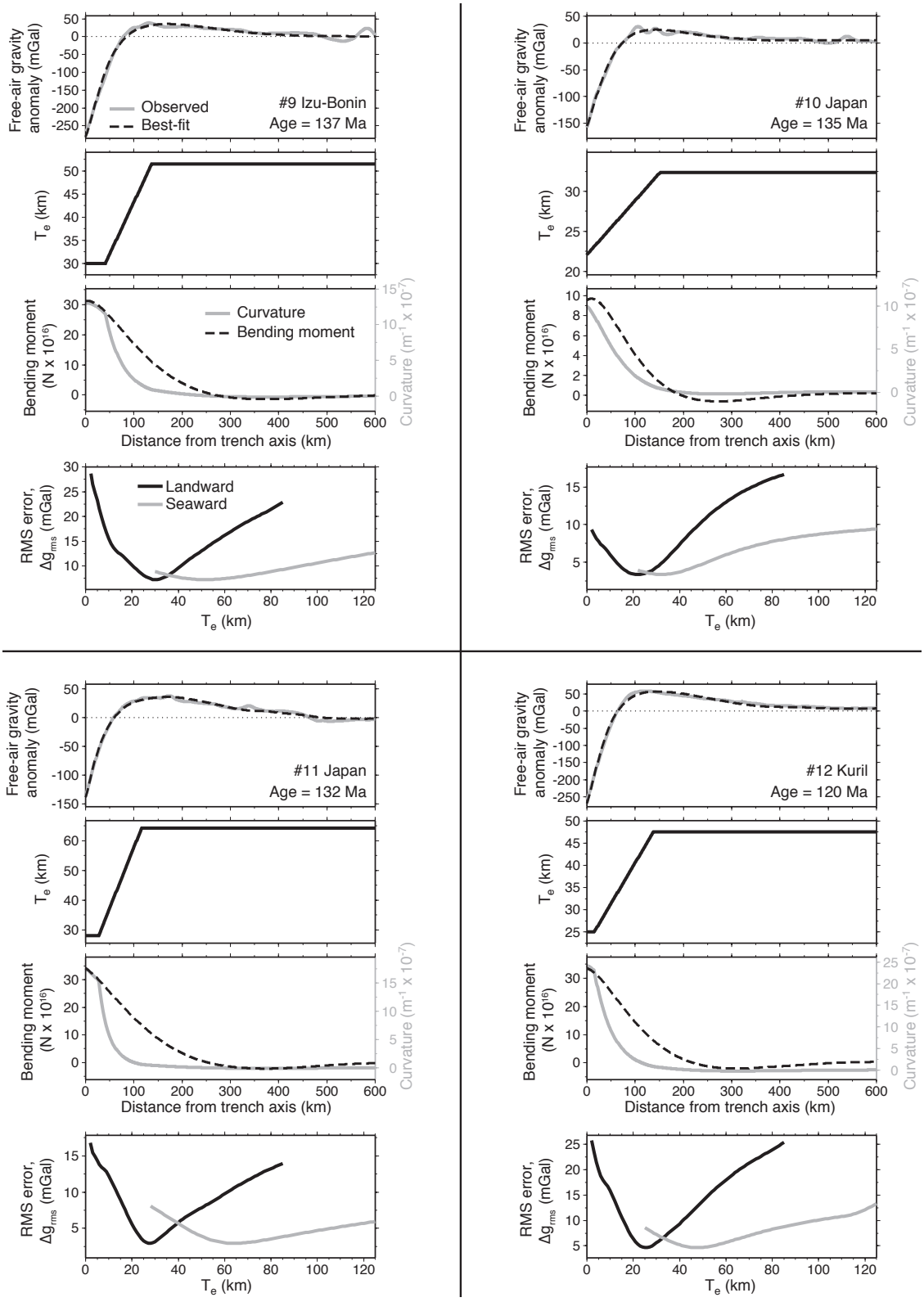
Free-air gravity anomaly (mGal)
Observed
Best-fit
#9 Izu-Bonin
Age = 137 Ma
#10 Japan
Age = 135 Ma
#11 Japan
Age = 132 Ma
#12 Kuril
Age = 120 Ma
T_e (km)
Bending moment (N x 10^{16})
Curvature
Bending moment
Curvature (m^{-1} x 10^{-7})
Distance from trench axis (km)
RMS error, Δg_{rms} (mGal)
Landward
Seaward
T_e (km)

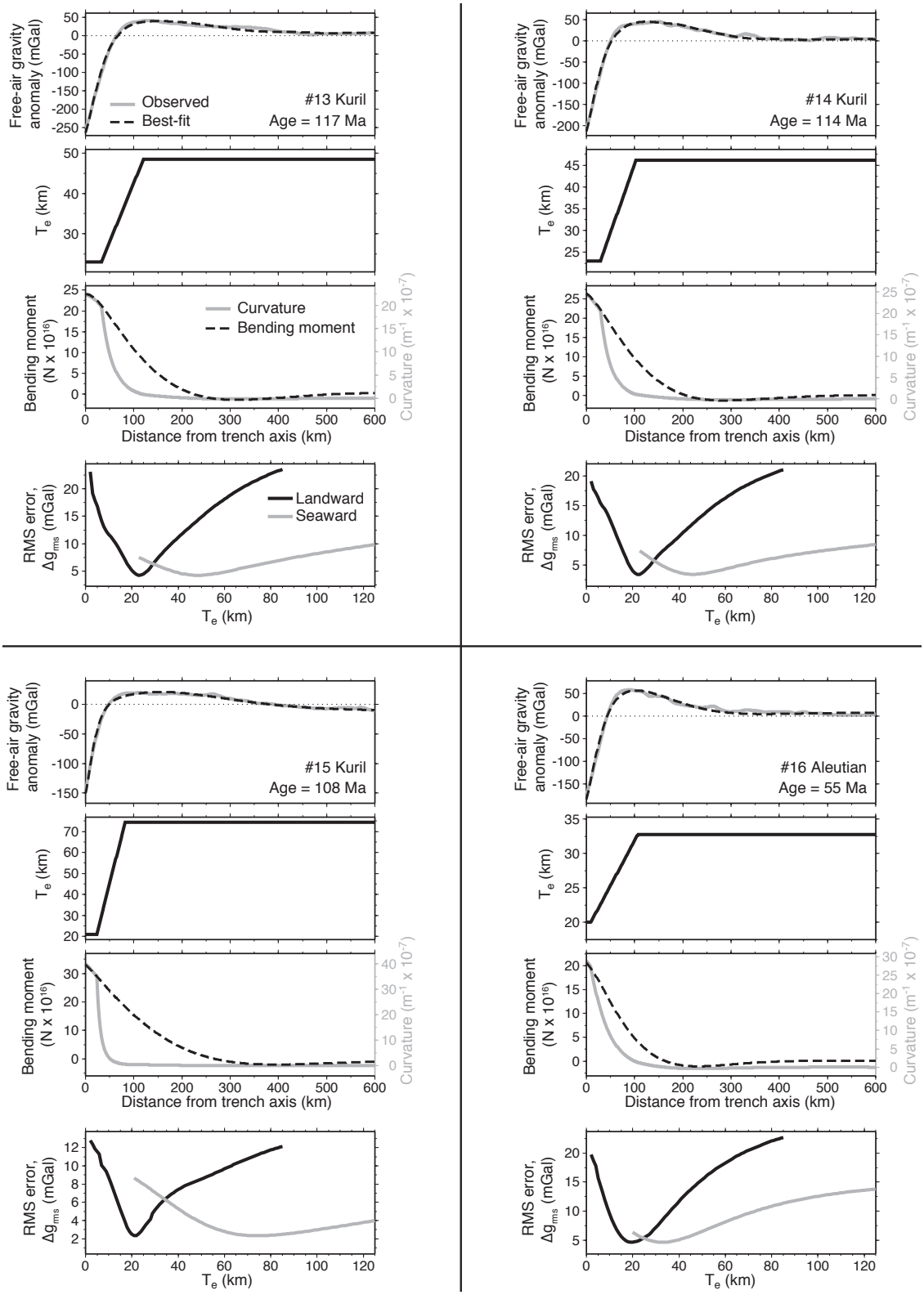
Free-air gravity anomaly (mGal)
Observed
Best-fit
#13 Kuril
Age = 117 Ma
#14 Kuril
Age = 114 Ma
#15 Kuril
Age = 108 Ma
#16 Aleutian
Age = 55 Ma
Te (km)
Bending moment (N x 10^16)
Curvature
Bending moment
Curvature (m^-1 x 10^-7)
Distance from trench axis (km)
RMS error, Δgrms (mGal)
Landward
Seaward
Te (km)

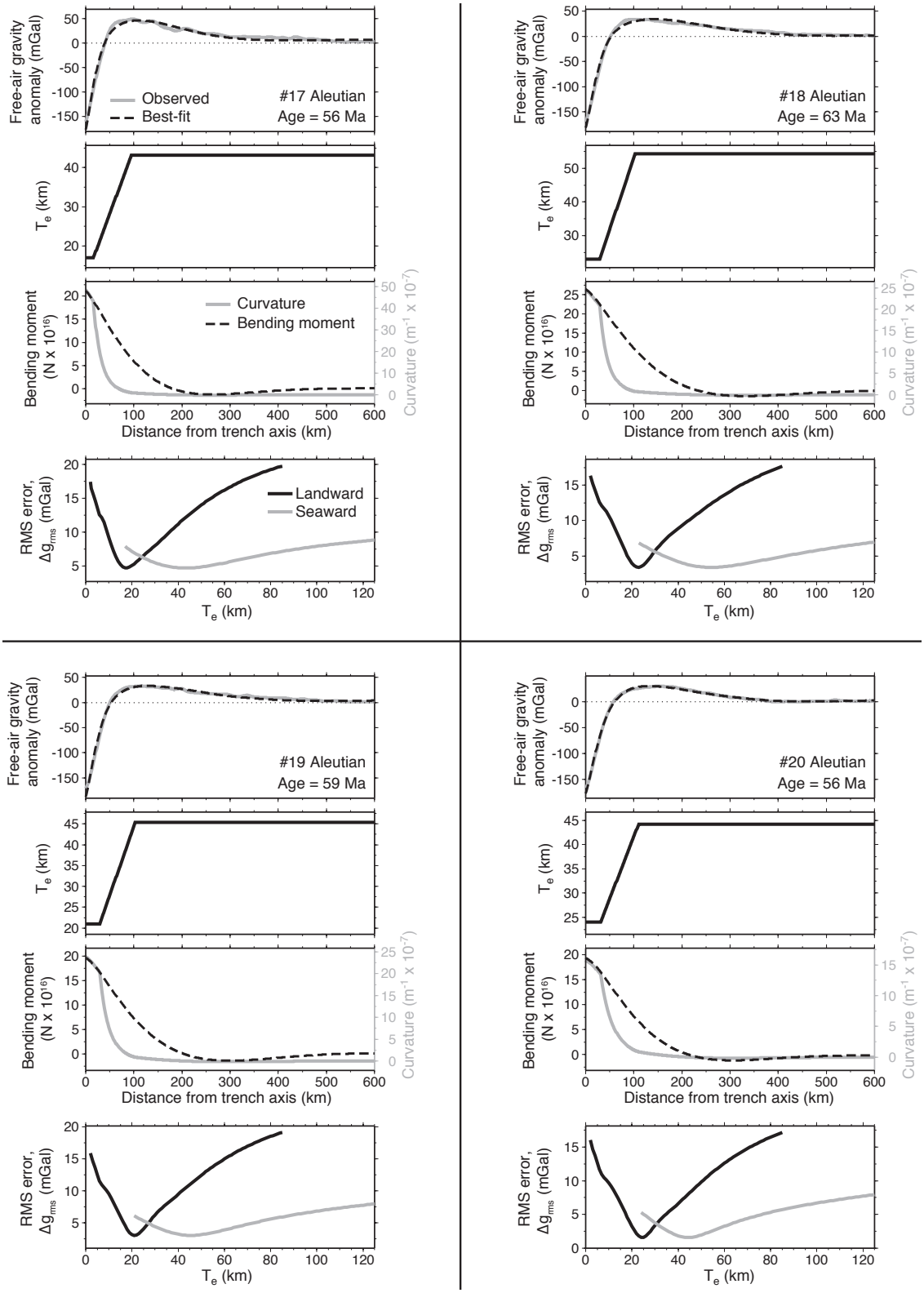
Free-air gravity anomaly (mGal)
Observed
Best-fit
#17 Aleutian
Age = 56 Ma
#18 Aleutian
Age = 63 Ma
#19 Aleutian
Age = 59 Ma
#20 Aleutian
Age = 56 Ma
Te (km)
Bending moment (N x 10^16)
Curvature
Bending moment
Curvature (m^-1 x 10^-7)
Distance from trench axis (km)
RMS error, Δgrms (mGal)
Landward
Seaward
Te (km)

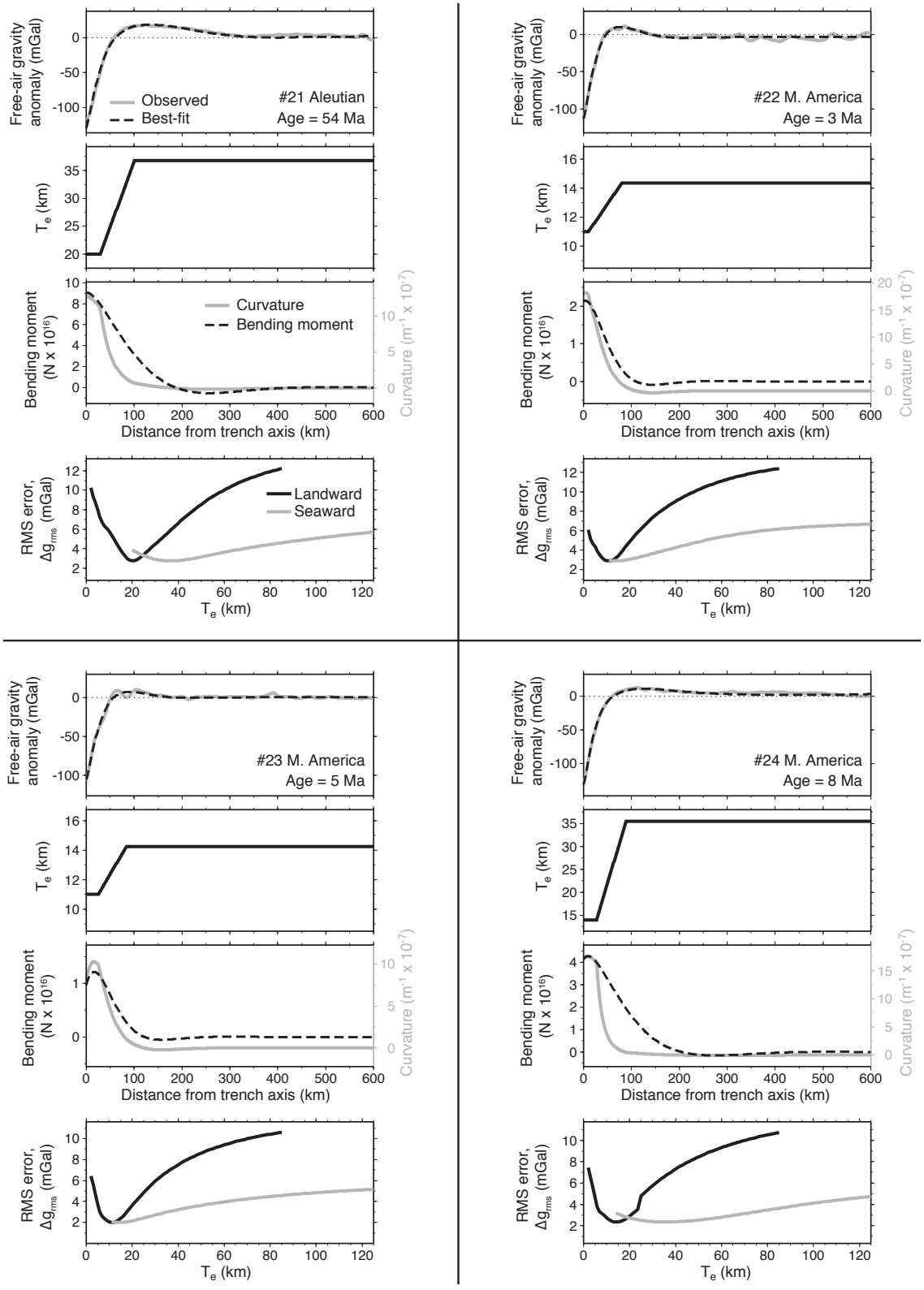
Free-air gravity anomaly (mGal)
Observed
Best-fit
#21 Aleutian
Age = 54 Ma
T_e (km)
Bending moment (N x 10^{16})
Curvature
Bending moment
Curvature (m^{-1} x 10^{-7})
Distance from trench axis (km)
RMS error, Δg_{rms} (mGal)
Landward
Seaward
T_e (km)
#22 M. America
Age = 3 Ma
#23 M. America
Age = 5 Ma
#24 M. America
Age = 8 Ma

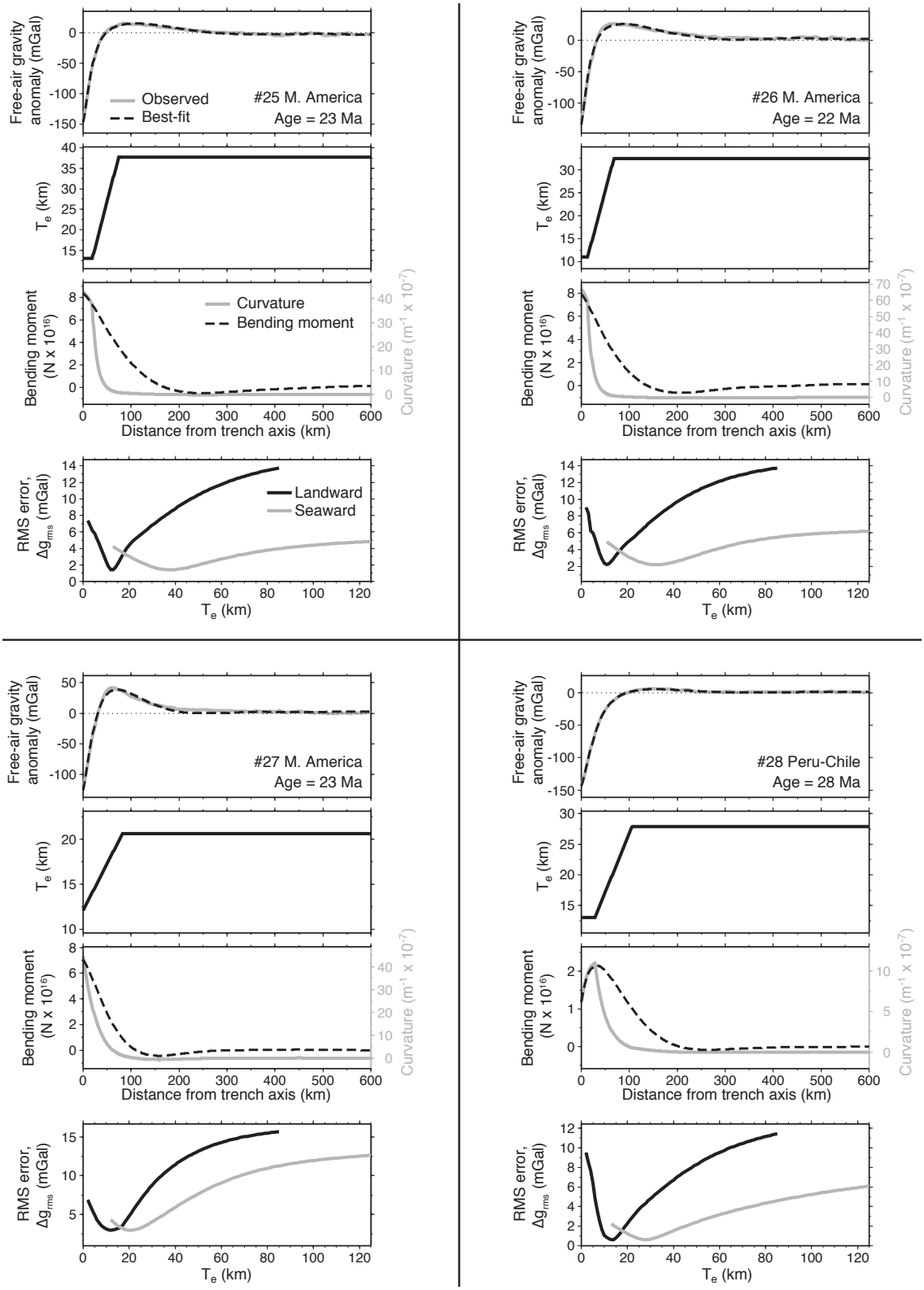
Free-air gravity anomaly (mGal)
Observed
Best-fit
#25 M. America
Age = 23 Ma
#26 M. America
Age = 22 Ma
#27 M. America
Age = 23 Ma
#28 Peru-Chile
Age = 28 Ma
Te (km)
Bending moment (N x 10^16)
Curvature
Bending moment
Curvature (m^-1 x 10^-7)
Distance from trench axis (km)
RMS error, Δgrms (mGal)
Landward
Seaward
Te (km)

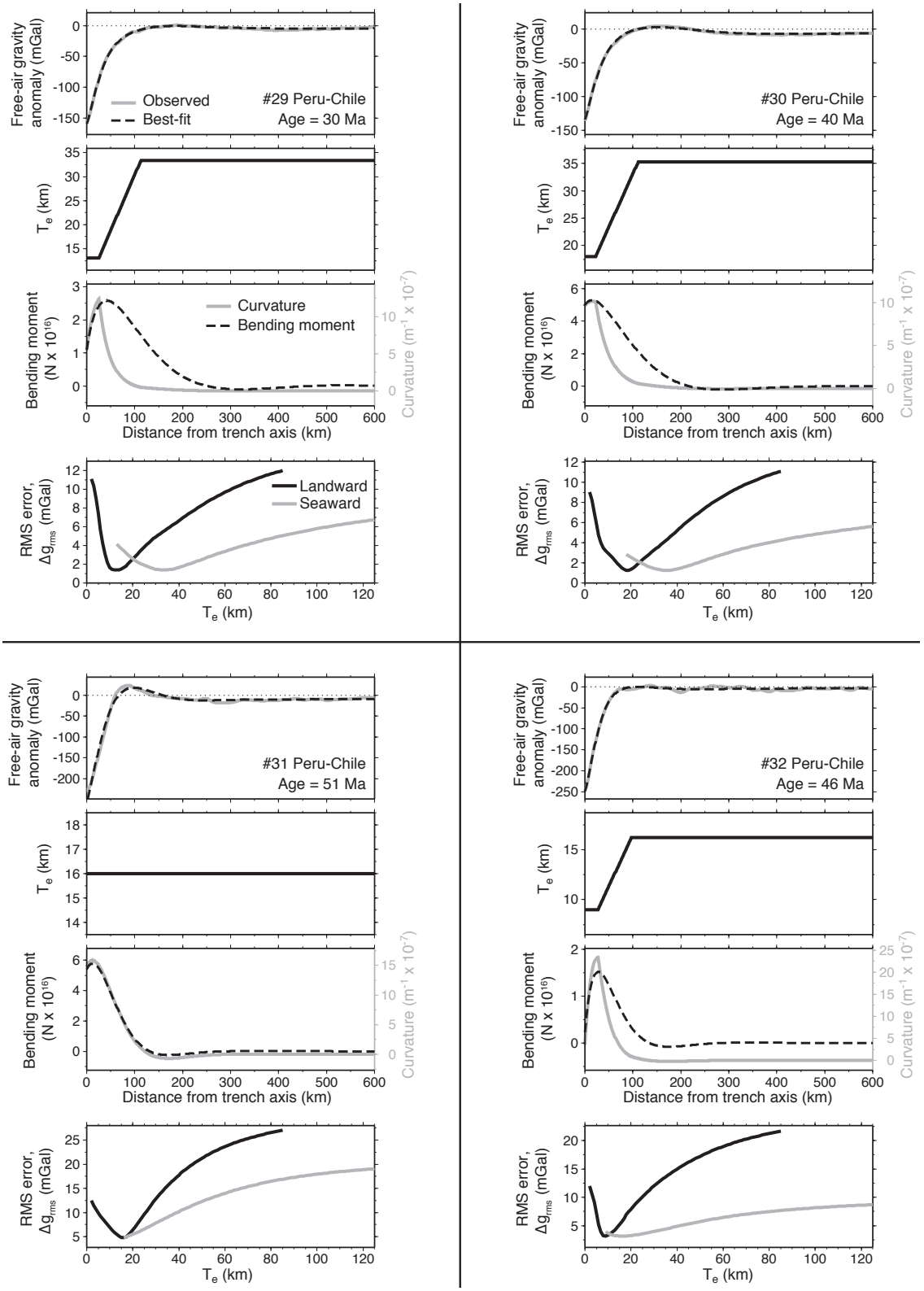
Free-air gravity anomaly (mGal)
Observed
Best-fit
#29 Peru-Chile
Age = 30 Ma
#30 Peru-Chile
Age = 40 Ma
#31 Peru-Chile
Age = 51 Ma
#32 Peru-Chile
Age = 46 Ma
Te (km)
Bending moment (N x 10^16)
Curvature
Bending moment
Curvature (m^-1 x 10^-7)
Distance from trench axis (km)
RMS error, Δgrms (mGal)
Landward
Seaward
Te (km)

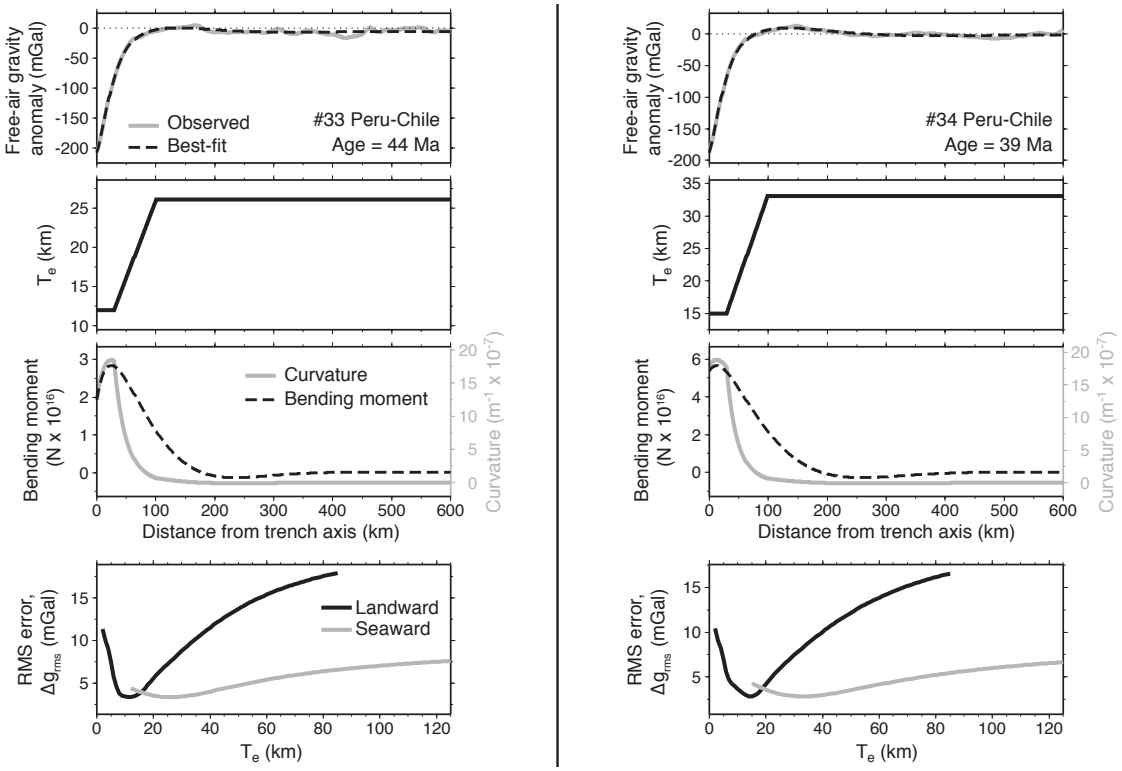
Free-air gravity anomaly (mGal)
Observed
Best-fit
#33 Peru-Chile
Age = 44 Ma
#34 Peru-Chile
Age = 39 Ma
Te (km)
Bending moment (N x 10^16)
Curvature
Bending moment
Curvature (m^-1 x 10^-7)
Distance from trench axis (km)
RMS error, Δgrms (mGal)
Landward
Seaward
Te (km)

C.2 Trench-bins

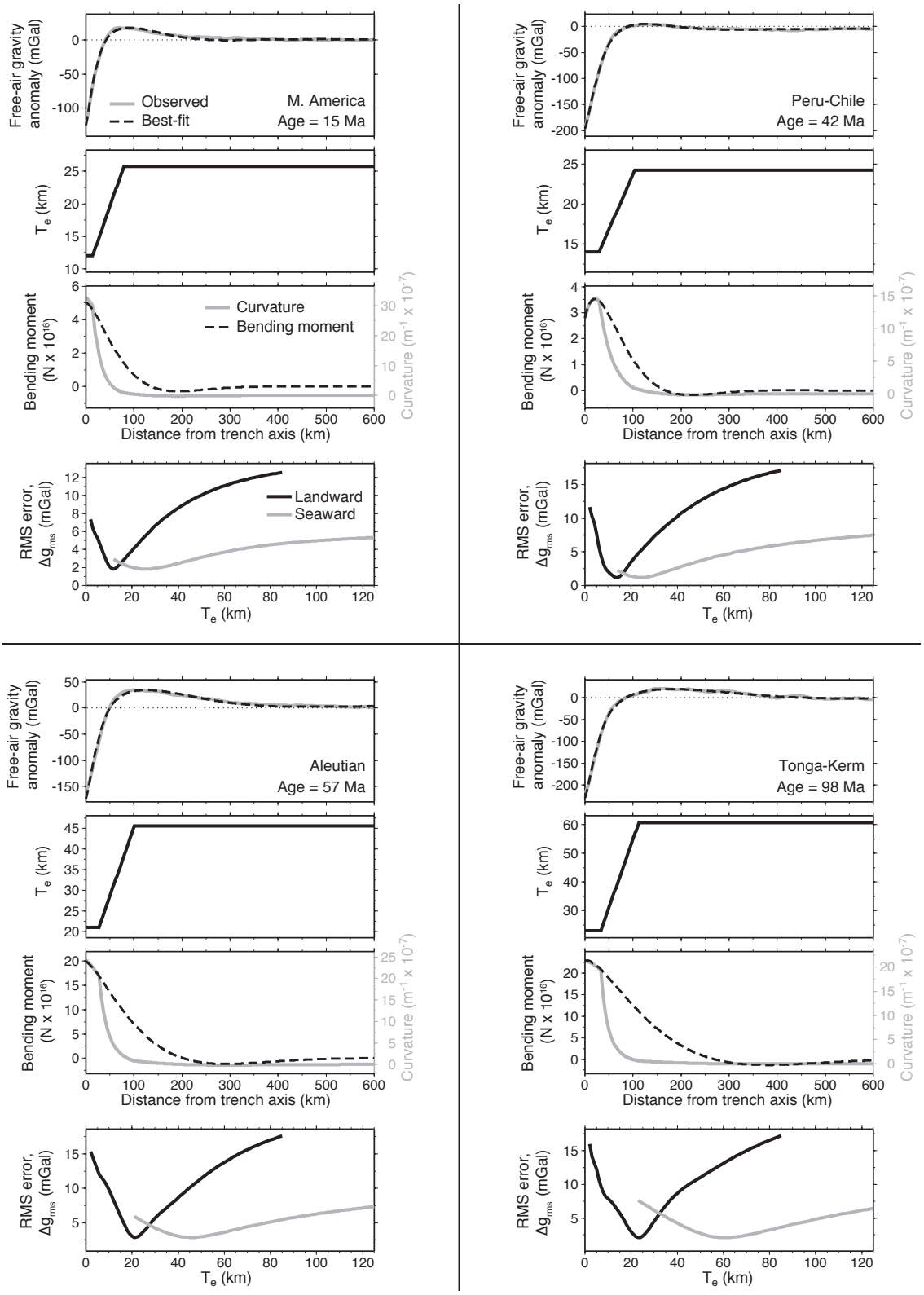

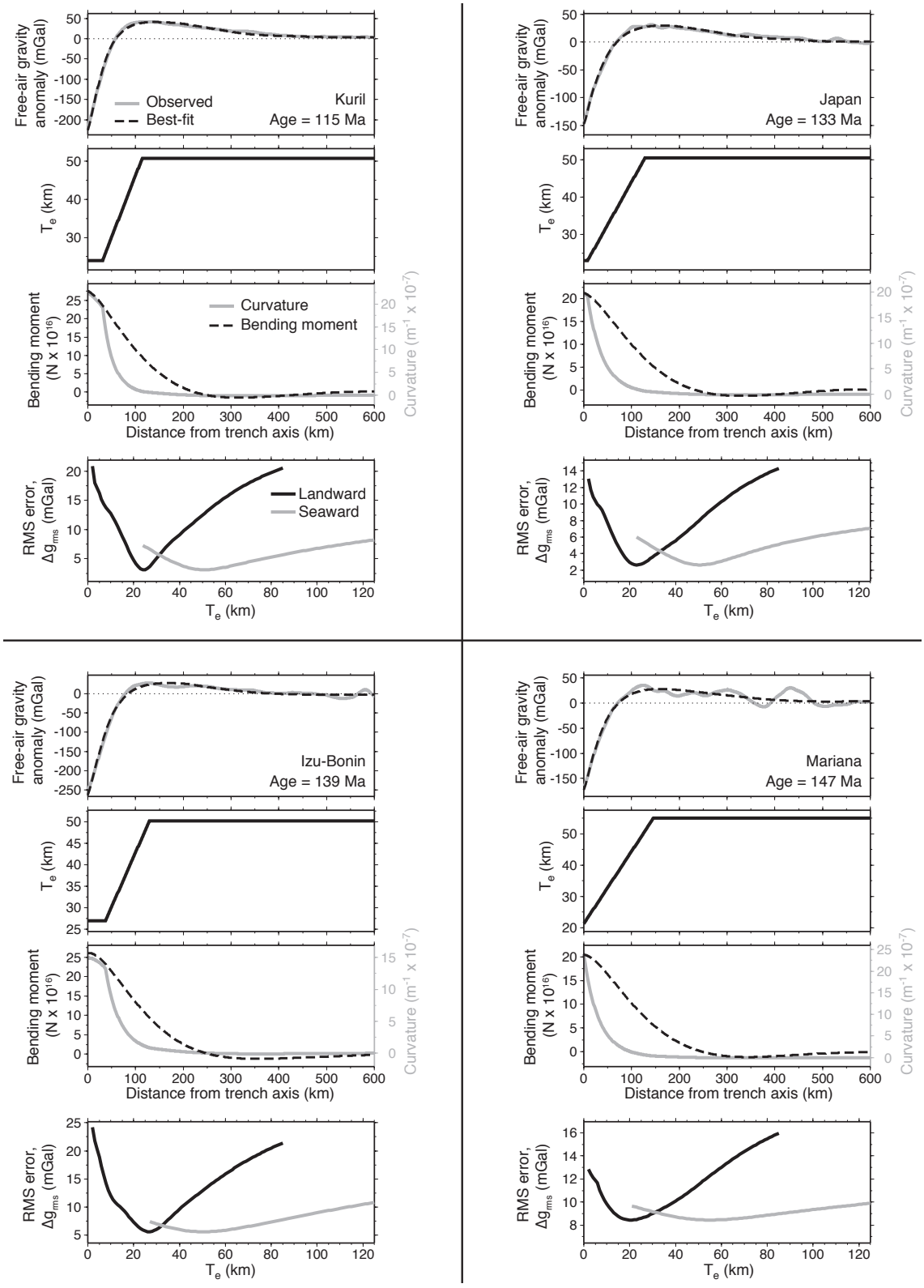
Free-air gravity anomaly (mGal)
Observed
Best-fit
Kuril
Age = 115 Ma
Japan
Age = 133 Ma
Izu-Bonin
Age = 139 Ma
Mariana
Age = 147 Ma
Te (km)
Bending moment (N x 10^16)
Curvature
Bending moment
Curvature (m^-1 x 10^-7)
Distance from trench axis (km)
RMS error, Δgms (mGal)
Landward
Seaward
Te (km)

References

Anderson, D. L. Seismic velocity, attenuation and rheology of the upper mantle. 1980.

Anderson, E. M. The dynamics of faulting. *Transactions of the Edinburgh Geological Society*, 8(3):387–402, 1905.

Anderson, E. M. *The dynamics of faulting and dyke formation with applications to Britain.* Hafner Pub. Co., 1951.

Asaadi, N., Ribe, N. M., and Sobouti, F. Inferring nonlinear mantle rheology from the shape of the Hawaiian swell. *Nature*, 473(7348):501–504, 2011.

Bai, Q. and Kohlstedt, D. L. Substantial hydrogen solubility in olivine and implications for water storage in the mantle. *Nature*, 357(6380):672–674, 1992.

Barazangi, M. and Isacks, B. L. Spatial distribution of earthquakes and subduction of the Nazca plate beneath South America. *Geology*, 4(11):686–692, 1976.

Barenblatt, G. I., Zhivago, A. V., Neprochnov, Y. P., and Ostrovskiy, A. A. The fractal dimension: a quantitative characteristic of ocean-bottom relief. *Oceanology*, 24(6):695–697, 1984.

Barrell, J. The strength of the Earth's crust. *The Journal of Geology*, pages 655–683, 1914.

Bassett, D. *The Relationship Between Structure and Seismogenic Behaviour in Subduction Zones.* PhD thesis, University of Oxford, 2014.

Bassin, C. The current limits of resolution for surface wave tomography in North America. *Eos Trans. AGU*, 2000.

Beaumont, C. Foreland basins. *Geophysical Journal International*, 65(2):291–329, 1981.

Behn, M. D., Hirth, G., and Elsenbeck, J. R. Implications of grain size evolution on the seismic structure of the oceanic upper mantle. *Earth and Planetary Science Letters*, 282 (1):178–189, 2009.

Bell, D. R. and Rossman, G. R. Water in Earth's mantle: the role of nominally anhydrous minerals. *Science*, 255(5050):1391, 1992.

Bell, T. H. Statistical features of sea-floor topography. In *Deep Sea Research and Oceanographic Abstracts*, volume 22, pages 883–892. Elsevier, 1975.

Bercovici, D. The generation of plate tectonics from mantle convection. *Earth and Planetary Science Letters*, 205(3):107–121, 2003.

Bevis, M. The curvature of Wadati-Benioff zones and the torsional rigidity of subducting plates. *Nature*, 323(6083):52–53, 1986.

Billen, M., Cowgill, E., and Buer, E. Determination of fault friction from reactivation of abyssal-hill faults in subduction zones. *Geology*, 35(9):819–822, 2007.

Billen, M. I. and Gurnis, M. Constraints on subducting plate strength within the Kermadec trench. *Journal of Geophysical Research: Solid Earth (1978–2012)*, 110(B5), 2005.

Billen, M. I. and Stock, J. Morphology and origin of the Osbourn Trough. *Journal of Geophysical Research: Solid Earth (1978–2012)*, 105(B6):13481–13489, 2000.

Blakely, R. J. *Potential theory in gravity and magnetic applications*. Cambridge University Press, 1996.

Bodine, J. H. and Watts, A. B. On lithospheric flexure seaward of the Bonin and Mariana trenches. *Earth and Planetary Science Letters*, 43(1):132–148, 1979.

Bodine, J. H., Steckler, M. S., and Watts, A. B. Observations of flexure and the rheology of the oceanic lithosphere. *Journal of Geophysical Research: Solid Earth (1978–2012)*, 86 (B5):3695–3707, 1981.

Bott, M. H. P. *GRAVN. Durham geophysical computer specification No. 1*. 1969.

Brace, W. F. An extension of the Griffith theory of fracture to rocks. *Journal of Geophysical Research*, 65(10):3477–3480, 1960.

Brace, W. F. and Kohlstedt, D. L. Limits on lithospheric stress imposed by laboratory experiments. *Journal of Geophysical Research: Solid Earth (1978–2012)*, 85(B11):6248–6252, 1980.

Brodie, J. W. Capricorn Seamount South-west Pacific Ocean. *TRANSTACTIONS OF THE ROYAL SOCIETY OF NEW ZEALAND-GEOLOGY*, 3(10):151, 1965.

Bry, M. and White, N. Reappraising elastic thickness variation at oceanic trenches. *Journal of Geophysical Research: Solid Earth*, 112(8), 2007. ISSN 21699356. doi: 10.1029/2005JB004190.

Buck, W. R. and Poliakov, A. N. B. Abyssal hills formed by stretching oceanic lithosphere. *Nature*, 392(6673):272–275, 1998.

Buck, W. R., Lavier, L. L., and Choi, E. Magma explains low estimates of lithospheric strength based on flexure of ocean island loads. In *EGU General Assembly Conference Abstracts*, volume 17, page 14525, 2015.

Buffett, B. A. Plate force due to bending at subduction zones. *Journal of Geophysical Research: Solid Earth (1978–2012)*, 111(B9), 2006.

Buffett, B. A. and Becker, T. W. Bending stress and dissipation in subducted lithosphere. *Journal of Geophysical Research: Solid Earth (1978–2012)*, 117(B5), 2012.

Bürgmann, R., Kogan, M. G., Steblov, G. M., Hilley, G., Levin, V. E., and Apel, E. Interseismic coupling and asperity distribution along the Kamchatka subduction zone. *Journal of Geophysical Research: Solid Earth (1978–2012)*, 110(B7), 2005.

Burov, E. and Gerya, T. Asymmetric three-dimensional topography over mantle plumes. *Nature*, 513(7516):85–89, 2014.

Burov, E. B. Rheology and strength of the lithosphere. *Marine and Petroleum Geology*, 28 (8):1402–1443, 2011.

Burov, E. B. and Diament, M. The effective elastic thickness (T e) of continental lithosphere: What does it really mean? *Journal of Geophysical Research: Solid Earth (1978–2012)*, 100 (B3):3905–3927, 1995.

Burov, E. B. and Watts, A. B. The long-term strength of continental lithosphere:" jelly sandwich" or" cr{è}me br{û}l{é}e"? *GSA today*, 16(1):4, 2006.

Burov, E. V., Kogan, M. G., Lyon-Caen, H., and Molnar, P. Gravity anomalies, the deep structure, and dynamic processes beneath the Tien Shan. *Earth and Planetary Science Letters*, 96(3):367–383, 1990.

Byerlee, J. Friction of rocks. *Pure and applied geophysics*, 116(4-5):615–626, 1978.

Byrne, T. Late Paleocene demise of the Kula-Pacific spreading center. *Geology*, 7(7):341–344, 1979.

Caldwell, J. G. and Turcotte, D. L. Dependence of the thickness of the elastic oceanic lithosphere on age. *Journal of Geophysical Research: Solid Earth (1978–2012)*, 84(B13):7572–7576, 1979.

Caldwell, J. G., Haxby, W. F., Karig, D. E., and Turcotte, D. L. On the applicability of a universal elastic trench profile. *Earth and Planetary Science Letters*, 31(2):239–246, 1976.

Capitanio, F. A., Morra, G., and Goes, S. Dynamics of plate bending at the trench and slab-plate coupling. *Geochemistry, Geophysics, Geosystems*, 10(4), 2009.

Cardozo, N. 3D flexural modeling code, 2009. URL `http://www.ux.uis.no/{~}nestor/work/matlabScripts.html`.

Caress, D. W. and Chayes, D. N. MB-System: Open source software for the processing and display of swath mapping sonar data. *Internet: http://www. mbari. org/data/mbsystem*, 2008.

Chapman, M. E. Techniques for interpretation of geoid anomalies. *Journal of Geophysical Research: Solid Earth (1978–2012)*, 84(B8):3793–3801, 1979.

Chapple, W. M. and Forsyth, D. W. Earthquakes and bending of plates at trenches. *Journal of Geophysical Research: Solid Earth (1978–2012)*, 84(B12):6729–6749, 1979.

Chapple, W. M. and Tullis, T. E. Evaluation of the forces that drive the plates. *Journal of geophysical research*, 82(14):1967–1984, 1977.

Chen, S., Hiraga, T., and Kohlstedt, D. L. Water weakening of clinopyroxene in the dislocation creep regime. *Journal of Geophysical Research: Solid Earth (1978–2012)*, 111(B8), 2006.

Chen, W.-P. and Molnar, P. Focal depths of intracontinental and intraplate earthquakes and their implications for the thermal and mechanical properties of the lithosphere. *J. geophys. Res*, 88(B5):4183–4214, 1983.

Chopra, P. N. The plasticity of some fine-grained aggregates of olivine at high pressure and temperature. *Geophys. Monogr., Am. Geophys. Union*, 36:25–33, 1986.

Chopra, P. N. High-temperature transient creep in olivine rocks. *Tectonophysics*, 279(1): 93–111, 1997.

Chopra, P. N. and Paterson, M. S. The experimental deformation of dunite. *Tectonophysics*, 78(1):453–473, 1981.

Chopra, P. N. and Paterson, M. S. The role of water in the deformation of dunite. *Journal of Geophysical Research: Solid Earth (1978–2012)*, 89(B9):7861–7876, 1984.

Christensen, D. H. and Ruff, L. J. Seismic coupling and outer rise earthquakes. *Journal of Geophysical Research: Solid Earth (1978–2012)*, 93(B11):13421–13444, 1988.

Clague, D. A. and Dalrymple, G. B. Age and petrology of alkalic postshield and rejuvenated-stage lava from Kauai, Hawaii. *Contributions to Mineralogy and Petrology*, 99(2):202–218, 1988.

Cloetingh, S. and Burov, E. B. Thermomechanical structure of European continental lithosphere: constraints from rheological profiles and EET estimates. *Geophysical Journal International*, 124(3):695–723, 1996.

Cloetingh, S., Burov, E., Matenco, L., Toussaint, G., Bertotti, G., Andriessen, P. A. M., Wortel, M. J. R., and Spakman, W. Thermo-mechanical controls on the mode of continental collision in the SE Carpathians (Romania). *Earth and Planetary Science Letters*, 218(1): 57–76, 2004.

Clouard, V., Campos, J., Lemoine, A., Perez, A., and Kausel, E. Outer rise stress changes related to the subduction of the Juan Fernandez Ridge, central Chile. *Journal of Geophysical Research: Solid Earth (1978–2012)*, 112(B5), 2007.

Cochran, J. R. An analysis of isostasy in the world's oceans: 2. Midocean ridge crests. *Journal of Geophysical Research: Solid Earth (1978–2012)*, 84(B9):4713–4729, 1979.

Coleman, R. G. and Keith, T. E. A chemical study of serpentinizationâĂŤBurro Mountain, California. *Journal of Petrology*, 12(2):311–328, 1971.

Conrad, C. P. and Lithgow-Bertelloni, C. How mantle slabs drive plate tectonics. *Science*, 298(5591):207–209, 2002.

Conrad, C. P., Bilek, S., and Lithgow-Bertelloni, C. Great earthquakes and slab pull: interaction between seismic coupling and plate–slab coupling. *Earth and Planetary Science Letters*, 218(1):109–122, 2004.

Contreras-Reyes, E. and Carrizo, D. Control of high oceanic features and subduction channel on earthquake ruptures along the Chile–Peru subduction zone. *Physics of the Earth and Planetary Interiors*, 186(1):49–58, 2011.

Contreras-Reyes, E. and Osses, A. Lithospheric flexure modelling seaward of the Chile trench: Implications for oceanic plate weakening in the Trench Outer Rise region. *Geophysical Journal International*, 182(1):97–112, 2010. ISSN 0956540X. doi: 10.1111/j.1365-246X.2010.04629.x.

Contreras-Reyes, E., Grevemeyer, I., Flueh, E. R., Scherwath, M., and Heesemann, M. Alteration of the subducting oceanic lithosphere at the southern central Chile trench-outer rise. *Geochemistry, Geophysics, Geosystems*, 8(7), 2007. ISSN 15252027. doi: 10.1029/2007GC001632.

Contreras-Reyes, E., Grevemeyer, I., Flueh, E. R., and Reichert, C. Upper lithospheric structure of the subduction zone offshore of southern Arauco peninsula, Chile, at˜ 38 S. *Journal of Geophysical Research: Solid Earth (1978–2012)*, 113(B7), 2008a.

Contreras-Reyes, E., Grevemeyer, I., Flueh, E. R., Scherwath, M., and Bialas, J. Effect of trench-outer rise bending-related faulting on seismic Poisson's ratio and mantle anisotropy: a case study offshore of Southern Central Chile. *Geophysical Journal International*, 173(1): 142–156, 2008b.

Courtney, R. C. and Beaumont, C. Thermally-activated creep and flexure of the oceanic lithosphere. 1983.

Craig, T. J., Copley, a., and Jackson, J. A reassessment of outer-rise seismicity and its implications for the mechanics of oceanic lithosphere. *Geophysical Journal International*, 197(1):63–89, 2014a. ISSN 0956540X. doi: 10.1093/gji/ggu013.

Craig, T. J., Copley, A., and Middleton, T. A. Constraining fault friction in oceanic lithosphere using the dip angles of newly-formed faults at outer rises. *Earth and Planetary Science Letters*, 392:94–99, 2014b.

Crawford, W. C., Hildebrand, J. A., Dorman, L. M., Webb, S. C., and Wiens, D. A. Tonga Ridge and Lau Basin crustal structure from seismic refraction data. *Journal of Geophysical Research: Solid Earth (1978–2012)*, 108(B4), 2003.

Dalrymple, G. B., Clague, D. A., Vallier, T. L., and Menard, H. W. 40Ar/39Ar age, petrology, and tectonic significance of some seamounts in the Gulf of Alaska. *Seamounts, islands, and atolls*, pages 297–315, 1987.

Davis, E. E. and Hyndman, R. D. Accretion and recent deformation of sediments along the northern Cascadia subduction zone. *Geological Society of America Bulletin*, 101(11): 1465–1480, 1989.

De Bremaecker, J.-C. Is the oceanic lithosphere elastic or viscous? *Journal of Geophysical Research*, 82(14):2001–2004, 1977.

Debayle, E. and Ricard, Y. Seismic observations of large-scale deformation at the bottom of fast-moving plates. *Earth and Planetary Science Letters*, 376:165–177, 2013.

DeMets, C., Gordon, R. G., and Argus, D. F. Geologically current plate motions. *Geophysical Journal International*, 181(1):1–80, 2010.

Dengo, C. A. and Logan, J. M. Implications of the mechanical and frictional behavior of serpentinite to seismogenic faulting. *Journal of Geophysical Research: Solid Earth (1978–2012)*, 86(B11):10771–10782, 1981.

Detrick, R. S. and Watts, A. B. An analysis of isostasy in the world's oceans, 3. Aseismic ridges. *J. geophys. Res*, 84(8687):8653, 1979.

Detrick, R. S., Von Herzen, R. P., Crough, S. T., Epp, D., and Fehn, U. Heat flow on the Hawaiian swell and lithospheric reheating. 1981.

Divins, D. L. Total Sediment Thickness of the World's Oceans and Marginal Seas, 2003.

Dmowska, R. and Lovison, L. C. Intermediate-term seismic precursors for some coupled subduction zones. *pure and applied geophysics*, 126(2-4):643–664, 1988.

Dolan, J. F. and Mann, P. *Active strike-slip and collisional tectonics of the northern Caribbean plate boundary zone*, volume 326. Geological Society of America, 1998.

Duncan, R. A. and Clague, D. A. Pacific plate motion recorded by linear volcanic chains. In *The ocean basins and margins*, pages 89–121. Springer, 1985.

Dziewonski, A. M., Chou, T.-A., and Woodhouse, J. H. Determination of earthquake source parameters from waveform data for studies of global and regional seismicity. *Journal of Geophysical Research: Solid Earth (1978–2012)*, 86(B4):2825–2852, 1981.

Edmond, J. M. and Paterson, M. S. Volume changes during the deformation of rocks at high pressures. In *International Journal of Rock Mechanics and Mining Sciences & Geomechanics Abstracts*, volume 9, pages 161–182. Elsevier, 1972.

Ekström, G., Nettles, M., and Dziewo\'nski, A. M. The global CMT project 2004–2010: Centroid-moment tensors for 13,017 earthquakes. *Physics of the Earth and Planetary Interiors*, 200:1–9, 2012.

Engdahl, E. R. and Scholz, C. H. A double Benioff zone beneath the central Aleutians: An unbending of the lithosphere. *Geophysical Research Letters*, 4(10):473–476, 1977.

Engdahl, E. R., van der Hilst, R., and Buland, R. Global teleseismic earthquake relocation with improved travel times and procedures for depth determination. *Bulletin of the Seismological Society of America*, 88(3):722–743, 1998.

England, P. and Wortel, R. Some consequences of the subduction of young slabs. *Earth and Planetary Science Letters*, 47(3):403–415, 1980.

Escartin, J., Hirth, G., and Evans, B. Nondilatant brittle deformation of serpentinites: Implications for Mohr-Coulomb theory and the strength of faults. *Journal of Geophysical Research: Solid Earth (1978–2012)*, 102(B2):2897–2913, 1997.

Escartin, J., Hirth, G., and Evans, B. Strength of slightly serpentinized peridotites: Implications for the tectonics of oceanic lithosphere. *Geology*, 29(11):1023–1026, 2001.

Evans, B. and Goetze, C. The temperature variation of hardness of olivine and its implication for polycrystalline yield stress. *Journal of Geophysical Research: Solid Earth (1978–2012)*, 84(B10):5505–5524, 1979.

Farrington, R. J., Moresi, L.-N., and Capitanio, F. A. The role of viscoelasticity in subducting plates. *Geochemistry, Geophysics, Geosystems*, 15(11):4291–4304, 2014.

Faul, U. H. and Jackson, I. Diffusion creep of dry, melt-free olivine. *Journal of Geophysical Research: Solid Earth (1978–2012)*, 112(B4), 2007.

Foley, B. J. and Becker, T. W. Generation of plate-like behavior and mantle heterogeneity from a spherical, viscoplastic convection model. *Geochemistry, Geophysics, Geosystems*, 10 (8), 2009.

Forsyth, D. and Uyeda, S. On the relative importance of the driving forces of plate motion. *Geophysical Journal International*, 43(1):163–200, 1975.

Forsyth, D. W. Determinations of focal depths of earthquakes associated with the bending of oceanic plates at trenches. *Physics of the Earth and Planetary Interiors*, 28(2):141–160, 1982.

Forsyth, D. W. Subsurface loading and estimates of the flexural rigidity of continental lithosphere. *Journal of Geophysical Research: Solid Earth (1978–2012)*, 90(B14):12623–12632, 1985.

Frohlich, C., Billington, S., Engdahl, E. R., and Malahoff, A. Detection and location of earthquakes in the central Aleutian subduction zone using island and ocean bottom seismograph stations. *Journal of Geophysical Research: Solid Earth (1978–2012)*, 87(B8):6853–6864, 1982.

Fryer, P. and Smoot, N. C. Processes of seamount subduction in the Mariana and Izu-Bonin trenches. *Marine Geology*, 64(1):77–90, 1985.

Gamage, S. S. N., Umino, N., Hasegawa, A., and Kirby, S. H. Offshore double-planed shallow seismic zone in the NE Japan forearc region revealed by sP depth phases recorded by regional networks. *Geophysical Journal International*, 178(1):195–214, 2009.

Garcia, E. S., Sandwell, D. T., and Luttrell, K. M. An iterative spectral solution method for thin elastic plate flexure with variable rigidity. *Geophysical Journal International*, 200(2): 1010–1026, 2015.

Garcia-Castellanos, D., Torne, M., and Fernandez, M. Slab pull effects from a flexural analysis of the Tonga and Kermadec trenches (Pacific Plate). *Geophysical Journal International*, 141(2):479–484, 2000.

Gere, J. and Goodno, B. Mechanics of materials. 2009.

Gilbert, G. K. *Lake Bonneville*, volume 1. US Government Printing Office, 1890.

Gilbert, L. E. and Malinverno, A. A characterization of the spectral density of residual ocean floor topography. *Geophysical Research Letters*, 15(12):1401–1404, 1988.

Goetze, C. The mechanisms of creep in olivine [and discussion]. *Philosophical Transactions of the Royal Society of London. Series A, Mathematical and Physical Sciences*, 288(1350): 99–119, 1978.

Goetze, C. and Evans, B. Stress and temperature in the bending lithosphere as constrained by experimental rock mechanics. *Geophysical Journal International*, 59(3):463–478, 1979.

Gordon, R. B. Diffusion creep in the Earth's mantle. *Journal of Geophysical Research*, 70(10):2413–2418, 1965. ISSN 2156-2202. doi: 10.1029/JZ070i010p02413. URL `http://dx.doi.org/10.1029/JZ070i010p02413`.

Grevemeyer, I., Kaul, N., Diaz-Naveas, J. L., Villinger, H. W., Ranero, C. R., and Reichert, C. Heat flow and bending-related faulting at subduction trenches: case studies offshore of Nicaragua and Central Chile. *Earth and Planetary Science Letters*, 236(1):238–248, 2005.

Grevemeyer, I., Ranero, C. R., Flueh, E. R., Kläschen, D., and Bialas, J. Passive and active seismological study of bending-related faulting and mantle serpentinization at the Middle America trench. *Earth and Planetary Science Letters*, 258(3):528–542, 2007.

Griffith, A. A. The phenomena of rupture and flow in solids. *Philosophical transactions of the royal society of london. Series A, containing papers of a mathematical or physical character*, pages 163–198, 1921.

Grim, P. J. and Erickson, B. H. Fracture zones and magnetic anomalies south of the Aleutian trench. *Journal of Geophysical Research*, 74(6):1488–1494, 1969.

Gunn, R. A quantitative evaluation of the influence of the lithosphere on the anomalies of gravity. *Journal of the Franklin Institute*, 236(1):47–66, 1943.

Gutscher, M.-A. Andean subduction styles and their effect on thermal structure and interplate coupling. *Journal of South American Earth Sciences*, 15(1):3–10, 2002.

Gutscher, M.-A., Olivet, J.-L., Aslanian, D., Eissen, J.-P., and Maury, R. The âĂIJlost Inca PlateauâĂİ: cause of flat subduction beneath Peru? *Earth and Planetary Science Letters*, 171(3):335–341, 1999.

Hager, B. H. Constraints on Mantle Rheology and Flow. *Journal of Geophysical Research*, 89 (B7):6003–6015, 1984.

Hager, B. H. and O'Connell, R. J. A simple global model of plate dynamics and mantle convection. *Journal of Geophysical Research: Solid Earth (1978–2012)*, 86(B6):4843–4867, 1981.

Hall, E. O. The deformation and ageing of mild steel: III discussion of results. *Proceedings of the Physical Society. Section B*, 64(9):747, 1951.

Hanks, T. C. The Kuril Trench-Hokkaido Rise system: large shallow earthquakes and simple models of deformation. *Geophysical Journal International*, 23(2):173–189, 1971.

Hansen, L. N., Zimmerman, M. E., and Kohlstedt, D. L. Grain boundary sliding in San Carlos olivine: Flow law parameters and crystallographic-preferred orientation. *Journal of Geophysical Research: Solid Earth (1978–2012)*, 116(B8), 2011.

Haskell, N. A. The motion of a viscous fluid under a surface load. *Journal of Applied Physics*, 6(8):265–269, 1935.

Hauri, E. H., Lassiter, J. C., and DePaolo, D. J. Osmium isotope systematics of drilled lavas from Mauna Loa, Hawaii. *Journal of Geophysical Research: Solid Earth (1978–2012)*, 101 (B5):11793–11806, 1996.

Hayes, G. P., Wald, D. J., and Johnson, R. L. Slab1. 0: A three-dimensional model of global subduction zone geometries. *Journal of Geophysical Research: Solid Earth (1978–2012)*, 117(B1), 2012.

Heiland, C. A. *Geophysical exploration*. Prentice-Hall, Incorporated, 1940.

Hetényi, M. *Beams on elastic foundation: theory with applications in the fields of civil and mechanical engineering*, volume 16. University of Michigan Press, 1946.

Heuret, A. and Lallemand, S. Plate motions, slab dynamics and back-arc deformation. *Physics of the Earth and Planetary Interiors*, 149(1):31–51, 2005.

Hilairet, N., Reynard, B., Wang, Y., Daniel, I., Merkel, S., Nishiyama, N., and Petitgirard, S. High-pressure creep of serpentine, interseismic deformation, and initiation of subduction. *Science*, 318(5858):1910–1913, 2007.

Hillier, J. K. and Watts, A. B. Relationship between depth and age in the North Pacific Ocean. *Journal of Geophysical Research: Solid Earth (1978–2012)*, 110(B2), 2005.

Hino, R., Azuma, R., Ito, Y., Yamamoto, Y., Suzuki, K., Tsushima, H., Suzuki, S., Miyashita, M., Tomori, T., Arizono, M., and Others. Insight into complex rupturing of the immature bending normal fault in the outer slope of the Japan Trench from aftershocks of the 2005 Sanriku earthquake (Mw= 7.0) located by ocean bottom seismometry. *Geochemistry, Geophysics, Geosystems*, 10(7), 2009.

Hirth, G. and Kohlstedt, D. Rheology of the upper mantle and the mantle wedge: A view from the experimentalists. *Inside the subduction Factory*, pages 83–105, 2003.

Hirth, G. and Kohlstedt, D. L. Water in the oceanic upper mantle: implications for rheology, melt extraction and the evolution of the lithosphere. *Earth and Planetary Science Letters*, 144(1):93–108, 1996.

International Seismological Centre. On-line Bulletin, 2013.

Ioc, Iho, and Bodc. Centenary Edition of the GEBCO Digital Atlas, published on CD-ROM on behalf of the Intergovernmental Oceanographic Commission and the International Hydrographic Organization as part of the General Bathymetric Chart of the Oceans, British Oceanographic Cen, 2003.

Isacks, B. L. and Barazangi, M. Geometry of Benioff zones. *Island arcs, deep sea trenches and back-arc basins*, pages 99–114, 1977.

Ismail, W. B. and Mainprice, D. An olivine fabric database: an overview of upper mantle fabrics and seismic anisotropy. *Tectonophysics*, 296(1):145–157, 1998.

Jackson, J. Strength of the continental lithosphere: time to abandon the jelly sandwich? *GSA today*, 12(9):4–9, 2002.

Jarrard, R. D. and Clague, D. A. Implications of Pacific island and seamount ages for the origin of volcanic chains. *Reviews of Geophysics*, 15(1):57–76, 1977.

Jeffreys, H. On the nature of isostasy. *Gerlands Beitrage zur Geophysik*, 15(2):167–186, 1926.

Jones, G. M., Hilde, T. W. C., Sharman, G. F., and Agnew, D. C. Fault patterns in outer trench walls and their tectonic significance. *Journal of Physics of the Earth*, 26 (Supplement):S85—-S101, 1978.

Jordan, T. A. and Watts, A. B. Gravity anomalies, flexure and the elastic thickness structure of the India–Eurasia collisional system. *Earth and Planetary Science Letters*, 236(3):732–750, 2005.

Judge, A. V. and McNutt, M. K. The relationship between plate curvature and elastic plate thickness: A study of the Peru-Chile Trench. *Journal of Geophysical Research: Solid Earth (1978–2012)*, 96(B10):16625–16639, 1991.

Kalnins, L. M. and Watts, A. B. Spatial variations in effective elastic thickness in the Western Pacific Ocean and their implications for Mesozoic volcanism. *Earth and Planetary Science Letters*, 286(1):89–100, 2009.

Karato, S.-i. *Deformation of earth materials: an introduction to the rheology of solid earth*. Cambridge University Press, 2008.

Karato, S.-i. Rheology of the Earth's mantle: A historical review. *Gondwana Research*, 18 (1):17–45, 2010.

Karato, S.-i. Water distribution across the mantle transition zone and its implications for global material circulation. *Earth and Planetary Science Letters*, 301(3):413–423, 2011.

Karato, S.-I. and Jung, H. Effects of pressure on high-temperature dislocation creep in olivine. *Philosophical Magazine*, 83(3):401–414, 2003.

Karato, S.-I., Paterson, M. S., and FitzGerald, J. D. Rheology of synthetic olivine aggregates: influence of grain size and water. *Journal of Geophysical Research: Solid Earth (1978–2012)*, 91(B8):8151–8176, 1986.

Karato, S.-i., Wu, P., and Others. Rheology of the upper mantle- A synthesis. *Science*, 260 (5109):771–778, 1993.

Karner, G. D. and Watts, A. B. Gravity anomalies and flexure of the lithosphere at mountain ranges. *Journal of Geophysical Research: Solid Earth (1978–2012)*, 88(B12):10449–10477, 1983.

Katayama, I. and Karato, S.-i. Low-temperature, high-stress deformation of olivine under water-saturated conditions. *Physics of the Earth and Planetary Interiors*, 168(3):125–133, 2008.

Kobayashi, K., Nakanishi, M., Tamaki, K., and Ogawa, Y. Outer slope faulting associated with the western Kuril and Japan trenches. *Geophysical Journal International*, 134(2): 356–372, 1998.

Kocks, W. F. Thermodynamics and kinetics of slip. *Progr. Mater. Sci.*, 19:291, 1975.

Kohlstedt, D. L. and Goetze, C. Low-stress high-temperature creep in olivine single crystals. *Journal of Geophysical Research*, 79(14):2045–2051, 1974.

Kohlstedt, D. L., Evans, B., and Mackwell, S. J. Strength of the lithosphere: constraints imposed by laboratory experiments. *Journal of Geophysical Research: Solid Earth (1978–2012)*, 100(B9):17587–17602, 1995.

Koppers, A. A. P., Duncan, R. A., and Steinberger, B. Implications of a nonlinear 40Ar/39Ar age progression along the Louisville seamount trail for models of fixed and moving hot spots. *Geochemistry, Geophysics, Geosystems*, 5(6), 2004.

Korenaga, J. Thermal cracking and the deep hydration of oceanic lithosphere: a key to the generation of plate tectonics? *Journal of Geophysical Research: Solid Earth (1978–2012)*, 112(B5), 2007.

Kusznir, N. and Karner, G. Dependence of the flexural rigidity of the continental lithosphere on rheology and temperature. 1985.

Lakes, R. S. *Viscoelastic materials*. Cambridge University Press, 2009.

Langseth, M. G., Le Pichon, X., and Ewing, M. Crustal structure of the mid-ocean ridges: 5. Heat flow through the Atlantic Ocean floor and convection currents. *Journal of Geophysical Research*, 71(22):5321–5355, 1966.

Lefeldt, M., Grevemeyer, I., Goßler, J., and Bialas, J. Intraplate seismicity and related mantle hydration at the Nicaraguan trench outer rise. *Geophysical Journal International*, 178(2): 742–752, 2009.

Levitt, D. A. and Sandwell, D. T. Lithospheric bending at subduction zones based on depth soundings and satellite gravity. *Journal of Geophysical Research: Solid Earth (1978–2012)*, 100(B1):379–400, 1995.

Li, X., Kind, R., Priestley, K., Sobolev, S. V., Tilmann, F., Yuan, X., and Weber, M. Mapping the Hawaiian plume conduit with converted seismic waves. *Nature*, 405(6789):938–941, 2000.

Liu, X. and McNally, K. C. Quantitative estimates of interplate coupling inferred from outer rise earthquakes. *pure and applied geophysics*, 140(2):211–255, 1993.

Lonsdale, P. A multibeam reconnaissance of the Tonga Trench axis and its intersection with the Louisville guyot chain. *Marine Geophysical Researches*, 8(4):295–327, 1986.

Lowry, A. R. and Smith, R. B. Flexural rigidity of the Basin and Range-Colorado Plateau-Rocky Mountain transition from coherence analysis of gravity and topography. *JOURNAL OF GEOPHYSICAL RESEARCH-ALL SERIES-*, 99:20–123, 1994.

Lyon-Caen, H. and Molnar, P. Constraints on the structure of the Himalaya from an analysis of gravity anomalies and a flexural model of the lithosphere. *J. Geophys. Res*, 88(B10): 8171–8191, 1983.

Macdonald, K. C., Fox, P. J., Alexander, R. T., Pockalny, R., and Gente, P. Volcanic growth faults and the origin of Pacific abyssal hills. *Nature*, 380(6570):125–129, 1996.

Maggi, A., Jackson, J. A., Mckenzie, D., and Priestley, K. Earthquake focal depths, effective elastic thickness, and the strength of the continental lithosphere. *Geology*, 28(6):495–498, 2000.

Mandelbrot, B. B. *The fractal geometry of nature*. Macmillan, 1983.

Manea, M., Manea, V. C., Ferrari, L., Kostoglodov, V., and Bandy, W. L. Tectonic evolution of the Tehuantepec Ridge. *Earth and Planetary Science Letters*, 238(1):64–77, 2005.

Manea, V. C., Pérez-Gussinyé, M., and Manea, M. Chilean flat slab subduction controlled by overriding plate thickness and trench rollback. *Geology*, 40(1):35–38, 2012.

Manríquez, P., Contreras-Reyes, E., and Osses, A. Lithospheric 3-D flexure modelling of the oceanic plate seaward of the trench using variable elastic thickness. *Geophysical Journal International*, 196(2):681–693, 2014.

Mareschal, J.-C. Fractal reconstruction of sea-floor topography. *pure and applied geophysics*, 131(1-2):197–210, 1989.

Markwardt, C. B. Non-linear least squares fitting in IDL with MPFIT. *arXiv preprint arXiv:0902.2850*, 2009.

Massell, C. G. *Large-scale structural variation of trench outer slopes and rises*. PhD thesis, University of California, San Diego, 2002.

Masson, D. G. Fault patterns at outer trench walls. *Marine Geophysical Researches*, 13(3): 209–225, 1991.

McAdoo, D. C. and Sandwell, D. T. Folding of oceanic lithosphere. *Journal of Geophysical Research: Solid Earth (1978–2012)*, 90(B10):8563–8569, 1985.

McAdoo, D. C., Caldwell, J. G., and Turcotte, D. L. On the elastic-perfectly plastic bending of the lithosphere under generalized loading with application to the Kuril Trench. *Geophysical Journal International*, 54(1):11–26, 1978.

McConnell, R. K. Viscosity of the mantle from relaxation time spectra of isostatic adjustment. *Journal of Geophysical Research*, 73(22):7089–7105, 1968.

McKenzie, D. Estimating Te in the presence of internal loads. *Journal of Geophysical Research: Solid Earth (1978–2012)*, 108(B9), 2003.

McKenzie, D. and Bowin, C. The relationship between bathymetry and gravity in the Atlantic Ocean. *Journal of Geophysical Research*, 81(11):1903–1915, 1976.

McKenzie, D. and Fairhead, D. Estimates of the effective elastic thickness of the continental lithosphere from Bouguer and free air gravity anomalies. *Journal of Geophysical Research: Solid Earth (1978–2012)*, 102(B12):27523–27552, 1997.

McKenzie, D. P. Some remarks on heat flow and gravity anomalies. *Journal of Geophysical Research*, 72(24):6261–6273, 1967.

McKenzie, D. P. Speculations on the consequences and causes of plate motions. *Geophysical Journal International*, 18(1):1–32, 1969.

McNutt, M. K. Lithospheric flexure and thermal anomalies. *Journal of Geophysical Research: Solid Earth (1978–2012)*, 89(B13):11180–11194, 1984.

McNutt, M. K. and Fischer, K. M. *The south Pacific superswell*. Wiley Online Library, 1987.

McNutt, M. K. and Judge, A. V. The superswell and mantle dynamics beneath the South Pacific. *Science*, 248(4958):969–975, 1990.

McNutt, M. K. and Menard, H. W. Constraints on yield strength in the oceanic lithosphere derived from observations of flexure. *Geophysical Journal International*, 71(2):363–394, 1982.

McQueen, H. W. S. and Lambeck, K. The accuracy of some lithospheric bending parameters. *Geophysical Journal International*, 96(3):401–413, 1989.

Mei, S. and Kohlstedt, D. L. Influence of water on plastic deformation of olivine aggregates: 2. Dislocation creep regime. *Journal of Geophysical Research: Solid Earth (1978–2012)*, 105(B9):21471–21481, 2000a.

Mei, S. and Kohlstedt, D. L. Influence of water on plastic deformation of olivine aggregates: 1. Diffusion creep regime. *Journal of Geophysical Research: Solid Earth (1978–2012)*, 105 (B9):21457–21469, 2000b.

Mei, S., Suzuki, A. M., Kohlstedt, D. L., Dixon, N. A., and Durham, W. B. Experimental constraints on the strength of the lithospheric mantle. *Journal of Geophysical Research: Solid Earth (1978–2012)*, 115(B8), 2010.

Meinesz, F. A. V. *Gravity over the Hawaiian Archipelago and over the Madeira area, conclusions about the Earth's crust*. 1941.

Menard, H. W. and McNutt, M. Evidence for and consequences of thermal rejuvenation. *Journal of Geophysical Research: Solid Earth (1978–2012)*, 87(B10):8570–8580, 1982.

Mitrovica, J. X. Haskell [1935] revisited. *JOURNAL OF GEOPHYSICAL RESEARCH-ALL SERIES-*, 101:555–569, 1996.

Mitrovica, J. X. and Peltier, W. R. The inference of mantle viscosity from an inversion of the Fennoscandian relaxation spectrum. *Geophysical Journal International*, 114(1):45–62, 1993.

Miura, S., Takahashi, N., Nakanishi, A., Tsuru, T., Kodaira, S., and Kaneda, Y. Structural characteristics off Miyagi forearc region, the Japan Trench seismogenic zone, deduced from a wide-angle reflection and refraction study. *Tectonophysics*, 407(3):165–188, 2005.

Miyazaki, T., Sueyoshi, K., and Hiraga, T. Olivine crystals align during diffusion creep of Earth/'s upper mantle. *Nature*, 502(7471):321–326, 2013.

Moody, J. B. Serpentinization: a review. *Lithos*, 9(2):125–138, 1976.

Moore, D. E., Lockner, D. A., Ma, S., Summers, R., and Byerlee, J. D. Strengths of serpentinite gouges at elevated temperatures. *Journal of Geophysical Research: Solid Earth (1978–2012)*, 102(B7):14787–14801, 1997.

Moore, J. G. Density of basalt core from Hilo drill hole, Hawaii. *Journal of volcanology and geothermal research*, 112(1):221–230, 2001.

Moore, J. G. and Clague, D. A. Volcano growth and evolution of the island of Hawaii. *Geological Society of America Bulletin*, 104(11):1471–1484, 1992.

Moré, J. J. The Levenberg-Marquardt algorithm: implementation and theory. In *Numerical analysis*, pages 105–116. Springer, 1978.

Morgan, J. P. The generation of a compositional lithosphere by mid-ocean ridge melting and its effect on subsequent off-axis hotspot upwelling and melting. *Earth and Planetary Science Letters*, 146(1):213–232, 1997.

Morgan, W. J. Convection plumes in the lower mantle. 1971.

Mortera-Gutiérrez, C. A., Scholl, D. W., and Carlson, R. L. Fault trends on the seaward slope of the Aleutian Trench: Implications for a laterally changing stress field tied to a westward increase in oblique convergence. *Journal of Geophysical Research: Solid Earth (1978–2012)*, 108(B10), 2003.

Mueller, S. and Phillips, R. J. On the reliability of lithospheric constraints derived from models of outer-rise flexure. *Geophysical Journal International*, 123(3):887–902, 1995.

Mueller, S., Choy, G. L., and Spence, W. Inelastic models of lithospheric stress-I. Theory and application to outer-rise plate deformation. *Geophysical Journal International*, 125(1): 39–53, 1996a.

Mueller, S., Spence, W., and Choy, G. L. Inelastic models of lithospheric stress-11. Implications for outer-rise seismicity and dynamics. *Geophysical Journal International*, 125(1): 54–72, 1996b.

Müller, R. D., Sdrolias, M., Gaina, C., and Roest, W. R. Age, spreading rates, and spreading asymmetry of the world's ocean crust. *Geochemistry, Geophysics, Geosystems*, 9(4):1–19, 2008. ISSN 15252027. doi: 10.1029/2007GC001743.

Nabarro, F. R. N. Deformation of crystals by the motion of single ions. In *Report of a Conference on Strength of Solids*, pages 75–90, 1948.

Nakada, M. and Lambeck, K. Glacial rebound and relative sea-level variations: a new appraisal. *Geophysical Journal International*, 90(1):171–224, 1987.

Naliboff, J. B., Billen, M. I., Gerya, T., and Saunders, J. Dynamics of outer-rise faulting in oceanic-continental subduction systems. *Geochemistry, Geophysics, Geosystems*, 14(7): 2310–2327, 2013.

Nishimura, C. E. and Forsyth, D. W. Anomalous Love-wave phase velocities in the Pacific: sequential pure-path and spherical harmonic inversion. *Geophysical Journal International*, 81(2):389–407, 1985.

Nishimura, C. E. and Forsyth, D. W. The anisotropic structure of the upper mantle in the Pacific. *Geophysical Journal International*, 96(2):203–229, 1989.

Nishizawa, A., Kaneda, K., Watanabe, N., and Oikawa, M. Seismic structure of the subducting seamounts on the trench axis: Erimo Seamount and Daiichi-Kashima Seamount, northern and southern ends of the Japan Trench. *Earth, Planets and Space*, 61(3):e5—-e8, 2009.

Ohuchi, T., Karato, S.-i., and Fujino, K. Strength of single-crystal orthopyroxene under lithospheric conditions. *Contributions to Mineralogy and Petrology*, 161(6):961–975, 2011.

Pacheco, J. F., Sykes, L. R., and Scholz, C. H. Nature of seismic coupling along simple plate boundaries of the subduction type. *Journal of Geophysical Research: Solid Earth (1978–2012)*, 98(B8):14133–14159, 1993.

Parker, R. L. The rapid calculation of potential anomalies. *Geophysical Journal International*, 31(4):447–455, 1973.

Parsons, B. and Molnar, P. The origin of outer topographic rises associated with trenches. *Geophysical Journal International*, 1(4):707–712, 1978.

Parsons, B. and Richter, F. M. A relation between the driving force and geoid anomaly associated with mid-ocean ridges. *Earth and Planetary Science Letters*, 51(2):445–450, 1980.

Parsons, B. and Sclater, J. G. An analysis of the variation of ocean floor bathymetry and heat flow with age. *Journal of geophysical research*, 82(5):803–827, 1977.

Pavlis, N. K., Holmes, S. A., Kenyon, S. C., and Factor, J. K. The development and evaluation of the Earth Gravitational Model 2008 (EGM2008). *Journal of geophysical research: solid earth*, 117(B4), 2012.

Peacock, S. M. Are the lower planes of double seismic zones caused by serpentine dehydration in subducting oceanic mantle? *Geology*, 29(4):299–302, 2001.

Peitgen, H.-O., Saupe, D., Barnsley, M. F., Fisher, Y., and McGuire, M. *The science of fractal images*. Springer New York etc., 1988.

Peltier, W. R. New constraints on transient lower mantle rheology and internal mantle buoyancy from glacial rebound data. *Nature*, 318:614–617, 1985.

Pérez-Gussinyé, M., Swain, C. J., Kirby, J. F., and Lowry, A. R. Spatial variations of the effective elastic thickness, Te, using multitaper spectral estimation and wavelet methods: examples from synthetic data and application to South America. *Geochemistry, Geophysics, Geosystems*, 10(4), 2009.

Petch, N. J. The cleavage strength of polycrystals. *J. Iron Steel Inst.*, 174:25–28, 1953.

Quinlan, G. M. and Beaumont, C. Appalachian thrusting, lithospheric flexure, and the Paleozoic stratigraphy of the eastern interior of North America. *Canadian Journal of Earth Sciences*, 21(9):973–996, 1984.

Raleigh, C. B. and Paterson, M. S. Experimental deformation of serpentinite and its tectonic implications. *Journal of Geophysical Research*, 70(16):3965–3985, 1965.

Ranalli, G. *Rheology of the Earth*. Springer Science & Business Media, 1995.

Ranero, C. R. and Sallares, V. Geophysical evidence for hydration of the crust and mantle of the Nazca plate during bending at the north Chile trench. *Geology*, 32(7):549–552, 2004.

Ranero, C. R., Morgan, J. P., McIntosh, K., and Reichert, C. Bending-related faulting and mantle serpentinization at the Middle America trench. *Nature*, 425(6956):367–373, 2003.

Ranero, C. R., Villaseñor, A., Phipps Morgan, J., and Weinrebe, W. Relationship between bend-faulting at trenches and intermediate-depth seismicity. *Geochemistry, Geophysics, Geosystems*, 6(12), 2005.

Raterron, P., Wu, Y., Weidner, D. J., and Chen, J. Low-temperature olivine rheology at high pressure. *Physics of the Earth and Planetary Interiors*, 145(1):149–159, 2004.

Ray, J. S., Mahoney, J. J., Duncan, R. A., Ray, J., Wessel, P., and Naar, D. F. Chronology and geochemistry of lavas from the Nazca Ridge and Easter Seamount Chain: an˜ 30 Myr hotspot record. *Journal of Petrology*, page egs021, 2012.

Rea, D. K. and Dixon, J. M. Late Cretaceous and Paleogene tectonic evolution of the north Pacific Ocean. *Earth and Planetary Science Letters*, 65(1):145–166, 1983.

Richards, M. A., Yang, W.-S., Baumgardner, J. R., and Bunge, H.-P. Role of a low-viscosity zone in stabilizing plate tectonics: Implications for comparative terrestrial planetology. *Geochemistry, Geophysics, Geosystems*, 2(8), 2001.

Richardson, R. M. Ridge forces, absolute plate motions, and the intraplate stress field. *Journal of Geophysical Research: Solid Earth (1978–2012)*, 97(B8):11739–11748, 1992.

Richter, F. M. and McKenzie, D. Simple plate models of mantle convection. *J. Geophys*, 44: 441–471, 1978.

Rychert, C. A. and Shearer, P. M. Imaging the lithosphere-asthenosphere boundary beneath the Pacific using SS waveform modeling. *Journal of Geophysical Research: Solid Earth (1978–2012)*, 116(B7), 2011.

Sandwell, D. and Schubert, G. Geoid height versus age for symmetric spreading ridges. *Journal of Geophysical Research: Solid Earth (1978–2012)*, 85(B12):7235–7241, 1980.

Sandwell, D. T. and Smith, W. H. F. Marine gravity anomaly from Geosat and ERS 1 satellite altimetry. *Journal of Geophysical Research: Solid Earth (1978–2012)*, 102(B5): 10039–10054, 1997.

Sandwell, D. T., Müller, R. D., Smith, W. H. F., Garcia, E., and Francis, R. New global marine gravity model from CryoSat-2 and Jason-1 reveals buried tectonic structure. *science*, 346 (6205):65–67, 2014.

Schellart, W. P. Quantifying the net slab pull force as a driving mechanism for plate tectonics. *Geophysical Research Letters*, 31(7), 2004.

Scholz, C. H. Microfracturing and the inelastic deformation of rock in compression. *Journal of Geophysical Research*, 73(4):1417–1432, 1968.

Scholz, C. H. The brittle-plastic transition and the depth of seismic faulting. *Geologische Rundschau*, 77(1):319–328, 1988.

Scholz, C. H. *The mechanics of earthquakes and faulting*. Cambridge university press, 2002.

Schroeder, W. The empirical age-depth relation and depth anomalies in the Pacific Ocean Basin. *Journal of Geophysical Research: Solid Earth (1978–2012)*, 89(B12):9873–9883, 1984.

Searle, R. GLORIA survey of the East Pacific Rise near 3.5 S: Tectonic and volcanic characteristics of a fast spreading mid-ocean rise. *Tectonophysics*, 101(3):319–344, 1984.

Seta, H., Nagaoka, S., and Kato, S. Landforms of the Izu-Ogasawara Trench by the narrow multi beam echo sounder. *Rep Hydrogr Res*, 31:173–180, 1991.

Shimamoto, T. Transition between frictional slip and ductile flow for halite shear zones at room temperature. *Science*, 231(4739):711–714, 1986.

Sleep, N. H. and Snell, N. S. Thermal contraction and flexure of mid-continent and Atlantic marginal basins. *Geophysical Journal International*, 45(1):125–154, 1976.

Smith, W. H. F., Staudigel, H., Watts, A. B., and Pringle, M. S. The Magellan Seamounts: Early Cretaceous record of the South Pacific isotopic and thermal anomaly. *Journal of Geophysical Research: Solid Earth (1978–2012)*, 94(B8):10501–10523, 1989.

Smoot, N. C. The Marcus-Wake seamounts and guyots as paleofracture indicators and their relation to the Dutton Ridge. *Marine geology*, 88(1):117–131, 1989.

Stein, C. A. and Abbott, D. H. Heat flow constraints on the South Pacific superswell. *Journal of Geophysical Research: Solid Earth (1978–2012)*, 96(B10):16083–16099, 1991.

Stesky, R. M. Mechanisms of high temperature frictional sliding in Westerly granite. *Canadian Journal of Earth Sciences*, 15(3):361–375, 1978.

Stewart, J. and Watts, A. B. Gravity anomalies and spatial variations of flexural rigidity at mountain ranges. *JOURNAL OF GEOPHYSICAL RESEARCH-ALL SERIES-*, 102: 5327–5352, 1997.

Swain, C. J. and Kirby, J. F. An effective elastic thickness map of Australia from wavelet transforms of gravity and topography using Forsyth's method. *Geophysical research letters*, 33(2), 2006.

Tackley, P. J. Self-consistent generation of tectonic plates in time-dependent, three-dimensional mantle convection simulations. *Geochemistry, Geophysics, Geosystems*, 1(8), 2000.

Talwani, M., Worzel, J. L., and Landisman, M. Rapid gravity computations for two-dimensional bodies with application to the Mendocino submarine fracture zone. *Journal of Geophysical Research*, 64(1):49–59, 1959.

Tilmann, F. J., Grevemeyer, I., Flueh, E. R., Dahm, T., and Goßler, J. Seismicity in the outer rise offshore southern Chile: indication of fluid effects in crust and mantle. *Earth and Planetary Science Letters*, 269(1):41–55, 2008.

Timoshenko, S., Woinowsky-Krieger, S., and Woinowsky-Krieger, S. *Theory of plates and shells*, volume 2. McGraw-hill New York, 1959.

Tsenn, M. C. and Carter, N. L. Upper limits of power law creep of rocks. *Tectonophysics*, 136(1):1–26, 1987.

Tsuji, T., Nakamura, Y., Tokuyama, H., Coffin, M. F., and Koda, K. Oceanic crust and Moho of the Pacific Plate in the eastern Ogasawara Plateau region. *Island Arc*, 16(3):361–373, 2007.

Tukey, J. W. An introduction to the calculations of numerical spectrum analysis. *Spectral analysis of time series*, 25, 1967.

Turcotte, D. L. and Schubert, G. Geodynamics: Applications of continuum physics to geological problems, 450 pp, 1982.

Turcotte, D. L., McAdoo, D. C., and Caldwell, J. G. An elastic-perfectly plastic analysis of the bending of the lithosphere at a trench. *Tectonophysics*, 47(3):193–205, 1978.

Von Herzen, R. P., Detrick, R. S., Crough, S. T., Epp, D., and Fehn, U. Thermal origin of the Hawaiian swell: heat flow evidence and thermal models. *Journal of Geophysical Research: Solid Earth (1978–2012)*, 87(B8):6711–6723, 1982.

Von Herzen, R. P., Cordery, M. J., Detrick, R. S., and Fang, C. Heat flow and the thermal origin of hot spot swells: the Hawaiian swell revisited. *Journal of Geophysical Research: Solid Earth (1978–2012)*, 94(B10):13783–13799, 1989.

Walcott, R. I. Flexural rigidity, thickness, and viscosity of the lithosphere. *Journal of Geophysical Research*, 75(20):3941–3954, 1970.

Walther, C. H. E. The crustal structure of the Cocos ridge off Costa Rica. *Journal of Geophysical Research: Solid Earth (1978–2012)*, 108(B3), 2003.

Wang, K. Unbending combined with dehydration embrittlement as a cause for double and triple seismic zones. *Geophysical research letters*, 29(18):31–36, 2002.

Warren, J. M. and Hauri, E. H. Pyroxenes as tracers of mantle water variations. *Journal of Geophysical Research: Solid Earth*, 119(3):1851–1881, 2014.

Warren, J. M. and Hirth, G. Grain size sensitive deformation mechanisms in naturally deformed peridotites. *Earth and Planetary Science Letters*, 248(1):438–450, 2006.

Watts, A. B. An analysis of isostasy in the world's oceans 1. Hawaiian-Emperor Seamount Chain. *Journal of Geophysical Research: Solid Earth (1978–2012)*, 83(B12):5989–6004, 1978.

Watts, A. B. The effective elastic thickness of the lithosphere and the evolution of foreland basins. *Basin Research*, 4(3-4):169–178, 1992.

Watts, A. B. *Isostasy and Flexure of the Lithosphere*. Cambridge University Press, 2001.

Watts, A. B. and Burov, E. B. Lithospheric strength and its relationship to the elastic and seismogenic layer thickness. *Earth and Planetary Science Letters*, 213(1):113–131, 2003.

Watts, A. B. and Cochran, J. R. Gravity anomalies and flexure of the lithosphere along the Hawaiian-Emperor seamount chain. *Geophysical Journal International*, 38(1):119–141, 1974.

Watts, A. B. and Talwani, M. Gravity anomalies seaward of deep-sea trenches and their tectonic implications. *Geophysical Journal International*, 36(1):57–90, 1974.

Watts, A. B. and Ten Brink, U. S. Crustal structure, flexure, and subsidence history of the Hawaiian Islands. *Journal of Geophysical Research: Solid Earth (1978–2012)*, 94(B8): 10473–10500, 1989.

Watts, A. B. and Thorne, J. Tectonics, global changes in sea level and their relationship to stratigraphical sequences at the US Atlantic continental margin. *Marine and Petroleum Geology*, 1(4):319–339, 1984.

Watts, A. B. and Zhong, S. Observations of flexure and the rheology of oceanic lithosphere. *Geophysical Journal International*, 142(3):855–875, 2000. ISSN 0956540X.

Watts, A. B., Cochran, J. R., and Selzer, G. Gravity anomalies and flexure of the lithosphere: a three-dimensional study of the Great Meteor Seamount, northeast Atlantic. *J. geophys. Res*, 80:1391–1398, 1975.

Watts, A. B., Bodine, J. H., and Steckler, M. S. Observations of flexure and the state of stress in the oceanic lithosphere. *Journal of Geophysical Research: Solid Earth (1978–2012)*, 85 (B11):6369–6376, 1980.

Watts, A. B., Karner, G. D., and Steckler, M. S. Lithospheric flexure and the evolution of sedimentary basins. *Philosophical Transactions of the Royal Society of London A: Mathematical, Physical and Engineering Sciences*, 305(1489):249–281, 1982.

Watts, A. B., Weissel, J. K., Duncan, R. A., and Larson, R. L. Origin of the Louisville Ridge and its relationship to the Eltanin fracture zone system. *Journal of Geophysical Research: Solid Earth (1978–2012)*, 93(B4):3051–3077, 1988.

Watts, A. B., Zhong, S. J., and Hunter, J. The behavior of the lithosphere on seismic to geologic timescales. *Annual Review of Earth and Planetary Sciences*, 41:443–468, 2013.

Weertman, J., White, S., and Cook, A. H. Creep Laws for the Mantle of the Earth [and Discussion]. *Philosophical Transactions of the Royal Society of London A: Mathematical, Physical and Engineering Sciences*, 288(1350):9–26, 1978.

Wessel, P. Thermal stresses and the bimodal distribution of elastic thickness estimates of the oceanic lithosphere. *Journal of Geophysical Research: Solid Earth (1978–2012)*, 97(B10): 14177–14193, 1992.

Wessel, P. A reexamination of the flexural deformation beneath the Hawaiian Islands. *Journal of Geophysical Research*, 98(12):112–177, 1993.

Wessel, P., Smith, W. H. F., Scharroo, R., Luis, J., and Wobbe, F. Generic mapping tools: improved version released. *Eos, Transactions American Geophysical Union*, 94(45):409–410, 2013.

Wicks, F. J. *X-ray and optical studies on serpentine minerals*. PhD thesis, University of Oxford, 1969.

Wiens, D. A. and Stein, S. Age dependence of oceanic intraplate seismicity and implications for lithospheric evolution. *Journal of Geophysical Research: Solid Earth (1978–2012)*, 88 (B8):6455–6468, 1983.

Wiens, D. A. and Stein, S. Intraplate seismicity and stresses in young oceanic lithosphere. *Journal of Geophysical Research: Solid Earth (1978–2012)*, 89(B13):11442–11464, 1984.

Wolfe, C. J. and McNutt, M. K. Compensation of Cretaceous seamounts of the Darwin Rise, northwest Pacific ocean. *Journal of Geophysical Research: Solid Earth (1978–2012)*, 96 (B2):2363–2374, 1991.

Wolfe, C. J., Solomon, S. C., Laske, G., Collins, J. A., Detrick, R. S., Orcutt, J. A., Bercovici, D., and Hauri, E. H. Mantle shear-wave velocity structure beneath the Hawaiian hot spot. *science*, 326(5958):1388–1390, 2009.

Wortel, M. J. R. and Cloetingh, S. Accretion and lateral variations in tectonic structure along the Peru-Chile Trench. *Tectonophysics*, 112(1):443–462, 1985.

Yamano, M. and Uyeda, S. Heat-flow studies in the Peru Trench subduction zone. In *Proc. Ocean Drill. Program, Sci. Results*, volume 112, pages 653–661, 1990.

Yáñez, G. A., Ranero, C. R., Huene, R., and Díaz, J. Magnetic anomaly interpretation across the southern central Andes (32–34 S): The role of the Juan Fern{á}ndez Ridge in the late Tertiary evolution of the margin. *Journal of Geophysical Research: Solid Earth (1978–2012)*, 106(B4):6325–6345, 2001.

Yoshii, T. A detailed cross-section of the deep seismic zone beneath northeastern Honshu, Japan. *Tectonophysics*, 55(3):349–360, 1979.

Zhang, F., Lin, J., and Zhan, W. Variations in oceanic plate bending along the Mariana trench. *Earth and Planetary Science Letters*, 401(0):206–214, 2014. ISSN 0012-821X. doi: http://dx.doi.org/10.1016/j.epsl.2014.05.032. URL `http://www.sciencedirect.com/science/article/pii/S0012821X14003343`.

Zhao, D. Seismic images under 60 hotspots: search for mantle plumes. *Gondwana Research*, 12(4):335–355, 2007.

Zhong, S. and Gurnis, M. Controls on trench topography from dynamic models of subducted slabs. *Journal of Geophysical Research: Solid Earth (1978–2012)*, 99(B8):15683–15695, 1994.

Zhong, S. and Watts, A. B. Lithospheric deformation induced by loading of the Hawaiian Islands and its implications for mantle rheology. *Journal of Geophysical Research: Solid Earth*, 118(11):6025–6048, 2013.

Zhou, Z., Lin, J., Behn, M. D., and Olive, J.-A. Mechanism for normal faulting in the subducting plate at the Mariana trench. *Geophysical Research Letters*, 2015.

Zimmerman, M. E. and Kohlstedt, D. L. Rheological properties of partially molten lherzolite. *Journal of Petrology*, 45(2):275–298, 2004.